Preface

This volume on organic light-emitting devices (OLEDs) has been written to serve the needs of the beginning researcher in this area as well as to be a reference for researchers already active in it.

From their very beginning, OLEDs, which include both small-molecular- and ploymer-based devices, were recognized as a promising display technology. As the dramatic improvements in the devices unfolded over the past two decades, the investment of research and development resources in this field grew exponentially. The fascination with these devices is due to several potential advantages: (1) Relative ease and low cost of fabrication, (2) their basic properties as active light-emitters (in contrast to liquid-crystal displays, which are basically polarizing filters requiring a backlight), (3) flexibility, (4) transparency, and (5) scalability. Once the performance of red-to-green OLEDs approached and then exceeded that of incandescent bulbs and fluorescent lights, it became clear that they are serious candidates for general solid-state lighting technology, competing directly with inorganic LEDs. Hence, while inorganic LEDs are the dominant solid-state lighting devices at present, OLEDs are expected to gradually replace the inorganic devices in more and more niche areas. Finally, OLEDs are attracting considerable attention as building blocks for some types of molecular electronic devices, and, most recently, for spintronic devices. In short, although their introduction into commercial products began only a few years ago, the breadth of their impact is widening rapidly.

The first reports of electroluminescence (EL) from an organic material can be traced back to 1907, and the first actual OLED, based on anthracene, was fabricated in 1963. However, it was not a thin-film device, and the operating voltage was extremely high. After years of efforts to improve its performance, interest in the subject waned. The breakthroughs that led to the exponential growth of this field and to its first commercialized products can be traced to two poineering papers. The 1987 paper by Tang and Van Slyke demonstrated that the performance of green-emitting thin film OLEDs based on the small organic molecule tris(8-hydroxy quinoline) Al (Alq_3) is sufficiently promising to warrant extensive research on a wide variety of thin film OLEDs. The 1990 paper by Bradley, Friend, and coworkers described the first ploymer OLED (PLED), which was based on poly(*p*-phenylene vinylene) (PPV), and demonstrated that such devices warrant close scrutiny as well. Since then, the competition between small-molecular OLEDs and PLEDs continues in parallel with the overall dramatic developments of this field. This volume has tried to mirror this competition by devoting comparable attention to these two subfields.

The first chapter provides an introduction to the basic physics of OLEDs and surveys the various topics and challenges in this field. It includes a description of the basic optical and transport processes, the materials used in some of the OLEDs that have studied extensively to date, the performance of various blue-to-red OLEDs, and a brief outlook.

Chapters 2 through 4 are devoted to small-molecular OLEDs. Chapter 2 focuses on design concepts for molecular materials yielding high performance small molecular OLEDs, including the recent developments in electrophosphorescent devices. Chapter 3 focuses on the degradation processes affecting Alq_3, which is arguably the small molecular device material that has been studied in more detail than any other. Chapter 4 is devoted to organic microcavity light emitting diodes, providing a review of the geometrical effects of the OLED geometry on its performance.

Chapters 5 through 9 are devoted to various PLEDs. Chapter 5 provides an extensive review of devices based poly(*p*-phenylene vinylene), which has been studied more than any other light-emitting polymer. Chapter 6 is devoted to the dominant effects of polymer morphology on device performance. Chapter 7 is devoted to studies of the transient EL in PPV-based PLEDs, which exhibit EL spikes and have provided considerable insight into details of carrier dynamics in these devices. Chapter 8 reviews the extensive work on EL of polyparaphenylenes (PPPs), which in 1993 were the first reported blue-light emitting polymers. Although other blue-light emitting polymers have been developed since then, notably polyfluorenes and phenyl-substituted polyacetylenes, PPPs were studied extensively and provided extensive insight into light-emitting polymers in general and blue emitters in particular. Chapter 9 reviews direct and alternating current light-emitting devices based on pyridine-containing conjugated polymers. In particular, it describes the symmetrically-configured AC light-emitters (SCALE) devices and discusses their potential. Finally, Chapter 10 focuses on polyflurorene-based PLEDs which developed during the past six years and are perhaps the most promising blue devices, and consequently provide a basis for full-color PLED-based displays.

In spite of the fast pace of developments on OLEDs, it is hoped that the topics provided in this volume will be valuable as tutorials for the beginning resercher and as a desktop reference for the advanced researcher for some time to come.

Joseph Shinar
Ames, IA, February, 2003

Contents

Preface v

Contributors xv

1 Introduction to Organic Light-Emitting Devices
Joseph Shinar and Vadim Savvateev 1
- 1.1 Introduction 1
- 1.2 Basic Electronic Structure and Dynamics of π-Conjugated Materials 5
- 1.3 Basic Structure of OLEDs 9
- 1.4 OLED Fabrication Procedures 10
  - 1.4.1 Thermal Vacuum Evaporation 10
  - 1.4.2 Wet-Coating Techniques 11
- 1.5 Materials for OLEDs & PLEDs 12
  - 1.5.1 Anode Materials and HTLs or Buffers 12
  - 1.5.2 Small Electron-Transporting and Emitting Molecules. . 17
  - 1.5.3 Small Molecular Guest Dye Emitters 18
  - 1.5.4 White OLEDs 18
  - 1.5.5 Phosphorescent Small Molecules & Electrophosphorescent OLEDs 19
  - 1.5.6 Fluorescent Polymers 19
  - 1.5.7 Cathode & Organic/Cathode Buffer Materials 21
- 1.6 Basic Operation of OLEDs 22
- 1.7 Carrier Transport in OLEDs 23
  - 1.7.1 Polaron vs Disorder Models for Carrier Hopping 24

1.7.2 Long-Range Correlations 25
1.7.3 Carrier Injection 26
1.7.4 Space-Charge Limited Versus Injection-Limited Current Mechanisms 28
1.8 The Efficiency of OLEDs 29
1.9 Degradation Mechanisms 31
1.10 Outlook for OLEDs 33
References 34

2 Molecular LED: Design Concept of Molecular Materials for High-Performance OLED
Chihaya Adachi and Tetsuo Tsutsui 43
2.1 Introduction 43
2.2 OLED Development from the 1960s to the 1980s 43
2.3 Working Mechanisms of OLED 45
2.3.1 Charge Carrier Injection and Transport 46
2.3.2 Carrier Recombination and Emission Process 50
2.3.3 Estimation of External and Internal Quantum Efficiency 50
2.4 Design of Multilayer Structures 53
2.5 Molecular Materials for OLED 55
2.5.1 Hole-Transport Material 55
2.5.2 Electron-Transport Material 58
2.5.3 Emitter Material 60
2.5.4 Dopant Material 60
2.5.5 Molecular Tuning for High EL Efficiency 62
2.5.6 Molecular Tuning for a High EL Durable OLED 63
2.6 Future Possibilities of OLED 64
2.7 Conclusion 65
References 65

3 Chemical Degradation and Physical Aging of Aluminum(III) 8-Hydroxyquinoline: Implications for Organic Light-Emitting Diodes and Materials Design
Keith A. Higginson, D. Laurence Thomsen III, Baocheng Yang, and Fotios Papadimitrakopoulos 71
3.1 Introduction 71
3.2 Chemical Stability of OLED Materials 72
3.2.1 Thermal Hydrolysis of Alq_3 72
3.2.2 Electrochemical Degradation of Alq_3 and Hq 78
3.3 Morphological Stability of Organic Glasses in LEDs 85
3.3.1 Crystallization of Alq_3 86
3.3.2 Guidelines for Amorphous Materials Selection 89
3.3.3 Crystallization and Aging of $AlMq_3$ and $Alq_3/AlMq_3$ blends 91

3.4 The Effect of Aging Processes on OLED Performance 95
References 98

4 Organic Microcavity Light-Emitting Diodes
Ananth Dodabalapur 103
4.1 Introduction 103
4.2 Types of Microcavities 104
4.3 Planar Microcavity LEDs 106
4.4 Single Mode and Multimode Planar Microcavity LEDs 110
4.5 Intensity and Angular Dependence in Planar Microcavities . . 114
4.6 Materials for Organic Microcavity LED Displays 121
4.7 Summary 123
References 124

5 Light-Emitting Diodes Based on Poly(p-phenylenevinylene) and Its Derivatives
Neil C. Greenham and Richard H. Friend 127
5.1 Introduction 127
5.2 The Electronic Structure of PPV 128
5.3 Synthesis of PPV and Derivatives 132
5.4 Single-Layer LEDs 134
5.5 Multiple-Layer Polymer LEDs 138
5.6 Transport and Recombination in Polymer LEDs 141
5.7 Optical Properties of Polymer LEDs 143
5.8 Novel LED Structures 146
5.9 Prospects for Applications of PPV-Based LEDs 149
5.10 Conclusions 150
References 150

6 Polymer Morphology and Device Performance in Polymer Electronics
Yijian Shi, Jie Liu, and Yang Yang 155
6.1 Introduction 155
6.2 The Control of Polymer Morphology 157
  6.2.1 The Polymer–Polymer Interactions in Solutions 157
  6.2.2 The Morphology Control of Polymer Thin Films via the Spin-Coating Process 161
6.3 The Control of Device Performance via Morphology Control. . 166
  6.3.1 Conductivity of the Polymer Film 166
  6.3.2 Charge-Injection Energy Barriers 167
  6.3.3 The Turn-on Voltages 172
  6.3.4 The Emission Spectrum of the Device 176
  6.3.5 The Device Quantum Efficiency 180
6.4 Conclusions 182
  6.4.1 The Solvation Effect and Polymer Aggregation 182

6.4.2 The Device Emission Color and the Quantum Efficiency . . . 182
6.4.3 The Conductivity of the Film . . . 182
6.4.4 The Turn-on Voltage of the PLED Device . . . 183
References . . . 183

7 On the Origin of Double Light Spikes from Polymer Light-Emitting Devices
Aharon Yakimov, Vadim Savvateev, and Dan Davidov . . . 187
7.1 Introduction . . . 187
7.2 Experimental . . . 188
7.3 Results and Analysis . . . 190
7.4 Discussion . . . 199
7.5 Conclusions . . . 202
References . . . 203

8 Electroluminescence with Poly(para-phenylenes)
Stefan Tasch, Wilhelm Graupner, and Günther Leising . . . 205
8.1 Introduction . . . 205
8.2 Physical Properties of Oligophenyls and Polyphenyls . . . 206
8.2.1 Processing and Stability . . . 206
8.2.2 Geometric Arrangement of *Para*-phenylenes . . . 208
8.2.3 Absorption Properties . . . 209
8.2.4 Emission Properties . . . 214
8.2.5 Excited States . . . 214
8.2.6 Charge Transport . . . 217
8.3 Electroluminescence . . . 220
8.3.1 Single-Layer LED Based on PPP-Type Polymers . . . 220
8.3.2 Emission Colors . . . 224
8.3.3 LEDs Based on Multilayer Structures . . . 225
8.3.4 LEDs Based on Polymer Blends . . . 229
8.3.5 Light-Emitting Electrochemical Cells Based on PPPs. . . 233
8.4 Conclusions . . . 238
References . . . 238

9 Direct and Alternating Current Light-Emitting Devices Based on Pyridine-Containing Conjugated Polymers
Y. Z. Wang, D. D. Gebler, and A. J. Epstein . . . 245
9.1 Introduction . . . 245
9.2 Experiments . . . 247
9.3 Results and Discussion . . . 249
9.4 Summary and Conclusion . . . 261
References . . . 262

10 Polyfluorene Electroluminescence

Paul A. Lane 265
10.1 Introduction 265
10.2 Synthesis and Characterization of Polyfluorene 266
  10.2.1 Polyfluorene Synthesis 266
  10.2.2 Optical and Physical Characterization 268
  10.2.3 Electronic Characterization 270
10.3 Electroluminescence 275
  10.3.1 Polyfluorene Electroluminescence 275
  10.3.2 Fluorene-Based Copolymers 282
  10.3.3 Doped Polyfluorene Light-Emitting Diodes 288
10.4 Concluding Remarks 298
References 299

Index **303**

Contributors

Editor:

Joseph Shinar, Ames Laboratory – USDOE & Department of Physics and Astronomy, Iowa State University, Ames, IA

Chapter 1:

Joseph Shinar, Ames Laboratory – USDOE & Department of Physics and Astronomy, Iowa State University, Ames, IA

Vadim Savvateev, 3M Corporate Research Center, St. Paul, MN

Chapter 2:

Chihaya Adachi, Department of Photonics Materials Science, Chitose Institute of Science & Technology (CIST), Chitose, Japan

Tetsuo Tsutsui, Department of Materials Science and Technology, Graduate School of Engineering Sciences, Kyushu University, Kasuga, Fukuoka, Japan

Chapter 3:

Fotis Papadimitrakopoulos, Department of Chemistry and Institute of Materials Science, University of Connecticut, Storrs, CT

Baocheng Yang, Department of Chemistry and Institute of Materials Science, University of Connecticut, Storrs, CT

Keith Higginson, Triton Systems Inc., Chelmsford, MA

D. Laurence Thomsen III, NASA Landley Research Center, Hampton, VA

Chapter 4:

Ananth Dodabalapur, Department of Electrical and Computer Engineering, Microelectronics Research Center, The University of Texas at Austin, Austin, TX

Chapter 5:

Neil C. Greenham, Cavendish Laboratory, Cambridge University, Cambridge, UK
Richard H. Friend, Cavendish Laboratory, Cambridge University, Cambridge, UK

Chapter 6:

Yang Yang, Department of Material Science and Engineering, University of California, Los Angeles, CA
Yijian Shi, Department of Materials Science and Engineering, University of California, Los Angeles, CA
Jie Liu, General Electric Global Research, Niskayuna, NY

Chapter 7:

Aharon Yakimov, GE Global Research Center, Niskayuna, NY 12309
Vadim Savvateev, 3M Corporate Research Center, St. Paul, MN
Dan Davidov, Racah Institute of Physics, The Hebrew University, Jerusalem, Israel

Chapter 8:

Stefan Tasch, Institut für Festkorpephysik, Technische Universitt Graz, Austria
Wilhelm Graupner, Austriamicrosystems AG, Schloss Premstaetten, Austria
Guenther Leising, Institut für Festkorpephysik, Technische Universität Graz, Austria

Chapter 9:

Arthur J. Epstein, Department of Physics, Department of Chemistry, and Center for Materials Research, The Ohio State University, Columbus, OH
D. Gebler, The Ohio State University, Columbus, OH
Y. Z. Wang, The Ohio State University, Columbus, OH

Chapter 10:

Paul A. Lane, Draper Laboratory, Cambridge, MA

1

Introduction to Organic Light-Emitting Devices

Joseph Shinar and Vadim Savvateev

1.1 Introduction

Using organic materials for light-emitting devices (LEDs) is fascinating due to their vast variety and the relative ease of controlling their composition to tune their properties by chemical means. The first organic electroluminescence (EL) cells were fabricated and studied in an ac mode in 1953 by Bernanose *et al.*,[1] and in a dc mode in 1963 by Pope and coworkers.[2] Soon after ac EL was also achieved using an emissive polymer.[3] The observation of bright EL with an external quantum efficiency η_{ext}, defined as the number of photons emitted from the face of the device per injected electron or hole, of 4–6% in anthracene crystals with powdered graphite electrodes marked another milestone.[4] However, single-crystal anthracene-based organic LEDs (OLEDs) were thick and hence required very high operating voltages. The fabrication of bright green multilayer thin film devices based on tris-(8-hydroxy quinoline) Al (Alq_3), which yielded $\eta_{ext} \sim 1\%$,[5] spawned a period of intense research and development, on both small molecular OLEDs and polymer LEDs (PLEDs), which continues to grow at a fast rate.[6,7,8] Figure 1.1 shows the molecular structures of some small molecules widely used in OLEDs; Figure 1.2 shows the structures of some π-conjugated and other polymers. Figure 1.3 shows several photoluminescence (PL) spectra of films and EL spectra of OLEDs based on these molecules.[9–12]

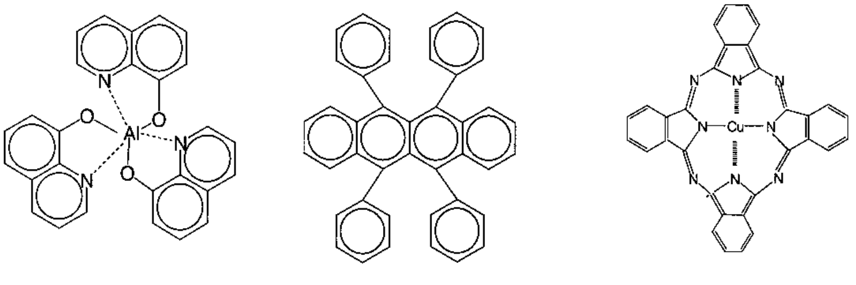

(a) Alq3 (b) Rubrene (c) CuPc

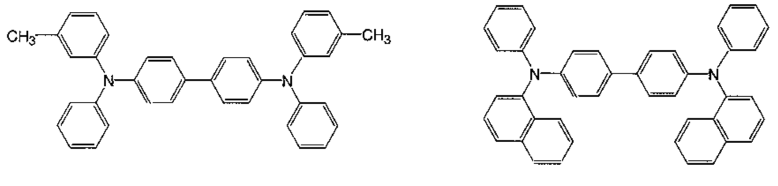

(d) TPD (e) (α-)NPB, (α-)NPD

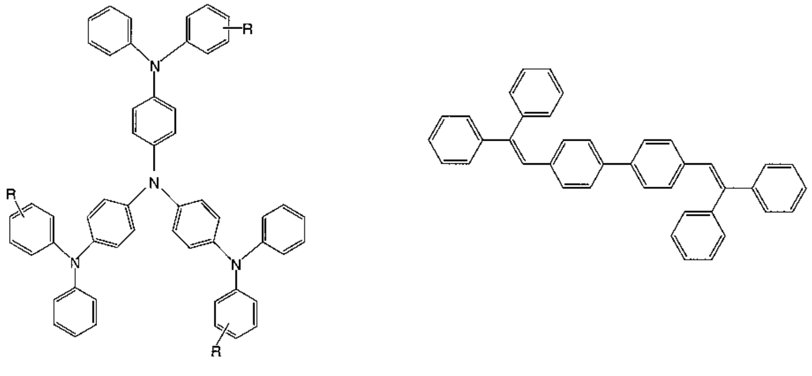

(f) TDATA (g) DPVBi

FIGURE 1.1. Molecular structure of widely used π-conjugated small molecules: (a) tris-(8-hydroxy quinoline Al) (Alq_3); (b) rubrene (5,6,11,12-tetraphenyl tetracene or 5,6,11,12-tetraphenyl naphthacene); (c) copper phthalocyanine, (CuPc); (d) N, N'-diphenyl-N, N'-bis(3-methylphenyl)-1,1′-biphenyl-4, 4′-diamine (TPD); (e) N, N'-diphenyl-N, N'-bis(1-naphthylphenyl)-1, 1′-biphenyl-4, 4′-diamine (NPB, α-NPB, NPD, or α-NPD); (f) 4, 4′, 4″-tris(diphenyl amino)triphenylamines (TDATAs); (g) 4, 4′-bis(2, 2′-diphenylvinyl)-1, 1′-biphenyl (DPVBi).

The work on Alq_3 and other small π-conjugated molecules that followed shortly thereafter[13,14] demonstrated that multilayer OLEDs could be fabricated simply by thermal evaporation of these molecules. In 1990 Friend and coworkers described the first PLED,[15] in which the luminescent poly(p-phenylene vinylene) (PPV)

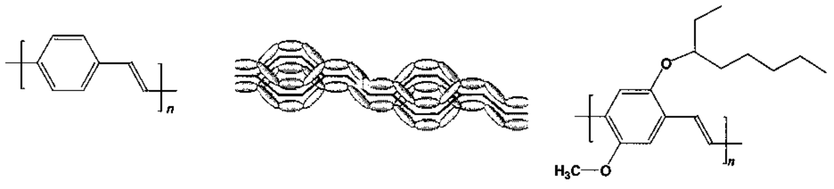

(a) PPV **(b) PPV** **(c) MEH-PPV**

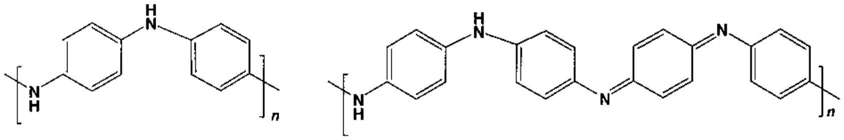

(d.1) LEB **(d.2) EB**

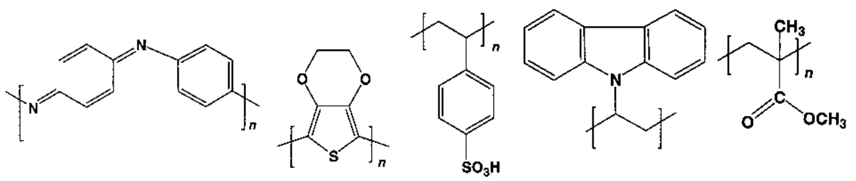

(d.3) PNB **(e) PEDOT-PSS** **(f) PVK** **(g) PMMA**

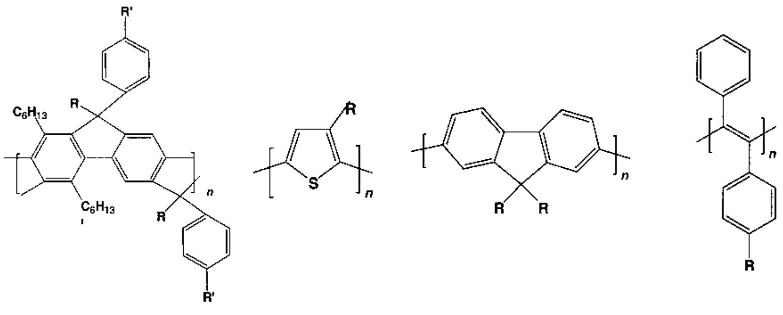

(h) m-LPPP **(i) P3AT** **(j) PFO** **(k) PDPA**

FIGURE 1.2. Molecular structure of widely used π-conjugated and other polymers: (a) poly(*para*-phenylene vinylene) (PPV); (b) σ (solid line along backbone) and π ("clouds" above and below the σ line) electron probability densities in PPV; (c) poly(2-methoxy-5-(2'-ethyl)-hexoxy-1,4-phenylene vinylene) (MEH-PPV); (d) polyaniline (PANI): (d.1) leucoemeraldine base (LEB), (d.2) emeraldine base (EB), (d.3) pernigraniline base (PNB); (e) poly(3,4-ethylene dioxy-2,4-thiophene)-polystyrene sulfonate (PEDOT-PSS); (f) poly(N-vinyl carbazole) (PVK); (g) poly(methyl methacrylate) (PMMA); (h) methyl-bridged ladder-type poly(p-phenylene) (m-LPPP); (i) poly(3-alkyl thiophenes) (P3ATs); (j) polyfluorenes (PFOs); (k) diphenyl-substituted *trans*-polyacetylenes (t-$(CH)_x$) or poly(diphenyl acetylene) (PDPA).

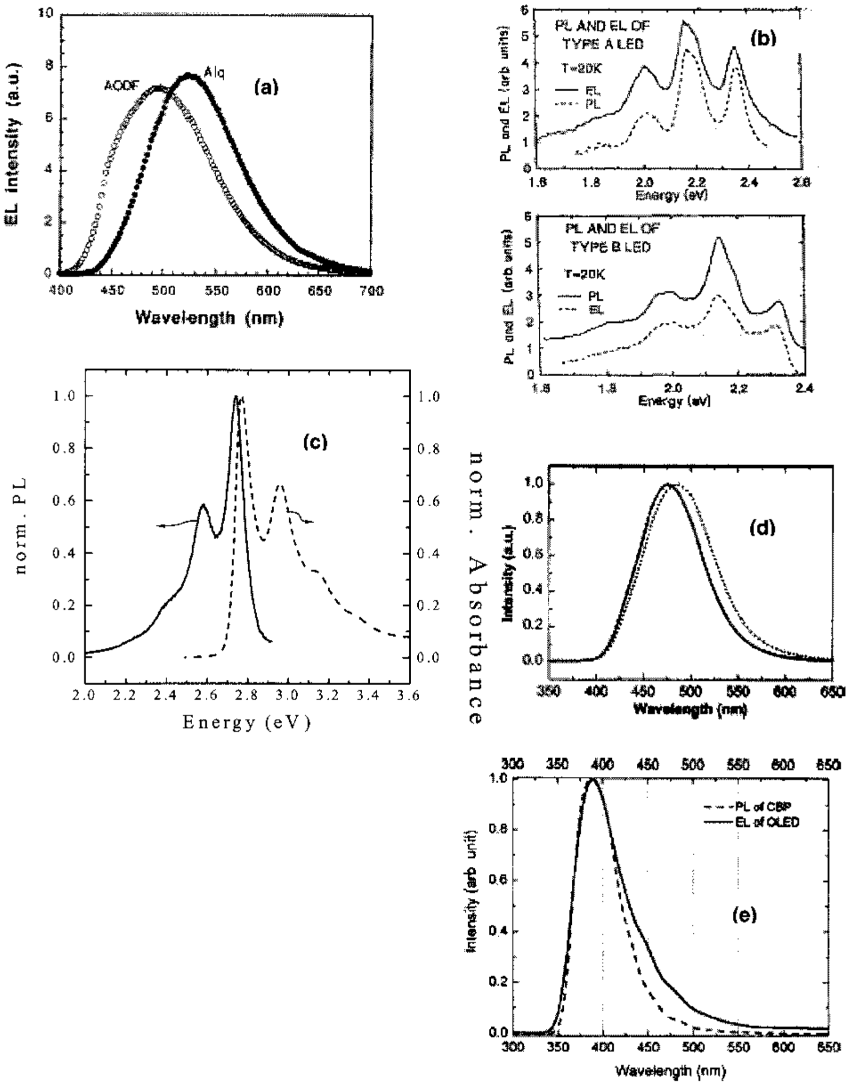

FIGURE 1.3. The photoluminescence (PL) and electroluminescence (EL) spectra of some representative π-conjugated films and OLEDs, respectively: (a) EL of blue aminooxadiazole fluorene (AODF) and green Alq$_3$ OLEDs,[9] (b) PL and EL of PPV films and PLEDs, respectively,[10] (c) PL of m-LPPP films, (d) EL of DPVBi (solid line) and DPVBi/Alq$_3$ (dashed line) OLEDs,[11] and (e) PL of CBP films and EL of CBP OLEDs.[12]

was fabricated by spin-coating a precursor polymer onto the transparent conducting indium-tin-oxide (ITO) anode substrate, thermally converting the precursor to PPV, and finally evaporating the Al thin film cathode on the PPV. The developments in both small molecular OLEDs and PLEDs since the seminal reports of Tang and VanSlyke and of Friend and coworkers have been truly spectacular: from very dim devices with a lifetime of less than 1 minute in air, to green OLEDs that can operate continuously for over 20,000 hours (833 days) at a brightness of 50–100 Cd/m^2 (i.e., comparable to a typical TV or computer monitor),[16] or in pulsed operation at $>10^6$ Cd/m^2,[17] or blue, white, and red devices with continuous dc lifetimes of over 2000 hours. Indeed, the developments have been so remarkable, that serious effort is now underway towards the most ubiquituos application: replacing the incandescent and fluorescent light bulbs with OLEDs as the primary source for general lighting applications. However, even as they now enter the marketplace,[18,19] outstanding challenges in the efficiency and long-term degradation processes of OLEDs remain. These are intimately tied to the dynamics of the basic excitations in these materials and devices, namely singlet excitons (SEs), triplet excitons (TEs), and p^- and p^+ polarons, to which the electrons and holes, respectively, relax as they are injected from the electrode into the organic layer of the OLED. This chapter reviews the basic properties of these devices, including the basic photophysics of these excitations.

1.2 Basic Electronic Structure and Dynamics of π-Conjugated Materials

Most luminescent organic molecules are π-conjugated compounds, i.e., materials in which single and double or single and triple bonds alternate throughout the molecule or polymer backbone. The second and third bonds of a double or triple bond are π bonds, i.e., if the backbone of the molecule or polymer is along the x axis, then the orbitals which define these π bonds are formed from overlapping atomic p_z or p_y orbitals. Since the energy of electrons in π orbitals is usually higher than in the σ orbitals (which are generated from sp^3, sp^2, or sp hybridized atomic orbitals), the gap between the highest occupied molecular π orbital (HOMO) and the lowest unoccupied molecular π^* orbital (LUMO) is typically in the 1.5–3 eV range, i.e., the materials are semiconductors.[20] Due to the overlap of π orbital wave functions of adjacent carbon atoms, the electrons occupying such orbitals are relatively delocalized. Figure 1.2(b) shows the π electron clouds in PPV, which are generated from electrons in the overlapping atomic p_z orbitals. Since these p_z orbitals have lobes above and below the x-y plane of the σ bonds of PPV, the π electrons lie above and below this plane. Although it is not reflected in Fig. 1.2(b), the distance between two C atoms is shorter and the π electron cloud between them is more dense in the double C=C than in the single C–C bond. The difference between these distances, or, equivalently, between the densities of the π electrons in the double vs. the single bond, is a measure of the "alternation parameter," and it may strongly impact the electronic structure of the molecule or polymer.[21,22]

Due to the π conjugation, in the perfect isolated polymer chain the delocalized π electron cloud extends along the whole length of the chain. However, in the real chain various defects, such as external impurities (e.g., H, O, Cl, or F atoms which eliminate the double bond, etc.) or intrinsic defects (e.g., kinks, torsional conformations, a cross-link with a neigboring chain, etc.) break the conjugation. In the typical polymer film, the length of a conjugated segment typically varies from ∼5 repeat units to ∼15 repeat units. The HOMO-LUMO gap decreases with increasing conjugation length to an asymptotic value usually reached at ∼10 repeat units.[21]

An important characteristic of both polymer and small molecular films is disorder. Although polymer chains may be quite long, typically the π-conjugation is interrupted by topological defects. Hence the conjugated polymers can be considered as an assembly of conjugated segments. The length of the segments is subject to random variation that is a major source of energetic disorder implying both inhomogeneous broadening of the absorption spectrum and a relatively broad density-of-states (DOS) energy distribution for neutral and charged excitations. However, the structural disorder in amorphous films of small π-conjugated molecules also leads to a similarly broad DOS distribution. The width of the DOS of the charge transport manifold, to a large degree, determines the charge transport characteristics of the material (see Sec. 1.7 below). Due to the broad DOS distribution, the tail states of this distribution can in principle act as the shallow trapping states for charge carriers at low temperatures (*intrinsic* localized states). On the other hand, *extrinsic* trapping, meaning the presence of localized states that differ from the majority of hopping states in that they require a larger energy to release the charge carriers back to the intrinsic DOS, is also possible.

The ground state of most of the luminescent molecules and polymers which are used as the emitters in OLEDs and PLEDs is the symmetric singlet 1^1A_g state.[22] Figure 1.4 shows the basic processes which may occur following photoexcitation of the molecule or conjugated segment of the polymer. Since the material is assumed to be luminescent, the antisymmetric 1^1B_u state must lie below the symmetric 2-photon 2^1A_g state. Otherwise, photoexcitation will still populate the 1^1B_u state, but that state will quickly decay to the 2^1A_g, and the latter will decay nonradiatively to the ground state, with lifetimes as short as ∼2 ps.[23]

As Figure 1.4 shows, several processes may occur following photoexcitation of the molecule or conjugated segment of the polymer into the vibrational manifold of the 1^1B_u:

(1) Rapid (∼100 fs) thermalization of the excited state to the lowest 1^1Bu vibrational state, followed by radiative decay to the ground state. The radiative lifetime is typically ∼ 1 ns.[20,24,25]

(2) Charge transfer from the 1^1B_u to an adjacent molecule or segment of a chain, i.e., dissociation of the 1^1B_u. This process may also be extremely fast.[24] Indeed, so fast that it has been suspected that this charge transfer state, aka a “spatially indirect exciton,” “charge transfer exciton (CTE),” or “intermolecular or interchain polaron pair,” may be generated directly from the ground state.[24]

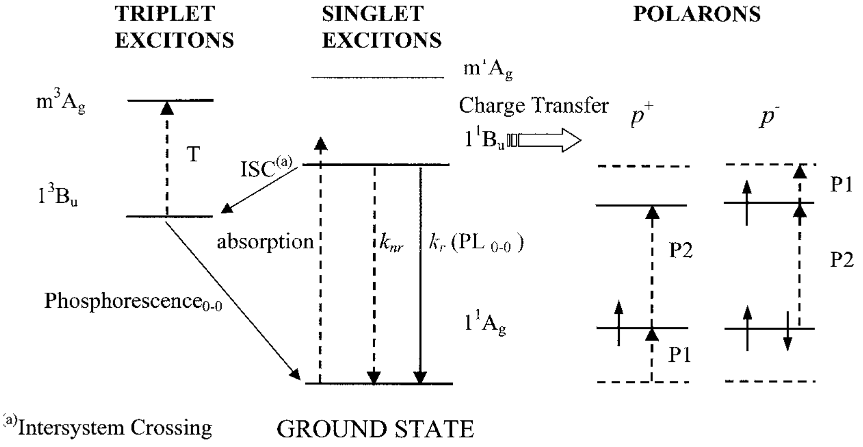

FIGURE 1.4. Basic processes following photoexcitation of a π-conjugated molecule or polymer.

(3) Intersystem crossing (ISC) from the 1^1B_u to the lowest state in the triplet manifold, assumed to be the 1^3B_u. Although the yield of this ISC process is known to be high in some specific molecules, e.g., anthracene[20] and C_{60},[26] it is apparently very low in most π-conjugated molecules and polymers. In some unusual cases such as solid rubrene (5,6,11,12-tetraphenyl tetracene or 5,6,11,12-tetraphenyl naphthacene; see Figure 1.1), where the energy $E(1^1B_u)$ of the 1^1B_u is about twice the energy $E(1^3B_u)$ of the lowest triplet, the 1^1B_u dissociates to two 1^3B_u triplets on neighboring molecules with a very high yield. This process quenches the PL yield of solid rubrene films down to ~ 10%. In contrast, the PL yield of dilute rubrene solutions is ~100%.[27]

The dynamics of the polarons and TEs, and their interactions with the SEs, have been the subject of numerous studies.[20–25,28–36] Although the source of the EL is the recombination of a polaron pair in the antisymmetric singlet configuration to a SE:

$$p^- + p^+ \rightarrow {}^1S^* \rightarrow 1^1B_u + \text{phonons} \rightarrow h\nu + \text{phonons}, \tag{1}$$

a polaron pair in the symmetric singlet configuration or the triplet configuration may recombine to a TE:

$$p^- + p^+ \rightarrow {}^3T^* \rightarrow 1^3B_u + \text{phonons}. \tag{2}$$

Indeed, spin statistics mandate that if the rates of reactions (1) and (2) are the same, then the nongeminate polaron pairs generated by carrier injection in OLEDs would yield 3 TEs for every SE. This SE/TE branching ratio is one of the most important factors suppressing the efficiency of OLEDs based on the fluorescent decay of SEs. However, recent studies suggest that in luminescent π-conjugated polymers the rate of reaction (1) is higher than that of (2), so the yield of SEs is higher than 25%.[37] While it may be as high as 50% in PPV-based PLEDs,[38] it may even be higher in most of the other PLEDs.[38] The issue of efficiency of OLEDs is treated in some detail in Sec. 1.8.

The copious generation of TEs in OLEDs (Eq. (2)) has motivated the recent successful development of OLEDs based on electrophosphorescence, i.e., on the radiative decay of TEs in molecules containing a heavy transition metal or rare-earth atom, where that decay is partially allowed due to strong spin-orbit coupling.[40,41,42] Although in the most recent study[42] it was shown that some of the emission was due to triplet-triplet annihilation to SEs,

$$1^3B_u + 1^3B_u \rightarrow {}^1S^* \rightarrow 1^1B_u + \text{phonons} \rightarrow h\nu + \text{phonons}, \tag{3}$$

it appears that in general this process is marginal in most π-conjugated polymer films, as well as both PLEDs and small molecular OLEDs, probably due to the strong localization and low diffusivity of TEs in these disordered systems.[30,34,35]

As mentioned in point (ii) above, the 1^1B_u SEs may decay nonradiatively by dissociating into an interchain or intermolecular polaron pair. This dissociation may be induced by an external electric field,[32] defects such as carbonyl groups (which, in PPV, are generated by photooxidation),[25] charged defects as may be found in the organic/organic or organic/cathode interfaces in OLEDs, or any other species generating an electric field. Hence, besides their recombination to singlet and triplet excitons, polarons may play another major role in π-conjugated films and OLEDs: Since they generate an electric field, they may also quench SEs:

$$p^{-/+} + 1^1B_u \rightarrow p^{-/+*} + \text{phonons} \tag{4}$$

or

$$p^{-/+} + 1^1B_u \rightarrow p^{-/+} + p^+ + p^- + \text{phonons}. \tag{5}$$

Indeed, considerable evidence for such quenching of SEs by polarons has accumulated over the past decade,[29–31] and recent modeling of the behavior of multilayer OLEDs[43] and optically detected magnetic resonance (ODMR) studies suggest that this quenching process may be a major mechanism in suppressing the efficiency of OLEDs, in particular at high injection current of OLEDs.[29] It should be noted, however, that in small molecular OLEDs it is believed that the quenching of SEs by polarons does not result in dissociation of the SE but rather in absorption of its energy by the polaron (Eq. 4).[20] Finally, TEs may quench the SEs as well,[20] and that mechanism may indeed be responsible for the triplet resonances observed in ODMR studies of these materials.[28–30]

The foregoing section attempted to provide an introduction to the dynamics of singlet excitons, generated either by photoexcitation or by polaron recombination, and the effects of polarons and TEs on the SE dynamics. We now turn to the basic structure and dynamics of OLEDs, which obviously reflect the basic processes described above.

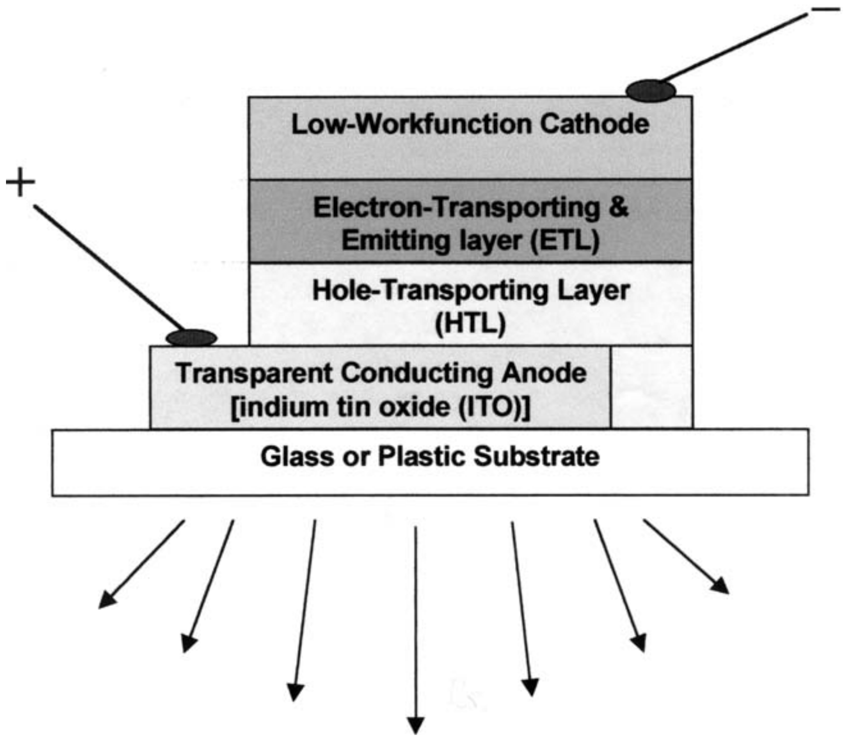
−
+
Low-Workfunction Cathode
Electron-Transporting & Emitting layer (ETL)
Hole-Transporting Layer (HTL)
Transparent Conducting Anode [indium tin oxide (ITO)]
Glass or Plastic Substrate

FIGURE 1.5. Basic structure of a bilayer OLED.

1.3 Basic Structure of OLEDs

The basic structure of a typical dc-biased bilayer OLED is shown in Figure 1.5. The first layer above the glass substrate is a transparent conducting anode, typically indium tin oxide (ITO). Flexible OLEDs, in which the anode is made of a transparent conducting organic compound, e.g., doped polyaniline (see Fig. 1.2),[44] or poly(3,4-ethylene dioxy-2,4-thiophene) (PEDOT)-polystyrene sulfonate (PEDOT-PSS) (see Fig. 1.2)[45] deposited on a suitable plastic, e.g., transparency plastic, have also been reported.

The single- or multi-layer small organic molecular or polymer films are deposited on the transparent anode. Appropriate multilayer structures typically enhance the performance of the devices by lowering the barrier for hole injection from the anode and by enabling control over the $e^- - h^+$ recombination region, e.g., moving it from the organic/cathode interface, where the defect density is high, into the bulk. Hence, the layer deposited on the anode would generally be a good hole transport material, providing the hole transport layer (HTL). Similarly, the organic layer in contact with the cathode would be the optimized electron transporting layer (ETL).

The cathode is typically a low-to-medium workfunction (ϕ) metal such as Ca ($\phi = 2.87$ eV), Al ($\phi = 4.3$ eV),[15] or $Mg_{0.9}Ag_{0.1}$ (for Mg, $\phi = 3.66$ eV)[5] deposited either by thermal or e-beam evaporation. However, in case of Al or Ca, addition of an appropriate buffer layer between the top organic layer and the metal cathode improves the device performance considerably. This issue is discussed in some detail in Sec. 1.5.8 below.

1.4 OLED Fabrication Procedures

The existing OLED fabrication procedures fall into two major categories: (1) thermal vacuum evaporation of the organic layers in small molecular OLEDs, and (2) wet coating techniques of the polymer layers in PLEDs.

1.4.1 Thermal Vacuum Evaporation

Thermal evaporation of small molecules is usually performed in a vacuum of $\sim 10^{-6}$ torr or better. However, it has been observed that the residual gases in the chamber may affect the performance of the devices significantly. For example, Brömas et al.[47] found that the performance of OLEDs in which a Ca film was deposited as the cathode in a high vacuum (HV; $\sim 10^{-6}$ torr) system was far better than that of OLEDs deposited under ultra-high vacuum (UHV; $\sim 10^{-10}$ torr). This was apparently due to the formation of an oxide buffer layer between the top organic layer and the metal cathode and, indeed, led to the deliberate introduction of an AlO_x buffer layer by Li et al.[48] In another case, it was found that Au/[organic]/Au device structures were rectifying when deposited under HV but symmetric when fabricated under UHV.[49]

One of the most salient advantages of thermal vacuum evaporation is that it enables fabrication of multilayer devices in which the thickness of each layer can be controled easily, in contrast to spin coating (see below). In addition, 2-dimensional combinatorial arrays of OLEDs, in which two parameters (e.g., the thickness or composition of two of the layers) may be varied systematically across the array, can be relatively easily fabricated in a single deposition procedure.[50,12] This combinatorial fabrication greatly enhances the efficiency of systematic device fabrication aimed at optimizing the various parameters.

The major appeal of vacuum deposition techniques is that they employ the generally available vacuum equipment existing in the semiconductor industry. Using properly matched shadow masks for depositing RGB emitting materials allows a relatively simple way to achieve multi-color displays in segmented-color, active-matrix (AM) full color, and passive-matrix (PM) configurations. The commercial Pioneer vehicular stereo OLED display (1999) and Motorola cell phone OLED display (2000) were prepared with Kodak-licensed small molecule vacuum sublimation technology.

1.4.2 Wet-Coating Techniques

General remarks and spin-coating

Since polymers generally crosslink or decompose upon heating, they cannot be thermally evaporated in a vacuum chamber (in case of PPVs, rapid photooxidation is an additional problem as even residual quantities of oxygen lead to significant emission quenching). Hence, they are generally deposited by wet-coating a thin film from a solution containing them. That, however, imposes restrictions on the nature of the polymers and the sidegroups attached to the polymer backbone, since the polymer must be soluble. For example, unsubstituted PPV (Fig. 2) is insoluble. Hence, it is generally fabricated by spin-coating a soluble precursor polymer onto the desired substrate (typically ITO). The precursor polymer film is then converted to PPV by annealing at a temperature $150 \leq T \leq 250°\text{C}$ for up to ∼24 hours.[15,34,51,52] As this conversion process yields an insoluble layer of PPV, additional layers may be deposited on it by spin-coating.[51,52] However, when soluble PPV derivatives such as 2,5-dialkoxy PPVs are spun-coated onto the substrate, only solvents which would not redissolve the deposited film can be used to deposit additional layers. Thus, Gustaffson et al.[44] fabricated flexible PLEDs by sequentially spin-coating an aqueous solution of water-soluble, conducting transparent polyaniline onto a transparency, and a xylene solution of poly(2-methoxy-5-(2'-ethyl)-hexoxy-1,4-phenylene vinylene) (MEH-PPV) (see Fig. 1.2).

Although the thickness of spun-coated films may be controlled by the concentration of the polymer in the solution, the spinning rate, and the spin-coating temperature, it is difficult to fabricate thick films and the thickness obviously cannot be monitored during deposition. In addition, no combinatorial fabrication methods have been developed for spun- coated PLEDs (see above).

Spin-coating is an established procedure in the semiconductor and display industries, widely used in photolithography of silicon and ITO and polycrystalline backplanes for liquid-crystal displays. However it may not be used for large size single plane displays for rapid web coating in reel-to-reel processes desired in flexible display manufacturing. An even more important limitation of spin-coating is that it does not provide a way to pattern full-color display. The whole surface of the substrate is covered with the light-emitting polymer, and the devices are created through cathode patterning.

Doctor blade technique

In this technique, a film of the solution containing the soluble polymer is spread with uniform thickness over the substrate using a precision "doctor blade."[53] In contrast to spin-coating, the doctor-blade technique is very useful for fabricating relatively thick films, but does not enable the fabrication of films <100 nm thick, which are commonly used in OLEDs.

Wet-Casting

An important development of wet-casting is inkjet printing, achieved by Yang and coworkers.[54] It is currently being utilized for the development of organic high-information content (HIC) displays by, e.g., Cambridge Display Technology, Seiko-Epson,[55] and Philips.[56] This technique is currently leading the pursuit for commercially viable HIC displays, as the organic layers are deposited directly as an array of pixels. While several companies have announced the development of ink-jet printed displays, the numerous intricacies of this technique are delaying the commercialization of PLEDs. As in the case of spin-coating, when used for patterning bilayer PLEDs, wet casting techniques impose an additional demand of mutual insolubility of organic layers.

Other important techniques currently studied in the area of wet casting are screen printing, micro-stamping, and hot microprint contact.[57]

1.5 Materials for OLEDs & PLEDs

The list of materials that have been incorporated in OLEDs is now too large to provide in this introductory chapter. The following list highlights some of the materials that have drawn considerable attention:

1.5.1 Anode Materials and HTLs or Buffers

Indium–Tin–Oxide (ITO)

In the most common "cathode on top" device configuration the OLED is prepared on a glass substrate pre-coated with ITO. The ITO-coated backplane is an established component in the LC-display industry with very large well-developed facilities dedicated to its preparation and handling. The availability of these elaborate facilities, each of which reflects a minimal investment of as much as \$400m, is an important prerequisite for OLED penetration of the existing flat-panel display (FPD) market. The fact that these facilities were not in place when the early attempts were made to introduce the inorganic EL displays contributed to their failure to enter the display market. The initial cost models for OLEDs manufacturing are all built on the assumption of low cost of retooling the LCD manufacturing facilities based on patterning and handling of ITO backplanes.[58] The commercial batches of ITO-coated glass are normally characterized by square or sheer resistance, material roughness, and layer transparency.[59] All of these parameters have important implications for device functionality and durability. However, it should be emphasized that ITO is a non-stoichiometric mixture of In, In_2O, InO, In_2O_3, Sn, SnO, and SnO_2 (it is sometimes even referred to as "In-doped tin oxide" or vice versa). It also appears that the workfunction ϕ_{ITO} of ITO films, typically $\sim$4.5 eV, increases with the O content up to $\sim$5.1 eV. It was found that device brightness and efficiency tend to increase with increased ϕ_{ITO}. Hence several procedures for saturating the O content of ITO have been developed. The most common is UV-ozone treatment, in which the ITO film is exposed to ozone produced by a UV lamp.[60] Other procedures involve partial etching of the ITO in aquaregia[61] or plasma etching.[62] However, since the excess oxygen typically evolves out of the treated ITO within a few hours, the organic layers must be deposited promptly on the ITO after the treatment.

Using ITO-coated glass in the common configuration is problematic in several respects. One of them is strong coupling of the emitted light to the evanescent mode inside the glass that leads to extremely high light losses. Therefore, an alternative "anode on top" configuration has also been developed.[63] We return to this issue below, when discussing device optimization.

Polyaniline (PANI; see Fig. 1.2)

The development of water-soluble-transparent-conducting-doped-PANI, enabled the first fabrication of an "all plastic" PLED.[44] In an interesting development of this anode, a mixture of an aqueous solution containing the PANI and an organic solution containing polystyrene was spun coated to yield a film, from which the polystyrene was then etched by an organic solvent, resulting in a highly porous PANI anode.[64] The high contact area between the anode and the emitting polymer layer enhanced h^+ injection, resulting in improved device performance.

Poly(3,4-ethylene dioxy-2,4-thiophene)-polystyrene sulfonate (PEDOT-PSS; see Fig. 1.2)[65]

This polymer is also water soluble, and hence, similar to PANI, can be used as a transparent anode.

Pt

Since Pt has a very high $\phi = 5.6$ eV, it could strongly enhance hole injection. However, since it must be very thin to be transparent, it would be deposited on, e.g., the conventional ITO. Indeed, Malliaras et al.[66] have very recently shown that a thin layer (≤ 10 Å) of Pt on ITO enhances hole injection by up to a factor of 100 relative to the uncoated ITO.

ZnO

Although ZnO also forms transparent conducting films, it has drawn surprisingly little attention for use as the anode in OLEDs.

On top of the ITO layer one usually deposites an HTL or more-recently "buffer" layer. It serves to planarize the irregularities present at the ITO surface, produces an interface with an emitting layer that confines charge carriers away from the electrodes, and provides the h^+ delivery for exciton formation.

Copper phthalocyanine (CuPc; see Figure 1.1)

CuPc is widely used as an HTL. However, it may either inhibit hole injection,[67] or enhance it,[68] depending on the other layers in the OLED.

N,*N*'-diphenyl-*N*,*N*'-bis(3-methylphenyl)-1,1'-biphenyl-4,4'-diamine, also dubbed "triphenyl diamine," (TPD; see Fig. 1.1)

This material has been used extensively as the HTL. However, its glass transition temperature T_g is a relatively low 65° C (see Table 1.1). Hence, it causes a failure of OLEDs as it recrystrallizes (see Section 1.9 below). The recrystallization may be suppressed and the device lifetime greatly enhanced by adding a guest molecule such as rubrene. However, in that case carriers may recombine on the rubrene, resulting in red EL from that guest molecule.[69]

N,*N*'-diphenyl-*N*,*N*'-bis(1-naphthylphenyl)-1,1'-biphenyl-4,4'-diamine, (NPB, α-NPB, NPD, or α-NPD; see Fig. 1.1)

NPB is very similar to TPD, but the methylphenyl groups are replaced by naphthylphenyls. This modification has been shown to enhance the stability of the OLEDs very significantly, apparently due to the higher glass transition temperature $T_g \sim 95^\circ$ C of NPB (see Table I).[70]

"Starburst molecules."

The synthesis and application of these compounds, in which three identical branches "radiate" from a central N atom or phenyl group, was pioneered by Shirota and coworkers.[71] They were synthesized for their nonplanar geometry, which inhibits easy packing and consequent crystallization. The most widely used materials of this class are the 4,4',4"-tris(diphenyl amino)triphenylamines (TDATAs), and among these the meta-methyl derivative *m*-MTDATA (see Fig. 1.1) is the most common.

Poly(3,4-ethylene dioxy-2,4-thiophene)-polystyrene sulfonate (PEDOT-PSS; see Fig. 1.2)[65]

As mentioned above, this material can be used as a transparent anode. However, it is now also commonly deposited on ITO as an HTL in PLEDs. Indeed, it has recently become the HTL of choice in most efforts to develop PLEDs for commercial products.

Doped or Guest-Host Materials

As mentioned above and treated in detail below, crystallization of compounds such as TPD is one of the main degradation processes in OLEDs (see Sec. 1.9 below). Doping of these compounds enhances stability by inhibiting the crystallization process and by localizing the excitation energy on the dopant or guest molecule (see Sec. 1.6 below).

TABLE 1.1. Values of the Glass Transition Temperature T_g, the HOMO and LUMO Levels (Relative to the Vacuum Level), and Typical Hole and Electron Mobilities (μ_h and μ_e, respectively) at Fields F of 10^5–10^6 V/cm of some Typical OLED Materials

Material	$T_g(^\circ C)$	HOMO (eV)	LUMO (eV)	$\mu_h(\mathrm{cm}^2/V\ s)$	$\mu_e(\mathrm{cm}^2/V\ s)$
CuPc		4.8[a]	3.1[a]	$\sim 10^{-3}$ [b]	
m-MTDATA				$1.5 \times 10^{-5} - 1.5 \times 10^{-4}$ [c]	$1.5 \times 10^{-7} - 1.5 \times 10^{-6}$ [c]
TPD	65[d]	5.6,[ef] 5.1[g]	2.5[ef]	$1\text{–}2\times 10^{-3}$[h]	
NPB, NPD	95[d]	5.6[8]		3×10^{-4} [i]	
AIq$_3$	> 170[d]	5.9[e,f], 5.7 – 5.9[8]	3.2[e,f]	2×10^{-8} [j]	1.4×10^{-6} [j]
Rubrene		5.4[f]	3.2[f]		
DPVBi	64[k]	5.9[1]	2.8[1]		
PVK		5.4,[m] 6.1[a]	1.9[m], 1.2[a]		
PPV		5.1[n]	2.5[n]		
2,5-Dialkoxy-PPV		4.9 – 5.1[o]	2.5 – 2.8[o]	5×10^{-7} [p], $10^{-10} - 10^{-9}$ [q]	
MEH-PPV		4.9[r]	2.8[r]	$5 \times 10^{-7} - 5 \times 10^{-6}$ [s]	6×10^{-8}
				$2.3 \times 10^{-7} - 6 \times 10^{-6}$ [t]	$1.2 \times 10^{-5}t$
m-LPPP		5.5[u]	2.3[u]	10^{-3} [v]	
Polythiophenes		5.5 – 6[W]	2 – 3.5[W]		
PFO		5.8[x]	2.1[x]	4×10^{-4} [y] $- 8 \times 10^{-3}$ [z]	

a. W.-L. Yu, J. Pei, Y. Cao, and W. Huang, J. Appl. Phys. **89**, 2343 (2001).

b. K.-O. Cheon and J. Shinar, unpublished results.

c. J. Staudigel, M. Stössel, F. Steuber, and J. Simmerer, J. Appl. Phys. 86, 3895 (1999).

d. D. F. O'Brien, P. E. Burrows, S. R. Forrest, B. E. Koene, D. E. Loy, and M. E. Thompson, Adv. Mater. **10**, 1108 (1998).

e. J. Kalinowski, in *Organic Electroluminescent Materials and Devices*, edited by S. Miyata and H. S. Nalwa, Chap. 1 Gordon & Breach, Amsterdam, 1997.

f. H. Murata, C. D. Merritt, and Z. H. Kafafi, IEEE J. Select. Topics Quantum Electron. **4**, 119 (1998).

g. H. Ishii, K. Sugiyama, E. Ito, and K. Seki, Adv. Mater. **11**, 605 (1999).

h. M. Stolka, J. F. Yanus, and D. M. Pai, J. Phys. Chem. **88**, 4707 (1984).

i. E. W. Forsythe, M. A. Abkowitz, Y. Gao, and C. W. Tang, J. Vac. Sci. Technol. A **18**, 1869 (2000).

j. R. G. Kepler, P. M. Beeson, S. J. Jacobs, R. A. Anderson, M. B. Sinclair, V. S. Valencia, and P. A. Cahill, Appl. Phys. Lett. **66**, 3618 (1995); at $F = 4 \times 10^5$ V/Cm.

k. H. Spreitzer, H. Schenk, J. Salbeck, F. Weissoertel, H. Riel, and W. Reiss, in *Organic Light Emitting Materials and Devices III*, edited by Z. H. Kafafi, Proc. SPIE 3797, SPIE, Bellingham, WA, 1999, p. 316.

l. C. Hosokawa, H. Higashi, H. Nakamura, and T. Kusumoto, Appl. Phys. Lett. **67**, 3853 (1995).

m. Z.-L. Zhang, X.-Y. Jiang, S.-H. Xu, and T. Nagamoto, in *Organic Electroluminescent Materials and Devices*, edited by S. Miyata and H. S. Nalwa, Chap. 5. Gordon & Breach, Amsterdam, 1997).

n. W. Reiss, in *Organic Electroluminescent Materials and Devices*, edited by S. Miyata and H. S. Nalwa, Gordon & Breach, Amsterdam, 1997, Chap. 2.

o. The values generally range from those of PPV to those of MEH-PPV.

p. P. W. M. Blom, M. J. M. de Jong, and J. J. M. Vleggaar, Appl. Phys. Lett. **68**, 3308 (1996).

q. H. C. F. Martens, H. B. Brom, and P. W. M. Blom, Phys. Rev. B **60**, R8489 (1999).

r. I. D. Parker, J. Appl. Phys. **75**, 1656 (1994).

s. I. H. Campbell, D. L. Smith, C. I Neef, and J. P. Ferraris, Appl. Phys. Lett. **74**, 2809 (1999).

t. L. Bozano, S. A. Carter, J. C. Scott, G. G. Malliaras, and P. J. Brock, Appl. Phys. Lett. **74**, 1132 (1999).

u. S. Tasch, E. J. W. List, C. Hochfilzer, G. Leising, P. Schlichting, U. Rohr, Y. Geerts, U. Scher and K. Müllen, Phys. Rev. B **56**, 4479 (1997).

v. D. Hertel, H. Bässler, U. Scherf, and H. H. Hörhold, J. Chem. Phys. **110**, 9214 (1999).

w. O.. Inganäs, in **Organic Electroluminescent Materials and Devices**, edited by S. Miyata and H. S. Nalwa, Gordon & Breach, Amsterdam, 1997, Chap. 3.

x. S. Janietz, D. D. C. Bradley, M. Grell, C. Giebeler, M. Inbasekaran, and E. P. Woo, Appl. Phys. Lett. **73**, 2453 (1998).

y. M. Redecker, D. D. C. Bradley, M. Inbasekaran, and E. P. Woo, Appl. Phys. Lett. **73**, 1565 (1998).

z. M. Redecker, D. D. C. Bradley, M. Inbasekaran, and E. P. Woo, Appl. Phys. Lett. **74**, 1400 (1999).

1.5.2 Small Electron-Transporting and Emitting Molecules

Alq_3 (see Figs. 1.1 and 1.3)

This green emitter has probably received more attention than any other small molecular emitter.[5,14,67,69] It is not only commonly used as a green emitter, but also as a host for lower-gap emitter guest molecules, to which the SE energy is transferred very efficiently via the radiationless Förster mecahanism (see Sec. 1.5.4 below).[20] Such dopant or guest molecules have typically included dyes such as yellow-emitting coumarin 540 or red-emitting DCM1.[14]

Oxadiazoles

These compounds provided the source material for the first blue OLEDs.[72] However, these devices were short-lived. Yet devices fabricated with improved blue-emitting amino oxadiazole fluorene did exhibit greater efficiency and stability,[9] although their performance was still inferior to that of polyfluorene-based PLEDs (see below).

Distyrylarylenes

These generally blue-emitting materials were studied extensively by Hosokawa and coworkers.[73] Among them, 4,4’-bis(2,2’-diphenylvinyl)-1,1’-biphenyl (DPVBi) (see Figs. 1.1 and 1.3) has proven to be a particularly promising material for blue OLEDs. The degradation of OLEDs based on this material is apparently due to its crystallization, which results from its relatively low $T_g \sim 64^\circ$ C. Indeed, the related spiro-DPVBi, with $T_g \sim 100^\circ$ C, yields considerably more stable devices.[70]

Other widely-used electron-transporting materials include 2-(4-biphenylyl)-5-(4-tert-butylphenyl)-1,3,4-oxadiazole (butyl-PBD), which is essentially nonemissive and often introduced between the cathode and the emitting layer precisely for that reason, and 3-(4-Biphenylyl)-5-(4-tert-butylphenyl)-4-phenyl-1,2,4-triazole (TAZ-1).[6,74]

Finally, although CuPc is used mostly as an HTL (see above), it is also effective as an intermediate layer between the emitting layer and sputter deposited cathode.[75,76] In these structures it serves a dual function, promoting electron injection during device operation and protecting the OLED from sputter damage during inorganic cathode deposition. As shown in ref. 75, the electron injection is promoted by damage-induced states at the inorganic/CuPc interface. This finding demonstrates again that the electronic function of organic materials in OLEDs are not derived only from their energy band characteristics. In case of the Li/Al inorganic cathode a significant amount of Li is incorporated into CuPC that leads to increased device efficiency.[76] When ITO is sputter-deposited on top of the CuPc layer,[75] the fully transparent cathode is formed and successfully utilized in stacked multi-color devices.

1.5.3 Small Molecular Guest Dye Emitters

4-dicyanomethylene-6-(p-dimethylaminostyryl)-2-methyl-4H-pyran (DCM) and 3-(2-benzothiazolyl)-7-diethylaminocoumarin (C540)

In 1989 Tang et al. described OLEDs obtained by doping the higher-gap $\mathrm{Alq_3}$ host with these lower-gap dye guests, to yield relatively efficient and long-lived red and yellow devices, respectively.[14] Since then, other dye guests have been described, including coumarin 6, TPB, Nile red, etc. A summary of spectra obained from guest-host layers containing these dyes is given by Kido.[77]

Rubrene (5,6,11,12-tetraphenyl tetracene or 5,6,11,12-tetraphenyl naphthacene; see Fig. 1.1)

As mentioned above, rubrene is a prominent red-emitting molecule, as its PL quantum yield is ∼100% in dilute solution, but that emission is strongly suppressed in the solid state due to fission of the 1^1B_u to two triplets. Hence, it yields bright red OLEDs when incorporated as a guest in hosts such as TPD.[69]

1.5.4 White OLEDs

White OLEDs may have far-reaching applications as paper-thin white light sources for, e.g., the backlight in LCD-based displays and for general lighting applications. As the power efficiency and lifetime of the best green OLEDs now exceeds ∼30 lumens/W and 20,000 hours, respectively, or more than twice the ∼14 lumens/W and more than 20 times the 1,000 hours of a standard incandescent bulb, respectively, the eventual replacement of the bulb by the OLED can be envisioned. This revolution in the lighting industry is still in its infancy, and its implementation will require efficient long-lived white OLEDs. Multilayer OLEDs with white CIE coordinates were described by Kido et al.,[78] and summarized later by Kido.[77] In brief, white emission was achieved by the following procedures:

1. Fabrication of multilayer devices such as ITO/(40 nm TPD)/(3 nm *p*-EtTAZ)/(5 nm $\mathrm{Alq_3}$)/(5 nm 1 mol% Nile Red-doped $\mathrm{Alq_3}$)/(40 nm $\mathrm{Alq_3}$)/$\mathrm{Mg_{0.9}Ag_{0.1}}$, where *p*-EtTAZ is the para ethyl derivative of the TAZ triazole.[77,79] The *p*-EtTAZ, with a very high ionization potential and HOMO-LUMO gap, partially blocks hole injection from the TPD into the $\mathrm{Alq_3}$ and electron injection from the $\mathrm{Alq_3}$ into the TPD. Hence, this device exhibits emission bands due to TPD, $\mathrm{Alq_3}$, and Nile red, resulting in a white CIE coordinate. The brightness of the device exceeded 2,000 Cd/m^2 at 16 V.
2. Multilayer devices with lanthanide chelate complexes. In these complexes, efficient energy transfer from the singlet or triplet exciton on the ligand of the complex to the lanthanide atom at its center results in efficient, atomic-like line emission spectra from the latter. By adjusting the identity and concentration of the different lanthanide complex dopants, a line spectrum with white CIE coordinates was achieved.[77]

The ability to transfer the ligand TE energy to an efficient emissive lanthanide atom state removes the 25% internal quantum efficiency barrier on such OLEDs, enabling very efficient electrophosphorescent devices–see Sec. 1.5.6 below.

(3) Multilayer and single layer dye-doped PLEDs.[77] In these devices, the polymer layer, typically poly(N-vinyl carbazole) (PVK; see Fig. 1.2) or poly(methyl methacrylate) (PMMA; see Fig. 1.3), is only weakly emissive, but is doped with several lower-gap guest dyes, to which the excitation energy is transferred. An appropriate concentration of dyes then yields a white OLED.

1.5.5 Phosphorescent Small Molecules & Electrophosphorescent OLEDs

As noted in Sec. 1.2 above, naïve spin statistics mandate that 75% of the electron-hole or positive-negative polaron recombination events result in the formation of the generally nonemissive TEs, imposing the upper limit of 25% on the internal quantum efficiency η_{EL}. However, consider guest-host devices in which the guest is a heavy-metal atom chelate complex, e.g., chelate lanthanide complexes,[77,80] 2,3,7,8,12,13,17,18-octaethyl-21H,23H-phorphyrin Pt (PtOEP),[81] or tris(2-phenyl pyridine) Ir ($\mathrm{Ir(ppy)_3}$).[82] Most or all of the recombination events occur on a ligand of that guest. Then, if efficient energy transfer occurs from the SE and TE states of the ligand to an emissive state of the metal atom, then η_{EL} can exceed 25%, and, in principle, may approach 100%. Indeed, Baldo et al. achieved internal and external η_{EL} of 23% and 4%, respectively, with PtOEP-based devices,[81] and Tsutsui et al. reported an external η_{EL} of 13.7% and a power efficiency of 38.3 lumens/W with $\mathrm{Ir(ppy)_3}$-based OLEDs.[82]

1.5.6 Fluorescent Polymers

PPVs

PPV derivatives and block copolymers have probably drawn more attention than any other class of π-conjugated polymers. Several surveys of PPVs have been published recently; see, e.g., the recent reiew by Friend et al.[34] or the chapter by Greenham and Friend in this volume.[52] The most commonly used PPV is the unsubstituted, which is typically deposited by spincoating a precursor polymer, followed by thermal conversion of the precursor to PPV, and various derivatives such as 2,5-dioctoxy PPV (DOO-PPV) or MEH-PPV. Similar to $\mathrm{Alq_3}$, PPVs have also been used as hosts for lower-gap emitters.

PPV-Based Block Copolymers

Since the HOMO-LUMO gap increases with decreasing conjugation length, copolymers containing blocks of oligophenylene vinylene (OPV) and an alkane segment emit at shorter wavelengths when the length of the OPV block decreases. Using this approach, Sokolik et al. were able to fabricate blue PPV-based PLEDs.[83]

Poly(p-phenylenes) (PPPs)

The blue-emitting PPPs have been studied extensively by Leising and coworkers.[84,85] Due to the relative freedom of rotation of the phenylene rings relative to each other, the "unplanarized" PPP exhibits broad absorption and emission spectra, with a relatively low η_{PL} and a large Stokes shift due to migration of the SEs to the lower-gap segments. In contrast, the planarized methyl-bridged ladder-type PPP (m-LPPP) (see Figs. 1.2 and 1.3) has a high $\eta_{\mathrm{PL}} \sim 30\%$ in the solid state and a very narrow Stokes shift.

Polythiophenes (PTs) and poly(3-alkylthiophenes) (P3ATs) (see Figs. 1.2 and 1.3)

PT and P3AT-based PLEDs were studied by Yoshino and coworkers,[86] Braun et al.,[87] Greenham et al.,[88] Hadziioannou and coworkers,[89] and Inganäs and coworkers.[90] Due to their relatively low gap, the "intrinsic" PTs are red emitters. However, the gap is very sensitive to the torsion angle between consecutive thiophene units, and a theoretical study has suggested that it may vary from 1.7 eV for the perfectly planarized chain to 4.5 eV for chains with a torsion angle of 90°. Hadziioannou and coworkers have shown that the gap, and hence the EL emission, can be tuned in poly(silanylene thiophene)s and in alkylated polythiophenes with well-defined regioregularity.[89] Inganäs and coworkers have shown that in appropriate polymer blends, the peak emission can be tuned from blue to red by the applied voltage.[90] However, the relatively poor lifetime of PT-based PLEDs inhibits their commercialization.

Polyfluorenes (PFOs) (see Figs. 1.2 and 1.3)

While the first blue PFO-based PLED was described by Yoshino and coworkers in 1991,[92] the major effort to develop commercially viable devices based on these polymers was conducted only recently by Woo and coworkers.[93] This effort has been highly successful, as highly efficient and stable blue-to-red PFO-based PLEDs, based mostly on the di-n-octyl derivative, and including devices with highly polarized emission, have been reported recently.[94]

Diphenyl-substituted *trans*-polyacetylenes (t-(CH)$_x$) or poly(diphenyl acetylene) (PDPA) (see Fig. 1.2)

In contrast to unsubstituted t-(CH)$_x$, which is nonluminescent,[21] the various diphenyl substituted t-(CH)$_x$-(PDPA; see Fig. 1.2) based films and devices emit a strong green or blue PL and EL.[95,96] The strong dependence of the emission on the sidegroups is apparently due to their effect on the energy levels of the polymer: In unsubstituted t-(CH)$_x$, the 2^1A_g level is below the 1^1B_u, but in the luminescent derivatives the sidegroups shift the 1^1B_u below the 1^1A_g.[97] In some phenyl disubstituted derivative films η_{PL} is sufficiently high to enable lasing by optical pumping of the film.[96]

Other materials

This Section 1.5 has provided a brief survey of the small molecules and polymers currently in use in various academic and industrial laboratories developing novel OLEDs and PLEDs. It is obviously incomplete, and only highlights some of the major molecules and polymers utilized to date. It is also obvious that an enormous variety of existing and novel compounds, yet to be synthesized, could be utilized for novel future devices.

1.5.7 Cathode & Organic/Cathode Buffer Materials

As mentioned above, the cathode is typically a low-to-medium workfunction (ϕ) metal such as Ca ($\phi = 2.87$ eV),[98] Al ($\phi = 4.3$ eV),[15] or $\text{Mg}_{0.9}\text{Ag}_{0.1}$ (for Mg, $\phi = 3.66$ eV),[5] deposited either by thermal or e-beam evaporation. In the latter case of $\text{Mg}_{0.9}\text{Ag}_{0.1}$, the Ag is codeposited with the Mg since the low sticking coefficient of Mg on most organic surfaces requires the presence of Ag to enable the deposition of the Mg.

X-ray and ultraviolet photoelectron spectroscopy (XPS and UPS, respectively) studies[99–101] and thermally stimulated current (TSC) measurements[102] revealed that the energy offsets at the organic/metal cathode interface generally cannot be predicted using the "affinity rule," which is based on the difference between the work functions. This is due to the chemical interactions between the metals and the organic films. In the case of PPV/Al, the Al may bind to the vinylene-carbon atom, with slightly more elaborate configurations in PPV derivatives.[103,104] The interface layer of Al atoms covalently bonded to the polymer or small molecule is typically 2–3 nm thick. Ca atoms diffuse into the organic layer and then donate their electrons to the π-electron system and form Ca^{2+} ions. This Ca-doped interface layer is also 2–3 nm thick. The deposition of these and some other metals onto clean surfaces of phenylenevinylene oligomers and Alq_3 were studied under high vacuum conditions.[105–107] It was found that deposition of even submonolayer quantities of metal leads to a dramatic quenching of photoluminescence from the field. On the other hand, independent studies[103,104] showed that deposition on the oxygen-contaminated interfaces leads to better OLEDs. The obvious scenario was that oxidation bonds the metallic atoms thus preventing bonding to organics. This scenario is supported by the recovery of the deposition-induced quenching by subsequent oxidation.[108] A special case is presented by Mg electrodes, which perform best when prepared under high vacuum conditions in the absence of oxygen.[109]

The quenching recovery provided the motivation for fabrication of OLEDs with Al_2O_3/Al cathodes.[48] The Al_2O_3 was obtained by the natural oxidation of a pre-deposited ultrathin layer of Al on the organic surface. It led to improved EL efficiency as long as the thickness of the initially deposited Al layer did not exceed the depth of the native oxide layer. Further improvement was achieved when the Al cathode was separated from the organic layer with a ∼1 nm layer of LiF.[110] It was found that significant improvement can be achieved by introduction of LiF or CsF composites with Al,[111] suggesting that the role of fluorides is to prevent chemical bonding of Al to organics and/or enable the alhali atoms to dope the organic as donors, rather than band matching.

Besides preventing the interaction between the organic layer and the Al or Ca cathode or n-type doping of the organic by alhali atoms, the insulating buffer layer introduced between them also results in the formation of a dipole charge layer. This dipole charge layer increases the vacuum level of the metal cathode, which reduces the barrier for electron injection from the metal to the organic layer. A detailed treatment of the changes in the vacuum level and band-bending effects at the organic-metal interface is given by Ishii et al.[112]

1.6 Basic Operation of OLEDs

In the basic operating mode of an OLED, holes are injected from the (transparent) anode and electrons from the metal cathode (see Figure 1.6). There is typically a roughly triangular barrier for both h^+ penetration into the HTL from the anode

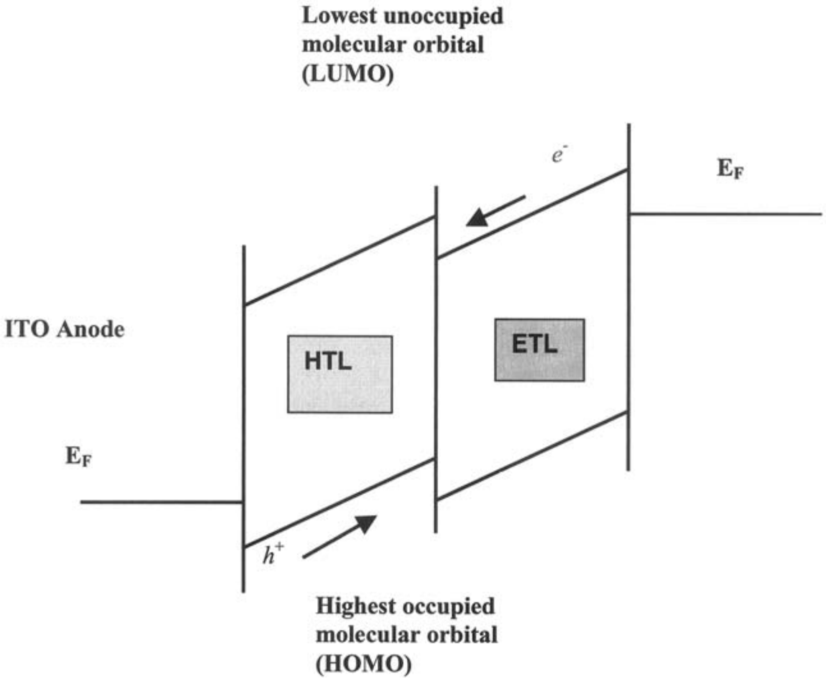

FIGURE 1.6. Basic operation of an OLED.

and e^- penetration of the ETL from the cathode. In the lower-current carrier-injection regime, the current is determined by the rate at which charge either hops over the barriers by thermionic emission, tunnels through it, or is transported through the barrier by hopping among localized gap states in the barrier. In the higher-current space-charge limited current (SCLC) regime, the current is determined by the intrinsic properties of the layers through which it flows. We now proceed to consider carrier transport in OLEDs in greater detail.

1.7 Carrier Transport in OLEDs

Carrier injection and transport in OLEDs has been treated in detail by, among others, Kalinowski.[113] Most of the organic electroluminescent materials, small molecules and conjugated polymers are low-conductance materials. The h^+ mobility in these materials is typically 10^{-7}–10^{-3} cm^2/(Vs), and the e^- mobility is typically lower by a factor of 10–100. However, it is now clear that the low mobility is due to the disorder in the amorphous or polycrystalline materials. Indeed, in high-quality single crystals of pentacene, the h^+ and e^- mobility are 2.7 and 1.7 cm^2/Vs at room temperature.[114] Given the HOMO–LUMO gap of ≥ 2 eV, the thermal concentration of carriers at room temperature is insufficient for light generation. However, the application of an external field causes injection of h^+'s from the ITO and of e^-'s from the cathode (see below). The injection from the metallic electrode is usually less efficient than from the ITO. The asymmetry in carrier injection leads to an imbalance in the concentrations of the injected carriers that reduces the device efficiency (see Sec. 1.8 below).

Unlike inorganic semiconductors, the transport and the injection properties in OLEDs are determined by intersite hopping of charge carriers between localized states[115,116] as well as hopping from delocalized states in the metal to localized states in the organic layer. The actual transition rate from one site to another depends on their energy difference and on the distance between them. The carriers may hop to a site with a higher energy only upon absorbing a phonon of appropriate energy. This decreases the probability of transition to a localized state with higher energy. The energetically allowed hops to a distant site are limited also by the localization length.[117] The energy states involved in the hopping transport of h^+'s and e^-'s form narrow bands around the HOMO and LUMO levels. The widths of these bands is determined by the intermolecular interactions and by the level of disorder.

The transport in OLEDs has been extensively studied by time-of-flight (TOF),[118] and analysis of the dc current-voltage characteristics.[119] In a number of cases the results produced by the two methods were compared and good agreement was generally found.[120] In other cases the mobilites were measured using Hall-effect[121] and delayed EL[122] techniques.

The universal dependence of charge carrier mobility on the electric field

$$\mu(E, T) = \mu(0, T) \exp(\gamma \sqrt{E}), \tag{6}$$

where $\mu(0, T)$ is the low-field mobility and γ is an empirically determined coefficient, is observed for the vast majority of materials. The method of delayed pulsed EL enabled measuring this dependence up to relatively high fields of ~1 MV/cm, while TOF[118] or dc[119] transport measurements usually do not exceed 0.3 MV/cm. Several models have been invoked to explain the observed carrier mobility. Choosing between them is related to the basic issue of the nature of charge carriers in organic films formed by conjugated molecules. The experimentally observed dependence is the same as observed earlier for the wide class of organic photoconductors used in the photocopying process.

1.7.1 Polaron vs Disorder Models for Carrier Hopping

As suggested from Sec. 1.2 above, the models based on polaron formation assume that a localized carrier interacts strongly with molecular vibrations of the host and neighboring molecules, so significant relaxation of the local molecular structure occurs around the carrier. That carrier can move to an adjacent molecule only by carrying that relaxation (or strain field) along with it. Clearly, that relaxation or stabilization lowers the energy of the negative carrier below the LUMO level and the energy of the positive carrier above the HOMO level.

The experimental evidence for polarons in PPV and related polymers is extensive. For PPV it emerges from the comparison of resonant Raman spectra of bulk samples with those of anions in model compounds equivalent to segments of PPV with different lengths. In actual samples the polaronic stabilization may also be induced by defects[123] such as chain breaks and various conjugation defects, e.g., sp^3 bonds, cross-links, and inclusions of catalysts and of precursor polymer that all act as chain breaks. The stabilization is found in calculations assuming the conjugation length is less than 50 sites. It is apparent, however, that on any length scale conjugation defects which are less severe than chain breaks, but raise the energy required to create the polaron on the segment, can help localize the polaron on other chain segments.

While experimental evidence for polaronic relaxation is extensive, other experiments render the polaron models problematic: (i) the use of the Arrhenius relation to describe the temperature dependence of the mobility (see above) leads to pre-factor mobilities well in excess of unity, and (ii) the polaron models cannot account for the dispersive transport observed at low temperatures. In high fields the electrons moving along the fully conjugated segments of PPV may reach drift velocities well above the sound velocity in PPV.[124] In this case, the lattice relaxation cannot follow the carriers, and they move as "bare" particles, not carrying a lattice polarization cloud with them. In the other limit, creation of an orderly system free of structural defects, like that proposed by recently developed self-assembly techniques, may lead to polaron destabilization and inorganic semiconductor-type transport of the h^+'s and e^-'s in the HOMO and LUMO bands, respectively.

The fundamental difference between disorder and polaron models is related to the difference in energy of hopping sites due to disorder and the change in molecular conformation upon addition or removal of a charge at a given site. In the disorder formalism it is assumed that the coupling of a charge carrier to molecular modes is weak, and the activation energy reflects the static disorder of the hopping sites. In the polaron models, it is assumed that the energetic disorder energy is small compared to the deformation energy.

The polaron models predict that the mobility is a product of a Boltzmann probability of energy coincidence and the probability that a carrier will jump between adjacent sites by thermal activation once energy coincidence occurs. The most widely accepted model, proposed by Emin, yields

$$\mu \propto \frac{\sinh(E/E_0)}{E/E_0}. \tag{7}$$

Yet this result agrees with the experimental results over a limited range only.

The calculations of the mobility of e^-'s hopping through the manifold of energetically and spatially disordered states yield Eq. (6), and they show that γ is related to the diagonal disorder parameter σ and the off-diagonal disorder parameter χ.[126–128] The former is usually interpreted as the width of the band of disordered states. Assuming a Gaussian distribution of site energies, σ is the full width of the distribution. Similarly, χ is interpreted as the full width of the distribution of the values of the overlap integrals. This distribution is also assumed to be Gaussian.

The field-dependent mobility expression is universal and applicable to a large class of materials including conjugated polymers, blends, and mixtures of polymers and dyes.

Generally, despite the better agreement between the disorder-based models and transport measurements, it is widely believed that the charge carriers exist as polarons rather than free e^-'s and h^+'s. It should be noted that the basic disorder-based calculations yield the experimentally observed field dependence of the carrier mobility for a relatively narrow range of fields only.

1.7.2 Long-Range Correlations

The range of agreement between the disorder-based models and the experimental results improves when the correlation of the energies of adjacent sites is taken into account.[129] Recently, analytical solutions which relate the field dependent mobility to intermolecular interactions in the polymer were obtained for this case.[130,131] This correlation model results in the following dependence of γ on the electric field:

$$\gamma = C_0 \left(\sigma_d^{3/2} - \Gamma\right) \sqrt{\frac{ea}{\sigma_d}} \tag{8}$$

with $C_0 = 0.78$, $\Gamma = 2$ and μ_0 containing the temperature dependence. The model treats carrier hopping among sites arranged on a cubic lattice of spacing a, but differs from the regular disorder models in the way site energies are determined. An independent and randomly oriented dipole of moment p is placed at each lattice site, and the energy of a carrier at a given site is then given by the Ewald method, i.e., the sum calculated through its interaction with dipoles at all sites except its own:[132]

$$U_m = -\sum_{n,m} \frac{e\vec{p}_n|\vec{r}_n - \vec{r}_m|^3}{\varepsilon|\vec{r}_n - \vec{r}_m|}. \tag{9}$$

The site energy distribution in this model has been extensively studied and shown to be approximately Gaussian with a width[133]

$$\sigma_d = 2.35\frac{ep}{\varepsilon a^2} \tag{10}$$

where p is a randomly oriented dipole moment, ε is the dielectric constant, and a is the spacing on a cubic lattice for which the calculation was carried out. The crux of the improved disorder models is that the many long-range contributions comprising U_m introduce correlations in the distribution of site energies, yielding a version of the disorder model with specific kinds of correlations. In addition, these equations are derived assuming a simple cubic lattice, and thus cannot be expected to be valid for the disordered material. However, they do show how the long-range interactions may be rationalized in terms of the experimentally observed dependence of the mobility on the electric field.

1.7.3 Carrier Injection

We now proceed to briefly describe e^- injection from the metallic electrode into the adjacent band of LUMO states and the hopping transport in this band.[134]

In the absence of e^- injection and an external electric field, the Fermi level of the metallic electrode is at negative energy Δ, with respect to the center of the LUMO band (see Figure 1.7). When a contact between the electrode and the organic is established, there is some initial injection of e^-'s into (probably trap) states in the organic/metal interface. This results in an "image force" potential ϕ_i (shown by a solid thick line in Figure 1.7) due to Coulomb attraction between these electrons and the holes which are left behind in the metal after the electron injection. This image potential lowers the energy of the interface states and renders them energetically available for the e^-'s hopping from the metal Fermi surface. However, the image force potential decreases with increasing distance from the interface and thus the bulk states deep in the organic layer remain energetically unavailable for charge hopping. Application of an external field lowers the energy of the available states in the bulk of the polymer. As a result, hopping into bulk states away from the interface becomes more probable. Figure 1.7 describes the energy of the available sites versus the distance x from the metallic electrode under the influence of the "image force" potential and the applied electric field. It should be emphasized that the carrier motion in the organic layer occurs everywhere through hopping, including injection from the metallic electrode through the interface and the hops in the opposite direction (or "back flow"[135]). At least one of the states involved in each hopping event is localized. Based on the above description of injection and transport, the current vs voltage $I(V)$ in OLEDs was calculated using a model for electron diffusion in an Onsager-type potential with random site energies.[134] It is

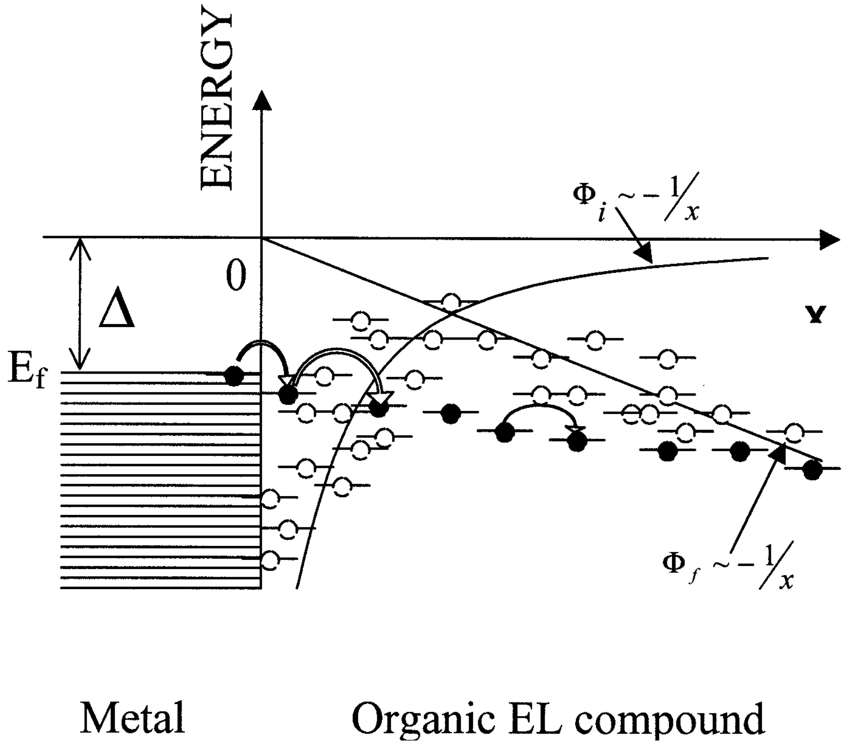

FIGURE 1.7. The energy of the available sites versus the distance x from the metallic electrode under the influence of the "image force" potential and the applied electric field.

noteworthy that this treatment not only predicts the correct dependence of I on V but the magnitude of I as well.

The voltage dependence of the injection-limited current resulting from this treatment, as well as experimentally observed $I(V)$ characteristics are Fowler-Nordheim (FN)-like, i.e., similar to that obtained by tunneling through a triangular barrier. This similarity suggested a number of treatments that analyzed injection into OLEDs in terms of this model, which predicts that

$$J \propto V^2 \exp\left(-\tfrac{b}{V}\right), \tag{11}$$

where J is the current density, V is the voltage and b is a constant that may be analytically derived as a combination of the energy band parameters for the semiconductor material and the contact metal.

Notwithstanding the similarities between the observed $I(V)$ in the current-injection regime and the FN relation (Eq. (11)), the physics that underlies e^- injection from the metal into the insulator described above differs radically from a FN mechanism and should not be mistaken for one. The localized states of the insulator become energetically available for the e^- at the metal Fermi energy due to the application of the external field that drives them down in energy, not unlike the energy bands of the semiconductor or the vacuum level in the original FN treatment. However, the k-vector is inappropriate for describing the e^- motion through the system of localized states. Hence, e^- injection into such a material cannot be treated as a plane wave scattered by a triangualar barrier , which is the basis for the FN model. The hopping mechanism is incoherent and the phase of the electron in the metal is completely lost during the first hopping step into the organic. The mirror image attraction significantly affects the process of the charge motion after hopping into the first organic site. Due to the low bulk mobility, this carrier is effectively trapped in the potential well near the interface, and may leave it only upon absorption of a phonon. Thus, the whole process resembles the Shottky-Richardson mechanism of thermally-stimulated emission, rather than the FN picture of coherent wave tunneling. As several in-depth numerical treatments show, the injection yield, i.e., the probability for a carrier at the first near-interface site to reach across the film, depends critically on the energy of the near-interface sites.[136] Several fundamental considerations defeat the mechanistic treatment of injection into the unperturbed LUMO state: (i) injection occurs into a polaron level;[137] (ii) in the close vicinity of the metallic electrode, the high-mobility image charges in it screen out the dipole terms in the Coulomb interactions at 5–7 nm at least;[138] (iii) even when contamination with, e.g., water vapor or oxygen are excluded, the interface is modified by the direct chemical interaction between the low-work function metal and the organic molecules. As result, no general treatment can be expected, with each process to be analysed on a case-by-case base.

1.7.4 Space-Charge Limited Versus Injection-Limited Current Mechanisms

Injection EL with characteristic efficiencies of 0.5–3 Cd/A that are standard in modern OLEDs demand current densities ≥ 3 mA/cm^2 for this purpose. Mobilities in organic luminescent materials are low, typically 10^{-5}-10^{-3} cm^2/(V·s). Such strong injection into low-mobility materials inevitably leads to charge accumulation in the organic film. This charge build-up partially screens out the applied electric field, leading to its redistribution. The resulting behavior of $I(V)$ is that of space-charge limited current (SCLC).[139] The $I(V)$ curves predicted by this model are supralinear, typically quadratic in the absence of traps or with a single shallow trap level. The local increase in the quasi-Fermi level due to strong injection may lead to charge immobilization in the deep states of the disorder-induced distribution of the HOMO and LUMO levels. In that case, however, the resulting trapped-charge limited current (TCLC) model predicts a generally high-exponent power law $I \propto V^{\alpha}$ with $7 \leq \alpha \leq 9$.[140] The study of trap levels in various electrically active organic films yielded the data required to explain the DC $I(V)$ curves in the most common types of OLEDs.[140]

Single-carrier-dominated transport, including a detailed treatment which includes space-charge effects that are prominent in single layer devices, have been developed to provide a satisfactory explanation of the $I(V)$ characteristics in

OLEDs.[141] Models accounting for the motion of both holes and electrons in single-layer PLEDs elucidated the issue of emission efficiency in these devices.[142] These approaches were later extended for the case of multilayer devices as well.[43] A deeper insight into the subband electronic structure and the dynamics of their charging under different injection conditions was achieved with application of impedance spectroscopy to studies of the space-charge in PLEDs.[143] While these experiments revealed a rich structure of charged gap states acting as traps, a number of recent studies show that the field-dependent mobility alone may account for the steep current-voltage characteristics, without invoking the complicated trap structure. This approach is particularly attractive due to its generality;[144] however, no description for the dependence of the efficiency on injection level or applied bias has been provided yet.

The SCLC-type mechanisms are invariably found to dominate the conduction in devices where strong injection is achieved from both electrodes. The structure of bilayer devices (and multilayer devices derived from them) gives rise to charge trapping and formation of charge dipole layers at the internal interfaces.[43,145] When the external electric field is applied, the holes are injected from the anode into the HTL and drift or hop across it. However, they decelerate at the internal interface due to the lower hole mobility in the ETL. This leads to substantial charge accumulation which is not unlike the most common type of injection-induced space charge build-up in low-mobility insulators. The same mechanism should also be true for electrons as they cross the organic/organic interface. We stress that for this "interface" trapping of charge carriers an energy offset at the internal interface is not necessary, as the carriers are immobilized by the mobility offset. In steady-state this carrier localization leads to increased charge concentration away from the electrodes where the majority of the radiative SEs would be quenched. On the other hand, at high injection levels strong carrier concentration gradients may build up at the interface, leading to increased local electric fields. Yet these field are formed exactly where most of the light is emitted. When the local field at the HTL/ETL interface exceeds the critical value for SE dissociation, it leads to a dramatic decrease in emission efficiency. This decreased efficiency has been observed at high injection levels in virtually all multi-layer OLEDs. Obviousely, balancing injection and mobility in the HTL and ETL respectively may significantly improve the steady-state efficiency at high brightness levels.

1.8 The Efficiency of OLEDs

Efficiency is a key issue not only for energy-consumption, but also for its effect on the longevity of the devices, since the ability to operate the device at a lower input power at a given luminance decreases ohmic heating and increases the device lifetime. A high power efficiency implies a low IV product for a given luminance. However, much of the analysis of the efficiency in the literature has been devoted to the external quantum efficiency η_{EL}, i.e., the number of photons emitted through the front face of the device per injected electron.[146] One of the forms in which the basic equation for the external quantum efficiency η_{EL} of the OLED can be written is

$$\eta_{\mathrm{EL}} = \xi \gamma r_{\mathrm{ST}} \eta_{\mathrm{PL}}, \tag{12}$$

where (i) ξ is the out-coupling efficiency (i.e., the fraction of the photons which are emitted from the front surface of the device), (ii) γ is the ratio of the number of exciton-forming events to the electrons flowing in the external circuit (basically a measure of the fraction of electrons & holes which recombine with each other), (iii) r_{ST} is the ratio of SEs to TEs formed from the recombining charge carriers, and (iv) η_{PL} is the PL quantum yield (i.e., the radiative yield of SEs). We now dwell briefly on each of these terms.

(1) It can be shown that for a large refractive index of the emitter layer n and for isotropic dipoles not subjected to optical interference with the cathode reflector,[38]

$$\xi \approx \frac{0.5}{n^2}. \tag{13}$$

Hence for $n \approx 1.7$, $\xi \approx 0.17$. However, the recent detailed analysis by Kim et al.[38] shows that if the optical interference with the cathode reflector is taken into account, for isotropic and in-plane dipoles $\xi \approx A/n^2$, where $A \approx 0.75 \pm 0.1$ and 1.2 ± 0.1, respectively.

(2) The factor $\gamma \leq 1$, which is a measure of the balance between h^+ and e^- injection, and of the probability that each of them will recombine with the other, is very difficult to measure, but it has been argued that in the relatively efficient OLEDs studied to date, it is close to 1.[38] This factor is optimized by varying the composition and thickness of the HTLs and ETLs, and monitoring the response of the $I(V)$ and $I_{\mathrm{EL}}(V)$ curves to these variations. For practical display devices however, there exists a certain tradeoff between a low turn-on voltage on the one hand, and high efficiency on the other. Hence considerable effort is being invested into promoting the injection of both types of carriers in order to restrict not only the active matrix but in particular passive matrix driving circuitry to lower operating voltages. However, strong injection of majority carriers (usually holes) leads to decreased efficiency, excess Joule heating, and should actually be avoided. Hence highly efficient devices generally operate in the injection-limited current regime. The validity of this approach for multi-layer OLEDs was recently confirmed by Forsythe et al., who introduced trap-free CuPc as a hole-limiting layer immediately on top of the ITO anode to control excessive hole injection.[147]

(3) As mentioned in Sec. 1.2 above, from spin-statistics the ratio r_{ST} of SEs to TEs formed from the recombining polaron pairs should be $r_{\mathrm{ST}} = 0.25$, since parallel spin pairs would recombine to TEs and antiparallel pairs would recombine equally to SEs and TEs. However, several recent independent studies suggest that the cross-section for SE formation (Eq. (1)) σ_S is greater than that for TE formation (Eq. (2)) σ_T, so $r_{\mathrm{ST}} > 0.25$.[37–39] However, the

actual value for different polymers is still not well-established, and for small π-conjugated molecules it is essentially unknown.

As mentioned in Sec. 1.2 above, electrophosphorescing OLEDs, i.e., devices in which the emission is due to partially-allowed radiative decay of the TEs, have been fabricated and studied,[40–42] and values of η_{EL} as high as $\sim$12% have been reported.[41]

(4) The PL quantum yield η_{PL}. While η_{PL} of many dyes is close to 100% in solution, in almost all cases that yields drops precipitously as the concentration of the dye increases. This well-known "concentration quenching" effect is due to the creation of nonradiative decay paths in concentrated solutions and in solid-state. These include nonradiative torsional quenching of the SE,[148] fission of SEs to TEs in the case of rubrene (see Sec. 1.2 above), or dissociation of SEs to charge transfer excitons (CTEs), i.e., intermolecular polaron pairs, in most of the luminescent polymers and many small molecular films,[20,24,29,32] or other nonradiative quenching of SEs by polarons or trapped charges.[25,29,31,32] In view of these numerous nonradiative decay paths, the synthesis of films in which η_{PL} exceeds 20%, such as in some PPVs,[149] exceeds $\sim$30%, as in some films of *m*-LPPP,[85] and may be as high as 60%, as in diphenyl substituted polyacetylenes,[95,96] is impressive.

In summary, in evaluating the upper limit of η_{EL} from Eq. (11), the upper limits of the different terms, appear to be $\xi \approx 0.35$, $\gamma \approx 1$, and $r_{\mathrm{ST}} \approx 0.5$. Hence fluorescence (as opposed to phosphorescence)-based OLEDs with these values of ξ, γ, and r_{ST} should yield $\eta_{\mathrm{EL}} \approx 0.15\eta_{\mathrm{PL}}$.

1.9 Degradation Mechanisms

The stability of OLEDs is obviously a key element in determining their technological impact. The common degradation mechanisms were recently summarized by Sato et al.[150] We now briefly review these mechanisms.

Dark spot formation

One of the most prominent mechanism of degradation in OLEDs is through the formation of non-emissive "dark" spots along with a long-term decrease in the device efficiency. As found for both OLEDs[151] and PLEDs,[152] these defects result from delamination of the metal at the organic/metal interface initiated by pinholes on the cathode in the presence of significant Joule heating. In-situ imaging of the electrode surface using time-resolved confocal laser-scanning microscope revealed the appearance of dome-shaped defects corresponding to the locations of the "dark spots."[153] Some parts of a strongly degraded sample are short-circuited by the carbonized polymer; in other parts an open circuit condition is found. Cumpston and Jensen[154] proposed that electromigration of the electrode material may occur in the areas where the local conductance is high. It leads to inhomogeneities and, in the final account, to the loss of electrode continuity.

Photooxidation

Many conjugated polymers undergo photooxidation during device operation.[155,156] The extended conjugation length of the polymer may increase the electron density at the double bond, thereby making it more reactive to the excited singlet $^1O_2$ electrophile than in the respective oligomers. There is also evidence that the presence of electron-rich groups on the phenyl rings, such as alkoxy groups, may increase the likelihood of 1,2-cycloaddition of $^1O_2$ at the vinyl double bond, which convert to two C=O carbonyl groups spontaneously.[25] These two carbonyl groups are not bonded to each other, so their formation physically cuts the polymer chain into two segments. In addition, the C=O group is a very efficient nonradiative SE quenching center, and hence its formation rapidly decreases the PL and EL yield of the PPV films and PLEDs.

The source for the formation of the highly reactive $^1O_2$ is the energy transfer from the polymer.[157] The SE of the polymer is responsible for light emission but it is too short lived to transfer energy to oxygen efficiently. However, the copious non-emissive triplet state has a far greater lifetime and is sufficiently energetic to excite the ground state $^3O_2$ to the singlet $^1O_2$ state.

It should be emphasized that neither exposure to *only* light or *only* O_2 lead to the degradation in PPV derivatives.[25] The combination of these factors, however, leads to the oxygen addition at the double bond in the vinyl group.[158] It is important to mention, however, that while many common derivatives of PPV, such as MEH-PPV, are highly vulnerable to photooxidation, others, such as unsubstituted PPV or other polymers such as poly(3-octylthiophene) (P3OT), photooxidation does not appear to be the leading limitation on the longevity.

Recrystallization

This process is one of the primary degradation mechanism of OLEDs based on amorphous organic layers, since SEs are efficiently quenched by defects and charge-dipole-induced fields at the surface of a grain boundary. Since any given amorphous layer will recrystallize slowly as its temperature reaches the glass transition temperature T_g, major efforts to synthesize materials with high Tg have been reported.[70,71] Indeed, as mentioned in Sec. 1.5.2, the considerably higher $T_g \approx 95^\circ$ C of NPB (see Fig 1) as compared to TPD (see Fig. 1.1), where $T_g \approx 63^\circ$ C,[70] is a major reason for the improved stability of NPB/Alq$_3$ devices relative to those of TPD/Alq$_3$ OLEDs.

The major efforts to increase T_g include two noteworthy innovative approaches: (i) Synthesis of "starburst molecules," suitable for HTLs, whose patently nonplanar structure inhibits recrystallization,[71] and (ii) synthesis of novel molecules in which familiar luminescent molecules are synthesized around a spiro-bifluorene core.[70] As shown by Spreitzer et al.,[70] T_g of these spiro derivatives, such as spiro-DPVBi, is considerably higher than that of the parent molecules, yet their PL and EL spectra are essentially identical. As expected, the lifetime of the OLEDs fabricated from the spiro derivatives is considerably higher than that of the parent-compound-based devices, both at room and at elevated temperatures.

Metal atom migration

Several studies have shown that while migration of cathode metal atoms such as Mg is not significant, indium migration from the ITO is a very considerable problem.[159,160] Indeed, Lee et al.[159] have shown that In migration occurs mainly during operation of the devices, i.e., it is an electromigration process, and that its presence is correlated with performance degradation.

Molecule-specific degradation processes

Some degradation processes are molecule-specific. The widely used Alq_3 was found to be unstable in the $+1$ oxidative state.[161] Therefore, hole migration from the HTL to the Alq_3 layer causes degradation unless the injected electrons first charge the Alq_3 negatively. In PPV-based devices, the hole injection process was also found to degrade the ITO/PPV interface.[162]

Electrical breakdown

Finally, damage patterns observed at the Al (Mg) interface with PPV in PLEDs under strong pulsed bias are reminiscent of those observed in AC thin-film inorganic devices. The mechanism of their formation is the electrical breakdown in the form of pinhole electrical arcs.[163] These breakdowns occur at some typical voltage, which in capacitor device technology is called the "clearing voltage." In this case the circuit opens around the pinhole that stops the arcing. The resulting burnout typically does not exceed 50 μm. It leaves an injury through which moisture can penetrate and lead to hydrolysis and subsequent delamination. Also, when the burn-outs become too numerous, they limit the light output and open up an entire circuit eventually. The interesting feature is the propagation of "tributaries." In inorganic devices they were found to be formed by arc-induced dielectric melting, which becomes conductive. The tributaries run all the way through to the opposite electrode, thus completing the electric circuit and leading to a short-circuit condition. This picture is completely compatible with experimental observations in PPV and appears to be adoptable without significant changes.

1.10 Outlook for OLEDs

The progress achieved in OLEDs and PLEDs during the last fifteen years is nothing short of spectacular. While the early devices barely lasted for a few minutes, and could only be observed in the dark, red-to-green OLEDs with lifetimes $\tau > 10^4$ hours and $\eta_{EL} > 4\%$, and numerous white and blue OLEDs with $\tau > 10^3$ hours and $\eta_{EL} \geq 4\%$ are now being routinely reported. In addition, optically-pumped lasing of polymer films such as PPV,[17,164] m-LPPP,[165] and disubstituted polyacetylene,[96] have also been reported. As the maximum theoretical value of η_{EL} may exceed 15%, the devices will become very attractive for an extremely wide variety of display and lighting purposes, and as mentioned above, for general lighting purposes as well.

Hence the intense research and development that the field is currently experiencing will undoubtedly continue into the forseeable future.

References

[1] A. Bernanose, M. Comte and P. Vouaux, J. Chim. Phys. 50, 65 (1953).

[2] M. Pope, J. Chem. Phys. 38, 2043 (1963).

[3] W. A. Hartman and H. L. Armstrong, J. Appl. Phys. 38, 2393 (1967).

[4] J. Gu, M. Kawabe, K. Masuda and S. Namba, J. Appl. Phys. 48, 2493 (1977).

[5] C. W. Tang and S. A. VanSlyke, Appl. Phys. Lett. 51, 913 (1987).

[6] S. Miyata and H. S. Nalwa, Editors, *Organic Electroluminescent Materials and Devices*, (Gordon and Breach Publishers, Overseas Publishers Association, Amsterdam, 1997).

[7] Z. H. Kafafi, Editor, *Organic Light-Emitting Materials and Devices*, SPIE Proc. 3148, (SPIE- The International Society for Optical Engineering, Bellingham, WA, 1997).

[8] Z. H. Kafafi, Editor, *Organic Light-Emitting Materials and Devices III*, SPIE Proc. 3797, (SPIE- The International Society for Optical Engineering, Bellingham, WA, 1999).

[9] H. Tang, F. Li, and J. Shinar, Appl. Phys. Lett. 71, 2560 (1997).

[10] L. S. Swanson, J. Shinar, A. R. Brown, D. D. C. Bradley, R. H. Friend, P. L. Burn, A. Kraft, and A. B. Holmes, Phys. Rev. B 46, 15072 (1992).

[11] S. E. Shaheen, G.E. Jabbour, M. M. Morell, Y. Kawabe, B. Kippelen, N. Peyghambarian, M.-F. Nabor, R. Schlaf, E. A. Mash, and N. R. Armstrong, J. Appl. Phys. 84, 2324 (1998).

[12] L. Zou, V. Savvate'ev, J. Booher, C.-H. Kim, and J. Shinar, Appl. Phys. Lett. 79, 2282 (2001).

[13] (a) C. Adachi, S. Tokito, T. Tsutsui, and S. Saito, Jap. J. Appl. Phys. 27, L269 (1988); (b) *ibid.*, L713 (1988); (c) C. Adachi, T. Tsutsui, and S. Saito, Appl. Phys. Lett. 55, 1489 (1989).

[14] C. W. Tang, S. A. VanSlyke, and C. H. Chen, J. Appl. Phys. 65, 3610 (1989).

[15] J. H. Burroughs, D. D. C. Bradley, A. R. Brown, R. N. Marks, K. Mackay, R. H. Friend, P. L. Burns and A. B. Holmes, Nature 347, 539 (1990).

[16] http://www.pioneer.co.jp/press/release39.html (9/28/98);
http://www.pioneerelectronics.com/features/0003_OEL1.asp

[17] (a) N. Tessler, N. T. Harrison, and R. H. Friend, Adv. Mat. 10, 64 (1998); (b) N. Tessler, Adv. Mat. 11, 363 (1999).

[18] M. T. Johnson and A. Sempel, Information Display 16(2), 12 (February 2000)

[19] N. Bailey, Information Display 16(3), 12 (Mar 2000).

[20] M. Pope and C. E. Swenberg, Electronic Processes in Organic Crystals and Polymers, Second Edition, Oxford University Press, NY, 1999.

[21] A. J. Heeger, S. Kivelson, J. R. Schrieffer, and W.-P. Su, Rev. Mod. Phys. 60, 781 (1988).

[22] (a) Z. G. Soos, S. Ramasesha, and D. S. Galvao, Phys. Rev. Lett. 71, 1609 (1993); (b) Z. G. Soos, S. Ramasesha, D. S. Galvao, R. G. Kepler, and S. Etemad, Syn. Met. 54, 35 (1993).

[23] Z. V. Vardeny, in *Primary Photoexcitations in Conjugated Polymers: Molecular Exciton Versus Semiconductor Band Model*, edited by N. S. Sariciftci (World Scientific, NY, 1997).

[24] M. Yan, L. J. Rothberg, F. Papadimitrakopoulos, M. E. Galvin, and T. M. Miller, Phys. Rev. Lett. 72, 1104 (1994).

[25] M. Yan, L. J. Rothberg, F. Papadimitrakopoulos, M. E. Galvin, and T. M. Miller, Phys. Rev. Lett. 73, 744 (1994).

[26] (a) M. R. Wasielewski, M. P. O'Neil, K. R. Lykke, M. J. Pellin, and D. M. Gruen, J. Amer. Chem. Soc. 113, 2774 (1991); (b) P. A. Lane, L. S. Swanson, Q.-X. Ni, J. Shinar, J. P. Engel, T. J. Barton, and L. Jones, Phys. Rev. Lett. 68, 887 (1992); (c) P. A. Lane and J. Shinar, Phys. Rev. B 51, 10028 (1995).

[27] V. I. Lesin, A. I. Pristupa, and E. L. Frankevich, Optics and Spectroscopy 51, 477 (1981).

[28] (a) L. S. Swanson, J. Shinar, and K. Yoshino, Phys. Rev. Lett. 65, 1140 (1990); (b) L. S. Swanson, P. A. Lane, J. Shinar, and F. Wudl, Phys. Rev. B 44, 10617 (1991); (c) L. S. Swanson, J. Shinar, A. R. Brown, D. D. C. Bradley, R. H. Friend, P. L. Burn, A. Kraft, and A. B. Holmes, Phys. Rev. B 46, 15072 (1992); (d) X. Wei, B. C. Hess, Z. V. Vardeny, and F. Wudl, Phys. Rev. Lett. 68, 666 (1992).

[29] (a) J. Shinar, Syn. Met. 78, 277 (1996); (b) W. Graupner, J. Partee, J. Shinar, G. Leising, and U. Scherf, Phys. Rev. Lett. 77, 2033 (1996); (c) N. C. Greenham, J. Shinar, J. Partee, P. A. Lane, O. Amir, F. Lu, and R. H. Friend, Phys. Rev. B 53, 13528 (1996); (d) J. Shinar, in *Handbook of Organic Conductive Molecules and Polymers: Vol. 3. Conductive Polymer: Spectroscopy and Physical Properties*, edited by H. S. Nalwa, Chap. 7., pp. 319-366 (J. Wiley, NY, 1997); (e) E. J. W. List, C. H. Kim, W. Graupner, G. Leising, and J. Shinar, Syn. Met. (in press).

[30] E. J. W. List, J. Partee, J. Shinar, U. Scherf, K. Müllen, E. Zojer, K. Petritsch, G. Leising, and W. Graupner, Phys. Rev. B 61, 10807 (2000).

[31] Z. V. Vardeny and X. Wei, Mol. Cryst. Liq. Cryst. 256, 465 (1994).

[32] (a) R. Kersting, U. Lemmer, M. Deussen, H. J. Bakker, R. F. Mahrt, H. Kurz, V. I. Arkhipov, H. Bässler, and E. O. Göbel, Phys. Rev. Lett. 73, 1440 (1994); (b) Yu. V. Romanovskii, A. Gerhard, B. Schweitzer, R. I. Personov, and H. Bässler, Chem. Phys. 249, 29 (1999); (c) B. Schweitzer, V. I. Arkhipov, and H. Bässler, Chem. Phys. Lett. 304, 365 (1999); (d) B. Schweitzer, V. I. Arkhipov, U. Scherf, and H. Bässler, Chem. Phys. Lett. 313, 57 (1999); (e) Yu. V. Romanovskii, A. Gerhard, B. Schweitzer, U. Scherf, R. I. Personov, and H. Bässler, Phys. Rev. Lett. 84, 1027 (2000); (f) B. Schweitzer and H. Bässler, Syn. Met. 109, 1 (2000).

[33] (a) E. M. Conwell and H. A. Mizes, Phys. Rev. B 51, 6953 (1995); (b) H. A. Mizes and E. M. Conwell, Syn. Met. 68, 145 (1995); (c) E. M. Conwell, Syn. Met. 83, 101 (1996); (d) E. M. Conwell, J. Perlstein, and S. Shaik, Phys. Rev. B 54, R2308 (1996); (e) E. M. Conwell, Phys. Rev. Lett. 78, 4301 (1997); (f) E. M. Conwell, Syn. Met. 85, 995 (1997); (g) M. W. Wu and E. M. Conwell, Phys. Rev. B 56, R10060 (1997).

[34] R. H. Friend, R. W. Gymer, A. B. Holmes, J. H. Burroughes, R. N. Marks, C. Taliani, D. D. C. Bradley, D. A. Dos Santos, J. L. Brédas, M. Lögdlund, and W. R. Salaneck, Nature 397, 121 (1999).

[35] V. Dyakonov, G. Rösler, M. Schwoerer, and E. L. Frankevich, Phys. Rev. B 56, 3852 (1997).

[36] J. Partee, E. L. Frankevich, B. Uhlhorn, J. Shinar, Y. Ding, and T. J. Barton, Phys. Rev. Lett. 82, 3673 (1999).

[37] Z. Shuai, D. Beljonne, R. J. Silbey, and J. L. Bredas, Phys. Rev. Lett. 84, 131 (2000).

[38] J.-S. Kim, P. K. H. Ho, N. C. Greenham, and R. H. Friend, J. Appl. Phys. 88, 1073 (2000).

[39] M. Wohlgenannt, Kunj Tandon, S. Mazumdar, S. Ramasesha, and Z. V. Vardeny, Nature 409, 494 (2001).

[40] (a) M. A. Baldo, D. F. O'Brien, Y. You, A. Shoustikov, S. Sibley, M. E. Thompson, and S. R. Forrest, Nature 395, 151 (1998); (b) D. F. O'Brien, M. A. Baldo, M. E. Thompson, and S. R. Forrest, Appl. Phys. Lett. 74, 442 (1999).

[41] T. Tsutsui, M.-J. Yang, M. Yahiro, K. Nakamura, T. Watanabe, T. Tsuji, Y. Fukuda, T. Wakimoto, and S. Miyaguchi, Jpn. J. Appl. Phys. 38, L1502 (1999).

[42] C. Adachi, M. A. Baldo, and S. R. Forrest, J. Appl. Phys. 87, 8049 (2000).

[43] J. Staudigel, M. Stössel, F. Steuber, and J. Simmerer, J. Appl. Phys. 86, 3895 (1999).

[44] G. Gustafsson, Y. Cao, G. M. Treacy, F. Klavetter, N. Colaneri, and A. J. Heeger, Nature 357, 447 (1992).

[45] Y. Gao, G. Yu, C. Zhang, R. Menon, and A. J. Heeger, Syn. Met. 87, 171 (1997).

[46] D. Braun and A. J. Heeger, Appl. Phys. Lett. 58, 1982 (1991).

[47] P. Brömas, J. Birgersson, N. Johansson, M. Lögdlund, W. R. Salaneck, Syn. Met. 74, 179 (1995).

[48] F. Li, H. Tang, J. Anderegg and J. Shinar, Appl. Phys. Lett. 70, 1233 (1997)

[49] A. Kahn, in *Organic Electroluminescent Materials and Devices*, edited by S.-T. Lee, Proc. of the International Union of Materials Research Societies' 6th International Conference in Asia, and J. Mat. Sci. Eng. B (in press).

[50] (a) C. Schmitz, P. Pösch, M. Thelakkat, and H.-W. Schmidt, Phys. Chem. Chem. Phys. 1, 1777 (1999); (b) H.-W. Schmidt, C. Schmitz, P. Pösch, and M. Thelakkat, in *Organic Light-Emitting Materials and Devices III*, edited by Z. H. Kafafi, Proc. SPIE 3797, 58 (1999).

[51] N. C. Greenham, S. C. Moratti, D. D. C. Bradley, A. B. Holmes, and R. H. Friend, Nature 365, 628 (1993).

[52] N. C. Greenham and R. H. Friend, this volume.

[53] (a) W. Reiss, in *Organic Electroluminescent Materials and Devices*, edited by S. Miyata and H. S. Nalwa, Chap. 2 (Gordon & Breach, NY, 1997); (b) www.erichsen.de.

[54] Y. Yang, this volume.

[55] http://www.cdtltd.co.uk.

[56] E. Haskal, P. C. Duineveld, C. Liedenbaum, P. v. d. Weijer, J. N. Huiberts, and R. J. Visser, in *Organic Electronic and Photonic Materials and Devices*, Proc. Mat. Res. Soc. Symp. 660 (2001), in press.

[57] Y. Koide, Q. Wang, J. Cui, D. D. Benson, and T. J. Marks, J. Amer. Chem. Soc. 122, 11266 (2000).

[58] For sources of the ITO supply see e.g. the industry directories at http://www.sid.org/.

[59] See e.g. http://www.appliedfilms.com/

[60] K. Sugiyama, H. Ishii, Y. Ouchi, and K. Seki, J. Appl. Phys. 87, 295 (2000).

[61] F. Li, H. Tang, J. Shinar, O. Resto, and S. Z. Weisz, Appl. Phys. Lett. 70, 2741 (1997).

[62] M. Ishii, T. Mori, H. Fujikawa, S. Tokito, and Y. Taga, J. Lumin. 87-89, 1165 (2000).

[63] See http://www.emagin.com/

[64] Y. Yang, W. Westerweele, C. Zhang, P. Smith, and A. J. Heeger, J. Appl. Phys. 77, 694 (1995).

[65] Y. Gao, G. Yu, C. Zhang, R. Menon, and A. J. Heeger, Syn. Met. 87, 171 (1997).)

[66] G. G. Malliaras, Y. Shen, and J. C. Scott, in *Organic Light-Emitting Materials and Devices IV*, edited by Z. H. Kafafi, Proc. SPIE 4105, xxx (2000).

[67] (a) H. Aziz, Z. D. Popovic, N.-X. Hu, A.-M. Hor, and G. Xu, Science 238, 1900 (1999); (b) E. W. Forsythe, M. A. Abkowitz, Yongli Gao, and C. W. Tang, J. Vac. Sci. Tech. A 18, 1869 (2000).

[68] W.-L. Yu, J. Pei, Y. Cao, and W. Huang, J. Appl. Phys. 89, 2343 (2001).

[69] H. Murata, C. D. Merritt, and Z. H. Kafafi, IEEE Journal of Selected Topics in Quantum Electronics 4, 119 (1998).

[70] H. Spreitzer, H. Schenk, J. Salbeck, F. Weissoertel, H. Riel, and W. Reiss, in *Organic Light Emitting Materials and Devices III*, edited by Z. H. Kafafi, Proc. SPIE 3797, 316 (SPIE, Bellingham, WA, 1999).

[71] Y. Shirota, J. Mater. Chem. 10, 1 (2000).

[72] (a) C. Adachi, T. Tsutsui, and S. Saito, Appl. Phys. Lett. 56, 799 (1990); (b) Y. Hamada, C. Adachi, T. Tsutsui, and S. Saito, Jpn. J. Appl. Phys. 31, 1812 (1992); (c) Y. Hamada, C. Adachi, T. Tsutsui, and S. Saito, Optoelectronics - Devices and Technologies 7, 83 (1992).

[73] (a) H. Tokailin, H. Higashi, and C. Hosokawa, U. S. Patent No. 5,130,630 (1992); (b) H. Tokailin, M. Matsuura, H. Higashi, C. Hosokawa and T. Kusumoto, in *Electroluminescence: New Materials for Devices and Displays*, edited by E. M. Conwell, M. Stolka, and M. R. Miller, SPIE 1910, 38 (1993); (c) C. Hosokawa, H. Tokailin, H. Higashi, and T. Kusumoto, J. Appl. Phys. 78, 5831 (1995); (d) C. Hosokawa, H. Higashi, H. Nakamura, and T. Kusumoto, .Appl. Phys. Lett. 67, 3853 (1995);

[74] See, e.g., http://www.aldrich.com, http://www.hwsands.com,
and http://www.dojindo.com.

[75] G. Parthasarathy, P. E. Burrows, V. Khalfin, V. G. Kozlov, and S. R. Forrest, .Appl. Phys. Lett. 72, 2138 1(998).

[76] L.S. Hung, L.S. Liao, C. S. Lee and S. T. Lee, J. Appl. Phys. 86, 4607 (1999).

[77] J. Kido, in *Organic Electroluminescent Materials and Devices*, edited by S. Miyata and H. S. Nalwa (Gordon & Breach, Amsterdam, 1997), Chap. 10.

[78] J. Kido, M. Kimura, and K. Nagai, Science 267, 1332 (1995).

[79] J. Kido, C. Ohtaki, K. Hongawa, K. Okuyama, and K. Nagai, Jap. J. Appl. Phys. 32, L917 (1993).

[80] Y. Hamada, in *Organic Electroluminescent Materials and Devices*, edited by S. Miyata and H. S. Nalwa (Gordon & Breach, Amsterdam, 1997), Chap. 9.

[81] M. A. Baldo, D. F. O'Brien, Y. You, A. Shoustikov, S. Sibley, M. E. Thompson, and S. R. Forrest, Nature 395, 151 (1998).

[82] T. Tsutsui, M.-J. Yang, M. Yahiro, K. Nakamura, T. Watanabe, T. Tsuji, Y. Fukuda, T. Wakimoto, and S. Miyaguchi, Jpn. J. Appl. Phys. 38, L1502 (1999).

[83] (a) I. Sokolik, Z. Yang, F. E. Karasz, and D. C. Morton, J. Appl. Phys. 74, 3584 (1993); (b) Z. Yang, I. Sokolik, F. E. Karasz, Macromol. 26, 1188 (1993).

[84] (a) G. Grem, G. Leditzky, B. Ulrich, and G. Leising, Adv. Mat. 4, 36 (1992); (b) G. Grem and G. Leising, Syn. Met. 55-57, 4105 (1993); (c) C. Ambrosch-Draxl, J. A. Majewski, P. Vogl, and G. Leising, Phys. Rev. B 51, 9668 (1995).

[85] (a) W. Graupner, S. Eder, M. Mauri, G. Leising, and U. Scherf, Syn. Met. 69, 419 (1995); (b) W. Graupner, G. Leising, G. Lanzani, M. Nisoli, S. De Silvestri, and U. Scherf, Chem. Phys. Lett. 246, 95 (1995); (c) G. Grem, V. Martin, F. Meghdadi, C. Paar, J. Stampfl, J. Sturm, S. Tasch, and G. Leising, Syn. Met. 71, 2193 (1995); (d) G. Grem, C. Paar, J. Stampfl, G. Leising, J. Huber, and U. Scherf, Chem. Mat. 7, 2 (1995); (e) J. Stampfl, W. Graupner, G. Leising, and U. Scherf, J. Lumin. 63, 117 (1995); (f) J. Stampfl, S. Tasch, G. Leising, and U. Scherf, Syn. Met. 71 2125 (1995); (g) S. Tasch, A. Niko, G. Leising, and U. Scherf, Appl. Phys. Lett. 68, 1090 (1996);

(h) W. Graupner, G. Leditzky, G. Leising, U. Scherf, Phys. Rev. B 54, 7610 (1996); (i) W. Graupner, G. Leising, G. Lanzani, M. Nisoli, S. De Silvestri, and U. Scherf, Phys. Rev. Lett. 76, 847 (1996); (j) W. Graupner, J. Partee, J. Shinar, G. Leising, and U. Scherf, Phys. Rev. Lett. 77, 2033 (1996); (k) G. Kranzelbinder, H. J. Byrne, S. Hallstein, S. Roth, G. Leising, U. Scherf, Phys. Rev. B 56, 1632 (1997).

[86] (a) Y. Ohmori, M. Uchida, K. Muro, and K. Yoshino, Jpn. J. Appl. Phys. 30, L1938 (1991); (b) Y. Ohmori, M. Uchida, K. Muro, and K. Yoshino, Sol. St. Comm. 80, 605 (1991); (c) Y. Ohmori, C. Morishima, M. Uchida, and K. Yoshino, Jpn. J. Appl. Phys. 31, L568 (1992).

[87] D. Braun, G. Gustafsson, D. McBranch, and A. J. Heeger, J. Appl. Phys. 72, 564 (1992).

[88] N. C. Greenham, A. R. Brown, D. Bradley, and R. H. Friend, Syn. Met. 57, 4134 (1993).

[89] (a) G. G. Malliaras, J. K. Herrema, J. Wildeman, and G. Hadziioannou, Adv. Mat. 5, 721 - 723 (1993); (b) R. E. Gill, G. G. Malliaras, J. Wildeman, and G. Hadziioannou, Adv. Mat. 6, 132 - 135 (1994).

[90] (a) M. Berggren, G. Gustafsson, O. Inganäs, M. R. Andersson, T. Hjertberg, and O. Wennerström, J. Appl. Phys. 76, 7530 (1994); (b) M. Berggren, O. Inganäs, G. Gustafsson, J. Rasmusson, M. R. Andersson, T. Hjertberg, and O. Wennerström, Nature 372, 444 (1994); (c) M. R. Andersson, M. Berggren, O. Inganäs et al., Macromol. 28, 7525 (1995); (d) O. Inganäs, in *Organic Electroluminescent Materials and Devices*, edited by S. Miyata and H. S. Nalwa (Gordon & Breach, Amsterdam, 1997), Chap. 3.

[91] B. Thémans, W. R. Salaneck, and J. L. Brédas, Syn. Met. 28, C359 (1989).

[92] Y. Ohmori, M. Uchida, K. Muro, and K. Yoshino, Jpn. J. Appl. Phys. 30, L1941 (1991).

[93] (a) A. W. Grice, D. D. C. Bradley, M. T. Bernius, M. Inbasekaran, W. W. Wu, and E. P. Woo, Appl. Phys. Lett. 73, 629 (1998); (b) M. Bernius, M. Inbasekaran, E. Woo, W. Wu, and L. Wujkowski, in *Organic Light Emitting Materials and Devices*, edited by Z. H. Kafafi, Proc. SPIE 3797, 129 (SPIE, Bellingham, WA, 1999).

[94] (a) W.-L. Yu, Y. Cao, J. Pei, W. Huang, and A. J. Heeger, Appl. Phys. Lett. 75, 3270 (1999); (b) D. Sainova, T. Miteva, H. G. Nothofer, U. Scherf, I. Glowacki, J. Ulanski, H. Fujikawa, and D. Neher, Appl. Phys. Lett. 76, 1810 (2000); (c) X. Jiang, S. Liu, H. Ma, and A. K.-Y. Jen, Appl. Phys. Lett. 76, 1813 (2000); (d) K. S. Whitehead, M. Grell, D. D. C. Bradley, M. Jandke, and P. Strohriegl Appl. Phys. Lett. 76, 2946 (2000).

[95] (a) K. Tada, H. Sawada, J. Kyokane, and K. Yoshino, Jpn. J. Appl. Phys. 34, L1083 (1995); (b) K. Tada, R. Hidayat, M. Hirohata, H. Kajii, S. Tatsuhara, A. Fujii, M. Ozaki, M. Teraguchi, T. Masuda, and K. Yoshino, in *Optical Probes of Conjugated Polymers*, edited by Z. Valy Vardeny and Lewis J. Rothberg, Proc. SPIE 3145, 171 (1997).

[96] I. Gontia, S .V. Frolov, M. Liess, E. Ehrenfreund, Z. V. Vardeny, K. Tada, H. Kajii, R. Hidayat, A. Fujii, K. Yoshino, M. Teraguchi, and T. Masuda, Phys. Rev. Lett. 82, 4058 (1999).

[97] A. Shukla and S. Mazumdar, Phys. Rev. Lett. 83, 3944 (1999).

[98] D. Braun and A. J. Heeger, Appl. Phys. Lett. 58, 1982 (1991).

[99] Y. Park, V. E. Choong, B. R. Hsieh, C. W. Tang, T. Wehrmeister, K. Mullen, and Y. Gao, J. Vac. Sci. technol A 15, 2574 (1997).

[100] Y. Park, V. E. Choong, Ettedgui, Y. Gao, B. R. Hsieh, T. Wehrmeister, and K. Mullen, Appl. Phys. Lett. 69, 1080 (1996).
[101] I. G. Hill, A. Rajopal, A. Kahn, and Y. Hu, Appl. Phys. Lett. 73, 662 (1998).
[102] W. Brutting, E. Buchwald, G. Egerer, M. Meier, K. Zuleeg, and M. Schwoerer, Synth. Met. 84, 677 (1997).
[103] J. Birgerson, M. Fahlman, P. Broms, and W. R. Salaneck, Synth. Met. 80, 125 (1996).
[104] W. R. Salaneck and J. L. Bredas, Adv. Mater. 8, 48 (1996).
[105] V. E. Choong, Y. Park, N. Shivaparan, C. W. Tang, and Y. Gao, Appl. Phys. Lett. 71, 1005 (1997).
[106] V. E. Choong, Y. Park, Y. Gao, T. Wehrmeister, K. Mullen, B. R. Hsieh, and C. W. Tang, . Vac. Sci. Technol. A 15, 1745 (1997).
[107] V. E. Choong, Y. Park, Y. Gao, T. Wehrmeister, K. Mullen, B. R. Hsieh, and C. W. Tang, Appl. Phys. Lett. 69, 1492 (1996).
[108] Y. Park, V. E. Choong, B. R. Hsieh, C. W. Tang, and Y. Gao, Phys. Rev. Lett. 78, 3955 (1997).
[109] P. Broms, J. Birgerson, and W. R. Salaneck, Syn. Met. 88, 255 (1997).
[110] L. S. Hung, C. W. Tang, and M. G. Mason, Appl. Phys. Lett. 70, 152 (1997).
[111] G. E. Jabbour, B. Kippelen, N. R. Armstrong and N. Peyghambarian, Appl. Phys. Lett. 73 (1998) 1185
[112] H. Ishii, K. Sugiyama, E. Ito, and K. Seki, Adv. Mater. 11, 605 (1999).
[113] J. Kalinowski, in *Organic Electroluminescent Materials and Devices*, edited by S. Miyata and H. S. Nalwa (Gordon & Breach, Amsterdam, 1997), Chap. 1.
[114] J. H. Schön, S. Berg, Ch. Kloc, and B. Batlogg, Science 287, 1022 (2000).
[115] M. Raikh and X. Wei, Mol. Cryst. Liq. Cryst. 256, 563 (1994).
[116] U Lemmer, M. Scheidler, R. Kersting, R. F. Mahrt, H. Kurz, H. Bässler, E. Gobel and P. Thomas, in *Hopping and Related Phenomena: Proceedings of the 6th international conference on Hopping and Related Phenomena*, edited by O. Millo and Z. Ovadyahu, p. 400 (Jerusalem, Israel. 1995).
[117] (a) A. Miller and E. Abrahams, Phys. Rev. 120, 7455 (1960) ; (b) S. V. Frolov, M. Leiss, P. A. Lane, W. Gellerman and Z. V. Vardeny, Phys. Rev. Lett. 78, 4285 (1997).
[118] (a) A. J. Pal, R. Osterbacka, K. M. Kallman, and H. Stubb. Appl. Phys. Lett. 71, 228 (1997); (b) S. Karg, V. Dyakonov, M. Meier, W. Reiss, G.Paasch, Synth. Met. 67, 165 (1994).
[119] (a) S. Naka, H. Okada, H. Onnagawa, Y. Yamaguchi, and T. Tsutsui, Synth. Met. 111-112, 331 (2000); (b) B. J. Chen, W. Y. Lai, Z. Q. Gao, C. S. Lee, S. T. Lee, and W. A. Gambling, Appl. Phys. Lett.75, 4010 (1999); (c) A. J. Campbell, D. D. C. Bradley, H. Antoniadis, M. Inbasekaran, W. W. Wu, and E. P. Woo, Appl. Phys. Lett.76, 1734 (2000); (d) E. W. Forsythe, M. A. Abkowitz, Y. Gao and C.W. Tang, J. Vac. Sci. & Tech. A18, 1869 (2000); (e) H. Meyer, D. Haarer, H. Naarmann, and H. H. Horhold, Phys. Rev. B 52, 2587(1995); (f) E. Lebedev, Th. Dittrich, V. Petrova-Koch, S. Karg, and W. Brutting, Appl. Phys. Lett. 71, 2686 (1997); (g) P. M. Borsenberger, L. Pautimeier, and H. Bässler, J. Chem. Phys. 95, 1258 (1991).
[120] (a) I. H. Campbell, D. L. Smith, C. J. Neef, and J. P. Ferraris. Appl. Phys. Lett. 74, 2809 (1999); (b) W. Brutting, E. Lebedev, S. Karg, T. Dittrich, V. Petrova-Koch, and M. Schwoerer, SPIE 3281, 251 (1998).
[121] N. Camaioni, G. Casalbore-Miceli, A. Geri, S. Nicoletti, Adv. Mater. 11, 472 (1999).
[122] (a) M. Dongge, I. A. Hummelgen, B.Hu, F.E. Karasz, J. Appl. Phys. 86, 3181 (1999); (b) P. W. M. Blom, M. J. M. de Jong, and M. G. van Munster, Phys. Rev. B 55, R656 (1997);

[123] H. A. Mizes and E.M. Conwell, Phys. Rev. Lett. 70, 1505 (1993).
[124] E. M. Conwell, Phys. Rev. B 57, R12670 (1998).
[125] L. B. Shein, Phil.Mag. B 65, 795 (1992).
[126] T. Blum and H. Bässler, Chem. Phys. 123, 431 (1988).
[127] P. M. Borsenberger, L. Pautmeier and H. Bässler, J. Chem. Phys. 95, 1258 (1991).
[128] D. H. Dunlap, P. E. Parris and V. M. Kenkre, Phys. Rev. Lett. 77, 542 (1996).
[129] Yu. N. Gartstein and E. M. Conwell, Chem. Phys. Lett. 245, 351 (1995).
[130] D. H. Dunlap, P. E. Parris and V. M. Kenkre, Phys. Rev. Lett. 77, 542 (1996).
[131] S. V. Novikov, D. H. Dunlap, V. M. Kenkre, P. E. Parris and A. V. Vannikov, Phys. Rev. Lett. 81, 4472 (1998).
[132] S. W. DeLeeuw, J. W. Perram and E. R. Smith, Proc. R. Soc. London A 373, 27 (1989).
[133] S. V. Novikov and A. V. Vannikov, JETP 79, 482 (1994).
[134] V. I. Arkhipov, E. V. Emelianova, Y. H. Tak and H. Bassler, J. Appl. Phys. 84, 848 (1998).
[135] P. S. Davids, Sh. M. Kogan, I. D. Parker, and D. L. Smith, Appl. Phys. Lett. 69, 2270 (1996).
[136] Yu.N.Gartstein and E.M.Conwell, Chem.Phys. Lett. 255, 93 (1996).
[137] E.M. Conwell and M.W. Wu, Appl. Phys. Lett. 70, 1867 (1997).
[138] V. N. Savvate'ev and Z. Ovadyahu, "Slow Relaxation in a Fermi Glass," in *Hopping and Related Phenomena: Proceedings of the 6th International Conference on Hopping and Related Phenomena*, edited by O. Millo and Z. Ovadyahu, p. 44 (1995).
[139] M. A. Lampert and P. Mark, *Current Injection in Solids*, (Academic Press, NY, 1970).
[140] P. E. Burrows, Z. Shen, V. Bulovic, D. M. McCarty, S. R. Forrest, J. A. Cronin, and M. E. Thompson, J. Appl. Phys. 79, 7991 (1996).
[141] (a) P. S. Davids, I. H. Campbell, and D. Smith. J. Appl. Phys. 82, 6319 (1997); (b) D. Ma, I. Hummelgen, B. Hu, and F. E. Karasz, J. Phys. D: Appl. Phys. 32, 2568 (1999); (c) M. Koehler and I. A. Hummelgen, J. Appl. Phys. 87, 3074 (2000).
[142] (a) P. W. M. Blom, M. J. M. de Jong, and S. Breedijk. Appl. Phys. Lett. 71, 930 (1997; (b) S. Berleb, W. Brutting, and M. Schwoerer, J. Appl. Phys. 83, 4403 (1998); (c) B. K. Crone, P. S. Davids, I. H. Campbell, and D. L. Smith, J.Appl. Phys. 84, 833 (1998).
[143] (a) M. G. Harrison, J. Gruner, and G. C. W. Spencer, Syn. Met. 76, 71 (1996); (b) A. J. Campbell, D. D. C. Bradley, and D. G. Lidzey, J. Appl. Phys. 82, 6326 (1997); (c) M. Meier, S. Karg, and W. Reiss, J. Appl. Phys. 82, 1961 (1997); (d) H. C. F. Martens, H. B. Brom, and P. W. M. Blom, Phys. Rev. B 60, R8489 (1999).
[144] A. Ioannidis, E. Forsythe, Yongli Gao, M. W. Wu, and E. M. Conwell, Appl. Phys. Lett. 72, 3038 (1998).
[145] M. Matsumura, A. Ito, and Y. and Miyama, Appl. Phys. Lett. 75, 1042 (1999).
[146] J.-S. Kim, P. K. H. Ho, N. C. Greenham, and R. H. Friend, J. Appl. Phys. 88, 1073 (2000).
[147] E. W. Forsythe, M. A. Abkowitz, Yongli Gao, J. Phys. Chem. B 104, 3948 (2000).
[148] (a) D. Oelkrug, A. Tompert, H.-J. Egelhaaf, M. Hanack, E. Steinhuber, M. Hohloch, H. Meier, and U. Stalmach, Syn. Met. 83, 231 (1996); (b) D. Oelkrug, A. Tompert, J. Gierschner, H.-J. Egelhaaf, M. Hanack, M. Hohloch, and E. Steinhuber, in *Optical Probes of Conjugated Polymers*, edited by Z. Valy Vardeny and L. J. Rothberg, SPIE Conf. Proc. 3145, 242 (1997).
[149] J. C. de Mello, H. F. Wittmann, and R. H. Friend, Adv. Mat. 9, 230 (1997).

[150] Y. Sato, S. Ichinosawa, and H. Kanai, IEEE Journal of Selected Topics in Quantum Electronics 4(1), 40 (1998).
[151] J. Mc Elvain, H. Antoniadis, M. R. Hueschen, J. N. Miller, D. M. Roitman, J. R. Sheats, and R. L. Moon, J. Appl. Phys. 80, 6002 (1996).
[152] V. N. Savvate'ev, A. V. Yakimov, D. Davidov, R. M. Pogreb, R. Neumann, and Y. Avny, Appl. Phys. Lett. 71, 3344 (1997).
[153] L. M. Do, K. Kim, T. Zyung, H. K. Shim and J. J. Kim, Appl. Phys. Lett. 70, 3470 (1997).
[154] B. H. Cumpston and K. F. Jensen, Appl. Phys. Lett. 69, 3941 (1996).
[155] B. H Cumpston and K. F. Jensen, Syn. Met. 73, 195 (1995).
[156] B. H. Cumpston, I. D. Parker, and K. F. Jensen, J. Appl. Phys. 81, 3716 (1997)
[157] B. H. Cumpston and K. F. Jensen, Trends in Polymers 4, 151 (1996).
[158] D. G. Sutherland, J. A. Carlisle, P. Elliker, G. Fox, T. W. Hagler, I. Jimenez, H. W. Lee, K. Pakbaz, L. J. Terminello, S. C. Williams, F. G. Himpsel, D. K. Shuh, W. M. Tong, J. J. Jia, T. A. Callcott and D. L. Ederer, Appl. Phys. Lett. 68, 2046 (1996).
[159] S. T. Lee, Z. Q. Gao, and L. S. Hung, Appl. Phys. Lett. 75, 1404 (1999).
[160] M. P. de Jong, D. P. L. Simons, M. A. Reijme, L. J. van Ijzendoorn, A. W. Denier van der Gon, M. J. A. de Voigt, H. H. Brongersma, and R. W. Gymer, Syn. Met. 110, 1 (2000).
[161] H. Aziz, Z. D. Popovic, N.-X. Hu, A.-M. Hor, and G. Xu, Science 238, 1900 (1999).
[162] V. Savvateev, A. Yakimov, and D. Davidov, Adv. Mat. 11, 519 (1999).
[163] L. E. Tannas, in *Flat-Panel Displays and CRTs*. Ed. L. E. Tannas, Van Nostrand Reinhold, NY, 1984, p.266
[164] N. Tessler, G. J. Denton, and R. H. Friend, Nature 382, 695 (1996).
[165] C. Zenz, W. Graupner, S. Tasch, G. Leising, K. Iskra, J. Flieser, and T. Neger, J. Appl. Phys. 84, 5445 (1998).

2

Molecular LED: Design Concept of Molecular Materials for High-Performance OLED

Chihaya Adachi and Tetsuo Tsutsui

2.1 Introduction

The recent rapid development of organic light-emitting diodes (OLEDs) has resulted in the commercialization of simple dot-matrix OLED displays.[1] The great success of OLED devices has also introduced a brand new organic semiconductor. Now, we are in the process of designing the physical and chemical makeup of this new type of organic semiconductor. In this chapter, first we will briefly describe the OLED development from the 1960s to the 1980s. Second, we will define the new organic semiconductor especially utilized for OLED devices and clarify what the organic semiconductor is and how it differs from the conventional inorganic semiconductor. Then, we will review the recent OLED progress by taking the following aspects into consideration: the design of multilayer cell structures, the design of each molecular constituents, hole transport, electron transport, and emitter and dopant molecules. Finally, we will discuss the future prospects of OLEDs.

2.2 OLED Development from the 1960s to the 1980s

The recent progress in OLEDs can be dated back to the early research of the 1950s. Thus, it has taken 40 years for this technology to become commercialized. Bernanose et al. first reported on electroluminescence (EL) by utilizing molecularly dispersed polymer films.[2–4] Although they insisted on the similar excitation and emission mechanisms that had been established in inorganic EL in those days, it was understood by Hercules et al. that the emission was induced from the secondary ultraviolet light by a glow discharge between two electrodes.[5] During these early experiments, a very interesting chance is the aluminum quinolinol (Alq), which is one of the most promising compounds in the recent OLED devices, used in this experiment.

In the 1960s, research moved on to the carrier-injection type of electroluminescence, namely OLED, by using a highly purified condensed aromatic single crystal, especially an anthracene. Pope et al.,[6,7] and W. Helfrich et al.,[8,9] in particular, experimented on carrier recombination and the emission mechanism, and their physical interpretation is still very useful today. Whereas a highly purified zone-refined anthracene single crystal essentially shows a conductivity of 10^{-20} S/cm, double injection of holes and electrons, however, were achieved efficiently based on space-charge-limited current (SCLC) with the equipment of charge-carrier-injection electrodes, and resulted in a successive carrier recombination, the creation of single and triplet excitons, and the radiative decay of them. Thus, the basic EL process has been established since the 1960s.

From the 1970s to the 1980s in addition to the studies on the EL mechanism [10–20] the focus of research shifted from single crystals to organic thin films. Based on the successful research on anthracene single crystals, various aromatic compounds were examined by using vacuum vapor deposition.[21–24] The morphology of polycrystalline films, however, was insufficient for stable current injection and transport. Moreover, although another thin-film fabrication method—the Langumir–Blodgett method—was examined, similar unstable behavior prevented further consideration.[25] Thus, in the thin-film devices, two major target areas for efficient EL were pointed out: improving the carrier-injection electrodes, in particular, electron injection, and forming pinhole-free thin films. This basic research was extremely important and provided a foundation for the continuation of EL development.

Judging from the present OLED status, the most important research was Partridge's report on the EL utilized poly(vinyl carbazole) (PVCz) thin films in 1982.[26–29] He used the 500-nm-thick PVCz thin films doped with fluorescent molecules as an emissive center, equipped with the efficient hole-injection electrode ($SbC1_5$/PVCz) and the electron-injection electrode (cesium) as a low-workfunction metal. Although no quantitative measurement of luminance was described, surprisingly the injection current density reached 1 mA/cm^2. Nowadays, we can fabricate very similar OLED devices with superior EL performance. Thus, Partridge's device contributed to establishing the prototypes of present OLED devices.

Next, in the 1980s, the organic multilayer structures, which are another key technology of present high-performance OLEDs, appeared. In 1986, Hayashi et al. observed a remarkable reduction of the driving voltage by inserting a polythiophene-electropolymerized thin film between an indium–tin–oxide (ITO) anode and a perylene-deposited film.[30] The insertion of the polythiophene thin film greatly contributed to the enhancement of hole-injection efficiency and also device stability. This is the first report on an organic double layer—a combination of a hole-transport layer (HTL) and an electron-transport layer (ETL). At the same time, in 1987, Tang et al. proposed the astonishing double-layer OLED device composed of ITO/HTL/ETL/MgAg, where an ETL was combined with an emitter function.[31] Using a 1,1-bis(4-di-*p*-tolylaminophenyl)-cyclohexane (TPAC) as an HTL and Alq as an ETL, high-EL quantum efficiency (1%), high luminous efficiency (1 lm/W), and fairly good stability (100 h) were reported. Tang et al.'s device demonstrated three major improvements: (1) The adequate combination of HTL and ETL that differs from an inorganic *p*-*n* junction. In particular, TPAC had a unipolar hole-transport characteristic and this layer could block electrons effectively, provided that there were efficient carrier recombination sites at the TPAC/Alq interface. (2) The use of pinhole-free amorphous films. In previous studies, no one examined such a thin-organic-film device at around 50–100 mn, because of the possibility of a strong electrical short circuit. The use of amorphous morphology, however, enabled us to construct submicrometer-sized devices. In addition, the thorough cleaning of ITO substrates, namely the preparation of minute dust-free substrates, was another unknown significant practical point. (3) The utilization of a MgAg alloy cathode, which remains fairly stable with efficient electron injection because of the low-workfunction of Mg atoms.

Based on the Tang's excellent work, the authors examined various combinations of organic molecules and proposed new OLED device structures.[32–36] In particular, the discovery of unipolar electron-transport materials, 2-(4′-biphenyl)-5-(4″*tert*-butylphenyl)-1,3,4-oxadiazole (PBD), greatly expanded the possibilities of OLED materials and cell structures. Thus, we could classify OLED cell structures into three categories.[37] A detailed classification of cell structures is described in Sections 3 and 4.

Now, in the 1990s, the research on OLED devices has proceeded from various aspects. In addition to the low-molecular materials, polymer materials have been widely examined also. Here, we will review the progress of molecular OLEDs in the past 10 years.

2.3 Working Mechanisms of OLED

Here, we have fluorescent organic thin films equipped with two electrodes. With the application of a dc voltage, hole and electron carriers are injected from electrodes, transported inside the organic layer, and recombined with the creation of excited states, to finally result in radiative decay. Although it is easy to misunderstand that OLED devices made of molecular materials have a very similar emission mechanism to conventional inorganic *p*-*n*-junction LEDs, the detailed behavior of inorganic LEDs and OLED is actually quite different. This difference originates from two intrinsically different electronic and optical properties between inorganic and organic semiconductors. The terms of carrier injection, SCLC (space charge limited current) and molecular exciton are the keys to understanding the OLED mechanism.

2.3.1 Charge Carrier Injection and Transport

First, we should recognize that all of the molecular materials useful for OLED behave electrically as an insulator under the condition's of a low electric field ($< 10^4$ V/cm), as was indicated in early studies on anthracene single crystals that demonstrated a resistivity of the order of $10^{20}\Omega$ cm.[38] Also, typical vacuum-sublimed anthracene films showed a resistivity of the order of $10^{15}\Omega$ cm. Furthermore, we need to remember that even one of the typical π-conjugated polymers, poly(p-phenylene vinylene), has an intrinsic resistivity of under $10^{16}\Omega$ cm.[39] These results indicate that carefully purified organic materials possess intrinsically no net charge carriers without chemical doping of donor and acceptor molecules. In OLED devices, however, we could achieve a very high current density of up to 1 A/cm^2 without any difficulty. This fact is inconsistent with the standard knowledge of organic semiconductors. Thus, it is necessary to understand what is controlling the principle of the current flow in organic semiconductors.

The large current density is provided by a carrier injection at an electrode/organic interface and SCLC.[40] The electronic structure of organic thin films is based on the HOMO (highest occupied molecular orbital) and the LUMO (lowest unoccupied molecular orbital) of individual molecules. As each molecule interacts with a weak Van der Waals' force, narrow conduction and valence bands are supposed to form. Furthermore, we can clearly describe the electronic structure of organic thin films using the ionization potential (I_p), electron affinity (E_a), and charge carrier densities (n_h, n_e) and mobilities (μ_h, μ_e) of holes and electrons. The I_p and E_a values relate to carrier injection phenomena, and the charge carrier densities (n_h, n_e) and mobilities (μ_h, μ_e) relate to carrier-transport phenomena. Here, we can point out that the intrinsic carrier densities of organic semiconductors, which presumably are based on unavoidable impurities and irregular structures of thin films, are very low — typically 10^5–10^{10} /cm^{-3}. Also, a typical mobility of organic semiconductors is fairly small, $10^{-3} - 10^{-7}$ cm^2/Vs, compared with that of inorganic materials, $1 - 10^3$ cm^2/Vs. Although these numerical characteristics seem to be obstacles for device fabrication, the formation of ultrathin films provides a possible way to produce organic semiconductors.

When we apply 10 V to a typical 100-nm-thick organic layer, we need to watch for an unexpected high electric field (10^6 V/cm^2), which enables us to induce carrier injection and SCLC. First, we turn our attention to the behavior of current injection from electrodes. We have two possible mechanisms to inject charge carriers: Schottky thermal emission and the tunneling injection processes, both of which are based on the theory of inorganic semiconductors. The Schottky emission process is described by[41]

$$J = \frac{4\pi qmk}{h^3} T^2 \exp\left(-\frac{q\Phi_{\mathrm{Bn}}}{kT}\right)\left[\exp\left(\frac{qV}{kT}\right) - 1\right] \qquad (1)$$

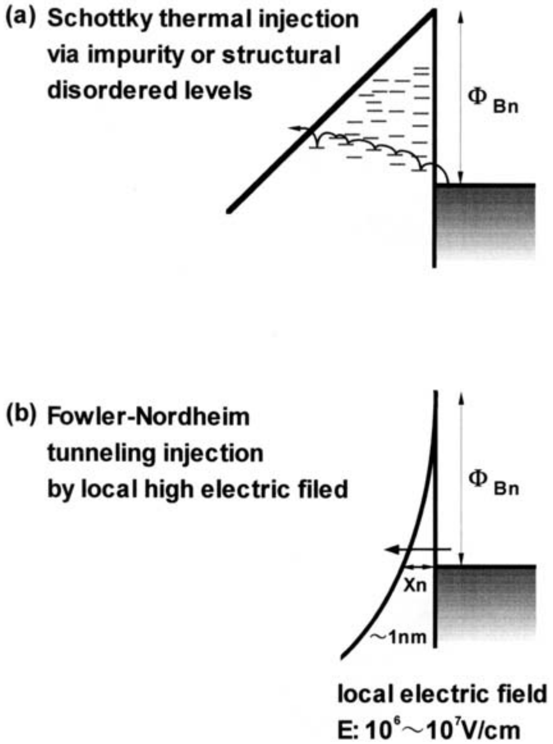
(a) Schottky thermal injection via impurity or structural disordered levels
Φ Bn
(b) Fowler-Nordheim tunneling injection by local high electric filed
Φ Bn
Xn
~1nm
local electric field
E: 10⁶~10⁷V/cm

FIGURE 2.1. Two possible carrier injection mechanisms at the organic/metal electrode; interface: (a) Schottky-type carrier injection via impurity or structural disordered levels with thermal assistance and (b) Fowler–Nordheim tunneling carrier injection with the assistance of a local high electric field (10^6–10^7 V/cm).

where m is the effective mass of the electron (hole); k is Boltzmann's constant, h is Planck's constant, T is the temperature, q is the elementary charge, Φ_{Bn} is the barrier height, and V is the applied voltage.

At the typical Alq/Mg interface, for example, the energy barrier was estimated to be 1.0 eV.[42] From the standpoint of Schottky emission, we could never achieve such a large current density over such a high-energy barrier of 1 eV. As the activation energy of typical OLEDs was found to be around 0.03 eV,[43,44] one of the possible injection mechanisms is through the localized levels induced by structural defects and unexpected impurities, as shown in Fig. 2.1(a). Another possibility of describing carrier injection is by Fowler–Nordheim tunneling injection, as shown in Fig. 2.1(b). The current flow is described by[41]

$$J = \left(\frac{q^3 V^2 m_0}{8\pi h \Phi_{\mathrm{Bn}} m^*}\right) \exp\left(-\frac{4(2m^*)^{0.5}\Phi_{\mathrm{Bn}}^{1.5}}{3\hbar q V}\right), \qquad (2)$$

where m_0 is the mass of the free electron and m^* is the effective mass.

On the basis of this equation, even with the applied electric field of 10^6 V/cm, the estimated tunneling distance exceeds 10 nm, which is not a realistic value. Thus, we have to anticipate the application of local high electric field ($\cong 10^7$ V/cm), between a molecule and a metal electrode; otherwise, the practical energy barrier must be lower than the estimated value if we want to use the tunneling mechanism.

We could inject charge carriers by the two possible mechanisms. Next, we will describe the carrier transport inside organic thin films. When the applied electric field is less than 10^4 V/cm weak and the injected current density (n_{ci}) is less than the intrinsic charge density (n_i), the current flow is governed by Ohm's law. When n_{ci} exceeds n_i with the application of over 10^5 V/cm, however, the injected charge carriers form space charges near the organic/electrode, interface because of low carrier mobility, as shown in Fig. 2.2. Thus, as the internal electric field is enhanced by the space charges, the current density (J) is governed by the SCLC described by[41]

$$J = \frac{9\varepsilon\varepsilon_0\mu V^2}{8L^3} \tag{3}$$

where ε is the relative dielectric constant, ε_0 is the dielectric constant, and L is the sample thickness.

As another aspect, we deal with the phenomenon not under electrostatic equilibrium but under dynamic charge equilibrium when devices are under operation. All charges are assumed to behave as space charges, and no local charge neutrality is expected within organic films. Here, we can estimate the possible current density. In the typical amorphous organic films, by the substitution of $\mu = 1\text{–}10^{-6}$ cm^2/Vs (mobility), $L = 100$ nm (sample thickness), and $V = 0.01\text{–}20$ V (applied voltage), we can obtain an unexpected large current density. Figure 2.2b compares ohmics current and SCLC. Interestingly, we can easily achieve the desired current density of 1 mA/cm^2 to 1 A/cm^2 with only 10 V, if the carrier mobility is larger than 10^{-4} cm^2/V s.

Therefore, by applying 10 V to the thickness of 100 nm ($\cong 10^6$ V/cm), the carrier injection and successive SCLC allow us to achieve practical current density of 1 mA cm^2 to 1 A/cm^2, even though organic semiconductors are a so-called "insulator." Thus, we obtained a new category of the real organic semiconductor. The previous studies on the conducting polymers with a chemical doping surely increased the carrier density under thermal equilibrium and showed semiconducting and metallic properties, similar to the inorganic semiconductors.[44] Thus, we obtained two types of organic semiconductor by distinct methods: chemical doping and the carrier injection–SCLC combination. Although the high conductivity by chemical doping certainly opened up the possibilities of new conducting materials such as solar cells, dielectric condensers, field effect transistors (FETs), and so forth, the chemical doping, however, took the fluorescence away from organic molecules, because of the formation of the charge-transfer complex between them. As it is impossible to maintain the compatibility of conductivity and fluorescence by the doping method, the carrier injection–SCLC combination is indispensible as the foundation of OLED devices.

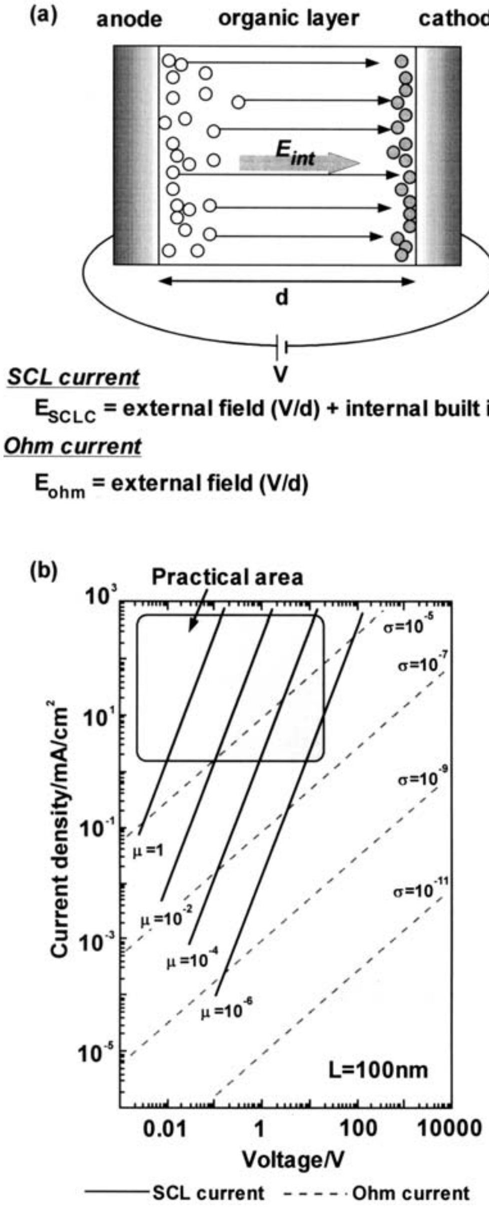

FIGURE 2.2. (a) Schematic view of SCLC. With an external electric field (V/d), an additional internal field (E') induced by injected excess charge carriers plays important role for the achievement of high current density. The total electric field, $E_{\text{total}} = V/d + E'$, significantly enhances current flow. Open symbols (○) corresponds to excess holes, closed symbols (●) correspond to excess electrons. (b) Comparison of J–V characteristics based on ohmic current (dashed line) and SCLC (solid line). The meshed area shows the J–V requisite for practical devices.

2.3.2 *Carrier Recombination and Emission Process*

Neutral excited states, typically singlet excitons, are produced by charge recombination, and emission is due to emissive transitions from neutral excited states to ground states. No experimental evidence on direct emission due to a recombination of positive and negative charges in OLED devices has been provided yet. The previous theoretical consideration[38,45] revealed that carrier recombination creates both singlet (S_1) and triplet excitons (T_1) at a ratio of 1 to 3:

$$4(e + h) \rightarrow S_1 + 3T_1. \tag{4}$$

Furthermore, the T_1–T_1, annihilation creates both of S_1, and T_1:

$$4(T_1 + T_1) \rightarrow S_1 + 3T_1. \tag{5}$$

Thus, in summary,

$$20(e + h) \rightarrow 5S_{\mathrm{dir}} + 3S_{\mathrm{ind}} \tag{6}$$

was estimated in the carrier recombination process. Therefore, even though the fluorescence efficiency is 100%, maximum EL quantum efficiency is limited to 40%.

In addition, we should mention the exciplex formation between adjoining molecules, which is frequent and poses a serious problem for obtaining pure EL colors and high efficiency in organic multilayer solid devices:[46]

$$D^+ + A^- \rightarrow (D \ldots A)^*, \tag{7}$$

$$D^+ + A^- \rightarrow A^* \quad \text{or} \quad D^* \rightarrow (D \ldots A)^*. \tag{8}$$

In most cases, because the exciplex formation results in a low-fluorescence efficiency with long-wavelength emission, we need to prevent it in order to achieve high luminance.

2.3.3 *Estimation of External and Internal Quantum Efficiency*

Figure 2.3 represents the elementary process for charge recombination, beginning with a recombination of holes and electrons and ending with light emission. The external and the internal efficiency are connected by the factor η_{ext}, which is approximately evaluated by using the refractive index of the emissive medium[47] n:

$$\eta_{\mathrm{ext}} = \frac{1}{2n^2}. \tag{9}$$

As the extraction efficiency of light from a thin-film device is limited by Eq. (8), new device structures were proposed to enhance extraction efficiency.[48]

Here, we define external EL quantum efficiency $\eta_\phi(\mathrm{ext})$ by the ratio of the number of emitter photons outside the device divided by the number of charge carriers injected into the device. The internal EL quantum efficiency η_ϕ is defined by the number of photons produced within a device divided by the number of

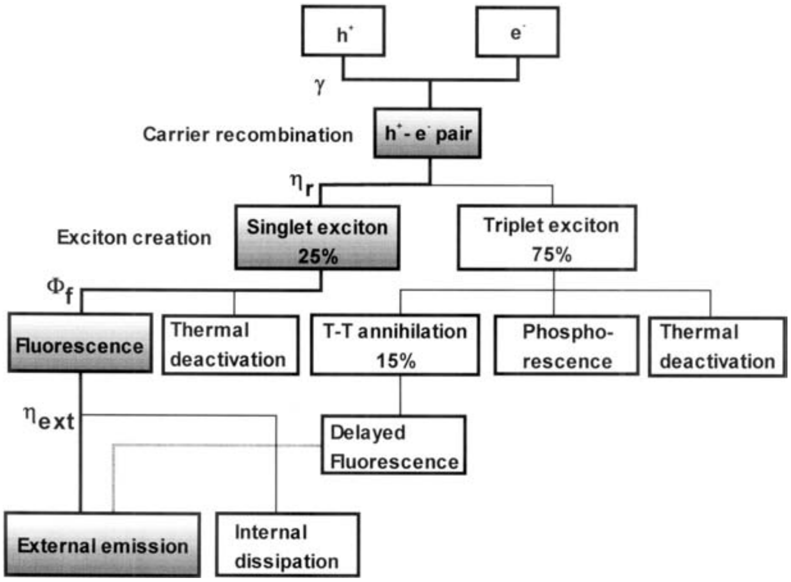

FIGURE 2.3. A schematic representation of the elementary processes for charge carrier recombination, production of molecular excitons, emission, and external emission.

injected charge carriers. Then, $\eta_\phi(\text{ext})$ is expressed by

$$\eta_\phi(\text{ext}) = \eta_\phi \eta_{\text{ext}}. \tag{10}$$

Using the charge-balance factory γ, the efficiency of production for singlet excitons η_r, and the quantum efficiency of fluorescence ϕ_f, the internal quantum efficiency η_ϕ, is given by[49]

$$\eta_\phi = \gamma \eta_r \phi_f. \tag{11}$$

The definition of the charge-balance factor γ can be defined by

$$\gamma = \frac{J_r}{J} \tag{12}$$

using circuit current J and recombination current J_r as shown in Fig. 2.4. Here, the amount of holes and electrons injected from an anode and a cathode is expressed by J_h and J_e, respectively. The amount of holes crossing through an organic layer without recombination with electrons and the amount of electrons crossing through an organic layer without recombination with holes are given by J_h' and J_e' respectively. Thus, the following two equations are derived:

$$J = J_h + J_e' = J_e + J_h' \tag{13}$$

and

$$J_r = J_h - J_h' = J_e - J_e'. \tag{14}$$

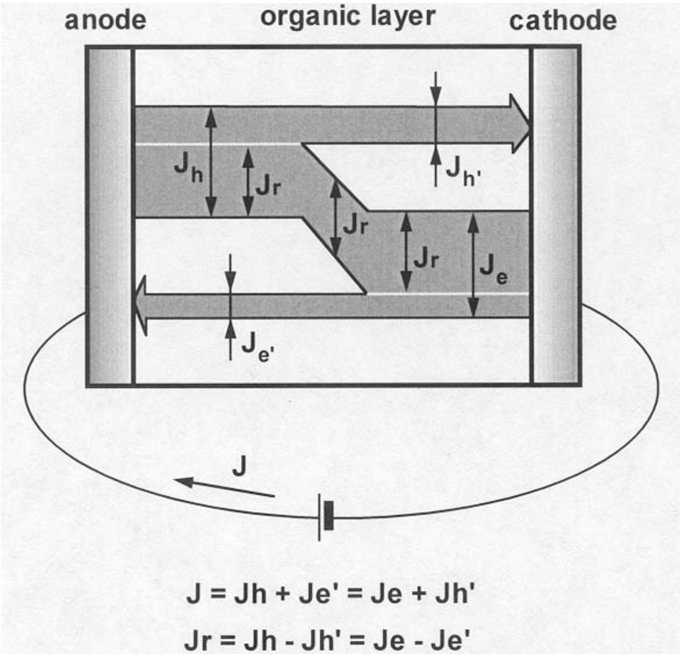

FIGURE 2.4. Current flow of holes and electrons injected and transported inside an organic layer. J_h and J_e are net hole and electron current density, respectively. J_r is the component of recombination current density. J'_h and J'_e correspond to the hole and electron current densities, respectively, without recombination.

Although no direct methods to estimate J_r exists, we can discuss J_r values based on the examination of charge carrier recombination regions.

The relation between the internal energy conversion efficiency η_E which is defined by the ratio of emitter light power and the input electric power (JV), and the internal quantum efficiency is given by

$$\eta_E = \frac{\eta_\phi \varepsilon_p}{eV}, \tag{15}$$

where ε_p and V are the average photon energy of emitter light and applied voltage. Then, applied voltage only appears in the expression of energy conversion efficiency.

Based on the above consideration, the following five issues are keys to maximizing OLED efficiencies:

1. We should attain the charge-balance factor $\gamma = 1.0$.
2. Various combinations of multilayer structures greatly enhance the γ value close to 1.0. [37,50–52]
3. The maximum value for the production of singlet excitons is assumed to be 25%, or 40% when we take into account T–T annihilation, so we should make full use of triplet excitons.

4. Fluorescent molecules with high quantum efficiency should be used. Because of the concentration quenching of molecules in nature, the doping of a slight amount of highly fluorescent molecules into host organic layers is effective.
5. The small carrier injection barrier between electrode and organic layers should be selected.

2.4 Design of Multilayer Structures

Recent studies revealed that organic multilayer structures greatly improved OLED device performance. The most significant aspect of a multilayer structure is the confinement of charge carriers inside an emitter layer by balanced carrier injection and transport.[37,50] Figure 2.5a summarizes three basic OLED structures: SH-H (single hetero-H structure), SH-E (single hetero-E structure), and DH (double heterostructure). We would like to stress that basic cell structures are organic double layers—the combination of HTL and ETL — even though recent high luminance and durable OLED structures are composed of four or five organic layers. In an SH-H structure proposed by Tang and VanSlyke,[31] the carrier recombination occurs inside the ETL, as the ETL has the ability to accept hole injection from the HTM. Thus, the ETL combines the emitter function with an electron transport. On the contrary, in an SH-B structure,[34] the HTL combines the emitter function with a

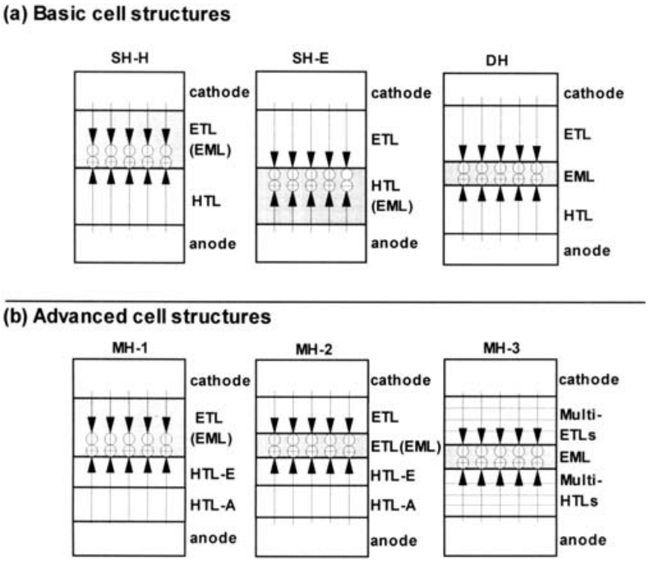

FIGURE 2.5. Three basic OLED structures; SH-H, SH-E, and DH. HTL hole-transport layer, ETL electron-transport layer and EML, and EML emitter-layer. SH-H and SH-E holds both carrier-transport and emitter characters. Advanced OLED structures MH-1, MH-2, and MH-3. Double HTLs and ETLs significantly increase device performance.

hole transport. Furthermore, the separation of the emitter function is attained by the double heterostructure (DH).[36] This structure, in particular, allows us to construct an extremely thin emitter layer of 5 nm that corresponds to a few molecular stacks. Thus, the molecular-size device in the direction vertical to the organic film was achieved, Here, we should stress that a key of the multilayer structures is the utilization of a unipolar HTL or ETL. The unipolar layers surely block the passage of hole or electron carriers and serve as a highly efficient carrier recombination region near the HTL/ETL interface. In fact, the recombination region of multilayer devices is restricted in a very narrow region, typically less than 10 nm, near the HTL/ETL interface. Presumably, the accumulation of hole or electron carriers at the interface contributes to the high recombination probability. On the contrary, in single-layer devices, the recombination region is rather widespreading over 50–100 nm, suggesting a low-carrier-capture cross section.[37,100]

Another significant merit of organic multilayer structures is keeping the energy of molecular excitons from dissipating into the metal electrodes — in other words, the retardation effect between an excited molecule and a metal mirror.[53] It is well known that if excited molecules located near a metal electrode are less than 20 nm, the nonradiative energy transfer to the metal electrode dominantly occurs. Thus, the 50–70-nm-thick HTL and ETL effectively protect molecular excitons from the dissipation process.

Based on the three basic OLED structures, the new multilayer structures (MH1–3) are proposed as summarized in Fig. 2.5b. MH-1 and MH-2 structures are composed of double HTLs[54–56] and ETLs,[57,58] as shown in Figs. 2.5a and 2.5b. The meaning of the double layers is a separation of carrier injection from an electrode and carrier transport. The following are five major requirements that the HTL should have:

1. The HTL should have a small barrier for hole injection from an anode electrode. For the low injection barrier between them, the I_p of HTL has to match with that of an anode. As we usually use an indium–tin–oxide (ITO) with I_p of 5.0 eV, the HTL should have similar value.
2. The HTL transports holes with a low driving voltage. High hole mobility over 10^{-3} cm^2/Vs is recommended.
3. The HTL blocks the passage of electrons transported by the ETL. The small E_a of the HTL is required.
4. The HTL should have larger exciton energy than that of the ETL to protect against exciton migration and the effective radiative decay of them inside an emitter layer.
5. The HTL should not form an exciplex with the ETL. The HTL having a low I_p value of less than 5.2 eV sometimes results in exciplex formation with the ETL.

Based on the above requirements, it is easy to recognize that it is very difficult to satisfy a single HTL with all of these assignments. In particular, requirement 1 is incompatible with requirement 4, resulting in a construction of double HTLs. In a similar manner, using a double ETL is necessary to enhance OLED performance.

In addition, the success of multilayer studies has caused the reexamination of single-layer devices. Although the combinations and contents of well-organized carrier transport and emitter materials resulted in the enhancement of EL efficiency, a higher efficiency than the multilayer structures has never obtained.[59,60] Thus, we anticipate that organic/organic interfaces will especially provide efficient carrier recombination sites.

2.5 Molecular Materials for OLED

Here, we describe the design concept of hole-transport materials (HTMs), electron-transport materials (ETMs), emitter materials (EMs), and dopant materials. We also mention the material design for obtaining highly efficient and durable OLED devices.

First, we point out two empirical guidelines, obtained in early studies, common to HTM, ETM, and EM:

1. Each organic layer should have uniform and pinhole-free thin films at a thickness of about 50 nm. Amorphous morphology was found to satisfy this requirement. Sometimes, polycrystalline thin films are also acceptable, when their grain sizes are less than 50 nm and they form dense pinhole-free films. The previous systematic studies proposed a molecular design for the formation of uniform thin films. It was reported that the introduction of bulky substituents and steric hindrance into molecular structures, as well as an appropriate three-dimensional steric configuration resulted in amorphous morphology.[35,58,61]
2. No exciplex or charge-transfer (CT) complexes between two adjoining organic layers. As HTMs have an electron-donating characteristic and ETMs have an electron-accepting characteristic by nature, most of the HTM–ETM combinations result in exciplex or CT complex formation.[62] Bulky substituents/components and a three-dimensional steric configuration also contribute to the relaxation of the complexes.[58]

These guidelines are common to all OLED materials. Many researchers have encountered these problem, and organic synthesis tailor-made for OLED materials was examined.

2.5.1 Hole-Transport Material

First, a single HTL was used in a simple anode/HTL/ETL/cathode structure. Aromatic amines, N, N'-diphenyl-N, N'-bis(3-methylphenyl)-1, 1′-biphenyl-4, 4′-diamine (TPD),[32] and TPAC[31] were widely used. Instead of a single HTL as mentioned in Section 2.4, however, it was revealed that the formation of double HTLs, HTL-A, and HTL-E, as shown in Fig. 2.6 became indispensible for high-performance OLEDs. It is required that the I_p of HTL-A should be similar to that

(a) Single HTL to double HTLs

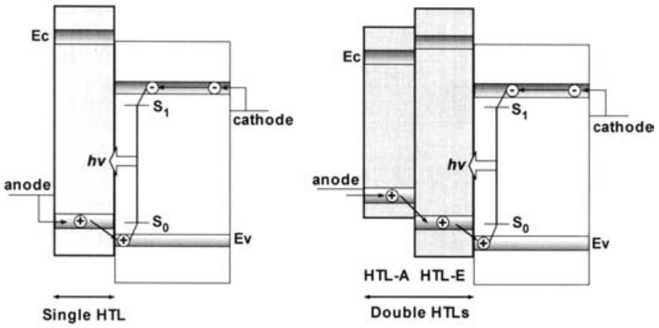

(b) Single ETL to double ETLs

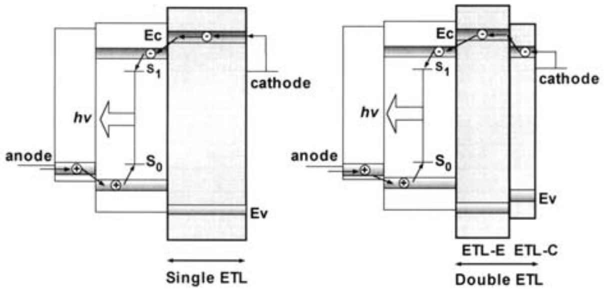

FIGURE 2.6. Schematic energy diagrams of a single HTL and double HTLs, also a single ETL and double ETLs.

of an anode for efficient hole injection. As we usually use an ITO anode having an I_p of about 5.0 eV, HTM-A having a similar I_p value is a good candidate. With regard to the bandgap (E_g) of HTL-A, we do not necessarily need to use wide-bandgap materials, because we insert a HTL-E with a wide-bandgap, which prevents exciton migration from an emitter layer. From the aspect of less reabsorption of EL by HTL-A, however, the wide-bandgap materials, those that are transparent to the EL wavelength, are preferred. First, Tang et al. demonstrated that phthalocyanines, CuPc and H_2Pc, with an I_p of $\cong$ 5.0 eV worked well as a HTL-A, although PCs have large absorption in the visible region.[54] Second, the starburst polyamine (m-MTDATA), proposed by Shirota et al.[56] has less absorption at a visible region over 460 nm, and it was confirmed to form an excellent interface between an ITO anode ($I_p = 5.0$ eV) and /m-MTDATA ($I_p = 5.1$ eV) for hole injection. In addition, it should be stressed that the excellent amorphous morphology of m-MTDATA largely enhanced device stability under continuous operation. Figure 2.7 summarizes six typical HTMs. Here, we should aware that the phenylene–diamine unit, which contributes to the reduction of the I_p value, is a representative structure in HTL-A. Nowadays, from the aspect of thermal stability, various advanced structures have been proposed.[63–65] In a similar manner, various

(a) HTM-A

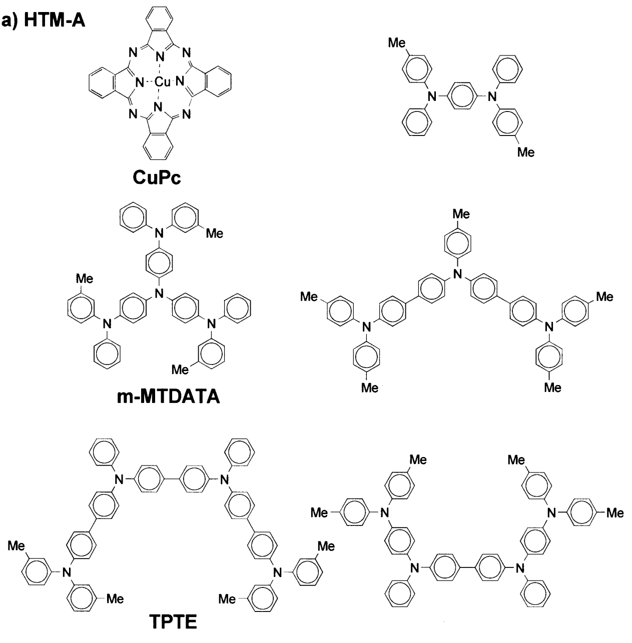

(b) HTM-E

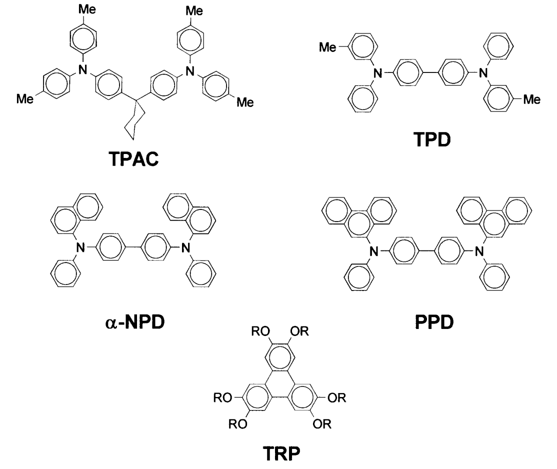

FIGURE 2.7. Molecular structures adequate for HTM-A and HTM-B.

conducting polymers, polyanilines[66,67] and polythiophenes,[68] were successfully reported as HTL-A.

Next, we mention the molecular design of HTL-E. Because HTL-E contacts with ETL, different characteristics are required. Significant requisites for HTL-E are conditions 2, 3, 4, and 5 as summarized in Section 2.4. In particular, HTL-E should bear the confinement of excitons and electrons. Various bendidine backbone structures were confirmed to be excellent candidates as HTL-E. Furthermore, trimer and tetramer structures and aromatic substituted bendidine structure were developed to enhance thermal stability. The α-naphthyl-substituted bendidine,[55] in particular, was widely used because of its thermal duration and electrochemical stability. Most recently, new backbone structures,[63,64] triphenylene[69–71] and spiro–spiro[72] have been proposed as HTL-E.

2.5.2 *Electron-Transport Material*

When we think about recent OLED devices from various viewpoints, we can say that the success of OLED is due to an active utilization of electron-transport materials. Especially, the discovery of various classes of organic ETMs has really opened the possibility of bipolar devices.

Based on a successful SH-A structure, we thought that if we had unipolar electron-transport materials, we could construct new device structures such as SH-B and DH structures. During that time, we had a few materials as a candidate of ETMs. In the research on organic photoconductors[73] (OPC), trinitrofluorenone (TNF) was known to transport only electron carriers. Other suggestive materials were Alq in EL and PV (perylene bis-benzimidazole) in organic solar cells.[74] TNF, which is a very strong electron acceptor, however, was found to form a CT complex between adjoining layers and resulted in a quenching of the luminescence, even though it selectively transports electrons well. Thus, strong electron-accepting characteristics need to be avoided for multilayer structures. Furthermore, using PV as an ETL, the large π-conjugation of PV resulted in a serious exciton migration from an emitter layer to PV and this is called the inferior exciton confinement effect.[75] Then, we examined various classes of organic molecule, focusing on whether the molecules were weak electron acceptors. In research on materials, some organic molecules containing nitrogen or oxygen heteroatoms were found to be weak electron acceptors. Finally, we obtained one of the oxadiazole derivatives (OXDs), PBD [2-(4-biphenylyl)-5-(4-*tert*-butylphenyl)-1,3,4-oxadiazole)], as shown in Fig. 2.8.[74] The double hetero structure with PBD as the ETL showed excellent electron transport and exciton confinement effect.[36] After this discovery, various PBD derivatives were synthesized. The new dimer, trimer, and tetramer structures[76–78] and the polymers[79–84] contributed to the enhancement of the film morphology and thermal stability.

Here, we mention the structure design of ETL. We have to form double ETLs (ETL-E/ETL-C), which are very similar to the double HTLs, for low electron injection from a cathode and the confinement of molecular excitons and hole carriers (Fig. 2.8b. For the efficient electron injection from a cathode into the ETL, the electron affinity (E_a) of ETL should be close to the level of the cathode's workfunction. The large E_a, however, mostly results in a small bandgap and insufficient exciton confinement. A typical example of the efficient combination of double ETLs is the OXD/Alq, in which OXD works well to confine excitons and the hole effect while the Alq layer injects and transports electrons from a cathode to an OXD layer.

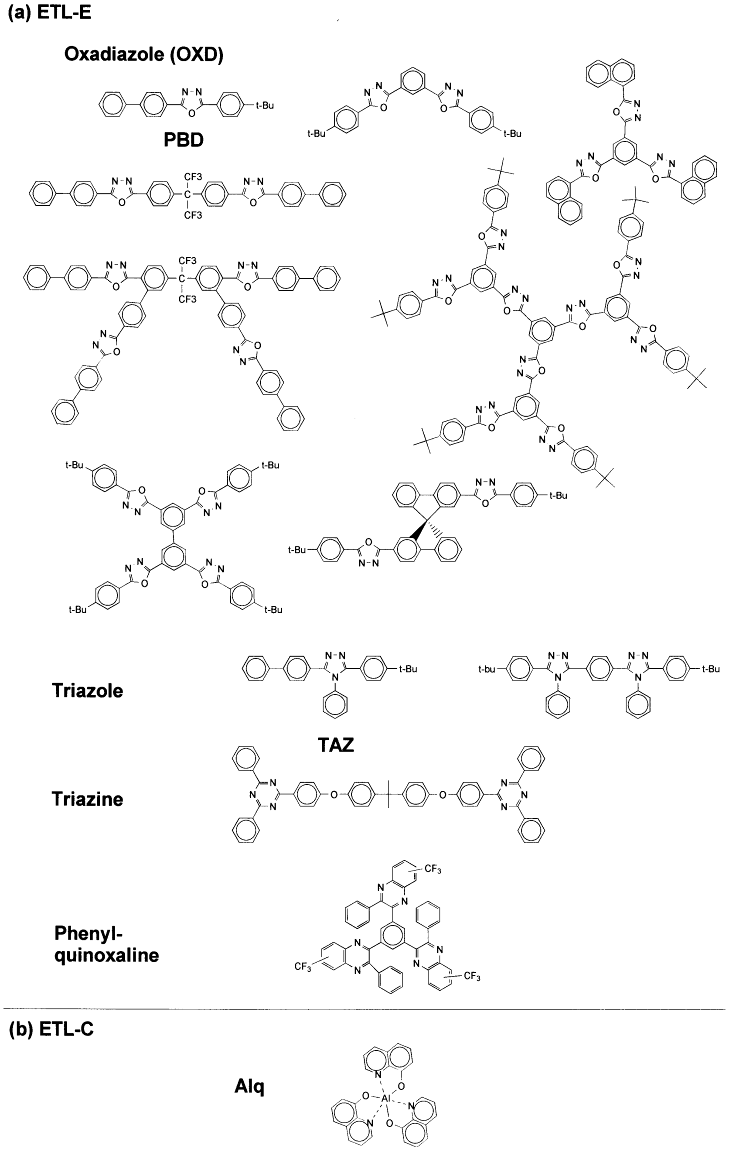

FIGURE 2.8. Molecular structures adequate for ETL-A and ETL-B.

A similar performance was reported by the BSA/Alq double structure, for which BSA holds both electron-transport and emitter functions.

Finally, we should point out that OXD derivatives lack durability under continuous device operation.[78] The best device ever reported had only a few hundred hours of continuous dc operation and ≅ 1000 h under pulse operation. This inferior duration is due to the lack of electrochemical stability.[78] Although a wide variety of HTMs were developed, particularly in the development of OPC, for the last 30 years, the development of ETM has just begun. Thus, we hope that many researchers will develop new ETMs for achieving durable bipolar devices that will eventually surpass inorganic semiconductors. Furthermore, new backbone structures, triazole (TAZ),[85] triazine, quinoqusaline,[86] and phenanthroline,[87] are also reported as an ETM.

2.5.3 *Emitter Material*

When the HTL or ETL possesses a bipolar carrier-transport characteristic and highly efficient fluorescence, these molecules can be a candidate for an emitter layer. So far, a variety of fluorescent molecules with high fluorescent efficiency in solid states have been reported to be useful as an emitter layer. Here, we can classify EM into two categories (Fig. 2.9). The first category is ETM-EM, for which a major carrier in ETM-EM is electrons and a minor carrier is holes, and this is suitable for the SH-A structure. Alq is a representative in this class, and a thorough investigation was conducted in which Alq derivatives were examined systematically.[88–90] Beq_2 (beryllium quinoline)[91] and Almq (4-methyl-8-hydroxyquinoline),[92] in particular, were found to have much better performance than Alq. Also, a blue emitter, BAlq,[93] was synthesized. Furthermore, ZnPBO (phenyloxazole),[94] ZnPBT (phenylthiazole), and azomethine[95] metal complexes have been successively reported. Because the metal complexes were found to show basically an electron-accepting characteristic, these materials are useful for ETM-EM. In addition to the metal complexes, BAS (bis-styrylarylene) derivatives[58,96] and bis-anthracene derivatives[97] are significant EMs. The thorough synthesis of BAS on this structure finally produced durable blue materials, even though this chemical structure is not accessible to the public. The success of the minute-molecular design of the bis-styrylarylene derivatives has encouraged organic chemists to take part in the development of new OLED materials.

Another category is HTM-EM is found in the SH-B structure. As shown in Fig. 2.9b, various kinds of styrylamine derivative, which have a strong fluorescence in solid states, are representative of this kind of structure.[98] The unique combination of a triphenylamine unit and a styrylbenzene unit or a condensed aromatic unit allowed us to use them as an HTM-EM.[99]

Finally, we should mention that the above-mentioned emitter materials are occasionally useful in a DH structure. Moreover, it is possible to form a single-layer EM if we could achieve balanced hole and electron injection and transport by equipping adequate carrier injection electrodes. In fact, BAS[96] and BczVBi[100] were known to show a fairly high EL efficiency in a single-layer structure.

2.5.4 *Dopant Material*

Dopant materials (DMs) are other keys for obtaining not only high EL quantum efficiency but also durable device performance. We know of various organic

(a) ETM-EM

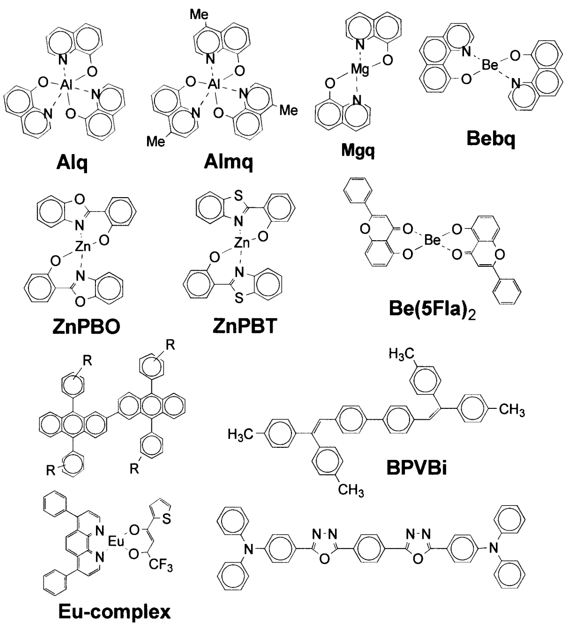

(b) HTM-EM

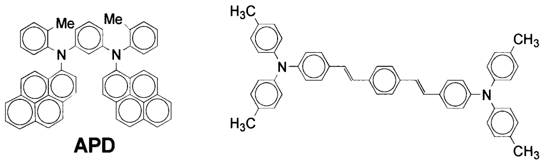

Emitter materials

FIGURE 2.9. Molecular structures adequate for an EML. Emitter materials are classified into two categories: ETM-EM and HTM-EM.

molecules which show nearly 100% of fluorescence efficiency, such as laser dyes in a dilute solution, whereas that in a solid state is extremely small because of concentration quenching.[101] Thus, the doping of highly fluorescent molecules into an emitter layer surely contributes to the enhancement of EL quantum efficiency, as most of host emitter layers have a fluorescence efficiency of only 1–30% in solid states. Figure 2.10 summarizes previously reported dopant molecules. In Alq-based devices, the increases of twofold or threefold EL efficiency were reported by using coumarin6,[50] quinacridone,[102–105] ruburene[106,107] and DCM.[50,100] During the development of dopant materials, in particular, red dopants were found to be most difficult to observe because many red fluorescent molecules unfortunately showed orange–red emission (580–650 nm) and abrupt concentration quenching due to the intramolecular donor–acceptor or the plane structure.[108,109] We have

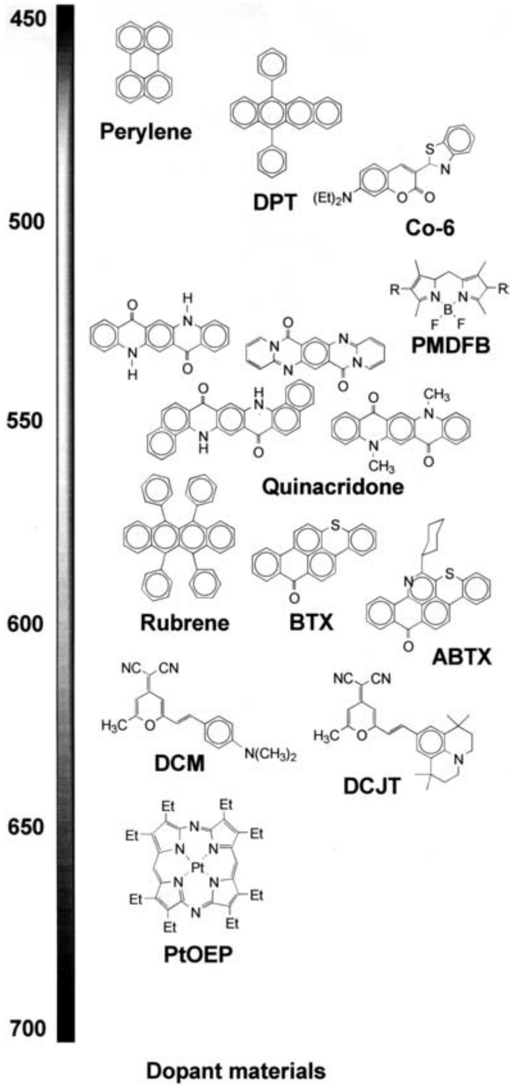

FIGURE 2.10. Molecular structures of dopant materials; blue to red materials are shown in sequence.

to introduce a new molecular concept to these problems in order to obtain highly efficient real red color.

2.5.5 Molecular Tuning for High EL Efficiency

For the enhancement of EL quantum efficiency, we should pay attention to two major subjects. The first subject relates on the exciplex between adjoining layers.

The exciplex, which results from mostly low emission efficiency in fluorescence and long-wavelength emission. It was revealed that a minute molecular tuning, even one methyl group, greatly influenced exciplex formation.[60] The second subject concerns the branching ratio of molecular excitons. We still have the basic unsolved question of whether the branching ratio of singlet and triplet exciton by carrier recombination is really 1:3.[38,45] Because the simple calculation on the branching ratio is based on hydrogen molecules, we believe that a branching ratio definitely changes depending on each molecular structure. Thus, there is a possibility of enhancing the production probability of singlet excitons by carrier recombination.

2.5.6 *Molecular Tuning for a High EL Durable OLED*

From the practical viewpoint, one of the most significant performances of OLEDs is device stability under continuous operation. Here, we summarize previous reports on durability.

First, the reduction of a carrier injection barrier between organic/electrode interfaces was reported to enhance device duration.[55,61] Although joule heat at the interfaces is supposed to induce microcrystallization of organic molecules and successive destruction of balanced hole and electron injection and transport, the precise degradation mechanism is still unclear.

Furthermore, two recent reports on the enhancement of device duration by a doping were very suggestive. Sano et al. reported the unique OLED structure: ITO/m-MTDATA/TPD doped with ruburene/Beq/MgIn.[106,107] The rubrene-doped TPD greatly contributed to enhanced device duration compared with the device without a doped TPD layer. The half-decay of initial luminance exceeded 3554 h, corresponding to an enhancement factor of 154. Although a detailed mechanism has not yet been revealed, the restraint of the formation of TPD anions by the rubrene doping seems to contribute the enhancement. Second, a variety of quinacridone derivatives were examined as a dopant in Alq. The introduction of bulky substituents, which prevents intermolecular hydrogen-bonding, into a basic quinacridone structure clearly increased device stability.[102–105] Moreover, a similar stabilizing effect was found in rubrene-doped Alq and perylene-doped BAlq.[93] The doping of both the HTL and ETL were also confined to enhance device stability. By the dopants with high PL quantum efficiency, as the final excited states are consumed by dopants as a light emission, other dissipation processes which induce unexpected degradation of molecules is expected to suppress. Recently, a few studies started to focus on the chemical stability of organic molecules:[99] the relationship between chemical structures and the stability of free radicals. We expect detailed consideration with a well-controlled moisture and oxygen atmosphere, because the lack of atmospheric control sometimes leads to unexpected results.

Another significant report is the development of the molecular structures of the HTM. Using (α-naphthyl-substituted TPD, α-NPD,[55] a long duration of over 4000 h (half-decay of initial luminance) was revealed without doping. The reversible behavior of the radical cation was pointed out as the main reason for stability. Also, the thermal stability of the film morphology was also considered to be a reason for the high duration.

2.6 Future Possibilities of OLED

In addition to the above-mentioned organic materials, many unique materials were examined. The EL from europium[110] and terbium[111] rare-earth complexes, J-aggregated cyanine dyes,[112] layered perovskite,[113] and CdS nanocrystals despersed into PVCz[114] are reported. Also, new backbone structures, spiro[72] and dendrimers,[115] for obtaining stable amorphous films were proposed. Furthermore, instead of amorphous films, special aggregated structures are being examined to create new device performance such as polazied emission,[116,117] submicrometer-sized emission,[118,119] and so on. The discotic liquid crystals, particularly triphenylene derivatives, were revealed to possess extremely high hole mobility (10 cm^2/Vs) and were confirmed to show similar high-EL performance compared with that of diamine-based devices.[69–71] Furthermore, the utilization of polymer materials opens unique possibilities for OLEDs, such as Melectrochemiluminescence (ECL),[120] DOLED,[121] and submicrometer-sized devices.[119]

Parallel to the improvement of OLED performance, another recent significant study deals with organic laser diodes. Now, various device structures such as microcavities[122,123] and optical waveguides[124,125] are proposed. From the materials aspect, the design of laser dyes in solid states is quite unknown. The materials possessing a high PL quantum yield does not necessarily show a low-threshold laser action.[126] Figure 2.11 shows solid states laser materials useful in a waveguide

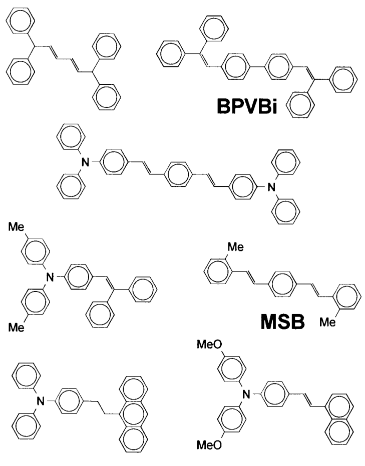

Organic solid state laser materials

FIGURE 2.11. Molecular structures of organic solid-state laser materials.

structure. The material design for solid-state laser diodes has just started and is a fascinating subject.

2.7 Conclusion

In this chapter, we showed that OLED performance is clearly defined based on the simplified working mechanism of carrier injection and successive SCLC. The balance of holes and electrons injected within an emitter layer is a major factor contributing to overall EL quantum efficiency. The unipolar-charged-transport layers, HTL and ETL, contribute to the increase of quantum efficiency.

We reviewed HTM, ETM, EM, and DM developed in the past 10 years and discussed the materials design of them from the aspect of high luminance, low driving voltage, and high duration.

Recent developments in OLEDs have established a new category of organic semiconductors. Thus, we are now faced with the chance of establishing new organic semiconductor physics and to create new organic semiconductors.

References

[1] In November 1997, Pioneer Co. Ltd. in Japan firstly commercialized the 256 × 64 dot-matrix OLED information display for automobiles.
[2] A. Bernanose, Br. J. Appl. Phys. 6, S54 (1955).
[3] A. Bernanose, J. Chim. Phys. 51, 255 (1954).
[4] A. Bernanose, J. Chim. Phys. 52, 396 (1955).
[5] G. D. Short and D. M. Herucles, J. Am. Chem. Soc. 87, 1439 (1965).
[6] M. Pope, H. Kallmann, and P. Magnate, J. Chem. Phys. 38, 2042 (1963).
[7] W. Helfrich and W. G. Schneider, Phys. Rev. Lett. 14, 229 (1965).
[8] M. Sano, M. Pope, and H. Kallmann, J. Chem. Phys. 43, 2920 (1965).
[9] W. G. Schneider and W. Helfrich, J. Chem. Phys. 44, 2902 (1966).
[10] T. C. Werner, J. Chang, and D. M. Hercules, J. Am. Chem. Soc. 92, 763 (1970).
[11] D. F. Williams and M. Schadt, J. Chem. Phys. 53, 3480 (1970).
[12] H. P. Schwob, D. Weitz, and D. F. Williams, Mol. Cryst. Liq. Cryst. 24, 271 (1973).
[13] L. L. T. Bradrey, H. P. Schwob, D. Weitz, and D. F. Williams, Mol. Cryst. Liq. Cryst. 23, 271 (1073).
[14] W. Hwang and K. C. Kao, J. Chem. Phys. 60, 3845 (1974).
[15] M. Witter and I. Zschokke-Granacher, J. Chem. Phys. 63, 4187 (1975).
[16] F. Lohmann and W. Mehl, J. Chem. Phys. 50, 500 (1969).
[17] C. E. Swenberg and M. Pope, Phys. Rev. 12, 4113 (1975).
[18] J. Kalinowski and J. Godlewski, Chem. Phys. Lett. 36, 345 (1975).
[19] J. Kalinowski, J. Godlewski, and R. Signerski, Mol. Cryst. Liq. Cryst. 33, 247 (1976).
[20] J. Glinski, J. Godlewski, and J. Kalinowski, Mol. Cryst. Liq. Cryst. 48, 1 (1977).
[21] G. G. Roberts, B. S. Keating, P. S. Vincett, and W. A. Barlow, J. Phys. C: Solid State Phys. 11, 3847 (1978).

[22] P. S. Vincett, W. A. Barlow, R. A. Hann, and G. G. Roberts, Thin Solid Films 94, 171 (1982).
[23] N. P. Sinha, Y. Misra, L. N. Tripathi, and M. Misra, Solid State Commun. 39, 89 (1981).
[24] R. M. Burgess, M. Gouterman, and G. E. Khalil, J. Lumin. 28, 377 (1983).
[25] G. G. Roberts, M. McGinnity, P. S. Vincett, and W. A. Barlow, Solid State Commun. 32, 683 (1979).
[26] P. H. Partridge, Polymer 24, 733 (1983).
[27] P. H. Partridge, Polymer 24, 739 (1983).
[28] P. H. Partridge, Polymer 24, 748 (1983).
[29] P. H. Partridge, Polymer 24, 755 (1983).
[30] S. Hayashi, H. Etoh, and S. Saito, Jpn. J. Appl. Phys. 25, L773 (1986).
[31] C. W. Tang and S. A. VanSlyke, Appl. Phys. Lett. 51, 913 (1987).
[32] C. Adachi, S. Tokito, T. Tsutsui, and S. Saito, Jpn. J. Appl. Phys. 27, L269 (1987).
[33] C. Adachi, S. Tokito, T. Tsutsui, and S. Saito, Jpn. J. Appl. Phys. 27, L713 (1987).
[34] C. Adachi, T. Tsutsui, and S. Saito, Appl. Phys. Lett. 55, 1489 (1989).
[35] C. Adachi, T. Tsutsui, and S. Saito, Appl. Phys. Lett. 56, 799 (1990).
[36] C. Adachi, T. Tsutsui, and S. Saito, Appl. Phys. Lett. 57, 531 (1990).
[37] C. Adachi, T. Tsutsui, and S. Saito, Optoelectron: Devices Technol. 6, 25 (1991).
[38] M. Pope and C. E. Swenberg, *Electronic Processes in Organic Crystals*, Oxford University Press, New York, 1982.
[39] S. Tokito, T. Tsutsui, and S. Saito, Polym. Commun. 27, 333 (1986).
[40] K. C. Kao and W. Hwang, *Electrical Transport in Solids, with Particular Reference to Organic Semiconductors*, International Series in the Science of the Solid States Vol. 14, Pergamon Press, London, 1981.
[41] S. M. Sze, *Physics of Semiconductor Devices*, Wiley, New York, 1981.
[42] K. Seki, E. Ito, and H. Ishii, Synth. Met. 91, 137 (1997).
[43] Z. Shen, P. E. Burrows, V. Bulovic, D. M. McCarty, M. E. Thompson, and S. R. Forrest, Jpn. J. Appl. Phys. 35, L401 (1996).
[44] Y. Abe, K. Onisawa, S. Aratani, and M. Hanazono, J. Electrochem. Soc. 139, 641 (1992).
[45] T. Yonezawa, T. Nagata, H. Kato, A. Imamura, and K. Morokuma, *Introduction of Quantum Chemistry*, Kagaku-Dojin, Japan, 1983, (in Japanese).
[46] N. J. Turro, *Molecular Photochemisrty*, Benjamin, San Francisco 1965.
[47] Text book of Basic Optics
[48] G. Gu, D. Z. Garbuzov, P. E. Burrows, S. Venkatesh, S. R. Forrest, and M. E. Thompson, Opt. Lett. 22, 396 (1997).
[49] T. Tsutsui and S. Saito, in *Intrinsically Conducting Polymer: An Emerging Technology*, edited by M. Aldissi, Kluwer Academic, Dordrecht 1993, p. 123.
[50] C. W. Tang, S. A. VanSlyke, and C. H. Chen, J. Appl. Phys. 65, 3610 (1989).
[51] T. Tsutsui, E. Aminaka, Y. Hamada, C. Adachi, and S. Saito, SPIE Proc. 1910, 180 (1993).
[52] T. Tsutsui, E. Aminaka, and S. Saito, J. Appl. Phys. 79, 8808 (1996).
[53] K. H. Drexhage, in *Progress in Optics, Volume 12*, edited by E. Wolf, North-Holland, Amsterdam, 1974, p. 165.
[54] S. A. VanSlyke and C. W. Tang, U.S. Patent 4, 720, 432.
[55] S. A. VanSlyke, C. H. Chen, and C. W. Tang, Appl. Phys. Lett. 69, 2160 (1996).
[56] Y. Shirota, Y. Kuwabara, H. Inada, T. Wakimoto, H. Nakada, Y. Yonemoto, S. Kawami, and K. Imai, Appl. Phys. Lett. 65, 807 (1994).

[57] C. Adachi, K. Nagai, and N. Tamoto, Jpn. J. Appl. Phys. 35, 4819 (1996).
[58] H. Tokailin, M. Matsura, H. Higashi, C. Hosokawa, and T. Kusumoto, SPIE Proceedings, 1910, 38 (1993).
[59] C. P. Lin, T. Tsutsui, and S. Saito, J. Polym. Res. 2, 133 (1995).
[60] J. Littman and P. Martic, J. Appl. Phys. 72, 1957 (1992).
[61] H. Azuma, C. Hosokawa, H. Tokailin, and M. Kusumoto, Nippon Kagakukai-shi, 10, 1162 (1992) (in Japanese).
[62] N. Tamoto, C. Adachi, and K. Nagai, Chem. Mater. 9, 1077 (1997).
[63] C. Adachi, N. Tamoto, and K. Nagai, Appl. Phys. Lett. 66, 2679 (1995)
[64] H. Tanaka, S. Tokito, Y. Taga, and A. Okada, Chem. Commun. 2175 (1996).
[65] TDK patent (Japanese)
[66] H. Antoniadis, M. R. Hueschen, J. McElvain, J. N. Miller, R. L. Moon, D. B. Roitman, and J. R. Sheats, Polymer. Prepr. (ACS) 382 (1997).
[67] Y. Yang, and A. J. Heeger, J. Appl. Phys. 64, 1245 (1994)
[68] TDK patent (Japanese)
[69] A. Bacher, I. Bleyl, C. H. Eedelen, D. Haarer, W. Paulus, and H. W. Schmidt, Adv. Mater. 9, 1031 (1997).
[70] T. Christ, V. Stumpflen, and J. H. Wendorff, Macromol. Rapid Commun. 18, 93 (1997).
[71] S. Tanaka, C. Adachi, T. Koyama, and Y. Taniguchi, Chem. Lett. 975 (1998).
[72] J. Salbeck, N. Yu, J. Bauer, F. Weissortel, and H. Bestgen, Synth. Met. 91, 209 (1997).
[73] W. G. Gill, J. Appl. Phys. 43, 5033 (1972).
[74] C. W. Tang, Appl. Phys. Lett. 48, 183 (1985).
[75] C. Adachi, T. Tsutsui, and S. Saito, Vol. 358, *Springer Proceedings in Physics Electroluminescence*, Springer-Verlag, New York, 1989.
[76] Y. Hamada, C. Adachi, T. Tsutsui, and S. Saito, Nippon Kagaku-kaishi 11, 1540 (1991) (in Japanese).
[77] Y. Hamada, C. Adachi, T. Tsutsui, and S. Saito, Jpn. J. Appl. Phys. 31, 1812 (1992).
[78] C. Adachi, K. Nagai, and N. Tamoto, Display Imaging 5, 325 (1997).
[79] M. Strukelj, F. Papadimitrakopoulos, T. Miller, and L. Rothberg, Science 267, 1969 (1995).
[80] E. Buchwald, M. Meier, S. Kag, P. Posch, H-W. Schmidt, P. Strohriegl, W. Reis, and M. Schwoerer, Adv. Mater. 10, 839 (1995).
[81] J. Kido, G. Harada, and K. Nagai, Chem. Lett. 161 (1996).
[82] Y. Yang and Q. Pei, J. Appl. Phys. 77, 4807 (1995).
[83] Q. Pei and Y. Yang, Adv. Mater. 7, 559 (1995).
[84] Q. Pei and Y. Yang, Chem. Mater. 7, 1568 (1995).
[85] J. Kido, M. Kimura and K. Nagai, Science 267, 1332 (1995).
[86] J. Bettenhausen, M. Greczmiel, M. Jandke, and P. Strohriegl, Synthe. Met. 91, 223 (1997).
[87] Y. Kijima, N. Asai, and S. Tamura, MRS Abstract, *1998 Spring Meeting*, 1998 p. 131.
[88] M. Morikawa, C. Adachi, T. Tsutsui, and S. Saito, Denshi Jyoho Tsushin Gakkai Ronbunshi C-2, 661 (1990).
[89] Y. Hamada, T. Sano, M. Fujita, T. Fujii, Y. Nishio, and K. Shibata, Jpn. J. Appl. Phys. 32, L514 (1993).
[90] P. E. Burrows, L. S. Sapochak, D. M. McCarty, S. R. Forrest, and M. E. Thompson, Appl. Phys. Lett. 64, 2718 (1994).

[91] Y. Hamada, T. Sano, M. Fujita, T. Fujii, Y. Nishio, and K. Shibata, Chem. Lett. 905 (1993).
[92] J. Kido and Y. lizumi, Chem. Lett. 963 (1997).
[93] S. A. VanSlyke, P. S. Bryan, and C. W. Tang, *Inorganic and organic electroluminescence/EL 96*, 1996, p. 195.
[94] N. Nakamura, S. Wakabayashi, K. Miyairi, and T. Fujii, Chem. Lett. 1741 (1994).
[95] Y. Hamada, K. Sano, M. Fujita, Y. Nishio, and K. Shibata, Nippon Kagakukai-shi, 879 (1993).
[96] C. Hosokawa, H. Hagashi, H. Nakamura, and T. Kusumoto, Appl. Phys. Lett. 67, 3853 (1995).
[97] TDK (unpublished).
[98] Ricoh Patent (Japanese)
[99] C. Adachi, K. Nagai, and N. Tamoto, Jpn. J. Appl. Phys. 35, 4819 (1996).
[100] E. Aminaka, T. Tsutsui, and S. Saito, J. Appl. Phys. 79, 8808 (1996).
[101] F. P. Schafer (ed.), *Dye Lasers*, Springer-Verlag, New York, 1973.
[102] T. Wakimoto, Y. Yoneyarna, J. Funaki, M. Tsuchida, R. Murayama, H. Nakada, H. Matsumoto, S. Yamamura, and M. Nomura, *ICEL*, Abstracts (Kitakyushu), 1997, p. 4 (1997).
[103] H. Nakada and T. Tohma, *Inorganic and Organic Electroluminescence/EL96*, 1996, p. 385.
[104] C. W Tang, SID 96 Digest 1996, p. 181.
[105] J. Shi and C. W. Tang, Appl. Phys. Lett. 70, 1665 (1997).
[106] T. Sano, M. Fujita, T. Fujii, and Y. Hamada, Jpn. J. Appl. Phys. 34, 1883 (1995).
[107] T. Sano, Y. Hamada, and K. Shibata, *Inorganic and Organic Electroluminescence/EL96*, 1996, p. 249.
[108] C. H. Chen and C. W. Tang, *Chemistry of Functional Dyes*, Mita Press, 1992, Vol. 2, p, 536.
[109] Y. Sato, T. Ogata, S. Ichinosawa, and Y. Murata, Synthe. Met. 91, 103 (1997).
[110] J. Kido, K. Nagai, Y. Okamoto, and T. Skotheim, Chem. Lett. 1267 (1991).
[111] J. Kido, K. Nagai, and Y. Okamoto, J. Alloys Compounds 192 (1993).
[112] M. Era, C. Adachi, T. Tsutsui, and S. Saito, Chem. Phys. Lett. 178, 488 (1991).
[113] O. B. Dabbousi, M. G. Bawendi, O. Onitsuka, and M. F. Rubner, Appl. Phys. Lett. 66, 1316 (1995).
[114] M. Era, S. Morimoto, T. Tsutsui, and S. Saito, Appl. Phys. Lett. 65, 676 (1994).
[115] A. Kraft, Liebigs Ann. 1463 (1997).
[116] R. N. Marks, F. Biscarini, R. Zamboni, and C. Taliani, EuroPhys. Lett. 32, 523 (1995).
[117] M. Era, T. Tsutsui, and S. Saito, Appl. Phys. Lett. 67, 2436 (1995).
[118] M. Granstrom and O. Inganas, Adv. Mater. 7, 1012 (1995).
[119] C. Adachi, S. Hibino, T. Koyama, and Y. Taniguchi, Jpn. J. Appl. Phys. 36, L827 (1997).
[120] Q. Pei, Y. Yang, G. Yu, C. Zhang, and A.J. Heeger, J. Am. Chem. Soc. 118, 3922 (1996).
[121] A. Yamamori, C. Adachi, T. Koyama, and Y. Taniguchi, Appl. Phys. Lett. 72, 2147 (1998).
[122] T. Tsutsui, C. Adachi, S. Saito, M. Watanabe, and M. Koishi, Chem. Phys. Lett. 182, 143 (1991).
[123] A. Dodabalapur, L. J. Rothberg, T. M. Miller, and E. W. Kwock, Appl. Phys. Lett. 64, 2486 (1994).

[124] F. Hide, B. Benjamin, J. Schwartz, M. A. Diaz-Garcia, and A. J. Heeger, Chem. Phys. Lett. 256, 424 (1996).
[125] V. G. Kozlov, V. Bulovic, P. E. Burrows, and S. R. Forrest, Nature 389, 362 (1997).
[126] M. Nagawa, C. Adachi, T. Koyama, and Y. Taniguchi, Appl. Phys. Lett. (submitted).

3

Chemical Degradation and Physical Aging of Aluminum(III) 8-Hydroxyquinoline: Implications for Organic Light-Emitting Diodes and Materials Design

Keith A. Higginson, D. Laurence Thomsen III,
Baocheng Yang, and Fotios Papadimitrakopoulos

3.1 Introduction

A traditional barrier to marketing organic light-emitting diode (OLED) technology has been achieving devices capable of sustaining brightness levels with minimum drift over long periods of time as well as maintaining longevity while operating at elevated temperatures (e.g., 60–80°C). In many cases, product developers have designed around these problems (e.g., by extensive passivation[1,2] or with the driving technology),[3] but understanding of the decay processes is still by many means insufficient, especially with respect to the intrinsic limitations imposed by the materials in question. This type of knowledge gives upper-bound design constraints and should give insight in materials or device designs with greater stability or longevity.

Several failure modes for OLEDs are enumerated. Often, poorly prepared OLEDs show failure locally, evidenced by the origination and growth of nonemissive regions. In parallel, a gradual decrease in brightness, accompanied by an increase in driving voltage, also occurs. The majority of the failure literature is summarized as follows:

- Resistive heating
    - Locally, originating from surface asperity and film defects, and resulting in short-circuits or other heating-related phenomena (see below) in that region[4–6]

  - Globally, due to poorly energy-level matching of the electrode and charge-transport material[7,8]
- Poor metal organic adhesion. This may be caused by (or facilitated by) the following:
  - Dewetting, either unassisted[9] or with water penetration[4]
  - Strain from expansion of electrodes upon oxidation by water[4–6]
  - Higher thermal expansion of organic layers compared to electrodes[10]
- Interdiffusion of organic layers[11]
- Breakdown of the indium–tin–oxide (ITO) anode and diffusion of elemental species[12–14]
- Chemical,[15–17] electrochemical,[18,19] and photochemical degradation[20,21]
- Structural relaxations in layers: crystallization and physical aging[17,22,25]

Many of these may be considered engineering issues. For example, the surface of ITO can be planarized and passivated by a variety of techniques.[26–29] There has been some work in stable metal/organic interface design, but a good deal more is known about the electronic properties of the interfaces than their physical ones.[13,30–34] The final two bulleted points, however, represent intrinsic bulk material properties and are the focus of this chapter. It will be shown that the homogeneous chemical aging of aluminum (III) 8-hydroxyquinoline (Alq_3) results in charge-trapping and quenching species and that physical aging or crystallization may similarly change the distribution of localized electronic states and hence the charge-transport and emissive properties. There is some inherent difficulty in such studies, due to the large number of tightly interrelated parameters affecting performance, as well as the few experimental methods available for the study of ultrathin films. Care has been taken to observe the limitations of extrapolating solution or powder measurements to thin solid films.

In this chapter, a review of our work regarding the chemical, electrochemical, and morphological stability of vacuum-deposited Alq_3 is presented. The effect of these processes on charge transport and light emission in OLEDs is also considered, and the readers may refer to some published work for more quantitative analysis.[35–37] The efficacy of “simple” passivation schemes as well as the fabrication of crystallization-resistant blends will also be briefly discussed.

3.2 Chemical Stability of OLED Materials

3.2.1 *Thermal Hydrolysis of* Alq_3

The detection of chemical reaction products in device geometries has largely been limited to the observation of indirect effects. Electrochemical instability has been used to explain the differences in the lifetimes of OLEDs based on compounds of a homologous series when the expected correlation with the glass transition temperature (T_g) or the ionization potential was not observed.[19] The oxidative

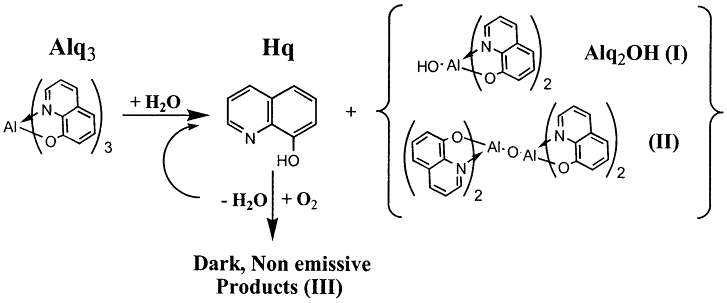

FIGURE 3.1. Overall mechanism for Alq$_3$ degradation in the presence of water. Water replaces one of the oxyquinolate ligands on the complex. The free Hq can then go on to form oxidized species which act as luminescence quenchers.

instability of Alq$_3$ in an actual device was reported in 2001 by Aziz et al., who observed a loss of fluorescence intensity in devices where Alq$_3$ was forced to transport holes (oxidized). The fluorescence decay was too great to be explained by chemical degradation alone [no change was observed in the Fourier transform infrared (FTIR) spectrum of Alq$_3$, which was being recorded simultaneously] and was explained by the formation of quenching materials which could affect the fluorescence quantum yield in very small concentrations.[38]

A few other techniques have been effectively used in the chemical study of OLEDs, including infrared spectroscopy [for the generation of carbonyl impurities in poly(*p*-phenylenevinylene)],[20] photoemission spectroscopy (capable of measuring valence and core electronic states at the surface of the material during deposition),[13,30,32,39] and gas chromatography (which is well suited for Alq$_3$ because some of the reactants and products are volatile).[16,35]

Figure 3.1 summarizes the hydrolytic decomposition of Alq$_3$.[15] Water replaces one of the ligands of the complex to produce 8-hydroxyquinoline (Hq). Its anion (q^-) is, in turn, particularly susceptible to oxidation reactions, which produce other luminescence-quenching products. The first evidence of Alq$_3$ chemical degradation was observed during attempts to develop an aqueous synthesis for the compound. Basic reaction mixtures, from which atmospheric oxygen was not carefully excluded, developed a characteristic brown color which could be cultivated in a controlled fashion. The degradation of both Alq$_3$ and Hq could be observed in a variety of solvents, as well as in the solid phase. Heating in air, as well as under oxygen pressure, readily produced a dark, nonemissive material, whereas no color change could be observed in solutions where oxygen was carefully removed with freeze–pump–thaw cycling.

The degradation products formed from Hq and Alq$_3$ were nearly identical by FTIR and ultraviolet–visible (UV-vis) spectroscopy and shared some characteristics of polymeric degradation products of Hq reported in the literature, although thorough characterization was not conducted in the reported case[40] and the samples prepared in our lab for FTIR analysis were highly oxidized. Reaction conditions which favored Hq oxidation as observed by darkening also promoted Alq$_3$ degra-

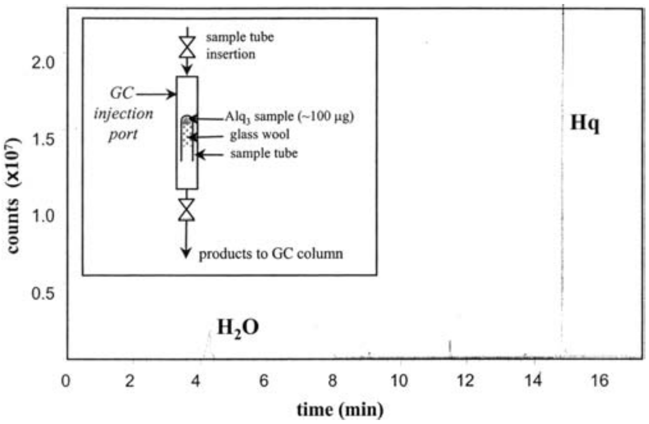

FIGURE 3.2. Typical chromatogram for the reaction experiment showing Hq and water peaks. Inset is a schematic of the injection port and sample cell.

dation, but with an apparent induction time. This early evidence, in conjunction with the similarity of the oxidation products, led us to suspect a two-part mechanism as suggested in Fig. 3.1, where quenching impurities originate from the liberation of Hq from its metal center, followed by its oxidation (because Hq alone does not quench the luminescence of Alq_3).

The hydrolysis of Alq_3 was characterized with a gas chromatography and mass spectroscopy (GC–MS) apparatus modified with a headspace accessory designed to study volatile products evolved from solid materials (illustrated in Fig. 3.2, inset).[41] Powder or film (deposited on foil) samples of Alq_3 were held in a constant-temperature injection port for a given time, and the eluents at the end of the heating period were fed to the GC column. The relative areas of water and Hq peaks were used to measure the conversion (a typical trace is shown in Fig. 3.2). The prepurified Alq_3 samples were allowed to absorb an equilibrium amount of water from the atmosphere, which occurred in about 3 min for the samples used.[16]

For kinetics studies, it was most convenient to measure the mole fraction (i.e., area fraction) of water or Hq in the gas phase. Fig. 3.3 shows the consumption of water and the production of Hq in the hydrolysis of Alq_3 at 125°C. The data fit a rate law which shows a power-law dependence on the mole fraction (or partial pressure) of water in the gas phase: $\mathfrak{R} = P_{\mathrm{H2O}}^{n}$ where $n \approx 2$–6. To explain this, a mechanistic model (Fig. 3.4) was developed considering the sorption and desorption of the volatile components. The first step of the reaction is the absorption of water into the solid and the formation of an intermediate where water hydrogen bonds with the electronegative oxygen atoms on the ligand. The reaction then follows where the water exchanges position with Hq and the products can be desorbed (or desolvated).

The reaction mechanism is based on the Langmuir–Hinshelwood model for heterogeneous catalysis. This represents sorption and desorption of reactants and products as equilibria; the ligand-exchange reaction is considered rate limiting. By

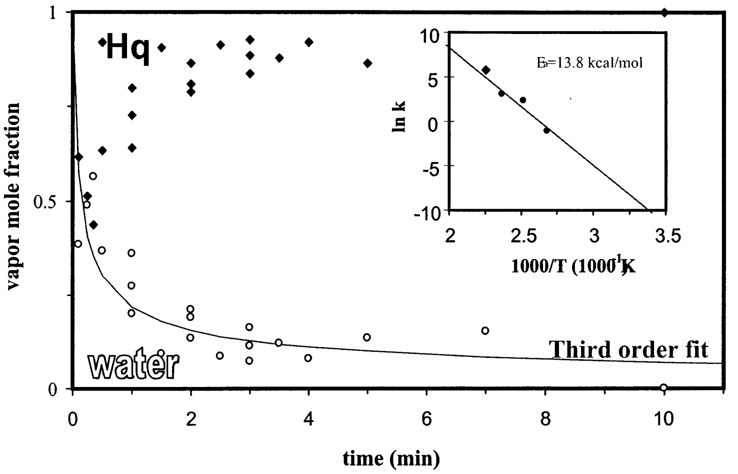

FIGURE 3.3. Rate data at 125°C showing the consumption of water and production of Hq in the vapor phase. The solid line is a fit for a third-order reaction. Inset is the temperature dependence of the rate constant.

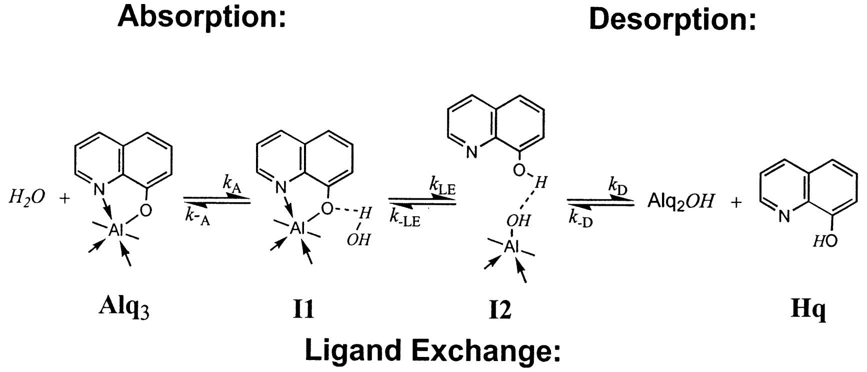

FIGURE 3.4. The full mechanism proposed for the reaction. It consists of sorption, ligand exchange, and desorption steps. The middle reaction is considered rate limiting.

lumping the sorption and solvation into one equilibrium expression, the kinetics also resemble the form suggested by Eigen and Tamm for the formation of complexes in solution.[42] It is assumed here that physical absorption of water into the film and the chemical solvation are occurring simultaneously. It is assumed that any surface effects are negligible and that the solid reactant (Alq$_3$) is in great excess. The first assumption is verified in part by observing that sorption transients could be observed in the GC experiment (monitoring the total peak area normalized by the initial mass), which were relatively fast (equilibrating within the initial 30 s). In this experiment, this is probably assisted by the small volume and high surface area of the films and powders studied, and samples were kept as small as possible to get more accurate kinetic data. The second assumption begins to fail at modest conversions, and the estimated generation rate of Hq, which will be discussed in Section 3.3, eventually becomes invalid for this reason.

The following equations represent the mechanism in Fig. 3.4:

absorption/solvation

$$\mathrm{Alq_3} + n\mathrm{H_2O} \underset{k_{-A}}{\overset{k_A}{\longleftrightarrow}} [\mathrm{Alq_3} \bullet n\mathrm{H_2O}], \tag{1}$$

ligand exchange

$$[\mathrm{Alq_3} \bullet n\mathrm{H_2O}] \underset{k_{-\mathrm{LE}}}{\overset{k_{\mathrm{LE}}}{\longleftrightarrow}} [\mathrm{Alq_2OH} \bullet \mathrm{Hq}(n-1)\mathrm{H_2O}] \tag{2}$$

desolvation/desorption

$$[\mathrm{Alq_2OH} \bullet \mathrm{Hq}(n-1)\mathrm{H_2O}] \underset{k_{-D}}{\overset{k_D}{\longleftrightarrow}} [\mathrm{Alq_2OH} + \mathrm{Hq}(n-1)\mathrm{H_2O} \tag{3}$$

and the rate laws for each component may be written as follows:

$$\mathfrak{R}_A = k_A P^n_{\mathrm{H_2O}} C_{\mathrm{Alq_3}} - k_{-\mathrm{A}} C_{\mathrm{I1}}, \tag{4}$$

$$\mathfrak{R}_{\mathrm{LE}} = k_{\mathrm{LE}} C_{\mathrm{I1}} - k_{-\mathrm{LE}} C_{\mathrm{I2}}, \tag{5}$$

$$\mathfrak{R}_D = -k_{-D} P^{n-1}_{\mathrm{H_2O}} P_{\mathrm{Hq}} C_{\mathrm{Alq_2OH}} + k_D C_{\mathrm{I2}}, \tag{6}$$

where the subscripts I1 and I2 represent the intermediates. P_i denotes partial pressures of vapor component i, and C_i is the concentration of component i in the film. This is convenient from a measurement and modeling standpoint and the rate constants may be considered to have the appropriate units. The middle reaction is considered rate limiting. By this assumption, k_{-A} and k_{-D} are large compared to the actual reaction rates of the fast reactions. Dividing Eq. (4) by k_{-A} (where $\mathfrak{R}_A/k_{-A} \cdot 0$) and Eq. (6) by k_{-D} and rearranging gives expressions for C_{I1} and C_{I2}:

$$C_{\mathrm{I1}} = K_A {P_{\mathrm{H_2O}}}^n C_{\mathrm{Alq_3}}, \tag{7}$$

$$C_{\mathrm{I2}} = K_{-D} {P_{\mathrm{H_2O}}}^{n-1} P_{\mathrm{Hq}} C_{\mathrm{Alq_2OH}}, \tag{8}$$

where $K_A = k_A/k_{-A}$ and $K_{-D} = k_{-D}/k_D$ are equilibrium constants. Substituting these into Eq. (5) and rearranging gives,

$$\mathfrak{R} = \mathfrak{R}_{\mathrm{LE}} = k_{\mathrm{LE}} C_{\mathrm{Alq_3}} \left[K_A P^n_{\mathrm{H_2O}} - K_{-D} \left(\frac{k_{-\mathrm{LE}}}{k_{\mathrm{LE}}} \right) P^{n-1}_{\mathrm{H_2O}} P_{\mathrm{Hq}} \left(\frac{C_{\mathrm{Alq_2OH}}}{C_{\mathrm{Alq_3}}} \right) \right], \tag{9}$$

which can be simplified because the reaction medium, $\mathrm{Alq_3}$, is in great excess. $C_{\mathrm{Alq_2OH}}$ is very small in comparison, and the ratio $C_{\mathrm{Alq_2OH}}/C_{\mathrm{Alq_3}}$ is approximately zero. Note that this is analogous to considering the ligand-exchange reaction [Eq. (2)] as irreversible. With these considerations, the rate law may now be written as

$$RT\mathfrak{R} = -\frac{dP_{\mathrm{H_2O}}}{dt} = \frac{dP_{\mathrm{Hq}}}{dt} = RTk_{\mathrm{LE}} K_A C_{\mathrm{Alq_3}} P^n_{\mathrm{H_2O}}. \tag{10}$$

This expression may be converted into vapor-phase mole fractions easily by substituting $P_i = y_i P$ for the partial pressures. Because the overall stoichiometry in this experiment is 1:1, the total pressure of the reaction should remain constant; for convenience, this constant-pressure assumption is continued in other situations. The mole fractions shown in Fig. 3.3 do not include the contribution of the carrier gas. Given the stoichiometry, the pressure at all times should be equal to the initial pressure of water. At a first approximation, the partial pressure of water is near that of the atmospheric, because the Alq_3 sample starts the experiment saturated at similar conditions. In terms of the empirically determined rate constant, k,

$$-\frac{dy_{H_2O}}{dt} = k y^{n}_{H_2O}, \tag{11}$$
$$k = k_{LE} C_{Alq_3} K_A R T P^2_{H_2O,0}.$$

Because $P_{H_2O,0}$ is more or less known for this case, this rate constant can be appropriately converted in order to apply Eq. (9) or (11) to real situations.

Simple complexes can be viewed as a series of concentric charged spheres. For hydrated Alq_3, the aluminum atom is the positive center, the oxyquinolate ligands form the negatively charged inner coordination sphere of the complex, and the hydrogen atoms of water molecules may occupy the outer coordination sphere. In reality, there is strong hydrogen-bonding with the electronegative atoms in the ligands.[43,44] The overall mechanism for ligand substitution reactions may be written $ML_1 + L_2 \xrightarrow{k_f} ML_2 + L_1$, where[42]

$$k_f = K_{OS,1} k^{M-H_2O} \tag{12}$$

k_f is the rate constant for the formation of the complex, $K_{OS,1}$ is the outer-sphere association equilibrium constant for a single L_2 ligand, and k^{M-H_2O} is the exchange rate constant of water molecules about Al^{3+}, which, according to this formulation, is equal to k_{LE} presuming that the presence of other ligands does not affect the exchange rate (as is the case for Hq complexes of magnesium).[42] k^{M-H_2O} is a first-order rate constant, which is correct for Alq_3, based on Eq. (2). Unlike Eq. (12), however, it is assumed that multiple ligands are coordinating in the outer sphere. K_A represents a third-order process. In fact, the exponent in the rate law has the physical significance of the number of water molecules coordinated by Alq_3, approximately three. If consecutive association reactions, that is,

$$\begin{aligned} Alq_3 + 3H_2O_{(v)} \overset{s}{\longleftrightarrow} Alq_3 + 3H_2O_{(solv)} \overset{K_{OS,1}}{\longleftrightarrow} Alq_3 \bullet 1H_2O + 2H_2O_{(solv)} \\ \overset{K_{OS,1}}{\longleftrightarrow} \cdots \overset{K_{OS,1}}{\longleftrightarrow} Alq_3 \bullet 3H_2O, \end{aligned} \tag{13}$$

have the same equilibrium coefficient, $K_{OS,1}$, then K_A can be represented as $K_A = (S K_{OS,1})^3$, where S is the solubility of water in Alq_3. Using the reported value for k^{M-H_2O} ($\approx k_{LE}$) of $0.27\ \text{min}^{-1}$[42] in conjunction with the extrapolated value of the measured rate constant of $k = 6.6 \times 10^{-5}\ \text{min}^{-1}$ and measured solubility of $0.0023\ \text{mol/cm}^3\ \text{cmHg}$,[35] predicts a first-order $K_{OS,1}$ of roughly $2.6 \times 10^3\ M^{-1}$, which is a typical high value for this parameter, signifying that the association of water with the complex is strong.[42]

The inset of Fig. 3.3 shows the temperature dependence of the reaction rate constants for Alq_3 hydrolysis. The data approximately fit an Arrhenius law in the

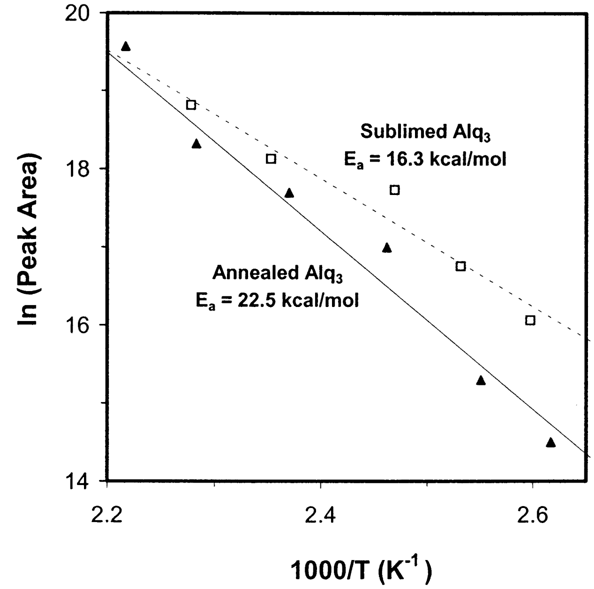

FIGURE 3.5. Reaction rates (elution area at constant reaction time) as a function of temperature for freshly sublimed and annealed Alq$_3$ samples. The greater resistance to hydrolysis shown in the annealed sample is attributed to lower water sorption or ligand association due to the crystallinity.

limited temperature range. This temperature dependence can also be obtained by observing the extent of reaction at constant time, as shown in Fig. 3.5. Immediately after deposition, Alq$_3$ is nearly amorphous. Annealing near the glass transition temperature causes the films to rapidly crystallize. The annealed films demonstrate a greater resistance to hydrolytic decomposition as a function of temperature than do freshly deposited ones,[17] which may be attributed to a lower degree of water absorption, because crystalline domains are generally impermeable to gaseous penetrants.

3.2.2 *Electrochemical Degradation of Alq$_3$ and Hq*

Degradation of Alq$_3$ and Hq was initially studied in solution, where the generation of the colored by-product could easily be observed when air or oxygen was present. Shown in Fig. 3.6 is the oxidation reaction of Hq in chlorobenzene in various reaction conditions, as monitored at the peak absorption of 600 nm. The oxidation reaction occurs slowly in neutral or acidic conditions, but when the solution is basic, it occurs very readily, suggesting that the anionic form of Hq may be particularly unstable. Similar results were obtained from Alq$_3$ solutions. This is of particular interest for device applications, because as an electron transporter, Alq$_3$ is constantly getting reduced. As previously suggested,[45] in a device and in the presence of O_2, the lifetime of an electron on a particular Alq$_3$ molecule might be long

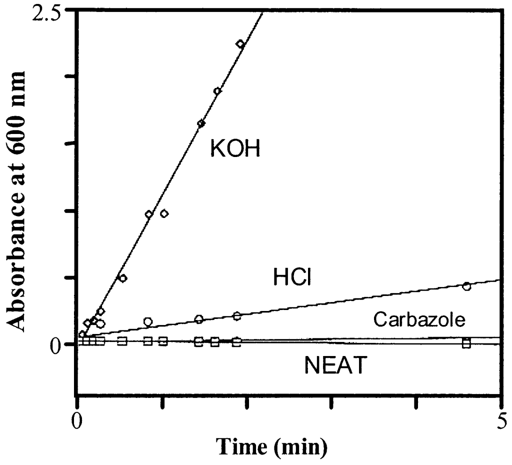

FIGURE 3.6. Preliminary oxidation kinetics heating chlorobenzene solutions of Hq in various conditions. Basic solutions of Hq oxidize most quickly. Similar behavior is observed for Alq_3.

enough to allow physical relaxation of the $[Alq_3]^-$ anion and subsequent reaction with molecular oxygen. The apparent chemical failure of Alq_3 in devices in oxidative device environments (bearing holes) has also been reported,[38] but based on the preliminary results of Fig. 3.6, this does not generate quenching species as quickly as when Alq_3 is reduced.

Cyclic voltammetry was used to generate and probe the chemical stability of the important Alq_3 anion.[18] Care must be taken when extrapolating electrochemical behavior to solid-state or optical behavior, where electronic transitions are many orders of magnitude faster than molecular diffusion and the interface structure is different, as well as essentially static. In general, however, a correlation exists between the ionization and oxidation potentials and between the electron affinity and reduction potential of a given compound.[46] As a low-order approximation, the electrochemical parameters may be used to estimate the optical (i.e., instantaneous) transitions, especially when comparing homologous materials.[46] The relaxed state of the Alq_3 anion in solution also assumes a somewhat different geometry than in the solid state. The effect of these factors should be held in mind while examining the stability of $[Alq_3]^-$ by this technique.

The chemical stability of the reduced forms of Alq_3 and Hq was examined using superoxide (O_2^-), which is a very strong nucleophile generated from the reversible reduction of oxygen dissolved in aprotic solvents.[47] A cyclic voltammogram of this process in DMF is shown in Figs. 3.7B and 3.8B. It is not unreasonable to suspect that dissolved or ITO-generated oxygen is being reduced in OLEDs, because it is certainly present in many cases, and devices generally operate at voltages well beyond the reduction potential of O_2. Examining the behavior of Alq_3 and Hq in the presence of superoxide, however, is used here primarily as a tool to examine their susceptibility to nucleophilic attack.

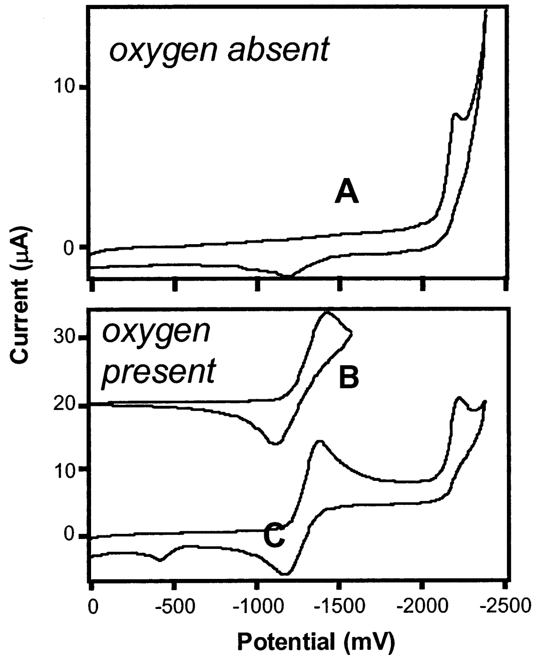

FIGURE 3.7. Cyclic voltammograms of Alq_3 in DMF. (A) When oxygen is absent, reduction of Alq_3 is seen at −2.3 V and its reoxidation at −1.2 V. (B) When oxygen is present, the reversible reduction of O_2 can be seen in the presence of Alq_3, (C) but once the reduction potential of Alq_3 is reached, a new peak appears on the reverse wave at −0.4 V, signifying a new chemical species.

The cyclic voltammograms for the reduction of Alq_3 in DMF are shown in Fig. 3.7 in the presence and absence of oxygen.[18] When oxygen was removed from the solution, reduction of Alq_3 could be seen on the cathodic wave at −2.3 V (Fig. 3.7A), followed by its reoxidation on the anodic wave at −1.3 V. Despite the large separation, it is currently believed that this is the reverse oxidation peak of the chelate, based primarily on the analogous behavior of Hq, as discussed below. When the Alq_3 solution was bubbled with pure oxygen, the reversible O_2/O_2-couple was observed at voltages below the reduction potential of Alq_3 (Fig. 3.7B) with no observable change in magnitude of the forward and reverse peaks. When the chelate was reduced, however, the reverse oxidation peak of O_2^- was diminished in height, and a new peak associated with the oxidation of the oxyquinolate anion (q^-) appeared at −0.4 V. It was not possible to distinguish a peak at −1.3 V, although it would probably be obscured by the oxidation of O_2^- (Fig. 3.7C).

The generation of a new peak not associated with either Alq_3 or oxygen is indicative of the formation of a new chemical species. The mechanism of this reaction is based on the nucleophilic character of the superoxide ion toward metal ions and organic compounds.[47] The neutral species shows no sensitivity to superoxide, but upon reduction, the chelate bonds are weakened enough to allow attack by the base

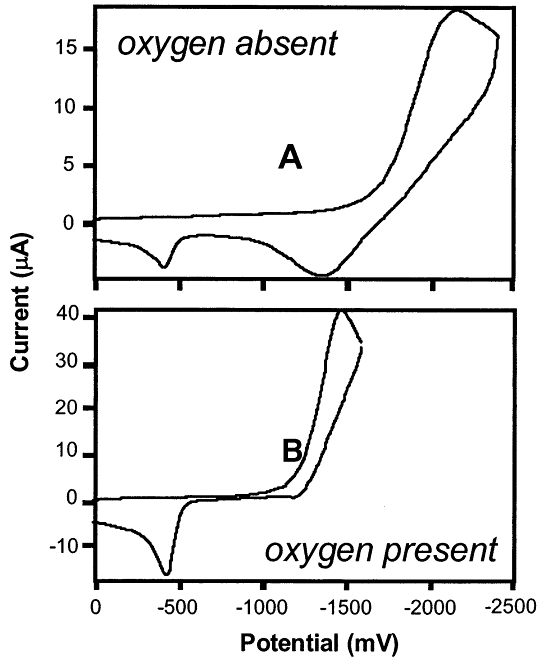

FIGURE 3.8. Cyclic voltammograms of Hq reduction. (A) When oxygen is absent, a broad reduction peak is seen beginning at -1.7 V and peaking at -2.3 V. Oxidation peaks are observed at -1.2 and -0.4 V, in an analogous fashion to Alq$_3$. (B) In the presence of dissolved oxygen, the peak at -0.4 V is recoverable as soon as the reduction potential O$_2$ is reached.

and the release of a negatively charged ligand. The oxidation of this free q^- anion is consistent with that observed during the reduction of free species.

Molecular orbital calculations of individual Alq$_3$ molecules have revealed that the lowest unoccupied state (LUMO) is localized on one of the oxyquinolate groups and that adding an electron to it shortens the Al-N bond on that ligand while lengthening the equivalent bond on the other two.[45] The resulting change in shape, as well as the destabilization of two of the ligands, may facilitate the nucleophilic addition of superoxide and the release of q^-. The metal peroxide will eventually disproportionate with other radicals to produce various other oxidation byproducts. The presence of nucleophiles other than O_2^- would also be expected to promote degradation of the complex, and their efficiency is probably affected by size and strength, although studies to generalize this observation have not yet been performed.

The first reduction of Hq in oxygen-free solvent is observed in the cyclic voltammogram as a broad peak beginning at approximately -1.7 V in DMF and ending at about -2.4 V (Fig. 3.8A).[18] On the anodic wave, oxidation peaks at -1.3 V and then at -0.4 V are observed. When oxygen is present, the peak at -0.4 V can be observed as soon as the formation of superoxide occurs (Fig. 3.8C). When Hq is reduced, it simultaneously eliminates hydrogen to form oxyquinolate anions

(q^-).[48] A second reduction soon follows to produce the doubly-charged oxyquinolate (q^{2-}).[48] These processes occur at similar potentials and were resolved as a single broad reduction peak at the scan rates used in the experiment. The peak at -1.3 V on the anodic wave of the oxygen-free samples is attributed to the removal of the second electron from the oxyquinolate ($q^{2-} \rightarrow q^- + e^-$). The peak at -0.4 V on the anodic wave is the oxidation of the q^- anion. When oxygen is present, however, the slightly acidic phenolic hydrogen on Hq is abstracted by highly basic O_2^- as soon as it is formed at -1.2 V (Fig. 3.8B).

In Alq_3, the ligand may be considered in its reduced state ($Al^{3+}q_3^-$). It is the ionic character of the ligand that allows for emission: Basic solutions of Hq are fluorescent. Similarly, varying the metal center shows marginal change in the electroluminescence (EL) emission spectra of OLEDs based on various other Mq_3 complexes.[45,49] Thus, the behavior of the chelate is roughly equivalent to that of the free q^- anion in reductive conditions. When these species are reduced ($Alq_3 \rightarrow [Alq_3]^-$, or $q^- \rightarrow q^{2-}$), the added electron is localized principally on the pyridine ring of the oxyquinolate.[45,48] In DMF, this reduction is shown at -2.3 V for Alq_3; for q^-, it occurs at apparently the same potential—the broad reduction peak begins with the dehydrogenation of Hq (at about -1.7 V) and includes the reduction of q^- (apparently at about -2.3 V). The reoxidation of both these species ($[Alq_3]^-$ and q^{2-}) occurs at -1.3 V on the reverse wave. The oxidation of q^- at -0.4 V is then observed only when the quinoid ion (q^-) is free; Alq_3 is a fairly stable compound, but when $[Alq_3]^-$ is formed in the presence of nucleophiles (O_2^-), a free q^- species is generated and its subsequent oxidation may be observed.

The chemical susceptibility of charged species in the glassy state and those in electrochemical solution are related, but the solvent and electrode surface may both alter the shape of the Alq_3 anion, probably destabilizing it further. Likewise, the diffusion of the attacking nucleophile and leaving q^- is likely facilitated in solution. The net effect is likely to, decrease the stability of solvated Alq_3 in comparison to glassy samples.

Still, the electrochemistry offers some useful insights into the stability of glassy Alq_3, especially when viewed in light of the solid-state thermal degradation (Sec. 3.2.1) and isomerization reaction[43] of the compound. Each of those processes suggest that decomposition of the chelate begins with the destabilization of the Al-N bonds. Furthermore, the coordination of solvent molecules into the outer sphere of Al^{3+} is an essential step in the thermal decomposition. In the previous section, the activity of water was described as a neutral ligand-exchange reaction, although it is also possible that neutral water is displacing a negatively charged ligand in processes similar to those mentioned earlier. The destabilization of the Al-N bond which occurs during reduction of Alq_3 is also suspected of facilitating dissociation of the complex by incoming nucleophiles, in this case, O_2^-.

Both the degradation of $[Alq_3]^-$ and the reduction of Hq result in the formation of the free oxyquinolate ligand (q^-). These materials may exist in OLED environments, held under high reductive bias or if the easily reduced Hq traps an incoming electron. Although neither q^- nor Hq offer avenues for energy transfer

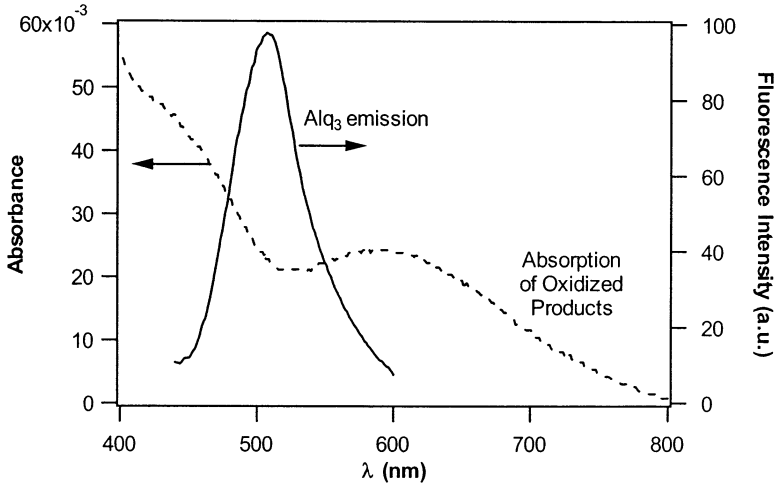

FIGURE 3.9. Absorbance of extracted oxidation products compared to the fluorescence of Alq$_3$. There is significant overlap of the spectra.

from Alq$_3$, their oxidation products do. In DMF, the oxidation potential of q^- is only −0.4 V versus a Ag/Ag$^+$ electrode (Figs. 3.7 and 3.8). Basic solutions of Hq (i.e., solutions of q^-) are also known to gradually oxidize in the presence of dissolved oxygen to form quinoid species.[48] Figure 3.9 shows the UV-vis absorption of the basic solutions of Hq heated in the presence of oxygen. These spectra strongly overlap the fluorescence of Alq$_3$, suggesting that energy transfer to these nonradiative products is likely.

Reactions such as those in Fig. 3.10 were prepared in a controlled fashion to produce impurity products in high enough concentrations for study. Considerable photoluminescence quenching occurs at impurity concentrations as low as 0.125 wt% in the solid state.[15] Cyclic voltammetry was also performed on these extracted compounds to characterize their HOMO and LUMO levels with respect to Alq$_3$. The lowest transition for the oxidized impurities lies nearly within that of Alq$_3$, showing that energy transfer from one compound to the other is probably thermodynamically allowed. The LUMO levels of these materials are similar and, alternatively, a charge-transfer quenching mechanism as has been shown for PPV[20] may also be possible in this case. The effect of these degradation products in the recombination interface of OLEDs was also investigated directly.[16] The introduction of the thin film at the interface of Alq$_3$ and a hole-transport layer caused complete extinction of the electroluminescence of the device, whereas the PL intensity of the combined layers was only diminished by about half due to nonradiative energy transfer. In this experiment, it was impossible to determine if this was due to recombination of holes and electrons in the nonemissive layer or the quenching of Alq$_3$ excitons formed near the interface.

When the q^- anion is exposed to oxidative environments, a variety of products can readily be formed. Figure 3.10 shows resonance forms of the oxyquino-

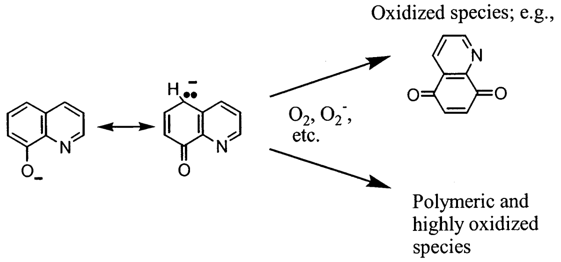

FIGURE 3.10. Resonant form of q^-. This anion is susceptible to oxidation at the 5-position to form quinones.

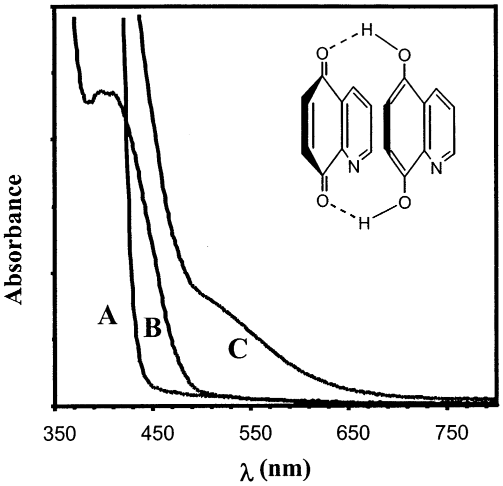

FIGURE 3.11. Absorbance spectra of (A) DHQQ, (B) QQ, and (C) the one-to-one mixture of these compounds. Inset is the probable structure of the charge-transfer complex observed in spectrum C.

late anion, indicating its susceptibility to addition at the 5-position. This results primarily in a number of quinoid species, which are normally in some equilibrium at room temperature. Furthermore, these species, in an analogous fashion with benzoquinones, easily form ground state charge-transfer complexes (CTCs) with electronic transitions in the visible spectrum. Further oxidation of Hq can result in the formation of insoluble species, which are probably polymeric in nature[15,40] and also act as luminescence quenchers. CTC formation was observed by the emergence of a new absorbance band when quinolinequinone (QQ) and dihydroquinolinequinone (DHQQ) were mixed in a 1:1 ratio (Fig. 3.11). The CTC arises via the partial donation of an electron from DHQQ to QQ, through π–π interactions of the two species. Such a complex is of the "quinhydrone" form as described by Mulliken and Person[50] and arises through the strong overlap of the nearly symmetric but differently populated π systems of QQ and DHQQ. The LUMO of QQ is essentially identical to the HOMO of DHQQ, which is consistent with the electrochemical measurements.[18] This symmetry allows significant donation of charge (about 0.2 e)[51] from DHQQ to QQ to form a relatively stable complex. Furthermore, the CTC formation is probably facilitated by hydrogen-bonding; the three-member linkage is of ideal geometry to maximize intramolecular π–π interactions.[52] The electronic states in a CTC are well defined and transitions are of lower energy than those in the parent molecules;[50,51] CTCs usually exhibit strong absorption in the visible region. The QQ/DHQQ complex shows a characteristic brown color, which is easily observed in solutions and even in solid samples. The breadth of the absorption bands, extending well into the red part of the spectrum (Fig. 3.11), is probably due to the interaction of the CTC with solvent, causing a distribution of possible orientations of the donor and acceptor species in the complex.

Neither QQ nor DHQQ is expected to act as a luminescence quencher for Alq_3, but the CTC has an absorption similar to that of the thermal oxidation products of Alq_3 and Hq, as shown in Fig. 3.9. For the extracted product, an absorbance band at 600 nm with an onset at 810 nin corresponds roughly to that of the QQ/DHQQ charge-transfer complex (Fig. 3.11). The differences between the spectra may be due to solvent effects or the presence of marginally soluble impurities (such as highly oxidized polymers or oligomers) generated during the harsh thermal oxidation. Infrared spectroscopy has also suggested that polymeric or heavily oxidized species may be present in the high-temperature samples and may result in other absorption bands or redox potentials, but it can, nonetheless, quench the luminescence of Alq_3.

3.3 Morphological Stability of Organic Glasses in LEDs

The efficacy of inorganic semiconductor technology is largely a result of the extraordinarily high degrees of purity and order attainable through sophisticated fabrication and growth procedures such as chemical vapor deposition or molecular beam epitaxy. It is not presently feasible to achieve this degree of crystallinity for organic electronic devices, and uniformly amorphous films are alternatively sought after. This is feasible with physical vapor deposition, where chemicals are usually condensed so rapidly from the gas phase that vitreous films result even from stubborn glass formers.[53,54] It has been demonstrated for OLEDs, however, that this amorphousness is not always a stable feature of the films. Raising the operating temperature of OLEDs to the vicinity of the materials' glass transition has caused an enormous drop in emission intensity.[24] The poor resistance to crystallization of commonly used hole-transport materials has also been recognized[22] and researchers have designed a variety of materials with high glass transition temperatures (T_g) to successfully increase the thermal stability of OLEDs.[23–25]

The crystallization of constituent OLED materials is likely to facilitate most of the extrinsic failure modes. If the cathode conforms to the volume shrinkage in the film that occurs with aging and/or crystallization, uneven charge injection and formation of hot spots could result that can lead to dielectric breakdown or penetration of the hot metal cathode through the softened material.[55–57] Alternatively, the strain from aging would likely assist the delamination of the cathode by oxidation or dewetting. Local heating is expected to occur at crystalline defects where current is disproportionately transported, greatly accelerating chemical and electrochemical degradation rates.

Physical aging is generally described as a relaxation of the free volume in a material, analogous to increasing the intermolecular interactions to a temperature-appropriate quasi-equilibrium.[58] Physical aging can also affect transport and EL properties even when uniformity is preserved on a meaningful scale. An amorphous material may be described as containing a spatially homogeneous distribution of defects states (i.e., the disorder in the film produces a variety of intermolecular interactions). The density and distribution in energy of these defect states often controls the transport and luminescence characteristics in an amorphous material.[59–62] The free-volume distribution, as well as the molecular or segmental mobility required for further relaxation, is strongly affected by thermal history. Materials which have a large amount of free volume frozen-in during a rapid quench will age more quickly.[58] Aging generally occurs within some window below T_g, where the segmental mobility is slow but not negligible; near the glass transition, the effects of sub-T_g aging can often be observed by calorimetry or by thermomechanical analysis.

3.3.1 Crystallization of Alq_3

Aluminum (III) 8-hydroxyquinoline is a good example of a high-T_g material (175°C) which does not form a stable glass.[17,63] In fact, little consensus has been reached in the literature as to the morphology of evaporated Alq_3 films in OLEDs, ranging from purely amorphous[64] to semicrystalline.[17,65] Substrate temperature, deposition rate, and purity levels probably account for some of the discrepancies in the reported values. Wide-angle X-ray diffraction (WAXD), as shown in the first curve of Fig. 3.12, showed that Alq_3 deposited at rates of 5–10 Å/s onto room-temperature substrates was noncrystalline. For a freshly sublimed sample, only a broad hump is visible, characteristic of a material with no long-range order. As the material is annealed, however, the trace rapidly resolves into crystalline peaks, even at temperatures 40°C below its T_g.

Figure 3.13 shows differential scanning calorimetry (DSC) traces for freshly deposited Alq_3 films. Large exotherms above T_g (165°C) are visible in the first heating scan of the newly sublimed sample. Below T_g, erratic, but reproducible, exotherms are also visible on the initial scan. These peaks have been attributed to crystallization based on the corroborating WAXD data. A broad featureless T_g at the reported value of about 175°C is visible on the subsequent trace, but there is no further evidence of crystallization. After annealing in the vicinity of the glass transition, the crystallization exotherms similarly disappear. The remaining amorphous material is in a state of metastable equilibrium with the crystal phase, exhibiting a broad spectrum of relaxations associated with the postannealed T_g.

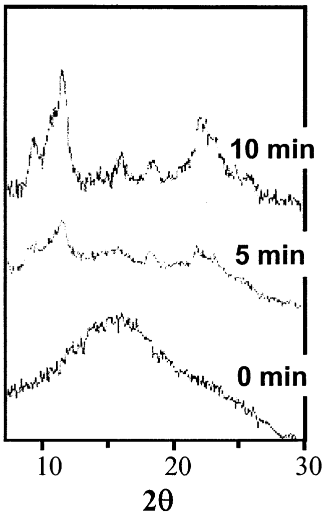

FIGURE 3.12. WAXD patterns of $\mathrm{Alq_3}$ as it is annealed at 145°C. The initial amorphous hump resolves rapidly into crystalline peaks.

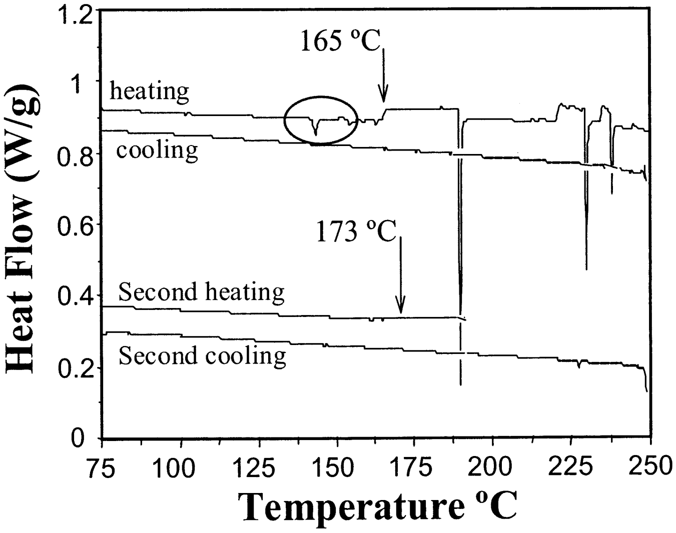

FIGURE 3.13. DSC of $\mathrm{Alq_3}$. Exotherms above and below T_g are due to crystallization. On subsequent scans and following annealing, these peaks disappear.

It is rare for materials to crystallize rapidly below their glass transition, and the rapid sub-T_g crystallization of the $\mathrm{Alq_3}$ samples is indicative of the instability of the glassy phase.

Crystallization of thin $\mathrm{Alq_3}$ films could easily be observed with optical microscopy as well. One thousand-angstrom films were fabricated by evaporation and

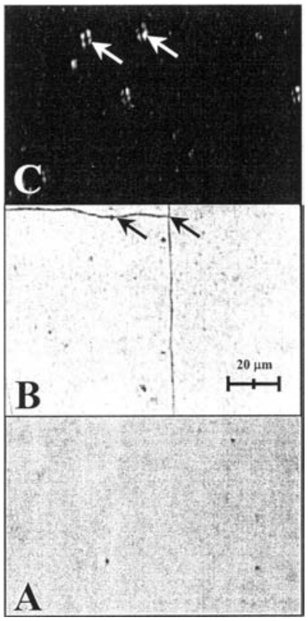

FIGURE 3.14. Optical micrographs of Alq_3 (A) as deposited on glass and (B) after annealing. (C) is the annealed sample viewed between crossed polarizers. At defects such as cracks, crystallites grow with spherical symmetry. In the homogeneous areas of the film, approximately one-dimensional crystals are visible.

annealed in a vacuum oven at the same temperatures as the diffraction experiments. Figure 3.14 shows micrographs of these films viewed at various times. Crystallites at film defects form rapidly and grow with spherical symmetry (shown by the cross pattern when viewed between crossed polarizers). After an apparent induction time, smaller cylindrical or needlelike crystallites become observable in defect-free areas.

Annealing 1000-Å Alq_3 films in the vicinity of their T_g resulted in a rapid decrease in fluorescence intensity accompanied by a slight red shift (by about 2 nm) of the emission maximum (Fig. 3.15). Both the photoluminescence (PL) decrease and red shift may be explained by the formation of aggregates or crystals which promote the formation of excimers or ground-state complexes. Excitons in the solid state tends to migrate to lower energy sites, commonly occurring at aggregates or crystallites, lowering the emission energy and increasing the quenching probability.[66–68] (There is a blue shift and intensity increase that occurs at long annealing times; this is not due to the change of the emission characteristics but to Rayleigh scattering of the excitation beam as the crystallites grow large.) From only fluorescence data, it cannot be determined whether the small red shift is due to a ground- or excited-state complex, although excimer emission usually occurs at a significantly lower energy than the single-component transition. It is convenient to assume that the red shift comes from splitting of the exciton in ground-state ag-

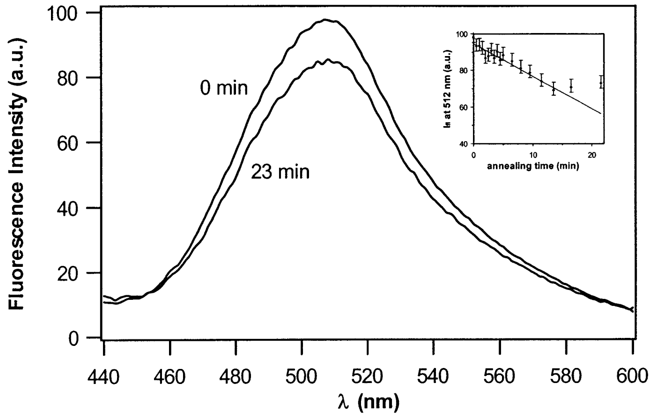

FIGURE 3.15. Fluorescence spectra of $\mathrm{Alq_3}$ films as a function of annealing near T_g. A small red shift is accompanied with a loss of fluorescence. The inset shows the peak intensity change as a function of time.

gregates, and the highest occupied molecular orbital (HOMO) level is unchanged, whereas the 2–3-nm shift will correspond to a reduction of about 0.1 eV in the lowest unoccupied molecular orbital (LUMO) energy level.

3.3.2 *Guidelines for Amorphous Materials Selection*

Crystallization of common hole transport materials in OLEDs has led to a variety of designs for high-T_g alternatives, comprised of highly asymmetric or bulky molecules, improving device longevity.[22–25] TPD in particular, although once nearly as ubiquitous as $\mathrm{Alq_3}$, is now rarely used because of its poor resistance to crystallization. The usual strategy for synthesis of high-T_g transport compounds is to increase the molecular weight and/or asymmetry of the structure. This approach reaches practical limits from both a purification and fabrication standpoint, as solution processing and sublimation become problematic as the size of the molecules is increased. Furthermore, as can be seen with $\mathrm{Alq_3}$, a high glass transition does not necessarily inhibit crystallization.

A more general tactic is to design for negligibly slow crystallization rates. The rate for the homogeneous, steady-state nucleation rate, I, of a single-component liquid (or glass) can be expressed by,[69]

$$I = \frac{n_v kT}{h}\left[\exp\left(\frac{-W^*}{kT}\right)\right]\left[\exp\left(\frac{-\Delta G_D}{kT}\right)\right], \tag{14}$$

where

$$W^* = \frac{16\pi^2\sigma^3 V_m^2}{2\Delta G_{\mathrm{gc}}^2}; \tag{15}$$

W^* is the Gibbs energy required to form a critical nucleus and ΔG_D is the activation energy for rearrangement. V_m is the molar free volume of the crystal; n_v is the number formula units (atoms) in the glass per unit volume; ΔG_{gc} is the free-energy difference between the glass and crystal phase; and σ is the interfacial energy of a critical nucleus. Similarly, the linear crystal growth rate u can be expressed as[70]

$$u = a_0 \nu_0 \left[1 - \exp\left(\frac{-\Delta G_{\text{gc}}}{kT} \right) \right] \left[\exp\left(\frac{-\Delta G_D}{kT} \right) \right], \tag{16}$$

where a_0 is a dimension and ν_0 is the "jump probability" of a formula unit.

These equations show that both the rate of nucleation and growth depend not only on the segmental mobility (associated with T_g and the activation energy ΔG_D) but also on the then-nodynamic driving force between the glassy (liquidlike) and crystal phases (represented as ΔG_{gc}). The activation energy term W^* varies inversely with ΔG_{gc}. In the case of Alq_3, the rapid crystallization is probably due to an anomalously large ΔG_{gc} term arising from the enhanced stability of a crystal phase containing extensive hydrogen-bonding and π–π stacking interactions.[71] (This is the case for Gaq_3 whose crystal structure is isomorphous with Alq_3.)[43]

When the nucleation is not homogeneous, the W^* term changes appropriately. Films tend to nucleate at surfaces or interfaces, where the mobility is higher, or at physical defects approximately the same size as a critical crystal nucleus.[69] One of the problems with using the above equations to predict nucleation rates is that the parameters ΔG_D and especially σ are difficult to obtain independently. ΔG_D can be estimated from viscosity data[69] or by calorimetry,[63,72] but σ is not easily determined outside of experiments related to nucleation and growth. Prediction of W^* for heterogeneous nucleation produces additional geometric considerations, although approximate magnitudes of the interfacial energy can be estimated from contact-angle experiments. As qualitative design criteria, however, they can be very useful. Selecting materials with high activation energies for rearrangement (high T_g) or which vitrify at low undercoolings (ΔG_{gc} is low) are both valid approaches to reduce the total rate of crystallization of a material.

According to the theory of Gibbs and DiMarzio, between the experimentally observed T_g and the true second-order transition temperature T_2, there is a finite probability for cooperative rearrangements of molecules or segments to occur. Similarly, physical aging is generally considered to occur within a window below T_g and above the temperature of the lowest-energy molecular rearrangement.[58] A rule of thumb developed by Adam and Gibbs for polymeric or low-molecular-weight systems is $T_g/T_2 \approx 1.3$.[73] By that argument, Alq_3 ($T_g = 175°\text{C}$) is perfectly frozen below about 75°C and forms a stable glass at room temperature. For TPD, a commonly used hole transporter ($T_g = 65°\text{C}$), T_2 is at about $-13°\text{C}$ and this material eventually crystallizes at ambient temperatures. For commercial-sized displays, the temperature rise due to power dissipation has been estimated to be as much as 60°C,[74] which may be a problem for Alq_3 and other materials. Also, thermal relaxation may occur in the top organic layers during the condensation of metal electrodes from a high-energy vapor phase.

In order to retard the crystallization rate by manipulating thermodynamic terms, Naito suggests designing organic dyes with minimal changes in enthalpy for glass–crystal transitions (ΔH) and low equilibrium melting points (T_m), in addition to high T_g's.[63,72] With similar reasoning, a small difference between T_g and T_m is often considered a useful indicator for high glass-forming ability.[54,75] Multicomponent liquids resist crystallization on this basis.[54,69] Mixing lowers the free energy of the liquid with respect to the single components (and lowers ΔG_{gc}). For non-polymeric, non-network systems (such as liquid metals), impurity concentrations as low as 1–2% are sufficient to observe glass formation at reasonable quenching rates. Mixing makes the liquid state more thermodynamically favorable by increasing its entropy, lowering the energy of the solution with respect to either single component. For an ideal solution, the free-energy change of mixing N components is simply expressed as

$$\Delta G^{\mathrm{mix}} = G - \sum x_i G_i = -RT \sum_{i=1}^{N} x_i \ln x_i, \qquad (17)$$

although ideal mixing, of course, is rare. Negative deviations from ideality (due to attractive intermolecular forces) can lower the free energy of the mixture even more. Figure 3.16A shows a generic free energy versus composition curve. As the material crystallizes, the final overall composition of the crystal phase may be that at one of the free-energy minima for the crystals or at a tie line between the two. For simple binary systems, stable glass-forming regions are usually centered about deep eutectics, where the free energy of mixing is largest. For real multicomponent systems, model parameters for mixture properties are fairly accessible, but it is generally impossible to predict the composition of the crystal phase beforehand. When the liquid and crystal phases have different net compositions, as is often the case, the analysis is generally fairly complicated. Although the free-energy term is still somewhat accessible, the activation energy ΔG_D and other parameters which now must make up W^* are quite difficult to quantify.[70]

For OLEDs, an added constraint is the compatibility of the diluent with the charge conduction and emissive properties of the host material. The blend system chosen for this study is Alq_3 and aluminum(III) 4-methyl-8-hydroxyquinoline ($AlMq_3$), a blue-green emitting material which has received recent attention for OLED applications.[76] These compounds are a good pair because Alq_3 acts as an energy-transfer acceptor for $AlMq_3$.[77] These materials are chemically similar and are expected to reasonably approximate an ideal solution in the liquidlike phase. As such, the maximum energy change on mixing will be at a 1:1 mole ratio (maximizing the combinatorial entropy). Blends were made by depositing the two materials simultaneously, either from the same evaporation source or from independent sources. When the materials were evaporated from the same source, the deposition rate was fast (about 20 Å/s) in order approximately preserve the mole ratio.

3.3.3 Crystallization and Aging of $AlMq_3$ and Alq_3/$AlMq_3$ blends

Melting of $AlMq_3$ could be observed with DSC, followed immediately by evaporation or decomposition. Figure 3.17 shows DSC traces of sublimed-scraped samples as well as films deposited directly onto the DSC pans. T_m was reproducible in the

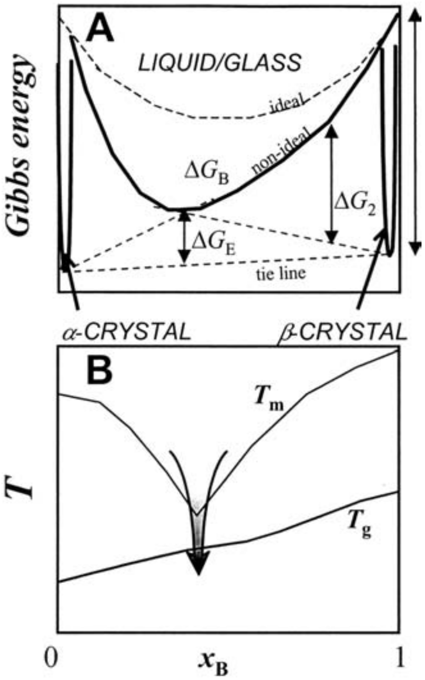

FIGURE 3.16. (A) Free-energy curve showing change in ΔG on mixing, as well as different crystallization regimes. ΔG_α is for a single component α, ΔG_E is for polymorphous crystallization; ΔG_2 is for the precipitation of the β phase from a glass of a different composition. (B) Quasi-phase equilibrium diagram showing the effect of undercooling. The glass-forming ability is usually high near eutectic points.

samples studied, but T_g was difficult to evaluate for this compound because it was associated with a maximum in the scraped samples that was rapidly followed by a cold crystallization peak. For the neat film, the sample weighed only 0.4 mg and the signal was too small to reliably extract a glass transition. Furthermore, this sample showed some sharp exothermic peaks between T_g and T_m, which may be similar to the rapid crystallization observed in Alq_3 calorimetry (Fig. 3.13), or simply artifacts. The thermal parameters for both compounds are summarized in

TABLE 3.1. Thermal parameters for Alq_3 and $AlMq_3$.

	T_g(°C)	T_c(°C)	T_m(°C)
Alq_3	165–175	130–240[a]	412[b]
$AlMq_3$	160–190	230–260[c]	297

[a] 20°C/min.

[c] 10°C/min.

[b] Data from Ref 63.

Table 3.1. The T_g of AlMq$_3$ varied from about 160°C to 190°C, with no apparent dependence on the quench rate (whether from the melt or vapor) for the few samples available for examination. Because the T_g of Alq$_3$ falls in such a close range with AlMq$_3$, no attempt was made to characterize the miscibility of the blend by observing the change in T_g with composition. Cold crystallization peaks were visible on every sample between T_g and T_m. The melting temperature was constant for each sample at 297°C. Crystal nucleation in AlMq$_3$ films apparently occurs homogeneously at some temperature between T_g and T_c, because even neat evaporated films exhibited a crystallization peak. No crystal nucleation was observed by optical microscopy at temperatures slightly below T_g. It is possible that some variation in the T_g and T_c temperatures observed for the sublimed films is due to small changes in the deposition rate or pressure.

The DSC analysis suggests that AlMq$_3$ is a better glass former than Alq$_3$. A glassy state can be obtained for this material by cooling from the melt as well as from the vapor phase. The addition of methyl groups does not appear to change the glass transition temperature significantly, but it lowers the melting point considerably. Presumably, this is due to decreased enthalpic interactions in the crystal by breaking up the hydrogen-bonding and stacking of Alq$_3$.[71] This can be witnessed by the lower 20 maximum of the amorphous AlMq$_3$ as opposed to Alq$_3$ (see bot-

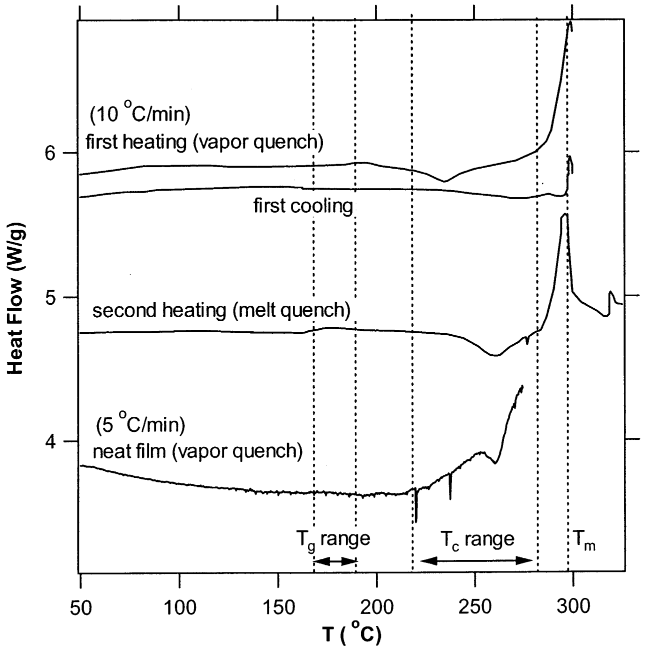

FIGURE 3.17. DSC traces for AlMq$_3$. Crystallization peaks could be seen in neat and scraped sublimed films. Endotherms associated with T_g are observable in the scraped sample, but the signal was too small in the neat sample. Thermal parameters are listed in Table 3.1.

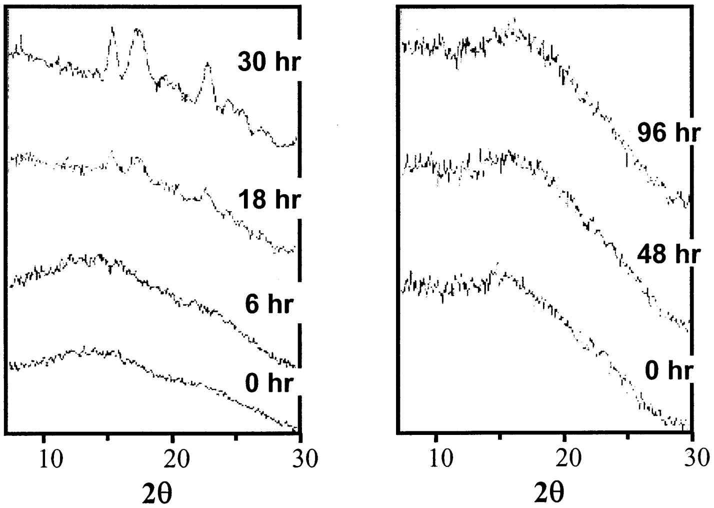

FIGURE 3.18. WAXD patterns for $AlMq_3$ and a 1:1 $AlMq_3$:Alq_3 blend for different annealing duration at 160°C. $AlMq_3$ is a more stable glass than Alq_3, crystallizing over the course of a day at the same temperature. The blend did not crystallize within a week of heating at temperatures approaching its T_g.

tom curves in Figure 3.18), indicating that the addition of methyl group do result in volume dilation.

Nucleation and growth rates can be measured independently by microscopy or DSC,[63,69,70,72] but only a small amount of $AlMq_3$was available for study. Optical microscopy revealed no macroscopic crystallites in the annealed $AlMq_3$ films (no birefringence was observed with crossed polarizers, although surface roughening occurred for all samples), and DSC experiments revealed erratic temperatures for both materials, requiring a large number of samples for statistical analysis. Similarly, WAXD patterns of these materials could not be obtained from any of the neat films, including Alq_3, where crystallites were clearly visible in the microscope. Vacuum-deposited samples were scraped from their substrates and placed in capillaries for powder WAXD measurements and the crystallization in these compounds was observed by directly annealing the capillaries at constant temperatures. $AlMq_3$ demonstrated greater thermal stability than Alq_3, but it still eventually resolved into crystalline peaks with sub-T_g annealing. The blend, however, did not crystallize even after 1 week of heating at 160°C. The nucleation rates may have been affected by scraping, because many irregular surfaces were introduced as potential heterogeneous nucleation sites (as in Alq_3 films, for example).

Because at early annealing times, all of the samples retained a clear amorphous contribution to the diffraction pattern, the fraction crystallinity, x_c, could be obtained by fitting the amorphous background and subtracting the spectrum [in this experiment, $1 - x_c = A_a/(A_a + A_c)$, where A_a and A_c are the areas of the amorphous and crystalline diffraction peaks, respectively]. The data for $AlMq_3$ and Alq_3

were fit to an Avrami equation, describing the combined nucleation and growth rate for a material:

$$\ln(1 - x_c) = -Zt^n. \tag{18}$$

Alq_3 crystallized too rapidly to produce meaningful results, but fits for $AlMq_3$ show an exponent of approximately 1 (with considerable scatter), which is consistent with crystals of low dimensionality and heterogeneous (or instantaneous) nucleation.[70] This also illustrates what can be readily seen in Fig. 3.18, that $AlMq_3$ is more stable to crystallization than Alq_3 at temperatures approaching its T_g. Based on the optical microscopy, it is possible that the sub-T_g crystallization in the film is limited by the nucleation rate in $AlMq_3$, although it can readily occur above T_g. Considering this, as well as the large degree of scatter in the data, the Avrami parameters acquired in the WAXD experiment were not particularly useful for predicting crystallization dynamics in the film, but they are used as qualitative indicators of the crystallization resistance of these materials.

The glass transitions for $AlMq_3$ show endothermic peaks associated with the step change of T_g. This is not distinguishable on the first heating sample because of the subsequent crystallization exotherm, but it is pronounced on the following heating scan. This is indicative that some physical aging of the sample occurred at temperatures below T_g in the time frame of the experiment. Energy is absorbed as segments become mobile to compensate for the decrease in the free energy as the material was aged at a lower temperature.[58] This may suggest that $AlMq_3$, although a better glass former, is susceptible to aging processes in the absence of crystallization. It will be worthwhile to compare the performance of OLEDs fabricated from $AlMq_3$ and $Alq_3/AlMq_3$ blends.

3.4 The Effect of Aging Processes on OLED Performance

Operating at constant current density, the light output (or efficiency) of an OLED tends to fall while the drive voltage (or device resistance) increases. At higher current densities, the rates of decay in Alq_3-based OLEDs increase.[29] This can be caused by the presence of carrier traps, such as would be generated by aging mechanisms. In similar metal–insulator–metal devices, conductivity switching phenomena have been ascribed to the presence of bulk trap states:[60–62,78,79] A resistive state exists as space charge is accumulated in the localized traps, whereas a conductive state could be obtained by neutralizing the space charge at high bipolar injection levels.[60–62] In Alq_3-based OLEDs, an alternating-current drive scheme has greatly increased luminous lifetimes,[29] which is supportive of trap-filling arguments if the traps are nonemissive.

Sernicrystalline polymers and amorphous network materials, where some degree of order persists (either in domains or over a short range), have been shown to exhibit trap-charge–limited (TCL) conduction in many cases.[59,80] These traps

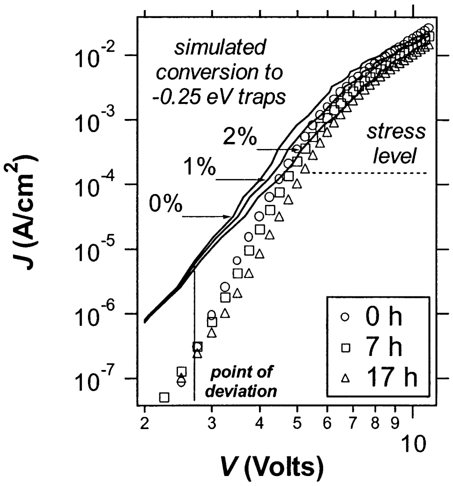

FIGURE 3.19. *J–V* characteristics taken at various times for a device stressed at 150 μA/cm^2. Successive curves begin to deviate from the original at about 3 V and then reconverge to the same square-law behavior at higher bias. This corresponds qualitatively to the simulations where traps are generated -0.25 eV below the Alq$_3$ LUMO, shown by the solid curves.

correspond to the disordered regions of the insulator which localize charge and they are frequently described by localized "tails" extending downward (upward) in energy from the conduction band (valence band).[59] The TCL model has been fit to Alq$_3$ with great success, possibly due to its semicrystalline nature or due to the physical relaxation of the localized electron;[45] this model has gained some criticism because it presupposes the existence of a conduction band in Alq$_3$.[81] Still, when the transport is effectively made unipolar by introducing nearly ohmic electron-injecting contacts[33] and effectively blocking hole injection,[36,82] then the entire predicted range of TCL transport can be observed, as shown in the first curve of Fig. 3.19. At low currents, ohmic transport ($J \propto V$) prevails, until the population of trapped electrons becomes significant and they start to fill rapidly as charge is injected ($J \propto V^n$; $n \approx 11$ for these data). At high enough injection levels, the strongly localized states become filled, and the current becomes space-charge limited (SCL; $J \propto V^2$).

The above laws arise from analytical solutions to the Poisson equation[83] in the bulk of the conducting layer, Alq$_3$. It can, however, also be solved numerically for an arbitrary trap distribution. Placing a narrow Gaussian spread of trap states, such as may arise from an impurity, against the "natural" background, presumed to originate from disorder, greatly affects the shape of the *J–V* curve.[37,78] Furthermore, the point at which the curve begins to deviate from the trap-free case is highly dependent on the energy level of the impurity traps. Therefore, by observing the change in shape of the *J–V* characteristic, it was possible to estimate the trap of the impurity level.

The calculated curves in Fig. 3.19 were obtained using a traps depth of 0.25 eV below the conduction band. (The low-current discrepancies between the model and experiment are either due to some field-effect component of the mobility or else to a non-negligible energy barrier for electron in ection.) This value is consistent with independently measured trap levels determined by thermally stimulated luminescence experiments.[84] It is also corresponds well with the difference in reduction potential of Hq and Alq$_3$, about 0.2 eV, as suggested in Figs. 3.7 and 3.8.

In addition to changing the apparent TCL power-law dependence and ohmic–TCL transition (Fig. 3.19), the presence of impurities will also affect the luminescence of Alq$_3$ by trapping otherwise viable carriers. If these traps are nonemissive, then the quantum efficiency of an OLED will decrease. Energy transfer to impurities will also decrease the emission. Based only on this trapping argument, the steady-state population of electrons in nonemissive traps can be calculated and compared to the total electron concentration, assuming that the hole–capture and recombination statistics are not affected by these traps.[37] The calculated decay curves (as a function of conversion of conduction band states to −0.25 eV traps) are shown in Fig. 3.20. The simulations show strong similarities with actual device data: A decrease in efficiency and increase in drive voltage, with the efficiency dropping faster than the voltage increases. Real devices have many other factors to consider, however, including chemical kinetics with varying/unknown initial conditions, Joule heating, and the eventual generation of quenching species.

For example, Hq provides a trap for electrons in Alq$_3$, but as shown earlier, this reduction is unstable. If oxygen is present, the easily oxidized q^- anion which results eventually produces species which efficiently quench the photoluminescence of Alq$_3$.[18,47–48] The breadth of the reduction peak in Fig. 3.8b is due to the reduction of Hq and the subsequent reduction of q^-. Most of the other species produce very deep electron traps and should are not expected, at a first approximation, to affect the J–V or efficiency characteristics by trapping.

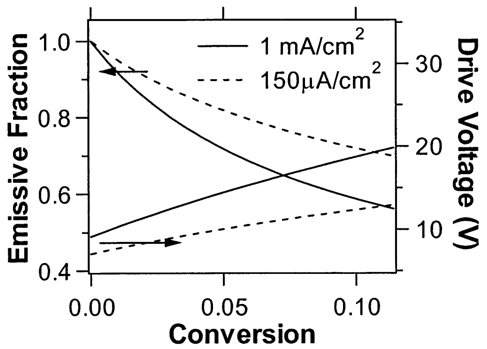

FIGURE 3.20. Simulated decay curves for devices stressed at 1 mA/cm^2 and 150 μA/cm^2. Evolution of −0.3-eV trap states is represented with a conversion.

Conclusions

Aluminum (III) 8-hydroxyquinoline undergoes a hydrolytic decomposition reaction, the principle product of which is Hq. The kinetics described here, in addition to other measured parameters, can be used to predict the rate of Hq generation in the film, which can then be linked to loss of performance due to quenching or charge trapping. Cyclic voltammetry shows that Hq is an electron trap, which will affect the resistance and luminescence of an OLED by capturing emissive carriers and generating a space charge. The trap depth estimated by observing the changes in $J-V$ behavior of Alq_3-based OLEDs is consistent with the measured value for Hq.

The reduction of this compound, however, is unstable, and q^- will readily be formed when an electron is added to Hq. This anion will also forin when Alq_3 is reduced in the presence of nucleophiles. q^- may then go on to form luminescence quenching species when oxygen is present. When a superoxide was present, the change in shape which arises as Alq_3 is reduced can account for the susceptibility of this species. Better understanding of this mechanism could be obtained by varying the size and strength of the invading nucleophile. This is extremely important from a device standpoint. Despite the intrinsic differences of the solution and solid-state processes, Alq_3 in an OLED is being constantly reduced. It has been proposed[1] that the electron lifetime is long enough to allow such physical relaxations. Furthermore, it is probable that neutral oxygen is present in devices and may be reduced as well.

Aluminum (III) 8-hydroxyquinoline is a high-T_g material which is nonetheless a poor glass former. Crystallization of this material is very rapid at temperatures far below its glass transition and it may be within the aging window during device operation. Alq_3 films become nonemissive as they are annealed. Greater glass forming ability is demonstrated with $AlMq_3$, although the resistance to physical aging appears to be poor. Electronically compatible blends of Alq_3 and $AlMq_3$ present an opportunity for excellent morphological control of OLEDs.

Acknowledgments

This work was supported by the Critical Technologies Program of Connecticut Innovations, Inc., Trans-Lux Corporation, and a fellowship from Hewlett Packard for K.A.H. and D.L.T. The authors would also like to thank Dr. H. Antoniadis, Dr. R. Budzilek, Dr. L. Rothberg, and Dr. F. Jain for helpful discussions. M. Mathai assisted in device preparation.

References

[1] S. P. Rogers (to Motorola, Inc.) U.S. Patent 5,874,804 (1999).

[2] T. Yamashita, T. Ogura, H. Nakaya, and M. Yoshida (to Sharp Kabushiki Kaisha) U.S. Patent 5,189,405 (1993).

[3] A. Dodabalapur, Z. Bao, A. Makhija, J. G. Laquindanum, V. R. Raju, and Y. Feng, Appl. Phys. Lett. 73, 142 (1998).

[4] P. E. Burrows, V. Bulovic, S. R. Forrest, L. S. Sapochak, D. M. McCarthy, and M. E. Thompson, Appl. Phys. Lett. 65, 2922 (1994).

[5] H. Antoniadis, M. R. Hueschen, J. McElvain, J. N. Miller, R. L. Moon, D. B. Roitman, and J. R. Sheats, ACS Polym. Prepr. 38, 382 (1997).

[6] J. McElvain, H. Andoniadis, M. Hueschen, J. Miller, D. Roitman, J. Sheats, and R. Moon, J. Appl. Phys. 80, 6002 (1996).

[7] X. Zhou, J. He, L. S. Liao, M. Lu, Z. H. Xiong, X. M. Ding, X. Y. Hou, F. G. Tao, C. E. Zhou, and S. T. Lee, Appl. Phys. Lett. 74, 609 (1999).

[8] C. Adachi, K. Nagai, and N. Tamoto, Appl. Phys. Lett. 66, 2679 (1995).

[9] C. Redon, F. Brochard-Wyart, and F. Rondelez, Phys. Rev. Lett. 66, 715 (1991).

[10] P. Fenter, F. Schreiber, V. Bulovic, and S. R. Forrest, Chem. Phys. Lett. 277, 521 (1997).

[11] M. Fujihira, L.-M. Do, A. Koike, and E.-M. Han, Appl. Phys. Lett. 68, 1787 (1996).

[12] A. R. Schlatmann, D. W. Floet, A. Hilberer, F. Garten, P. J. M. Smulders, T. M. Klapwick, and G. Hadziaioannou, Appl. Phys. Lett. 69, 1764 (1996).

[13] Y. Hirose, A. Kahn, V. Aristov, and P. Soukiassian, Appl. Phys. Lett. 68, 217 (1996).

[14] E. Gautier, A. Lorin, J.-M. Nunzi, A. Schalchli, J.-J. Benattar, and D. Vital, Appl. Phys. Lett. 69, 1071 (1996).

[15] F. Papadimitrakopoulos, X-M. Zhang, D. L. Thomsen, and K. A. Higginson, Chem. Mater. 8, 1363 (1996).

[16] F. Papadimitrakopoulos and X-M. Zhang, Synth. Met. 85, 1221 (1996).

[17] K. A. Higginson, X-M. Zhang, and F. Papadimitrakopoulos, Chem. Mater. 10, 1017 (1997).

[18] D. L. Thomsen, Ph.D. thesis, University of Connecticut, 1999.

[19] C. Adachi, K. Nagai, and N. Tamoto, Jpn. J. Appl. Phys. Part 1 35, 4819 (1996).

[20] F. Papadimitrakopoulos, M. Yan, L. J. Rothberg, H. E. Katz, E. A. Chandross, and M. E. Galvin, Mol. Cryst. Liq. Cryst. 256, 663 (1994).

[21] I. Sokolik, A. D. Walser, R. Priestley, R. Dorsinville, and C. W. Tang, SPE Prepr. (1996).

[22] E.-M. Han, L.-M. Do, N. Yamamoto, and M. Fujihira, Thin Solid Films 273,202 (1996).

[23] Y. Shirota, Y. Kuwabara, H. Inada, T. Wakimoto, H. Nakada, Y. Yonemoto, S. Kawami, and K. Imai, Appl. Phys. Lett. 65, 807 (1994).

[24] S. Tokito, H. Tanaka, K. Noda, A. Okada, and Y. Taga, IEEE Trans. Electron Devices 44, 1239 (1997).

[25] B. E. Koene, D. E. Loy, and M. E. Thompson, Chem. Mater. 10, 2235 (1998).

[26] B. R. Hsieh, unpublished (2003).

[27] Y. Yang and A. J. Heeger, Applied Physics Letters 64, 122-124 (1994).

[28] A. Yarnamori, C. Adachi, T. Koyama, and Y. Taniguchi, Appl. Phys. Lett. 72, 2147 (1998).

[29] S. A. VanSlyke, C. H. Chen, and C. W. Tang, Appl. Phys. Lett. 69, 2160 (1996).

[30] P. Dannetun, M. Logdlund, C. Fredriksson, M. Boman, S. Stafstrom, W. R. Salaneck, B. E. Kohler, and C. Spangler, in *Polymer-Solid Interfaces*, edited by J. J. Pireaux, P. Bertrand, and J. L. Bredas, IOP, Bristol, 1992.

[31] S. Egusa, N. Gemma, A. Miura, K. Mizushima, and M. Azuma, J. Appl. Phys. 71, 2042 (1992).

[32] Y. Hirose, A. Kahn, V. Aristov, P. Soukiassian, V. Bulovic, and S. R. Forrest, Phys. Rev. B 54, 13,748 (1996).

[33] L. S. Hung, C. W. Tang, and M. G. Mason, Appl. Phys. Lett. 70, 152 (1997).

[34] R. Schlaf, B. A. Parkinson, P. A. Lee, K. W. Nebesny, G. Jabbour, B. Kippelen, N. Peyghambarian, and N. R. Armstrong, J. Appl. Phys. 84, 6729 (1998).

[35] K. A. Higginson, Ph.D. thesis, University of Connecticut, 1999.

[36] K. A. Higginson, M. Mathai, F. Papadimitrakopoulos, and B. R. Hsieh, Inter. Soc. Opt. Eng. Proc. 4105, 243, (2001).

[37] M. K. Mathai, K. A. Higginson, B. R. Hsieh, and F. Papadimitrakopoulos, Appl. Phys. Lett. submitted (2003).

[38] H. Aziz, Z. D. Popovic, N.-X. Hu, A.-M. Hor, and G. Xu, Science 283, 1900 (1999).

[39] R. Lazzaroni, M. Lodglund, A. Calderone, J.-L. Bredas, P. Dannetun, C. Fauquet, C. Fredriksson, S. Stafstron, and W. R. Salaneck, Synth. Met. 71, 2159 (1995).

[40] A. V. Ragimov, B. A. Mamedov, and S. I. Mustafaeva, Polymer 30,1851 (1989).

[41] M. Ezrin and G. Lavigne, SPE–ANTEC Proc. 2230 (1991).

[42] D. W. Margerum, G. R. Cayley, D. C. Weatherburn, and G. K. Pagenkopf, in *Coordination Chemistry*, edited by A. E. Martell, American Chemical Society, Washington, DC, 1978, Vol. 2, pp. 1–220.

[43] H. Schmidbauer, J. Lettenbauer, D. L. Wilkinson, G. Muller, and O. Kumberger, Zeitschr. Naturforsch. 46b (1991).

[44] J. P. Phillips, Chem. Rev. 56, 271 (1956).

[45] P. E. Burrows, Z. Shen, V. Bulovic, D. M. McCarty, S. R. Forrest, J. A. Cronin, and M. E. Thompson, J. of Appl. Phys. 79, 7991 (1996).

[46] V. Khodorkovsky and J. Y. Becker, in *Organic Conductors*, edited by J. P. Farges, Marcel Dekker, New York, 1994.

[47] D. T. Sawyer, G. Chiericato, C. T. Angells, E. J. Nanni, and T. Tsuchiya, Anal. Chem. 54, 1720 (1982).

[48] T. Fujinaga, K. Izutsu, and K. Takaoka, J. Electroanal. Chem. 16, 89 (1968).

[49] Y. Hamada, T. Sano, M. Fujita, T. Fujii, Y. Nishio, and K. Shibata, Jpn J. Appl. Phys., Part 2 32, 514 (1993).

[50] R. S. Mulliken and W. B. Person, *Molecular Complexes: A Lecture and Reprint Volume*, Wiley–Interscience, New York, 1969.

[51] E. Kampar and O. Neilands, Russ. Chem. Rev. 55, 637 (1986).

[52] N. J. Turro, *Modern Molecular Photochemistry*, University Science Books, Mill Valley, CA, 1991.

[53] M. Xia, X. Liu, and P. Gu, Appl. Opt. 32, 5443 (1993).

[54] H. A. Davies, in *Amorphous Metallic Alloys*, edited by F. E. Luborsky, Butterworths, London, 1983, pp. 8–25.

[55] L. F. Pender and R. J. Fleming, J. Appl. Phys. 46, 3426 (1974).

[56] H. Pagnia and N. Sotnik, Phys. Status Solidii (A) 108, 11 (1988).

[57] J. C. Scott, J. H. Kaufman, P. J. Brock, R. DiPietro, J. Salem, and J. A. Goitia, J. Appl. Phys. 79, 2745 (1996).

[58] L. C. E. Struik, *Physical Aging in Amorphous Polymers and Other Materials*, Elsevier, Amsterdam, 1978.

[59] P. Nagels, in *Amorphous Semiconductors, Volume 36*, edited by M. H. Brodsky, Springer-Verlag, Berlin, 1979, pp. 113–130.

[60] N. F. Mott, Phil. Mag. 24, 911 (1971).

[61] I. Lucas, J. Non-Cryst. Solids 6, 136 (1970).

[62] H. K. Henisch, E. A. Fagen, and S. R. Ovshinsky, J. Non-Cryst. Solids 4, 538 (1970).

[63] K. Naito and A. Miura, J. Phys. Chem. 97, 6240 (1993).

[64] T. Wada, Y. Yogo, I. Kikuma, M. Masui, M. Anzai, and M. Takeuchi, Appl. Surface Sci. 65/66, 376 (1993).

[65] C. W. Tang and S. A. VanSlyke, Appl. Phys. Lett. 51, 913 (1987).

[66] N. T. Harrison, D. R. Baigent, I. D. W. Samuel, R. H. Friend, A. C. Grimsdale, S. C. Moratti, and A. B. Holmes, Phys. Rev. B 53, 15,815 (1996).

[67] J. W. Blatchford, S. W. Jessen, L.-B. Lin, T. L. Gustafson, D.-K. Fu, H.-L. Wang, T. M. Swager, A. G. MacDiarmid, and A. J. Epstein, Phys. Rev. B 54, 9180 (1996).

[68] R. M. Silverstein, G. C. Bassler, and T. C. Morrill, *Spectrometric Identification of Organic Compounds*, 5th ed., Wiley, New York, 1991.

[69] P. F. James, in *Nucleation and Crystallization in Glasses*, Volume 4, edited by J. H. Simmons, D. R. Uhlmann, and G. H. Beall, American Chemical Society, Columbus, OH, 1982, pp. 1–47.

[70] M. G. Scott, in *Amorphous Metallic Alloys*, edited by F. E. Luborsky, Butterworths, London, 1983, pp. 144–168.

[71] Y. Wang, W. Zhang, Y. Li, L. Ye, and G. Yang, Chem. Mater. 11, 530 (1999).

[72] K. Naito, Chem. Mater. 6, 2343 (1994).

[73] J. Zarzycki, *Glasses and the Vitreous State*, Cambridge University Press, Cambridge, 1991.

[74] J. C. Sturm, W. Wilson, and M. lodice, IEEE J. Select. Topics Quantum Electron. 4, 75 (1998).

[75] W. J. MacKnight, F. E. Karasz, and J. R. Fried, in *Polymer Blends*, edited by D. R. Paul and S. Newman, Academic Press, San Diego, 1978, Vol. 1, pp. 186–243.

[76] J. Kido, Chem. Lett. 963 (1997).

[77] H. Mattoussi, H. Murata, C. D. Merritt, Z. H. Kafafi, Y. lizumi, and J. Kido, J. Appl. Phys. (1999).

[78] J. Adolph, E. Baldinger, W. Czaja, and I. Granacher, Phys. Lett. 6, 137 (1963).

[79] J. G. Simmons and R. R. Verderber, Roy. Soc. Proc. Series A 301, 77 (1967).

[80] R. Nath and N. N. Perlman, J. Appl. Phys. 65, 4854 (1989).

[81] A. Ioannidis, E. Forsythe, Y. Gao, M. W. Wu, and E. M. Conwell, Appl. Phys. Lett. 72, 1038 (1998).

[82] H. Antoniadis, J. N. Miller, and D. M. Roitman, in *Effects of Hole Carrier Injection and Transport in Organic Light-Emitting Diodes*, 1996.

[83] M. A. Lampert and P. Mark, *Current Injection in Solids*, Academic Press, New York, 1970.

[84] E. W. Forsythe, D. C. Morton, C. W. Tang, and Y. Gao, Appl. Phys. Lett. 73, 1457 (1998).

4

Organic Microcavity Light-Emitting Diodes

Ananth Dodabalapur

4.1 Introduction

Microcavities have been extensively studied over the past several decades.[1,2] The motivations for such studies range from the most fundamental to the very applied. Microcavities have been useful in clarifying some fundamental problem in electrodynamics such as the effect of vacuum field fluctuations on an emitting dipole.[3,4] Microcavity-based devices have been suggested for display applications[5] and in enhancing the efficiency of conventional light-emitting diodes.[6,7,8,9] Microcavity LEDs based on III–N semiconductors have been proposed as sources for optical communication systems.[7,9] This interest has led to numerous contributions, both theoretical and experimental, that have considerably enhanced our understanding of the optical processes in microcavities. We need to point out that there are many types of microcavities and some of the more technologically important ones are described in the following section. In most of this chapter, we will be concerned with the properties and applications of one microcavity type: planar microcavities, often simply referred to as “microcavities.”

Microcavity studies have employed a number of optically active materials: inorganic semiconductors,[6,9] organic liquids,[2] and organic thin-film structures capable of charge transport.[10,19] In this chapter, we shall be concerned with the latter class of materials, which include evaporated small molecules and conjugated polymers. These materials are used in device configurations that often include electron- and hole-transporting layers to improve performance. Impressive strides have been made in understanding some of the many fundamental phenomena involved as well as in improving reliability of nonmicrocavity LEDs based on these materials.[20] This progress has resulted in device lifetimes in excess of 5×10^4 h at display brightness levels, which is considered adequate for many applications.

4.2 Types of Microcavities

A microcavity is a resonator with dimensions of a few times the wavelength or less. An important figure of merit for a resonator is the quality factor or Q, which is the number of optical cycles the cavity will sustain before the field drops to $1/e$ times the initial value. A microcavity with a large Q means that despite the small dimensions of the cavity, the optical field does not decay rapidly; this, in turn, implies that the losses in the cavity are very small. Such low-loss cavities are useful in implementing low-threshold lasers. It is not always necessary to have very high–Q values in microcavities, and a variety of interesting and useful effects can result from cavities of modest $Q(< 100)$. In the following, we describe three categories of microcavities which can be technologically useful in the context of emissive organic materials.

A planar Fabry–Perot microcavity generally refers to a cavity of short optical length ensconced between two mirrors, as illustrated in Fig. 4.1a. One or even both of these mirrors could be partially transmitting in order to couple light out of the cavity. Such planar Fabry–Perot microcavities (often simply referred to as planar microcavities) have been used to make organic LEDs and photoexcited lasers. This generic type of microcavity has been the subject of numerous experimental investigations and may be useful for display applications, the enhancement of the external quantum efficiency of organic LEDs, and controlling the directionality of the emitted light. The basic physics of such cavities is described in the following

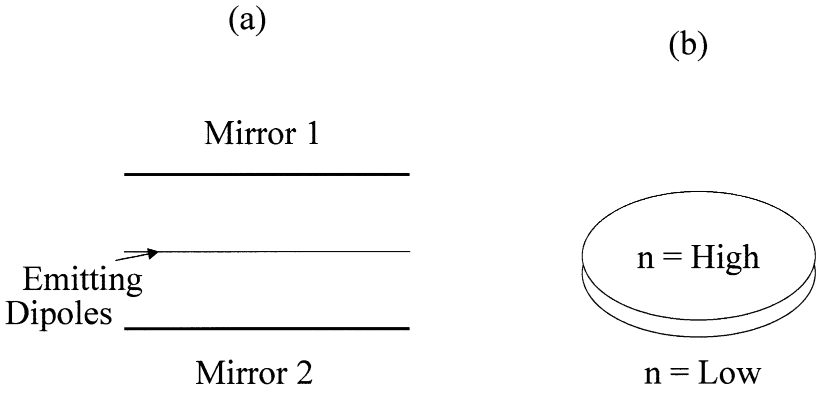

FIGURE 4.1. Structures of two types of microcavities: (a) planar microcavity and (b) microdisk.

section, and much of this chapter is devoted to a description of devices made with such cavities.

A second type of microcavity is called a "microdisk" because of its shape and is illustrated in Fig. 4.1b. Such a cavity requires that a waveguide be formed in the plane parallel to the substrate. The layer structure is patterned so as to be disk shaped. A fraction of the light generated in such structures is vertically confined by the waveguide. Some of the waveguided light is trapped by total internal reflection along the edge of the disk at the interface between the organic and air. If this boundary is smooth, then the losses in such a cavity can be made very small and will result in high Q values. The optical modes of such cavities are analogous to the modes in acoustic whispering galleries such as in St. Paul's Cathedral and for this reason are called "whispering galley modes." Microdisks with Q values estimated to be ~ 100 have been experimentally realized with organic systems.[21] Such cavities are not very effective in modifying the spontaneous emission characteristics of emissive media below the threshold for stimulated emission. They are, therefore, not very useful in LED applications. However, they are very promising for laser applications, and photoexcited microdisk lasers have been made with both dye-doped polymers[21] and sublimed molecular solids.[22] In additions to planar disks, other resonators with circular symmetry — such as rings and spheres/spheroids — can have whispering gallery modes and lasers have been made with such cavities as well.[21]

Microcavities based on photonic bandgap (PBG) structures are emerging as an interesting class of resonators potentially useful for both LED and low-threshold laser applications. A PBG structure or photonic crystal is a structure in which the dielectric constant varies in a periodic manner in one, two, or three dimensions[23] and on a spatial scale slightly smaller than a wavelength. Two-dimensional PBG structures are attractive because of their relative simplicity of fabrication (in comparison with three-dimensional PBG structures) and because many of the advantageous properties of PBG structures can be realized in two-dimensional photonic gap structures in combination with planar waveguiding, which provides some confinement in the third dimension. One example of a photonic bandgap structure is illustrated in Fig. 4.2 and consists of a two-dimensional array of holes of circular cross section in a material such as SiN_x or SiO_2. If such a structure were to be coated with a layer of an emissive organic such that (1) the organic medium surrounds but does not fill the holes and (2) a planar waveguide is formed by the organic, the SiO_2, and air, then it may be possible, under appropriate conditions, to realize two-dimensional PBG-based microcavities as outlined next.

For the formation of microcavities, it is necessary that a complete two-dimensional PBG exists at least for one polarization (TE or TM) and ideally for both polarizations. This involves careful design and requires that there be a sufficient index difference between the two materials. The photonic band structure of a triangular lattice of air holes in a membrane of SiO_2 coated with a thin layer of organic semiconductor has been described in Ref 24. Such a structure has been shown to possess a complete bandgap for TE polarized light. In a photonic lattice which possesses a complete bangap, it is possible to create a microcavity

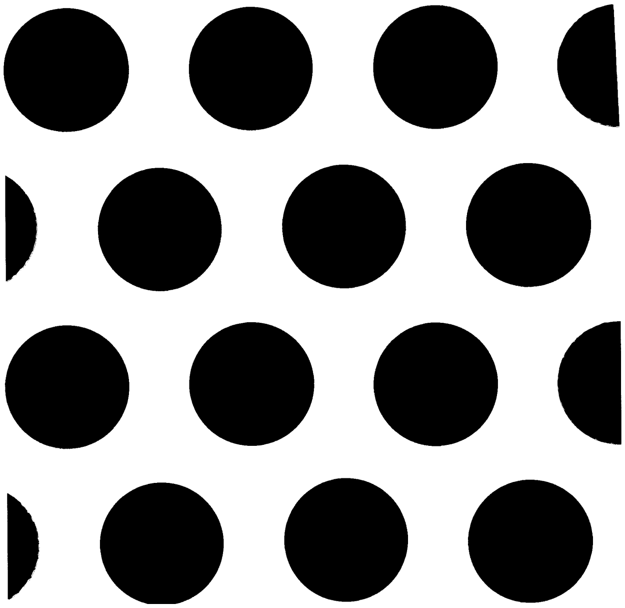

FIGURE 4.2. Illustration of a two-dimensional photonic bandgap structure in which the white regions possess a high refractive index and the black regions represent air holes. Such structures can have a complete photonic bandgap under appropriate conditions. When a defect is introduced in the perfectly periodic lattice, a microcavity can be created.

by introducing a point defect, which could simply be a missing lattice point and which will be a site for a localized photonic state. Photonic bandgap structures could be used to control the spontaneous emission spectrum (in LEDs) as well as serve as resonators for organic-based lasers. Photonic crystals can also be useful in increasing the amount of light that gets coupled out of an organic LED. Planar microcavities can be regarded as a one-dimensional PBG structure with a defect.

4.3 Planar Microcavity LEDs

The principal effect of a planar microcavity, illustrated in Fig. 4.1a, on the spontaneous emission is to redistribute the photon density of states such that only certain wavelengths, which correspond to allowed cavity modes, are emitted in a given direction. The spontaneous emission intensity is enhanced in the direction normal to the cavity axis relative to a noncavity device. The external quantum efficiency or integrated intensity may also be enhanced in some cases. The conditions under which efficiency enhancement occurs are described in detail later in the chapter. There is also an angular dependence to the emission wavelength, linewidth, and intensity. Modest changes (of the order of 10%) in exciton lifetime have been observed in organic microcavities with Qs in the range 20–50.[17] There are, however, conditions under which even cavities with Q values < 100 can, as a consequence of exciton–photon coupling, significantly alter exciton dynamics.[14] This is surveyed later in this section.

The use of electroluminescent organic materials as the active medium in planar microcavities results in a number of interesting and potentially useful effects.[10,19] For example, the electroluminescent molecule 8-hydroxyquinoline aluminum (Alq) has been the subject of many recent reports on organic LEDs.[25] Undoped Alq has a fairly broad free-space emission spectrum covering the range 450–650 nm, and LEDs with external quantum efficiencies of 0.3–1.3% photons/electron have been made with Alq together with a hole-transporting material such as triphenyl diamine (TAD). The Alq/TAD system, in which only the Alq emits light in a LED device, is used in many of the experiments described in this chapter and is representative of a broad-band organic emitter. Alq doped with small quantities of the fluorescent dye pyrromethene (PM) 580 has a narrower free-space emission spectrum than undoped Alq. Such a system is very suitable for studying angular and integrated enhancements due to cavity effects. The magnitude of such effects in both Alq and Alq + PM and their possible applications are also discussed.

The schematic structure of a typical planar microcavity organic LED is shown in Fig. 4.3a. The bottom mirror usually consists of a dielectric quarter-wave stack (QWS). The stop band of the QWS must be wide enough to cover the free-space spectral range of the electroluminescent semiconductor used. The width of the stop band is approximately $\lambda(\Delta n/n)$, where Δn is the index difference between the layers that constitute the stack, λ is the center wavelength of the stop band, and n is the average index. Using a pair of dielectrics with a high index difference results in a broad stop band. The peak reflectivity of the stack (R_2) is given by

$$R_2 = \tanh \sum_i \tanh^{-1}(r_i), \tag{1}$$

where r_i is the index difference between a pair of layers in the stack. The reflectivity of such a stack depends on the wavelength and also on the angle of incidence. The total optical thickness of the cavity, L, is given by

$$L(\lambda) \approx \frac{\lambda}{2}\left(\frac{n}{\Delta n}\right) + \sum_j n_j L_j + \left|\frac{\varphi_m}{4\pi}\lambda\right|. \tag{2}$$

The first term in Eq. (2) is the penetration depth of the electromagnetic field into the dielectric stack, the second term is the sum of optical thicknesses of the layers between the two mirrors, and the last term is the effective penetration depth into the top metal mirror. The phase shift at the metal reflector (ϕ_m) is given by[26]

$$\varphi_m = \arctan\left(\frac{2n_s k_m}{n_s^2 - n_m^2 - k_m^2}\right), \tag{3}$$

where n_s is the refractive index of the organic material in contact with the metal and n_m and k_m are the real and imaginary parts, respectively, of the refractive index of the metal. The positions of the cavity modes are given by the relation $m\lambda = 2L(\lambda)$, where m is the mode index. The mode positions and spacings can

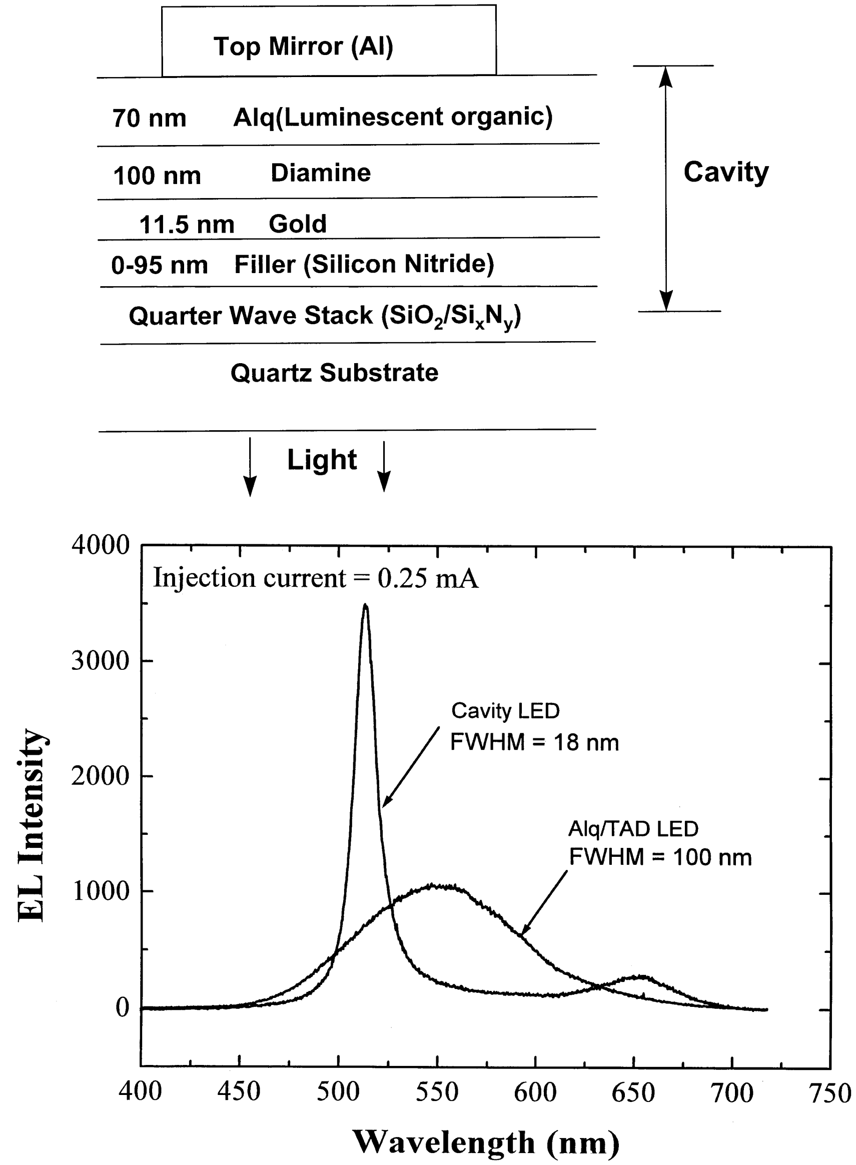

FIGURE 4.3. (a) Schematic structure of a microcavity LED with an Alq emitting layer. The top mirror is the electron-injecting contact and the bottom mirror is a three-period dielectric quarter-wave stack (QWS) with $SiO_2(n = 1.5)$ and $Si_xN_y(n = 2.2)$. (b) Electroluminescence spectrum from a cavity LED compared with that from a noncavity LED. The noncavity LED possesses the same layer structure as shown in (a), but has no QWS.

be adjusted by varying $L(\lambda)$. The maximum spacing is largely determined by the first term in Eq. (2), which depends on the index difference between the layers that constitute the stack.

The approximate theoretical spectrum for emission normal to the plane of the device layers can be calculated following the approach of Deppe et al.[8] The calculated spectrum can be approximated by

$$|E_{\mathrm{cav}}(\lambda)|^2 = \frac{\frac{1-R_2}{i}\sum_i \left[1 + R_1 + 2(R_1)^{0.5}\cos\left(\frac{4\pi x_i}{\lambda}\right)\right]}{\left[1 + R_1 R_2 - 2(R_1 R_2)^{0.5}\cos\left(\frac{4\pi L}{\lambda}\right)\right]} |E_{\mathrm{nc}}(\lambda)|^2, \tag{4}$$

where x_i are the effective distances of the emitting dipoles from the metal mirror, R_1 and R_2 are the reflectivities of the metal and dielectric mirrors, respectively, L is the total optical thickness of the cavity, and $|E_{\mathrm{nc}}(\lambda)|^2$ is the free-space electroluminescence intensity at λ. Eq. (4) provides a qualitative understanding of the main effects produced by the microcavity. For a more complete and rigorous description, it is necessary to construct a theoretical model from first principles. Rothberg et al. have developed such a model which satisfactorily accounts for nearly all the observed phenomena *quantitatively*.[27] In this model, the density of photon modes at a given wavelength and propagation angle $D(\omega, \mathbf{k})$ and the field intensity at frequency ω are computed by a transfer-matrix formalism. Calculated results from this model are compared to experimental results in several instances that follow.

An inspection of Eq. (4) reveals the importance of the spatial location of the emitting dipoles in determining the nature of the emission spectrum. If the emitting dipoles are located at a node of the standing wave formed between the two end mirrors, then the emission would be greatly suppressed, and, likewise, if the emitting dipoles are located at an antinode, the emission intensity would be a maximum, all other factors being the same.

Fig. 4.3b illustrates the modifications to the free-space emission produced by the planar microcavity device whose structure is shown schematically in Fig. 4.3a. The principal effect is a narrowing of the emission spectrum in most directions. The cavity device spectrum is taken along the cavity axis, and the full width at half-maximum (FWHM) is lowered from $\sim$ 100 nm for a noncavity device to 18 nm. With higher-Q cavities, it is possible to get narrower spectra, and Tokito et al. have reported LEDs with a FWHM of 8 nm.[28]

It must be mentioned that there are some weak microcavity effects present in typical organic and polymer LEDs[25] which do not have a quarter-wave stack. These arise as a result of the high reflectivity of the cathode and because the refractive indices of the organic layers and indium–tin-oxide (ITO) are higher than that of typical substrates such as glass. Bulovic et al. have examined such weak microcavity effects and have found that the polarization and spectral peak positions of light emitted normal to the active layers can be significantly different from those of light directed parallel to the layers.[19]

Lidzey et al. have demonstrated that, under appropriate conditions, there can be strong coupling between excitons and photons in organic semiconductor microcavities.[14] Clear evidence has been found for the formation of polariton branches and Rabi splittings between the upper and lower polariton branches $\geq$ 80 meV have been reported. Such large values are uncommon in compound semiconductor microcavities, indicating that organic semiconductors are a useful medium for studying the physics of strong exciton–photon coupling and its consequences. The large value of the Rabi splitting means that the consequences of such coupling will be left even at room temperature.

4.4 Single Mode and Multimode Planar Microcavity LEDs

The positions of the cavity modes (resonance wavelengths) can be altered by changing the cavity thickness [see Eq. (2)], and by doing this in a controlled fashion, it is possible to get emission at the three primary color wavelengths. This could be accomplished by patterning and etching an electriclly inactive filler layer. One scheme to realize such patterned filler microcavity LEDs is illustrated in Fig. 4.4. It consists of a three-period dielectric QWS consisting of alternate layers of $\mathrm{Si}_x\mathrm{N}_y(n = 2.2)$ and $\mathrm{SiO}_2(n = 1.5)$. The QWS is designed to have a broad stop band of $>$ 200 nm FWHM, centered at 550 nm, and a peak reflectivity of $\sim$ 80%. This is followed by the deposition of a 100-nm-thick silicon nitride ($n = 1.92$) filler layer which is used to regulate the total cavity thickness. One or two steps, each having heights of approximately 40 nm, are etched on part of this layer to change the device color from blue to green and red, respectively. Thin

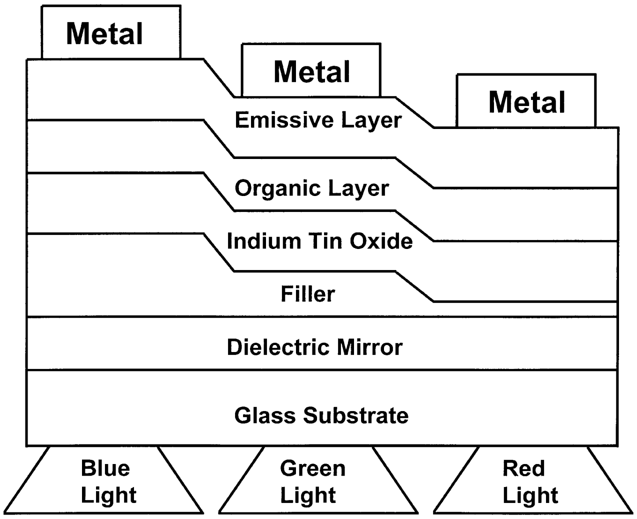

FIGURE 4.4. Schematic structure of a patterned planar microcavity in which the $\mathrm{Si}_3\mathrm{N}_4$ filler layer is etched to three different thicknesses to change the optical thickness. The step heights are $\sim$ 40 nm, which is sufficient to change the resonance position by 45–60 nm.

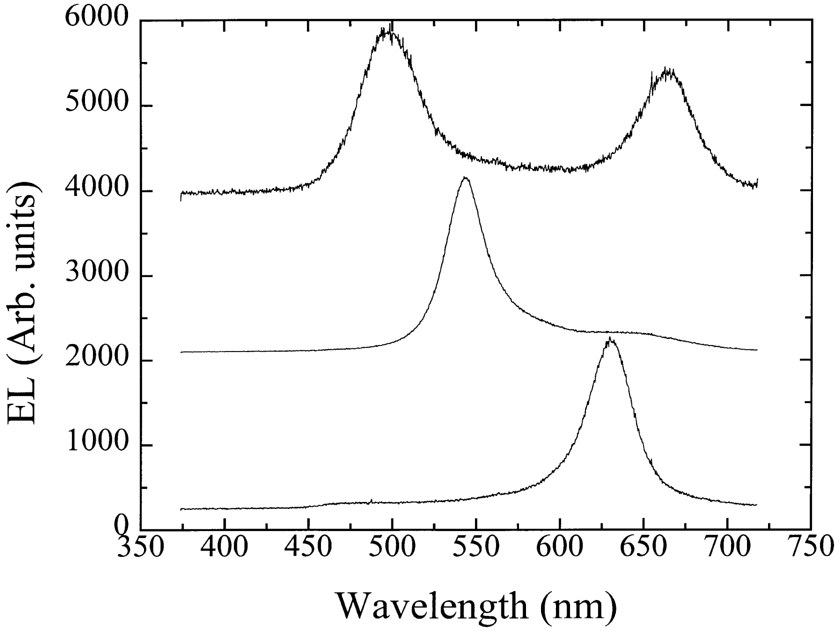

FIGURE 4.5. Electroluminescence spectra from three devices which have different optical thicknesses. The presence of a second mode in one of the spectra is a result of a closer than ideal mode spacing, If the refractive index difference between the materials that constitute the QWS is enhanced, the total optical thickness will be reduced and the mode spacing increased.

gold (11.5 nm) which forms a semi-transparent layer, is evaporated above the filler layer and forms the hole-injecting contact or anode. Layers of TAD (100 nm) and Alq (70 nm) are sublimed over the gold, followed by the evaporation of Al dots of diameter 1 mm, which serve both as cathodes and as the top mirrors of the cavity. The top mirror has a theoretical maximum reflectivity ~ 90%;[29] however, in actual devices, the reflectivity was less than this value. The spectra corresponding to the three filler thicknesses are shown in Fig. 4.5.

It must be emphasized that, with the exception of the preformed filler layer, all three devices function with identical structures which are formed simultaneously. Only the total optical thicknesses of the Fabry–Perot cavities that contain the three LEDs are different, and it is this difference that is responsible for the color change. Thus, by patterning a well-characterized material such as Si_3N_4, it is possible to control the emission wavelength over a range of ~ 150 nm without requiring three different materials or patterning of the organic layers. We expect this to be an advantage in making color displays with organic LEDs. Alq has a free-space emission that is relatively weak in the blue; in Section 5, alternate materials are described which will further improve the above-described spectral characteristics of the LEDs. Patterned planar microcavities have been implemented by many groups.[12,30]

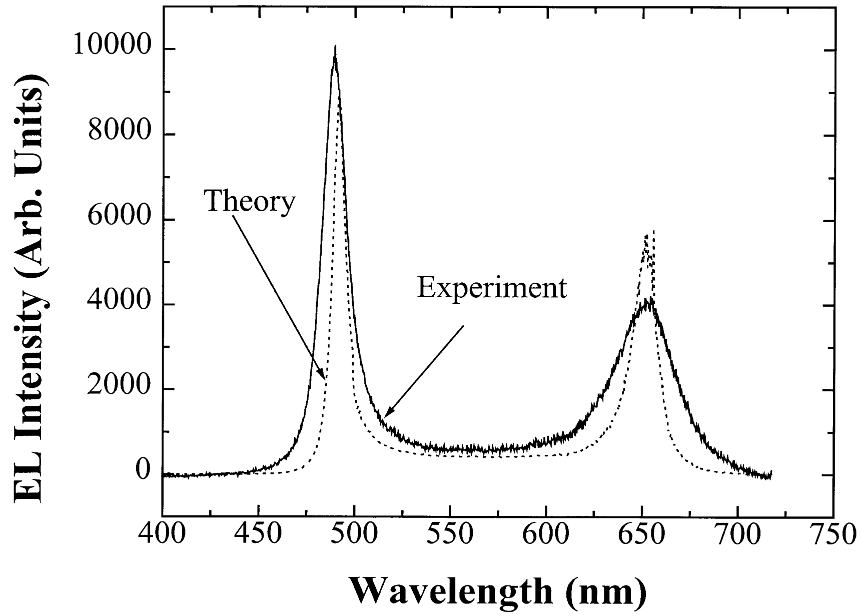

FIGURE 4.6. Electroluminescence spectrum of a two-mode LED which has CIE coordinates close to that of pure white. The CIE coordinates are (0.34, 0.386) and the Alq thickness is 30 mn. Also shown is the calculated spectrum using Eq. (4.4).

The EL spectrum has multiple peaks when more than one mode of the cavity overlaps the free-space emission spectrum. It is possible to realize a white LED with a single electroluminescent material such as Alq by employing a two-mode microcavity device structure in which one of the modes is centered near 480 nm and the other near 650 nm. Such an electroluminescence spectrum, for which the CIE coordinates are (0.34, 0.386),[13] is shown in Fig. 4.6. The approximate spectrum calculated with Eq. (4) is also shown in Fig. 4.6. With very minor changes in the device design, it is easy to achieve (0,33, 0.33). For comparison, the CIE coordinates of a noncavity Alq LED are (0.39, 0.56).

The location of the emitting dipoles with respect to the profile of the electromagnetic field in the microcavity is important in determining the intensity of emission. In a two-mode cavity, we can vary the relative intensities of modes by changing the location of the dipoles (by changing the thickness of the Alq film, which is easily controllable). This is illustrated in Fig. 4.7 in which where electroluminescence spectrum of a two-mode LED is shown. In this case, the Alq thickness is ~ 70 nm, compared to 30 mn for the LED in Fig. 4.6; however, the total optical thickness of the cavity is approximately the same. The calculated spectrum is also shown in the Fig. 4.7 for a lower value of R_1 [modifying reflectivities is yet another way to change the perceived color, as Eq. (4) suggests] compared to the device whose spectrum is shown in Fig. 4.6. It is also important to note that an Alq thickness of 30–100 mn is optimal from the electrical standpoint; larger thicknesses will lead

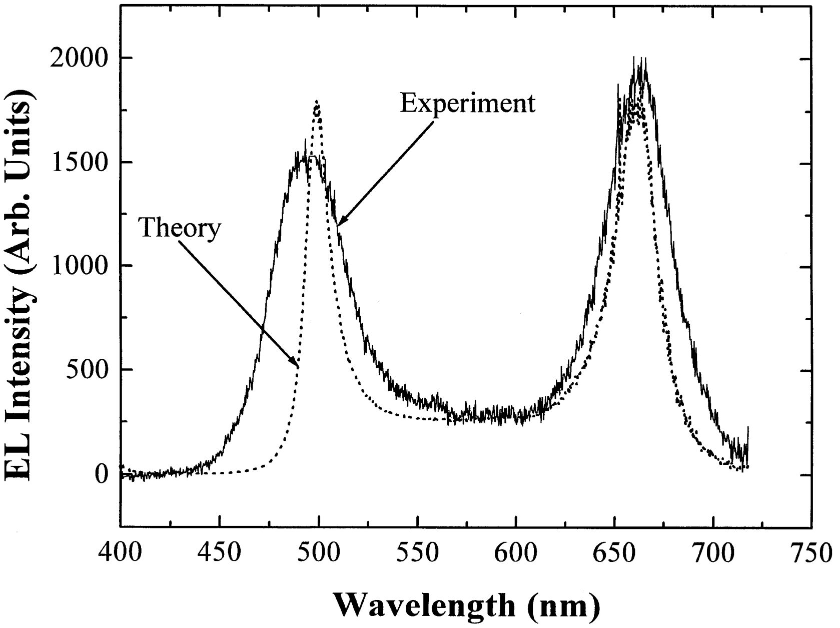

FIGURE 4.7. Electroluminescence spectrum of a two-mode LED in which the total optical thickness is the same as that for the device in Fig. 4.4. The Alq thickness (70 nm) is higher, leading to a larger-enhancement of the longer-wavelength mode.

to significant increases in the forward voltage drop, whereas smaller thicknesses will result in a substantial lowering of electroluminescence efficiency because of exciton quenching at the Alq/metal interface.

The calculated spectra in Figs. 4.6 and 4.7 assume that the emitting dipoles are distributed in an $\sim$ 20-nm-thick region of Alq adjacent to the Alq/TAD junction. This gave the best fit in terms of the relative peak magnitudes, which is strongly dependent on the location of the emitting dipoles [Eq. (4)]. Our assumption that the exciton recombination region is approximately 20 mn in lateral extent is consistent with the findings of Tang et al. using an alternate approach.[25] This illustrates the utility of two-mode cavity LEDs in profiling the exciton recombination region in organic LEDs. Two-mode LEDs (where the mode spacing is large) are more accurate for this purpose than single-mode LEDs.

In addition to white LEDs, it is possible to produce mixed-color LEDs which are not easily realized with a single organic or inorganic LED. For example, we get different shades of purple and magenta in two-mode devices which have blue and red modes (but with less green than the white LED), It is sometimes useful to have a three-mode device with emission peaks corresponding to the primary colors. Such devices, in which the emission spectra match the transmission maxima of color filters, might find application as backlights in light-valve-based color displays. The electroluminescence spectrum of one such LED is shown in Fig. 4.8. The three peaks corresponding to the 10th, 9th, and 8th modes are located at 488 nm, 543 nm,

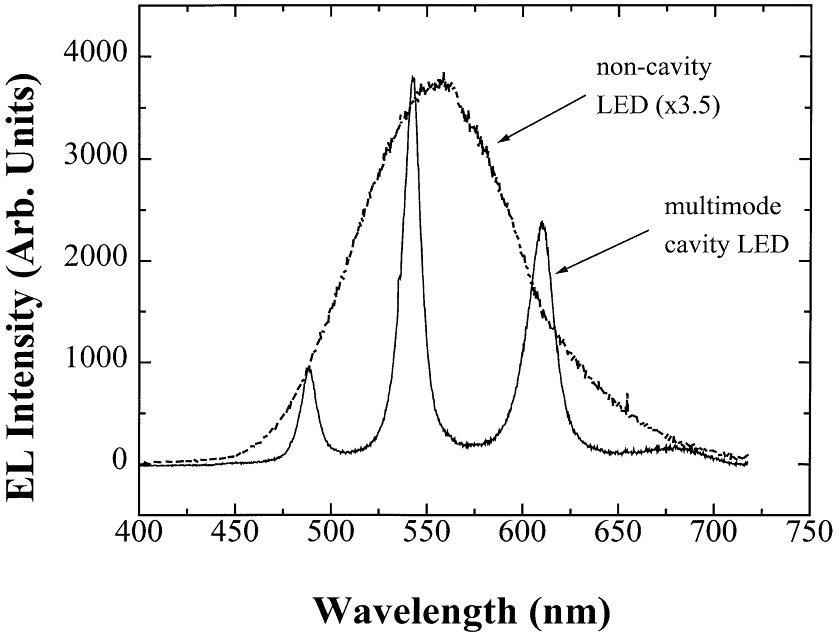

FIGURE 4.8. Electroluminescence spectrum from a three-mode microcavity LED, in which the three peaks are at 488, 543, and 610 nm. The EL spectrum from a noncavity device is shown for comparison.

and 610 nm, respectively. The silicon nitride filler thickness in this case is 835 nm, resulting in a total optical thickness of about 2.5 μm. Also shown in Fig. 4.8 is the scaled electroluminescence spectrum of a noncavity Alq/diamine LED. It is important to reemphasize that in a microcavity, the angular distribution of spontaneous emission of a broad-band emitter is altered such that most of the emission in a narrow spectral range [coinciding with the allowed cavity mode(s)] escapes the cavity, whereas in other spectral regions, it is lost. Thus, it is not merely a filtering effect, and one can achieve integrated intensity similar to that of a noncavity device. These issues are examined in more detail next.

4.5 Intensity and Angular Dependence in Planar Microcavities

It is important to compare the relative intensity of light emitted from a microcavity LED with light emitted from a noncavity LED possessing the same active-layer structure. In a typical noncavity organic/polymeric LED, the emissive and transport layers are placed above ITO-coated glass. An analysis[31] of the optics in such a LED structure has shown that only a fraction of approximately $1/2n^2$ (where n is the index of refraction of the active layers) of the total light generated escapes through the back of the glass substrate into air. The rest of the light is totally internally reflected and either escapes through a waveguide mode or the substrate or is reabsorbed. The use of the microcavity LED architecture offers a way to alter this emission pattern (in which most of the light does not go out through the back of the substrate); indeed, in some cases, an enhancement in intensity can be achieved. Such enhancement is strongly dependent on the free-space emission linewidth of the emitting material. In general, it is easier to obtain an enhancement in external quantum efficiency with narrow-band emitters. The characteristics of a broad-band emitter (Alq)-based microcavity LEDs are described next, followed by those of relatively narrower-band Alq+PM emitter-based LEDs.

The relative comparisons between intensities of cavity and noncavity devices was made using two techniques. The experimental data were supplemented by detailed theoretical calculations. In the first set of experiments, the external quantum efficiency of both the cavity and noncavity LEDs are measured by placing a large-area Si photodiode very close to the back of the glass substrate. A large fraction of the total light emitted through the back of the substrate into air is absorbed by the photodiode, which has a known responsivity. In this manner, comparisons can be made of the spatially and spectrally integrated intensities. Such measurements were made for several sets of devices, including cavity LEDs with different on-axis resonance wavelengths and noncavity LEDs.

In Figs. 4.9a-4.9c are shown the electroluminescence spectra measured along the cavity axis for three cavity LEDs possessing different resonance wavelength. These spectra are typical of many others measured on the same patterned substrate. The LEDs possess identical active-layer dimensions; it is only the patterned Si_3N_4 filler that creates differences in the optical thickness of the cavity. As mentioned earlier, the emissive material is undoped Alq. Also shown in each of the figures is the external quantum efficiency as measured with the Si photodiode. The external quantum efficiency, which is a measure of the integrated intensity of light that exits though the back of the substrate, is extracted from such L–I characteristics. For comparison, noncavity LEDs have an external quantum efficiency of 0.32 – 0.4%, which is only slightly more than those of the cavity LEDs. The cathode metal/top mirror is Al in both the cavity LEDs and the reference noncavity LEDs. It can be noticed in Fig. 4.9b that two modes contribute to the light collected by the photodiode. However, over most angles of interest, devices a and c are substantially single mode. The small peak near 460 nm in Fig. 4.9a is very weak and disappears over most angles away from the cavity axis. Thus, these results indicate that the integrated intensities in cavity and noncavity devices in which Alq is the emissive material are essentially similar. Before we discuss the significance of this result, the details of the second set of experiments to compare intensities in cavity and noncavity devices are described next.

In these experiments, two different substrates were employed: one quartz substrate with a three-period SiO_2/Si_3N_4 quarter-wave stack and the other plain quartz. Thirty nanometers of ITO was deposited on both substrates by pulsed-laser deposition of a commercial ITO target in 1 mtorr of O_2 at a substrate temperature of 250° C.[32] This was followed by depositing 60 nm of TAD and $\sim$ 60 run of Alq,

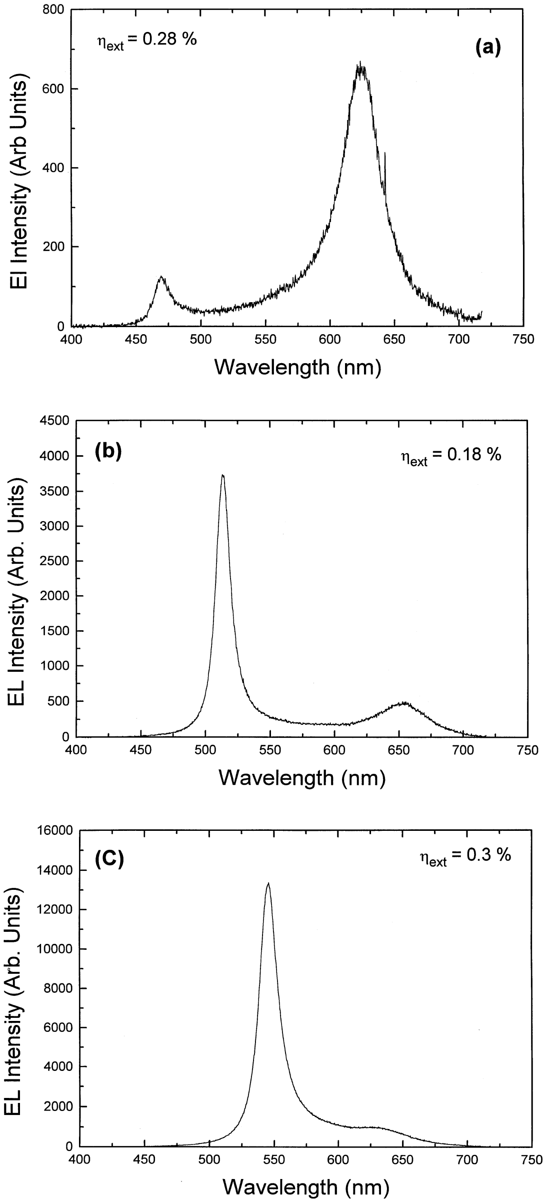

FIGURE 4.9. Electroluminescence spectra (along the cavity axis) from three representative cavity devices from the same substrate but with a terraced filler (as in Fig. 4.2). The anode is a 55-nm-thick ITO layer. The three spectra have major peaks at (a) 625 run, (b) 512 nm, and (c) 545 nm. The measured external quantum efficiencies (in units of photons/electron) are also indicated in each case.

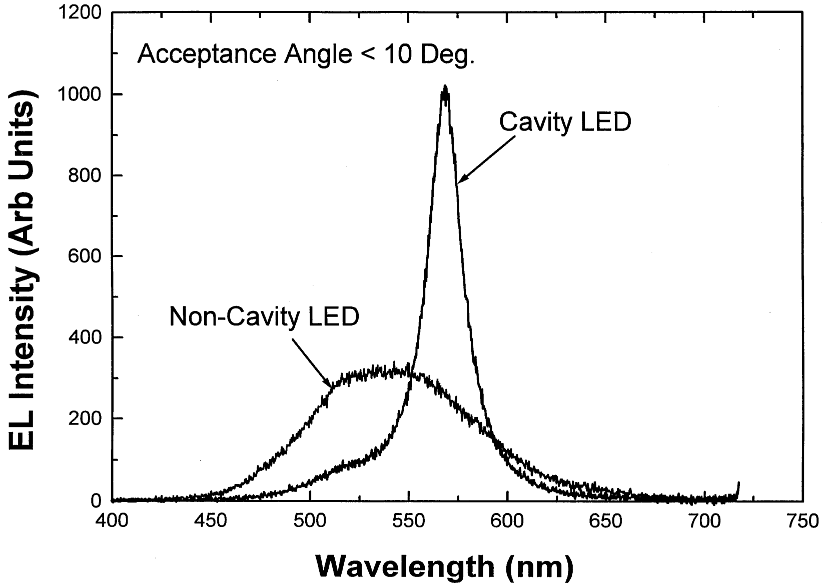

FIGURE 4.10. Electroluminescence spectra (along the normal to the plane of the substrate) from a cavity LED and a reference noncavity LED excited by the same injection current. The active materials for both devices were deposited simultaneously.

and then defining arrays of 1-mm-diameter Al dots on each of the two substrates. Thus, the two sets of devices — cavity and noncavity — possess identical layer structures (including the ITO), which were deposited simultaneously. The LEDs were then excited by a constant-current source, and the light emitted was collected by a high-transmission liquid light guide placed some distance away from the back of the glass substrate along the cavity axis. The light guide is positioned so as to only collect light very close to the cavity axis (collection angle $< 10^\circ$). The collected light is dispersed in a 0.5-m spectrometer and detected with a liquid-nitrogen-cooled CCD detector. Several cavity and noncavity LEDs were excited by equal injection currents and their on-axis EL spectra were recorded for the same period of time (10 s). A typical cavity LED spectrum and a noncavity spectrum are shown in Fig. 4.10. The on-axis resonance wavelength for the cavity LED is 570 nm. The spectrally integrated angular intensities (intensities over a small angular range) of the cavity and noncavity LEDs are almost identical.

The enhancement of the emission intensity along the cavity axis (at the resonance wavelength) is given by:[9]

$$G_e = \frac{\zeta}{2}\frac{(1+\sqrt{R_1})^2(1-R_2)}{(1-\sqrt{R_1R_2})^2}\frac{\tau\mathrm{cav}}{\tau}, \tag{5}$$

where R_1 is the reflectivity of the top (metal) mirror, R_2 is the reflectivity of the dielectric mirror, and ζ is the antinode enhancement factor. ζ has a maximum value of 2 when the emitting dipoles (i.e., exciton recombination zone) is located exactly at the antinode of the standing wave. τ_{cav}/τ is the ratio of exciton lifetimes in the cavity device and the noncavity device, respectively. Lifetime changes due to cavity effects have been measured for Alq doped with the dye pyromethene 580 and were found to be of order 10%.[17] Thus, we can make a first-order approximation that $\tau_{\mathrm{cav}} \sim \tau$. The value of R_1R_2 can be found from:[6]

$$Q = \frac{\lambda}{\Delta\lambda} = \frac{2\pi L}{\lambda}[-\ln(R_1 R_2)^{0.5}]^{-1}, \tag{6}$$

which relates the Q of the cavity to the resonance wavelength (λ), cavity optical thickness (L), and mode linewidth ($\Delta\lambda$). From Eq. (6), $(R_1 R_2)^{1/1} = 0.69$, which is lower than what is predicted by detailed theoretical calculations[27] and what is expected from reflectivity measurements. Taking $R_1 = 0.8$, $R_2 = 0.6$, and $\zeta = 1.4$ (because the exciton recombination zone is spread over about 20 nm) gives $G_e = 4.9$, which agrees quite well with the measured value of 4.1. It must be remembered that in the “noncavity” device, there are some cavity effects present which would lower the measured G_e. Fig. 4.10 and Eq. (5) together imply that if the cavity resonance wavelength was in the range 520–550 nm instead of 570 nm, the angular enhancement would have been 1.3 along the cavity axis. This small increase would be a result of better alignment between the maximum intensity band of the Alq free-space emission spectrum and the microcavity resonance.

Theoretical calculations of the integrated intensity for the microcavity LED structure described earlier indicate that the integrated intensity (over the range of wavelengths that escape from the back of the glass substrate into the air) is slightly less than that of a noncavity LED. This was determined by calculating the emission spectrum at different angles for both types of LEDs. The cavity resonance wavelength is assumed to be 570 nm, as in Fig. 4.10. The two sets of emission spectra are integrated over all relevant angles. This procedure is illustrated in Fig. 4.11 in which the results of theoretical calculations are plotted.[27] The calculations indicate that the integrated intensity of the cavity device relative to the noncavity device is 0.65, which agrees with the results of the integrated intensity comparisons between cavity and noncavity LEDs made by photocurrent measurements.

We have indicated how a modest (1.3) enhancement in angular intensity can be obtained in cavity devices with Alq emissive layers. Further enhancements in angular intensity are possible by choosing emissive layers with narrower free-space emission spectra than Alq. Alq doped with small quantities of the laser dye pyrromethene 580 (PM) results in the emission spectrum of the system becoming narrower than that of Alq. This is result of resonance energy transfer[33] from the excited states of Alq to the excited states of PM580. The full width at half-maximum of the luminescence drops from $\sim$ 100 nm to $\sim$ 45 nm. The spectra are shown in Fig. 4.12. The external quantum efficiency of noncavity devices is enhanced in comparison with devices with an undoped Alq emissive layer. For a device with a ITO/TAD/Alq+0.5%PM (20 nm)/Alq/Li (1 nm)/A1(200 m) structure, an external quantum efficiency of 1.8–2% photons/electron was measured. For comparison, equivalent LEDs without the pyromethene dye had an external quantum efficiency (with Li/Al cathodes) of 0.8%.

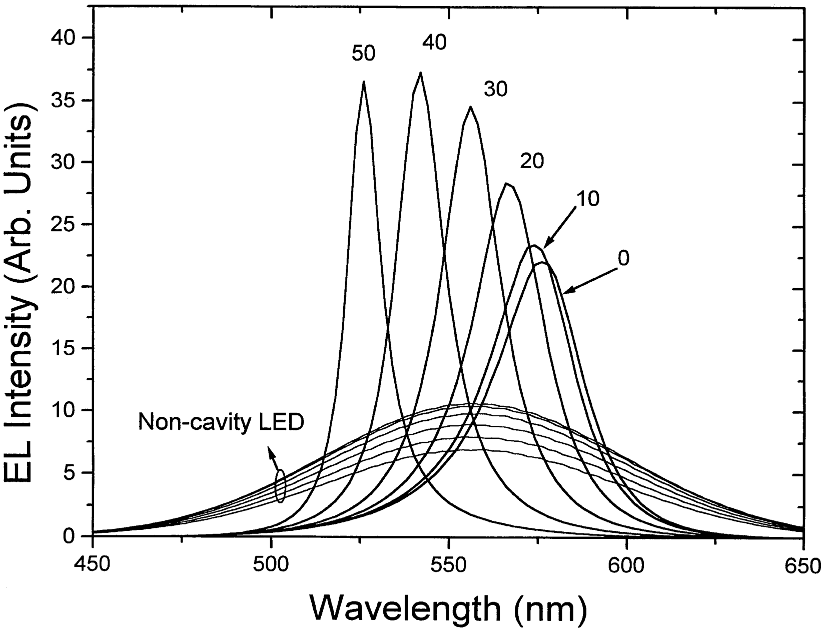

FIGURE 4.11. Calculated spectra as a function of angle for the cavity and noncavity LED in Fig. 4.10. The calculations were made with the matrix formalism developed by Rothberg et al. [4.27]. The calculations indicate that the integrated intensities of the two devices are very similar.

Jordan et al. have evaluated the performance of microcavity LEDs with an emissive layer of Alq doped with 0.5% PM. A maximum angular enhancement of 3.3–3.7 and an integrated enhancement of 1.8 relative to noncavity LEDs with the same emissive layer have been measured.[17] The higher angular and integrated enhancements for the Alq+PM system relative to the undoped Alq is a result of the narrower linewidth of the free-space emission spectrum. The results are summarized in Table 4.1. It is possible to get even larger angular enhancements if active layers with very narrow free-space emission spectra such as the europium

TABLE 4.1. Angular and Integrated Enhancements of Cavity Devices with Alq+0.5% PM Emissive Layers Relative to Noncavity Devices with the Same Emissive Material.

Cavity Resonance	Integrated Enhancement	Angular Enhancement (max θ)
545 nm	0.85	3.3 (0°)
560 nm	1.76	3.7 (10°)
580 nm	1.62	1.6 (40°)
630 nm	0.31	1.2 (60°)

Note: The maximum θ is the angle with respect to the cavity axis at which the maximum angular intensity is attained.

complex reported in Ref 34 are used. Larger enhancements in a given material system are possible by increasing the *Q* of the cavity (i.e., by increasing the mirror reflectivity). These values are eventually limited by what can be attained in practice with Al or Ag top mirrors at visible wavelengths.

The angular dependence of the emission wavelength or effective color in a microcavity LED has been briefly addressed earlier. This angular dependence arises naturally from the changing resonance position caused by the dielectric stack mirror. This could limit the usefulness of the patterned planar microcavity scheme outlined in Section 3 to fabricate full-color displays. However, it is possible by means of a simple modification to the LED architecture to obtain an averaging effect over a significant range of angles. Rothberg et al. have shown that by employing a modified cavity LED, the effective color over a range of +45° changes very little.[27] Tessler et al. and Lidzey et al. have proposed several schemes to mitigate the angular dependence of emission color in polymer LEDs.[35,36] Such approaches may enhance the utility of cavity LEDs for display applications by combining the color selectivity and (possibly) efficiency enhancement of the cavity architecture with the averaging effect (over a range of wavelengths).

For monochrome displays, backlights, and indicators, the Alq+PM system described in the previous section, or its equivalent, would be very suitable. High efficiencies are attainable with this material system and the free-space emission range is centered near 545 nm, which coincides with the maximum sensitivity of

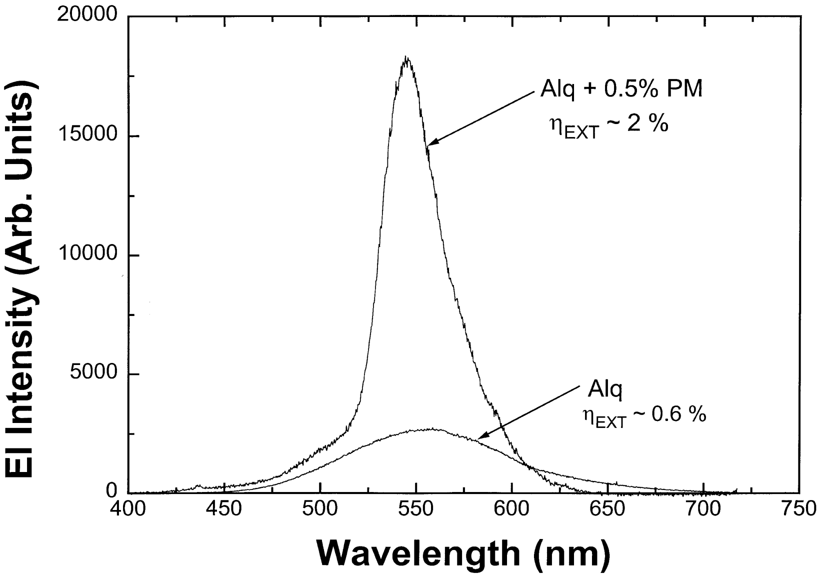

FIGURE 4.12. Electroluminescence spectra from a noncavity LED with an emissive layer consisting of Alq doped with 0.5% pyrromethene. Also shown is the EL spectrum of a LED with an Alq emissive layer. The spectra have been scaled so that the areas are proportional to the measured external quantum efficiencies.

the eye. An additional advantage of this wavelength range is that the off-axis shift in emission wavelength results in much less of a detectable color change. Indeed, for cavity LEDs with a peak resonance wavelength of 560 nm along the cavity axis, the CIE coordinates are (0.38, 0.61) along the axis and change to (0.31, 0.65) at 40°. This results in almost no difference in the hue. The angular-intensity enhancement may also prolong device lifetime, because a smaller current is required to produce a given brightness. This is expected to translate into longer lifetimes because a reciprocal relationship exists between the lifetime and the excitation current level.

4.6 Materials for Organic Microcavity LED Displays

In this section, we discuss the characteristics required of the emissive materials for a full-color-display technology based on the patterned planar microcavity idea and also for monochrome backlight applications. In an earlier section, it was shown that although Alq has a broad molecular emission spectrum spanning the 450–650-nm range, it is weak in the blue and red components. Alq is a very useful model material for studying a variety of microcavity effects. However, it is not ideal in terms of its intensity distribution. Several groups have reported organic LED materials which result in substantially white (or broad band) emission.[37,38]

Jordan et al. have developed a white organic LED technology also based on the Alq/TAD system.[37] The blue component of the spectrum is augmented by introducing a thin layer of a blue-green emitting material between the Alq and the TAD. The use of a dye-doped Alq layer in the device adds to the red component of the combined emission spectrum. In this manner, efficient (0.7% external quantum efficiency) and bright (4750 Cd/m^2) LEDs have been fabricated with emission colors that are close to white.

Introducing a thin layer of 2-napthyl-4,5-bis(4-methoxyphenyl)-1,3-oxazole (NAPOXA) between the Alq and TAD causes the emission spectrum to shift to the blue (shown in Fig. 4.13). The external quantum efficiency, however, remains practically constant for small thicknesses ($<$ 20 nm) of NAPOXA. The increasing blue component of the emission spectrum, as the thickness of the NAPOXA is increased, originates in the NAPOXA layer. Indeed, the EL spectrum of LEDs with a thick NAPOXA layer is almost identical to the photoluminescence spectrum of thin films of NAPOXA. It is necessary to introduce a thin layer of Alq doped with 0.3–0.5% DCM in the device structure for white-light emission (shown in Fig. 4.14). The purpose of this layer is to boost the red component of the NAPOXA/Alq emission. It was found that if the DCM-doped Alq layer was too close to the NAPOXA, the blue and green components of the combined emission spectrum are suppressed. It was therefore necessary to have an undoped Alq layer between the NAPOXA and DCM/Alq layers, as shown in Fig. 4.14. Adjusting the thickness of this undoped Alq layer allows us to control the combined emission spectrum. The device with a 30-nm-thick undoped Alq layer has CIE coordinates

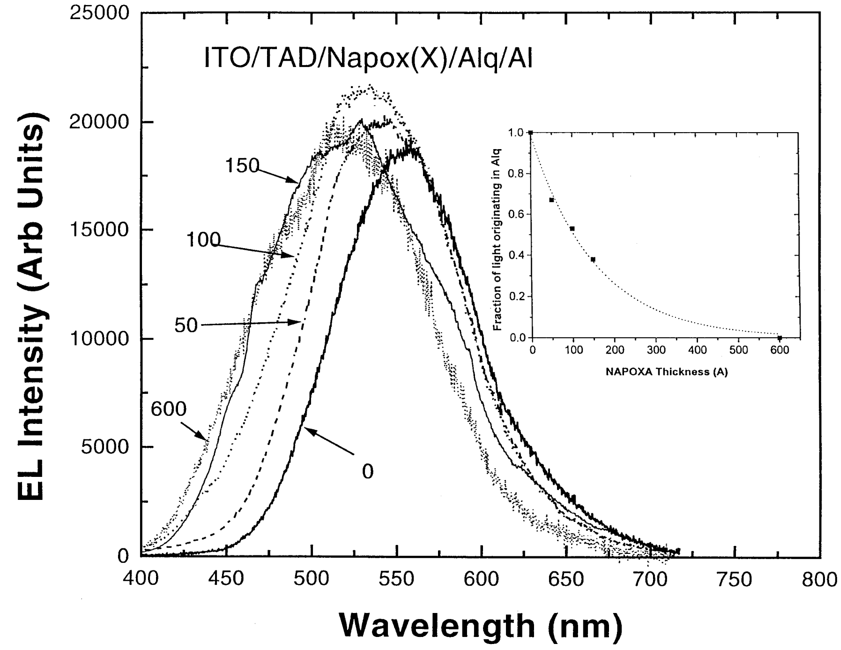

FIGURE 4.13. Normalized electroluminescence spectra of Alq/NAPOXA/TAD LEDs as a function of NAPOXA thickness x (in Å). In the inset is shown the fraction of the total LED light output originating in the Alq as a function of x together with a fit to the data points.

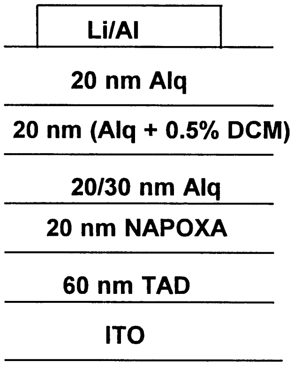

FIGURE 4.14. Device structure of LEDs with multiple emitting layers.

of (0.31, 0.41), which are the closest to white (0.33, 0.33) that we have achieved and is most suitable for use as the broad-band emitter in microcavity LEDs. The spectra are shown in Fig. 4.15. For comparison, the CIE coordinates of Alq/TAD LEDs are (0.39, 0.56). The external quantum efficiencies of LEDs with NAPOXA are 0.5–0.7% with Li/Al contacts. The whitest LED with CIE coordinates (0.31, 0.41) had an external efficiency of 0.7%, and a maximum luminance of 4750 Cd/m^2

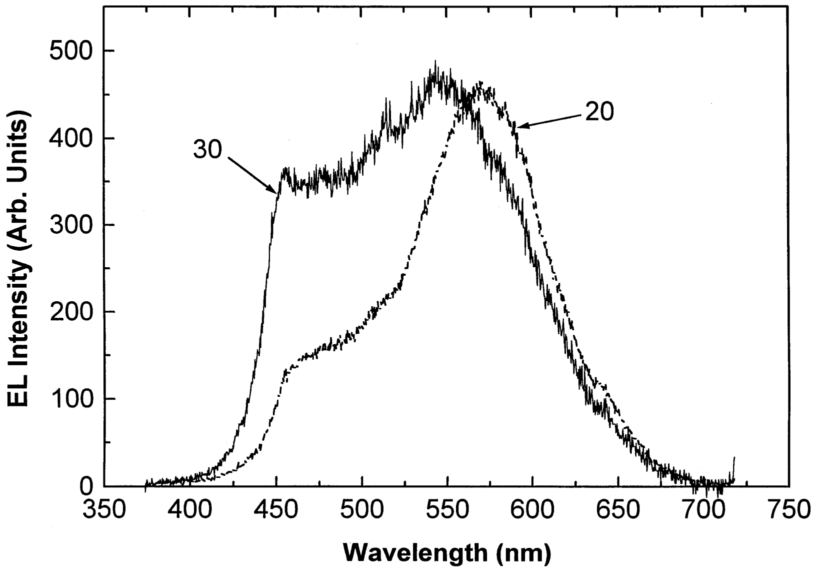

FIGURE 4.15. Electroluminescence spectra from two noncavity devices with the structure shown in Fig. 4.14b. The thicknesses of the undoped Alq layers in the two devices are 20 nm and 30 nm.

(at 20 V and 380 mA/cm^2). Recent advances in white organic LED technology have raised the maximum luminance achieved to more than 30,000 Cd/m^2.[39]

When TiO$_2$ ($n = 2.5$)/SiO$_2$ ($n = 1.46$) mirrors are employed in the QWS, the effective penetration depth into the stack is lowered in comparison with SiO$_2$/Si$_x$N$_y$ mirrors because of the greater index contrast. The mode spacing is commonly increased to $>$ 180 nm from the 125–130 nm that is the case with SiO$_2$/Si$_x$N$_y$ mirrors. Reflectance measurements on cavity devices with typical active-layer thicknesses do indicate that mode spacings of 180–190 nm are possible, which is more suitable for full-color applications. In recent work, Tokito et al. have reported saturated red, green, and blue single-mode LEDs with TiO$_2$/SiO$_2$ dielectric mirrors.[40] In another recent development, the resonance wavelength of a microcavity structure has been tuned over ~ 50 nm by the incorporation of a liquid-crystal layer within the cavity.[41]

4.7 Summary

The effects produced by a planar microcavity on the electroluminescence characteristics of organic materials have been described. A number of organic and polymeric semiconductors have been employed by various groups in studies on microcavity LEDs. However, for detailed descriptions, three categories of emissive materials have been considered: undoped Alq, Alq doped with 0.5% pyrromethene, and Alq+NAPOXA. Alq has a broad free-space emission spectrum spanning the

450–650-nm range (albeit, with a weak blue component). In cavity devices with an Alq emissive layer, it is possible to realize saturated colors with peak wavelengths in the 495–625-nm range and a variety of unsaturated colors, including white. With other emissive materials, saturated red, green, and blue LEDs have been fabricated. The patterned planar microcavity scheme to realize full-color organic-LED-based displays has been described. For the broad-band emitters such as Alq, the external quantum efficiency (or integrated intensity) of cavity devices are slightly lower than those of equivalent noncavity device. This is an expected result because of the large free-space emission linewidth ($\sim$ 100 nm). Theoretical calculations based on a transfer-matrix formalism also indicate that that the integrated intensity of cavity LEDs is, at best, equal to those of noncavity LEDs. However, with Alq emitters, it is possible to realize modest enhancements in *angular* intensity. The angular dependence of the emission characteristics in cavity LEDs have been well documented by many groups and there has been work on ameliorating its effects. When the emissive material is changed to Alq doped with pyrromethene, the free-space emission linewidth is lowered to about 45 nm. Cavity devices with this emissive material show integrated enhancements of 1.8 and angular enhancements of up to 3.7.

Acknowledgments

The authors wish to thank L.J. Rothberg, R.E. Slusher, and the late S. McCall for useful discussions.

References

[1] Y. Yamamoto and R. E. Slusher, Phys. Today 66, (June 1993).
[2] H. Yokoyama, Science 256, 66 (1992).
[3] D. Klepner, Phys. Rev. Lett. 47, 233 (1981).
[4] R. K. Chang and A. J. Campilo (eds.), *Optical Processes in Microcavities*, World Scientific, Singapore, 1996.
[5] A. Dodabalapur, L. J. Rothberg, R. H. Jordan, T. M. Miller, R. E. Slusher, and J. M. Phillips, J. Appl. Phys. 80, 6954 (1996).
[6] T. J. Rogers, D. G. Deppe, and B. G. Streetman, Appl. Phys. Lett. 57, 1858 (1990).
[7] E. F. Schubert, Y. -H. Wang, A. Y. Cho, L. -W. Tu, and G. J. Zydzik, Appl. Phys. Lett. 60, 921 (1992).
[8] D. G. Deppe, C. Lei, C. C. Lin, and D. L. Huffaker, J. Mod. Opt. 41, 325 (1994).
[9] E. F. Schubert, N. E. J. Hunt, M. Micovic, R. J. Malik, D. L. Sivco, A. Y. Cho, and G. J. Zydzik, Science 265, 943 (1994).
[10] N. Takada, T. Tsutsui, and S. Saito, Appl. Phys. Lett. 63, 2032 (1993).
[11] T. Nakayama, Y. Itoh, and A. Kakuta, Appl. Phys. Lett. 63, 594 (1993).
[12] A. Dodabalapur, L. J. Rothberg, T. M. Miller, and E. W. Kwock, Appl. Phys. Lett. 64, 2486 (1994); A. Dodabalapur, L. J. Rothberg, and T. M. Miller, Electron. Lett. 30, 1000 (1994).

[13] A. Dodabalapur, L. J. Rothberg, and T. M. Miller, Appl. Phys. Lett. 65, 2308 (1994).
[14] D. G. Lidzey, D. D. C. Bradley, T. Virgili, A. Armitage, M. S. Skolnick, and S. Walker, Phys. Rev. Lett. 82, 3316 (1999); D. G. Lidzey, D. D. C. Bradley, M. S. Skolnick, T. Virgili, S. Walker, and D. M. Whitaker, Nature 395, 53 (1998).
[15] H. F. Wittmann, J. Gruner, R. H. Friend, G. W. C. Spencer, S. Moratti, and A. B. Holmes, Adv. Mater. 7, 541 (1995).
[16] U. Lemmer, R. Hennig, W. Guss, A. Ochse, J. Pommerehne, R. Sander, A. Greiner, R. F. Mahrt, H. Bassler, J. Feldmann, and E. O. Gobel, Appl. Phys. Lett. 66, 1301 (1995).
[17] R. H. Jordan, L. J. Rothberg, A. Dodabalapur, and R. E. Slusher, Appl. Phys. Lett. 69, 1997 (1996).
[18] M. Berggren, O. Inganas, T. Granlund, S. Guo, G. Gustafsson, and MR. Andersson, Synth. Met. 76, 121 (1996).
[19] V. Bulovic, V. B. Khalfin, G. Gu, P. E. Burrows, D. Z. Garbuzov, and S. R. Forrest, Phys. Rev. B58, 3730 (1998).
[20] R. H. Friend et al., Nature 397, 121 (1999)
[21] M. Gonokami, R. H. Jordan, A. Dodabalapur, H. E. Katz, M. L. Schilling, R. E. Slusher, and S. Ozawa, Opt. Lett. 20, 2093 (1995)
[22] M. Berggren, A. Dodabalapur, and R. E. Slusher, Appl. Phys. Lett. 71, 2230 (1997).
[23] J. D. Joannopoulos, R. D. Meade, and J. N. Winn, *Photonic Crystals*, Princeton University Press, Princeton, NJ., 1995.
[24] A. Mekis, M. Meier, A. Dodabalapur, R. E. Slusher, and J. D. Joannopoulos, Appl. Phys. A69, 111 (1999).
[25] C. W. Tang and S. A. VanSlyke, Appl. Phys. Lett. 51, 913 (1987); C. W. Tang, S. A. VanSlyke, and C. H. Chen, J. Appl. Phys. 65, 3610 (1989).
[26] A. Chin and T. Y. Chang, J. Lightwave Technol. 9, 321 (1991)
[27] L. J. Rothberg, unpublished results.
[28] S. Tokito, S. Noda, and Y. Taga, Electron. Lett. 32, 691 (1996).
[29] *CRC Handbook of Chemistry and Physics*, 73rd ed., CRC Press, Boca Raton, Fl., 1992.
[30] T. Nakayama, Opt. Rev. 2, 39 (1995)
[31] N. C. Greenham, R. H. Friend, and D. D. C. Bradley, Adv. Mater. 6, 491(1994).
[32] J. M. Phillips, R. J. Cava, S. Y. Hou, J. J. Krajewski, J. Kwo, J. H. Marshall, W. F. Peck, Jr, D. H. Rapkine, G. A. Thomas, and R. B. van Dover, Mater. Res. Soc. Symp. Proc. 345, 255 (1994).
[33] T. Forster, Ann. Phys. 2, 55 (1948
[34] J. Kido, K. Nagai, Y. Okamoto, and T. Skotheim, Chem. Lett., 1267 (1991)
[35] N. Tessler, S. Bums, H. Becker, and R. H. Friend, Appl. Phys. Lett. 70, 556 (1997).
[36] D. G. Lidzey, D. D. C. Bradley, S. J. Martin, and M. A. Pate, IEEE J. Select. Topics Quantum Electron. 4, 113 (1998).
[37] R. H. Jordan, A. Dodabalapur, M. Strukelj, and T. M. Miller, Appl. Phys. Lett. 68, 1192 (1996).
[38] J. Kido, M. Kimura, and K. Nagai, Science 267, 1332 (1995).
[39] C. H. Cheun and Y. T. Yao, Appl. Phys. Lett. vol. 81, 4499 (2002).
[40] S. Tokito, T. Tsutsui, and Y. Taga, J. Appl. Phys. 86, 2407 (1999).
[41] H. Becker, T. D. Wilkinson, and R. H. Friend, Adv. Mat. Opt. and Electron, 9, 9 (1999).

5

Light-Emitting Diodes Based on Poly(p-phenylenevinylene) and Its Derivatives

Neil C. Greenham and Richard H. Friend

5.1 Introduction

The report of electroluminescence in the conjugated polymer poly(p-phenylenevinylene), (PPV) in 1990[1] has led to a major effort to develop light-emitting diodes (LEDs) based on PPV and its derivatives and to understand the chemistry and physics which underpins the fabrication and operation of these devices. In this chapter, we review some of this work, concentrating on the relationship between the fundamental semiconductor physics of conjugated polymers and their performance in LEDs. There are several previous reviews covering polymer LEDs, by us[2] and by other authors;[3–6] we aim here to concentrate on more recent developments in the field up to the date of writing (1997). The enormous number of articles published on polymer electroluminescence means that it is impossible to mention more than a small fraction of work in the field, and we deliberately draw most of our examples from the work with which we are most familiar — that from the Cambridge group.

Figure 5.1 shows the structure of a simple conjugated polymer LED. In this structure, a thin film of conjugated polymer is sandwiched between two electrodes, one of which is semitransparent, typically indium tin oxide (ITO) on a glass substrate. A voltage is applied between the electrodes, with the positive voltage applied to the ITO, causing electrons and holes to be injected from the negative and positive electrodes, respectively. The charge carriers drift through the device under the

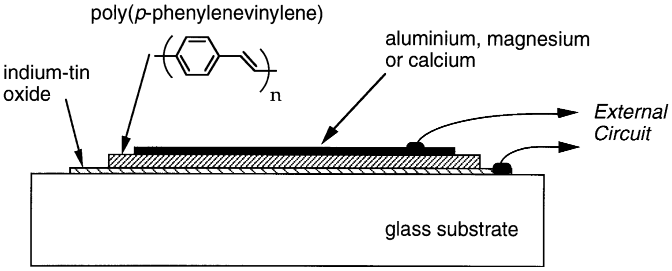

FIGURE 5.1. Structure of a polymer light-emitting diode.

action of the applied field, and electrons and holes may recombine to form bound neutral excited states, known as excitons. Those excitons formed in the singlet spin state may decay radiatively to the ground state, giving out light which is observed through the semitransparent electrode. The color of the emission depends on the energy gap of the polymer, which can be altered by chemical substitution. Polymer LEDs thus provide the opportunity for producing large-area displays with emission throughout the visible range.

Attention has focused on developing new polymers and device structures in order to control the emission color, to improve the efficiency of light emission, and to understand the physical processes which determine the device performance. In the following sections, we first outline the electronic properties of PPV and review some of the synthetic routes to PPV and its derivatives. We then describe how high efficiencies and a range of emission colors have been achieved in PPV-based LEDs, and we examine the processes of charge injection, transport, recombination, and exciton decay, which control the device properties. Industrial interest in polymer LEDs is based on the potential for low-cost solution processing of large-area displays. Considerable effort has been put into improving the operating lifetime of polymer LEDs to values which are acceptable for commercial applications. We review this area in the final section.

5.2 The Electronic Structure of PPV

The chemical structure of PPV is shown in Figure 5.1. The polymer backbone is held together by σ bonds formed by the three sp^2 hybridised electrons on each carbon atom. The remaining valence electron on each carbon is a p_z electron, with a wavefunction as shown in Fig. 5.2. In the polymer, the p_z, atomic orbitals overlap to form a delocalized π molecular orbital, along with a corresponding unoccupied π^* orbital, separated by an energy gap E_g. Electronic transitions may occur between the highest occupied molecular orbital (HOMO) and the lowest unoccupied molecular orbital (LUMO), corresponding to the π and π^* orbitals, respectively. In the language of conventional semiconductor physics, the HOMO and LUMO levels may be considered as the valence and conduction bands, respectively.

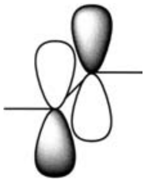

FIGURE 5.2. p_z orbitals along a conjugated polymer backbone.

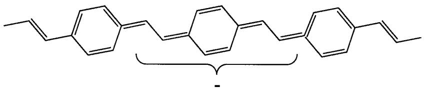

FIGURE 5.3. Rearrangement of bonding geometry around a negative charge in PPV.

Whereas simple Hückel-like models can give a relatively good description of the ground-state properties of conjugated polymers, the situation is more complicated in the case of excited states, due to both electron–electron and electron–lattice interactions. Because the interactions between neighboring repeat units within a polymer chain are much stronger than the interactions between neighboring chains, the electronic structure of conjugated polymers may be considered as one dimensional. In such a one dimensional system, there is strong coupling between the electronic excitations and the chain geometry. A charge on a PPV chain will therefore be accompanied by a local reorganization of the nuclear geometry, leading to a region of chain where the bond alternation amplitude is weakened or even reversed (see Fig. 5.3). Such an excited state is termed a polaron and has an energy level which is relaxed within the energy gap. The energy levels for positive and negative polarons, and the corresponding optical transitions which they produce are shown in Fig. 5.4. For simplicity, when discussing charge carriers in conjugated polymer devices, we will use the terms "electron" and "hole" to refer to negative and positive charge carriers, respectively. Theory also predicts the existence of doubly-charged, spin-zero excited states, termed bipolarons, where the state is stabilized by further lattice relaxation, producing energy levels relaxed further within the gap.[7,8] In real materials, there is considerable debate about the degree to which bipolarons require the presence of disorder, chemical defects, or counterions in order to be stable.[9,11]

In the simplest terms, photoexcitation in conjugated polymers can be thought of as exciting an electron from the HOMO to the LUMO. In detail, however, it is necessary to take into account both the interaction with the lattice and the coulombic attraction between electron and hole. In a conventional inorganic semiconductor, the electron and hole are delocalized in all three dimensions, so their overlap is small, leading to a coulombic exciton binding energy which is much smaller than the thermal energy at room temperature. In a conjugated polymer, however, the electron and hole are confined to the same chain, so the binding energy is much larger. The magnitude of the binding energy depends on the extent of delocalization along the polymer chain and has been a matter of considerable recent debate.[12,15]

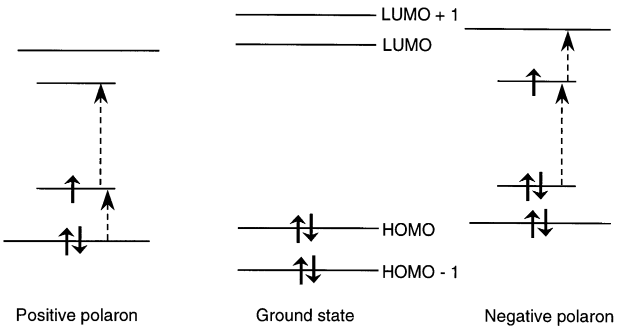

FIGURE 5.4. Electronic transitions (dotted arrows) due to positive and negative polarons. Occupation of electronic energy levels is denoted by solid arrows. The ground state is shown as a reference.

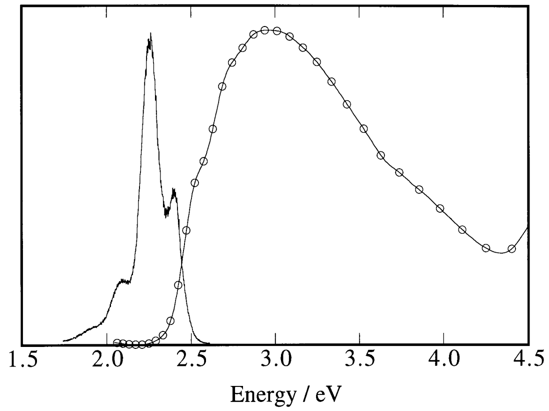

FIGURE 5.5. Absorption (circles) and emission (line) spectra of PPV.

Although there is still no firm agreement on the value of the exciton-binding energy in PPV, the consensus of opinion is that the binding energy is several tenths of an electron volt and that it is therefore appropriate to consider the neutral excited state as a bound exciton at room temperature. In the absence of conformational or chemical defects which disrupt the conjugation of the polymer chain, singlet excitons are believed to extend over as many as 10 repeat units in PPV.[16]

The singlet exciton in PPV can therefore be considered as a molecular excited state which will couple strongly to vibrations of the chain, giving a series of vibrational side bands which may be observed in the absorption and emission spectra. Absorption and emission spectra for PPV are shown in Fig. 5.5. Real solid-state samples of PPV in fact contain a range of different conjugation lengths (defined as the distance between topological or chemical defects which break the conjugation) and a range of physical environments for conjugated segments. Because the energy gap depends on both the conjugation length and the local environment, the absorption spectrum of PPV shows significant inhomogeneous broadening. Excitons created on high-energy segments may hop to lower-energy segments by Förster transfer, a nonradiative energy-transfer process mediated by the near-field dipole–dipole interaction between two molecules. Emission therefore tends to come from the lower-energy regions of the sample, and its spectrum is less broadened than the absorption spectrum.

The excitons produced by photoexcitation are in the singlet spin state. Excitons produced by the recombination of opposite charges can be in either the singlet or triplet state, with spin statistics dictating a ratio of 3:1 between the generation of triplet and singlet excitons. Triplet excitons are not coupled radiatively to the ground state and have lifetimes of the order of 1 ms in PPV at low temperatures.[17] The presence of triplet excitons may be detected by the occurrence of an additional absorption at 1.4 eV, corresponding to a transition from the lowest triplet exciton to a higher-lying triplet.[17] Triplet excitons are localized largely within a single phenyl ring[18] and are consequently more strongly bound and lower in energy than singlet excitons. The absolute position of the lowest triplet state not well known, but theoretical calculations suggest that it is approximately 0.65 eV below the first excited singlet state.[16]

The radiative decay of singlet excitons is clearly an important process in the operation of polymer LEDs. This rate is denoted by k_r, where for PPV, $(k_r)^{-1} \approx 1200$ ns.[19] Radiative decay competes with various nonradiative decay processes, such as quenching of excitons by defects, exciton dissociation, and intersystem crossing to form triplet states. Assuming that both radiative and nonradiative decays are monoexponential, the photoluminescence quantum efficiency, $\mathrm{PL}_{\mathrm{eff}}$, defined as the number of photons emitted per photon absorbed, is given by

$$\mathrm{PL}_{\mathrm{eff}} = b\frac{k_r}{k_r + k_{\mathrm{nr}}},$$

where k_{nr} is the nonradiative rate and b is the fraction of absorbed photons which generate singlet excitons. The PL efficiency of standard PPV has been measured to be 0.27, with an overall decay rate $k_r + k_{\mathrm{nr}}$ of $(320\ \mathrm{ps})^{-1}$.[20] On the basis of these figures, the efficiency can be accounted for solely by the competition between radiative and nonradiative decay, with a value of b close to 1, implying that singlet excitons are the predominant product of photoexcitation in PPV.

In PPV, there is strong evidence that singlet excitons are localized on a single chain, although they may hop between chains by Förster transfer. However, in some PPV derivatives, such as the cyano-substituted PPV shown in Fig. 5.6, there is evidence that the emissive state is delocalized over at least two neighboring chains. In these materials, the emission in the solid state is significantly red-shifted with respect to that in solution (where the emission is assumed to be intrachain).[21] The radiative lifetime is almost 10 times longer in the solid state than in solution, implying that the excited state is only weakly coupled to the ground state. These factors, combined with the lack of vibronic coupling to the emission, suggest that the emissive species is an interchain state, either an excimer or a physical dimer.

Other interchain excited states are possible in PPV, including bound polaron pairs, where the positive and negative polarons reside on neighboring chains.

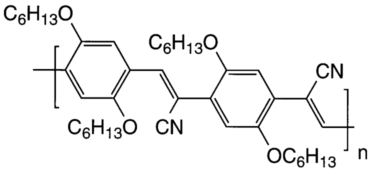

FIGURE 5.6. Chemical structure of CN-PPV.

From stimulated emission measurements on picosecond timescales, Rothberg and co-workers found that 90% of photons absorbed in their PPV samples produced nonemissive species, and they proposed that these nonemissive species were polaron pairs.[22] These polaron pairs are believed to be responsible for an induced absorption which overlaps with the PL.[23] For PPV prepared in Cambridge with special care taken to avoid photo-oxidation, we have found that a much smaller fraction of absorbed photons produce polaron pairs, with a consequent decrease in the picosecond photoinduced absorption.[24] For the soluble PPV derivatives, the formation of interchain excited states is strongly dependent on the film morphology, which can be controlled through the choice of solvent for spin-coating.[25]

5.3 Synthesis of PPV and Derivatives

One of the major attractions of conjugated polymers as materials for LEDs is their processability from solution, using spin-coating or other solution-processing techniques. PPV in its final form, however, is insoluble, so it is processed via a soluble precursor polymer, which is then heated to remove a leaving group and form the final conjugated polymer. The standard route uses an alkyl-sulfonium leaving group, as developed originally by Wessling and Zimmermann.[26] Much of the recent LED work has been performed using the tetrahydothiophenium leaving group precursor,[27] synthesized as shown in Fig. 5.7 by the base-induced polymerization of bis-xylylenetetrahydrothiophenium chloride.[28] This polymer is soluble in methanol and can be converted to the final polymer by heating at around 220°C in vacuum.

By substituting alkoxy groups at the 2- and 5-positions on the benzene ring, it is possible to achieve polymers which are soluble in their final form.[29] The energy gaps of these polymers are typically smaller than in PPV, due to the electron-donating nature of the substituents, although by using sufficiently bulky side groups, it is possible to disrupt the conjugation though steric effects and return the energy gap to the green. The orange-red emitting polymer poly(2-methoxy, 5-(2′-ethyl-hexyloxy)-*p*-phenylenevinylene), MEH-PPV, as shown in Fig. 5.8, has been extensively investigated in LEDs.[30] Although precursor routes to dialkoxy-PPVs have been used,[31] they are typically produced by direct dehydrohalogenation polymerization of 1,4-bischloromethyl(2, 5-dialkoxy)benzene derivatives,[32] as shown in Fig. 5.9.

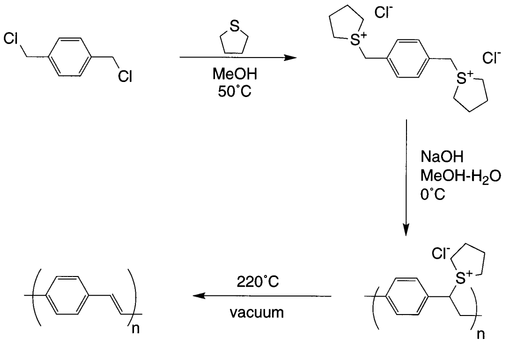

FIGURE 5.7. Synthesis of PPV precursor and its conversion to form PPV.

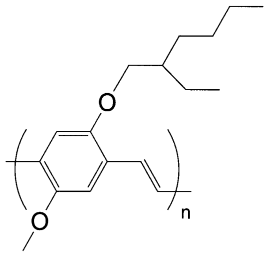

FIGURE 5.8. Chemical structure of MEH-PPV.

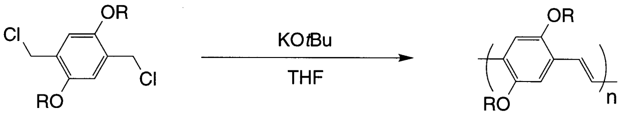

FIGURE 5.9. Synthesis of dialkoxy-PPV.

Copolymerization of various substituted PPV monomer units has been used to tune the electronic properties. In particular, the introduction of nonconjugated units into the polymer chain has been found to produce enhanced photoluminescence efficiencies by preventing diffusion of excitons along the chains to defect sites.[33,34]

Substitution at the vinylic carbons can also be used to alter the electronic properties. For example, the substitution of electronegative -CN groups has been found to increase the electron affinity and ionization potential of PPV derivatives, thus improving the electron-injection characteristics.[35,36] The synthesis is performed by the Knovenagel condensation polymerization of a terephthaldehyde and a benzene-1,4-diacetonitrile derivative, as shown in Fig. 5.10.

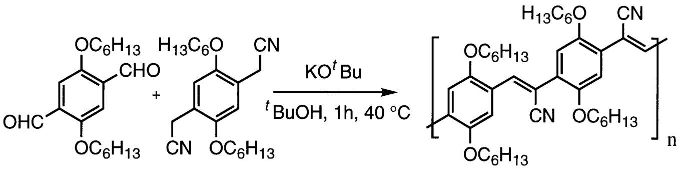

FIGURE 5.10. Synthesis of CN-PPV.

5.4 Single-Layer LEDs

The structure and basic operation of a single-layer polymer LED were described in Section 5.1. PPV was the first conjugated polymer in which electroluminescence was observed, initially using thin oxide-coated aluminum, and subsequently using ITO, as the hole-injecting electrode.[1] The internal efficiency of a polymer LED, η_{int}, defined as the number of photons generated within the emissive layer per charge carrier flowing in the external circuit, is the product of a number of factors:

$$\eta_{\text{int}} = \text{PL}_{\text{eff}}(f_{\text{singlet}})(\eta_{\text{recomb}}),$$

where PL_{eff} is as defined in Section 5.2 (assuming that photoexcitation only produces singlet excitons), f_{singlet} is the fraction of excitons generated in the singlet state in the LED, taken to be 0.25, and η_{recomb} is the number of recombination events taking place in the LED per charge flowing in the external circuit. To achieve efficient electroluminescence, it is necessary to have a highly photoluminescent material, to have closely balanced rates of electron and hole injection, and to ensure that a large proportion of the injected charges recombine within the device, rather than escaping at the opposite electrode.

The first PPV LEDs were relatively inefficient, and a great deal of effort has been put into improving their efficiency. Photoluminescence efficiencies have been improved by reducing the level of chemical defects (including photo-oxidation products), which act as quenching sites for excitons, and values of 27% have been achieved for standard PPV.[20] By introducing nonconjugated units into the polymer backbone and using a bromide counterion in the precursor salt, PL efficiencies as high as 80% have been achieved.[37]

The balance of charge carrier injection is usually limited by the electron-injecting characteristics of the negative electrode. For example, the barrier to electron injection from aluminum to PPV is significantly larger than the barrier to hole injection from ITO. The current is thus made up largely of holes which do not recombine with electrons, leading to low efficiencies. Major improvements have been made by using lower-workfunction metals such as calcium for electron injection.[30,38,39] This technique was first demonstrated by Braun and co-workers,[30,38] who achieved quantum efficiencies in the region of 1% using MEH-PPV between electrodes of calcium and ITO.

Color is another important factor for control in polymer LEDs. The emission spectrum of PPV, shown in Fig. 5.5, corresponds to green emission. As mentioned in Section 5.3, alkoxy substitution can be used to shift the emission toward the red, as in MEH-PPV, which gives orange-red emission. In CN-PPV (Fig. 5.6), the emission is further shifted to the red because the emissive state is able to lower its energy by spreading onto more than one chain.[21,35] Slight shifts in PPV emission toward the blue can be achieved by copolymerization with nonconjugated units,[33] although, in general, it is difficult to achieve large shifts in random copolymers due to the migration of excitons to the low-energy regions. Oligomers of PPV can be used to give blue emission, either dispersed in an inert matrix,[40] attached to a polymer chain as side groups,[41] or within the main chain.[42]

Although the basic principles of polymer LED operation are well established, the details of what determines the current–voltage and current–luminance characteristics of polymer LEDs are still a matter of intense debate. The problem is complicated by the range of different materials being studied, the lack of detailed information about mobilities, doping levels and recombination mechanisms, and the possibility of interfacial layers at the polymer/electrode interface. The current–voltage and luminance–current curves of a typical PPV LED are shown in Fig. 5.11. The diodelike characteristics are typical of most polymer LEDs and are consistent with the simple band diagram shown in Fig. 5.12, where the barriers for charge injection in reverse bias are much larger than those for injection in forward bias.

The problem of detailed modeling can be divided into three parts: (1) What is the shape of the energy bands within the device, particularly close to the electrodes? (2) What is the mechanism for injection of charges through any barriers which are formed at the interface? (3) To what extent are the characteristics of the device determined by transport and recombination within the bulk of the polymer, rather than by injection at the interfaces?

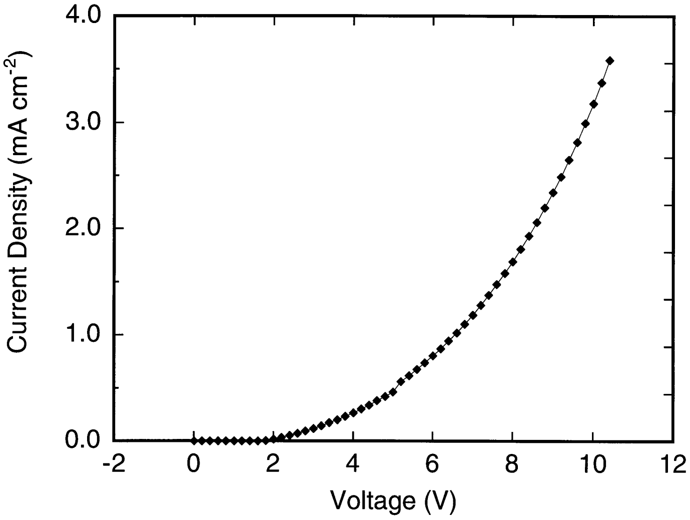

FIGURE 5.11. Current density as a function of voltage for a typical ITO/PPV/Ca LED.

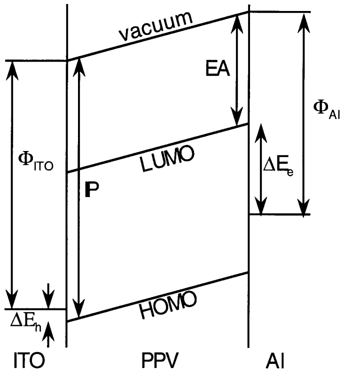

FIGURE 5.12. Schematic energy-level diagram for an ITO/PPV/Al LED, showing the workfunctions, Φ, of the electrodes and the electron affinity (EA) and ionization potential (IP) of the polymer. The barriers to electron injection (ΔE_e) and hole injection (ΔE_h) are also shown.

For an ideal polymer/metal interface, the form of the band bending in the proximity of the interface is determined by the doping level in the polymer. Conjugated polymers are usually synthesized with doping levels as low as possible. For low doping levels, the width of the band-bending region will be considerably greater than the thickness of a typical polymer LED,[2] implying that the electric field is constant throughout the device, as shown in Fig. 5.11. In PPV devices, it is sometimes found that the PPV is significantly more conducting than expected from the synthetic route.[43] This is attributed to doping of the polymer by indium impurities, probably caused by the reaction of the acid produced during the thermal elimination process with the ITO electrode. For these devices, a model has been proposed where a depletion region exists close to the negative electrode, causing a conventional Schottky barrier to form at this interface. It has been proposed that thermionic emission of holes over this barrier controls the hole current in the device.[43]

For soluble PPV derivatives and for PPV devices where the ITO has been protected to avoid attack by acid, the bands are likely to be flat, as shown in Fig. 5.12. The fully depleted nature of MEH-PPV LEDs, for example, was demonstrated using impedance spectroscopy by Campbell et al.[44] In this case, it has been proposed that both electron and hole currents are determined by tunneling through triangular barriers at the electrodes. The dependence of the electron and hole currents on the electrode workfunction was clearly demonstrated by Parker,[45] who obtained reasonable agreement with Fowler–Nordheim theory for the barrier heights in devices constructed so that only electron or only hole currents were observed. However, the magnitudes of the currents observed in polymer LEDs are several orders of magnitude smaller than those predicted from Fowler–Nordheim theory, and there are serious problems in fitting the current–voltage characteristics of double-carrier devices. Progress in resolving the problem of the magnitude of the observed current has been made by Davids et al., who have allowed for diffusion of injected carriers back into the contact, which is important due to the low mobility of carriers in conjugated polymers.[46]

An alternative approach has been taken by Blom and co-workers, who have developed a model in which the electron and hole currents are limited not by the injection process but by the transport capability of the bulk polymer.[47,48] The maximum single-carrier current that can be supported in a trap-free semiconductor is the space-charge-limited current J_{SCL}, given by

$$J_{\mathrm{SCL}} = \frac{9}{8}\epsilon_0\epsilon_r\mu\frac{V^2}{L^3},$$

where μ is the mobility of the carrier in question, V is the applied voltage, and L is the device thickness. By constructing single-carrier dialkoxy-PPV devices, Blom et al. showed that the hole current could be described by a trap-free (or trap-filled) space-charge-limited current with a field-dependent mobility and that the electron current is limited by strong trapping. They then extended this model to double-carrier ITO/polymer/Ca devices and found that good fits could be obtained to the experimental current–voltage and luminance–voltage characteristics by including bimolecular recombination in the model. A similar approach was applied in molecular organic LEDs by Burrows et al.[49] and in polymer LEDs by Conwell.[50] This approach is attractive, but it only applies when the barriers to injection are small enough to allow the space-charge-limited current to be supplied. The dependence of the device characteristics on electrode material clearly indicates that frequently this is not the case and that the intermediate regime where both injection and space charge are important remains to be modeled in detail, although some progress in this direction has been made by Scott et al.[51]

A further complication arises from the possible presence of chemically modified layers, particularly at the interface between the polymer and the negative electrode. The interface between PPV and aluminum has been studied using X-ray and ultraviolet photoelectron spectroscopy (XPS and UPS). For PPV surfaces carefully cleaned in ultrahigh vacuum (UHV) conditions before deposition, covalent bonding of aluminum at the vinylic carbon positions has been observed.[52] For calcium/PPV interfaces, a region of doped polymer is formed at the interface.[53] For less carefully prepared surfaces, as are likely to be found in LEDs, an oxide layer is found at the interface.[53,54] This oxide might be expected to act as a barrier to charge transport. LEDs fabricated in typical high-vacuum conditions (10^{-5} mbar) have been found to have higher efficiencies than those fabricated in UHV; this effect has been attributed to the interfacial oxide layer.[53] Meier et al. have deposited thin layers of aluminum oxide between the emissive polymer and the cathode in ITO/PPV/Al devices and have found that the quantum efficiency of the device is optimized with an insulator thickness between 3 and 5 nm.[55]

At the ITO interface, various conducting polymers have been introduced between the luminescent polymer and the ITO. These include polyaniline[56] and polyethylenedioxythiophene (PEDOT) (Fig. 5.13).[37] There are several potential benefits from this approach, including the smoothing out of surface features on the ITO which may lead to short-circuits, the possibility of dopants from the con-

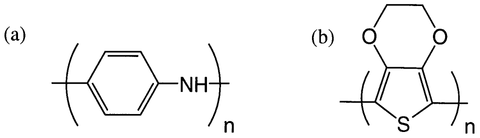

FIGURE 5.13. Chemical structures of the undoped forms of (a) polyaniline and (b) PEDOT.

ducting polymer beneficially modifying the emissive polymer at the interface, and, for precursor-route PPV devices, the protection of the ITO from elimination products of the precursor. Yang et al. have found that further reductions in drive voltage can be achieved by creating a high-surface-area electrode using polyaniline blended with polyester resin, which is subsequently removed to leave a polyaniline network.[57] This is believed to lead to an increased area for hole injection and to an increase in the local electric field at the electrode. Other groups have studied the effect of surface treatment of the ITO by organic solvents, acids, and oxygen plasmas and have found that the device characteristics can be significantly altered by these treatments.[58,59]

5.5 Multiple-Layer Polymer LEDs

The use of two semiconducting layers to improve the efficiency of organic light-emitting diodes was first demonstrated by Tang and co-workers using molecular materials.[60,61] These ideas were subsequently extended to three-layer systems by Adachi et al.[62,63] The principle of using more than one semiconducting layer is to optimize the energy barriers to electron and hole injection at the metal/semiconductor and semiconductor/semiconductor interfaces within the device.

The first two-layer device based on a conjugated polymer was demonstrated by Brown et al.[39] They introduced an electron-transporting layer (ETL) between PPV and the negative electrode, as shown in Fig. 5.14. The electron-transporting layer used was the molecule 2-(4-biphenylyl)-5-(4-*tert*-butylphenyl)-1,3,4-oxadiazole, dispersed in a matrix of polymethylmethacrylate. Quantum efficiencies were typically increased by a factor of 10 compared to devices without the electron-transport

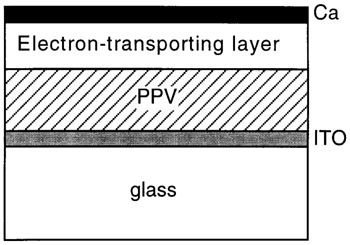

FIGURE 5.14. Schematic structure of a PPV LED incorporating an electron-transporting layer.

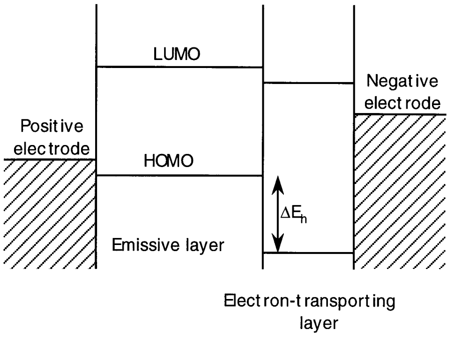

FIGURE 5.15. Schematic energy-level diagram for the device shown in Fig. 5.14.

layer. The energy-level diagram for such a device is shown in Fig. 5.15. The improvement in efficiency is largely due to the barrier for hole transport from the PPV into the ETL. This barrier reduces the number of holes passing through the device without recombination. In addition, the increased charge density at the interface may increase the probability of electrons recombining and will also redistribute the electric field in the device in such a way as to promote electron injection at the negative electrode. Finally, the recombination region is moved away from the metallic negative electrode where the efficiency of radiative decay is reduced, as discussed in Section 5.6.

Electron-transporting layers have been used in conjunction with conjugated polymers by several other groups, with a similar effect.[64,65] Unfortunately, the stability of LEDs using molecular electron-transporting materials dispersed in polymeric matrices tends to be poor, probably due to slow recrystallization of the electron-transporting molecules. This problem has led to the development of various polymeric electron-transporting materials, which show improved stability.[66]

An alternative approach to improving the electron injection in polymer LEDs is to use materials which have been designed to have higher electron affinities and hence lower barriers to electron injection. This strategy has been demonstrated by Greenham et al., who attached electron-withdrawing -CN groups at the vinylic carbons in poly(2,5-dihexyloxy-*p*-phenylenevinylene) in order to increase the electron affinity (see Fig. 5.6).[35] Both the electron affinity and ionization potential were found to be increased by 0.5– 0.6 eV in this polymer (CN-PPV) compared to the corresponding polymer without the -CN groups. LEDs were fabricated as shown in Fig. 5.16, with the structure ITO/PPV/CN-PPV/metal. Due to the improved electron-injection characteristics of CN-PPV, high efficiencies (approximately 4% internal quantum efficiency) were achieved using aluminum as the negative electrode, thus removing the necessity to use low-workfunction metals such as calcium. A schematic energy-level diagram for such a device is shown in Fig. 5.17, showing the barriers to both hole and electron transport at the PPV/CN-PPV interface. The emission in these devices is found to come entirely from the

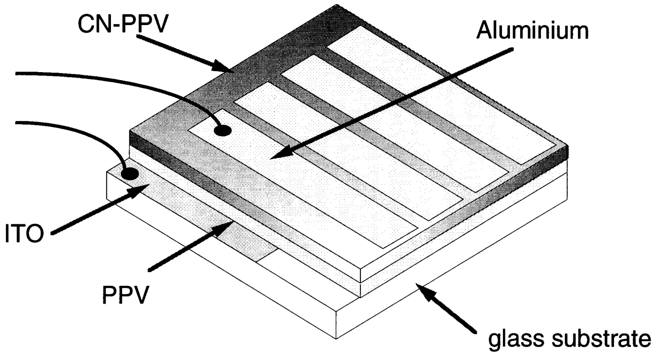

FIGURE 5.16. Heterostructure LED based on CN-PPV.

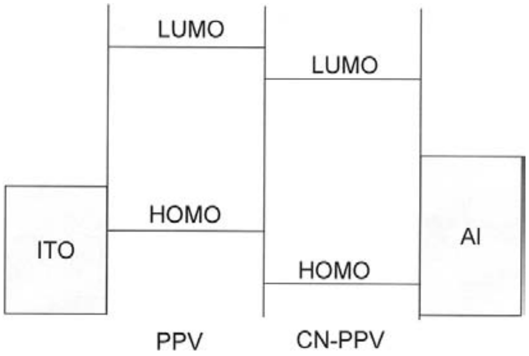

FIGURE 5.17. Schematic energy-level diagram for the device shown in Fig. 5.16.

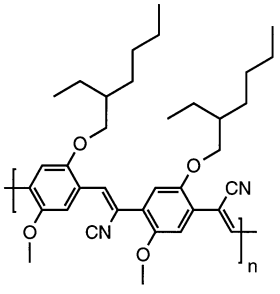

FIGURE 5.18. A cyano-substituted PPV derivative with asymmetric side chains.

CN-PPV layer, implying that recombination occurs only in this layer and that the PPV acts solely as a hole-transport layer.

Other electronegative polymers have been investigated in this role, and particular success has been achieved using the substituted MEH-PPV derivative shown in Fig. 5.18. This polymer can be spin-coated from toluene to form uniform thin layers, and it emits at slightly shorter wavelengths than CN-PPV, which has allowed

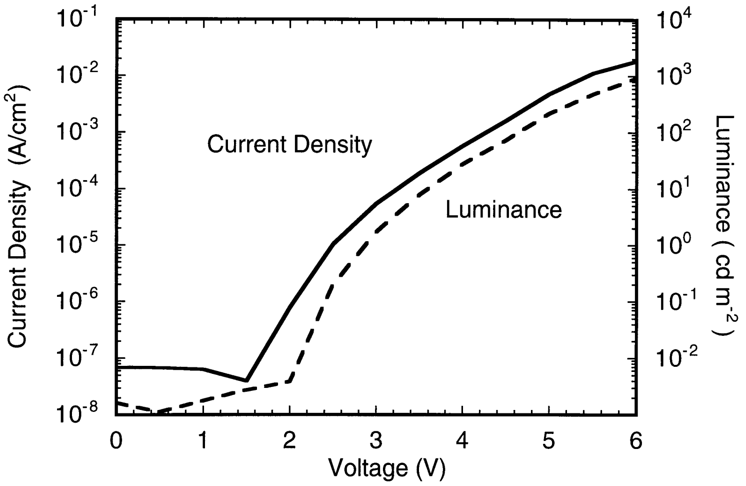

FIGURE 5.19. Current and luminance as a function of voltage for a heterostructure LED using PPV and the polymer shown in Fig. 5.18.

brightnesses in excess of 100 cd/m^2 to be achieved at only 5 V, as shown in Fig. 5.19. Detailed modeling of the performance of double-layer LEDs is a difficult task because both injection and space-charge effects are likely to be important.[67]

5.6 Transport and Recombination in Polymer LEDs

The processes of charge carrier transport and recombination are crucial to the operation of polymer LEDs and, in the case of good injection, can directly determine the electrical characteristics. However, both these processes are difficult to study at a fundamental level and remain poorly understood.

Transport properties are usually described by the effective mobilities, μ_{eff}, of electrons and holes, such that the current density, J, due to a single carrier type is given by

$$J = ne\mu_{\text{eff}}F,$$

where F is the applied field and n is the total number density of charge carriers present, including those in traps. The traditional way to determine carrier mobilities in organic materials is by time-of-flight experiments: however, in PPV and its derivatives, it is extremely difficult to extract meaningful data from time-of-flight experiments due to the dispersive nature of the transport, although Lebedev et al. have recently been able to extract values of 10^{-5} cm^2/V s from time-of-flight measurements on carefully prepared PPV samples.[68] Values of mobility may be extracted from measurements of metal–insulator–semiconductor field-effect transistors using a conjugated polymer as the semiconductor layer, although undoped PPV does not show a field effect.[69] The mobility measured is highly sensitive to the dopant concentration, and for lightly doped PPV films, field-effect hole mobilities as low as 10^7 cm^2/V s have been found.[69] However, it is not clear whether the mobility values extracted from field-effect measurements are relevant to the operation of LEDs, due to the difference in electric field, charge densities, and trap filling between the two devices. Further differences may arise due to the presence of the insulator layer close to the active region in the field-effect transistor and to the different direction of transport relative to the plane of the polymer film.

The operation of polymer LEDs themselves can give information about the mobilities of charge carriers in conjugated polymers. Assuming a model where the hole current is space-charge-limited, Blom et al. have extracted a hole mobility in poly(2-methoxy,5-decyloxy-*p*-phenylenevinylene) of 5×10^{-7} cm^2/V s at low fields, increasing by a factor of 5 at 10^5 V/cm.[70] Such a field dependence is expected in a disordered hopping system. An alternative approach is to study the transient response of the light output in a polymer LED to an applied voltage pulse.[71–73] The delay between the voltage turn-on and the light turn-on then gives some measure of the transit time of carriers in the device. Great care must be taken when interpreting these results to ensure that recombination between injected carriers is being observed, rather than recombination of injected carriers with extrinsic or trapped carriers already present in the device.[71,74] In PPV devices, Karg et al. extracted a mobility of between 10^{-7} and 3×10^{-6} cm^2/V s, depending on the applied field[71] although significantly higher values have been deduced under conditions of a high excitation density.[73]

The recombination of carriers in polymer LEDs is clearly critical to their operation. The recombination rate, R, is related to the density of electrons and holes (n and p) by

$$R = np\gamma.$$

The theory for recombination in a system where the mean free path of a carrier is small was developed by Langevin[75] who showed that the recombination rate constant is given by

$$\gamma = \frac{e}{\varepsilon}(\mu_e + \mu_h),$$

where μ_e and μ_h are the electron and hole mobilities, respectively.

This formalism has been applied to polymer LEDs to estimate the position of the recombination zone. Particularly useful experimental data here come from studies of multiple-layer LEDs, where the emission spectrum can be used to determine the amount of recombination occurring in each layer.[76] The simple theory has been extended by Gartstein et al. to take into account the discrete nature of the hopping process and the distribution in site energies.[77]

The presence of singlet excitons in polymer LEDs can be clearly deduced from the emission spectrum. Triplet excitons, however, are more difficult to detect because they are not coupled radiatively to the ground state. Triplet excitons in PPV may be detected by the presence of an induced absorption at approximately 1.4 eV.[17] The presence of this induced absorption in PPV LEDs was demonstrated by Brown et al., who detected the modulation of a probe beam that was passed through the active layer and reflected from the negative electrode.[78] The spectral shape and lifetime of the induced absorption were similar to those of the triplet induced absorption seen in photoinduced absorption experiments, thus confirming the presence of triplet excitons in PPV LEDs.

Further evidence for the presence of triplet excitons in LEDs comes from electroluminescence-detected magnetic resonance experiments. In this technique, the LED is placed in a microwave cavity where a dc magnetic field can be applied. Using lock-in detection, the change in EL output is monitored as the magnetic field is scanned through the resonance condition for the microwave frequency applied. Triplet excitons produce a characteristic resonance corresponding to $\Delta m_s = \pm 2$ and can, therefore, be easily detected. Resonance alters the population of triplet excitons (which can act as quenching centers for singlet excitons) and, therefore, changes the EL output. This technique has been used to demonstrate the presence of triplet excitons in LEDs using both PPV[78] and CN-PPV as the emissive material.[79] From the shape of the observed resonances, the spatial extent of the triplet exciton can be estimated; it is found that the triplet exciton is localized largely on a single phenyl ring.[18]

Charged excited states can also produce subgap absorptions in polymer LEDs.[78] These absorptions can be distinguished from triplet–triplet absorptions by their spectrum, temperature dependence, and dependence on chopping frequency. The charge carriers responsible for electroluminescence can thus be directly observed in a device.[80] Knowledge of the optical cross section for the transition allows an estimate to be made of their density and, hence, of their average mobility. Mobilities of 5×10^{-7} cm^2/V s have been obtained for holes in tris-(dimethylamino-stilbene)-amine using this method,[80] and recent measurements at higher peak current densities performed on PPV-based LEDs have shown considerably higher mobilities.[73]

5.7 Optical Properties of Polymer LEDs

The optical structure of a polymer LED can have an extremely important effect on the efficiency, angular distribution, and spectrum of the emitted light. A polymer LED comprises several layers with different optical properties, including at least one metal electrode. Reflection and refraction of light at the dielectric interfaces within the device must be taken into account in order to model the light emission. Interference of light reflected at different interfaces within the device can modify the angular distribution of the emitted light and will also modify the spectrum of the emission at a given angle. Given the optical constants of the various materials within the device, the transmission and reflection can be modeled as a function of wavelength and angle using the transfer-matrix formalism.

For a molecule emitting within a complex dielectric structure, the radiative rate can be strongly modified relative to the rate in an infinite isotropic medium.

A simple example of this is the case of a molecule (modeled as an oscillating dipole) close to a perfect mirror. If the dipole is parallel to the mirror, destructive interference between directly emitted light and reflected light causes a reduction in the radiative rate. In the presence of competing nonradiative decay processes, this leads to a reduction in the efficiency of emission. The variation of radiative rate with position and orientation for a molecule within an arbitrary planar dielectric structure has been modeled by Crawford.[81] This model has been applied to polymer LEDs by Burns et al.,[82] and Becker et al.,[83] who predict significant variations in the efficiency of radiative decay in polymer LEDs depending on the distribution of exciton generation within the device.

The presence of interfaces within a polymer LED can also introduce additional nonradiative decay channels. This is particularly important in proximity to a metal electrode. Excitons which are able to diffuse to the metal surface are liable to be quenched directly by interaction with the metal wavefunction. This mechanism is therefore active only within a few nanometers of the interface. At larger distances (up to about 100 nm), excited molecules can couple to the surface plasmon excitations in the metal, thus providing a further nonradiative decay channel. The combined effects of changes in the radiative and nonradiative rates in two-layer LED structures have been modelled by Becker et al.,[83] who have been able to model the variation in EL efficiency with layer thickness due to changes in the efficiency of exciton decay.

Recently, considerable effort has been put into developing microcavity structures where the optical structure is deliberately modified to control the luminescence spectrum and efficiency. In a microcavity, the polymer film, which has a thickness of some fraction of the wavelength of the emitted light, is placed between two reflective layers, which may either be metals or dielectric stacks designed to give a high reflectivity over a certain spectral range. Only optical modes which satisfy the boundary conditions defined by the cavity may be supported in these structures, and the excited molecule can therefore only radiate into these modes. Microcavities can therefore be used to obtain spectrally narrow emission from a molecule which would have a broad emission spectrum in free space; this may be used as a strategy to tune the emission color in display applications. The sharpness of the peaks is determined largely by the quality of the mirrors.

Organic microcavity LEDs were first demonstrated using molecular materials.[84,85] The first (optically pumped) polymer microcavities were demonstrated by Ochse et al.,[86] who obtained a significant modification of the emission spectrum relative to the free-space emission in poly(phenyl-phenylenevinylene). The coupling of emission from polymer molecules into the cavity modes has been demonstrated by Burns et al.,[87] and by Lidzey et al.,[88] who placed thin emissive layers at different positions within the microcavity. Emission intensities varied by more than a factor of 15 depending on whether the emissive layer was placed at a node or an antinode of the optical cavity. Microcavity polymer LEDs were first demonstrated by Wittmann et al., using a partially reflecting gold electrode in place of the ITO electrode.[89] Although the Q factor of these cavities was not high, significant spectral shifts and narrowing of the emission were observed. Subsequent experiments using distributed Bragg reflectors (dielectric stacks) underneath the ITO electrode have shown more pronounced narrowing of the emission.[90]

If population inversion is achieved in a microcavity structure, conditions may be reached where stimulated emission dominates over spontaneous emission, leading to laser operation. In principle, because spontaneous emission can be suppressed in a microcavity, thresholdless lasing may be achieved. To achieve lasing in a conjugated polymer, one must have high excitation densities, a high-quality cavity, a highly luminescent material, and low losses due to absorption. Stimulated emission in PPV films was first observed by Yan et al., using picosecond pump-probe techniques.[22] However, there was an overlapping induced absorption in the same spectral range, which, after about 20 ps, overcame any gain achieved through stimulated emission, making lasing impossible.[91] Interchain charge-separated species were proposed as the cause of the absorption.[91] Subsequently, it has been found that this induced absorption is highly sensitive to the synthesis, processing, and subsequent handling of the polymer film.[25] By careful handling and avoidance of photo-oxidation, it has been possible to produce PPV films where net gain can be achieved over a significant spectral range.[24,92]

Using a film of PPV deposited on a distributed Bragg reflector (DBR), with an evaporated silver top mirror, Tessler et al. were able to demonstrate optically pumped lasing in a conjugated polymer film.[92] Excitation was provided by the frequency-tripled output of a regeneratively amplified Nd:YAG laser, giving pulses of 200–300 ps, with a repetition rate of 1 kHz and a center wavelength of 355 nm. The distributed Bragg reflector was partially transparent at this wavelength. The emission spectrum of the microcavity at both low and high excitation intensities is shown in Fig. 5.20. At low energy, spontaneous emission into three cavity modes is observed. These modes arise from the structure of the DBR mirror, which contains various stacks with different layer thicknesses. The narrow emis-

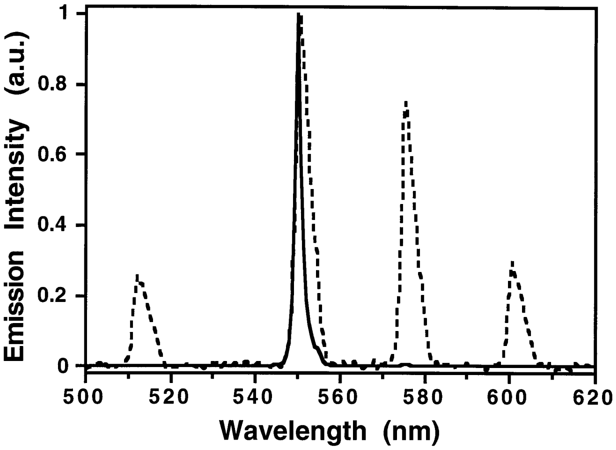

FIGURE 5.20. Emission spectrum for a PPV microcavity structure at low (dotted line) and high (solid line) excitation intensities.[92]

sion demonstrates the high Q factor of the cavity. At high excitation energy, the emission comes predominantly from one cavity mode and becomes strongly directional. This provides clear evidence for lasing, where stimulated emission from one mode dominates over spontaneous emission.

Another phenomenon related to stimulated emission has been observed by several groups. [25,93–95] Emission from a simple polymer film on a transparent substrate is found to be significantly narrowed at high excitation densities. Emission widths of less than 1 nm have been reported. The origin of this "line-narrowing" has been a matter of considerable debate, with some authors proposing cooperative effects such as superradiance or superfluorescence as the origin of the narrow emission.[93,96] The concencuss now is that the predominant mechanism is that of amplified spontaneous emission (ASE). Spontaneous emission which is waveguided within the polymer film produces stimulated emission due to the high excitation density in the surrounding film. Repeated multiplication of the emission by the gain spectrum of the excited medium leads to spectral narrowing of the light, which is eventually scattered out of the film.

Electrically pumped lasing in polymers remains a considerable challenge, as it will require much higher excitation densities than are typically achieved in polymer LEDs. Operation will therefore only be possible by driving with short pulses. Other challenges involve introducing the various electrodes and transport layers which are required in an electrically pumped device without introducing unacceptably high levels of loss in the cavity. Metallic electrodes are particularly problematic in this respect. Absorptions due to the high density of charged excitations also need to be considered.

Progress in achieving high excitation densities has been achieved recently by Tessler et al., who have driven PPV devices with high voltages and low-duty cycles.[73] Rise times for the electroluminescence were approximately 10 s, and peak brightnesses of 5×10^6 cd/m^2 were reached. The efficiency of the electroluminescence was found not to decrease significantly with increasing excitation density. High brightnesses are likely to be important in passive-matrix multiplexed displays, where each row of pixels is illuminated successively. Tessler et al. deduce that the charge carrier mobility is significantly increased under the conditions of high field and high charge carrier densities in their devices, thus helping to increase the maximum current allowed by space-charge considerations.

5.8 Novel LED Structures

The LEDs discussed so far have all been simple planar structures, typically on glass substrates. The unique processing advantages of conjugated polymers also allow a range of novel device structures to be considered, some of which are discussed here.

The flexibility and low-temperature processing of polymers allow them to be deposited onto plastic substrates. This fact was exploited by Gustafsson et al., who were able to make flexible MEH-PPV LEDs.[97] Polyethylene terephthalate was used as the flexible substrate, onto which polyaniline was coated as a semitransparent hole-injecting electrode. These devices can be bent though sharp angles without damage. Other substrates may also be used, including ITO-coated plastics. Flexible substrates may allow reel-to-reel processing of polymer LEDs and also allow LEDs to be formed on nonplanar surfaces in various consumer electronics applications, however, plastic substrates do not provide such good protection against the ingress of water and oxygen as glass substrates.

For some applications, it is useful to be able to fabricate LEDs onto opaque substrates. This requires a transparent top electrode, which can, in general, be a thin metal, or indium–tin–oxide. ITO has the advantage of being stable against atmospheric degradation, but because it is typically deposited by sputtering, it can be difficult to deposit without damaging the underlying polymer. Baigent et al., however, took advantage of the robustness of unsubstituted PPV to deposit ITO as the top contact in a double-layer LED as shown in Fig. 5.21, using aluminum as the bottom contact, on a silicon substrate.[98] This type of device gives efficient surface emission and may be important in interfacing polymer LEDs directly to silicon driving circuitry.

Transparent electrodes also allow the fabrication of stacked LEDs with electrodes within the device structure. By applying voltages between different adjacent pairs of electrodes, it is possible to control the amount of emission from each layer and hence to control the color of the emission (see Fig. 5.22), taking advantage of the fact that blue emitters, for example, are transparent to red, green and blue emission. This strategy was first demonstrated in polymer LEDs by Martens et al.,[99] and has also been used in molecular organic LEDs.[100]

To generate useful display devices from polymer LEDs requires lateral definition of the emissive areas. Simple arrays can be generated by patterning top and bottom

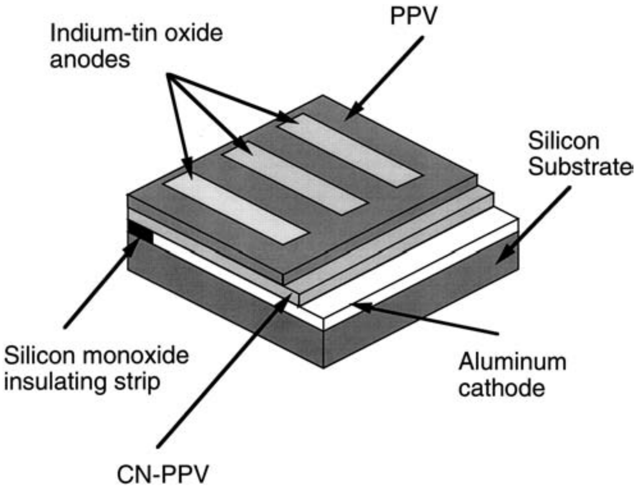

FIGURE 5.21. Heterostructure LED on a silicon substrate.[98]

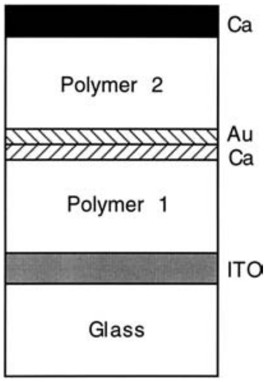

FIGURE 5.22. Stacked LED using semitransparent electrodes.

electrodes into perpendicular stripes. For relatively coarse arrays, the top electrode can be defined by shadow evaporation, but lithographic patterning is required to achieve high definition. With PPV, which has the advantage of being robust and insoluble in its final form, various photolithographic techniques, including lift-off,[101] may be used to pattern the top electrode. For more sophisticated structures, including multicolor displays with pixels of different colors, some patterning of the emissive material itself is necessary. Patterning PPV has been demonstrated using light to initiate selective conversion of the precursor to the insoluble final polymer.[102,103]

Conventional devices using PPV and its derivatives have been fabricated using polymers with low doping levels and low concentrations of mobile impurities. Recently, Pei et al. showed that it is possible to produce light-emitting devices by mixing MEH-PPV with an ion-conducting polymer (polyethylene oxide) and an electrolyte (lithium triflate),[104,105] These devices gave characteristic emission from the MEH-PPV, but operated at much lower voltages than conventional polymer LEDs, even with large thicknesses and relatively high-workfunction cathodes. The devices require an initial period to reach steady state after the initial application of the voltage, during which time motion of the ions occurs within the polyethylene oxide. Pei et al. propose that a *p–n* junction forms within the bulk of the device, and that recombination occurs in this region. They have also fabricated planar devices with electrode spacings of 15 μm, where the emission comes from a narrow region between the electrodes.

De Mello et al. have proposed an alternative model for the operation of these devices, where they point out that, given a sufficient density of mobile ionic charge, the ions will move in such a way as to cancel out any field within the bulk of the device.[106] The potential across the device is therefore dropped largely in narrow regions close to the electrodes, allowing charge injection to occur without requiring good matching of the electrode workfunctions with the polymer energy levels. The injected charges then travel through the bulk of the device largely under the influence of diffusion, where they recombine with oppositely charged carriers.

5.9 Prospects for Applications of PPV-Based LEDs

The performance and processing advantages of polymer LEDs have been described earlier and make polymer LEDs an attractive technology for display applications. However, to transform polymer LEDs from a laboratory demonstration into a manufacturable and marketable technology requires a great deal of effort. Particular issues which must be addressed include lifetime, both under operation and under storage, encapsulation, scale-up of polymer synthesis, and volume production of repeatable large-area devices. Rapid progress is being made by a number of industrial companies in all of these areas, much of which is not publicly reported. At the time of writing (1997), prospects appear good for the successful commercialization of polymer LEDs.

Operating lifetime is a particular concern for any organic electronic device; for most display applications, 20000 h of operating lifetime are required. Many of the early polymer LEDs degraded rapidly, either by gradual decay of luminance, formation of dark spots, or catastrophic failure by shorting. Encouraging results for PPV devices were reported by Cacialli et al., who achieved lifetimes of 1200 h for PPV LEDs using calcium cathodes encapsulated with aluminum, operated under a vacuum of 10^{-2} mbar.[107] Both oxygen and water are important in causing degradation, both by attack on the bulk of the polymer and by degradation of the electrodes, particularly in the region of the metal/polymer interface. Photooxidation is a well-known process in conjugated polymers and has been found to lead to the formation of carbonyl species at the vinylic carbons in PPV.[108] These carbonyl groups act as efficient quenching centers for singlet excitons.[108] Water is particularly important in causing degradation of the polymer/cathode interface by delamination of the electrode, leading to the formation of dark spots in the device. For practical devices, effective encapsulation is critical to achieve long lifetimes.

Recent encouraging results have been reported by Carter et al., who have obtained room temperature lifetimes in excess of 7000 h for encapsulated ITO/PPV/Ca devices at current densities of 60 mA/cm^2.[37] The polymer used was the PPV copolymer shown in Fig. 5.23, where the conjugation is interrupted by nonconjugated α-acetyloxy-*p*-xylylene units. The efficiency of these devices was typically 0.02 lm/W. Devices operating at 80° C had lifetimes in excess of 1100 h. Carter et al., also reported devices based on the same emissive polymer giving efficiencies between 0.5 and 2 lm/W. These devices used a layer of conducting polymer (polyethylenedioxythiophene/polystyrene sulfonate) between the ITO and the PPV, and a sputtered aluminum/lithium alloy as the cathode. The devices

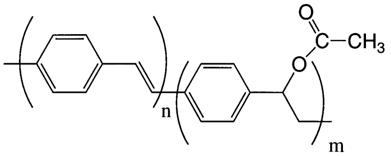

FIGURE 5.23. PPV copolymer with high luminescence efficiency.

gave brightnesses of 1000 Cd/m^2 at voltages between 4 and 5 V and lifetimes of more than 1400 h at 100 Cd/m^2.

5.10 Conclusions

Polymer LEDs based on PPV and its derivatives have made rapid progress since their discovery in 1989. The available emission colors have been extended into the red and into the blue, and efficiencies have been improved to useful levels. This rapid development has been facilitated by the development of the basic science of conjugated polymer physics and chemistry, which has addressed the various issues important in the operation of polymer LEDs. Nevertheless, there remain many important questions to be addressed about the operation of polymer LEDs, particularly concerning the details of the charge injection, transport, and recombination processes. Photonic properties of polymer-based device structures and the operation of LEDs at high excitation densities are also areas of great current interest. Significant effort is being invested in the development of PPV-based LEDs for commercial applications, and the rapid rate of improvement in device lifetime and processing is encouraging for applications in flat-panel displays.

References

[1] J. H. Burroughes, D. D. C. Bradley, A. R. Brown, R. N. Marks, K. Mackay, R. H. Friend, P. L. Burn, and A. B. Holmes, Nature 347, 539 (1990).

[2] N. C. Greenham and R. H. Friend, in *Solid State Physics*, edited by H. Ehrenreich and F. Spaepen Academic Press, San Diego, 1995, pp. 1–149.

[3] D. Bradley, Curr. Opin. Solid State Mater. Sci. 1, 789 (1996).

[4] J. R. Sheats, H. Antoniadis, M. Hueschen, W. Leonard, J. Miller, R. Moon, D. Roitman, and A. Stocking, Science 273, 884 (1996).

[5] J. Salbeck, Ber. Bunsenges. Phys. Chem. 100, 1667 (1996).

[6] L. J. Rothberg and A. J. Lovinger, J. Mater. Res. 11, 3174 (1996).

[7] K. Fesser, A. R. Bishop, and D. K. Campbell, Phys. Rev. B 27, 4804 (1983).

[8] H.-Y. Choi and M. J. Rice, Phys. Rev. B 44, 10,521 (1991).

[9] Y. Furukawa, Synth. Met. 69, 629 (1995).

[10] M. Deussen and H. Bässler, Chem. Phys. 164, 247 (1992).

[11] E. M. Conwell and H. A. Mizes, Synth. Met. 78, 201 (1996).

[12] J.-L. Brédas, J. Cornil, and A. J. Heeger, Adv. Mater. 8, 447 (1996).

[13] P. Gommes da Costa and E. M. Conwell, Phys. Rev. B 48, 1993 (1993).

[14] M. Chandross, S. Mazumdar, S. Jeglinski, X. Wei, Z. V. Vardeny, E. W. Kwock, and T. M. Miller, Phys. Rev. B 50, 14,702 (1994).

[15] K. Pakbaz, C. H. Lee, A. J. Heeger, T. W. Hagler, and D. McBranch, Synth. Met. 64, 295 (1994).

[16] D. Beljonne, Z. Shuai, R. H. Friend, and J. L. Brédas, J. Chem. Phys. 102, 2042 (1995).

[17] N. F. Colaneri, D. D. C. Bradley, R. H. Friend, P. L. Burn, A. B. Holmes, and C. W. Sprangler, Phys. Rev. B, 42, 11,670 (1990).

[18] L. S. Swanson, P. A. Lane, J. Shinar, and F. Wudl, Phys. Rev. B 44, 10,617 (1991).

[19] M. Yan, L. J. Rothberg, F. Papadimitrakopoulos, M. E. Galvin, and T. M. Miller, Phys. Rev. Lett. 73, 744 (1994).

[20] N. C. Greenham, I. D. W. Samuel, G. R. Hayes, R. T. Phillips, Y. A. R. R. Kessener, S. C. Moratti, A. B. Holmes, and R. H. Friend, Chem. Phys. Lett. 241, 89 (1995).

[21] I. D. W. Samuel, G. Rumbles, and C. J. Collison, Phys. Rev. B 52, 11,573 (1995).

[22] M. Yan, L. J. Rothberg, F. Papadimitrakopoulos, M. E. Galvin, and T. M. Miller, Phys. Rev. Lett. 72, 1104 (1993).

[23] M. Yan, L. Rothberg, B. R. Hsieh, and R. R. Alfano, Phys. Rev. B 49, 9419 (1994).

[24] G. J. Denton, N. Tessler, N. T. Harrison, and R. H. Friend, Phys. Rev. Lett. 78, 733 (1997).

[25] F. Hide, M. A. Diazgarcia, B. J. Schwartz, M. R. Andersson, Q. B. Pei, and A. J. Heeger, Science 273, 1833 (1996).

[26] R. A. Wessling and R. G. Zimmerman, U.S. Patent 3,401,152 (1968).

[27] R. W. Lenz, C.-C. Han, J. Stenger-Smith, and F. E. Karasz, J. Polym. Sci. A 26, 3241 (1988).

[28] P. L. Burn, D. D. C. Bradley, R. H. Friend, D. A. Halliday, A. B. Holmes, R. W. Jackson, and A. Kraft, J. Chem. Soc. Perkin Trans. 1, 3225 (1992).

[29] S. H. Askari, S. D. Rughooputh, F. Wudl, and A. J. Heeger, Polym. Prepr. 30, 157 (1989).

[30] D. Braun and A. J. Heeger, Appl. Phys. Lett. 58, 1982 (1991).

[31] F. Wudl, P.-M. Allemeand, G. Srdanov, Z. Ni, and D. McBranch, in ACS Symp. Ser., edited by S. R. Marder, J. E. Sohn, and G. D. Stucky, American Chemical Society, Washington DC, 1991, pp. 683–686.

[32] S. Doi, M. Kuwabara, T. Noguchi, and T. Ohnishi, Synth. Met. 55-57, 4174 (1993).

[33] P. L. Burn, A. B. Holmes, A. Kraft, D. D. C. Bradley, A. R. Brown, R. H. Friend, and R. W. Gymer, Nature 356, 47 (1992).

[34] E. G. J. Staring, R. C. J. E. Demandt, D. Braun, G. J. Rikken, Y. A. R. R. Kessener, T. H. J. Venhuizen, H. Wynberg, W. ten Hoeve, and K. J. Spoelstra, Adv. Mater. 6, 934 (1994).

[35] N. C. Greenham, S. C. Moratti, D. D. C. Bradley, R. H. Friend, and A. B. Holmes, Nature 365, 628 (1993).

[36] S. C. Moratti, D. D. C. Bradley, R. Cervini, R. H. Friend, N. C. Greenham, and A. B. Holmes, Proc. SPIE 2144, 108 (1994).

[37] J. C. Carter, I. Grizzi, S. K. Heeks, D. J. Lacey, S. G. Latham, P. G. May, O. R. Delospanos, K. Pichler, C. R. Towns, and H. F. Wittmann, Appl. Phys. Lett. 71, 34 (1997).

[38] D. Braun, A. J. Heeger, and H. Kroemer, J. Electron. Mater. 20, 945 (1991).

[39] A. R. Brown, D. D. C. Bradley, J. H. Burroughes, R. H. Friend, N. C. Greenham, P. L. Burn, A. B. Holmes, and A. Kraft, Appl. Phys. Lett. 61, 2793 (1992).

[40] A. R. Brown, Ph.D. thesis, University of Cambridge, (1992).

[41] D. R. Baigent, R. H. Friend, J. K. Lee, and R. R. Schrock, Synth. Met. 71, 2171 (1995).

[42] I. Sokolik, Z. Yang, F. E. Karasz, and D. C. Morton, J. Appl. Phys. 74, 3584 (1993).

[43] S. Karg, M. Meier, and W. Riess, J. Appl. Phys. 82, 1951 (1997).

[44] I. H. Campbell, D. L. Smith, and J. P. Ferraris, Appl. Phys. Lett. 66, 3030 (1995).

[45] I. D. Parker, J. Appl. Phys. 75, 1656 (1993).

[46] P. S. Davids, S. M. Kogan, I. D. Parker, and D. L. Smith, Appl. Phys. Lett. 69, 2270 (1996).
[47] P. W. M. Blom, M. J. M. de Jong, and J. J. M. Vleggaar, Appl. Phys. Lett. 68, 3308 (1996).
[48] P. W. A Blom, A J. A de Jong, and S. Breedijk, Appl. Phys. Lett. 71, 930 (1997).
[49] P. E. Burrows, Z. Shen, V. Bulovic, D. M. McCarty, S. R. Forrest, J. A. Cronin, and A E. Thompson, J. Appl. Phys. 79, 7991 (1996).
[50] E. M. Conwell, and M. W. Wu, Appl. Phys. Lett. 70, 1867 (1997).
[51] J. C. Scott, S. Karg, and S. A. Carter, J. Appl. Phys. 82, 1454 (1997).
[52] P. Dannetun, M. Lögdlund, M. Fahlman, M. Boman, S. Stafström, W. R. Salaneck, R. Lazzaroni, C. Fredriksson, J. L. Brédas, S. Graham, R. H. Friend, A. B. Holmes, R. Zamboni, and C. Taliani, Synth. Met. 55–57, 212 (1993).
[53] W. R. Salaneck, and J.-L. Brédas, Adv. Mater. 8, 48 (1996).
[54] Y. Gao, K. T. Park, and B. R. Hsieh, J. Chem. Phys. 97, 6991 (1992).
[55] A Meier, M. Cölle, S. Karg, E. Buchwald, J. Gmeiner, W. Riess, and M. Schwoerer, Mol. Cryst. Liq. Cryst. 283, 197 (1996).
[56] Y. Yang, and A. J. Heeger, Appl. Phys. Lett. 64, 1245 (1994).
[57] Y. Yang, E. Westerweele, C. Zhang, P. Smith, and A. J. Heeger, J. Appl. Phys. 77, 694 (1994).
[58] C. C. Wu, C. I. Wu, J. C. Sturm, and A. Kahn, Appl. Phys. Lett. 70, 1348 (1997).
[59] F. Li, H. Tang, J. Shinar, O. Resto, and S. Z. Weisz, Appl. Phys. Lett. 70, 2741 (1997).
[60] C. W. Tang, and S. A. VanSlyke, Appl. Phys. Lett. 51, 913 (1987).
[61] C. W. Tang, S. A. VanSlyke, and C. H. Chen, J. Appl. Phys. 65, 3610 (1989).
[62] C. Adachi, S. Tokito, T. Tsutsui, and S. Saito, Jpn. J. Appl. Phys. 27, L269 (1988).
[63] C. Adachi, S. Tokito, T. Tsutsui, and S. Saito, Jpn. J. Appl. Phys. 27, L713 (1988).
[64] I. D. Parker, Q. Pei, and M. Marrocco, Appl. Phys. Lett. 65, 1272 (1994).
[65] G. Leising, G. Grem, G. Leditzky, and U. Scherf, Proc. SPIE, 1910, 70 (1993).
[66] M. Strukelj, F. Papadimitrakopoulos, T. M. Miller, and L. J. Rothberg, Science 267, 1969 (1995).
[67] D. V. Khramtchenkov, H. Bässler, and V. I. Arkhipov, Appl. Phys. Lett. 79, 9283 (1996).
[68] E. Lebedev, T. Dittrich, V. Petrova-Koch, S. Karg, and W. Brütting, Appl. Phys. Lett. 71, 2686 (1997).
[69] K. Pichler, C. P. Jarrett, R. H. Friend, B. Ratier, and A. Moliton, J. Appl. Phys. 7, 3523 (1995).
[70] P. W. M. Blom, M. J. M. de Jong, and M. G. van Munster, Phys. Rev. B 55, 656 (1997).
[71] S. Karg, V. Dyakonov, M. Meier, W. Rieß, and G. Paasch, Synth. Met. 67, 165 (1994).
[72] D. Braun, D. Moses, C. Zhang, and A. J. Heeger, Appl. Phys. Lett. 61, 3092 (1992).
[73] N. Tessler, N. T. Harrison, and R. H. Friend, Adv. Mater. 10, 64 (1998).
[74] H. Vestweber, R. Sander, A. Greiner, W. Heitz, R. F. Mahrt, and H. Bässler, Synth. Met. 64, 141 (1994).
[75] P. Langevin, Ann. Chim. Phys. 28, 433 (1903).
[76] H. Vestweber, H. Bässler, J. Gruner, and R. H. Friend, Chem. Phys. Lett. 256, 37 (1996).
[77] Y. N. Gartstein, E. M. Conwell, and M. J. Rice, Chem. Phys. Lett. 249, 451 (1995).
[78] A. R. Brown, K. Pichler, N. C. Greenham, D. D. C. Bradley, R. H. Friend, and A. B. Holmes, Chem. Phys. Lett. 210, 61 (1993).

[79] N. C. Greenham, J. Shinar, J. Partee, P. A. Lane, O. Amir, F. Lu, and R. H. Friend, Phys. Rev. B 53, 13,528 (1996).

[80] M. Redecker, and H. Bässler, Appl. Phys. Lett. 69, 70 (1996).

[81] O. H. Crawford, J. Chem. Phys. 89, 6017 (1988).

[82] S. E. Burns, N. C. Greenham, and R. H. Friend, Synth. Met. 76, 205 (1995).

[83] H. Becker, S. E. Burns, and R. H. Friend, Phys. Rev. B 56, 1893 (1997).

[84] T. Tsutsui, N. Takada, S. Saito, and E. Ogino, Appl. Phys. Lett. 65, 1868 (1994).

[85] A. Dodabalapur, L. J. Rothberg, and T. M. Miller, Electron. Lett. 30, 1000 (1994).

[86] A. Ochse, U. Lemmer, A Deussen, J. Feldmann, A. Greiner, R. F. Mahrt, H. Bässler, and E. O. Göbel, Mol. Cryst. Liq. Cryst. 256, 335 (1994).

[87] S. E. Burns, N. Pfeffer, J. Gruner, M. Remmers, T. Javoreck, D. Neher, and R. H. Friend, Adv. Mater. 9, 395 (1997).

[88] D. G. Lidzey, M. A. Pate, D. D. C. Bradley, D. M. Whittaker, T. A. Fisher, and M. S. Skolnick, Appl. Phys. Lett. 71, 744 (1997).

[89] H. F. Wittmann, J. Grüner, R. H. Friend, G. W. Spencer, and A. B. Holmes, Adv. Mater. 7, 541 (1995).

[90] J. Grüner, F. Cacialli, and R. H. Friend, J. Appl. Phys. 80, 207 (1996).

[91] M. Yan, L. Rothberg, B. R. Hsieh, and R. R. Alfano, Phys. Rev. B 49, 9419 (1993).

[92] N. Tessler, G. J. Denton, and R. H. Friend, Nature 382, 695 (1996).

[93] H. J. Brouwer, V. V. Krasnikov, A. Hilberer, and G. Hadziioannou, Adv. Mater. 8, 935 (1996).

[94] S. V. Frolov, M. Ozaki, W. Gellermann, Z. V. Vardeny, and K. Yoshino, Jpn. J. Appl. Phys. Part 2 Lett. 35, L1371 (1996).

[95] G. J. Denton, N. Tessler, M. A. Stevens, and R. H. Friend, Adv. Mater. 9, 547 (1997).

[96] S. V. Frolov, W. Hellermann, M. Ozaki, K. Yoshino, and Z. V. Vardeny, Phys. Rev. Lett. 78, 729 (1997).

[97] G. Gustafsson, Y. Cao, G. M. Treacy, F. Klavetter, N. Colaneri, and A. J. Heeger, Nature 357, 477 (1992).

[98] D. R. Baigent, R. N. Marks, N. C. Greenham, and R. H. Friend, Appl. Phys. Lett. 65, 2636 (1994).

[99] J. H. F. Martens and R. H. Friend, (1995).

[100] P. E. Burrows, S. R. Forrest, S. P. Sibley, and M. E. Thompson, Appl. Phys. Lett. 69, 2959 (1996).

[101] D. G. Lidzey, M. A. Pate, M. S. Weaver, T. A. Fisher, and D. D. C. Bradley, Synth. Met. 82, 141 (1996).

[102] W. Schmidt, R. Dankesreiter, J. Gmeiner, T. Vogtmann, and M. Schwoerer, Acta Polym. 44, 208 (1993).

[103] M. L. Renak, G. C. Bazan, and D. Roitman, Adv. Mater. 9, 392 (1997).

[104] Q. B. Pei, G. Yu, C. Zhang, Y. Yang, and A. J. Heeger, Science 269, 1086 (1995).

[105] Q. B. Pei, Y. Yang, G. Yu, C. Zhang, and A. J. Heeger, J. Amer. Chem. Soc. 118, 3922 (1996).

[106] J. C. de Mello, N. Tessler, S. C. Graham, and R. H. Friend, Phys. Rev. B. 57, 12951 (1998).

[107] F. Cacialli, R. H. Friend, S. C. Moratti, and A. B. Holmes, Synth. Met. 67, 157 (1994).

[108] F. Papadimitrakopoulos, K. Konstadininis, T. M. Miller, R. Opila, E. A. Chandross, and M. E. Galvin, Chem. Mater. 6, 1563 (1994).

6

Polymer Morphology and Device Performance in Polymer Electronics

Yijian Shi, Jie Liu, and Yang Yang

6.1 Introduction

Since the first successful fabrication of the polymer light-emitting diode (PLED) using poly(p-phenylenevinylene) (PPV) as the active material,[1] there has been widespread research interest in conjugated polymers. The lightweight, flexibility, ease of processing, and the unique electrical and photonic semiconducting properties are among the most attractive characteristics of this class of materials. Because some of these materials can be obtained in solution form, spin-coating has become the most commonly used technique for obtaining uniform thin films of these materials. It is often noted that results published by different groups are inconsistent. For example, as shown in Fig. 6.1, emission spectra of poly(2-methoxy-5-(2′-ethylhexyloxy)-1,4-phenylenevinylene (MEH-PPV) thin films can be dramatically different. In addition, fluorescence decay dynamics of MEH-PPV films with a photoluminescence (PL) spectrum similar to curve a in Fig. 6.1 reported by Jakubiak Rothberg[2] are significantly different from that with a PL spectrum similar to curve b in Fig. 6.1 reported by Samuel et al.[3] The dispute of the charge carriers' mobility is another example. Scott et al.,[4,5] found that the electron is highly mobile in MEH-PPV films. Blom et al.[6] suggested that the charge recombination zone is next to the cathode, which suggests that the holes move faster than the electrons. It was also noted that hole transport is dispersive and, therefore, an interpretation in terms of charge carrier mobility is not meaningful.[7]

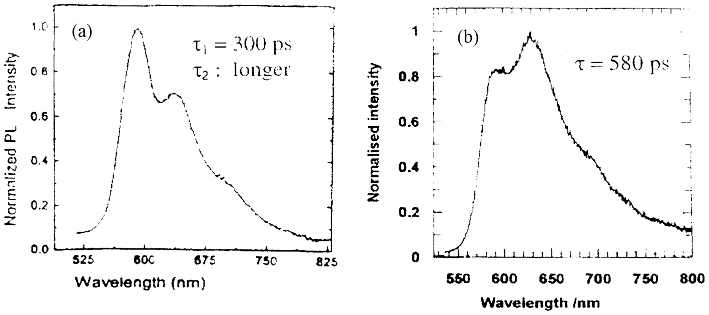

FIGURE 6.1. Two examples of different emission spectra of MEH-PPV thin films. The emission maximum of curve a appears at 580 nm, and that of while curve b appears at 630 nm.

Although the microcavity effect[8,9] could be a possible explanation for the difference in emission spectra observed in Fig. 6.1, it does not explain the different fluorescence decay dynamics. It has been shown that the PL spectrum of a spin-coated poly(*p*-pyridyl vinylene) thin film is dependent on the solvent used for the spin-coating.[10] This observation suggests that the morphology or the aggregation of polymer chains has a remarkable effect on its emission spectrum. This also led to the question of whether the above discrepancies are actually due to morphological differences or differences in the aggregation style of the polymer chains in the polymer film.

The aggregation of the polymer chains[11] and its effect on the photoluminescence properties[10,12–14] of conjugated polymers is another area which has been heavily investigated in recent years. It is generally believed that both the electroluminescence and the photoluminescence of the polymer films are originated from the same excited state.[1,15] It is also believed that the aggregation of polymer chains enhances the excimer formation, which reduces the PL quantum efficiency.[16] Recently, however, this traditional belief has been questioned by Shi et al.[17] They observed that proper aggregation could actually enhance the electroluminescence (EL) quantum efficiency of the polymer light-emitting diodes (PLED). They also found that many physical properties of the polymer film are affected by the morphology of the polymer film. In fact, other researchers have also observed similar morphologically dependent phenomena. For example, Yang et al.[18] reported that the threshold for the gain narrowing of the films prepared from tetrahydrofuran is lower than that of the films prepared using chlorobenzene and *p*-xylene. They attributed this phenomenon to the different chain orientation in those films. In the past, however, little attention has been paid to understanding the insight of these morphological effects, whereas significant efforts had been devoted to understand the device operating mechanism.[19–23] Recently, our group has performed a systematical study on these morphological effects.[17,24,25] Results from this study have revealed important information regarding the control of the morphology of polymer thin films, the morphological effects on the electrical properties of the film, and the correlations between film morphology and device performance. In this chapter, we will present a detailed discussion on these issues in the following order:

In Section 2, we will reveal the general guidelines for controlling the morphology of the polymer thin films by using different solvents, different spin speeds, and by varying the concentration of the polymer solutions. In Section 3, we will discuss the correlation between film morphology and device performance. We will reveal how the polymer morphology affects the conductivity of the polymer film (Sec. 3.A), the metal/polymer interfaces, and the energy barriers for charge injection (Sec. 3.B), the device turn-on voltage (Sec. 3.C), the emission spectrum (Sec. 4.D), and the emission quantum efficiency (Sec. 3.D), of a PLED device.

6.2 The Control of Polymer Morphology

6.2.1 The Polymer–Polymer Interactions in Solutions

6.2.1.1 The Effect of Concentration

It is commonly observed that polymers tend to aggregate in polymer solutions of sufficiently high concentration. The origin of the aggregation of polymer chains is the interchain attraction forces. Such interactions have been considered to be the cause of deviations from ideal solution behavior.[26] In dilute solutions, the polymer chains are isolated. Because the polymer–polymer interactions are short-range forces, these intermolecular forces can be neglected. Therefore, the probability of the polymer chains entangling with each other in dilute solutions is small. As the concentration increases and the distance between the polymer chains becomes smaller, these interchain forces become more significant. As a result, polymer chains have a higher chance of entangling with each other. It is predicted that a further increase in the concentration will eventually result in strong aggregation, in which the polymer chains are heavily entangled. Simha and Ultrachi[27] suggest that these concentration regions could be characterized using the product of the concentration (c) and the intrinsic viscosity (η_{in}) of the polymer solution. According to this method,[27,28] the polymer solutions are classified into four regimes. For concentrations such that $c\eta_{\text{in}} \leq 1$ the solution showed ideal solution behavior; when $c\eta_{\text{in}} = 1$–4, marked deviation from ideal behavior was observed; when $c\eta_{\text{in}} = 4$–10, interpolymer interactions became possible; and when $c\eta_{\text{in}} \geq 10$, interpenetration of polymer chains occurred (Fig. 6.2).

More recently, Shi et al.[17] proposed a new method to characterize these concentration regions based on the reduced viscosity (η/η^*), where η and η^* are the viscosities of the polymer solution and the solvent, respectively. In this method, η/η^* is plotted versus the concentration of the polymer solution. It is found that the plot has three distinct regimes: the linear region at low concentration, the curved region at middle concentration, and another linear region at high concentration. An example for such a plot using MEH-PPV is shown in Fig. 6.2. It is suggested that the polymer chains are not aggregated at the linear region of low concentrations

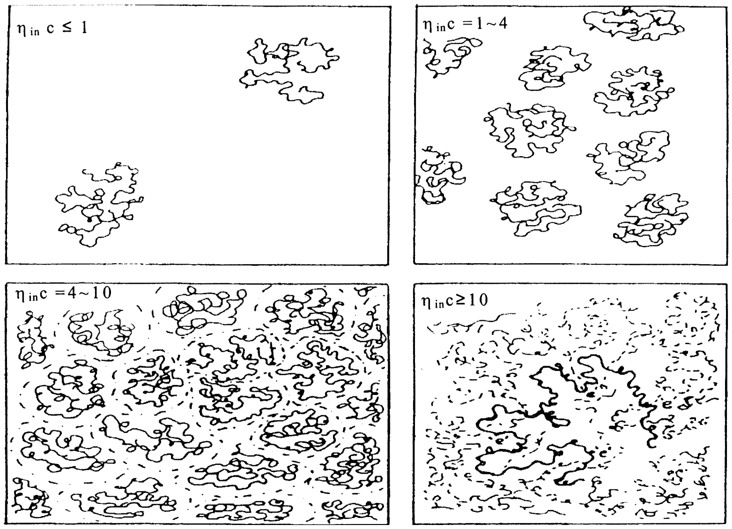

FIGURE 6.2. Schematic diagrams of aggregations of polymer chains in solutions. In dilute solution (left), polymer chains are isolated by solvent molecules. As the concentration increases, the spacing between polymer chains decreases. Eventually at high concentrations (right), the polymer chains will aggregate and form entangled structures.

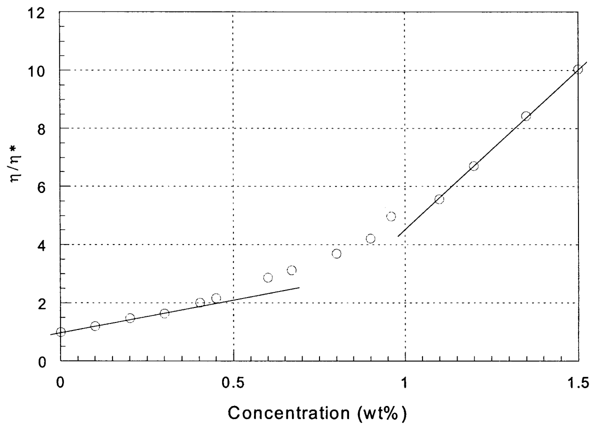

FIGURE 6.3. The reduced viscosity of MEH-PPV solutions (solvent: cyclohexanone) as a function of the concentration of the polymer solution. The curved region represents the concentrations for loose aggregation.

(i.e., $c < 0.4\%$ in Fig. 6.3) and heavily aggregated at the linear region of the high concentration ($c > 1\%$). The middle region, where the plot is curved, has been defined as the concentration for loose aggregation (CLA). In this region, it is observed that the morphology of a spin-coated polymer thin film strongly depends on the spin speed (see below).

6.2.1.2 The Effect of Solvent

The driving force for the mixing of two species (1 and 2) is the loss of free energy ($\Delta G_M < 0$), which is determined by

$$\Delta G_M = \Delta H_M - T\Delta S_M < 0, \tag{1}$$

where T is the absolute temperature of the system and ΔH_M and ΔS_M are the changes in enthalpy and entropy, respectively, due to mixing. Generally, ΔS_M is always positive, whereas ΔH_M can be either positive or negative. When dissolved in an ordinary organic solvent, the polymer chains should achieve the conformations that can minimize the free energy (largest negative ΔG_M). In other words, the thermodynamically stable conformation should have the minimum ΔH_M and the maximum ΔS_M. Generally, the major contribution in ΔH_M is the internal energy change ΔE_M due to the physical mixing of the two components, which is determined by

$$\Delta E_M = \tfrac{1}{2}(\varepsilon_{1-1} + \varepsilon_{2-2}) - \varepsilon_{1-2}, \tag{2}$$

where ε_{1-1}, ε_{2-2}, and ε_{1-2} are the interaction energies between the 1-1, 2-2, and 1-2 pairs, respectively. Usually, ΔE_M and ΔH_M are small when the two components are similar in structure, and larger when the two components are dissimilar. For example, the heats of mixing for the aromatic/aromatic or alkane/alkane systems either equal zero or a very small (several tens of joules per mole), positive number.[29,30] For aromatic/alkane systems, however, the ΔH_M is significantly larger (hundreds of joules per mole).[31] When a polymer molecule has multiple functional groups, it is expected that these functional groups will have different interaction energies with the solvent molecules. Consequently, some of the functional groups are preferentially solvated more heavily than the others. For example, the chemical structure of the MEH-PPV molecule consists of an aromatic polymer backbone and many ethyl-hexyloxy side chains. It is expected that the aromatic solvents can solvate the polymer backbone better than the alkyl side chains. In contrast, the aggregation of the alkyl side chains in aromatic solvents may lower the ΔH_M. It is therefore expected that strands of MEH-PPV aggregate lengthwise in the form of a spiral cylinder; the aromatic backbones of the long molecules form the shell of the cylinder due to greater solvation. The alkyl side chains of the molecules point radially inward inside the cylinder (Fig. 6.4). We defined this as the Ar-type aggregation style.

Results from molecular dynamic calculations suggest that for a MEH-PPV strand, a twisted conformation shown in Fig. 6.5 is the most stable conformation. Such a conformation may also benefit from gaining more configurational entropy because the side chains have higher freedom of rotation in comparison with those shown in Fig. 6.4. However, the twisting of the polymer backbone will interfere with the conjugation along the chain and thus lead to an extra internal energy increase ($\Delta E_{\text{conj}} > 0$). Therefore, the final conformation of the polymer chains should reflect a good balancing of all of these factors in order to reach the minimum free energy. In this regard, this twisted conformation will not be the best

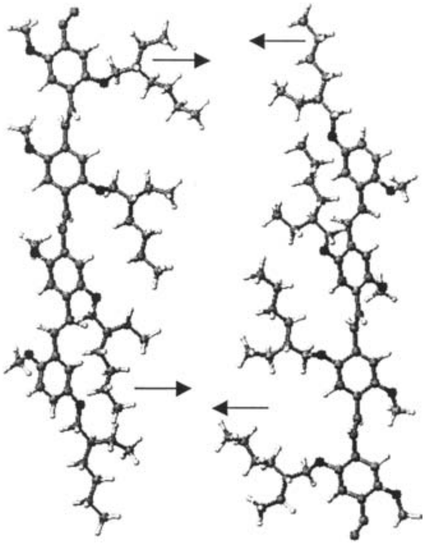

FIGURE 6.4. The Ar-type aggregation style of MEH-PPV molecules in an aromatic solvent: The polymer backbones are solvated by the solvent molecules while the side chains entangle to each other, resulting in an aggregate with the conducting backbones arranged outside and the insulating side chains pointing inward toward each other.

choice unless $2\varepsilon_{1-2}$ is much larger than the sum of ε_{1-1} and ε_{2-2} [Eq. (2)] so that ΔE_M (or ΔH_M) is sufficiently negative to compensate for ΔE_{conj}. Although the exact ΔE_M or ΔH_M values for MEH-PPV dissolved in many ordinary organic solvents are not known at this time, a qualitative estimation can be made based on the heats of mixing for similar, smaller molecular systems. For example, mixing many aromatic compounds with nonaromatic tetrahydrofuran (THF) or $CHCl_3$ yields relatively large negative heats of mixing (hundreds to nearly 1000 J/mol),[31] suggesting especially strong solvent–solute interactions (large ε_{1-2}). In contrast, the heats of mixing between two aromatic compounds are usually zero or only slightly positive. Therefore, the twisted conformation (defined as non-Ar conformation) shown in Fig. 6.5 is more likely to be attained in nonaromatic solvents, such as THF and $CHCl_3$.

According to the above discussion, it is expected that the MEH-PPV molecules should have a more planar (more conjugated) conformation in aromatic solvents and attain a more twisted conformation in nonaromatic solvents such as THF. Experimentally, it is observed that the absorption $\lambda_{\max}$ of a MEH-PPV solution in THF is significantly smaller than that observed in aromatic solvents,[32] indicating better conjugation in aromatic solvents. Furthermore, many other physical properties of the polymer are also solvent dependent (*vide infra*).

It should be noted that the solvation effect depends on concentration. The effect becomes more significant at sufficiently high concentrations and becomes less

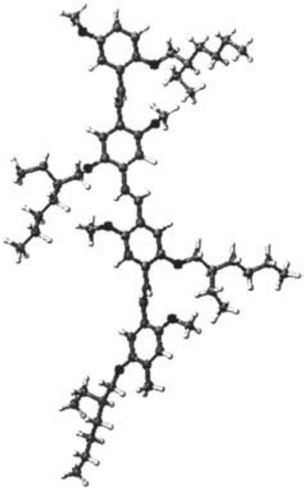

FIGURE 6.5. The non-Ar type of aggregation style: Nonaromatic solvents result in the twisted conformation of the MEH-PPV molecules with the side chains arranged around the polymer backbone, which hinder the interchain π–π interactions.

pronounced in more dilute solutions. This is because $T\Delta S_M$ is usually much larger than ΔH_M in highly dilute solutions. Therefore, the solvent–polymer interactions (ΔH_M) have a minor contribution to ΔG_M [refer to Eq. (1)], whereas the entropy term ($T\Delta S_M$) dominates. It is expected that the polymer molecules in dilute solutions should attain the more extended/open conformations in order to reach the maximal entropy. This explains the fact that the absorption $\lambda_{\max}$ of MEH-PPV solutions reaches a maximum value ($\sim$ 510 nm) in highly dilute solutions and this value is essentially independent of the solvent used. As the concentration increases, the interchain interactions and/or the interchain penetrations become more significant, which limits the free movement of the polymer chains and thus decreases ΔS_M. Therefore, the contribution from ΔH_M becomes more significant [refer to Eq. (1)]. This solvation effect is also reflected on the surface energy of the spin-coated polymer thin films (see Sec. 6.2.2.3).

6.2.2 The Morphology Control of Polymer Thin Films via the Spin-Coating Process

During the spin-coating process, the centrifugal force and the radial flow of solvent have a tendency to stretch the polymer chain radially against the cohesive force of the solution. If the centrifugal force is larger than the cohesive force of the solution, one would expect that spin-coating results in a more extended/stretched conformation of the polymer molecules. In contrast, if the cohesive force is stronger than the centrifugal force, one would expect that there would be less conformational change due to the spinning process. Therefore, depending on the viscosity of the solution, the spin speed could dramatically change the morphology of the polymer film from its solution state. Additionally, the solvent also plays an important role in controlling the conformation and the aggregation style of the polymer chains. Thus, the morphology of a spin-coated polymer thin film can be varied via the proper selection of the concentration (or viscosity) of the polymer solution, the solvent, and the spin speed, in order to accommodate different application requirements. These will be discussed in more detail in the following subsections.

6.2.2.1 The Effect of Solution Concentration

In conjugated polymers, the stretching of the coiled polymer chain usually results in a better conjugation of the π electrons. It is expected that the absorption λ_{max} of the film should be red-shifted as the polymer chains are stretched further. This phenomenon is indeed observed experimentally. Shi et al.[17] have observed that the absorption λ_{max} of a spin-coated polymer film obtained from a more dilute solution is significantly red-shifted in comparison to that spun from a more concentrated solution. Fig. 6.6 shows the absorption spectra of two films spun at the same speed (8000 rpm) but at two different concentrations: a thinner film (180 Å) spun from a 0.3-wt% MEH-PPV solution and a thicker film (900 Å) spun from a 1-wt% MEH-PPV solution in cyclohexanone (CHO). For easy comparison, the spectrum of the thinner film has been normalized. It can be easily seen from Fig. 6.6 that the absorption of the polymer film spun with the more dilute solution is significantly red-shifted ($\lambda_{max} = 510$ nm) as compared to that spun with the more concentrated solution ($\lambda_{max} = 496$ nm). This indicates that the polymer chains in the film spun from the more dilute solution are more extended and the π electrons in the polymer backbone are more conjugated.

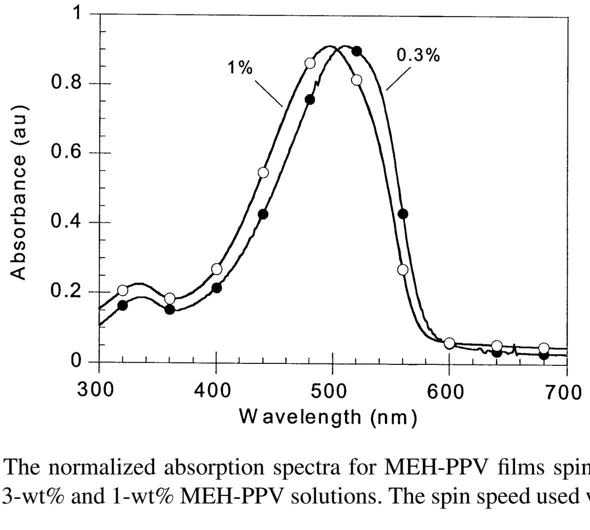

FIGURE 6.6. The normalized absorption spectra for MEH-PPV films spin-cast on glass plates using 0.3-wt% and 1-wt% MEH-PPV solutions. The spin speed used was 8000 rpm.

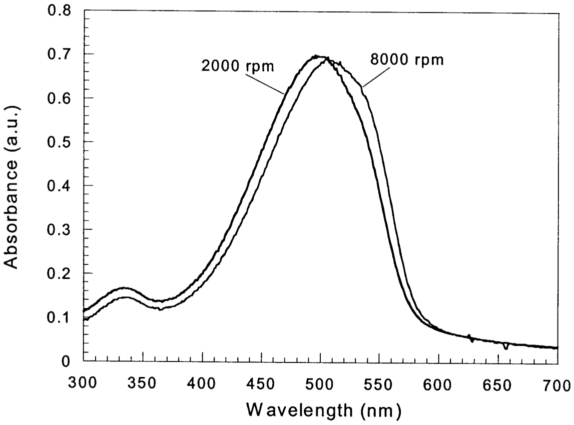

FIGURE 6.7. The normalized absorption spectra for MEH-PPV films spin-cast on glass plates using different spin speeds (2000 and 8000 rpm). The MEH-PPV solution used was 0.7 wt% in cyclohexanone.

6.2.2.2 The Effect of Spin Speed

A spectral red-shift similar to that shown in Fig. 6.6 can also be demonstrated by varying the spin speed if the polymer concentration is within the CLA region. For example, a 0.7-wt% MEH-PPV solution in CHO (refer to Fig. 6.3) spun at 2000 rpm resulted in a film with an absorption peak at $\lambda_{\max} = 499$ nm (film thickness $= 700$Å), whereas the same solution spun at 8000 rpm resulted in a film with $\lambda_{\max} = 509$ nm (film thickness $= 300$ Å) (Fig. 6.7). At higher (≥ 1 wt%) or lower (< 0.4 wt%) concentrations, however, the ultraviolet–visible (UV-vis) spectra were not observed to shift with spin speed. These effects are also reproducible in other solvents such as THF, chloroform, *p*-xylene, and so forth, although the exact CLA regions for the individual solvents are slightly different.

Based on the above discussion, the fact that a spin-speed dependence is not observed for films spun at concentrations > 1 wt% can be explained by the formation of strong aggregates. The spinning of this solution at up to 8000 rpm is insufficient to break the aggregates apart. Because high concentrations and the heavy entanglement of the polymer chains also decreases the effective conjugation length of the polymer backbone, it is not surprising that the films resulting from high concentrations have smaller absorption $\lambda_{\max}$ values (496 nm). As the concentration decreases, the cohesive force of the polymer solutions decreases, thus the aggregation becomes “looser.” It is therefore expected that such “loose aggregates” can be more easily separated by the centrifugal force. This explains the observation that within the CLA region, the absorption spectrum ($\lambda_{\max}$) of the polymer film is strongly affected by the spin speed. When the spin speed is lower than a “threshold,” the cohesive force dominates and a smaller absorption $\lambda_{\max}$ value is expected. In contrast, when the spin speed is high enough to overcome the cohesive force, a spectral red-shift (larger $\lambda_{\max}$) is expected (Fig. 6.7).

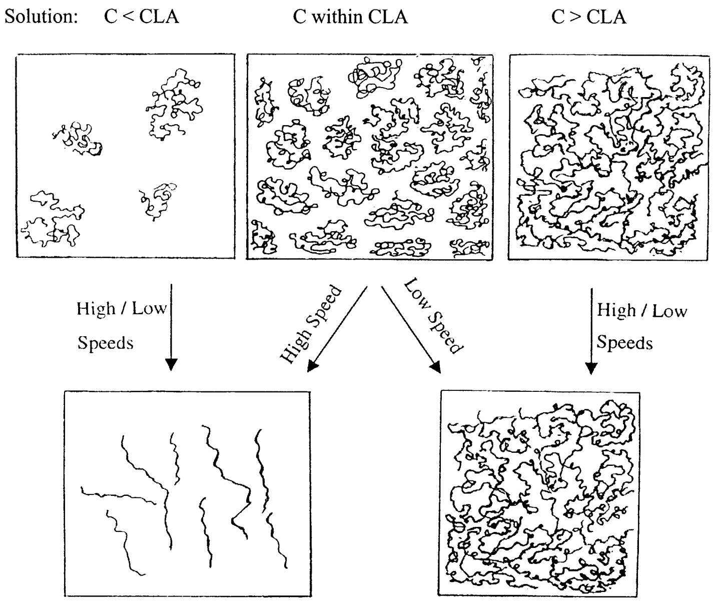

FIGURE 6.8. Schematic diagram of conformations of polymer chains in thin films fabricated with different spin speeds and from solutions with different concentrations.

At concentrations below the CLA region (e.g., < 0.4 wt% in Fig. 6.2), the $\lambda_{\max}$ of the resulting films is usually close to 510 nm and is nearly independent of the spin speed (within 1000–8000 rpm). This suggests that the polymer chains are easily stretched to the more extended conformations. In addition, polymer films spun at these lower concentrations are usually so thin that they dry almost instantaneously during the spin-coating process and, therefore, this more extended (and thus more conjugated) metastable conformation is "locked-in" upon the vaporization of the solvent. Upon annealing the film at $70°C$ for 48 h, the absorption peak is slightly blue-shifted (to 507 nm). This suggests that $\lambda_{\max} = 510$ nm reflects the maximum conjugation that can be achieved in this polymer. The above rationalization is summarized in Fig. 6.8.

6.2.2.3 The Effect of Solvent

As discussed earlier, different solvents may result in distinct conformations and aggregation styles of the polymer chains in the solution. It is expected that such differences will be carried on into the spun film. The direct evidence for this is the solvent dependence of the surface energy for spin-coated polymer films. Shi et al.[17] have observed that the contact angles (86°–87°) between H_2O and the polymer films spun from THF and $CHCl_3$ are significantly smaller than those (average $\sim 95°$) spun from aromatic solvents (Table 6.1). This indicates that these films have different surface energies. On the other hand, an MEH-PPV film spun from a cyclohexanone solution has a contact angle of 94° with water, which is close to that of the aromatic solvents. This is consistent with its aromatic-like behavior observed in the spin-speed-dependent EL spectrum experiments.[17] Although not technically an aromatic solvent, it is obvious that the six-member ring structure of this molecule leads to an aromatic-like behavior. The fact that films spun with THF and $CHCl_3$ have smaller contact angles with water indicates that these films are less hydrophobic (or more hydrophilic). Because water is a highly polar and an H-bonding solvent, the increase in hydrophilicity indicates that the surface of the film is more polar. In general, the polarity of a surface can be quantitatively characterized by the polar component (γ^p) of its surface tension, which can be computed from the θ values with water and CH_2I_2 using the method demonstrated by Wu.[33] The results for the dispersion (γ^d) and the polar (γ^p) components of the surface tension computed by this method are tabulated in Table 6.1. It can be seen from the data that the films spun with THF and $CHCl_3$ have much larger polar terms ($\gamma^p \approx 7$ dyn/cm) than those spun with aromatic solvents and cyclohexanone (γ^p =1–3 dyn/cm), indicating that nonaromatic solvents result in more polar surfaces. The contact angles with CH_2I_2, however, are distributed irregularly. This is because the differences between the θ values are too small in this case and are thus hidden by the relatively large experimental error.

Because the above MEH-PPV solutions were made from the same batch of polymer, the different surface tension values observed in Table 6.1 should be due to the different aggregation states (or packing) styles of the polymer chains, resulting from the different solvation effects.

As discussed earlier, the solvation effect is expected to become less significant at lower concentrations. Thus, the above solvent dependence of the contact angle should become less significant when more dilute solutions are used. This is indeed observed experimentally. For example, the contact angle between water and an MEH-PPV film spun with a 0.4% solution in THF has the same value (95°) as that spun from *p*-xylene under the same concentration (0.4%) and the same spin speed (4800 rpm).

TABLE 6.1. Contact Angles (θ) and Surface Tension of MEH-PPV Films

Solvent	θ (H_2O)	θ (CH_2I_2)	γ^d (dyn/cm)	γ^d (dyn/cm)
Toluene	96°	37°	41	2.0
Chlorobenzene	96°	40°	39	2.3
1,2-Dichlorobenzene	97°	34°	45	1.2
p-Xylene	95°	35°	42	2.3
Cyclohexanone	94°	38°	39	3.1
Chloroform	86°	41°	33	7.2
Tetrahydrofuran	87°	42°	33	6.8

Note: Polymer films were spun from ∼ 0.7% MEH-PPV solutions at ∼ 2000 rpm. There is no noticeable spin speed dependence of the contact angles at this concentration for all solvents.

It should be pointed out that the twisted conformation shown in Fig. 6.5 is a metastable state, which should only exist in the presence of a proper solvent. Once the solvent is removed, the polymer chains should spontaneously recover the more conjugated conformations, although such recovery is perhaps limited by the restricted motion of the polymer molecules in the solid state. This prediction is supported by the experimental observation that although the absorption $\lambda_{\max}$ of the polymer solution in THF is significantly smaller than the $\lambda_{\max}$ in aromatic solvents,[32] the films spun with aromatic and nonaromatic solvents have essentially the same $\lambda_{\max}$ value.

6.3 The Control of Device Performance via Morphology Control

6.3.1 *Conductivity of the Polymer Film*

It is known that the polymer chains are lying in the plane of the surface.[34] In a typical polymer device structure "anode/polymer/cathode," the charge carriers are traveling across the polymer film, which is perpendicular to the plane of the film. Therefore, the conductivity of the film will, to a large extent, depend on the rate for interchain hopping of the carriers or on the rate for the interchain electron transfer. If a polymer film is dominated by the Ar-type aggregation style shown in Fig. 6.4, where the bulky side chains (the insulators) are trapped inside the aggregate and

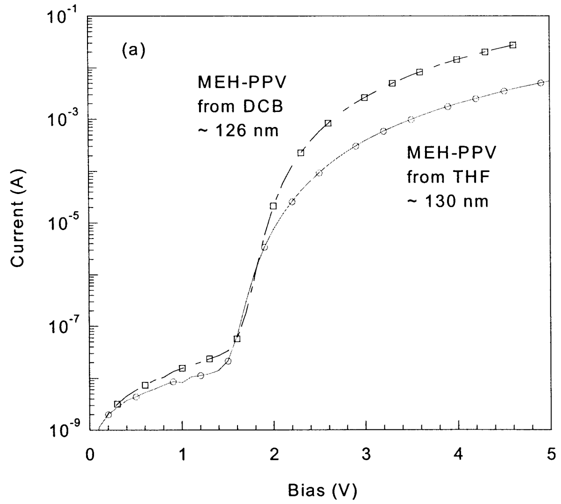

FIGURE 6.9. *I–V* curves for devices spun from DCB and THF. Although both devices have essentially the same polymer film thickness, the device using DCB as spin-coating solvent has significantly higher current injection than that using THF.

the conducting polymer backbones are exposed, it is expected that the interchain π–π interaction and thus the interchain electron transfer should be favorable (lower-energy barrier for electron transfer). In contrast, if the bulky side chains are arranged around the conducting polymer backbones (Fig. 6.5), the interchain electron transfer will be hindered by the side chains (higher-energy barrier for the interchain electron hopping). It can be predicted that the MEH-PPV films spun from aromatic solvents should have higher conductivity than those spun from nonaromatic solvents.

Liu et al.[24] have observed experimentally that the devices spun with aromatic solvents have a significantly higher current than those spun with nonaromatic solvents. Shown in Fig. 6.9 are the current–voltage (I–V) curves of a device spun with 1,2-dichlorobenzene (DCB) and a device spun with THF. Although these devices have the same film thickness ($\sim$ 130 nm), the former has much higher current than the latter at the same operating voltage. For example, at 4 V the current of the device spun with DCB reaches 13 mA, whereas that of the device spun with THF is only 2 mA.

6.3.2 Charge-Injection Energy Barriers

The current density of the device can also be affected to some extent by the charge-injection properties of the polymer/electrode interfaces or, more specifically, the energy barriers for the injection of the charge carriers into the polymer thin film. Based on the rigid-band theory, which was widely adopted in polymer LEDs, it was previously believed that this charge-injection voltage was determined by the difference of the workfunctions (also called built-in potential V_{bi}) between the Ca cathode and the ITO anode.[35,36] This implies that the energy barrier for charge injection depends only on the workfunctions of the electrodes and the HOMO/LUMO energy levels of the polymer. Recently, Malliaras has indicated that this is only true in an extreme case when there is an ohmic contact (barrierless contact) for the injection of the majority carrier. In reality, V_{bi} usually does not equal the difference between the workfunctions of the two electrodes, and a correction factor is required.[37] The origin of this derivation is the nonideal ohmic contact, which produces an extra energy barrier for the injection of the charge carriers across the interfaces. When the anode and cathode materials remain unchanged, these energy barriers will depend on the contact properties of the anode/polymer and cathode/polymer interfaces, which can dramatically vary with the processing conditions of the polymer film and the electrode.

In a typical polymer LED device, the anode is the electrode with a high workfunction used for hole injection. Usually, the polymer thin film is spun on top of the anode. On the other hand, the cathode of the device is a metal electrode with a low workfunction used for electron injection. It is usually produced by the thermal evaporation of the metal on top of the polymer film. For the hole-only devices that will be discussed here, both electrodes consist of the same metal. Therefore, there is no logical cathode and anode. However, for the sake of consistency, we still define the cathode as the electrode formed by the thermal deposition of the metal onto the polymer thin film. The anode is the electrode onto which the polymer film is spun.

6.3.2.1 The Cathode

When there is a direct contact between the metal and the π electrons of the conjugated polymer backbone, the energy barrier for the charge injection predominately depends on the energy gap between the workfunction of the metal and the energy levels of the HOMO (for hole injection) or the LUMO (for electron injection). This situation can be satisfied or nearly satisfied when the metal electrode is produced via evaporation of the metal on top of the polymer film, defined as a metal-on-polymer (MOP)-type contact. Since the metal atoms can diffuse into the polymer film, up to several nanometers,[38–40] a direct metal/π electron contact is formed in the mop-type contacts. Additionally, it is expected that the vapor deposition of metal atoms on the polymer surface should also result in maximum contact area (the metal atoms fill into the empty space of the polymer film near the surface). Because the energy levels of the HOMO and LUMO of the polymer and the workfunction of the metal are the intrinsic properties of the materials, this energy barrier is expected to be independent of the processing conditions of the polymer film. This is found to be nearly true in room temperature (see below). For example, the electron injection from a Ca cathode into the MEH-PPV film was found to be almost barrierless.[41] In other words, this energy barrier depends only on the materials (the polymer and the metal), which has been defined as the intrinsic energy barrier (ϕ_i) for the charge injection.[25]

6.3.2.2 The Anode

The Metal/Polymer Interface

At the anode side, the polymer was spun on top of a smooth metal surface, defined as the polymer-on-metal (POM) contact. It is now impossible for the metal to diffuse into the polymer film to form a perfect contact with the π electrons of the polymer chains. Furthermore, the evaporation of the solvent will create a significant amount of empty space inside the polymer film (and also near the metal/polymer interface). Therefore, a poorer polymer/metal contact is expected. On the other hand, this empty space may also allow the polymer chains to relax during the operation of the device, which may break down the existing contact and eventually result in a decrease of the charge-injection efficiency of the electrode. In this regard, the contact at the cathode side (MOP type) is expected to be more stable and more efficient. Therefore, the observed energy barrier for the POM contact should be higher than the intrinsic energy barrier. Liu et al.[25] defined the observed energy barrier ϕ as the sum of the intrinsic barrier ϕ_i and a contact-dependent component $\Delta\phi$ as follows

$$\phi = \phi_i + \Delta\phi.$$

According to this definition, the intrinsic energy barrier ϕ_i represents the minimum energy required for the charge injection from the metal into the polymer molecule, which is a constant for a given polymer and metal pair. On the other hand, the contact-dependent component $\Delta\phi$ should depend on the quality of the metal/polymer interface, which is morphology dependent.

The direct evidence for this morphological dependence of $\Delta\phi$ comes from the observation of the unsymmetrical I–V curves observed in a series of hole-only devices.[25,37] For example, it is observed that a hole-only device consisting of Au(anode: POM contact)/polymer/Au(cathode: MOP contact) has different I–V curves under forward and reversed biases.[37] This phenomenon is also observable with other high-workfunction metals such as Cu and Ag.[25] In these devices, if the anode/polymer and the cathode/polymer interfaces have the same ϕ values, it is expected that the I–V curves under forward and reverse biases should be exactly the same. In other words, the built-in potential of these devices should be equal to zero. However, it is observed that these devices have a built-in potential on the order of a few tenths of a volt.[37] In contrast, for a device Cu(anode: POM contact)/MEH-PPV/Al(cathode: MOP contact), the I–V curves under forward and reversed biases are expected to be significantly different since the two metals have different workfunctions (4.5 eV for Cu and 4.3 eV for Al). However, it was found by Roman et al. that the I–V curves were almost identical under forward and reverse biases.[36]

These results indicate that the interface energy barrier is not simply the energy gap between the workfunction and the LUMO or HOMO energy levels. The introduction of the contact-dependent component $\Delta\phi$ can perfectly explain these unexpected experimental observations. That is, the $\Delta\phi$ for the cathode/polymer interface (MOP contact) is lower (nearly zero, see above discussion) than that of the anode/polymer interface (POM contact). Therefore, the energy barrier for hole injection under forward bias (via a POM contact) is higher (therefore, a smaller current) than under reverse bias, where the hole injection is via a MOP contact (Figs. 6.10 and 6.11). The fact that the above Cu(POM contact)/polymer/Al(MOP contact) device has almost symmetrical I–V curves suggests that the barriers for hole injection from the cathode and the anode are similar. Because the workfunction of Cu is 0.2 V higher than Al, $\Delta\phi$ for the Cu anode can be estimated to be approximately 0.2 V for the above device (assuming that the $\Delta\phi$ of the MOP contact is zero), which compensates for the difference in the workfunction between the two metals.

The Effect of Solvent

From the above discussion, one will expect that the Ar type of aggregation style (Fig. 6.4), which has the conducting polymer backbones exposed, should have a better electrical contact with the metal electrode (Fig. 6.12a) than the non-Ar type of aggregation (Fig. 6.5), where the metal electrode and the conducting π system

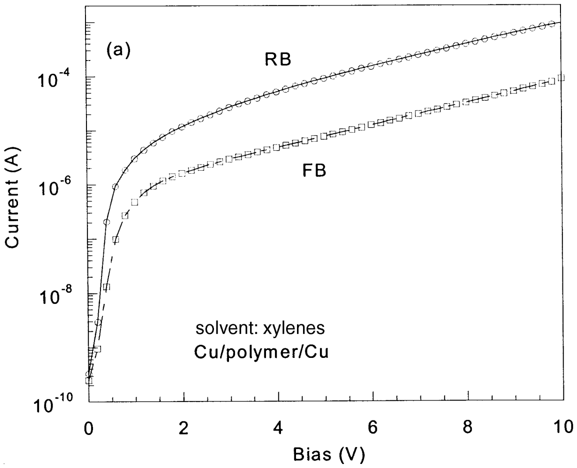

FIGURE 6.10. I–V curves under forward and reversed biases for a hole-only device using Cu electrodes. Xylenes was the solvent used for spin-coating.

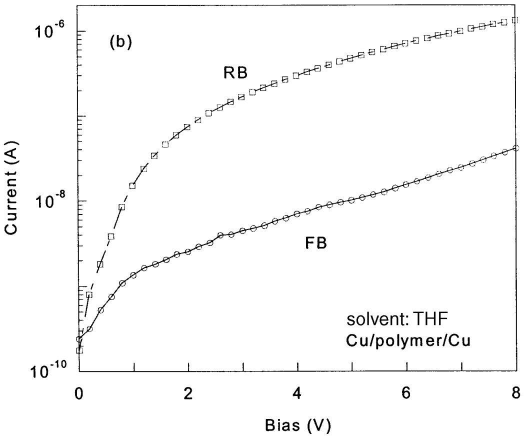

FIGURE 6.11. The I–V curves under forward and reversed biases for a hole-only device using Cu electrodes. Solvent used for spin-coating was THF.

are now isolated by the bulky ethyl-hexyloxy side chains (Fig. 6.12b). In other words, the contact shown in Fig. 6.12b should have a higher $\Delta\phi$ value than that shown in Fig. 6.12a. This prediction is confirmed experimentally. It is found that the built-in potential for devices processed using THF is significantly larger than those processed using an aromatic solvent (Table 6.2). This suggests higher $\Delta\phi$ values when the polymer films are processed using THF.

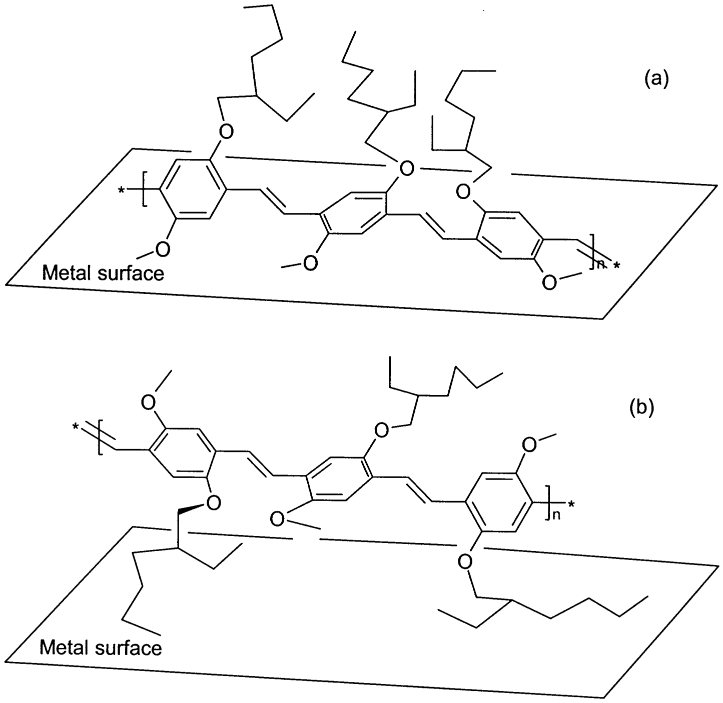

FIGURE 6.12. The effect of morphology on metal/polymer contact: (a) polymer processed with aromatic solvent; (b) polymer processed with non-aromatic solvents.

TABLE 6.2. Effects of Solvent on the $\Delta\phi$ for Hole-Only MEH-PPV Devices

System	Solvent	$\frac{j_R}{j_F}$	$\Delta\phi = \phi_F - \phi_R$ (eV)
Ag/MEH-PPV/Ag	P-Xylene	12 ± 3	0.063 ± 0.006
	Tetrahydrofuran	55 ± 5	0.104 ± 0.003
Cu/MEH-PPV/Cu	P-Xylene	9 ± 3	0.055 ± 0.009
	Tetrahydrofuran	45 ± 5	0.099 ± 0.003

The ITO/PEDOT Anode

For devices using ITO/PEDOT anodes, because the PEDOT layer is much more conductive than the MEH-PPV film, the major energy barrier for hole injection depends on the PEDOT/MEH-PPV interface. If the organic solvent used to dissolve the MEH-PPV does not dissolve the PEDOT layer, it is expected that the resulting PEDOT/MEH-PPV interface will be similar to those obtained by spin-coating the polymer on top of a metal electrode. This is true (or nearly true) in most cases, because PEDOT has a very limited solubility in many commonly used organic solvents. In fact, it was found that the MEH-PPV film spun on top of the PEDOT layer could be easily pealed off from the PEDOT surface by a piece of Scotch tape, indicating very weak binding forces across the interface. Therefore, it is expected that the energy barrier for the hole injection from a ITO/PEDOT anode should also be morphologically dependent in a way similar to the POM contact. It is indeed observed that the voltage for the hole injection in a PLED device is dependent on the processing conditions (e.g., solvent and spin speed) of the MEH-PPV film (see below). In this regard, it is expected that this contact could be improved if the hole injection layer could be partially dissolved during the spin-coating of the PEH-PPV layer, so that a significant interpenetration of the MEH-PPV and the PEDOT layer can result.

6.3.3 The Turn-on Voltages

It is commonly observed that in a regular PLED device, the voltage for current injection is different from the voltage required for the device to emit photons.[19,24] Generally, the voltage for current injection ($V_{\text{I-ON}}$) is defined as the voltage at which the current "switches on" in a semilog plot. Similarly, the light-emitting voltage ($V_{\text{L-ON}}$) is defined as the onset voltage at which the light "switches on" in a semilog plot. Based on numerical simulations, Malliaras and Scott[22] have recently reported that the carrier-injection efficiency of a PLED is primarily dominated by the carrier-injection rate. The carrier mobility only matters if the injection abilities are similar. Thus, the light-emitting voltage $V_{\text{L-ON}}$ is determined by the minority carrier injection. For a classical MEH-PPV device using ITO/PEDOT as an anode and Ca as a cathode, it is believed that the holes are the minority carriers.[23] Therefore, $V_{\text{I-ON}}$ should reflect the voltage for the electron injection and V_{L-ON} for hole injection. As a result, the device is a single-carrier (electron-only) device when operated between $V_{\text{I-ON}}$ and $V_{\text{L-ON}}$, and the voltage difference $\Delta V = V_{\text{L-ON}} - V_{\text{I-ON}}$ reflects the energy barrier for hole injection.

6.3.3.1 The Current-Injection Voltage

It is well accepted that $V_{\text{I-ON}}$ is related to the built-in potential V_{bi}, which is the difference in the workfunction of the cathode and the anode[35,36] in addition to a correction term primarily due to interfacial effects:[37]

$$V_{\text{I-ON}} = V_{\text{bi}} = \Delta\Phi + \varphi, \tag{3}$$

where $\Delta\Phi$ is the workfunction difference between the anode and the cathode and φ is a correction term primarily determined by the quality of the interface. φ is expected to be temperature dependent. When there is an ideal ohmic contact in the interface, $\varphi = 0$, Eq. (3) can be rewritten as $V_{\text{I-ON}} = \Delta\Phi = V_{\text{bi}}$. When operated at $V_{\text{I-ON}} < V < V_{\text{L-ON}}$, the MEH-PPV LED device is an electron-only device. Therefore, φ has the same meaning as the energy barrier for electron injection ($\Delta\phi$) from the cathode. As discussed earlier, $\Delta\phi$ for a MOP contact is expected to be very small and independent of the polymer morphology. It is indeed observed that the $V_{\text{I-ON}}$ of the MEH-PPV LED devices is essentially independent of the spin speed and the solvent used for the spin-coating.[42] This can also be seen from

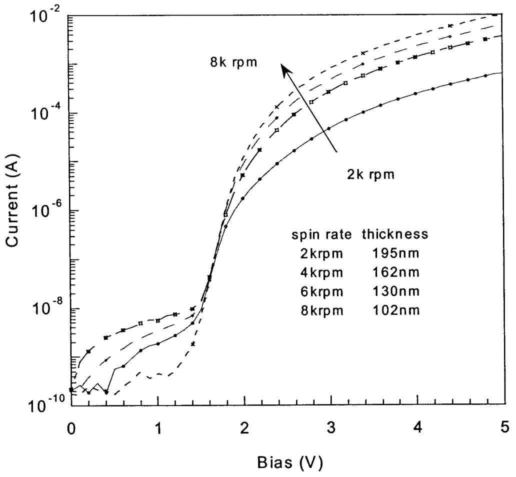

FIGURE 6.13. The *I–V* curves for a series of PLED devices, in which the MEH-PPV films were spun at different spin speeds (solvent: xylenes).

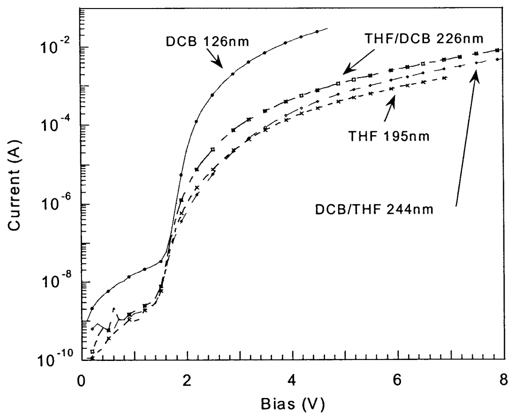

FIGURE 6.14. *I–V* curves for a series of PLED devices processed with different solvents. Shown are two “single layer” devices curve-DCB 126nm (solvent: DCB) and curve-THF 195nm (solvent: THF), and two “double layer” devices curve-THF/DCB 226nm (first spin-coat using THF followed by a second spin-coat using DCB) and curve-DCB/THF 244nm (first spin-coat using DCB followed by a second spin-coat using THF).

Figs. 6.13 and 6.14. The $V_{\text{I-ON}}$ determined from these Figures are independent of spin-speed, solvent, and thickness of the MEH-PPV film. The $V_{\text{I-ON}}$ value is approximately equal to $\Delta\Phi$ ($\sim$ 1.6 V) This suggests that the electron injection from the Ca/polymer interface is very small or even barrierless at room temperature, consistent with the findings of Campbell et al.[41]

However, $V_{\text{I-ON}}$ is found to increase as the temperature decreases. This can be easily seen from Fig. 6.15, where $V_{\text{I-ON}}$ is approximately 1.60 V at 298 K and

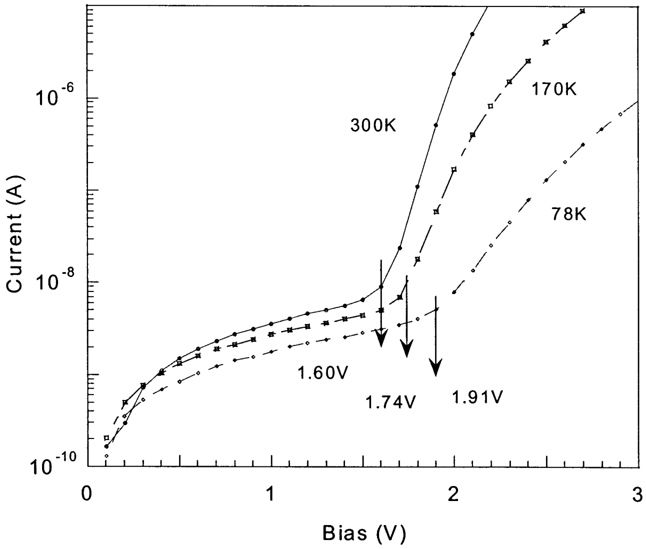

FIGURE 6.15. The temperature dependence of current injection voltage. Shown are the I–V curves of the same device taken under different temperature.

progressively increases to 1.91 V at 78 K. Because $\Delta\Phi$ is independent of temperature, the observed temperature dependence on $V_{\mathrm{I-ON}}$ suggests that φ of the polymer/Ca interface becomes more significant at low temperature, which is consistent with its contact-dependent characteristics.

6.3.3.2 The Light-Emitting Voltage

Although $V_{\mathrm{I-ON}}$ is essentially independent of the spin-coating conditions at room temperature, the light-emitting voltage $V_{\mathrm{L-ON}}$ is strongly dependent on the spin-coating conditions. Because $V_{\mathrm{L-ON}}$ is determined by the hole-injection ability of the anode, which is a POM-type contact, it is expected that the hole-injection energy barrier should be more sensitive to the film morphology. As discussed previously, it is expected that a film processed with nonaromatic solvents should have a higher $\Delta\phi$ for hole injection. Therefore, the $V_{\mathrm{L-ON}}$ is also expected to be higher for devices processed with non-aromatic solvents than those processed with aromatic solvents. This is exactly what has been observed experimentally. For example, the $V_{\mathrm{L-ON}}$ for a device processed with DCB is 1.75 V, whereas that for a device processed with THF is 1.94 V (Fig. 6.16).

On the other hand, the poor anode/polymer contact shown in Fig. 6.12b can be improved to some extent by using higher spin speeds (Fig. 6.17). At high spin speeds, the polymer coils are stretched open, allowing the conducting polymer backbone to settle closer to the ITO surface. This results in a better contact and thus a lower hole-injection barrier and lower $V_{\mathrm{L-ON}}$.

In contrast, the $V_{\mathrm{L-ON}}$ for devices processed with aromatic solvents is much less sensitive to the spin speed.[19] Shown in Fig. 6.18 are plots of the brightness

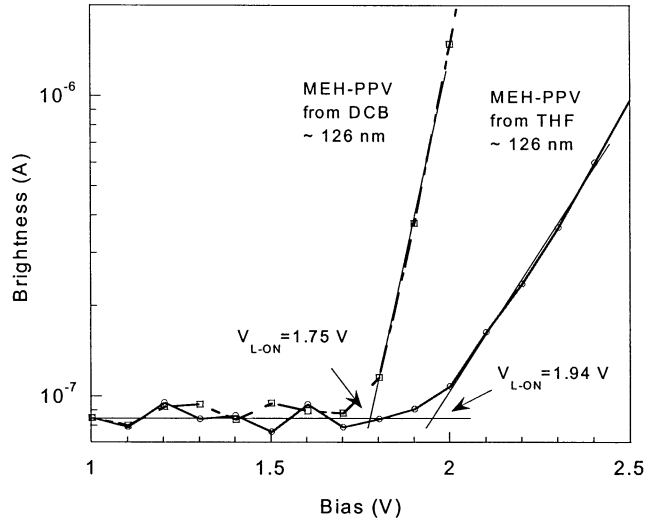

FIGURE 6.16. Brightness-voltage curves for PLED devices fabricated from DCB and THF. The device using aromatic solvent (DCB) has lower light-emitting voltage.

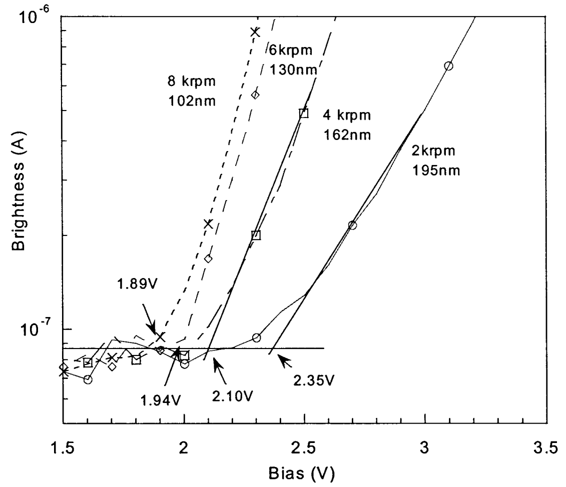

FIGURE 6.17. The light-emitting voltage for MEH-PPV LED devices processed with non-aromatic solvents is spin-speed dependent: higher spin speed results in lower light-emitting voltage.

(represented by the photocurrent of the detector) versus the operating voltage (B–V curves) for a series of devices processed with DCB. It can be seen from Fig. 6.19 that these devices have almost identical $V_{\text{L-ON}}$ values ($\sim 1.75V$), corresponding to a $\Delta\phi$ value of approximately 0.15 eV for hole injection.

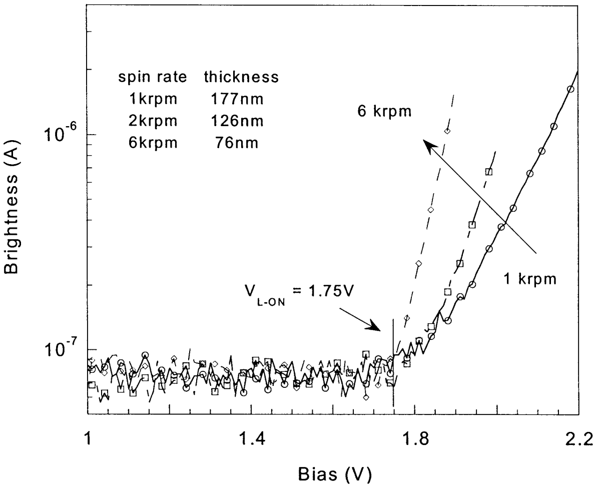

FIGURE 6.18. The light-emitting voltage for MEH-PPV LED devices processed with aromatic solvent (DCB) is found to be almost independent on spin-speed.

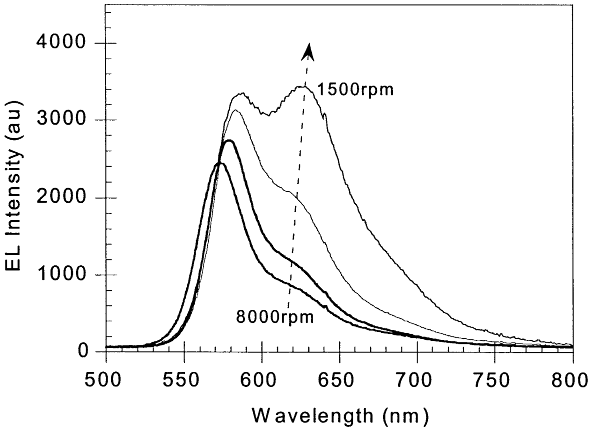

FIGURE 6.19. The EL emission spectra for devices processed with aromatic solvents within the CLA are spin speed dependent: higher speed results in stronger yellow emission, while lower spin speed results in stronger red emission.

6.3.4 The Emission Spectrum of the Device

6.3.4.1 MEH-PPV Processed Using Aromatic Solvents

The electroluminescence (EL) and photoluminescence (PL) spectra of spin-cast films are also morphologically dependent. It is found that within the CLA region, the EL and PL spectra of spin-cast MEH-PPV films are strongly dependent on spin speed (Fig. 6.19). It is consistently observed that when the polymer solution is coated at high speeds (e.g., 4000–8000 rpm, 0.7 wt%), the resulting devices have a strong yellow emission peak ($\lambda_{\max} \approx 575$ nm) and a weak red shoulder (~ 630 nm, Fig. 6.19). The spectrum of this yellow emission is similar to the PL spectrum of a highly dilute MEH-PPV solution, corresponding to the unaggregated single-chain exciton emission. As discussed earlier, it is expected that films resulting from high spin speeds should consist mostly of the more extended and less coiled polymer chains. Therefore, it is reasonable to suggest that this yellow EL emission (~ 575 nm) observed in films is also due to the single-chain exciton from the more extended polymer chains. As the spin speed decreases, the spectrum red-shifts and the intensity of the red emission peak (630nm) increases (refer to Fig. 6.19). This effect is observable in all aromatic solvents studied such as chlorobenzene, 1,2-dichlorobezene, toluene, and *p*-xylene and is independent of the applied electric field. Similar effects are also seen in the PL spectra of the thin films. However, these changes are limited to those devices spun within the CLA. At concentrations above the CLA, the red emission (630 nm) always dominates. In contrast, the yellow emission (575 nm) dominates at concentrations below the CLA.

Although the 630-nm peak in the emission spectrum of the MEH-PPV film has traditionally been considered as the intrinsic vibronic structure of the spectrum, the above spectrum changes are easily correlated to the microcavity effect.[8,9,43–45] This traditional belief has been challenged by Shi et al.[17] They observed that the above effect is independent of the thickness of the polymer film, suggesting that it is not due to the microcavity effect. Therefore, they suggested that the 630-nm emission more likely results from an excimer interchain species, namely the Ex-I species. As discussed earlier, the film morphology varies with spin speed when the polymer concentration is within the CLA. As the spin speed decreases, more and more "loose" aggregates survive the centrifugal force. On the other hand, lower spin speeds also result in thicker films, in which the rate for solvent evaporization from inside the film is slower. This allows more time for the polymer chains to relax into a more thermodynamically favorable conformation rather than being "locked in" to an unfavorable conformation caused by the spin-coating process. Because the polymer coils will tend to entangle and interpenetrate more heavily as the concentration increases, it is expected that slow evaporation of the solvent (and thus a slow increase of the polymer concentration within the film) should favor the entanglement of the polymer chains and the formation of stronger aggregates, which should favor the formation of the interchain species. Therefore, the spin speed dependence of the EL emission spectra can be rationalized as follows: A lower spin speed results in a more significant aggregation of the polymer chains, which favors the formation of the interchain species emitting at red. A study on the PL spectrum of MEH-PPV films using the microscopic fluorescence technique by Huser and Yan[46] also suggests that the yellow and the red peaks are probably due to different emitting species.

It is generally observed for many polymers that the aggregation of the polymer chains leads to a spectral red-shift in their absorption spectra.[11] Quantum mechanics calculations also suggest that a π–π stacking of the polymer backbones can red-shift the absorption spectrum.[47] If this explanation also applies to MEH-PPV films, a spectral red-shift in the absorption spectrum is expected as the aggregation of a MEH-PPV film increases. However, this prediction is inconsistent with the experimental observations for MEH-PPV, in which the absorption spectrum of a film resulting from a lower spin speed, implying more aggregation, is blue-shifted. This suggests that the π–π stacking of the polymer backbones in MEH-PPV is hindered in the ground state, probably due to the bulky 2-ethyl-hexyloxy side chains. Such interactions only become more pronounced in the excited state.

The PL decay dynamics of MEH-PPV in the film as well as in the solution have been studied extensively.[3,14] However, results obtained by different research groups are usually inconsistent. For example, Samuel et al.[3] have shown that the kinetics of the MEH-PPV films at 600 nm is dominated by exponential decay with a time constant of 580 ps, whereas Rothberg and co-workers[2,48] have reported that the PL decay dynamics of the MEH-PPV film at room temperature is nonexponential and consists of a fast component ($\tau \approx 300$ ps) and a slower component. The authors suggested that the nonexponential dynamics were probably due to the inhomogeneity of emission rates and to the dynamics of excited-state diffusion to the quenching defects. Although it is possible that this discrepancy is due to the intrinsic difference between the polymer samples used by the two groups, the fact that they have markedly different PL spectra could not be ignored. The PL spectrum reported by Samuel et al.[3] closely resembles the EL spectrum of the orange–red devices, whereas that reported by Rothberg and co-workers is similar to that of a yellow device. It is therefore very likely that the spectrum of Samuel et al. was dominated by the Ex-I species, whereas that reported by Rothberg and co-workers contained more emission from the single-chain exciton. Thus, it is not surprising that the Ex-I-dominated spectrum decays significantly slower than the typical single-chain exciton decay (300 ps) observed in dilute solutions and films.[14,52,49,50]

6.3.4.2 MEH-PPV Processed Using Nonaromatic Solvents

In nonaromatic solvents such as THF and $CHCl_3$, the spin-speed dependence of the emission spectrum is more complicated. At the lower end of the CLA, the observed spin-speed effect is similar to that observed for aromatic solvents and cyclohexanone; a higher spin speed results in a stronger yellow emission and a lower speed results in a stronger red emission. This is demonstrated in Figure 6.20 using a 0.4% polymer solution in THF (CLA $\approx$ 0.3–0.7% in THF). A notable result is that this effect is reversed at the higher end of the CLA. For example, spin-coating a 0.7% MEH-PPV solution (THF) at high spin speeds (e.g., 6000–8000 rpm) results in orange–red devices, whereas lower speeds (e.g., ≤ 2500 rpm), result in yellow-dominated devices (Fig. 6.21). The absorption λ_{max} of the film is almost unaffected by the spin speed at this concentration (0.7% THF). A similar effect is also observed when the polymer is spun with $CHCl_3$. This "reverse effect" clearly indicates that both the molecular conformation in the solution and the morphology of the film are substantially different from those obtained using aromatic solvents and cyclohexanone. Heeger and co-workers[51] have also indicated that the polymer films spun with THF and *p*-xylene have different morphologies. All of this suggest

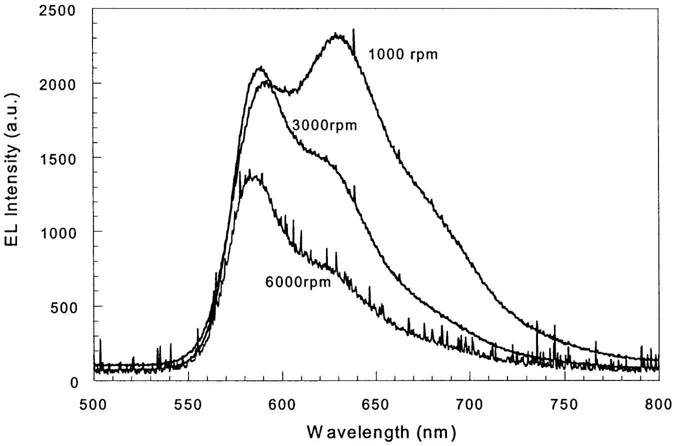

FIGURE 6.20. The EL emission (normalized) of devices fabricated from a 0.4% MEH-PPV solution in THF (the lower end of CLA in this solvent). Lower spin speed results in stronger red emission.

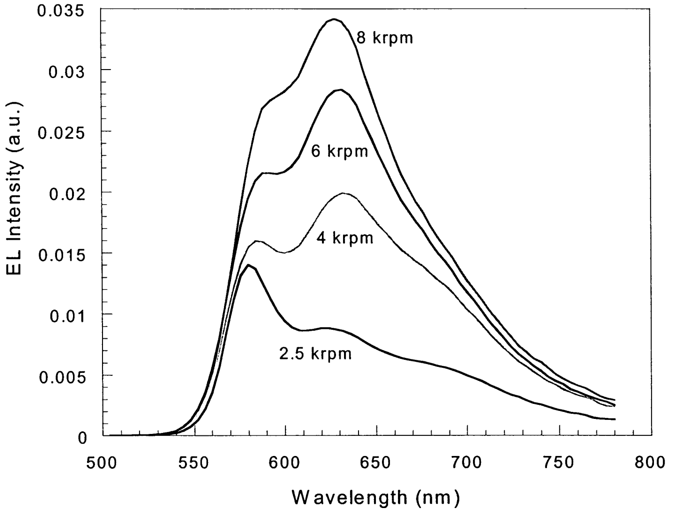

FIGURE 6.21. The spin-speed dependent EL spectra (normalized) of MEH-PPV films observed at the higher end of CLA (0.7%) in THF. Higher spin speed results in stronger red emission.

that the solvation effect plays an important role in the morphology of the spin-cast films.

The assignment of the 630-nm emission to the Ex-I interchain species can also explain the reverse effect observed in Fig. 6.21. When sufficiently viscous solutions (e.g., 0.7–0.8% in THF or $CHCl_3$) and low spin speeds (e.g., $\leq$ 2500 rpm) are used, the non-Ar type conformation (Fig. 6.5) is "memorized" by the polymer film. It is expected that with the bulky side chains pointing irregularly in all directions, the π–π stacking of the polymer backbones will be hindered. Therefore, the excimer emission should be less. It is therefore not surprising that films spun at low speeds give yellow-dominated emissions (Fig. 6.21). The fact that high spin speed enhances the interchain emission ($\lambda_{\max} \approx 630$ nm, Fig. 6.21) suggests that the centrifugal force results in a large conformational change. However, there is no noticeable spectral change observed in the absorption spectra, nor in the contact angles (*vide supra*). This indicates that the centrifugal force is not sufficient to completely break apart the heavily entangled polymer chains. Instead, the polymer coils are stretched more openly, allowing the insertion of additional polymer chains and thereby resulting in the formation of the interchain species. In contrast, the Ar-type aggregation style shown in Fig. 6.4 allows a better π–π overlapping and thus favors the formation of the Ex-I interchain species. At high spin speeds, this aggregation style is destroyed by the centrifugal force, which results in fewer Ex-I interchain species.

It should be noted that due to the complexity of the polymer system, the emission spectrum of a device may include many species with similar emissions. In fact, Rothberg and co-workers also observed an interchain species at $\lambda_{\max}$ 700 nm, denoted as the Ex-II species in the following discussion. Therefore, the Ex-I species should be considered as a series of interchain species with similar emission spectra rather than a single species.

6.3.5 The Device Quantum Efficiency

There have been extensive discussions in recent years regarding the role of aggregation and excimer formation in conjugated polymers. It is generally believed that aggregation quenches the excited state.[14,16] The mechanism for this aggregation quenching has been attributed to interchain interactions.[48,52] These issues have also been addressed theoretically by Conwell and co-workers.[53,54] In the meantime, tremendous efforts have been made to modify the polymer structure at the molecular level,[55–60] with the intention of suppressing such interchain interactions and thus achieving better quantum efficiencies. However, this traditional belief has been questioned recently by Shi et al.[17] They suggested that proper aggregation of the polymer chains could actually enhance the device quantum efficiency (QE). They also suggested that QE has a strong correlation with the emission spectrum and the polymer morphology rather than the thickness of the polymer film, which is contrary to Heeger and co-workers.[61] They observed that the orange–red devices always give a higher QE (by 30–80% higher) than the yellow devices (Table 6.3). This observation is reproducible in all the solvents that have been studied and it is independent of the thickness (within a range of 500–1500 Å) of the MEH-PPV films. This strongly suggests that the formation of the Ex-I species actually enhances the quantum efficiency, which is contrary to the general belief that the formation of interchain species quenches the PL quantum yield of the MEH-PPV polymer film.[31–35]

TABLE 6.3. Spin-Speed-Dependent Quantum Efficiency and Emission Color

Solvent	Speed (rpm)	Thickness (Å)	QE (%)	CIE X	CIE Y	λ_{max} (nm)
DCB	2500	860	3.0	0.62	0.38	632
	4000	720	2.4	0.59	0.40	588
	6000	630	2.1	0.57	0.43	584
	8000	590	2.0	0.56	0.43	580
THF	2500	1150	2.1	0.59	0.41	580
	4000	970	2.2	0.61	0.39	630
	6000	850	2.8	0.61	0.39	632
	8000	780	3.8	0.62	0.38	632

The formation of the excimer has traditionally been associated with aggregation,[14] whereas the possibility for the unaggregated chains to form excimers has rarely been addressed. In dilute solutions, excimer formation in the unaggregated polymer chains is relatively improbable, because the small diffusion rates of these macromolecules cannot compete with the decay of the excited state. In films, however, the polymer chains are closely packed. It is likely that the nonentangled species are close enough in the film to form excimers. Rothberg and co-workers[14] have indicated that the Ex-II excimer species ($\lambda_{max} \approx 700$ nm) is only weakly emissive in the PL spectrum of MEH-PPV films. This emission is also observed in the EL spectra of MEH-PPV films (Fig. 6.21). It is consistently observed that the Ex-II emission is always accompanied by the appearance of a reasonably strong yellow emission ($\lambda_{max} \approx 575$ nm, refer to Fig. 6.21). This observation implies that there is a connection between the Ex-II species and the yellow emissive species. The fact that the Ex-II emission has a longer lifetime[3] (820 ps) and a longer emission wavelength ($\lambda_{max} \approx 700$ nm) than the Ex-I species suggests that it probably results from a better aligned π–π overlap. In contrast, the Ex-I is more likely due to a partial or angled π–π overlap within the aggregates. Rothberg and co-workers[14,48] have shown by time-resolved fluorescence experiments that the exciton fluorescence is quenched by the rapid formation of the much less emissive Ex-II species. If this is also the case in the EL emission, the correlation between the QE and the color of the device can be rationalized by the relative rates for the formation of the Ex-I, the single-chain exciton, and the Ex-II species (Scheme I). It can be easily seen from Scheme I that there are two possible pathways that could result in a stronger Ex-I emission (a red device with higher QE): (1) $k_1 \gg k_2 + k_3$ and (2) although k_2 is significantly large, yet $k_4 \gg k_5 + k_f + k_d$, where k_f is the irradiative decay rate and k_d is the nonirradiative decay rate of the single-chain exciton. If a yellow device is required, effort should be made to enhance k_2 (or suppress k_1 and especially k_3) and to minimize k_4 and especially k_5 in order to achieve a better QE. This can also be achieved by the proper control of film morphology (i.e., using a mixed-solvent system).[62] In contrast, if k_3 is significantly large, or k_2 is significantly large but $k_5 \gg k_4$ and k_f, the QE of the device is lower. Therefore, the highest QE can be achieved if the conformations of the polymer chains are

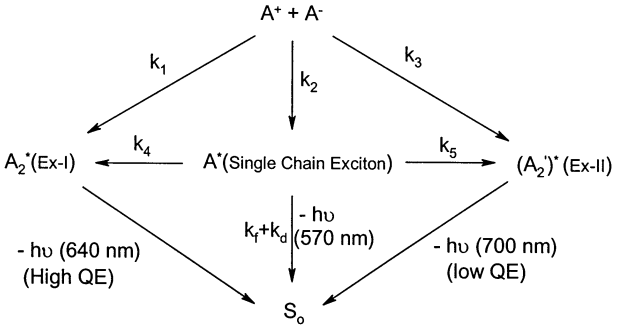

FIGURE 6.22. Scheme 1.

optimized in such a way that the rate of Ex-I formation is maximized, whereas the rates of Ex-II formation and the single-chain exciton formation are minimized, or $k_1 \gg k_2 + k_3$. This can be achieved by the proper selection of the spin-coating conditions (i.e., the solvent, the concentration, and the spin speed).

6.4 Conclusions

6.4.1 *The Solvation Effect and Polymer Aggregation*

The aggregation style of the MEH-PPV molecules can be changed by the use of different solvents, by the concentration of the polymer solution, and by the spin speed. At sufficiently high concentration, the polymer molecules aggregate in a style either similar to that shown in Fig. 6.4 (the Ar-type aggregation) in aromatic solvents or similar to the non-Ar-type conformation (Fig. 6.5) in nonaromatic solvents. When the concentration is below or within the CLA region, a high spin speed could result in a significant stretching of the polymer chains, making the molecular conformation and aggregation in the film different from that in the solution. Such morphological changes can result in large impacts on the device electrical and optical performance.

6.4.2 *The Device Emission Color and the Quantum Efficiency*

The emission peak of MEH-PPV films at $\lambda_{max} \approx 580$ nm is predominately due to the single-chain exciton emission, whereas that at 630 nm is most likely due to an interchain species (the Ex-I species). The devices with a stronger red (630 nm peak) emission usually have higher quantum efficiency.

6.4.3 *The Conductivity of the Film*

The conductivity of a spin-coated polymer film is solvent dependent. The films of the Ar-type aggregation style, resulting from aromatic solvents, usually have higher conductivity than films with the non-Ar-type aggregation style. This is due to the fact that the interchain electron transfer is more favorable in the former.

6.4.4 The Turn-on Voltage of the PLED Device

The current-injection voltage $V_{\mathrm{I-ON}}$, the voltage required for electron injection from the Ca calcium, is nearly independent of film morphology due to the direct contact between the metal and the π electrons of the polymer. On the other hand, the light-emitting voltage $V_{\mathrm{L-ON}}$, representing the voltage for hole injection from the anode, is significantly dependent on the polymer morphology. Generally, aromatic solvents result in a higher-quality contact (Fig. 6.13a) than the nonaromatic solvents (Fig. 6.13b). Therefore, any improvement on the anode/polymer interface, such as the use of a PEDOT layer on top of the anode, is able to reduce the $V_{\mathrm{L-ON}}$ of the device. In this regard, it is expected that the best contact will result if there exists a significant interpenetration between the charge-injection layer and the MEH-PPV layer. This could be achieved by using a proper solvent which can partially dissolve the charge injection polymer during spin-coating.

References

[1] J. H. Burroughes, D. D. C. Bradley, A. R. Brown, R. N. Marks, K. Mackay, R. H. Friend, P. L. Burns, and A. B. Holmes, *Nature* 347, 539 (1990).

[2] R. Jakubiak, and L. Rothberg, *J. Phys. Chem. A* 103, 2394 (1999).

[3] I. D. W. Samuel, G. Rumbles, C. J. Collison, R. H. Friend, S. C. Moratti, and A. B. Holmes, *Synth. Met*. 84, 497 (1997).

[4] J. C. Scott, S. Karg, and S. A. Carter, *J. Appl. Phys*. 82(3), 1454 (1997).

[5] G. G. Malliaras, and J. C. Scott, *J. Appl. Phys*. 85(10), 7426 (1999).

[6] P. W. M. Blom, M. J. M. de Jong, C. T. H. F. Liedenbaum, and J. J. M. Vleggaar, *Synth. Met*. 85, 1287 (1997).

[7] P. W. M. Blom, *Phys. Rev. Lett*. 80, 3819 (1998).

[8] H. F. Wittmann, J. Grüner, R. H. Friend, G. W. C. Spencer, S. C. Moratti, and A. B. Holmes, *Adv. Mater*. 7, 541 (1995).

[9] V. Cimrová, and D. Neher, *J. Appl. Phys*. 79(6), 3299 (1996).

[10] J. W. Baltchford, S. W. Jessen, L.-B. Lin, T. L. Gustafson, D.-K. Fu, H.-L. Wang, T. M. Swager, A. G. MacDiarmid, and A. J. Epstein, *Phys. Rev. B* 54, 9180 (1996)

[11] J. W. Baltchford, S. W. Jessen, L.-B. Lin, T. L. Gustafson, D.-K. Fu, H.-L. Wang, T. M. Swager, A. G. MacDiarmid, and A. J. Epstein, *Phys. Rev. B* 54, 9180 (1996); J. W. Baltchford, T. L. Gustafson, A. J. Epstein, D. A. Vanden Bout, J. Kerimo, D. A. Higgins, P. F. Barbara, D.-K. Fu, T. M. Swager, and A. G. MacDiarmid, *Phys. Rev. B* 54, R3683 (1996); T. Pauck, R. Hennig, M. Perner, U. Lemmer, U. Siegner, R. F. Mahrt, U. Scherf, K. Müllen, H. Bässler, and E. O. Göbel, *Chem. Phys. Lett*. 244, 171 (1995); U. Lemmer, S. Heun, R. F. Mahrt, U. Scherf, M. Hopmeier, U. Siegner, E. O. Göbel, K. Müllen, and H. Bässler, *Chem. Phys. Lett*. 240, 373 (1995); R. F. Mahrt, T. Pauck, U. Lemmer, U. Siegner, M. Hopmeier, R. Hennig, H. Bässler, and E. O. Göbel, *Phys. Rev. B* 54, 1759 (1996).

[12] U. Lemmer, S. Heun, R. F. Mahrt, U. Scherf, M. Hopmeier, U. Siegner, E. O. Göbel, K. Müllen, and H. Bässler, *Chem. Phys. Lett*. 240, 373 (1995)

[13] R. F. Mahrt, T. Pauck, U. Lemmer, U. Siegner, M. Hopmeier, R. Hennig, H. Bässler, and E. O. Göbel, *Phys. Rev. B* 54, 1759 (1996)

[14] M. Yan, L. J. Rothberg, F. Papadimitrakopoulos, M. E. Galvin, and T. M. Miller, *Phys. Rev. Lett*. 73, 744 (1994).

[15] T. A. Skotheim, R. L. Elsenbaumer, J. R. Reynolds, *Handbook of Conducting Polymers*, 2nd ed., New York, 1998.

[16] R. Jakubiak, C. J. Collison, W. C. Wan, L. J. Rothberg, and B. R. Hsieh *J. Phys. Chem. A* 103, 2394 (1999)

[17] Y. Shi, J. Liu, and Y. Yang, *J. Appl. Phys*. 87, 4254 (2000).

[18] C. Y. Yang, F. Hide, M. A. Diaz-Garcia, A. J. Heeger, and Y. Cao, *Polymer* 39, 2299 (1998).

[19] I. D. Parker, *J. Appl. Phys*. 75, 1656 (1994).

[20] I. H. Campbell, T. W. Hagler, D. L. Smith, and J. P. Ferraris, *Phys. Rev. Lett*. 76, 1900 (1996)

[21] P. W. M. Bolm, M. J. M. de Jong, and S. Breedijk, Appl. *Phys. Lett*, 71, 930 (1997).

[22] G. G. Malliaras and J. C. Scott, *J. Appl. Phys*. 83, 5399 (1998).

[23] J. C. Scott, G. G. Malliras, W. D. Chen, J. C. Breach, J. R. Salem, and P. J. Brock, *Appl. Phys. Lett*. 74, 1510 (1999).

[24] J. Liu, Y. Shi, and Y. Yang, *J. Appl. Phys*. 88, 605 (2000); J. Liu, Y. Shi, and Y. Yang, *J. Appl. Phys*. 89, 3668 (2001).

[25] J. Liu, Y. Shi, and Y. Yang, *Appl. Phys. Lett*. 79, 578 (2001), J. Liu, Y. Shi, and Y. Yang, *Adv. Funct. Mater*., in press.

[26] E. Wyn-Jones and J. Gormally, *Aggregation Process in Solution*, Elsevier Scientific, Amsterdam, 1983.

[27] R. Simha, and L. Ultrachi, J. Polym. Sci., A 2 (5), 853 (1967)

[28] R. A. Pethrick, *Aggregation Processes in Solution*, edited by E. Wyn-Jones, and J. Gormally, Elsevier Scientific, Amsterdam 1983, p. 594.

[29] C. P. Brown, A. R. Mathieson, and J. C. J. Thynne, *J. Chem. Soc*. 4141 (1955).

[30] A. R. Mathieson, and J. C. J. Thynne, *J. Chem. Soc*. 3708 (1956).

[31] J. J. Christensen, R. W. Hanks, and R. M. Izatt, *Handbook of Heats of Mixing*, Wiley, New York, 1982.

[32] M. Zheng, F. Bai, and D. Zhu, *J. Photochem. Photobiol*. A 116, 143 (1998).

[33] S. Wu, *J. Polym. Sci. C* 34, 19 (1971).

[34] D. McBranch, I. H. Campbell, and D. L. Smith, *Appl. Phys. Lett*. 66 (10), 1175 (1995).

[35] G. G. Malliaras, J. R. Salem, P. J. Brock, and J. C. Scott, *J. Appl. Phys*. 84, 1583 (1998).

[36] L. S. Roman, M. Berggren, and O. Inganas, *Appl. Phys. Lett*. 75, 3557 (1999).

[37] G. G. Malliaras, J. R. Salem, P. J. Brock, and J. C. Scott, *Phys. Rev. B* 58, R13,411 (1998).

[38] W. Salaneck, M. Logdlund, J. Birgersson, P. Barta, R. Lazzaroni, and J. Bredas, *Synth. Met*. 85, 1219 (1997).

[39] E. I. Haskal, A. Curioni, P. F. Seidler, and W. Andreoni, *Appl. Phys. Lett*. 71, 1151 (1997).

[40] L. S. Hung and C. W. Tang, *Appl. Phys. Lett*. 74, 3209 (1999).

[41] I. H. Campbell, T. W. Hagler, D. L. Smith, and J. P. Ferraris, *Phys. Rev. Lett*. 76, 1900 (1996).

[42] G. Yu, C. Zhang, and A. J. Heeger, *Appl. Phys. Lett*. 64, 1540 (1994).

[43] A. Dodabalapur, L. J. Rothberg, T. M. Miller, and E. W. Kwock, *Appl. Phys. Lett*. 64 (19), 2486 (1994).

[44] A. Dodabalapur, L. J. Rothberg, and T. M. Miller, *Appl. Phys. Lett*. 65(18), 2308 (1994).

[45] S. K. So, and W. K. Choi, *Appl. Phys. Lett*. 74, 1939 (1999).

[46] T. Huser, and M. Yan, *Fourth International Topical Conference on Optical Probes of Conjugated Polymers and Photonic Crystals*, 2000, abstract P1-46.

[47] J. Cornil, D. A. dos Santos, X. Crispin, R. Silbey, and J. L. Bredas, *J. Am. Chem. Soc*. 120, 1289 (1998).

[48] R. Jakubiak, L. J. Rothberg, W. Wan, and B. R. Hsieh, *Synth. Met*. 101, 230 (1999).

[49] L. Smilowitz, A. Hays, A. J. Heeger, G. Wang, and J. E. Bowers, *J. Chem. Phys*. 98(8), 6504 (1993).

[50] I. D. W. Samuel, B. Crystall, G. Rumbles, P. L. Burn, A. B. Holmes, and R. H. Friend, *Chem. Phys. Lett*. 213, 472 (1993).

[51] M. A. Diaz-Garcia, F. Hide, B. J. Schwartz, M. R. Andersson, Q. Pei, and A. J. Heeger, *Synth. Met*. 84, 455 (1997).

[52] M. Yan, L. J. Rothberg, E. W. Kwock, and T. M. Miller, *Phys. Rev. Lett*. 75, 1992 (1995).

[53] E. M. Conwell, *Phys. Rev. B* 57, 14200 (1998).

[54] E. M. Conwell, J. Perlstein, and S. Shaik, *Phys. Rev B* 54, R2308 (1996).

[55] B. R. Hsieh, Y. Yu, E. W. Forsythe, G. M. Schaaf, and W. A. Feld, *J. Am. Chem. Soc*. 120, 231 (1998).

[56] L. J. Rothberg, M. Yan, S. Son, M. E. Galvin, E. W. Kwock, T. M. Miller, H. E. Katz, R. C. Haddon, and F. Papadimitrakopoulos, *Synth. Met*. 78, 231 (1996).

[57] S. Son, A. Dodabalapur, A. J. Lovinger, and M. E. Galvin, *Science* 269, 376 (1995).

[58] C. L. Gettinger, A. J. Heeger, J. M. Drake, and D. J. Pine, *J. Chem. Phys*. 101, 1673 (1994).

[59] B. Hu and F. E. Karasz, *Synth. Met*. 92, 157 (1998).

[60] B. J. Sun, Y. -J. Miao, G. C. Bazan, and E. M. Conwell, *Chem. Phys. Lett*. 260, 186 (1996).

[61] Y. Cao, I. D. Parker, G. Yu, C. Zhang, and A. J. Heeger, *Nature* 397, 414 (1999).

[62] Y. Shin, J. Liu, and Y. Yang, unpublished results.

7

On the Origin of Double Light Spikes from Polymer Light-Emitting Devices

Aharon Yakimov, Vadim Savvateev,
and Dan Davidov

7.1 Introduction

The two decades of intensive research following the discovery of EL in thin organic-film based device by Tang and VanSlyke,[1] and later in polymer films by Burroughs et al[2] brought significant improvements in their characteristics. Currently the organic EL is seen as a candidate for a new generation of full-color displays and lighting applications. Major efforts have been concentrated on improving device efficiency, color gamut, lifetime and patterning techniques for achieving the full color displays.

The mechanism for light emission thin organic films is widely recognized as a radiative recombination of exciton states formed by positively and negatively charged polarons moving in the electric field applied to the device. These polarons are formed by the polarization of the organic matrix around electrons and holes injected from the cathode and anode respectively into the organic films. In the most common bi-layer configuration, the excitons form high concentration near the internal organic-organic interface where most of emission occurs. Several groups have studied the transient effects in OLEDs and related structures when the exciting voltage is applied as a short pulse.[3–7] Such transient measurements became an important tool in studying the general characteristics of the devices with implications for the dc operation. In particular, under low duty cycles with short pulses the effect of Joule heating may be eliminated, and the recombination rates and trap distribution in the emitting material may be elucidated from the EL decay rate at the device turn-on. The delays in the EL turn-on at the voltage pulse leading edge have been used to determine the carrier mobility and generally yield the μ values in agreement with those determined by other techniques.[8–10] At the turn-off of the voltage pulse some OLEDs emit a light flash that may last 10 ns–10 μs, and the peak intensity may exceed the steady state emission during the pulse by order of magnitude or even more.[11]

In an earlier paper Kirstein et al reported the occurrence of the light flashes at the pulse onset and turn-on in polymer based devices.[12] These flashes were found to be more prominent in thicker-film based devices. In a later paper we reported the observations of light flashes induced by ultra short ($\sim$ 10ns) voltage pulses in thicker films of poly (phenylene-vinylene).[13] In this work we report the new findings pertaining to the phenomenon of transient flashes induced by voltage pulses applied to polymer films. We consider several features of the phenomenon that distinguish it from the EL induced by a dc or video-rate bias in thin-film devices. While not immediately practical for display or lighting applications, the thick-film organic EL may become of considerable interest in long term.

We find that the emission spectra measured at the both turn-on and turn-off of the driving pulses are the same as with dc-excitation in thin films prepared with the same polymer, therefore the microscopic emission mechanism is apparently the same. However, the differences in transport mechanisms, especially injection and space charge distribution between thin and thick-film devices are enormous, and suggest completely different physics underlying EL excitation in these two cases. On the other hand, comparison of temporal characteristics of the emission in thick films to those observed in thick inorganic EL devices shows significant similarities. This may indicate connection of transient EL in emissive polymers to general behavior observed in insulating films in micron thickness range. In particular, the fast-decaying flash EL at the onset and turn-off of the driving voltage pulse may be related to the build-up and decay of the internal polarization counter-field induced by external bias when applied. The dynamics of EL decay would then reflect the build-up and decay of this polarization. We discuss details of the possible mechanisms for charge injection in the bulk and interfaces of the micron-range polymer film leading to light emission.

7.2 Experimental

In this study we used devices of two different architectures, namely the regular, down emitting and the inverted, or up emitting. The regular device employs ITO-covered glass as an anode, polymer film, and Mg-Ag opaque cathode on top of the device. The inverted device employs an Al opaque cathode that is deposited first onto the glass substrate, while semitransparent gold, deposited on top of the device, serves as an anode. Films of poly-2-methoxy,5-(2'-ethylhexoxy)-1,4-

phenylenevinylene (MEH-PPV) were spin-cast from chlorobenzene solution onto the sample substrate.

Film thickness could be varied from 500 nm to 800 nm by changing the polymer concentration in the solution and the spinning speed. The film thickness was measured either by means of the X-ray grazing angle reflectivity method, or by an Alpha-step profilometer, in the case of thicker films. Independent low-signal capacitance measurements yield consistent results for film thickness.

In order to observe the fast response of EL, we adjusted the RC time constant of the EL cell. We fabricated samples with low capacitance by lowering the device working area from 3 mm^2 to 0.3 mm^2, thus obtaining capacitance less than 50 pF for 800 nm thick films. Since the achieved capacitance values are of the same order of magnitude as that of the coaxial cables used in the experimental set-up, further sample capacitance reduction was not necessary.

The series resistance was determined mainly by the resistance of the electrodes, that is 20 Ω for ITO, or $\sim$ 50 Ω for Au. Other resistances in series with the sample had negligible values. Therefore, the RC time constant was estimated to be less than 5 nsec. Such a short charging time is necessary to observe the EL spikes, as will be shown below.

Pulses with time duration of 100 nsec to 10 μsec were generated using an Avtech high voltage pulse generator. The transition time of the voltage leading and trailing edges from 10% to 90% was 30 nsec and dominated not by the RC time constant of the sample, but by that of the generator. The pulse repetition rate was 100 Hz and voltage pulses of amplitude up to 200 V were applied to the sample.

Alternatively, pulses with rise times as short as 3–5 ns could be generated using a homemade setup schematically shown in Figure 7.1. It comprises a high voltage source, a transmission line and a photo-switch, governed by optical pulses from Nd:YaG laser. The circuit operates in a following way: first, the transmission line is charged by the high voltage source, while the photo-switch remains open. After the line charging, the photo-switch can be closed by a light flash of the laser. This leads to discharge of the line through the load (the sample). The rise time of the resulting voltage pulse is determined by the rise time of the laser flash. The duration of the voltage pulse is equal to the electromagnetic wave propagation time in the transmission line, and can be changed by using transmission lines of various lengths.

Using Velonex 350 as a high voltage source we were able to reach peak voltages exceeding 1 kV; the pulse width could be varied from 10 ns to 250 ns.

The EL signal was measured by a Hamamatsu photomultiplier and recorded by either a Tektronics fast storage oscilloscope or by a gated photon counter SR-400. Spectroscopy measurements were performed either in repetitive mode where the photomultiplier signal from the output of the CVI monochromator was scanned with the photon-counter, or alternatively by means of a cooled CCD camera connected to the CVI spectrograph.

For reduced temperature measurements the samples were placed in a low temperature microprobe chamber (MMR Technologies) that allow temperature variation

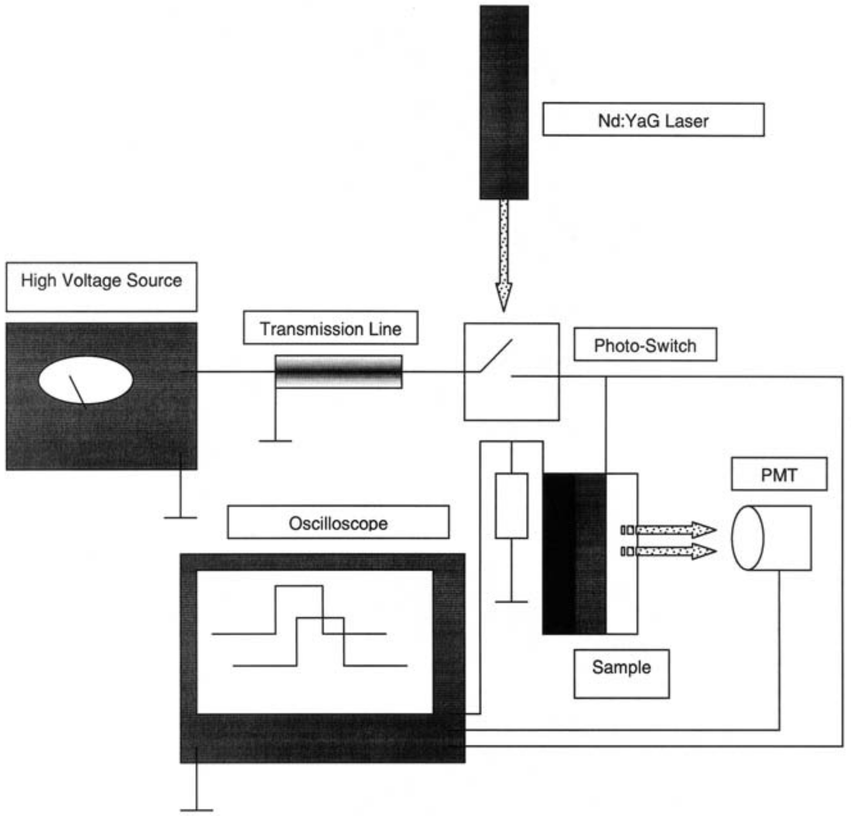

FIGURE 7.1. Experimental set-up for transient EL measurements under steep voltage pulses.

in the range of 90 K to 340 K. The chamber with the sample was evacuated to at least 10^{-5} Torr at room temperature prior the operation.

In evaluating the experimental data obtained from the time-resolved measurements we have taken into account artificial time lags of different origins, such as the electron transit time of the photomultiplier. The experimental data presented here was corrected for these time lags.

7.3 Results and Analysis

Typical light response to a forward bias (when the ITO serves as anode) voltage pulse is shown in Figure 7.2. Three main features of time-resolved EL can be easily seen: (a) EL spike after "turn-on" of the voltage pulse (T_{ON}); (b) EL spike after "turn-off" of the voltage pulse (T_{OFF}), and (c) a stationary EL appears when applied bias is strong enough to excite a dc emission; this stationary EL is usu-

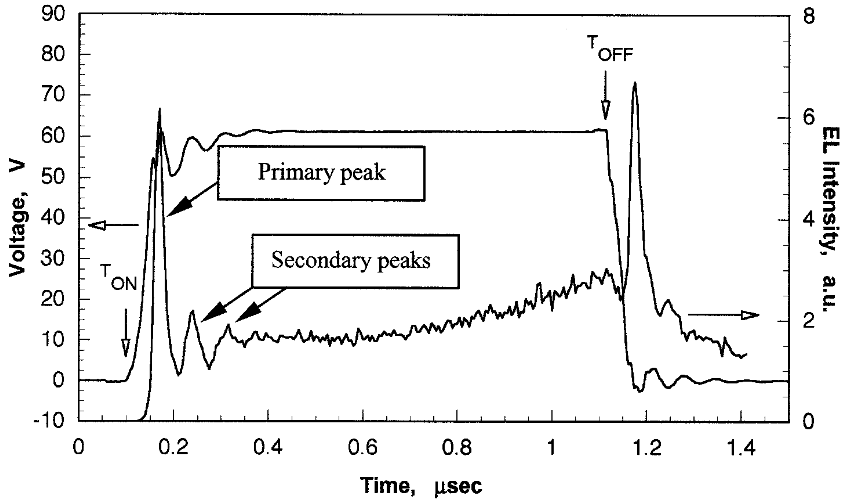

FIGURE 7.2. Light response to applied voltage pulse. Note light spikes after T_{ON} and T_{OFF}. Impedance mismatch leads to the fast voltage oscillations, that in turn leads to light oscillations. Note also short (~40 nsec) delay between the T_{OFF} and the light spike.

ally delayed versus the leading edge of the bias pulse. An additional feature often observed in practical conditions when ideal pulse shape is not easily achievable as shown in Figure 7.2 is the appearance of the secondary light peaks, or oscillations of the light intensity. These secondary peaks are time-correlated with voltage signal maxima, which apparently due to impedance mismatch between the line and the sample. Intensity of secondary peaks is much lower than that of a primary peak.

Stationary EL is simply the EL of the type that is emitted by the OLEDs when dc bias is applied. After the external field turns on, it may take certain time for the emission to develop and stabilize at a stationary level. After that it remains constant and limited only by device degradation. In the experiment shown in Figure 7.2, the gradual increase of emission that is registered starting 0.6 μsec after the pulse turn-on is apparently due to stationary EL. When the pulse polarity is reversed, this feature does not appear just as one would expect for a dc EL signal in a non-symmetric device. The emergence of stationary EL is even shown in more detail in Figure 7.3 as a function of the pulse amplitude. Higher bias accelerates the onset and increases the slope of the stationary EL. It starts to decrease promptly when the bias is turned off (at $t = T_{OFF}$).

Turn-off EL spikes were found to occur 30-40 nsec after the pulse turn-off and the decay of the stationary EL. Therefore, these two phenomena are well separated in time. The observation is also significant because it indicated that the delay between the voltage turn-off and the EL spike is not an artifact of the scope channel synchronization: the disappearance of stationary EL marks the synchronization of the light-readout channel. The time at which the turn-off spike reaches its maximum

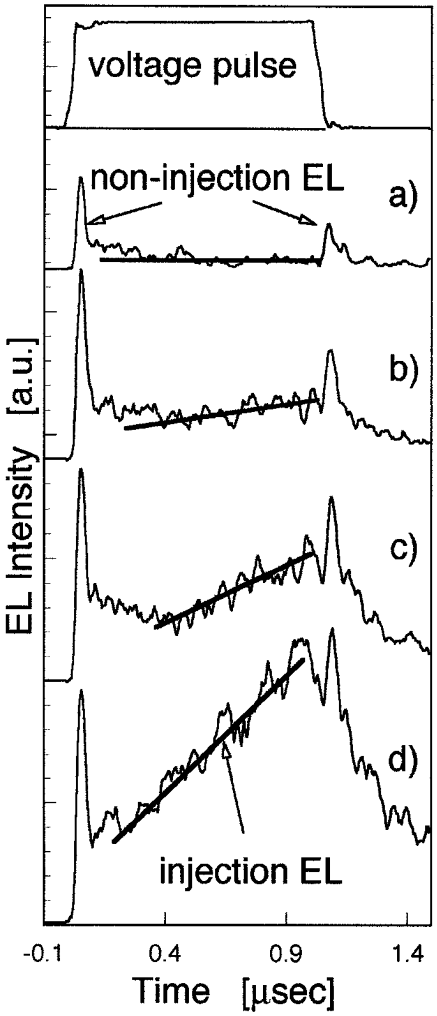

FIGURE 7.3. Transient EL under voltage pulses of 1 μsec duration. The amplitudes of the voltage pulses are: a) 55 V; b) 70 V; c) 75 V; d) 80 V. The spikes at the turn-on and turn-off of the voltage pulse are attributed to the transient EL response. The delayed EL in (c) and (d) is the regular, stationary EL.

coincides with the end of the voltage pulse fall edge. Therefore the decay of the turn-off spike occurs in the absence of an external field.

To measure spike intensity versus steepness of voltage pulse edges we introduced small variable capacitor connected in parallel with the sample. Increase in capacitive load led to a commensurate increase of the voltage pulse rise time. As we varied pulse rise-time from 2 ns to 90 ns, we observed the attenuation and eventual disappearance of transient EL peak. Therefore transient EL spikes can only be observed at sufficiently low circuit capacitance (or RC time) of the sample. This observation is consistent with, and explains why transient EL has not been observed in thin-layer samples.

Figure 7.3 exhibits an example of experiment where rectangular voltage pulse of microsecond duration (upper panel) was applied and led to the respective EL responses for varied pulse magnitudes. The stationary EL appears when voltage pulse magnitude is raised above a certain threshold (∼ 70 V in the conditions of Figure 7.3). The appearance of the regular EL is associated with noticeable current through the device due to injection of the charge carriers, as will be shown below.

In addition to the stationary EL (Figure 7.3d), two transient EL flashes appear at the rising and the falling edges of the voltage pulse. The voltage at which these spikes first appear is below the threshold voltage for the regular EL. Also, there is very small time delay between the onset of the voltage pulse and the EL spikes. Apparently, the emission of transient EL spikes is not limited by the drift of charge carriers across the film, which is believed to be responsible for the delay in rise of stationary EL upon application of the external bias.

Figure 7.4 shows the current-voltage and EL-voltage characteristics of the device. The measurements were carried out by applying forward bias pulses and

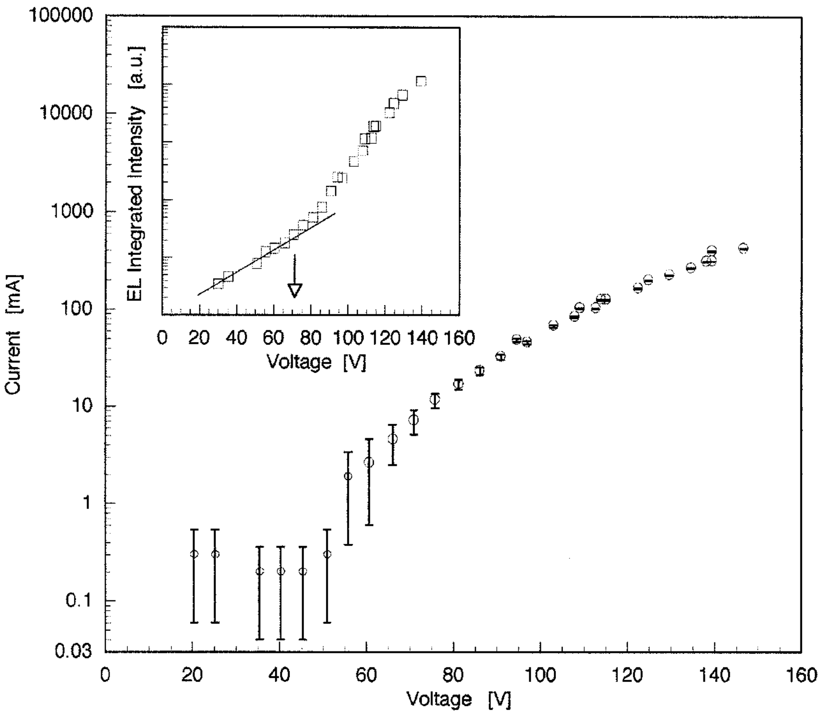

FIGURE 7.4. I-V curve under voltage pulses. The inset shows integrated EL signal vs voltage. The vertical arrow shows the threshold voltage for the regular EL. The spike EL integrated intensity is clearly seen at voltages below the threshold for the regular EL.

monitoring the current, as well as the time-integrated EL response. The current values are measured just before the end of the voltage pulse, when the current have reached the steady state. Therefore the measured current values are associated with charge injection from the electrodes and transport across the device. Note that there is only very small current below 60V (less than 0.3 mA/cm^2 which can be barely measured by this method), although the EL spikes can be detected already at 30V. Note also the dramatic increase of the current at ~70 V associated with the appearance of the regular, injection EL. The vertical arrow indicates the threshold voltage for the stationary EL. We emphasize that the EL spikes can be rather strong even below 70V. However, these spikes are very sharp and narrow, so their contribution to the time-integrated intensity can be rather small.

These observations along with the independence of the EL spikes on the applied voltage polarity[13] suggests that the EL spikes appearance can not be directly related to regular injection of charge carriers from the electrodes and their transport across the device, as it is in the case of stationary EL.

EL spectra measured for different voltage pulse amplitudes are shown in Figure 7.5. To exclude the contribution of the stationary EL, the transient emission was excited using voltage pulses of *reversed* polarity and of only 100 nsec pulse width. The plot of integrated EL intensity versus voltage is shown in the inset of Figure 7.5; the solid line shows an exponential fit to the data.

The spectral peak locations at 580 nm and 630 nm are identical to what can usually be seen with photoluminescence and regular EL measurements of MEH-PPV. Therefore we conclude that microscopic light emission mechanism in transient

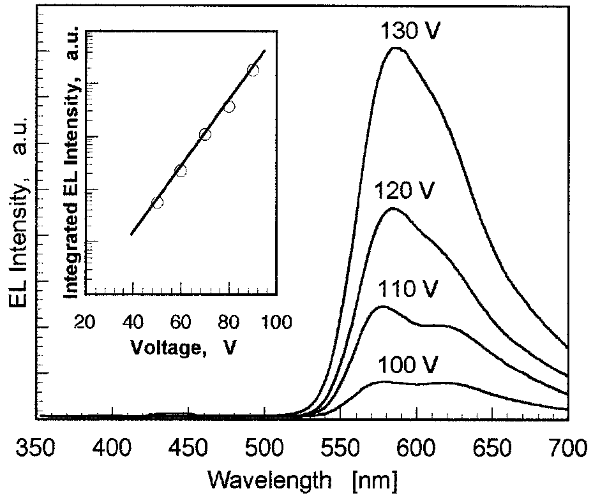

FIGURE 7.5. EL spectra of ITO/MEH-PPV/Mg:Ag upon voltage pulses of different amplitude. Inset shows integrated EL intensity as a function of applied voltage; the solid line is an exponential fit to the data.

EL does not differ from that in stationary light emission observed from the same films.

We recorded the EL decay patterns when a voltage pulse of 10 μsec duration was applied to the sample at room temperature (Figure 7.6A). We found that decay patterns of turn-on and turn-off EL spikes are similar: initial fast-decay part followed by slower decay. The observed curves were fitted to bi-exponential decay law with characteristic times $\tau_1 = 0.07$ μsec and $\tau_2 = 1.15$ μsec (Figure 7.6B). The drastic difference in time scales indicates the presence of two different mechanisms playing role in transient EL. Thus we may consider two different time scales for counter-field build-up, which presumably controls the EL spike decay. However, these time scales should be the same for the turn-on and turn-off spikes.

Reducing device temperature leads to increase in transient EL intensity, but the EL decay *dynamics* does not change, as shown in Figure 7.7. The temperature dependence of EL peak intensity was found to be the same for light emission at turn-on and at turn-off (inset of Figure 7.7). Such luminescence intensity dependence on temperature is not uncommon,[14–16] and falls into a pattern modeled with Fermi-Dirac function

$$I(T) \propto \frac{1}{1 + a \cdot \exp\left(-\frac{\Delta E}{kT}\right)}. \tag{1}$$

The best-fit parameters obtained are $a = 37$, and $\Delta E = 83$ meV. The ΔE value may be interpreted as activation energy for exciton quenching. Since the value of 83 meV is significantly lower than the MEH-PPV singlet exciton binding energy (usually measured as 0.3–0.4 eV) we cannot attribute this quenching to simple phonon-induced dissociation of emissive exciton. The study of exact mechanism of temperature induced quenching process is beyond the scope of this work; the dependence indicates however, the connection with the occupancy of the energy level through thermal activation of spin-1/2 particles across a gap of 83 meV.

The turn-off spike intensity as a function of the applied pulse width increases with an increase of the voltage pulse width, and it achieves saturation at a certain value, as shown in Figure 7.8. The dependence was successfully fitted with

$$S_2^{\max}(t) = A \cdot \left(1 - a \cdot \exp\left(-\frac{(t - t_0)}{\tau_1}\right) - b \cdot \exp\left(-\frac{t - t_0)}{\tau_2}\right)\right). \tag{2}$$

Where $S_2^{\max}$ is the measured maximum intensity of the turn-off spike and independent variable t is the applied pulse width. The best-fit parameters are: $A = 150$, $a = 1.4$, $b = 0.1$, $t_0 = 50$ nsec, $\tau_1 = 63$ nsec and $\tau_2 = 1150$ nsec. Thus, the dependence reveals two characteristic times, that are very close to those found in EL decay upon the voltage switching.

It is interesting to compare the EL response of the polymer-based device to that of the inorganic device. For time resolved measurements described below we used ac thin-film EL (ACTFEL) device, based on ZnS:Cu, and commercially available from EL-AM, Jerusalem.[17]

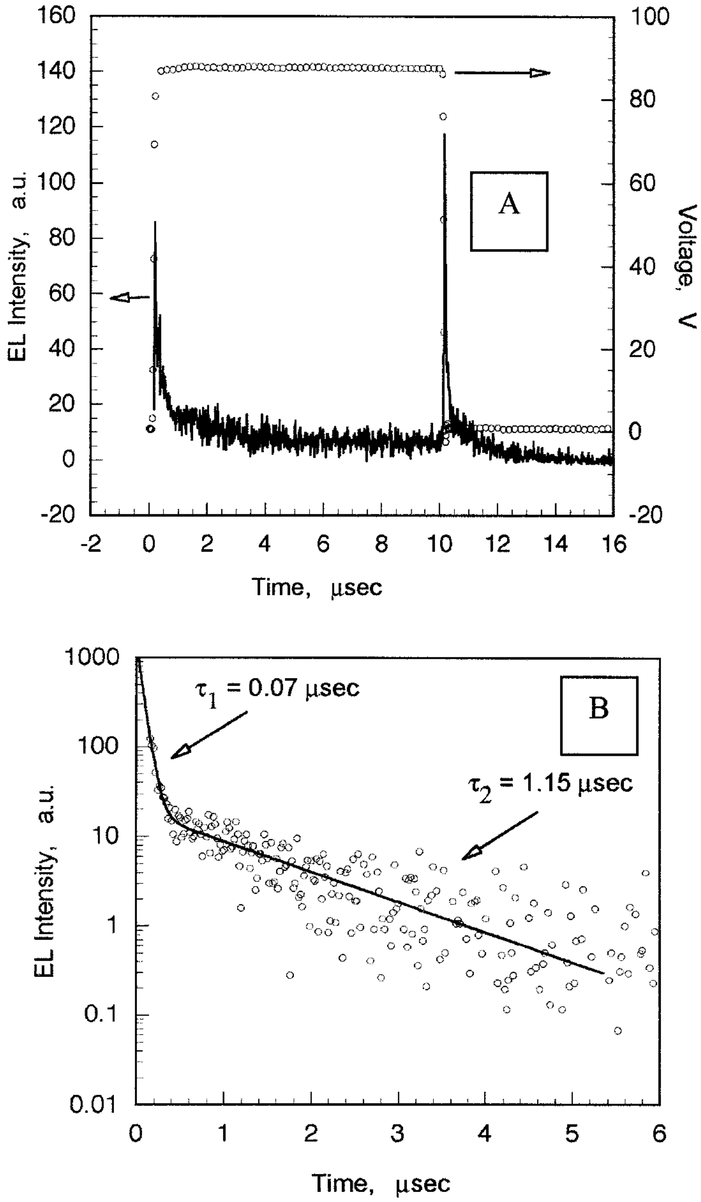

FIGURE 7.6. Panel (A): Transient EL response to the voltage pulse. The voltage pulse is shown by the open circles, EL spikes - by the solid line; panel (B): Bi-exponential fit to the EL spike decay.

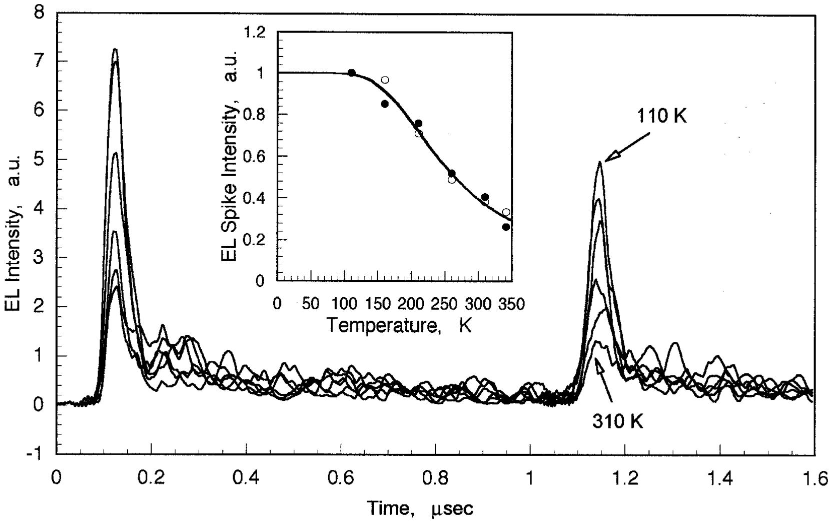

FIGURE 7.7. Time-resolved EL upon application of reversed bias pulse at different temperatures. Only EL intensity changes with temperature, not the decay characteristic times. In the inset: plot of the “turn-on” (open circles) and “turn-off” (closed circles) spike intensity versus temperature. The solid line represents the fitting function.

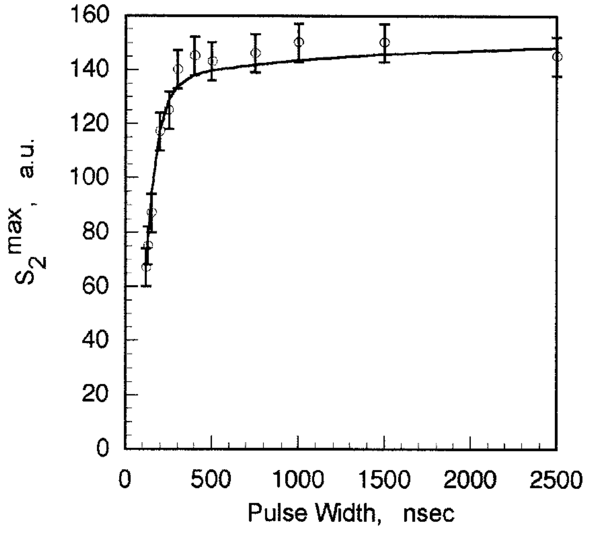

FIGURE 7.8. Turn-off spike intensity, S_2^{max}, dependence on the applied voltage pulse width. The solid line represents a fit to bi-exponent. The characteristic times and relative weights are the same, as for the turn-on spike decay.

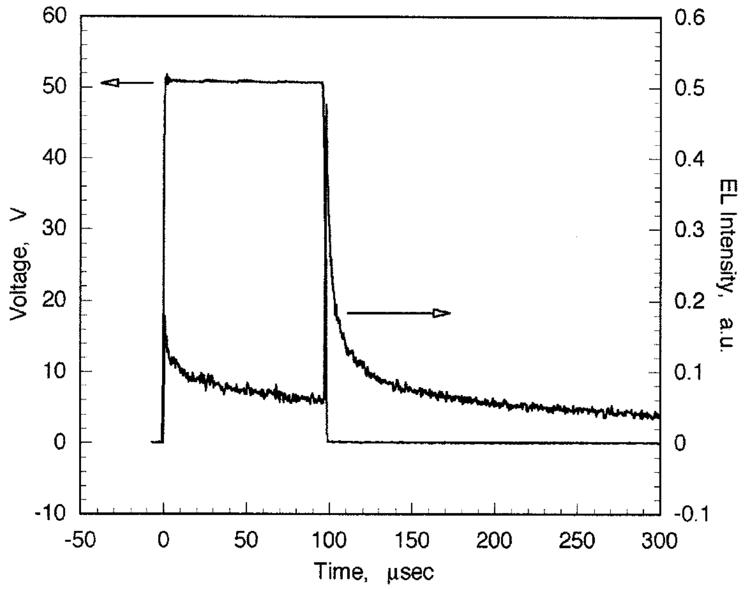

FIGURE 7.9. Transient EL response of inorganic-based device to applied voltage pulse (52 V). Note different time scales here and in Figure 7.6.

Shown in Figure 7.9 transient EL response consists of two light flashes, both having the same decay pattern. Note that the time-scale associated with the EL decay in the case of inorganic device is of the order of microseconds to tens of microseconds, which is much longer than that of polymer-based device.

Figure 7.10 shows the measured EL decay (dots) along with bi-exponential (dashed line) and stretched exponential (solid line) fit functions. The fitting functions and the best-fit parameters are:

Bi-exponential: $A \cdot \exp\left(-\frac{t}{\tau_1}\right) + B \cdot \exp\left(-\frac{t}{\tau_2}\right)$,
With $A = 0.8$, $B = 0.2$, $\tau_1 = 4.11\ \mu\text{sec}$, $\tau_2 = 212\ \mu\text{sec}$.
Stretched exponential: $\exp\left(-\frac{t}{\tau_0}\right)^{\alpha}$,
With $\tau_0 = 6.86\ \mu\text{sec}$, $\alpha = 0.29$.

Unfortunately, these functions fail to accurately describe the EL decay. However, the close analysis shows that at first several microseconds the EL decay follows the exponent, although at larger time-scale the decay can be fitted better with the stretched exponential fit function.

Striking similarity of the transient EL behavior for organic and inorganic-based devices indicates an apparent analogy in the underlying physic. However, the observed differences in the decay patterns reflect the different nature of the processes controlling the EL decay.

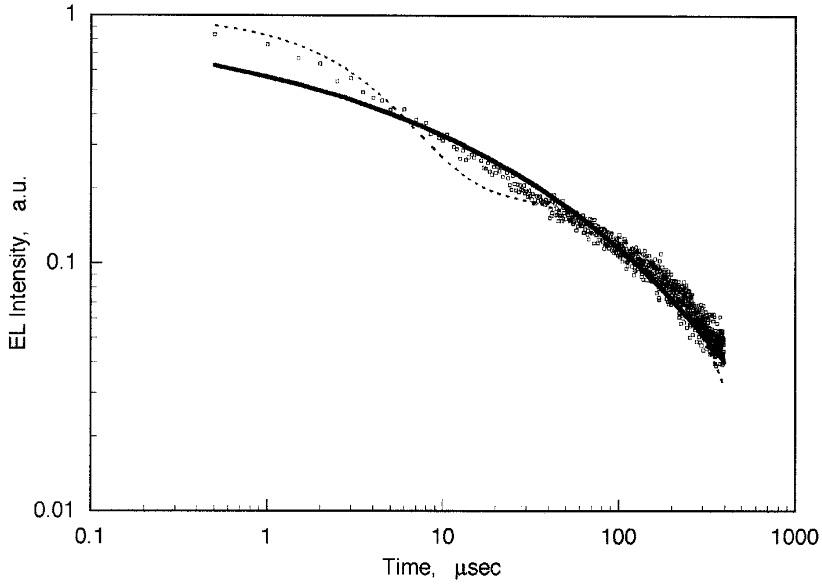

FIGURE 7.10. Measured EL decay (dots), the fitting curves: bi-exponential (dashed line) and stretched exponential (solid line). Note the log-log scale.

7.4 Discussion

In the experiments reported above we manage to separate the stationary EL, and the transient EL as distinct phenomena when excited by the voltage pulse. It appears that the basic microscopic emission mechanism in both cases is the same, which is confirmed by spectral measurements. The difference may be rising from the details in charge carrier excitation and injection into the film, and conditions influencing the radiative recombination of excitons inside it. The transient light emission occurs when the bias applied to the device is switched. The qualitative measure to the transient nature of this effect is provided by the experiment with parallel capacitor. The decrease of the ramp at the leading edge of the voltage pulse leads to a decrease of the EL output, until the voltage rise time becomes comparable with the relaxation time inside the sample, and the EL spike vanishes. The existence of this relaxation time is clearly indicated, and may be related to the onset of electrical polarization inside the film.

The nature of the polarization is of interest, i.e., whether the polarization is due to the rotational motion of structural dipoles or to the rearrangement of the space charge in the bulk of the film. To clarify this point we have carried out time-resolved EL studies at different temperatures and compare the previously measured temperature dependence of the dielectric polarization time[18] with that of the EL spike decay time.

Calculated from the time resolved measurements decay characteristic times at different temperatures are shown on Figure 7.11 (τ_1–open squares and τ_2–open

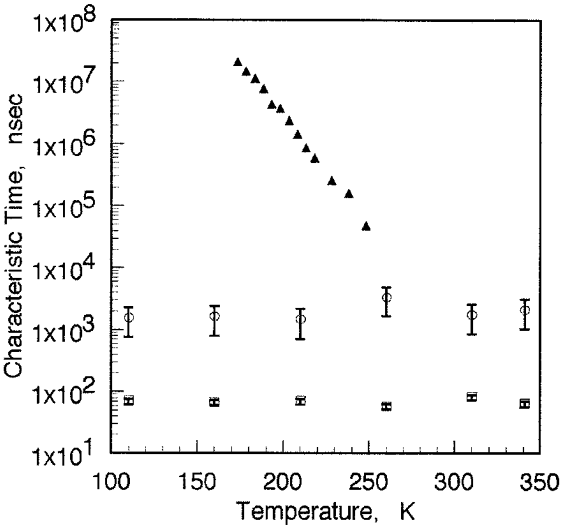

FIGURE 7.11. EL decay time constants (fast decay–open squares, slow decay–open circles) are independent on temperature. This is in contrast with the temperature dependence of the polymer matrix polarization time (closed triangles).

circles), along with the measured temperature dependent polymer relaxation time (closed triangles).

The absence of temperature dependence of the EL decay dynamics indicates that the counter field is produced mainly by redistribution of charges, rather than by the motion of structural dipoles, since the latter is highly temperature dependent.

Regardless of the origin of this polarization, the EL transient in the form of spikes appears to be related to the instantaneous difference between the applied field and the polarization field inside the film.

The transient polarization may play role in possible mechanisms of EL excitation, we will consider two of those: (i) field-induced de-trapping of the charge in the bulk of the film, and (ii) the charge injection via the electrode/polymer interface that is quenched by the polarization counter-field build-up.

We propose the following scenario for transient EL via field-induced de-trapping in the bulk of the film:

Immediately following the end of the voltage rise the effective field is high (and roughly equal to the applied field) and concentration of the de-trapped carriers is high, hence the distances between them are short. Therefore the probability to meet a counterpart for recombination is high. At this stage, the polarization counter-field increases rapidly due to fast movement of large amount of charge carriers. The polarization field build-up results in decrease of the effective field, that in turn leads to lower de-trapping rate, thus limiting the EL intensity. Therefore the EL intensity decreases rapidly, resulting in a light output in a form of a spike.

After first 50–100 nsec the effective field becomes lower than the de-trapping threshold and the carrier supply stops. Most of the carriers have either recombine, or re-trapped, thus compensating the external electric field. Now both the effective field and concentration of excess carriers are low, so that the recombination probability (and EL intensity) is low. The recombination limiting process at this stage becomes the slow carrier movement in a low electric field. Hence, long decay time is observed.

The EL output achieves the peak intensity within 30–40 nsec after the turn-on, when the polarization field is not yet significant and the effective field is roughly equal to the external field. Therefore, the EL peak intensity is determined mainly by the de-trapping rate, proportional to the exponent of the applied voltage, as indeed can be seen in the inset to Figure 7.5.

Just after the turn-off of the external voltage—more precisely, when the external voltage becomes small enough to enable the de-trapping by the polarization residual field—charge carriers can be released from the traps again. The released carriers move in the effective field and consequently recombine. The effective field again governs the recombination probability. Therefore the changes of the EL intensity (short-term decay of the turn-off spike) reflect appropriate changes of the residual field. Again, after the main relaxation of the residual field, there is a relatively small number of excess carriers that can recombine in the course of the movement in the slowly relaxing residual field. This leads to the long tail of light emission after the turn-off of the external voltage pulse. This scenario explains also why the decay pattern should be the same for the turn-on and the turn-off EL spikes, in agreement with the experimental results.

As an alternative to de-trapping in the bulk of the film, one can consider charge injection from electrodes. Efficient charge carrier injection is usually associated with energy match between the electrodes work function and polymer HOMO (holes injection) or LUMO (electrons injection) energy levels. The difference in work functions of the two injecting electrodes translates into non-symmetric dc current-voltage characteristic, and consequently, stationary emission occurs only if forward bias is applied. However, our experiments show the appearance of the transient EL signal independent of the applied voltage polarity. Therefore, we can consider charge injection from the opposite electrodes under high electric field even in *reversed* direction. Apparently, the energy match or mismatch on the polymer-electrode interface become not relevant under high field conditions, and this is strikingly different from the regular injection.

The injection leading to transient EL, may be possible through band-gap states at the electrode-polymer interface, and is essentially limited by the field strength across the interface. Upon injecting sufficient amount of charge the interface field will be screened by that charge, hence ceasing further injection. Therefore, the excitation is field-assisted and transient in nature, in accord with our experimental observations. Calculated order of magnitude delay time according to well known[19]

$$t_d = \frac{L}{\mu_0 \cdot E \cdot \exp(\gamma \cdot \sqrt{E})}, \tag{3}$$

is in the tens of nanoseconds range (film thickness $L = 1$ μm, electric field $E = 10^8$ V/m, $\gamma = 8.7 \cdot 10^{-3}$ (cm/V)$^{1/2}$, $\mu_0 = 10^{-6}$ cm^2/Vsec) that also fits well into the experimental data. Note that the case of injection from electrodes resembles the mechanism of EL excitation in inorganic ACTFEL devices. The main differences are in charge transport details and, of course, the nature of light emission.

We have assumed that the turn-off spike originates from the recombination of charges accumulated in the bulk of the polymer layer (bulk de-trapping case), or at the opposite polymer/electrode interface (electrodes injection case) during the voltage pulse. Comparison of the EL decay pattern with pulse-width dependence of the turn-off spike helps to prove this assumption. Indeed, during the voltage pulse some of the de-trapped (injected) charges form excitons, giving rise to light emission (this charge density will be denoted hereafter as $\mathrm{n_{EL}}$), while others contribute to the space-charge ($\mathrm{n_{SC}}$) being trapped either in the bulk, or at the opposite interface. Before the end of the voltage pulse we have a new distribution of charges, such that their mutual electric field diminishes the external field. After the external voltage is removed the charges can move in the residual field with subsequent recombination.

The light intensity integrated over the pulse duration is proportional to the number of charges that formed excitons (i.e., n_{EL}). Assuming the constant luminescence quantum efficiency during the voltage pulse, we find that the ratio $\mathrm{n_{EL}/n_{SC}}$ is constant. Now, if the turn-off spike originates from the accumulated space charge ($\mathrm{n_{SC}}$), then the intensity of the turn-off spike (S_2) should be proportional to the integrated EL intensity during the voltage pulse (S_1). Shown in Figure 7.12 is S_2 versus S_1 with the pulse duration as an implicit parameter. The obtained proportionality allows us to conclude that the accumulated charge during the external voltage pulse is indeed the source of the turn-off spike.

Finally, it is interesting to estimate the optimum ac-drive frequency, ω_0, for polymer-based ac-coupled device. This can be done by measuring the EL decay time to 25% of the initial light intensity value ($t_{0.25}$) and assuming $\omega_0 = (2t_{0.25})^{-1}$.

Calculated in this way optimum frequency for inorganic device is equal to 33 kHz, that is in reasonable agreement with the experimentally measured value of 28 kHz. For our polymer device we get $t_{0.25} = 0.4$ μsec, that corresponds to $\omega_0 = 1.25$ MHz. So, the optimum ac-drive frequency for the polymer-based device is much higher than that for the inorganic device.

7.5 Conclusions

We have carried out time-resolved EL measurements of polymer-based light-emitting devices. The transient EL spikes exhibit bi-exponential decay pattern. Temperature independence of the decay pattern allows us to rule out polarization due to polymer matrix relaxation as an EL governing process. According to our interpretation, the phenomenon of double light spikes under pulsed electrical

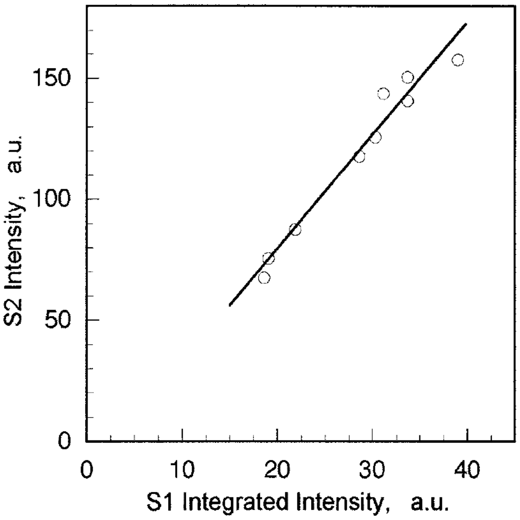

FIGURE 7.12. Plot of the turn-off spike intensity (S_2) versus integrated EL during the pulse (S_1) for different pulse widths. The solid line is a linear fit to the data.

excitation originates from recombination of charges accumulated in the polymer layer.

We stress the analogy between this phenomenon and ac-coupled EL from inorganic devices, although the microscopic mechanisms of transport and light emission are different in organic and inorganic devices.

The transient organic EL spikes effect may find practical application in addressing devices in which the EL peak intensity and fast modulation ability are of critical importance. While not immediately practical for display or lighting applications, the thick-film transient organic EL may become of considerable interest in long term.

References

[1] Tang, C. W.; VanSlyke, S. A. Appl. Phys. Lett. 1987, 51, 913;

[2] J. H. Burroughs, D. D. C. Bradley, A. R. Brown, R. N. Marks, K. Mackay, R. H. Friend, P. L. Burns, A. B. Holmes, Nature 1990, 347, 539;

[3] H. Vestweber, R. Sander, A. Greiner, W. Heitz, R. F. Mahrt, and H. Bassler, Synth. Met. 64, 141, 1994;

[4] P. W. M. Blom and M. C. J. M. Vissenberg, Phys. Rev. Lett. 80, 3819, 1998;

[5] D. J. Pinner, R. H. Friend, and N. Tessler, J. Appl. Phys. 86, 5116, 1999;

[6] J. C. Scott, S. Ramos, and G. G. Malliaras, J. Imaging Sci. Technol. 43, 233, 1999;

[7] D. J. Pinner, R. H. Friend, and N. Tessler, Synth. Met. 111-112, 257, 2000;

[8] H. Meyer, D. Haarer, H. Naarmann, H. H. Horhold, Phys. Rev. B 1995, 52, 2587;

[9] W. Brutting, E. Lebedev, S. Karg, T. Dittrich, V. Petrova-Koch, M. Schwoerer, Proc. SPIE 1988, 3281, 257;
[10] P. W. M. Blom, M. J. M. deJong, M. G. van Munster, Phys. Rev. B 1997, 55, R656;
[11] V. Savvate'ev, J. H. Friedl, L. Zou, J. Shinar, K. Christensen, W. Oldham, L. J. Rothberg, Z. Chen-Esterlit, and R. Kopelman, Appl. Phys. Lett. 76, 1501, 2000;
[12] Kirstein, G. Cohen, D. Davidov, U. Scherf, M. Klapper, K. Chmil, and K. Mullen, Synth. Met. 69, 415, 1995;
[13] V. N. Savvateev, A. Yakimov, and D. Davidov, Adv. Mater. 11, 519, 1999;
[14] C. Klick, J. H. Schulman, Solid State Physics, Vol. 5; Academic Press: New York, 1957;
[15] D. C. Bradley, and R. H. Friend, J. Phys.: Condens. Matter 1, 3671, 1989;
[16] Lifshitz, A. Kaplan, E. Ehrenfreund, and D. Meissner, J. Phys. Chem. B 102, 967, 1998;
[17] U.S. Patent # 5485355, Voskoboinik et al, 1996;
[18] A. V. Yakimov, V. N. Savvateev, D. Davidov, S. Pfeiffer, and H. H. Horhold, SPIE 3787, 237, 1999;
[19] M. Pope and C. Swenberg, "Electronic processes in organic crystals and polymers," Oxford University Press, New York, 1999.

8

Electroluminescence with Poly(para-phenylenes)

Stefan Tasch, Wilhelm Graupner, and Günther Leising

8.1 Introduction

Among the class of conjugated materials, the systems based on paraphenyl building blocks possess outstanding properties concerning their electronic structure, crystal structure, photophysical behavior, processibililty, and environmental stability. The enormous progress in defined chemical synthesis of precursor polymers and soluble ladder-type polyparaphenylenes have improved the quality of this polymers and enabled the fabrication of efficient blue-light-emitting electroluminescence devices (LEDs), light-emitting electrochemical cells, as well as the realization of optically pumped blue polymer lasers.

In this chapter, we discuss the physical properties of oligophenylenes and polyphenylenes with their processing, stability, and crystal structure. The absorption and emission properties, together with the discussion of the nature of the excited states are important for the understanding of the basic processes and for the application in optoelectronic devices. In the latter case, charge transport is also an essential part that is discussed in terms of the intrinsic and extrinsic properties. The main part of this chapter is dedicated to electroluminescence with polyphenylene-based materials, the generation of a variety of emission colors in the visible spectral range with different physical processes based on external color conversion techniques, and internal color conversion techniques, like excitation energy transfer in electroluminescence devices fabricated with multilayers and from polymer blends. The final section describes the appealing way of using a solid-state electrochemical cell to realize electroluminescence cells with quite fast response times and low driving voltages.

8.2 Physical Properties of Oligophenyls and Polyphenyls

The physical properties of bulk films of oligophenyls and polyphenyls strongly depend on the chemical structure of the molecules and on the structural arrangement of the molecules in the film. The most important parameters of the chemical composition are as follows:

1. Ortho, meta, or para substitution of the phenyl ring
2. Type of link between the phenyl rings
3. Number of phenyl rings connected with each other
4. Substitution of the phenylene backbone with side groups.

In order to illustrate these effects, we have compiled a few selected examples of well-investigated oligophenyls and polyphenyls in Fig. 8.1 and we discuss their properties in the following subsections. Although oligophenyls are known for decades as laser dyes,[1] it is also known that a linear arrangement (para substitution) of the phenyl rings composing the electronically active backbone of the oligo/polyphenyl are preferable over a ortho or meta substitution, which both result in smaller emission wavelengths and higher thresholds for lasing.[1] Therefore, we will restrict ourselves to the treatment of *para*-phenylenes in the subsequent subsections.

8.2.1 Processing and Stability

As for all conjugated molecules, the insolubility of *para*-phenylenes longer than five phenyl rings poses a severe obstacle to easy solution processing and film fabrication via simple drop, dip, or spin-casting as well as doctor blade processing. However, there are several strategies widely used to circumvent this problem:

1. **Evaporation of molecules**. This can be achieved in a very controlled way for the short oligomers. The evaporation of polymeric material leads to the deposition of fractional polymer segments (oligomers) and therefore results in layers composed of molecules with different lengths. The evaporation of the oligomers leads to polycrystalline layers with random orientation of the crystallites. However, under certain conditions, films of predominantly standing or lying molecules can be achieved. Pretreatment of the substrates onto which the evaporation takes place can even result in molecules which lie on the substrate and show a preferential orientation along a chosen axis within the substrate plane. Films of this type are suitable for large-area emission of linearly polarized light. For the melting points of oligophenyls, see Ref.2.

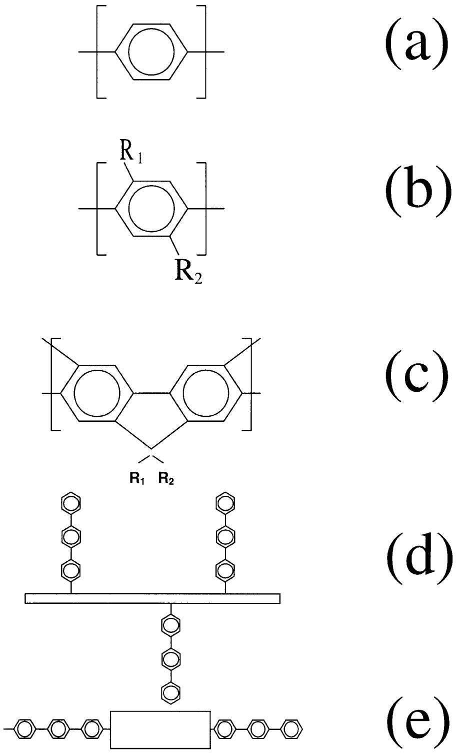

FIGURE 8.1. Selected representatives of poly(1,4-phenylene) or poly(*para*-phenylene) (PPP): (a) shows the unsubstituted poly(*para*-phenylene), (b) shows substituted poly(*para*-phenylene) with side-groups R_1 and R_2, (c) represents the ladder-type poly(*para*-phenylene) (LPPP), (d) and (e) represent graft–copolymer and main-chain copolymer approaches, with the three phenyl rings representing the insoluble conjugated backbone and the rectangles representing soluble molecules.

2. **Precursor routes**. This approach uses so-called precursor polymers, which are soluble and therefore easily processible. After production of the films via a casting technique, the precursor polymers are converted to the conjugated molecules. During this step, which is usually induced by heating and, in some cases, by light, the morphology of the obtained film can still be influenced (e.g., by cross-linking between the chains or by stretch orientation of the converting film).
3. **Solubilizing side groups**. Another very common approach is the attachment of solubilizing side groups to the *para*-phenylene backbone (Fig. 8.1b). The final product are molecules showing the desired electronic properties of the *para*-phenylene backbone and the processability of a soluble nonconjugated polymer. The external forces due to stress of the side groups on the phenyl rings do slightly alter the electronic properties of the *para*-phenylene backbone. Typically, higher photoluminescence quantum yields and blue-shifted absorption and emission

spectra are obtained with respect to the unsubstituted molecules. If suitable side groups are chosen, there is no principal limit for the length of the obtainable *para*-phenylene backbone. In Fig. 8.1c, there is depicted a bridged PPP with planarized backbone. The properties of this polymer representing a special modification of poly(*para*-phenylenes) (PPPs) with solubilizing side chains will be intensively discussed in this chapter.

4. **Side-chain copolymers**. This approach (Fig. 8.1d) is the inverse application of the strategy described in the previous paragraph. The backbone is a soluble nonconjugated polymer, whereas *para*-phenylene molecules are attached to it. For this approach, there is a fundamental limit in both the number and the length of the attached *para*-phenylene molecules; exceeding this limit results in the loss of solubility.
5. **Main-chain copolymers**. In this case, the polymer consists only of one main chain which alternately shows soluble nonconjugated segments and insoluble conjugated segments (Fig. 8.1e). This approach has the same limitation as strategy, 4, but both strategies 4 and 5 lead to electronic properties of the *para*-phenylene molecule, which are not altered as in strategy 3.

Para-phenylenes are comparably stable materials under environmental conditions; for the degradation and stability of conducting polymers, see Ref. 2. Both theoretical and experimental studies find their oxidation and ionization potentials about 1 eV higher than for conjugated molecules based on pyrrole or thiophene.[3]

8.2.2 Geometric Arrangement of Para*-phenylenes*

Para-phenyls, which have bulky side chains, are typically amorphous materials. In fact, this has the advantage that no recrystallization processes or rearrangement of the polymer chains will occur during device operation. However, in thin layers, an orientation of the polymer chains in the plane of the substrate is observed, leading to anisotropic macroscopic optical[4] and electrical properties.[5]

In contrast, the unsubstituted oligomer *para*-hexaphenyl is a highly crystalline material.[6] In the crystalline state, the oligomer chains are arranged in layers forming a herringbone-type structure as shown in Fig. 8.2, characterized by a unit cell $a = 8.091$ Å, $b = 5.568$ Å, $c = 26.241$ Å, and $\beta = 98.17^\circ$. Two types of preferred crystalline growths are observed.[7] One of them is oriented with the $(00l)$ and the other with the (22-3) plane parallel to the surface of the substrate.

Figure 8.2 shows one of the possible geometric arrangements of an ensemble of the linear *para*-hexaphenyl molecules, representing a monoclinic crystal structure of space group $P2_1/a$.[8,9] The crystallite size and the type of preferred growth can be controlled by the deposition parameters as the substrate temperature and the deposition rate.[10] The herringbone structure is known to lead to quite unique optical properties.[11] In contrast to other crystalline organic materials, a thermal annealing of the crystalline phase occurs[12,13] which is important for LED applications.

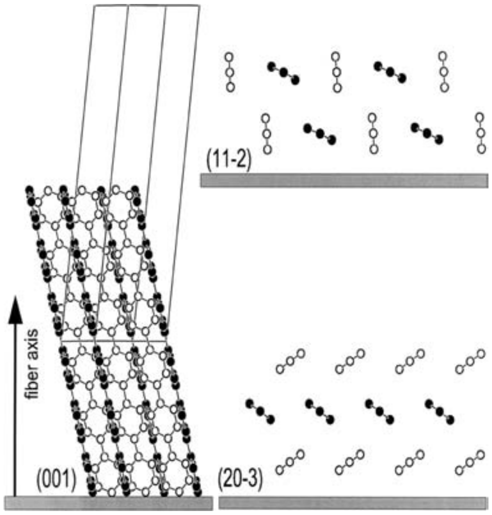

FIGURE 8.2. Geometrical arrangement of *para*-hexaphenyl. The thin solid lines in the left panel denote the monoclinic unit cell of the crystal. The solid gray bars represent the respective crystal planes (001, 11-2, and 20-3); therefore, the figures represent a cross section through the crystal along these planes. In the right panels, the herringbone structure becomes evident. (Reproduced from Ref. 158).

8.2.3 Absorption Properties

Absorption of light in the ultraviolet, visible, and near-infrared regions in conjugated polymers is caused by several entities: (1) ground-state absorption due to the promotion of a π electron to a higher electronic state, (2) absorption due to nonconjugated segments (i.e., chemical defects), (3) absorption due to excited states which are created either upon absorption of light or injection of charges (see Section 8.3).

The optical properties of materials are determined by the so-called dielectric function. This dielectric function for *para*-phenyl-type molecules was determined by first-principles band-structure calculations on PPP.[14] In Fig. 8.3, we depict one of the main results, namely the dependence of the imaginary part of the dielectric function (which is proportional to the optical absorption coefficient) on the orientation parallel (ϵ_c) and perpendicular (ϵ_a, ϵ_b) to the chain axis. From a comparison to the experiment, one can see that the optical absorption in the visible and ultraviolet ranges is mainly determined by the dielectric function parallel to the polymer chain. This is shown in Fig. 8.4, where the calculated absorption coefficient of *para*-hexaphenyl perpendicular to the chains is compared to the experimentally determined absorption perpendicular and parallel to the chains.

The observed π–π^* transition is therefore the result of an optical excitation with the dipole moment parallel to the PPP chains. The above-described anisotropy of the optical absorption is also valid for photoluminescence emission and can be used to obtain polarized electroluminescence (EL) spectra from Langmuir–Blodgett

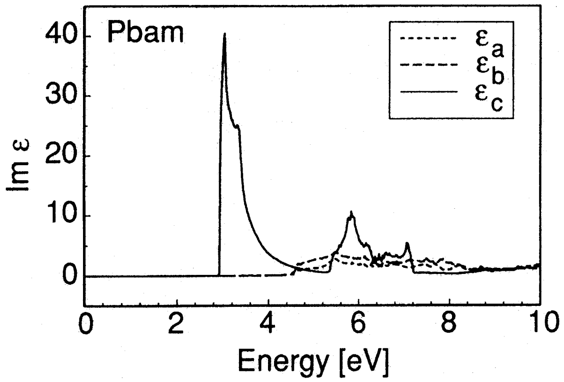

FIGURE 8.3. Calculated imaginary part of the dielectric tensor in crystalline PPIP in the *Pbam* phase. The ϵ_c is parallel to the chain axis, ϵ_a and ϵ_b are perpendicular to the chain axis. Reproduced from Ref. 14.

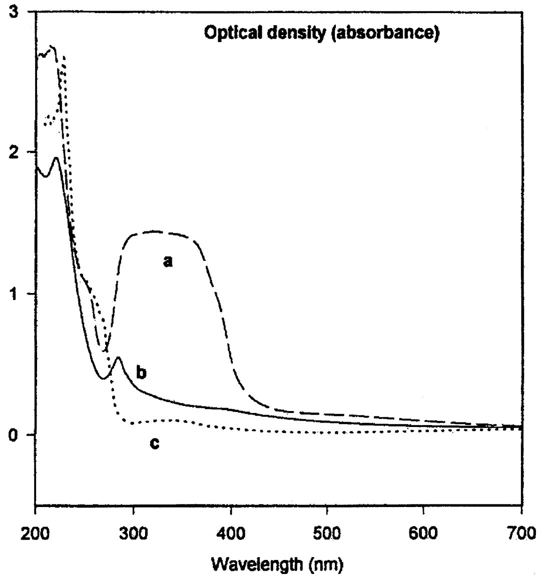

FIGURE 8.4. Calculated absorption coefficient perpendicular to *para*-hexaphenyl chains (c) compared to the experimentally determined absorption perpendicular (b) and parallel (a) to the chains. (Reproduced from Ref. 159.)

films made from soluble PPPs[15] or from oriented hexaphenyl films.[16] In a simple model,[17] that describes the π electrons of conjugated polymers as particles in a box, the energetic distance between the highest occupied molecular orbital (HOMO) and the lowest unoccupied molecular orbital (LUMO) shows a linear dependence on the inverse chain length of the molecule. Because the HOMO–LUMO distance is probed by optical absorption spectroscopy, this model can be applied to the

TABLE 8.1. Photoluminescence Quantum Yields of Selected *Para*-phenylene-Type Oligomer and Polymer Films and Solutions.

Molecule	Solution	Film	Reference
DO-PPP	85%	35%	59
EHO-PPP	85%	40%	59
CN-PPP	85%	46%	59
Para-terphenyl	93%		1
Para-quaterphenyl	98%		1
Para-hexaphenyl		30%	87
m-LPPP	100%	30%	5
Spiro P6			168

Note: Abbreviations: DO-PPP=poly(2-decyloxy-1,4-phenylene); EHO-PPP=Poly(2-(2'-ethylhexyloxy)-1,4-phenylene); CN-PPP=poly(2-(6'-cyano-6'-methyl-heptyloxy)-1,4-phenylene); m-LPPP=methyl-substituted ladder-type poly(1,4-phenylene).

absorbance spectra of oligophenyls and it leads to the following relation.[18,19]

$$E_a = \left(3.36 + \frac{3.16}{n}\right) \text{eV} \tag{1}$$

where E_a is equal to the energy of the peak of the absorbance and n is equal to the number of phenyl rings along the chain.

The electronic properties of conjugated polymers depend significantly on the structural regularity of the materials also. Because it is known that both the type of substitution as well as the planarity of the molecules influence the photoluminescence quantum yield of PPPs (see Table 8.1), chemical defects like branching, cross-linking, or meta and ortho substitutions and the degree of torsion between neighboring phenyl rings are important parameters.[20,21] These defects reduce the overlap of the π-electron wavefunctions and, therefore, they reduce the degree of conjugation. Hence, PPP molecules with a degree of polymerization as high as 100 phenyl rings can show optical properties equivalent to short oligomers. The inversion of Eq. (1) can be used to determine the *effective conjugation length* n_{eff} via the absorbance peak. Typical values for n_{eff} are 9–10 phenyl rings for PPP.[22]

The strength of the ground-state absorption of conjugated molecules is of the order of 10^5 cm^{-1}, which leads to penetration depths of visible light of the order of 100 nm. Therefore, light, penetrating *para*-phenylene layers in the spectral region of the ground-state absorption, can only travel a few hundred nanometers. This leads to a strong reabsorption of emitted light; therefore, efficient emission can only occur at quantum energies well below the ground-state absorption. In this region, the residual absorption is governed by defects and/or species created by optical or electrical excitation. In Fig. 8.5, we show that the absorption of a ladder-type PPP changes by more than four orders of magnitude when going from the spectral region of ground-state absorption to the residual absorption above 500 nm. This corresponds to absorption coefficients and penetration depths of 10 cm^{-}1 and 1 mm, respectively, at around 500 nm. In the same material, it was shown that this high penetration depth is sufficient to allow for efficient interaction between

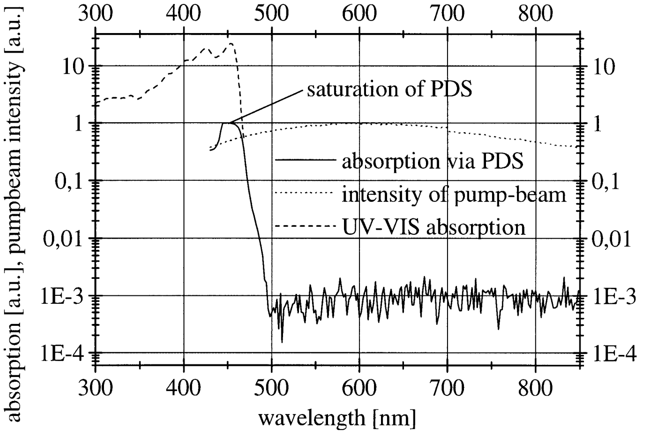

FIGURE 8.5. Absorption spectrum of a ladder-type PIPP as determined by conventional UV/vis transmission spectroscopy (dashed line) and photothermal deflection spectroscopy (PIDS, solid line); the dotted line shows the intensity of the PIDS pump beam. (Reproduced from Ref. 160.)

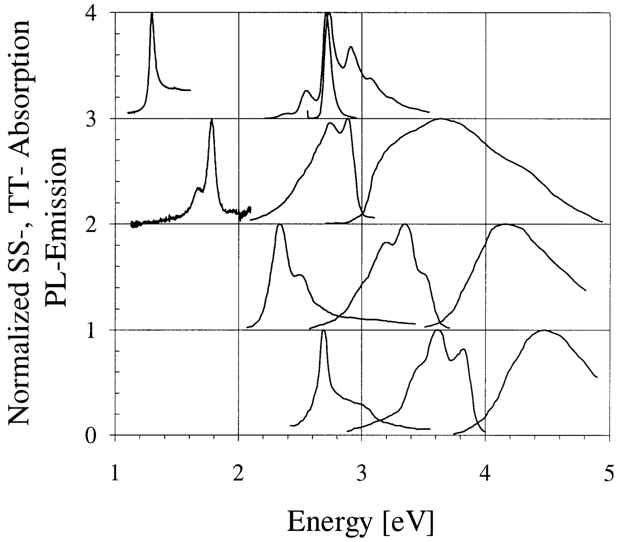

FIGURE 8.6. Triplet absorption, singlet emission, and absorption (from left to right) of (from top to bottom) m-LPPP[161] and hexaphenyl films [162] at 90 K, and *para*-quater-, and terphenyl at 77 K in tetrahydro-2-methylfuran.[25]

emitters in order to sustain amplified spontaneous emission (ASE) in waveguide structures; ASE is not observed at the peak of the photoluminescence emission of this material at 460 nm (see Fig. 8.6), as there, the residual absorption is still too high.[23]

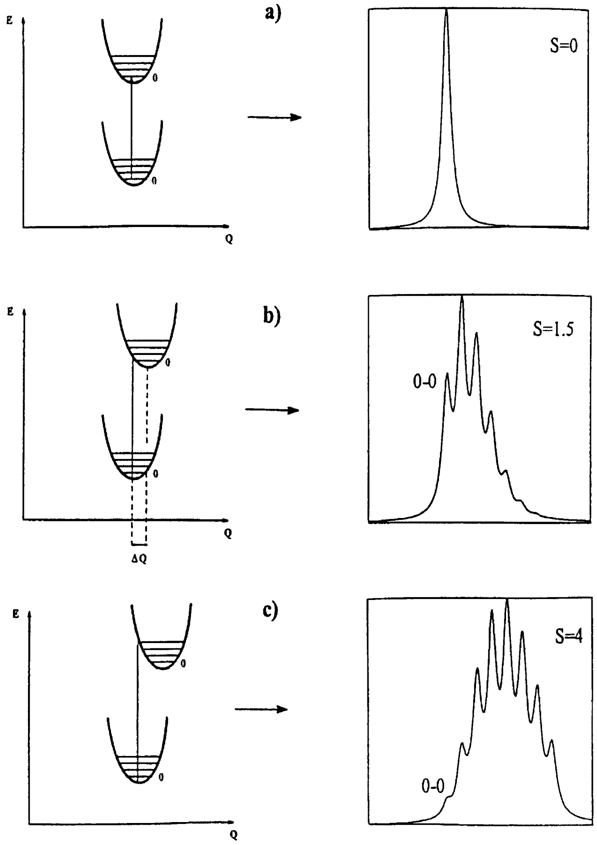

FIGURE 8.7. Schematic representation of the vibronic transitions observed in a situation where the equilibrium geometries of the ground and excited electronic states are (a) identical ($S =$), (b) weakly displaced ($S = 1.5$), and (c) strongly displaced ($S = 4$). S is the Huang Rhys factor as defined in the text. (Reproduced from Ref. 163.)

In Fig. 8.6, we have summarized the singlet–singlet (SS) and triplet–triplet (TT) absorption as well as the photoluminescence (PL) emission of *para*-, ter-, quater-, and hexaphenyl as well as of a ladder-type PPP. For the nonplanar oligophenyls, the SS absorption at room temperature does not show any vibrational replica which can be explained by the torsional degree of freedom of neighboring phenyl rings in the ground state.[24] This freedom leads to significant differences between the geometry of the ground and excited states, which involves phonon creation both in absorption and emission processes. The parameter which describes how many phonons are involved in an absorption or emission process is called the Huang Rhys factor; situations for different Huang Rhys factors are described in Fig. 8.7. When comparing Fig. 8.7 to the experimental results in Fig. 8.6, it becomes evident that both the absorption and the emission of light in the planar ladder-type PPP are significant for a smaller Huang Rhys factor in comparison to the nonplanar oligophenylenes. This is completely in accordance with the theoretical background, because the chemical planarization of the ladder-type PPP does not allow significant differences between ground- and excited-state geometry.

8.2.4 Emission Properties

The photoluminescence emission spectra of several *para*-phenylene molecules are shown in Fig. 8.6. In accordance with the previous discussion of a small Huang Rhys factor for the ladder-type PPP, it is evident that the energy difference between absorption and emission is very small for this material; this leads to a very small apparent Stokes shift. For the nonplanar molecules, this difference is much higher. When comparing absorption and emission properties, one has to keep one basic fact in mind: An absorption experiment probes all molecules in the film, whereas the emission experiment probes only the emitting molecules. Although molecules with a high HOMO–LUMO distance will definitely absorb light, they are not necessarily the emitters due to the phenomenon of excitation energy transfer (EET) to molecules with lower HOMO–LUMO distances. This phenomenon can even be observed in *para*-hexaphenyl film, which consists of chemically identical molecules. In Fig. 8.8, we have summarized the results of so-called site-selective spectroscopy, where the emission spectra of a *para*-hexaphenyl film were probed under various excitation wavelengths. It becomes evident that the emission spectra change below excitation energies of 3.1 eV. This is indicative for the suppression of significant EET below this energy (i.e., below this energy, the absorbers become also emitters). Correspondingly, the emission peaks shift to the red and become narrower with increasing excitation wavelength because only the molecules with the lowest HOMO–LUMO distances are excited and also emit; there is no contribution from all the other molecules.

8.2.5 Excited States

In this subsection, we want to treat the properties of states created either via charge injection or the absorption of light in *para*-phenylene-type systems. The emission of light via singlet excitons is always in competition with at least three other processes: (1) the formation of nonemissive excited species (e.g., triplet excitons), (2) nonradiative recombination of singlet excitons, (3) reabsorption of the light emitted by singlet excitons. Excited states play a role in all three areas. In light-emitting diodes, it is generally accepted that 75% of the excited species formed via the combination of a positive and a negative polaron are triplet excitons. They are nonemissive, but they also absorb emitted light. On the way to the organic laser diode, this process is a very important design issue. Therefore, a sufficiently large spectral separation between absorption of light due to triplet excitons and the singlet-exciton emission is desirable. As can be seen from Fig. 8.6, this is reasonably well fulfilled for the longer *para*-phenylene systems. Under optical pumping all the materials depicted in Fig. 8.6 show stimulated emission. The quaterphenyl does not show lasing as efficiently as the terphenyl due to stronger

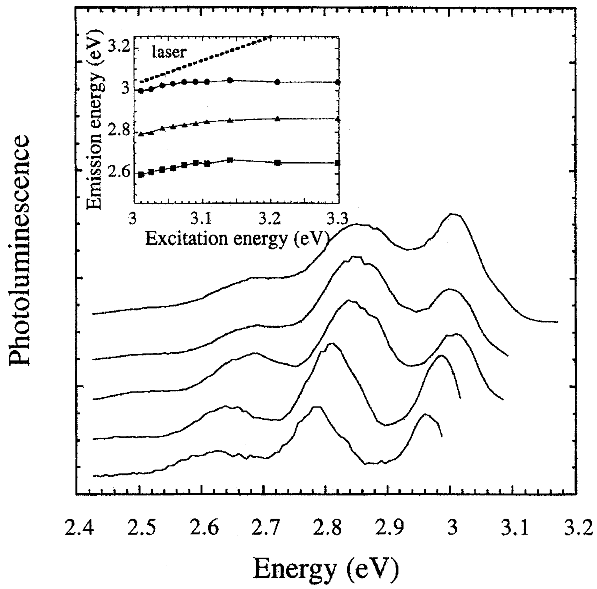

FIGURE 8.8. Site-selective photoluminescence spectra of *para*-hexaphenyl at 10 K: emission spectra at excitation energies of 3.30 (top curve), 3.21, 3.14, 3.04, and 3.01 eV; inset: evolution of the emission peaks versus excitation energy; the dotted line represents the quantum energy of the exciting photons.(Reproduced from Ref. 164. and 165.)

overlap of the emission with the triplet absorption.[25] However, one has to keep in mind that only very few triplets are produced by light, via intersystem crossing from the singlet to the triplet state, in comparison to charge injection; hence, for laser diodes, the triplet absorption can be an issue. Furthermore, the shape of the triplet absorption reveals a basic fact about the molecular geometry: A broad triplet absorption indicates that the molecules in their triplet state are not planar.[25]

Another absorbing species present both in photo excited and electrically excited para-phenylenes are polarons. In Fig. 8.9, we have summarized the absorption and emission spectra encountered in *para*-hexaphenyl: (1) the triplet absorption, (2) the stimulated emission observed in time-resolved experiments with a 200-fs resolution, (3) the polaron absorption, and (4) the continuous-wave photoluminescence emission. A clearer picture for the polaronic state can be derived from experiments on the ladder-type PPPs.

Singly charged states or polarons can be created in conjugated polymers via (1) exciton dissociation following the absorption of light, (2) chemical redox reactions, or (3) direct injection of electrons and holes into the organic film. Figure 8.10 summarizes this effect for ladder-type PPP. The polaronic species in all three cases have the same signature: two clear peaks at 1.9 and 2.1 eV plus higher-lying replicas with the same vibronic splitting as the ground-state absorption in these materials.

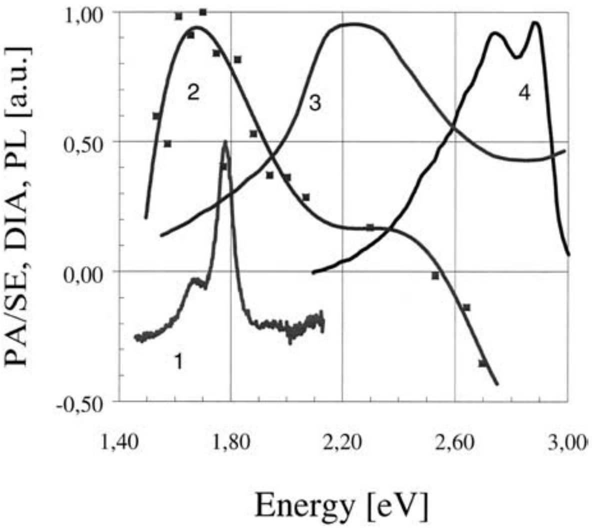

FIGURE 8.9. The solid line peaking at 1.78 eV (1) describes the triplet continuous-wave (cw) absorption spectrum of hexaphenyl; squares (2) represents the femtosecond pump/probe spectra at zero delay between pump and probe (solid line to guide the eye), (3) the polaronic absorption peaks at at 2.3 eV, and (4) the cw emission spectrum of peaks at roughly 2.9 eV.

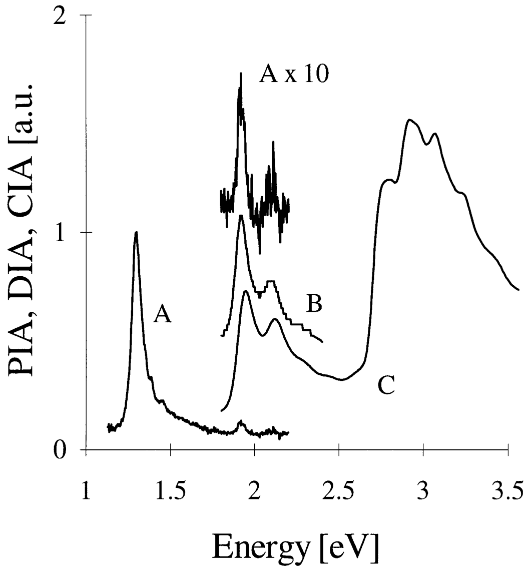

FIGURE 8.10. Doping-induced (C), charge-induced (B), and photoinduced (A) absorption in a ladder-type PPP.

High intrachain order and, therefore, low defect contents can be obtained in oligo/polyphenyls by forcing the PPP backbone into a planar ladder-type poly (*para*-phenylene) structure[26] (LPPP) in a very special synthetic route, which avoids torsional degree of freedom and decreases the concentration of chemical defects drastically. In order to prove that polymers obtained via this synthetic route have very low electronic defect contents, one can probe the electrical and optical signatures of charges (=polarons) trapped at such chemical defects. In agreement with results obtained on high-quality poly(*para*-phenylenevinylene) (PPV),[27] we find a very low number of long-living polarons created via photoexcitation. This is also illustrated by the very weak polaron signature in Fig. 8.10 [e.g., the photoinduced triplet absorption is much higher (for PPV, see Ref. 27)]. The results of a combined study of thermally stimulated currents and photoinduced absorption[28] revealed a number of electronic traps in ladder-type PPPs, which is on the order of 1 defect in 1000 monomer units.

8.2.6 Charge Transport

In *para*-phenylene molecules single charges exist in the form of positive and negative polarons (P^+, P^-) (i.e., a charge and the corresponding lattice distortion surrounding it). This can be shown by optical spectroscopy of *para*-phenylenes (Figs. 8.10 and 8.11). Films of *para*-phenylene molecules are wide-gap quasi one-dimensional semiconductors with respect to most of their properties. The electrical conductivity is determined by the product of carrier concentration and carrier mobility, forming so-called polarons which can be positive or negative. Therefore, the conductivity σ is a sum of both the conductivity of positive and negative polarons:

$$\sigma = en_{\mathrm{P}^-}\mu_{\mathrm{P}^-} + en_{\mathrm{P}^+}\mu_{\mathrm{P}^+}, \tag{2}$$

where n and μ are the concentration and the mobility of the respective species P^+ and P^-, and e denotes the elementary charge. In contrast to carrier injection, which depends on the properties of the polymer/electrode interfaces, carrier transport is a bulk property of the polymer layer. In organic electroluminescent devices, both interface and bulk properties are essential for the performance. The region of radiative recombination, for example, is determined by the different transport properties of negative and positive polarons.

Three different contributions determine the carrier concentration in organic semiconductors used as active layers in an electronic device:

- The intrinsic carrier concentration due to thermal excitation across the gap
- Carriers due to ionized defects
- Injected carriers

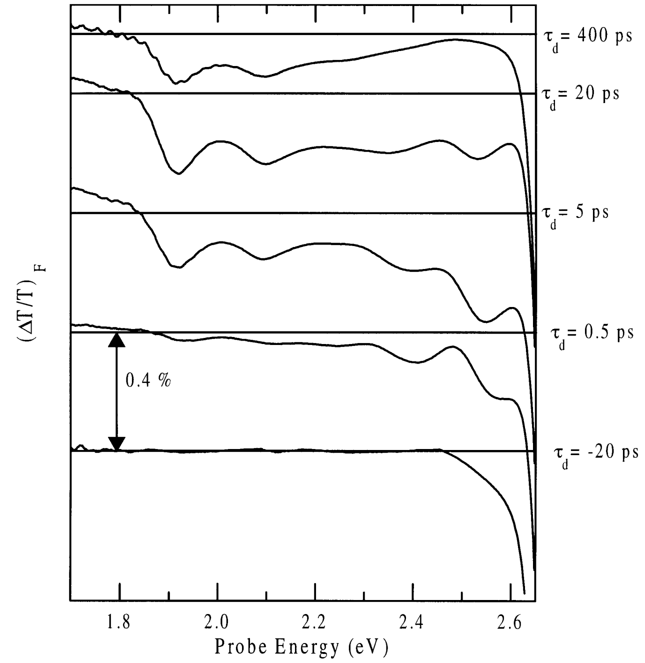

FIGURE 8.11. Femtosecond field-induced pump/probe spectra of ladder-type PPP at different pump/probe delays (τ_d). Within a few hundred picoseconds, the electric field leads to the dissociation of excitons which can be seen by (1) the decrease in stimulated emission at 2.4 and 2.55 eV and (2) the absorption of the created polarons at 1.9 and 2.1 eV. (Reproduced from Ref. 166.)

For an *intrinsic semiconductor*, the effective density of states $N_{C,V}$ of the valence (V) or conduction (C) band is given by the following relation:[29]

$$N_{C,V} = 2.4 \times 10^{19} \left(\frac{m^*_{C,V}}{m}\right)^{3/2} \left(\frac{T}{300\,K}\right)^{3/2} \text{cm}^{-3}, \tag{3}$$

where $m^*_{C,V}$ is the effective mass of the charge carriers, m is the electron mass, and T is the temperature of the semiconductor. Taking $m^*_{C,V} = m$ and $T = 300$ K, we obtain a value of 2.4×10^{19} cm^{-3} for the density of states. To obtain the intrinsic carrier concentration $n_i = n_p$ due to the thermal generation of charge carriers at a given temperature, the value of the energy gap E_g has to be known as well:

$$n_i = n_p = 2.4 \times 10^{19} \left(\frac{m^*_C m^*_V}{m^2}\right)^{3/4} \left(\frac{T}{300\,K}\right)^{3/2} \exp\left(-\frac{E_g}{2kT}\right) \text{cm}^{-3}. \tag{4}$$

Again taking the effective masses to be equal to the electron mass, using 300 K for room temperature, and using 2.7 eV for the energy gap of the ladder-type PPPs, we obtain an intrinsic carrier concentration of 10^{-4} cm^{-3}. This value will rise to 41 cm^{-3} upon increasing the temperature to 400 K. These values have to be compared to common inorganic semiconductors at room temperature: 2.7

carriers/cm^3 for GaP with an energy gap of 2.24 eV and 1.8×10^6 carriers/cm^3 for GaAs with a gap of 1.43 eV.

To determine the conductivity contribution from intrinsic charge carriers at 300 K, the carrier concentration of 10^{-4} cm^{-3} has to be multiplied by the elementary charge and the mobility, which is found around 10^{-4} cm^2/Vs in conjugated polymers.[30] This leads to a value of $1.6 \times 10^{-27} \Omega^{-1}$ cm. This value is in accordance with experiments by Chiu et al.,[31] who deduced the conductivity of pure PPP to be less than $10^{-17} \Omega^{-1}$ cm. The room-temperature conductivity of pure LPPP was determined to be $5 \times 10^{-15} \Omega^{-1}$ cm^{-1}. Its mobility is found to be higher than in typical conjugated polymers, namely 10^{-3} cm^2/V s.[145] PPPs in general are reported[2] to cover the range of 10^{-16}–$10^4 \Omega^{-1}$ cm^{-1}. The experimental values together with the calculated value for the conductivity due to intrinsic charge carriers show that the contribution of these carriers to charge transport is negligible. For completeness, we want to add here that the previous results were obtained in the conventional semiconductor model, developed for inorganic semiconductors. However, the weak coupling between the structural elements in nondegenerate conjugated polymers and oligomers and the moderate dielectric constant favors the description of conjugated materials in an exciton model. This will even further reduce the calculated concentration of charge carriers.

Chemical defects on the polymer chain may serve as sources for charge carriers. In PPP, it was shown that annealing samples at temperatures up to 250° C resulted in higher conductivities.[18] This effect was attributed to the increase of crystallinity[33,34] and, therefore, better mobility of charge carriers. However, increasing the annealing temperature beyond this value leads to the release of residual chlorine. Because the chlorine acted as a weak electron acceptor, its release leads to a decrease of conductivity, stressing the role of defects as sources for charge carriers. Instead of relying on residual impurities, charges can also be added to PPP by redox reactions; the introduction of a finite charge carrier concentration by a redox reaction even started the whole field of conducting conjugated polymers.[35] By doping with strong oxidizing or reducing agents, PPP is converted to a metallic conductor.[36] An ionic process such as the dominating charge transport mechanism was excluded and the electronic nature was established by a series of experiments comprising the thermal annealing of PPP.[31] Unfortunately, the strong doping required to achieve high conductivities such as 200 S/cm^{-1} quenches luminescence totally.[37] However, the defects present in the "pure" materials still occur at concentrations high enough to influence charge transport. In the following paragraphs, we want to summarize which kind of defects are believed to occur in conjugated polymers and their influence on charge transport.

From picosecond transient photoconductivity measurements on PPP films,[22] we know that mobile charged states decay within 110 ps. In conventional routes to PPPs, defects like branched chains and large torsion angles of neighboring rings are known to occur. These defects act as shallow or deep traps for positive and negative polarons,[38,39] which limit the mobility of charge carriers.[40] The synthetic route toward the PPP-type ladder-polymers prevents the described defects and leads to a trap concentration of less than 1 trap per 1000 monomer units,[28] whereas substituted PPV, for example, exhibits trap concentrations of one trap per monomer.[41] The former value, which corresponds to a concentration of 10^{17} traps/cm^3, further emphasizes that intrinsic carrier concentrations of 10^{-4} cm^{-3} are negligible for electrical transport in the PPPs.

For a quantitative treatment analogous to intrinsic charge carriers, we have to take the defect concentration N_d and the energetic defect-band distance E_d into account:

$$n_d = \sqrt{2N_d}\left(\frac{m_e kT}{2\pi\hbar^2}\right)^{3/4} \exp\left(-\frac{E_d}{2kT}\right)\ \mathrm{cm}^{-3}. \tag{5}$$

Trapping of charge carriers plays an important role in these materials, because the I–V-curves are also influenced by trapped charges.[42,43] These space charges distort the fields in the charge injection region at low voltages. From time-of-flight measurements, it is known for PPVs that negative polarons, in contrast to positive ones, are severely trapped,[40] which results in an unbalanced charge transport. The influence of unbalanced charge transport on the device operation was shown for PPV, where the limitation of the charge transport by traps leads to a bias-dependent efficiency:[44] At low bias, the injected electrons, which convert into negative polarons, are trapped and do not contribute to the radiative recombination process. With increasing bias, the traps are filled, giving rise to a strong increase of the number of free polarons, which participate in recombination; hence, it increases the device efficiency.

For a comprehensive treatment of *charge injection* and the importance of this process in device operation, we point to the subsequent section, in which this topic is described in detail.

8.3 Electroluminescence

Electroluminescence (EL) is the generation of light induced by an electrical current. Around 20 years after the invention of electroluminescence in 1907 by H. J. Round,[45] the first reports on organic electroluminescence were presented.[46,47] However, it lasted until the 1990s that the interest in science and industry on organic EL rapidly increased after Tang et al.[48] had presented thin-film organic EL based on organic metal complexes and Friend et al.[49] had demonstrated thin-film EL devices based on conjugated polymers.

8.3.1 Single-Layer LED Based on PPP-Type Polymers

After the application of conjugated polymers as organic semiconductors in light-emitting devices has been demonstrated,[49,50] poly(*para*-phenylene) (PPP) was the first simple conjugated polymer to produce visible blue light emission when used as an active layer in polymer LEDs.[51]

Light-emitting diodes (LEDs) based on PPP[52] (see Fig. 8.12), obtained by a precursor polymer route after Ballard et al.,[53] give blue-light emission ($\lambda_{\max} =$

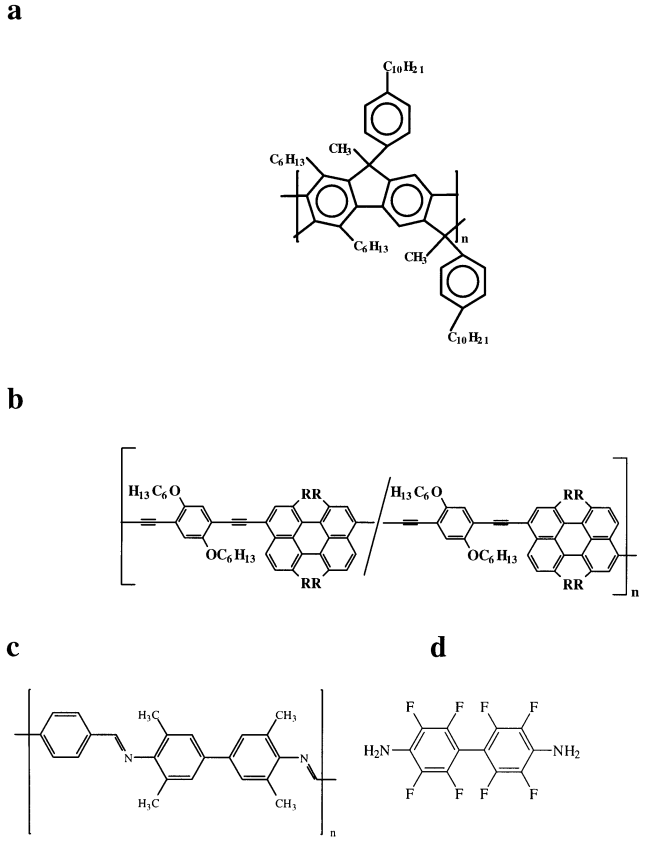

FIGURE 8.12. Chemical structure of materials used for the production of organic light-emitting diodes: (a) poly(*para*-phenylene) (PPP); (b) alkoxy-substituted PPP; (c) ladder-type PPP; R_6:C_6H_{13}; R_{10}: $C_{10}H_{21}$; LPPP (Y:-H) or m-LPPP (Y:-CH_3), LPPP block copolymer; (d) hexaphenyl; (e) poly(perylene-*co*-diethynyl benzene) (PPDB); R=phenoxy-t-butyl); (f) oligoazomethine (OAM); (g) diaminoctofluorobiphenyl (DOB).

470 nm, see Fig. 8.13) and show EL efficiencies up to 0.05% [with indium–tin oxide (ITO) and Al as the electrodes].[51–55] This value for the EL efficiency is remarkably high, if one considers the appreciable disorder and high impurity concentrations due to the film formation process in the PPP material prepared by this precursor technique. The working principle of LEDs based on polymers with such a high defect concentration can be described similar to Schottky-type diodes.[51,56] A substantial improvement of the performance of the polymer in EL devices was expected for the following:

- Using soluble PPPs (achieved by solubilizing side chains); Section 8.3.1.1
- Tying the PPP backbone into a planar, rigid ribbon structure (see Fig. 8.12), so that a polymer of a defined conformation is obtained; Section 8.3.1.2
- Using oligomers of PPP instead of the polymer; Section 8.3.1.3

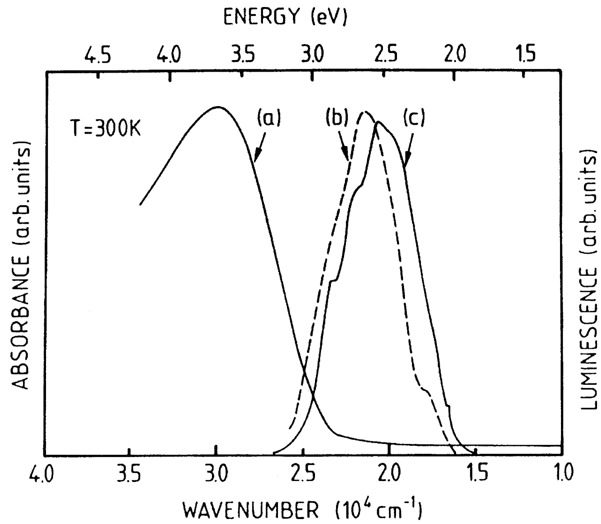

FIGURE 8.13. Absorption, PL, and EL of PPP obtained from the precursor route. (Reproduced from Ref. 54.)

8.3.1.1 EL Devices Based on Soluble PPPs

The emission spectra of PPP having solubilizing side chains are blue-shifted compared to that of PPP because of the steric hindrance of the side chains, which leads to an increased twisting angle between the phenyl rings (see Sec. 3.1.2). Alkoxy-substituted PPPs (see Fig. 8.12) were successfully applied in polymer LEDs.[57–62] Yang et al.[59] reported EL quantum efficiencies of 1.8% in single-layer devices using ITO and Ca as the electrodes and up to 0.8% (with ITO and Al) in polymer LEDs based on poly(2-decyloxy-1,4-phenylene) (DO-PPP). In order to obtain pinhole-free layers with that polymer, the active-layer thickness has to be increased to a value of around 300 nm, which is distinctly above the typical thickness d of the active layers in LEDs. In single-layer LEDs based on such a polymer with a low defect concentration, the electric field E seems to be the driving force for charge carrier injection.[56] For that reason, comparably high threshold voltages ($=Ed$) above 15 V are observed in LEDs based on DO-PPP.[59]

With LED based on alkoxy-substituted PPPs, Cimrova et al. realized polarized light-emitting devices by casting the active polymer layer by a Langmuir–Blodgett technique, in order to arrange the polymer chains parallel to the plane of the substrate.[63]

8.3.1.2 EL Devices Based on Ladder PPPs

This approach has been realized by Scherf and Müllen in the synthesis of ladder-type PPP (LPPP); (see Refs. 26, 64, and 65). In the following, an overview over the performance of polymer LEDs based on LPPP-type polymers is presented.

Ladder-type PPP is a soluble and easily processible polymer. The LPPP (with a hydrogen atom at the substitution position R_1, see Fig. 8.12) shows a PL quantum efficiency higher than 70% in solution.[66] The optical and electronic properties of the LPPP are well characterized (see Sec. 8.2).[67–70] The LPPP polymer was successfully used in EL devices, but an improvement of the EL efficiency and lifetime compared to PPP, which was expected especially due to the high intrachain order, was not obtained[69–73] (except for m-LPPP; see the next paragraph). The EL and the PL spectra of the LPPP are dominated by a yellowish component due to interchain interaction leading to the formation of aggregates in the ground state or in the excited state (excimers).[66,70] The influence of the aggregate emission on the emission color in LEDs is discussed in the next subsection. It has been shown that the broad shape of the EL spectrum can be changed from red to blue by varying the thickness of the active LPPP layer due to interference phenomena in Au/LPPP/Al devices.[74] These aggregate formations in LPPP are initiated by temperature[75] and, to a lesser extent, by degradation processes of the polymer. The degradation of the LPPP is the limiting factor for the application in polymer LEDs and mainly occurs via a photo-oxidation of the hydrogen atom (at substituent position R_1; see Fig. 8.12) induced by the combination of oxygen and ultraviolet light.

To improve the environmental stability, a LPPP polymer was synthesized by Scherf et al. with a methylene group on the position of the substituent R, (compare Figs. 8.1 and 8.12). This so-called m-LPPP shows the highest and most uniform effective conjugation length in the family of the LPPPs up to now and exhibits, as a consequence of its high intrachain order, a PL quantum efficiency with values up to 100% in solutions and higher than 30% in thin m-LPPP films. The EL devices produced with m-LPPP as the active layer show already high EL quantum efficiencies with maximum values around 1%,[5] when used as single layer with Al and ITO as the electrodes. Moreover, this m-LPPP polymer does not show the yellowish emission color of the other LPPP homopolymers, but it exhibits a bluish emission color (see Fig. 8.14) (similar to the LPPP copolymers).[69,76]

The absorption spectrum of m-LPPP (see Figs. 8.5 and 8.14) is characterized by a steep onset of the absorption above the energy gap ($\alpha_{\max} \approx 1.1 \times 10^5\ \mathrm{cm}^{-1}$ at 453 nm) and a very low subgap absorption ($\alpha_{\min} < 12\,\mathrm{cm}^{-1}$).[4,5,77] The minimum value of α is more determined by scattering effects than by true absorption, so that this value can be drastically decreased if the film quality of the polymer film is further improved, which is essential for the application of this polymer in waveguide structures for optical[23,78,79] and electrically pumped lasers.

8.3.1.3 EL Devices Based on PPP-Type Oligomers

Some oligomers of PPP are very suitable as blue-light-emitting material in LEDs due to their high PL efficiency and high environmental stability. These oligomers are most efficient in LEDs when applied in their insoluble unsubstituted form by vacuum deposition (as hexaphenyl;[22,80,81] see Sec. 8.3.2). Recently, PPP-type oligomers, which have been realized by a Spiro-type coupling of two oligomers, have attracted much interest for application LEDs, as this spiro systems form either

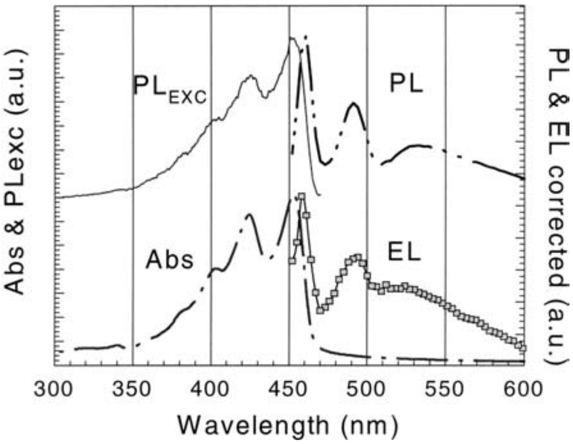

FIGURE 8.14. Absorbance spectrum (–.–), PL excitation spectrum (—) (emission at 491 nm), PL emission spectrum (–..–) (excitation at 420 nm), and EL spectrum (squares) (ITO/m-LPPP/Al) of a m-LPPP layer ($d \approx 90$ nm) (PL and EL are corrected for self-absorption).

amorphous or highly crystalline thin films.[82] Quarter- and hexaphenyl oligomers have also been incorporated in block copolymers, which have been used as active layers in LEDs.[83]

8.3.2 Emission Colors

As outlined in the previous sections, the isolated polymer chains of the class of PPPs are characterized by a bluish emission color. However, for some PPPs (e.g., some ladder-type PPPs; see Sec. 8.3.1), significant emission occurs in the yellow spectral range. This is due to an interchain emission process where various different polymer chains are involved in one emission process. This so-called aggregate emission will preferably occur, if the polymer backbones are densely packed one over the other (see also Ref. 84). One can assume that such a type of packaging can easily occur for polymers consisting of a rigid planar backbone (e.g., LPPPs) (similar interchain emission effects as have also been observed in polyfluorenes.)[85] For that reason, such aggregate emission processes usually dominate the emission spectra of LPPPs except for LPPP block copolymers (consisting of LPPP and PPP-type subunits)[66,73,86–88] and except for m-LPPP, where a cross-linking between polymer chains, which occurs during the synthesis, seems to prevent the aggregate formation.[89] EL efficiencies up to 0.4% were reported for the LPPP block colpolymer.[73,86]

The blue EL emission color, which, for example, can be realized with these PPP-type polymers, is absolutely necessary for the application of polymer LEDs in self-emissive flat-panel color displays. Moreover, any visible emission color can be realized with the blue emission because blue is located at the high-energy side of the visible spectral range.

The realization of red–green–blue (RGB) color dots (pixels) building up a color flat-panel display (CFPD)-based polymer LEDs can be achieved via several techniques:[56]

1. Blue, green, and red light-emitting organic LEDs[90,91]
2. Organic LEDs tunable from blue to red emission controlled by the voltage,[56,92–96] current, local temperature, or another device parameter
3. Large-area EL devices with a spectrally broad white emission, covered with red, green, or blue absorption filters or broad-band width emitter assembled in microcavity structures[97,98]
4. Blue large-area EL devices covered with appropriate dye layers, which *convert* the blue EL emission into the required emission color.[99–103]

Methods 1 and 4 are currently the most promising ones for realizing multicolor devices. The latter method exhibits the advantage that the whole display can be built up with the same blue-light-emitting polymer LED, so that the same I–V response for all pixels (in contrast to the method 1) can be expected.

From the PPP-related materials, especially the oligomer *para*-hexaphenyl (PHP) (see Fig. 8.2) seems to be very suitable for such an external energy conversion process. This is due to the highly efficient EL devices, which can be fabricated based on PHP and due to the deep blue PHP emission with an emission maximum located at 425 nm.[104] With that material, a substantial increase of the efficiency and a reduction of the onset voltages has been achieved in multilayer structures (see Sec. 8.3.3).[105,106]

8.3.3 LEDs Based on Multilayer Structures

The overall performance of single-layer polymer LEDs can be drastically improved if hole- and/or electron-transport layers are inserted at the interface between the polymer and the electrodes (see Fig. 8.15).[107,108] The working principle of single-layer and multilayer LEDs, which is outlined in Refs. 56 and 109, can be well described in various models.[110–112]

The influence of charge-transport layers in polyphenylene devices can be visualized by looking at the properties and performance of single-layer and multilayer EL devices based on the oligomer *para*-hexaphenyl (PHP).

When the function of the charge-transport layer in LEDs is discussed, one has to consider that the quality and the properties of the interfaces between the electrodes and the organic layers strongly affect the device performance.[113–116] Important parameters in that concern are the interdiffusion range[117] of the electrode material into the organic material and the interaction[113,116] between the electrode material and the organic material at the interface. The insertion of transport layers between the active layer and the electrodes is also a means to control or to change the interface region in the polymer, which, in fact, strongly depends on the preparation conditions.

In air-stable single-layer EL devices based on PHP with ITO and Al as electrodes, highly efficient blue LEDs (EL quantum efficiency up 1%) are obtained,[80,104]

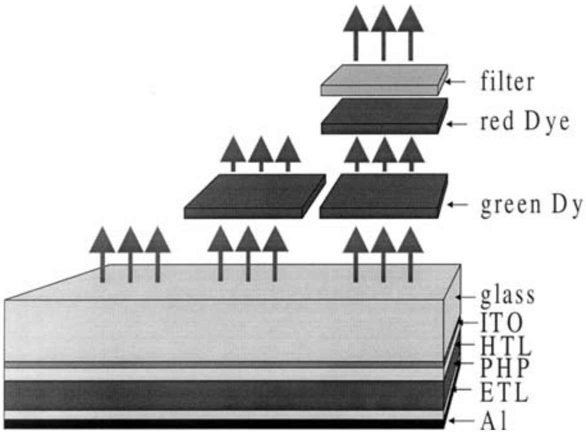

FIGURE 8.15. Construction of the organic LED: glass substrate/transparent electrode indium–tin-oxide (ITO)/hole-transport layer (HTL)/active layer *para*-hexaphenyl (PHP)/ electron-transport-layer (ETL)/aluminum (Al). The blue PHP electroluminescence emission light is converted by covering the PHP organic LED with a green dye layer (→green emission color) and a red dye layer together with a suitable dielectric filter (→red emission color).

although the band discontinuities at the interfaces in this configuration are of the order of 1 eV. The latter value is just a crude estimation obtained by calculating the difference between the literature values for the workfunction of the electrodes[118] and band edges of the oligomer.[119]

By applying an oligoazomethine (OAM) (see Fig. 8.12) as a hole-transport layer (HTL) between the ITO and PHP, the electric field required for the onset of the current in the forward direction is decreased (see Fig. 3.16).[105,106] For the ITO/OAM/PHP/Al structures, the onset of the electric field occurs at values of around 0.3 MV/cm compared to 0.8 MV/cm obtained for single-layer PHP under the same preparation conditions. OAM has been produced by a poly-condensation reaction of the successively deposited monomers in a vacuum chamber.[120] The decrease of the onset electric field with the application of OAM as the HTL compared to single-layer devices can be attributed to a reduction of the barrier height at the anode/HTL interface. The increased EL quantum efficiency of up to 2% emitted photons/injected electron is attributed to reduced quenching effects of the emitting species at the electrodes[121] because the recombination is spatially separated from the electrodes by the insertion of OAM.

In a multilayer structure applying electron-transport and hole-transport layers, the advantages, which are contributed by each layer, can be combined.[122] In the case of the PHP devices, the best EL quantum efficiencies ($> 2\%$), the lowest electric threshold field (≈ 0.25 MV/cm) (see Fig. 3.16), and the best stabilities up to now are obtained in a multilayer structure ITO/OAM/PHP/diaminoctofluorobiphenyl/Al (see Fig. 3.16).[105,106,123]

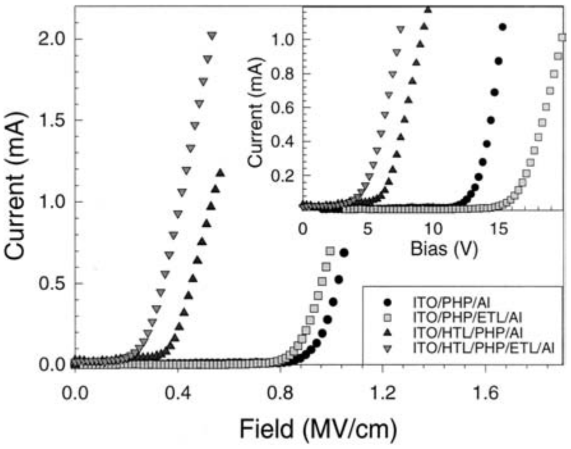

FIGURE 8.16. Current versus electric field characteristics for PHP single-layer and multilayer EL devices (inset: current versus bias voltage).

These efficient and bright multilayer LEDs based on PHP can be used to generate *any* other visible color by a *down* conversion process. An efficient color conversion can be realized by covering the EL device with appropriate dye/matrix layers of high PL quantum efficiency (*external color conversion technique*).[101,102] A dye absorbing in the blue spectral range is excited when illuminated with the blue PHP EL emission and, subsequently, emits PL light in a lower energetic range. The spectral range of the emitted light can be narrowed (or specifically shaped) with a minimum energy loss by a dielectric mirror/filter, so that spectrally pure emission light is obtained.

Regarding the realization of color flat-panel displays, the efficient production of the two other basic colors (besides blue), green and red, is of great interest. With this all-organic color-conversion technique, RGB emission colors with CIE coordinates (blue: $x = 0.15$, $Y = 0.06$, green: $x = 0.27$, $y = 0.62$; red: $x = 0.65$, $y = 0.34$) similar to the basic colors which are commonly used in commercial color displays were produced (see Fig. 8.17).[101] The spectra of the blue PHP EL emission together with the converted green and red emission light are presented in Fig. 8.17. Practically, the green was produced by covering the blue-emitting device with a layer of the dye coumarin 102 in poly(methylenemethacrylate) (PMMA) (optical density$>$ 3). The absolute external conversion efficiency from the blue PHP EL emission into the green was recorded to be around 40%.[101] In this case, the green emission (luminance$\approx$ 1100 Cd/m^2) is around three times brighter to the human eye than the blue pumping light from the PHP (360 Cd/m^2). This is due to the fact that the human eye sensitivity is much higher in the green spectral range than in the blue.

To obtain emission colors in the red–orange spectral range, the red dye layer usually has to be coupled with the green dye layer in order to transform the blue excitation light into the green spectral range, where the absorption of the red

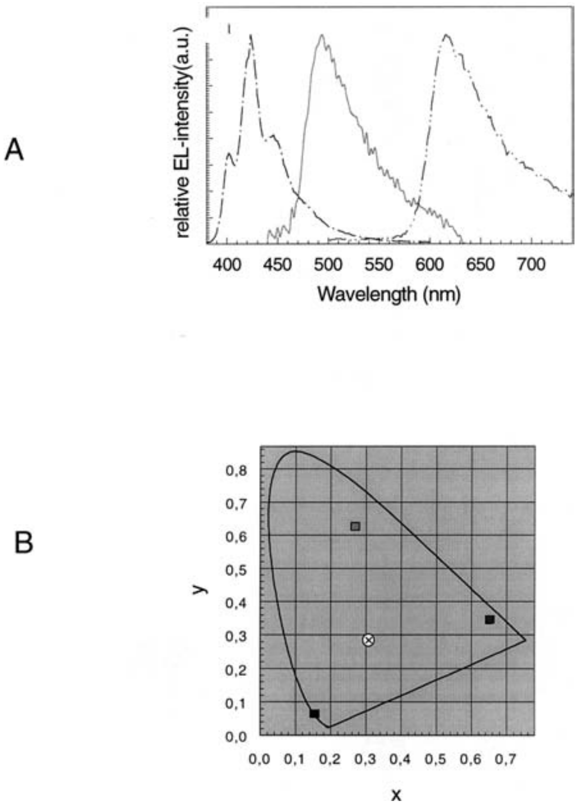

FIGURE 8.17. (a) From left to right: electroluminescence of the PHP organic LED (–.–), photoluminescence of the green dye (—), and the red dye (–..–) excited by the PHP EL emission; the spectra are normalized for better visibility. (b) CIE graph containing the CIE coordinates of the produced RGB colors (squares) compared to RGB colors used in cathode-ray tubes (circles) (the dotted line marks all colors, which can be produced by the RGB colors).

dye is much higher than in the blue range. This can be realized by covering the coumarin/PMMA layer with a layer of the red dye Lumogen F300 in PMMA.[101]

The experimental conversion quantum efficiency, which was reported to be 10% for the conversion from blue to red (via green),[101] can be significantly increased when the phase matching of the dye/matrix layers to the EL devices is improved, so that waveguiding losses are reduced.[102] This can be experimentally realized by directly depositing the color-conversion layer onto the device. Quantum efficiencies for color conversion from the blue into the green of around 90% and for the blue into the red of around 80% can then be obtained.[102,103] With this external excitation energy-transfer technique, a significant improvement of the power efficiency can be achieved: Based on a blue PHP LED with a power efficiency of

0.5 lm/W, one obtains pure green emission of a power efficiency of 3.5 lm/W and pure red emission of a power efficiency of 1.3 lm/W.

8.3.4 LEDs Based on Polymer Blends

The properties of various polymers can be combined if blends of polymers are used in the active layer of LEDs.[124,125] Compared to a LED consisting of a single polymer, significantly different device characteristics with respect to its electrical and its emission properties are obtained. One precondition for the polymers to be blended together is that they are miscible and therefore possess similar dissolution properties because the layer is cast from the same solution (and therefore it is critical to use these polymers together in multilayer structures). For instance, in devices based on alkoxy-PPPs, a significant increase in the efficiency (up 2%)[59] was obtained by blending the active layer with electron- and/or hole transporting materials.

In addition to the opportunity to increase the overall device performance in LEDs based on polymer blends,[126,127] another interesting aspect is that their emission color can be internally converted.[128–130] Based on blue-light-emitting polymers,[131] therefore, any other emission color can be realized for those also, which intrinsically are difficult to achieve with pure conjugated polymers, as is the case for pure white[132,133] and red[134,135] emission colors.

The internal color-conversion technique—in contrast to the external color conversion technique described in Section 3.3—is based on an internal excitation energy transfer (Förster transfer) and charge transfer from the wide-bandgap host to the low-bandgap guest material, so that a down conversion of the emission color is achieved. In order to realize efficient and stable LEDs with this technique, guest materials with a high PL quantum efficiency and/or good charge-transport properties are required.[131]

An efficient internal color-conversion technique will only occur if the polymers in the blend are only weakly phase separated. Otherwise, the various polymers in the blend behave similar to independent parallel diodes and hence a strongly voltage–dependent emission color will be observed.[131,137]

In the following, we discuss an internal color-conversion technique based on m-LPPP devices as an example.[131,137] The absorption and PL spectrum of a poly(perylene-*co*-diethynyl benzene) (PPDB) films[131] are depicted in Fig. 8.18. In the m-LPPP/PPDB films, no phase separation can be detected within the resolution ($>$ 10 nm) of an atomic-force microscope (tapping mode), which, as described earlier, is one of the preconditions for a stable internal color conversion. When the energetic levels of the two polymers are compared, it can be seen that the ionization potential and the lowest excited states of PPDB are located inside the energy gap of m-LPPP (see Fig. 8.19). An effective excitation energy transfer therefore occurs from the m-LPPP into the PPDB, where they have a high probability for radiative recombination, so that a significant increase in the PL efficiency can be achieved (see Fig. 8.19).[138] The solid-state PL efficiency of m-LPPP increases from $\eta_F \approx 30\%$ by doping of the red-light-emitting polymer PPDB into m-LPPP

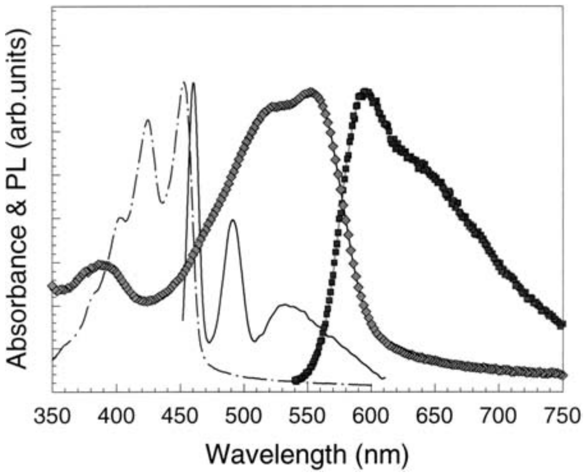

FIGURE 8.18. Absorption of m-LPPP (–.–), photoluminescence of m-LPPP (—), absorption of PPDB (diamond), and photoluminescence of PPDB (squares).

UP to $\eta_F \approx 41\%$ for very small PPDB concentrations of 0.7% in the blend. For higher doping concentrations, η_F then slowly decreases (down to 11% for a concentration of 10% PPDB in the blend) and approaches the η_F-value of pure PPDB films, which only is 0.6% (see Fig. 8.19).

The PL spectra of the m-LPPP/PPDB blends were recorded at an excitation wavelength of 420 nm, where mainly m-LPPP is excited, because the absorption of m-LPPP in the blend at this wavelength is much stronger than that of PPDB (see Fig. 8.20). The PL spectra of this blend, in which the concentration of m-LPPP is much higher than that of PPDB, however, are dominated by the red-orange PPDB emission due to an efficient energy transfer from m-LPPP to PPDB (see Fig. 8.20).

The color conversion occurring in the EL cannot be solely ascribed to an excitation energy transfer (Förster-type), because the change in the emission color and the dependence of the EL efficiency on the doping concentration are slightly but distinct different from that of the PL (see Figs. 8.19 and 8.20). We therefore propose that additional to the Förster transfer, a charge transfer (polarons) occurs from m-LPPP to PPDB.

For the LEDs based on m-LPPP:PPDB, a maximum external EL quantum efficiency of 1.6% is obtained for doping concentrations of only 0.2 wt% PPDB in m-LPPP (see Fig. 8.19). This value is higher than that of single-layer LEDs based on pure m-LPPP (maximum η_{EL} under cw operation around 1%; see Sec. 8.3.1).

In organic LEDs, the EL quantum efficiency η_{EL} can be described in a simplified way using the following equation:[139]

$$\eta_{\mathrm{EL}} = \gamma \eta_R \eta_F, \tag{6}$$

where γ is a double charge injection factor, η_R is the efficiency of singlet-exciton formation, and η_F is the quantum efficiency of fluorescence.

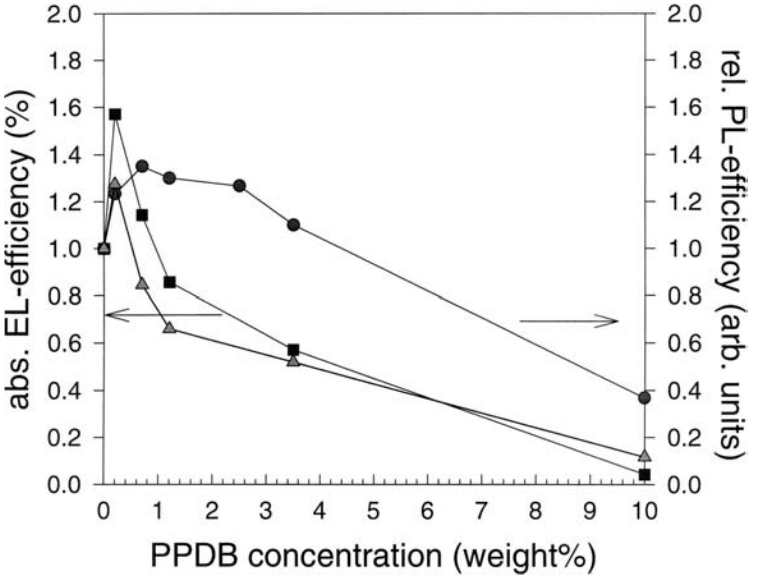

FIGURE 8.19. (a) Absolute electroluminescence quantum yield η_{EL} (■), relative photoluminescence quantum yield η_F (●), and the efficiency of singlet exciton formation η_R (σ) [obtained from Eq. (1) using the experimental data for η_{EL} and η_F, under the assumption that γ = constant] of the m-LPPP/PPDB blend depending on the PPDB concentration (in wt %) in the blend. (b) Scheme of the energetic levels of m-LPPP and PPDB. The values for the highest occupied states were deduced from cyclic voltammetry. The position of the excitonic levels was obtained by adding the energy gap to the ionization potential. The difference between exciton states (E_S) and the lower edge of the unoccupied states corresponds to the exciton binding energy ($E_B \approx 0.5$ eV for m-LPPP). (Reproduced from Ref. 167.)

At least one of the two other parameters in Eq. (6), besides η_F, strongly depends on the PPDB concentration in the blend because the EL and PL efficiencies depend in a different way on the PPDB concentration in the matrix (see Fig. 8.19). The charge carrier injection and, implicitly, γ are only slightly influenced by doping m-LPPP with PPDB (for PPDB concentrations up to 3.5%), as the threshold electric field and the slope of the current and of the EL intensity of these EL devices are not significantly different compared to homopolymer m-LPPP devices.

In contrast, the third factor in Eq. (6), the efficiency of singlet-exciton formation, η_R, is strongly altered by the amount of PPDB (see Fig. 8.19). For *low* concentrations of PPDB ($< 0.2\%$) in the polymer blend, the charge transport in the EL device is mainly provided by m-LPPP. PPDB acts as effective trap for electrons and holes in the blend and, therefore, enhances the singlet-exciton formation η_R at the PPDB sites. However, for higher PPDB concentrations ($> 0.2\%$), the effective trapping of positive and negative charge carriers is a drawback for efficient singlet-exciton formation because the charge transport is, therefore, strongly decreased.[131]

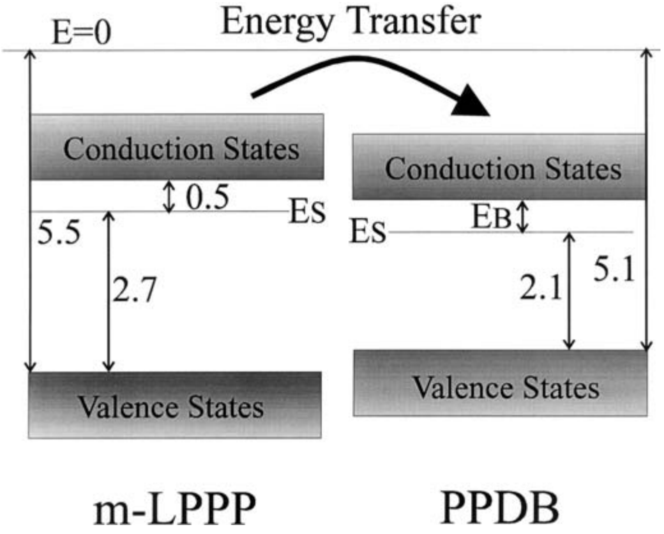

FIGURE 8.20. Electroluminescence (recorded from an ITO/m-LPPP:PPDB/Al device with a bias voltage of 15 V; $d_{\text{polymer}} \approx 85$ nm) and photoluminescence ($\lambda_{\text{excitation}} = 420$ nm) spectra of the m-LPPP/PPDB blend depending on the PPDB concentration in the blend.

Additionally, the efficiency for radiative recombination η_F of the created emitting species decreases for higher PPDB concentrations, so that according to Eq. 6, the EL efficiency is strongly reduced for high PPDB concentrations in the blend (see Fig. 8.19).

The internal color conversion in the m-LPPP:PPDB blend can also be used to realize a stable white EL emission, which could be applied to realize a multicolor display according to the method in Sec. 8.2 or it could be used as backlight (e.g., for LCDs).[137,140]

The blue m-LPPP emission can be quantified in CIE coordinates[141] $x = 0.24$ and $y = 0.30$ (see Fig. 8.21). In dilute (nonpolar) liquid or solid solutions of PPDB, the PL spectrum ($\gamma_{\max} = 580$nm) gives an orange color (CIE coordinates $x = 0.53$, $y = 0.46$).[140]

According to colorimetry, the coordinates of a color, which is produced by the mixture of two colors, can be found on the connecting line between the coordinates of the two colors in the CIE graph. A mixture of the m-LPPP and PPDB emission colors therefore can produce white-light emission near the equienergy white point ($x = 1/3$, $y = 1/3$) (see Fig. 8.21).

A white-light-emitting polymer LED (CIE $x = 0.31$, $y = 0.33$) can be obtained when using an 80-nm active layer of a m-LPPP/PPDB polymer blend containing 0.05 wt% PPDB.[140] Polymer LEDs of that concentration emit stable white light to the human eye fairly *independent* of the bias voltage.[131] The external EL quantum efficiency of the white polymer LED is around 0.8%, which represents the highest value reported for single-layer white polymer LEDs up to now. The EL efficiency

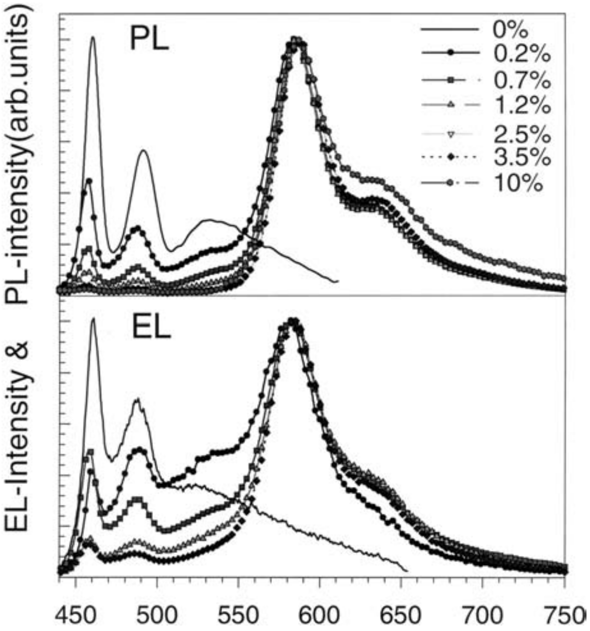

FIGURE 8.21. (a) EL (—) spectrum of m-LPPP ($d_{\mathrm{m-LPPP}} = 100\,\mathrm{nm}$), PL spectrum of PPDB-solution (squares) compared to EL spectra of the white organic LED ITO/m-LPPP:PBD/Al (thickness of active polymer layer is 80 nm) recorded at 30 V (circles); (b) CIE coordinates of the EL of m-LPPP ($x = 0.31$, $y = 0.33$), the PL of a PPDB ($x = 0.53$, $y = 0.46$), and the white polymer LEDs operated at 30 V ($x = 0.31$, $y = 0.33$).

of this white polymer LED can be further increased up to 1.2% by introducing PMMA 140 in the polymer blend.[140]

8.3.5 Light-Emitting Electrochemical Cells Based on PPPs

As mentioned earlier, light-emitting diodes based on conjugated polymers (polymer LEDs) can be realized with high efficiencies over the whole visible spectral range.[49,51,56,107,142,143] The most attractive potential application of polymer LEDs is their use in emissive flat-panel displays. In order to realize polymer LEDs with operating lifetimes which fulfill the values required for industrial applications (> 10, 000 h), efficient devices are required with operating voltages that are close to the lowest values that are energetically possible. Low operating voltages are more easily realized with small-band-gap conjugated polymers, because the mismatch between the energy bands of the polymers and the workfunctions of the electrodes[56] is smaller than for wide-band-gap polymers. Thus, it has been proven to be easier to realize red-orange and green polymer LEDs with low operating voltages and high power efficiencies. For these emissions, color power efficiencies up to 16 lm/W have been reported.[144] In order to achieve similar power efficiencies with LEDs based on m-LPPP, the PL efficiency of the polymer has to be improved.

Furthermore, polymer blends have to be applied consisting of excellent miscible guest materials with high PL efficiency and appropriate energetic levels relative to m-LPPP for an charge and energy transfer. Furthermore, the electron transport in devices based on m-LPPP, which has a significantly higher hole mobility ($\approx 10^{-3}$ cm^2/V s) than PPV and its derivatives,[145] has to be increased by improved device architectures.

However, the fabrication of blue polymer LEDs with sufficient lifetimes is absolutely necessary to realize multicolor flat-panel displays (see Sec. 8.2). Recently, a new type of polymer light-emitting device, the polymer light-emitting electrochemical cell (LEC), has been presented,[146,147] which has the advantage that the EL onset occurs for *all* emission colors at a bias voltage which is equal or even below the single-particle gap $E_{g,s}$ divided by the elementary charge.[148] The different performance of LECs compared to polymer LEDs is due to the fact that the charge carrier injection in these devices relies on completely different physical mechanisms.[56] In contrast to polymer LEDs, in LECs, an electrochemical doping of the conjugated polymer occurs, due to the interaction of ions with the injected positive and negative charges. This process takes place at both electrodes and, hence, a *p*- and a *n*-type doped region is created and the whole device forms an in situ created *p*-*i*-*n*-junction.[146]

The formation of the *p*-*i*-*n* junction is not an instantaneous process but depends on the mobility of the ions in the three-component blend consisting of an electron conductive and light-emitting polymer, an ionic conductive polymer, and an ionic salt. Therefore, the response times of conventional LECs typically are longer than those of polymer LEDs. However, if the motion of the ions can be suppressed after the junction has been formed, the response of the LECs can be drastically increased and it, therefore, should be possible to obtain fast response times similar to LEDs.

The first LECs based on a polymer from the family of the polyfluorenes was presented by Yang and Pei.[149] They used a poly(ethylene oxide) (PEO) with oligoethylene (ionic conductive) side chains. This polymer, which combines electronic and ionic transport properties, shows a bluish color in the emission of the LEC turning into a yellowish one after some time of operation. The response times of these LECs were rather long (in the range of minutes), but a very high efficiency and a high brightness were achieved.

Also, m-LPPP is very suitable to act as an active layer in LECs:[150] by using a blend of m-LPPP, PEO, and $LiCF_3SO_3$ in a weight ratio of 20:10:3, luminance values of around 250 Cd/m^2 were obtained at an operating voltage of 10 V.[150] The reported values for the external EL quantum efficiencies (0.3%)[150] of these LECs are below that obtained for ITO/m-LPPP/Al LEDs ($\eta_{EL} < 1\%$; see Sec. 8.1), but the threshold voltages of the LECs are distinct below that for LEDs.

The I–V and L–V characteristics of LECs based on m-LPPP do not show the characteristic symmetric shape usually observed in LECs. In contrast to polymer LEDs, the current–voltage (I–V) and the luminance–voltage (L–V) characteristics for LECs, which are not operated in a frozen junction regime (see below) should be fairly symmetric. This holds even for different electrode materials, because

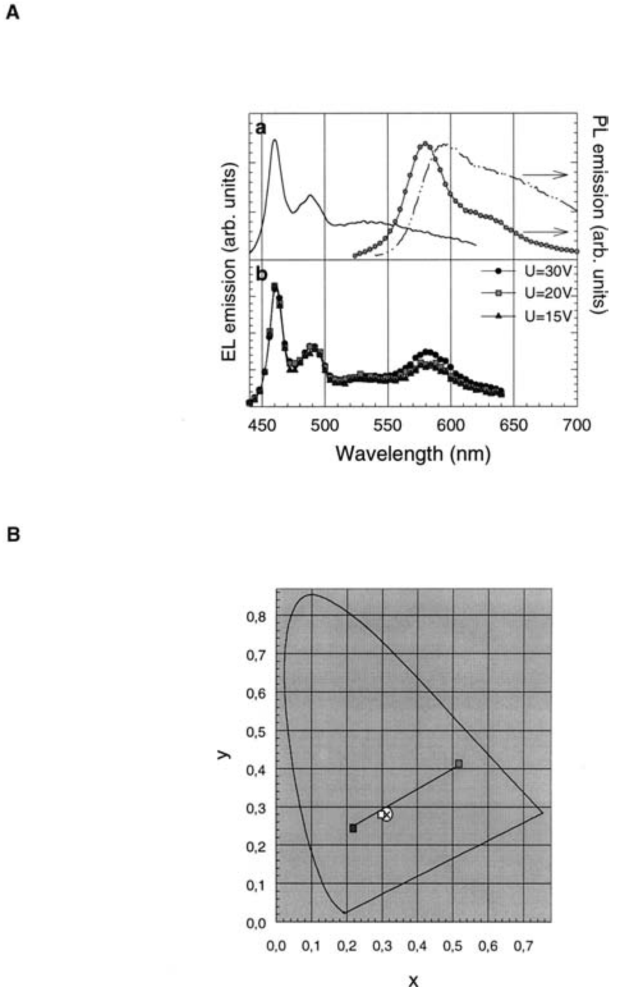

FIGURE 8.22. Current–bias and brightness–bias characteristics of an ITO/m-LPPP:PEO:$LiClO_4$/Al LEC (●, brightness; ■, current). The concentration of m-LPPP:PEO:$LiClO_4$ is 20:10:3. The thickness of the active layer is 200 nm. The characteristics were recorded in a pulsed mode with stepwise increase in the applied voltage.

the contacts between the electrodes and the relatively high doped polymer are of ohmic character (see Refs. 146–148 and 151).

In reverse bias [bottom electrode (e.g., ITO) as the cathode], light emission was clearly observable with the naked eye above 2.7 V, with Al as the top electrode (see Fig. 8.22). For LECs with ITO as the bottom electrode and Au as the top electrode, even the lower onset voltages were obtained. In these LECs the blue m-LPPP emission spectrum was already recorded at a bias voltage of only 2.2 V) (the energy gap of m-LPPP is at 2.7 eV!),[152] which is one of the lowest reported onset voltages for blue-light emission in EL devices up to now. The occurrence of EL emission below voltage values of E_g/e has also been reported and discussed for other LECs.[151,153] This low onset voltage is the main advantage of the LECs compared to polymer LEDs based on m-LPPP. In the forward direction, the onset of emission is usually between 4 and 10 V and hence distinctly higher than in the reverse direction.

An explanation for this unexpected behavior can be found by analyzing the distribution of the ions within the active layer of the LEC by secondary ion mass spectroscopy (SIMS) (a detailed analysis of the SIMS results is published elsewhere).[154] For an active-layer spin-cast onto ITO, the overall concentration of the Liions and triflateions ions is significantly higher near the ITO electrode than near the surface of the active layer (by a factor 15 and 2.5, respectively). After evaporating Al as the top electrode on the active layer, the negative triflate ions drift toward the top electrode (which acts as the anode) due to the internal electric built-in field. A detailed theoretical description of this scenario can be found in Ref. 155.

In the case that the polarity of the internal built-in field is reversed[154] (by using, e.g., ITO as the bottom electrode and Au as the top electrode), a shift of the negative triflate ions toward the anode is observed. In contrast, the position of the positive (Li^+) ions is *not* significantly altered by changing the polarity of the internal built-in field, but they stay preferentially near the (ITO) bottom electrode. This suggests, that the motion of the Li^+ions is restricted within the active layer and that they seem to be anchored near the bottom electrode. The reason for that interesting behavior of the positive ions in the active layer is currently being investigated.

It therefore seems as the Li^+ions are anchored near the bottom electrode, whereas the triflateions can move within the active layer. Because the presence of the ions is necessary for an electrochemical doping, *n*-doping of m-LPPP and hence the formation of the *p-i-n* junction is only possible if the bottom electrode is wired as the cathode (*reverse* direction). This observation is in agreement with the recorded I–V-characteristics of the m-LPPP LECs (see above).[150]

The asymmetric motion of the ions with respect to the polarity of the applied voltage was assigned to be the main reason for the observed long response of the LECs based on m-LPPP, which exhibit turn-on response times (the time required to reach 90% of the maximum EL brightness) of only 30–40 μs (see Fig. 8.23).[150] This value is significantly below the reported value for the turn-on response of other LECs, which range from 30 ms (achieved by optimizing the phase morphology of the active layer of the LEC by additives[153] to several minutes.[149] Similarly, fast response times have been reported for "frozen junction" LECs.[156] Such a "frozen junction" is generated by cooling the LEC — after the formation of the *p-i-n* junction – down below the glass transition temperature of the ionic conductive polymer. In that temperature regime, the ions are not mobile in the active layer. Because no ionic motion takes place at these low temperatures, fast response times in the microsecond regime can be achieved.[156]

The turn-on response of fresh and discharged LECs (without any space-charge zones) based on m-LPPP is significantly slower (approximately 20 s when operated at a bias voltage of 6 V) than that of LECs, which have already been operated

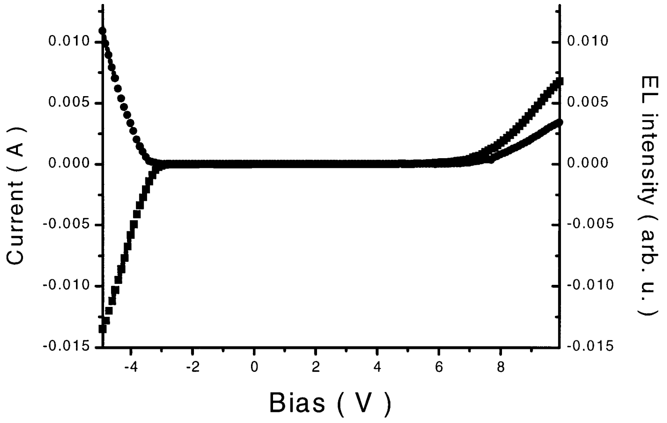

FIGURE 8.23. Time response of the current (square) and the EL (circle) of LEC based on a blend of m-LPPP:PEO: $LiCF_3SO_3$=20:10:3 under pulsed excitation (solid line-voltage pulse; dash-dot line-EL emission).

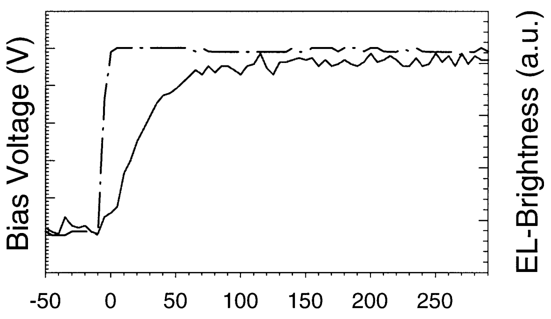

FIGURE 8.24.

at room temperature. This gives evidence that triflate$^+$ions, which can move to the anode under operation (see above), do not return immediately to their initial positions if there is no potential applied, but will stay near the anode (the Li$^+$ions seem to be always located near the bottom electrode anyway). Similar driving-cycle-dependent response times have also been described for LECs based on PPV derivatives recently.[157]

If the LEC devices are driven under pulsed operation, the ions are frozen in their position — similar to the *frozen junction* LECs but without needing to form the junction at elevated temperatures (see also Ref. 156). This formation effect in combination to the fine-phase morphology of the active layer in m-LPPP LECs is responsible for achieving *intrinsically* low response times in the range of microseconds under pulsed operation.[150]

In summary, LECs based on the PPP-type material m-LPPP exhibit extremely low onset voltages between 2.2 and 2.7 V in reverse direction for blue emission. In addition to the low onset voltages, their *intrinsically* low response time under pulsed operation in the microsecond regime, which is attributed to the restricted motion of the ions in the LEC, makes these LECs based on m-LPPP interesting for display application.

8.4 Conclusions

Phenylene-based oligomers and polymers are materials which attract high interest in basic research due to their physical properties as well as technological importance related to their processability. The paraphenylene oligomers and the planarized ladder-type polymers possess high-photoluminescence quantum yields in solution and in the solid state and a low concentration of electronic defects (traps). High intrachain order is observed in the ladder-type material, which leads to very low subgap absorption, triplet absorption with an outstanding narrow line, and polaron absorption spectra with narrow lines and a pronounced vibrational structure. Highly efficient electroluminescence devices are fabricated with para-phenylene materials showing blue-light emission at high external quantum efficiencies. Excitation energy transfer (Förster transfer) is used in polyphenylene blends to achieve efficient orange and white electroluminescence devices. Ladder-type *para*-phenylenes blends with ionically conducting polymer are applied in light-emitting electrochemical cells with good efficiency and response times in the microsecond range. Because optically pumped lasers have been built and characterized with phenylene-based systems, we propose that *para*-phenylenes are excellent candidates for the realization of an electrically pumped organic laser.

Acknowledgments

We want to thank the colleagues in the group in Graz, especially Barbara Herz, Christian Zenz, Egbert Zojer, Emil List, Markus Wuchse, Christian Hochfilzer, Franz-Peter Wenzl, Leonhard Holzer, Klaus Petritsch, Gerald Meinhardt, Gerald Kranzelbinder, Markus Moser, Stefan Eder, Roland Resel, and Farideh Meghdadi. Furthermore, we acknowledge exciting discussions with Guglielmo Lanzani, Giulio Cerullo, Mauro Nisoli, Sandro De Silvestri, Valy Vardeny, Joseph Shinar, and Alan Heeger. It was a pleasure to work with colleagues in chemistry, especially with Arnulf Dieter Schlueter, Franz Stelzer, Walter Fischer, Berthold Winkler, Ullrich Scherf, Yves Geerts, and Klaus Müllen.

References

[1] H. W. Furumoto, and H. L. Ceccon, IEEE J. Quantum Electron 6, 262 (1970).
[2] F. Mohammad, in *Handbook of Organic Conductive Molecules and Polymers, Vol. 3*, edited by H. S. Nalwa, Wiley, Chichester, 1997, p. 795.

[3] J. L. Bredas, R. Silbey, D. S. Boudreaux, and R. R. Chance, J. Am. Chem. Soc. 105, 6555 (1983).

[4] J. Sturm, S. Tasch, A. Niko, G. Leising, E. Toussaere, J. Zyss, T. C. Kowalczyk, and K. D. Singer, Thin Solid Films 298,138 (1997).

[5] S. Tasch, A. Niko, G. Leising, U. Scherf, Appl. Phys. Lett. 68, 1090 (1996).

[6] L. Athouel, G. Froyer, and M. T. Riou, Synth. Met. 55–57, 4734 (1993); B. Müller, T. Kuhlmann, K. Lischka, H. Schwer, R. Resel, and G. Leising, Surface Sci. 418, 256 (1998).

[7] R. Resel and G. Leising, Surface Sci. 409, 302 (1998).

[8] R. Resel, N. Koch, F. Meghdadi, G. Leising, N. Unzog, and K. Reichmann, Thin Solid Films 305, 232 (1997).

[9] K. N. Baker, A. V. Fratini, T. Resch, H. C. Knachel, W. W. Adams, E. P. Socci, and B. L. Farmer, Polymer 34, 1571 (1993).

[10] R. Resel, W. Graupner, C. Hochfilzer, N. Koch, S. Tasch, M. Wohlgenannt, G. Leising, and K. Reichmann, *Proc. of XVII Conference of Applied Crystallography*, 1998, p. 413.

[11] B. Stevens, Spectrochim. Acta 18, 439 (1962).

[12] E. M. Han, L. M. Do, N. Yamamoto, and M. Fujihara, Mol. Cryst. Liq. Cryst. 267, 411 (1995).

[13] L. Torsi, A. Dodabalapur, A. J. Lovinger, H. E. Katz, R. Ruel, D. D. Favis, and K. W. Baldwin, Chem. Mater. 7, 2247 (1995); A. J. Lovinger, D. D: Davis, R. Ruel, L. Torsi, A. Dodabalapur, and H. E. Katz and J. Mater. Soc. 10, 2958 (1995).

[14] C. Ambrosch-Draxl, J. A. Majewski, P. Vogl, and G. Leising, Phys. Rev. B 51, 668 (1995).

[15] G. Wegner, D. Neher, M. Remmers, V. Cimrova, and M. Schulze, Mater. Res. Soc. Symp. Proc. 413, 23 (1996).

[16] M. Era, T. Tsutsui, and S. Saito, Appl. Phys. Lett. 67, 2436 (1995).

[17] H. Kuhn, Fortschr. Chem. Org. Naturstof. 16, 169 (1958); 17, 404 (1959).

[18] G. Leising, K. Pichler, F. Stelzer, Springer Series in Solid State Sciences, Vol. 91, Springer-Verlag, New York, 1989, p. 100.

[19] R. K. Khanna, Y. M. Jiang, B. Srinivas, C. B. Smithhart, and D. L. Wertz, Chem. Mater. 5, 1792 (1993).

[20] A. Heim, G. Leising, and H. Kahlert, J. Lumin. 31 & 32, 573 (1984).

[21] A. Heim and G. Leising, Mol. Cryst. Liq. Cryst. 118, 309 (1985).

[22] W. Graupner, G. Grem, F. Meghdadi, Ch. Paar, G. Leising, U. Scherf, K. Müllen, W. Fischer, and F. Stelzer, Mol. Cryst. Liq. Cryst. 256, 549 (1994).

[23] C. Zenz, W. Graupner, S. Tasch, G. Leising, K. Müllen, and U. Scherf, Appl. Phys. Lett. 71 2566 (1997).

[24] F. Momicchioli, M. C. Bruni, and I. Baraldi, J. Phys. Chem. 76, 3983 (1972).

[25] T. G. Pavlopoulos and P. R. Hammond, J. Am. Chem. Soc. 96, 6568 (1974).

[26] U. Scherf and K. Müllen, Makromol. Chem., Rapid Commun. 12, 489 (1991).

[27] K. Pichler, D. A. Halliday, D. D. C. Bradley, P. L. Burn, R. H. Friend, and A. B. Holmes, J. Phys.: Condens. Matter 5, 7155 (1993).

[28] W. Graupner, G. Leditzky, G. Leising, and U. Scherf, Phys. Rev. B 54, 7610 (1996).

[29] M. S. Sze, *Physics of Semiconductor Devices*, Wiley–Interscience, New York, 1981; B. L. Sharma (ed.), *Metal–Semiconductor Schottky Barrier Junctions and Their Applications*, Plenum Press, New York, 1984.

[30] A. Dodabalapur, L. Torsi, and H. E. Katz, Science 268, 270 (1995).

[31] H. T. Chiu, T. Tsutsui, and S. Saito, Polym. Commun. 26, 61 (1985).

[32] G. Leditzky, Ph.D. thesis, Technische Universität Graz, 1994.
[33] P. Kovacic, M. B. Feldman, J. P. Kovacic, and J. B. Lando, J. Appl. Polym. Sci. 12, 1735 (1968).
[34] G. Leising, O. Leitner, F. Aldrian, and H. Kahlert, Synth. Met. 17, 635 (1987).
[35] C. K. Chiang, C. R. Fincher, Y. W. Park, A. J. Heeger, H. Shirakawa, E. J. Louis, S. C. Gau, and A. G. MacDiarmid, Phys. Rev. Lett. 39, 1098 (1977).
[36] D. M. Ivory, G. G. Miller, J. M. Sowa, L. W. Shacklette, R. R. Chance, and R. H. Baughman, J. Chem. Phys. 71, 1506 (1979).
[37] L. W. Shacklette, R. R. Chance, D. M. Ivory, G. G. Miller, and R. H. Baughman, Synth. Met. 1, 307 (1979).
[38] D. Moses and A. J. Heeger, in *Relaxation in Polymers*, edited by T. Kobayashi, World Scientific, Singapore, 1993.
[39] B. R. Hsieh, H. Antoniadis, M. A. Abkowitz, and M. Stolka, Polym. Prepr. 33, 414 (1992), and references therein.
[40] H. Antoniadis, M. A. Abkowitz, and B. R. Hsieh, Appl. Phys. Lett. 65, 2030 (1994).
[41] R. I. Frank, and J. G. Simmons, J. Appl. Phys. 38, 832 (1967).
[42] H. Meyer, D. Haarer, H. Naarmann, and H. H. Hörhold, Phys. Rev. B 52, 2587 (1995).
[43] M. Kryszewski and A. Szymanski, Macromol. Rev. 4, 245 (1970).
[44] P. W. M. Blom, M. J. M. de Jong, and J. J. M. Vleggaar, Appl. Phys. Lett. 68, 3308 (1996).
[45] H. J. Round, Elektron World 19, 309 (1907).
[46] A. Bernanose and P. Vouaux, Extr. J. Chim. Phys. 4, 261 (1953).
[47] M. Pope, H. P. Kallmann, and P. Magnante, J. Chem. Phys. 38, 2042 (1963).
[48] C. W. Tang and S. A. VanSlyke, Appl. Phys. Lett. 51, 913 (1987).
[49] J. H. Burroughes, D. D. C. Bradley, A. R. Brown, R. N. Marks, K. Mackay, R. H. Friend, P. L. Burn, A. Kraft, and A. B. Holmes, Nature 347, 539 (1990).
[50] Y. Ohmori, M. Uchida, K. Muro, and K. Yoshino, Jpn. Appl. Phys. 30, L1941 (1991).
[51] G. Grem, G. Leditzky, B. Ullrich, and G. Leising, Adv. Mater. 4, 36 (1992).
[52] C. Kvarnström and A. Ivaska, in *Handbook of Organic Conductive Molecules and Polymers*, Vol. 4, edited by H. S. Nalwa, Wiley, Chichester 1997, p. 487.
[53] D. G. H. Ballard, A. Courtis, L. M. Shirley, and S. C. Taylor, Macromolcules 21, 294 (1988).
[54] G. Grem and G. Leising, Synth. Met. 55–57, 4105 (1993).
[55] G. Leising, G. Grem, G. Leditzky, and U. Scherf, Proc. SPIE, 1910, 70 (1993).
[56] G. Leising, S. Tasch, and W. Graupner, in *Handbook of Conducting Polymers*, edited by T. Skotheim, Marcel Dekker, New York, 1997, p. 847.
[57] W.-X. Jing, A. Kraft, S. C. Moratti, J. Grüner, F. Cacialli, P. J. Hamer, A. B. Holmes, and R. H. Friend, Synth. Met. 67, 161 (1994).
[58] M. Hamaguchi and K. Yoshino, Jpn. J. Appl. Phys. 34, L587 (1995).
[59] Y. Yang, O. Pei, and A. J. Heeger, Appl. Phys. Lett. 79, 934 (1996).
[60] J. Grüner, M. Remmers, and D. Neher, Adv. Mater. 9, 964 (1997).
[61] J. Birgersson, K. Kaeriyama, P. Barta, P. Bröms, M. Fahlmann, T. Granlund, and W. R. Salaneck, Adv. Mater. 8, 982 (1996).
[62] J. Huang, H. Zhang, W. Tian, J. Hon, Y. Ma, J. Shen, and S. Liu, Synth. Met. 87, 105 (1997).
[63] V. Cimrova, M. Remmers, D. Neher, and G. Wegner, Adv. Mater. 8, 146 (1996).
[64] U. Scherf and K. Müllen, Macromol. Chem., Rapid. Commun. 12, 489 (1991).
[65] U. Fahnenstich, K.-H. Koch, M. Pollmann, U. Scherf, M. Wagner, S. Wegener, and K. Müllen, Macromolec. Chem., Macromolec. Symp. 54/55, 465 (1992).

[66] J. Stampfl, W. Graupner, G. Leising, and U. Scherf, J. Lumin. 63, 117 (1995).

[67] G. Leditzky, and G. Leising, J. Phys. D: Appl. Phys. 27, 2185 (1994).

[68] W. Graupner, M. Mauri, J. Stampfl, G. Leising, U. Scherf, and K. Müllen, Solid State Commun. 91, 7 (1994).

[69] G. Grem, C. Paar, J. Stampfl, G. Leising, J. Huber, and U. Scherf, Chem. Mater. 7, 2 (1995).

[70] U. Lemmer, S. Heun, R. F. Mahrt, U. Scherf, M. Hopmeier, U. Siegner, E. 0. Göbel, K. Müllen, and H. Bässler, Chem. Phys. Lett. 240, 373 (1995).

[71] T. Pauck, R. Hennig, M. Perner, U. Lemmer, U. Siegner, R. F. Mahrt, U. Scherf, K. Müllen, H. Bässler, and E. O. Göbel, Chem. Phys. Lett. 244, 171 (1995).

[72] G. Grem and G. Leising, Synth. Met. 57, 4105 (1993).

[73] J. Grüner, H. F. Wittmann, P. J. Hamer, R. H. Friend, J. Huber, U. Scherf, K. Müllen, S. C. Moratti, and A. B. Holmes, Synth. Met. 67, 181 (1994).

[74] V. Cimrova, U. Scherf, and D. Neher, Appl. Phys. Lett. 69, 608 (1996).

[75] J. Huber, K. Müllen, J. Salbeck, H. Schenk, U. Scherf, T. Stehlin, and R. Stern, Acta Polym. 45, 244 (1994).

[76] J. F. Grüner, H. F. Wittmann, P. J. Hamer, R. H. Friend, J. Huber, U. Scherf, K. Müllen, S. C. Moratti, and A. B. Holmes, Synth. Met. 67, 181 (1994).

[77] M. Moser, S. Tasch, and G. Leising, Synth. Met. 84, 651 (1997).

[78] A. Haugeneder, M. Hilmer, C. Kallinger, M. Perner, W. Spirkl, U. Lemmer, J. Feldmann, and U. Scherf, Appl. Phys. B 66, 389 (1998).

[79] B. Schweitzer, G. Wegmann, H. Giessen, D. Hertel, H. Bässler, R. F. Mahrt, U. Scherf, and K. Müllen, Appl. Phys. Lett. 72, 2933 (1998).

[80] W. Graupner, G. Grem, F. Meghdadi, Ch. Paar, G. Leising, U. Scherf, K. Müllen, W. Fischer, and F. Stelzer, Mol. Cryst. Liq. Cryst. 256, 549 (1994).

[81] M. Era, T. Tsutsui, and S. Saito, Appl. Phys. Lett. 67, 2436 (1995).

[82] J. Salbeck in *Inorganic and Organic Electroluminescence/EL 96*, edited by R. H. Mauch and H.-E. Gumlich, Wissenschaft und Technik Verlag, Berlin, (1996).

[83] M. Keegstra, V. Cimrova, D. Neher, and U. Scherf, Macromol. Chem. Phys. 197, 2511 (1996).

[84] J. Comil, A. J. Heeger, and J. L. Bredas, Chem. Phys. Lett. 272, 463 (1997); J. Cornil, D. A. dos Santos, X. Crispin, R. Silbey, and J. L. Bredas, J. Am. Chem. Soc. 120, 1289 (1998).

[85] M. Grell, D. D. C. Bradley, M. Inbasekaran, and E. P. Woo, Adv. Mater. 9, 798 (1997), and further private communication.

[86] C. Paar, S. Tasch, H. Bässler, and G. Leising, Solid State Commun. 96 167 (1995).

[87] J. Stampfl, S. Tasch, G. Leising, and U. Scherf, Synth. Met. 71, 2125 (1995).

[88] J. Grüner, R. H. Friend, J. Huber, and U. Scherf, Chem. Phys. Lett. 251, 204 (1996).

[89] U. Scherf, private communication.

[90] C. C. Wu, J. C. Sturm, R. A. Register, and M. E. Thompson, Appl. Phys. Lett. 69, 3117 (1996).

[91] T. Noda, H. Ogawa, N. Noma, and Y. Shirota, Adv. Mater. 9, 720 (1997).

[92] M. Berggren, O. Inganäs, G. Gustafsson, J. Rasmusson, M. R. Andersson, T. Hjertberg, and O. Wennerström, Nature 372, 444 (1994).

[93] M. Hamaguchi and K. Yoshino, Appl Phys. Lett. 69, 143 (1996).

[94] F. Meghdadi, E. Eder, F. Stelzer, and G. Leising, Conf. Proc. ANTEC 2, 1291 (1997).

[95] Z. Shen, P. E. Burrows, V. Bulovic, S. R. Forrest, and M. E. Thompson, Science 276, 2009 (1997).

[96] Y. Ohmori, N. Tada, Y. Kurosaka, H. Ueta, T. Sawatani, A. Fuji, and K. Yoshino, IEICE Trans Electron. E81-C, 1041 (1998).

[97] T. Tsutsui, N. Noriyuki, and S. Saito, Synth. Met. 71, 2001 (1995).

[98] S. Tokito, K. Noda, and Y. Taga, Appl. Phys. Lett. 68, 2633 (1996).

[99] H. Tokailin, C. Hosokawa, and T. Kusomoto, U.S. Patent 5,126,214 (1992); Matsura, H. Tokailin, M. Eida, C. Hosokawa, Y. Hironaka and T. Kusumoto, Proc. Asia Diplay '95 1995, p. 269.

[100] C. W. Tang, D. J. Williams, and J. C. Chang, U.S. Patent 5,294,870 (1994).

[101] S. Tasch, C. Brandstätter, F. Meghdadi, G. Leising, L. Athouel, and G. Froyer, Adv. Mat. 9, 33 (1997).

[102] A. Niko, C. Brandstätter, S. Tasch, and G. Leising, J. Appl. Phys. 82, 4177 (1997).

[103] A. Niko, S. Tasch, F. Meghdadi, C. Brandstätter, and G. Leising, Opt. Mater. 9, 188 (1998).

[104] G. Leising, G. Köpping-Grem, F. Meghdadi, A. Niko, S. Tasch, W. Fischer, L Pu, M. W. Wagner, R H. Grubbs, L. Athouel, G. Froyer, U. Scherf, and J. Huber, Proc. SPIE 2527, 307 (1995).

[105] F. Meghdadi, S. Tasch, B. Winkler, W. Fischer, and G. Leising, Synth. Met. 85 1441 (1996).

[106] B. Winkler, F. Meghdadi, S. Tasch, B. Evers, I. Schneider, W. Fischer, F. Stelzer, and G. Leising, Synth. Met. (in press).

[107] D. Braun and A. J. Heeger, Appl. Phys. Lett. 58, 1982 (1991).

[108] A. R. Brown, D. D. Bradley, J. H. Burroughes, R. H. Friend, N. C. Greenham, P. L Burn, A. B. Holmes, and A. Kraft, Appl. Phys. Lett. 61, 2793 (1992).

[109] N. C. Greenham and R. H. Friend, in *Solid State Physics*, edited by H. Ehrenreich and F. Spaepen, Academic Press, London, 1995.

[110] H. Bässler, Y. H. Tak, D. V. Khramtchenkov, and V. R. Nikitenko, Synth. Met. (in press).

[111] P. W. M. Blom, M. J. M. de Jong, and J. J. M. Vleggaar, Appl. Phys. Lett. 68,3308(1996).

[112] P. S. Davids, A. Saxena, and D. L. Smith, J. Appl. Phys. 82, 6319 (1997).

[113] P. Dannetun, M. Lögdlund, C. Fredriksson, R. Lazzaroni, C. Fauquet, S. Stafström, C. W. Spangler, J. L. Bredas, and W. R. Salaneck, J. Chem. Phys. 100, 6765 (1994).

[114] P. Bröms, J. Birgersson, N. Johnsson, M. Löglund, and W. R. Salaneck, Synth. Met. 74, 179 (1995).

[115] E. Ettedgui, H. Razafitrimo, Y. Gao, and B. R. Hsieh, Appl. Phys. Lett. 67, 2705 (1995).

[116] W. R. Salaneck and J. L. Bredas, Adv. Mater. 8, 48 (1996)

[117] N. Koch, A. Pogantsch, R. Boyd, M. Ramsey, F. Netzer, and G. Leising, unpublished data.

[118] David R. Lide, *Handbook of Chemistry and Physics*, CRC Press, Boca Raton, (1995).

[119] K. Seki, U.0. Karlsson, R. Engelhardt, E.-E. Koch, and W. Schmidt, Chem. Phys. 91, 459 (1984).

[120] W. Fischer, F. Meghdadi, F. Stelzer, and G. Leising, Synth. Met. 76, 201 (1996).

[121] H. Becker, S. Burns, and R. H. Friend, Phys. Rev. B 56, 1893 (1997).

[122] C. Adachi, T. Tsutsui, and S. Saito, Appl. Phys. Lett. 57, 531 (1990).

[123] B. Winkler, F. Meghdadi, S. Tasch, R. Müllner, R. Resel, R. Saf, G. Leising, and F. Stelzer, Opt. Mater. 9, 159 (1998).

[124] B. Hu, Z. Yang, and F. E. Karasz, J. Appl. Phys. 76, 2419 (1994).

[125] J.-I. Lee, I.-K. Kang, D.-H. Hwang, H.-K. Shin, S. C. Jeoung, and D. Kim, Chem. Mater. 8, 1925 (1996).

[126] H. Vestweber, R. Sander, A. Greiner, W. Heitz, R. F. Mahrt, and H. Bässler, Synth. Met. 64, 141 (1994).

[127] U. Albrecht and H. Bässler, Chem. Phys. 199, 207 (1995).

[128] C. Zhang, H. von Seggern, K. Pakbaz, B. Kraabel, H.-W. Schmidt, and A. J. Heeger, Synth. Met. 62, 23 (1994).

[129] H. Suzuki and S. Hoshino, J. Appl. Phys. 79, 8816 (1996); G. Wang, C. Yuan, Z. Lu, and Y. Wie, J. Lumin. 68, 49 (1996).

[130] K. Yoshino, K. Tada, K. Yoshimoto, M. Yoshida, T. Kawai, H. Araki, M. Hamaguchi, and A. Zakhidov, Synth. Met. 78, 301 (1996).

[131] S. Tasch, C. Hochfilzer, E. J. W. List, G. Leising, H. Quante, P. Schlichting, U. Rohr, Y. Geerts, U. Scherf, and K. Müllen, Phys. Rev. B 56, 4479 (1997).

[132] T. Christ, A. Greiner, R. Sander, V. Stüpflen, and J. H. Wendorff, Adv. Mater. 9, 219 (1997).

[133] S.-A. Chen, K. R. Chuang, C.-I. Chao, and H. T. Lee, Synth. Met. 82, 207 (1996).

[134] N. C. Greenham, I. D. W. Samuel, G. R. Hayes, R. T. Phillips, Y. A. R. R. Kessener, S. C. Moratti, A. B. Holmes, and R. H. Friend, Chem. Phys. Lett. 241, 89 (1995).

[135] D. Braun, G. Gustafsson, D. McBranch, and A. J. Heeger, Appl. Phys. Lett. 72, 564 (1992); I. D. Parker, Appl. Phys. Lett. 75, 1656 (1994); I. H. Campbell, D. L. Smith, and J. P. Ferraris, Appl. Phys. Lett. 66, 3030 (1995); S. Tasch, W. Graupner, G. Leising, L. Pu, M. W. Wagner, and R. H. Grubbs, Adv. Mater. 7, 903 (1995).

[136] M. Granström and O. Inganäs, Appl. Phys. Lett. 68, 147 (1996).

[137] E. J. W. List, S. Tasch, C. Hochfilzer, G. Leising, P. Schlichting, U. Rohr Y. Geerts, U. Scherf, and K. Müllen, Optical Materials 9, 183 (1998).

[138] M. Wohlgenannt, W. Graupner, F. P. Wenzl, S. Tasch, E. J. W. List, G. Leising, M. Graupner, A. Hermetter, U. Rohr, P. Schlichting, Y. Geerts, U. Scherf, and K. Müllen, Chem. Phys. 227, 99 (1998).

[139] T. Tsutsui and S. Saito, in *Intrinsically Conducting Polymers: An Emerging Technology*, edited by M. Aldissi, NATO ASI Series E: Appl. Sciences 246, 1993, p. 123.

[140] S. Tasch, E. J. W. List, 0. Ekström, W. Graupner, G. Leising, P. Schlichting, U. Rohr, Y. Geerts, U. Scherf, and K. Müllen, Appl. Phys. Lett. 71, 2883 (1997).

[141] *Colorimetry*, 2nd ed., CIE, Vienna, 1986.

[142] N. C. Greenham, S. C. Moratti, D. D. C. Bradley, R. H. Friend, and A. B. Holmes, Nature 365, 628 (1993).

[143] Y. Ohmori, M. Uchido, K. Muro, and K. Yoshino, Jpn. J. Appl. Phys. 30, L1938 (1991).

[144] R. E. Gill, P. van de Weijer, C. T. Liedenbaum, H. F. Schoo, AJ Berntsen, JJ Vleggaar, and R. J. Visser, Proc. SPIE 3476. (1998).

[145] D. Hertel, H. Bässler, and U. Scherf, unpublished.

[146] Q. Pei, G. Yu, C. Zang, Y. Yang, and A. J. Heeger, Science 269, 1086 (1995).

[147] Q. Pei, Y. Yang, G. Yu, C. Zhang, and A. J. Heeger, J. Am. Chem. Soc. 118, 3922(1996).

[148] Q. Pei and Y. Yang, Synth. Met. 80,131 (1996).

[149] Y. Yang and Q. Pei, J. Appl. Phys. 81, 3294 (1997).

[150] S. Tasch, J. Gao, F. P. Wenzl, L. Holzer, A. J. Heeger, and G. Leising, J. Electrochem. Soc. (in press).

[151] J. C. deMello, N. Tessler, S. C. Graham, and R. Friend, Phys. Rev. B. 57, 12,951 (1998).

[152] F. P. Wenzl, S. Tasch, J. Gao, L. Holzer, U. Scherf, A. J. Heeger, and G. Leising, Mater. Res. Soc. Symp. 448, 57 (1998).

[153] Y. Cao, G. Yu, A. J. Heeger, and C. Y. Yang, Appl. Phys. Lett. 68, 3218 (1996).

[154] L. Holzer, F. P. Wenzl, R. Sotgiu, M. Gritsch, S. Tasch, H. Hutter, M. Sampietro, and G. Leising, Synth. Met. (in press).

[155] D. L. Smith, J. Appl. Phys. 81, 2869 (1997).

[156] J. Gao, G. Yu, and A. J. Heeger, Appl. Phys. Lett. 71, 1293 (1997); G. Yu, Y. Cao, M. Andersson, J. Gao, and A. J. Heeger, Adv. Mater. 10, 35 (1998).

[157] G. Yu, Y. Cao, C. Zhang, Y. Li, J. Gao, and A. J. Heeger, Appl. Phys. Lett. 73, 111 (1998).

[158] R. Resel, N. Koch, F. Meghdadi, G. Leising, N. Unzog, and K. Reichmann, Thin Solid Films 305, 232 (1997).

[159] A. Niko, F. Meghdadi, C. Ambrosch-Draxl, P. Vogl, and G. Leising, Synth. Met. 76, 177 (1996).

[160] M. Moser, S. Tasch, and G. Leising, Synth. Met. 84, 651 (1997).

[161] W. Graupner, S. Eder, K. Petritsch, G. Leising, and U. Scherf, Synth. Met. 84, 507 (1997).

[162] W. Graupner, F. Meghdadi, G. Leising, G. Lanzani, M. Nisoli, S. De Silvestri, W. Fischer, and F. Stelzer, Phys. Rev. B 56, 10,128 (1997).

[163] J. L. Bredas, J. Cornil, F. Meyers, and D. Beljonne, in *Handbook of Conducting Polymers*, 2nd ed., edited by T. A. Skotheim, R. L. Elseenbaumer, and J. R. Reynolds, Marcel Dekker, New York, 1998, p. 1.

[164] A. Piaggi, G. Lanzani, G. Bongiovanni, A. Mura, W. Graupner, F. Meghdadi, and G. Leising, Phys. Rev. B 56, 10,133 (1997).

[165] A. Piaggi, G. Lanzani, G. Bongiovanni, M. A. Loi, A. Mura, W. Graupner, F. Meghdadi, and G. Leising, Opt. Mater. 9, 489 (1998).

[166] W. Graupner, G. Cerullo, M. Nisoli, S. De Silvestri, G. Lanzani, E. J. W. List, and G. Leising, Phys. Rev. Lett. 81, 3259 (1998).

[167] G. Meinhardt, A. Horvath, G. Leising, and G. Weiser, Synth. Met. 84, 669 (1997).

[168] N. Johansson, D. A. dos Santos, S. Guo, J. Comil, M. Fahlman, J. Salbeck, H. Schenk, H. Arwin, J. L. Bredas, and W. R. Salaneck, J. Chem. Phys. 107, 2542 (1997).

9

Direct and Alternating Current Light-Emitting Devices Based on Pyridine-Containing Conjugated Polymers

Y. Z. Wang, D. D. Gebler, and A. J. Epstein

9.1 Introduction

In the past decade, there has been great interest in organic molecular and polymeric electroluminescent devices, particularly conjugated-polymer-based light-emitting devices (LEDs).[1−4] Electroluminescence (EL) combined with other unique properties of polymers, such as solution processability, bandgap tunability, and mechanical flexibility, make conjugated polymers excellent candidates for low-cost large-area display applications.

Most "conventional" polymer LEDs have been shown to be tunneling diodes and can be operated only under forward dc bias.[5] Among the most important limitations associated with many of the "conventional" polymer LEDs are poor stability and short shelf life. Devices degrade even during storage. The double charge-injection mechanism of the "conventional" polymer LEDs requires the matching of the cathode (anode) workfunction to the corresponding lowest unoccupied molecular orbital (LUMO) highest occupied molecular orbital [highest occupied molecular orbital (HOMO)] level of the polymer in order to achieve efficient charge injection. The relatively low electron affinity of most conjugated polymers requires metals with very low workfunctions to achieve efficient electron injection. However, because low-workfunction metals are generally oxygen reactive, devices with a low-workfunction cathode usually are unstable. Thus, light-emitting devices with high-workfunction electrodes and high-electron-affinity polymers are highly desirable. A number of high-electron-affinity polymers have been synthesized and successfully utilized in polymer LEDs, among which, cyano-[6] and pyridine-containing conjugated polymers[7] are very promising.

Recently, there have been reports of new device configurations such as symmetrically configured ac light-emitting (SCALE) devices[8] and light-emitting electrochemical cells (LECs).[9] These devices modify the charge-injection and/or charge-transport characteristics such that the device can be operated under both forward and reverse biases and their operation is insensitive to the electrode materials used. As a consequence, more stable metals such as Au can be used as electrodes, potentially reducing unwanted chemical reactions. Although the response of the LECc is slow due to the involvement of the motion of ionic species in the device operation, the SCALE devices can be operated under ac modes up to $\sim$ 100 kHz.

To date, a variety of conjugated polymers and/or copolymers have been found to exhibit electroluminescent properties such that all of the colors necessary for display applications are obtainable. However, for most devices, the color of the emitted light is fixed once the device is fabricated. Recently, there has been substantial interest in developing color-variable light-emitting devices (i.e., individual devices that can generate two or more colors of light). The colors can be controlled by either magnitude[10] or polarity[11–13] of the driving voltage.

We present a series of novel LEDs based on pyridine-containing conjugated polymers and copolymers. Pyridine-containing conjugated polymers have been shown to be promising candidates for LEDs.[7] The pyridine-containing polymers are highly luminescent, especially the copolymers. For example, the internal photoluminescent quantum efficiencies of the copolymers consisting of alternating units of pyridylvinylene and phenylenevinylene have been measured to be 75–90% in solution and 18–30% in film. As compared to phenylene-based analogs, one of the most important features of the pyridine-based polymers is the higher electron affinity. As a consequence, the polymer is more resistant to oxidation and shows better electron-transport properties. In contrast, most other conjugated polymers are susceptible to oxidation and exhibit better hole-transport properties. The high electron affinity of pyridine-based polymers enables the use of relatively stable metals such as A1, Au, or indium–tin oxide (ITO) and doped polyaniline as electrodes. Taking advantages of the better electron-transport properties of the pyridine-containing polymers, we fabricated bilayer devices utilizing poly(9-vinyl carbazole) (PVK) as a hole-transporting/electron-blocking polymer, which improves the device efficiency and brightness significantly due to the charge confinement and exciplex emission at the PVK/emitting-polymer interface. The incorporation of conducting polyaniline network electrode into PVK reduces the device turn-on voltage significantly while maintaining the high efficiency and brightness. The high electron affinity of the pyridine-based polymers enables the use of ITO as an electron-injecting contact (in addition to its use as a hole-injecting contact as in typical polymer light-emitting diodes) to fabricate inverted LEDs.[14] A metal with a high workfunction, such as Au, is used as a hole-injecting contact. By inserting a layer of emeraldine base (EB) form of polyaniline on both sides of the emitting polymer, we fabricated symmetrically configured ac light-emitting (SCALE) devices[8]

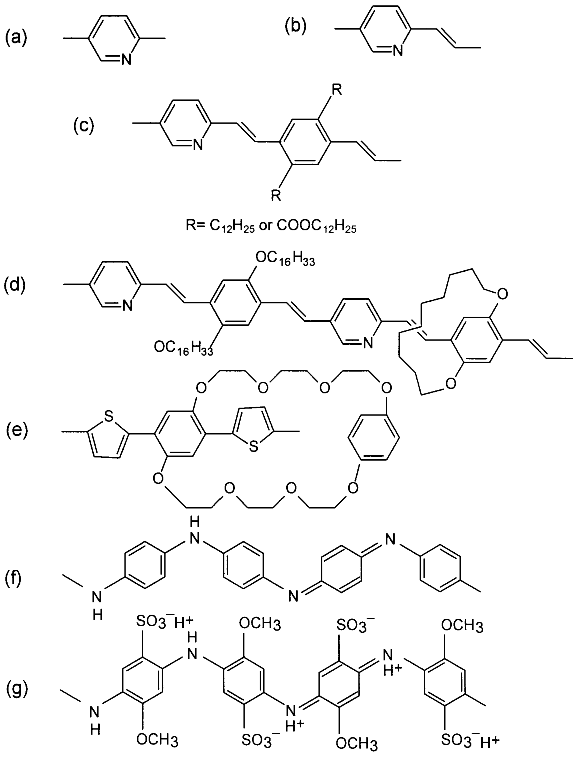

FIGURE 9.1. Repeat units of the pyridine-containing polymers and other polymers used in the study: (a) poly(*p*-pyridine) (PPy); (b) poly(*p*-pyridyl vinylene) (PPPyV); (c) copolymer of PPV and PPyV [PPyVP(R)2V]; (d) wrapped copolymer of pyridylvinylene and penylenevinylene (@PPyVPV); (e) wrapped copolymer of dithienylene and phenylene (@PTP); (f) emeraldine base (EB) form of polyaniline; (g) sulfonated polyaniline (SPAN).

which work under both forward and reverse dc biases as well as in ac modes. When we replace the EB layer on the cathode side of the SCALE device with sulfonated polyaniline (SPAN) and modify the emitting layer to appropriately balance electron and hole transport, color-variable bipolar/ac light-emitting devices are fabricated that can generate different colors of light depending on the polarity of the driving voltage: red under forward bias and green under reverse bias. Figure 9.1 shows the repeat units of the pyridine-containing polymers and other polymers that were used in these devices.

9.2 Experiments

For single-layer devices, the emitting layer was spin-cast at 1000–2000 rpm from solutions in formic acid [for polypyridine (PPy) and poly(pyridylvinylene) (PPyV)] or xylenes [(for copolymers of pyridylvinylene (PyV) and phenylenevinylene

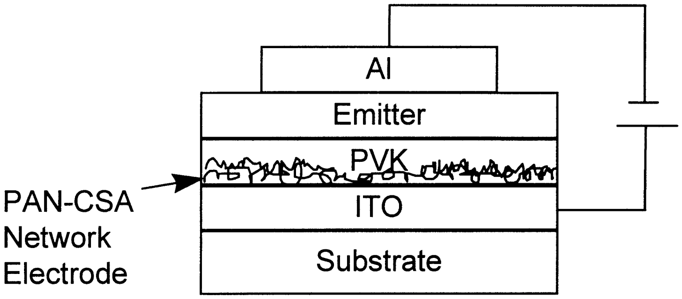

FIGURE 9.2. Schematic structure of a bilayer device with conducting polyaniline network electrode.

(PV)] (with a concentration of $\sim$ 10 mg/mL) onto precleaned patterned ITO substrates with a sheet resistance of $\sim$ 15 Ω/square. For bilayer devices, the PVK layer was spin-coated onto the ITO substrate from solution in tetrahydrofuran (THF) ($\sim$ 10 mg/mL) at $\sim$ 3000 rpm. The emitting layer was then spin-coated on top of the PVK layer from appropriate solutions (typically xylenes). As the solvent for the emitting layer does not dissolve PVK, no significant intermixing of the two polymers is expected. The conducting polyaniline network electrode was formed by spin-casting from a blend (1:4 ratio) of camphor-sulfonic-acid-doped polyaniline (PAN-CSA) and a low-molecular-weight host polymer poly(methyl methacrylate) (PMMA) (from Aldrich Chemical Co.) in *m*-cresol. The host polymer PMMA was subsequently washed away by xylenes. As xylenes are an excellent solvent for PMMA but a poor solvent for PAN-CSA, the extraction of the PMMA left a porous network of PAN-CSA. The PVK and emitting layers were subsequently coated as in the bilayer device. The PVK layer is expected to partially fill the PAN-CSA network, resulting in a structure schematically illustrated in Fig. 9.2. Similar effects has been reported for the formation of a PAN-CSA network within a PPV derivative.[15] For the inverted bilayer device, the emitting layer (PPy) was first spin-coated from formic acid onto ITO, followed by the PVK coated from THF. The SCALE devices were fabricated by spin-casting a solution of EB in *N*-methyl pyrrolidinone (NMP) ($\sim$ 5 mg/mL) onto an ITO substrate. After drying in dynamic vacuum, a layer of the emitting polymer was spin-coated on the EB surface. Another EB layer was similarly coated on top of the emitting layer. The spinning speed for all layers is $\sim$ 2000 rpm. The color-variable/ac light-emitting devices were similarly fabricated as the SCALE devices, except that the top EB layer was replaced by SPAN cast from aqueous solution and the emitting layer was comprised of a blend of polymers. All of the spin-coating procedures were carried out inside a class 100 clean room in air. The top metal electrode was deposited by vacuum evaporation at a pressure below 10^{-6} torr. To prevent damage to the polymers, the substrate was mounted on a cold-water-cooled surface during the evaporation.

Absorption spectra were measured on spin-cast films using a Perkin-Elmer Lambda 19 UV/VIS/NIR spectrometer. Photoluminescence (PL) and EL were

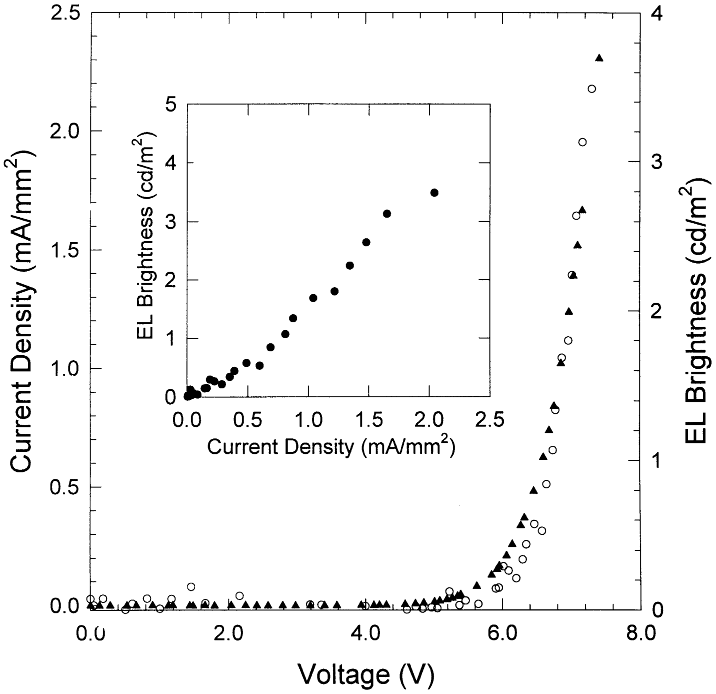

FIGURE 9.3. Current–voltage and brightness–voltage characteristics of a single-layer device using @PPyVPV as the emitting layer. Inset: brightness–current characteristics of the same device.

measured using a PTI fluorometer (model QM-1). The current–voltage characteristics were measured simultaneously with EL using two Keithley model 195A multimeters while de voltage was applied by a HP model 6218A DC power supply. Quantum efficiency and brightness were measured using a calibrated photodiode (UDT UV 100). We note that all of the device testing procedures were performed in air on as-made devices without any encapsulation.

9.3 Results and Discussion

Figure 9.3 shows the current–voltage and brightness–voltage characteristics of a single-layer device using the wrapped copolymer @PPyVPV as the emitting player. The single-layer devices have a typical operating voltage of 5–10 V. The EL intensity follows closely with the current and shows a linear relationship. The quantum efficiency of the single-layer devices is relatively low, typically ~ 0.001% photon/electron. The performance of a bilayer devices using PVK as the hole-transporting/electron-blocking layer improves dramatically as compared to single-layer devices. The internal quantum efficiency and brightness of the bilayer devices increase two to three orders of magnitude, reaching ~ 0.5% and over

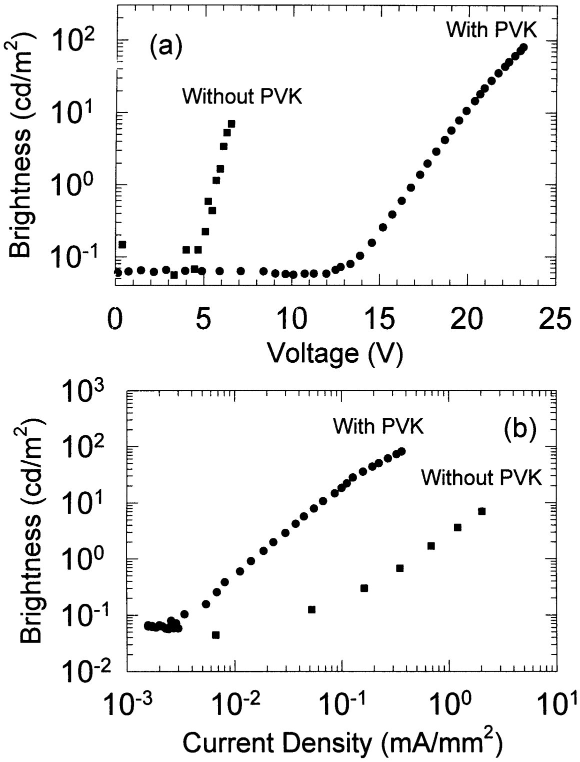

FIGURE 9.4. Comparison of (a) brightness–voltage and (b) brightness–current characteristics for a single-layer device (square) and a bilayer device (circle).

300 Cd/m^2, respectively. Figure 9.4 compares the electroluminescence–voltage and electroluminescence–current characteristics for a single-layer device and a bilayer device using the wrapped copolymer as the emitting layer. As a well-known hole-transporting/electron-blocking polymer, PVK enhances the transport of holes injected from the anode and blocks the transport of electrons injected from the cathode such that the electrons accumulate at the PVK/copolymer interface. This charge confinement greatly increases the probability of radiative recombination. In addition, the PVK layer removes the recombination zone from the vicinity of the electrode so that the radiative recombination is protected against the nonradiative quenching at the electrode/polymer interfaces.

An unwanted side effect of using the PVK layer is that it increases the device operating voltage substantially. One effective way to reduce the device turn-on voltage is to use a high-surface-area network electrode.[14] The rough electrode will create a nonuniform high electric field that enhances the charge injection. This technique has been successfully applied to PPV-based single-layer devices.[15] Figure 9.5 compares the electroluminescence–voltage and electroluminescence–current characteristics of the bilayer devices with and without the network

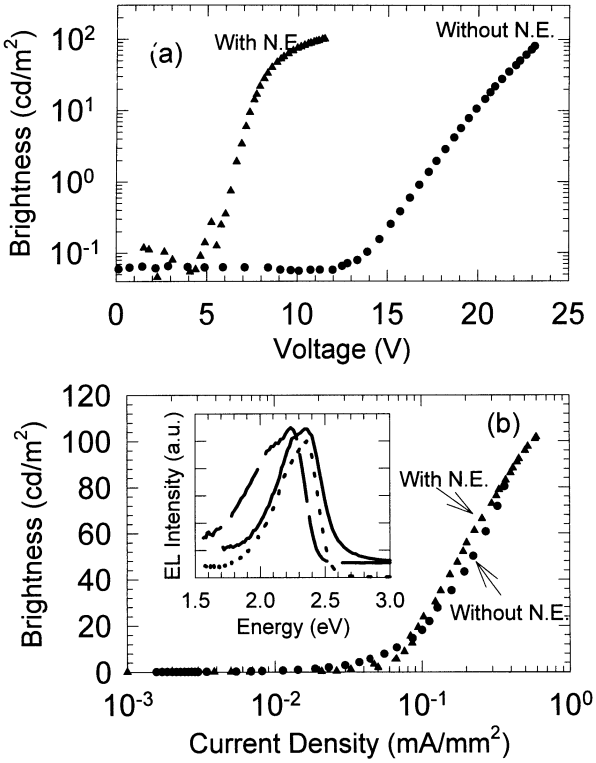

FIGURE 9.5. Comparison of (a) brightness–voltage and (b) brightness–current characteristics for a bilayer device (circle) and a bilayer device with a PAN-CSA network electrode.

electrode. For a device emitting at ∼ 50 Cd/m^2, the operating voltage is reduced from over 20 V to less than 10 V by introducing the network electrode. Because the incorporation of the PAN-CSA network electrode does not modify the PVK/copolymer interface, the high quantum efficiency and brightness of the bilayer device are maintained. Thus, the incorporation of the network electrode to the bilayer device dramatically improves the power efficiency (light output power/electrical input power) from ∼ 0.07% to ∼ 0.22%. The bilayer devices with and without a PAN-CSA network electrode show similar EL spectra, which are blue-shifted as compared to that of the single-layer device; see Fig. 9.5 inset. The slightly reduced intensity at the high-energy tail for the device with network electrode is probably due to absorption by the PAN-CSA.

The light generation in the bilayer device is attributed to the decay of exciplexes formed at the PVK/copolymer interface. Figure 9.6 compares the PL of a pure wrapped copolymer, pure PVK, and a bilayer of PVK/copolymer, as well as the EL spectra of the bilayer device. The PL of the PVK film excited at 3.6 eV has an emission peak at 3.06 eV. The PL of pure wrapped copolymer film excited at

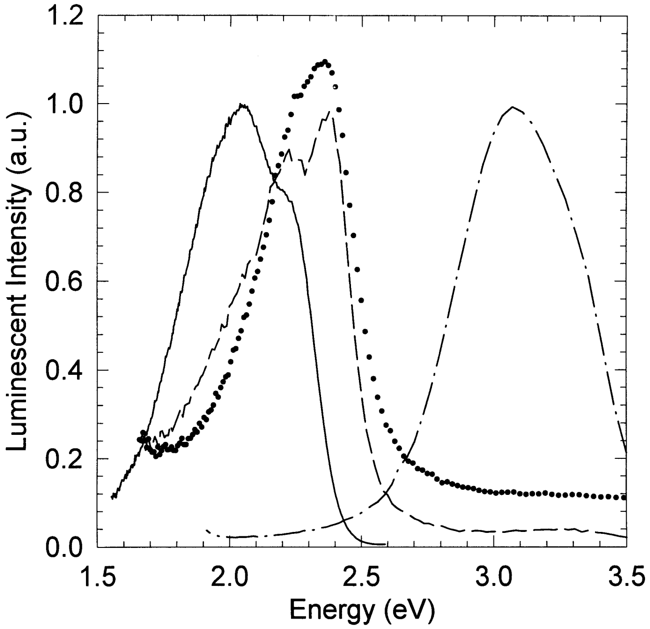

FIGURE 9.6. Normalized PL spectra of pure wrapped copolymer film (solid line) excited at 2.65 eV, pure PVK film (dash-dot line) excited at 3.6 eV, bilayer of PVK/copolymer (dashed line) excited at 3.6 eV, and the EL of the bilayer device (filled circle). The EL spectra are offset for clarity.

2.65 eV peaks at 2.03 eV with a shoulder at 2.25 eV. When the PVK/copolymer bilayer film is excited at 3.6 eV, a new peak appears at 2.38 eV with another peak at 2.23 eV. The new peak is assigned to exciplex emission at the PVK/copolymer interface. This assignment is supported by the optical absorption and photoluminescence excitation (PLE) measurements. Both the absorption and PLE of the bilayer PVK/copolymer film are the sum of those of individual PVK and copolymer films with no additional new features. Similar results are found for other unwrapped copolymers.[16] The EL of the bilayer device follows closely with the PL of the bilayer film in accord with the EL emission originating primarily from the exciplex formed at the PVK/copolymer interface.

The high electron affinity of the pyridine-based polymers enables novel device configurations such as inverted LEDs that are capable of eliminating the use of low-workfunction metals. Poly(*p*-pyridine) has an electron affinity of $\sim$ 3.5 eV, which allows metals with relatively high-workfunctions as electron-injecting contacts. In the inverted LEDs, ITO was used as an electron injecting contact, in contrast to most polymer LEDs which use ITO as the hole-injecting contacts. Au, a metal with even higher workfunction ($\sim$ 5.3 eV), was used as a hole-injecting electrode. The inverted (−) ITO/PPy/Au (+) devices show improved device performance, including quantum efficiency, brightness, operating stability, and storage lifetimes as compared to the usual (+) ITO/PPy/Al (−) device. By inserting a PVK layer

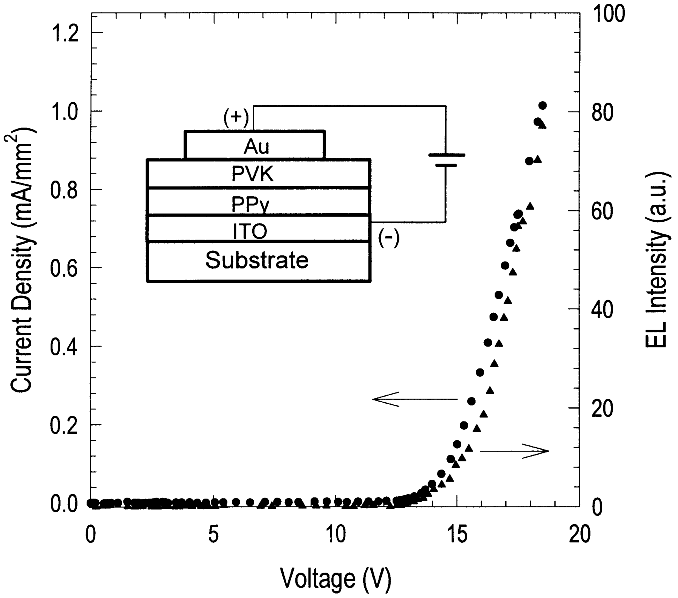

FIGURE 9.7. Current–voltage characteristics of an inverted LED with PPy as the emitting layer and PVK as the hole-transporting layer. Inset: schematic device structure of the device.

in between the PPy and Au, the device performance improves further. Figure 9.7 shows the current–voltage characteristics of a typical (−) ITO/PPy/PVK/Au (+) device. The device has a typical turn-on voltage of ∼ 10 V, and light follows closely with current after turn on. The device structure is shown schematically in the Fig. 9.7 inset.

The single-layer devices, the bilayer devices (with and without the PAN-CSA network electrode), and the inverted devices discussed are unipolar devices operating under a single-bias condition. We now discuss two novel device configurations that can be operated in both forward and reverse dc biases as well as in ac modes: the SCALE devices and color-variable bipolar/ac light-emitting devices.

The SCALE devices consist of a light-emitting layer sandwiched between two "insulating" redox polymer layers. The whole structure is then sandwiched between two electrodes. The SCALE device configuration is quite general; it can be applied to a variety of emitting and redox polymers, as well as electrodes. For the SCALE device presented here, PPy was used as the emissive layer; the emeraldine base (EB) form of polyaniline was utilized as the redox material; ITO and Al were used as electrodes. The Figure 9.8 inset shows schematically the structure of such SCALE devices. They emit light under both forward and reverse dc biases as well as under the ac driving voltage. Under low-frequency ac (sinusoidal) driving voltage, light pulses with twice the driving frequency were observed. Figure 9.8 shows the variation of the EL intensity of a ITO/EB/PPy/EB/Al device driven by a 60-Hz sinusoidal voltage. Under dc bias, these devices emit light in both

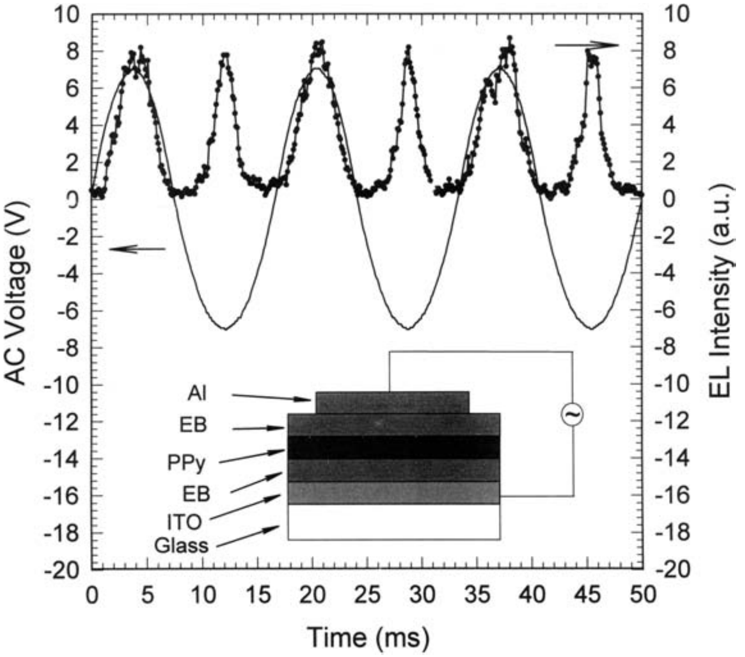

FIGURE 9.8. EL intensity as a function of time for a SCALE device driven by a 60-Hz sinusoidal voltage. Inset: schematic device structure of the SCALE device.

forward and reverse biases with almost symmetric current–voltage and brightness–voltage characteristics. This unusual behavior is attributed to the effects of charge accumulation at the polymer/polymer interfaces.[8] We examine the role of EB layers in the SCALE device operation by fabricating several single-layer and multi-layer devices, ITO/PPy/Al, ITO/EB/PPy/Al, ITO/PPy/EB/Al, ITO/EB/PPy/EB/Al, and ITO/EB/PPy/EB/Au, and comparing the device characteristics.

Figure 9.9 compares the current–voltage characteristics for ITO/PPy/Al, ITO/EB/PPy/Al, ITO/PPy/EB/Al, and ITO/EB/PPy/EB/Al devices. The light intensity follows closely with the corresponding current–voltage curve except for the ITO/PPy/EB/Al device in reverse bias, in which case no light was observed although there is significant current flow. Note that the tum-on voltage is lower and the current is higher at any given applied voltage when EB layers are added, indicating that EB facilitates, instead of limits, charge injection into the emitting polymer.

Photoinduced optical studies show that positive (P^+) and negative (P^-) polaron levels exist inside the π–π^* bandgap of EB associated with benzenoid and quinoid levels, respectively.[17] They are believed to play an important role in charge injection and transport. We propose the following mechanism for the SCALE device operation. Under low bias voltages, electrons and holes can be injected from the electrodes into the quinoid and benzenoid levels of EB and form negative and positive polarons, respectively. These polarons transport to the EB/PPy interfaces via

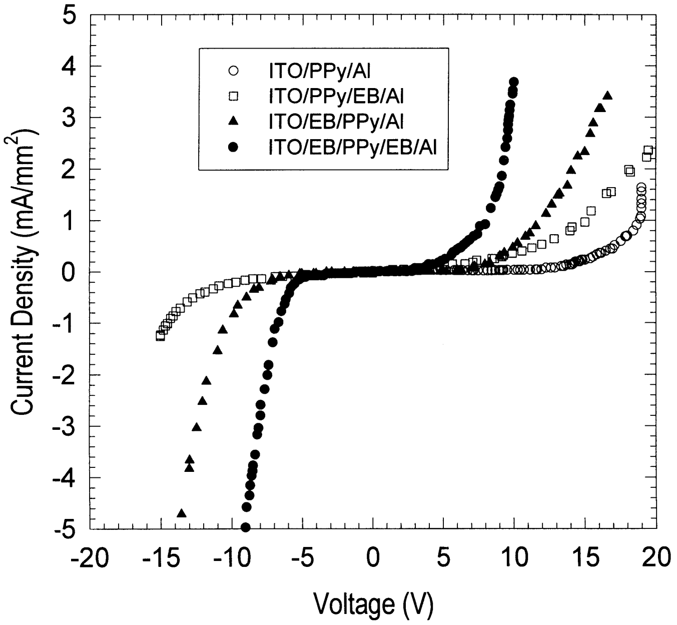

FIGURE 9.9. Current–voltage characteristics of four devices with different structures as shown in the legend. Note that the turn-on voltage *decreases* as the total number of layers *increases*.

a hopping mechanism and populate the EB/PPy interfaces at the polaron levels, as shown in Fig. 9.10. Because the polarons levels are within the π–π^* bandgap of EB and are also likely within the bandgap of PPy, the barriers for charge injection from electrodes to polaron levels of EB are significantly reduced as compared to injection directly to conduction and valence bands of PPy. Within this model, the limiting barriers for charge injection are changed from the electrode/polymer contacts as proposed for conventional polymer LEDs to the polymer/polymer (EB/PPy) interfaces of the SCALE devices. When the applied electric field is high enough, the stored charges begin to tunnel into the conduction and valence bands of PPy. When they meet, the injected charges may form intrachain excitons and decay radiatively to emit photons or follow other nonradiative decay paths. If the charge injection is not balanced, as is the case for most polymer LEDs, the excess charge carriers may migrate through the PPy layer without decaying. Most of these charges will be trapped in the opposite PPy/EB interface. When the bias voltage is reversed, the shallow trapped charges will be released from the interfaces and contribute to the recombination current. The deep trapped charges which act as quenchers or injection limiters in DC devices will be neutralized. We point out that the use of stable high-workfunction metals, such as Au, as electrodes to inject both electrons and holes for the SCALE devices may reduce the problems of aging of contacts of polymer light-emitting devices. Also, continuous reversal of the sign of the driving voltage under ac operation may reduce degradation.

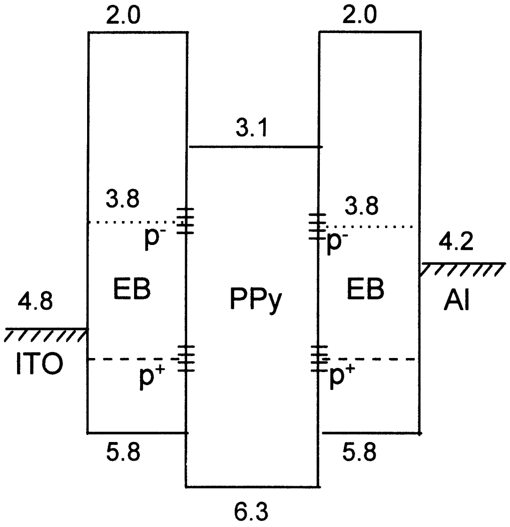

FIGURE 9.10. Energy diagram showing the role of positive (P^+) and negative (P^-) polaron levels of EB and the interface states in the SCALE device operation.

The SCALE devices generate the same color of light under both forward and reverse biases. Recently there has been great interest in developing color-variable polymer LEDs, (i.e., individual devices that can generate two or more colors of light). A number of approaches have been reported. One approach was based on blends of polythiophene derivatives in which different components emit different colors of light simultaneously with the intensity of each component varying with the applied voltage.[10] Although such devices can emit multiple colors of light, they have very limited control of the brightness at a desired color. Another approach is color-variable light-emitting electrochemical cells (LECs)[11] which emit two independent colors of light. The two color LECs offer an improved control of the color and brightness: The color is controlled by the polarity and the brightness is controlled by the magnitude of the driving voltage. However, due to the involvement of ionic species in the device operation, the response of the devices is intrinsically slow and not suitable for applications that requires rapid switching of colors. More recently, multilayer light-emitting devices which generate two independent colors were achieved at liquid-nitrogen temperature by inserting a blocking layer in between two different emitting polymer layers.[12] The two colors also can be controlled by the polarity of the driving voltage. Such an approach improves the device response time. However, it raises the device operating voltage due to the introduction of the charge-blocking layer and retains the stability concerns of "conventional" polymer LEDs. We have reported a new approach to the color-variable polymer light-emitting devices based on SCALE device structure: color-variable bipolar/ac light-emitting devices.[13] In this approach, we replace the EB layer on the cathode side of the SCALE device structure with sulfonated polyaniline (SPAN). Because the SPAN is capable of modifying the emission properties of certain

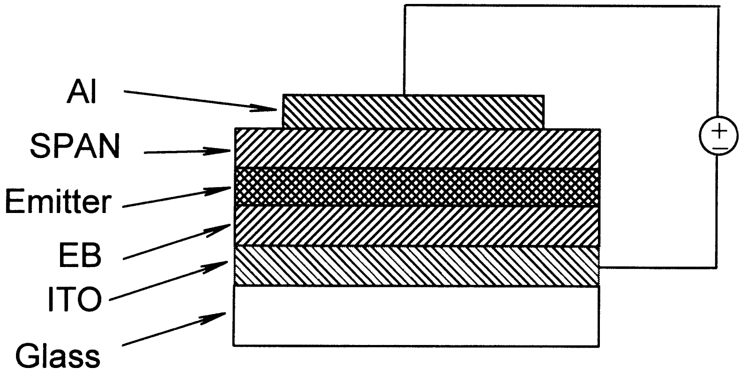

FIGURE 9.11. Schematic structure of the color-variable light-emitting devices.

pyridine-containing polymers at the interface such that the interface emits different colors of light than the bulk does, the device is able to generate a different color of light under forward and reverse biases. In this approach, the colors of light are controlled by selecting the desired emission locations, which, in, turn are controlled by the polarity of driving voltage and the charge-injection and charge-transport properties of the polymer layers. Because motion of ionic species is not required for device operation, a relatively fast time response is achieved, allowing the colors to be switched rapidly.

For the devices presented here, the wrapped copolymer @PPyVPV and a wrapped copolymer of polythiophene and polyphenylene derivative, @PTP, were used as the emitting materials; SPAN and EB were used as the redox materials; ITO and Al were used as electrodes. Figure 9.11 shows the schematic diagram of the device structure of the color-variable bipolar/ac light-emitting devices.

Figure 9.12 shows the typical current–voltage and brightness–voltage characteristics of the color-variable devices. The devices have typical turn-on voltages of $\sim$ 4-8 V depending on film thickness and work equally well under both polarities of driving voltage, as reported earlier for similar SCALE devices, with different colors of light being emitted. The light appeared red and green to the eye under forward and reverse biases, respectively, and was clearly visible under normal indoor lighting. Internal device efficiencies of 0.1% photons/electron has been achieved for the initial devices. Figure 9.13 shows the EL spectra of the color-variable device under forward and reverse biases. For comparison, the EL spectra for single-layer @PPyVPV and @PTP are also shown. The CIE chromaticity x, and y coordinates of the two spectra are calculated to be (0.654, 0.345) and (0.471, 0.519), respectively, showing both colors to be relatively pure (see Fig. 9.12 inset). The colors of the devices can be switched rapidly, up to $\sim$ 20 kHz, depending on device impedance and geometry.

The EL spectrum under forward bias is substantially different from that of the single-layer devices of either @PPyVPV or @PTP, suggesting that the light is generated from the interface between the emitter blend and either EB or SPAN under forward bias. To further clarify this, we fabricated the following de-

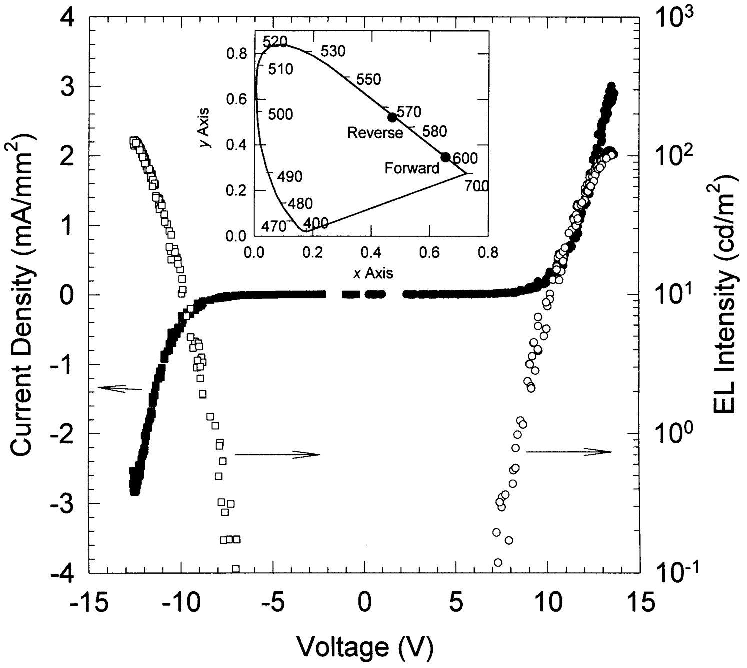

FIGURE 9.12. Current–voltage and brightness–voltage characteristics of a color-variable light-emitting device under forward and reverse bias conditions. The inset shows the colors of the device under forward and reverse biases in the CIE chromaticity diagram.

vices: ITO/@PPyVPV/Al; ITO/SPAN/@PPyVPV/Al; ITO/@PPyVPV/SPAN/Al; ITO/SPAN/@PPyVPV/SPAN/Al, and similar devices replacing SPAN with EB. All of these devices were fabricated and tested under similar conditions in forward bias. Among all these devices, only ITO/@PPyVPV/SPAN/Al and ITO/SPAN/@PPyVPV/SPAN/Al show dramatically red-shifted EL. This clearly demonstrates that the red light is generated from the @PPyVPV/SPAN interface on the cathode side under forward bias. Similar studies using @PTP as the emitting layer show that the emission properties of @PTP are not affected significantly by the presence of the SPAN layer.

The EL spectrum of the color-variable device under reverse bias are similar to those of the single-layer @PPyVPV and @PTP devices, implying that the light is generated either in the bulk of the emitting polymer or at the EB interface. The EB layer functions as a charge-injection enhancement layer, playing a similar role to that in SCALE devices reported earlier.[8] Under reverse bias, the SPAN layer on the cathode side plays a similar role.

It is noted that when the blend in the color-variable devices is replaced by pure @PPyVPV polymers, the devices emit red light in forward bias and red–orange light in reverse bias. This indicates that under reverse biases, the light is still generated near @PPyVPV/SPAN interfaces. This can be understood in terms of different

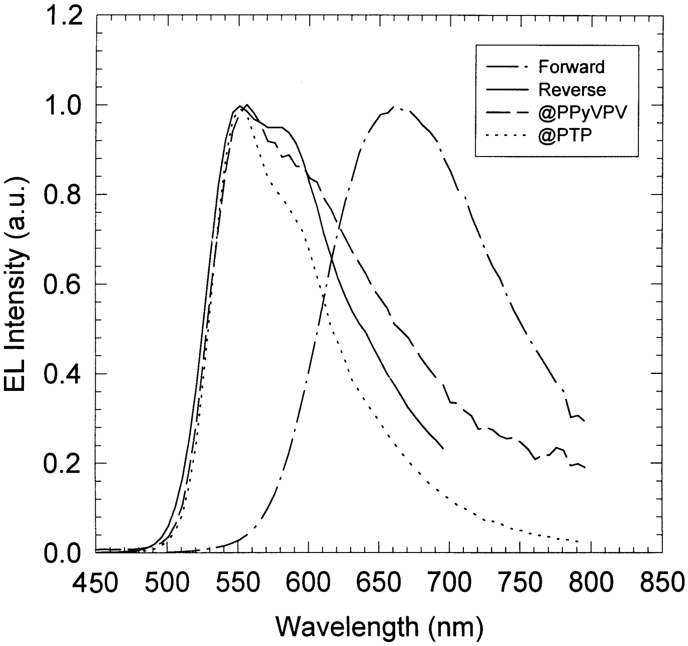

FIGURE 9.13. EL spectra of the color-variable device under forward and reverse bias conditions. For comparison, the EL spectra for single-layer PPyVPV and PTP devices also are shown.

electron- and hole-transport properties of the @PPyVPV and @PTP polymers. It is known that most conjugated polymers, including poly(phenylenevinylene) (PPV), poly(*p*-phenylene) (PPP), and polythiophene, have better hole-transport than electron-transport properties.[3] The addition of a high-electronegativity unit, pyridine, to the backbone is expected to improve the electron-transport properties. Therefore, tinder reverse bias, the light is still generated near the SPAN interface for the ITO/EB/@PPyVPV/SPAN/Al device. By adding @PTP, which is expected to have better hole-transport properties, to @PPyVPV, the overall hole-transport properties of the blend is improved and, hence, the light is generated away from the SPAN interface for the ITO/EB/Blend/SPAN/Al device under reverse bias, emitting green light. In fact, a gradual EL spectra shift toward green has been observed for the devices with increasing concentration of @PTP in the blend, as shown in Fig. 9.14.

The mechanism for the SPAN layer changing the emission properties of the @PPyVPV polymer is attributed to the formation of new emissive species due to protonation of the pyridyl units by SPAN. These species was identified by both absorption and PL experiments. Figure 9.15 shows the absorbance spectra of a @PPyVPV layer, a SPAN layer, and a bilayer of @PPyVPV/SPAN. SPAN is a self-doped, water-soluble conducting polymer with a room-temperature conductivity of 10^{-2} S/cm.[18] It has a wide optical window from green to near infrared @PPyVPV

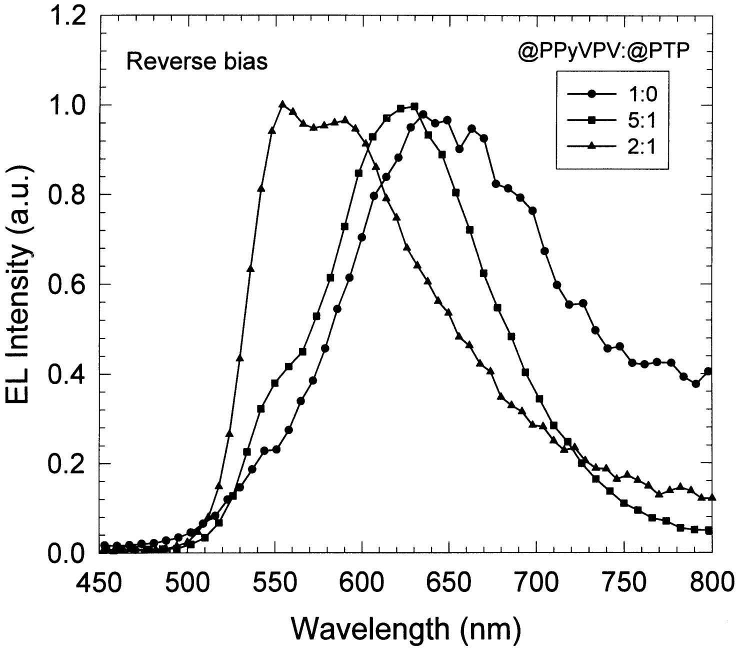

FIGURE 9.14. Comparison of the EL spectra of ITO/EB/@PPyVPV:@PTP/SPAN/Al with different @PPyVPV:@PTP ratios. When the concentration of @PTP increases, the EL spectrum under reverse bias shifts from red to green.

has an absorption band peaked around 480 mn. An extra shoulder around 500 nm is present in the absorption spectra of the bilayer of @PPyVPV/SPAN. The extra feature, assigned to the absorption at the interface, is clearly shown in the inset of Fig. 9.15 as a result of subtraction of the absorbance of each individual layers from that of the bilayer. We attribute the interface absorption to new species due to protonation of @PPyVPV by SPAN. One special feature of SPAN is that it is acidic in aqueous solution (it is often termed polyaniline sulfonic acid). On the other hand, the pyridyl unit is known to be susceptible to protonation or quarternization by acid.[19] To further clarify this, we performed the same absorption experiment on the films with the same configurations as above, but replacing the SPAN with toluene sulfonic acid (TSA). An almost identical absorbance feature to @PPyVPV/SPAN was found in the @PPyVPV/TSA bilayer, confirming that the new species at the @PPyVPV/SPAN interface originates from the protonated pyridyl units. The new species are emissive and emit red-shifted light as compared to a nonprotonated polymer.

Our approach to the color-variable LEDs presented here has a number of important advantages: (1) The two redox polymers modify the charge-injection properties of the polymer/metal interfaces, allowing the use of high-workfunction metals as electrodes. This potentially reduces the aging problems associated with "conventional" polymer LEDs, which must use reactive low-workfunction metals to

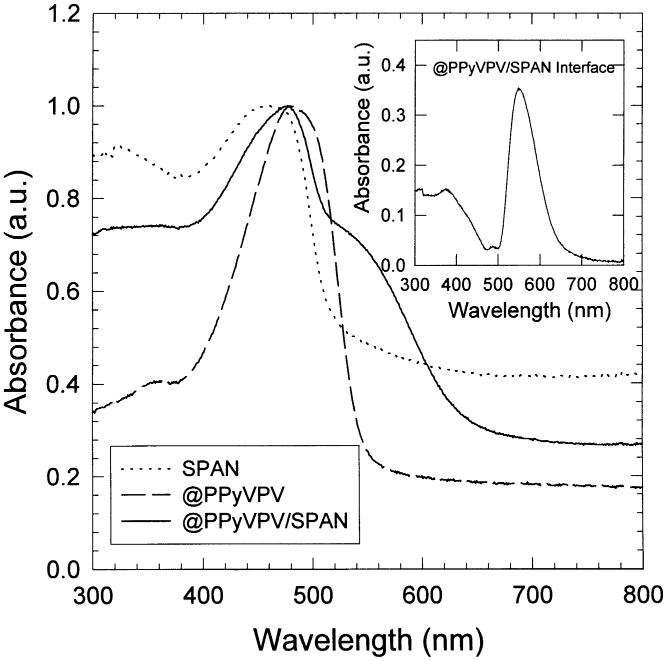

FIGURE 9.15. Absorbance spectra of a @PPyVPV film spin-cast from xylene solution, a SPAN film spin-cast from aqueous solution, and a bilayer of @PPyVPV/SPAN. Inset: absorbance spectra as a result of subtraction of the absorbance of each individual layers from that of the bilayer.

achieve efficient electron injection. (2) The introduction of the two redox polymers allows the devices to operate in both forward and reverse biases. Because no ionic species are involved directly in the device operation, the colors can be switched very rapidly, in sharp contrast to intrinsically slow response LECs. (3) The emission zone is confined in between the two emitting polymer/redox polymer interfaces and away from the electrodes, thereby avoiding EL quenching effects near the metal electrodes. (4) The emitting polymers are protected by the redox polymers against direct exposure to air, potentially improving the device stability. (5) Alternating current or periodically reversed operation may retard failure due to migration of metals from the electrodes into the polymer. Such an operation also may dissipate the build up of space charges.

9.4 Summary and Conclusion

In summary, we have presented a number of dc and ac light-emitting devices based on pyridine-containing conjugated polymers and copolymers. The high electron affinity of pyridine-based polymers enables the use of relatively stable metals such as Al as efficient electron-injecting contacts. Taking advantages of the better electron-transport properties of the pyridine-containing polymers, we have fabricated bilayer devices utilizing PVK as hole-transporting/electron-blocking polymer. The bilayer device structure improves the device quantum efficiency and brightness significantly due to the charge confinement and exciplex emission at the PVK/emitting polymer interface. The incorporation of the conducting polyaniline network electrode within PVK reduces the device turn-on voltage significantly while maintaining the high efficiency and brightness of the bilayer device. The high electron affinity of the pyridine-based polymers also enables the fabrication of novel devices such as inverted light-emitting devices, SCALE devices, and color-variable bipolar/ac light-emitting devices, which are capable of eliminating the use of low-workfunction metals as electrodes, potentially further improving the device operating stability and shelf life.

Acknowledgments

This work was supported in part by Office of Naval Research. We thank Dr. D. K. Fu, Dr. H. L. Wang, Professor T. M. Swager, and Professor A. G. MacDiarmid for providing us with samples used in this work.

References

[1] C. W. Tang and S. A. VanSlyke, Appl Phys. Lett. 51, 913 (1987).
[2] J. H. Burroughes, D. D. C. Bradley, A. R. Brown, R. N. Marks, K. Mackay, R. H. Friend, P. L. Bums, and A. B. Holmes, Nature 347, 539 (1990).
[3] D. D. C. Bradley, Synth. Met. 54, 401 (1993); J. Kido, Trends Polym. Sci. 2, 350 (1994).
[4] See, for example, Proc. Int. Confs. Sci. Tech. Synth. Met., 1994 [Synth. Met. 69–71 1995]; [Synth. Met. 84–86 1997]; J. W. Blatchford and A. J. Epstein, Am. J Phys. 64, 120 (1996), and references therein.
[5] I. D. Parker, J Appl. Phys. 75, 1656 (1994).
[6] N. C. Greenham, S. C. Moratti, D. D. C. Bradley, R. H. Friend, and A. B. Holmes, Nature 365, 628 (1993).
[7] A. J. Epstein, J. W. Blatchford, Y. Z. Wang, S. W. Jessen, D. D. Gebler, L. B. Lin, T. L. Gustafson, H. L. Wang, Y. W. Park, T. M. Swager, and A. G. MacDiarmid, Synth. Met. 78, 253 (1996).
[8] Y. Z. Wang, D. D. Gebler, L. B. Lin, J. W. Blatchford, S. W. Jessen, H. L. Wang, and A. J. Epstein, Appl. Phys. Lett. 68, 894 (1996).
[9] Q. Pei, G. Yu, C. Zhang, and A. J. Heeger, Science 269, 1086 (1995).
[10] M. Berggren, O. Inganas, G. Gustafsson, J. Rusmusson, M. R. Ansersson, T. Hjertberg, and O. Wennerstrom, Nature 372, 444 (1994).
[11] Y. Yang and Q. Pei, Appl. Phys. Lett. 68, 2708 (1996).
[12] M. Hamaguchi and K. Yoshino, Appl. Phys. Lett. 69, 143 (1996).
[13] Y. Z. Wang, D. D. Gebler, D. K. Fu, T. M. Swager, and A. J. Epstein, Appl Phys. Lett. 70, 3215 (1997).

[14] Y. Z. Wang, D. D. Gebler, D. K. Fu, T. M. Swager, and A. J. Epstein, Synth. Met. 85, 1179 (1997).

[15] Y. Yang, E. Westerweele, C. Zhang, P. Smith, and A. J. Heeger, J. Appl. Phys. 77, 694 (1995).

[16] D. D. Gebler, Y. Z. Wang, J. W. Blatchford, S. W. Jessen, T. L. Gustafson, D.-K. Fu, T. M. Swager, A. G. MacDiarmid, and A. J. Epstein, Appl. Phys. Lett. 70, 1644 (1997).

[17] R. P. McCall, J. M. Ginder, J. M. Leng, H. J. Ye, S. K. Manohar, J. G. Masters, G. E. Asturias, and A. G. MacDiarmid, Phys. Rev. B 41, 5202 (1990).

[18] W. Lee, G. Du, S. M. Long, A. J. Epstein, S. Shimizu, T. Saitoh, and M. Uzawa, Synth. Met. 84, 807 (1997).

[19] D. K. Fu, B. Xu, and T. M. Swager, Tetrahedron (in press).

10

Polyfluorene Electroluminescence

Paul A. Lane

10.1 Introduction

Fluorene-based polymers have been used as the emissive element in commercially available polymer displays, announced in October 2000.[1] The reported displays have a start emitting light below 2.5 V and an efficiency as high as 16 lm/W, and can emit 10 times the brightness of a CRT television screen at just 5 V. This achievement is all the more remarkable given that the synthesis of polyfluorene was first reported only in 1989.[2] Ironically, polyfluorene was synthesized shortly before Burroughes et al. reported the discovery of the polymer LED in 1990.[3] This pair of discoveries 1 year and half the world apart paved the way for the recent breakthrough.

The physical, optical, and electrical properties of polyfluorene derivatives have stimulated widespread interest in these polymers and their applications. Alkyl- and dialkyl-substituted polyfluorenes were first synthesized by Fukuda et al. in 1989.[2] These polymers are stable above their melting points, permitting melt processing not possible for many conjugated polymers. Such processing was crucial in the development of LEDs with highly polarized emission.[4] Polyfluorene has an optical gap of approximately 3 eV and efficient, blue fluorescence[5] — a key property needed for the development of full-color polymer displays. The optical and electronic properties of polyfluorenes have been modified through copolymerization of fluorene monomers with other molecular subunits.[6] Other notable properties

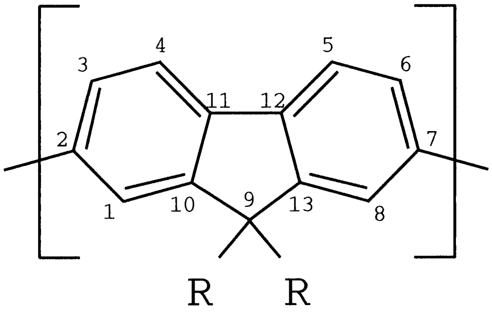

FIGURE 10.1. The chemical structure of poly(9,9′-dialkyl-fluorene-2,7-diyl). The positions of carbon atoms are labeled 1 through 13 and R=C_nH_{2n+1}.

of polyfluorenes include electron mobility as high as[7] 0.085 cm^2/Vs and unusual sensitivity of the optical properties to film morphology.[8–10]

10.2 Synthesis and Characterization of Polyfluorene

10.2.1 Polyfluorene Synthesis

Polyfluorene was first synthesized by Fukuda et al. via oxidative polymerization of fluorene monomers using ferric chloride as a catalyst.[2,11] Both mono- and dialkyl-substituted polyfluorenes were synthesized. Figure 10.1 shows the repeat unit of poly(9,9′-dialkyl-fluorene-2,7-diyl). The polymers are soluble in common solvents such as chloroform, dichloromethane, and toluene. Figure 10.2 shows the absorption and fluorescence spectra of a solution of poly(9,9′-dihexylfluorene-2,7-diyl) (PDHF) in chloroform.[11] The onset of the π–π^* absorption is at 420 nm, rising to a peak at 380 nm, yielding an optical gap of 2.95 eV. The fluorescence spectrum contains vibronic peaks at 417 and 440 nm and a shoulder at 470–480 nm.

The most notable property of these polymers is that they were fusible at relatively low temperatures. From visual inspection, Fukuda et al. reported a melting point that decreased from 100°C for PDHF to a minimum of approximately 30°C for poly(9,9-didodecylfluorene). In light of later differential scanning calorimetry studies of poly(9,9-dioctylfluorene),[12] it is possible that the glass transition temperature was observed rather than the melting point. The molecular weights of the polymers were evaluated by gel permeation chromatography (GPC) and calibrated with polystyrene standards. The molecular weight (M_W) and mean (M_n) average of the dialkyl-substituted polyfluorenes are summarized in Table 10.1. The number-average molecular weights are relatively low, with degrees of polymerization of approximately 10 repeat units.

Polyfluorenes synthesized by Fukuda et al. have relatively local molecular weights and some degree of branching and nonconjugated linkages via conjugation at carbon atoms at positions other than 2 and 7.[11] Inbasekaran and co-workers chose to minimize such effects by using transition-metal-catalyzed reactions of

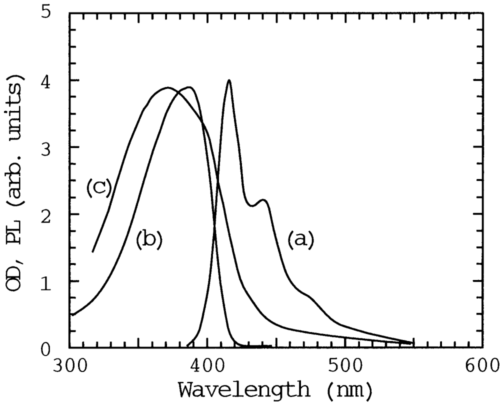

FIGURE 10.2. Absorption and fluorescence spectra of PDHF: (a) absorption and (b) fluorescence spectra in chloroform solution; (c) absorption spectrum of a film. (From Ref. 11.)

TABLE 10.1. Molecular Weights of Dialkyl-Substituted Polyfluorenes.

Chain length	M_W	M_n	PD	Repeat units
6	31,400	4,620	6.8	13.9
6	**44,700**	**18,600**	**2.4**	**48**
8	10,700	3,280	3.3	8.5
8	**56,000**	**34,000**	**1.65**	**100**
10	9,940	4,020	2.5	9.1
16	15,600	5,160	3.0	8.4

Note: The typical number of repeat units was calculated from the number-weight average (M_n). The boldfaced values are for polymers synthesized via the improved Suzuki coupling reaction Ref. 13 and 25.

2,7-dihalogenated fluorenes.[13,14] When applying this reaction to 2,7-dichloro-9,9-di-*n*-hexylfluorene and its dibromo analog, PDHF was synthesized with a significantly higher degree of polymerization and lower polydispersity than the ferric-chloride-synthesized polyfluorenes (see Table 1 for comparison). It was concluded that the major impediment to synthesizing higher-molecular-weight polymers was the limited solubility of PDHF and other short-chain dialkyl-substituted polyfluorenes in solvents required for the reaction. Consequently, the polymer precipitates out of solution, terminating polymerization.

The palladium-catalyzed synthesis of mixed biphenyls from phenylboronic acid and aryl bromide, discovered by Suzuki et al.,[15] is tolerant of functional groups and is insensitive to water and can be used to provide true alternating (not statistical) copolymers. Dow researchers have synthesized a variety of very pure polyfluorenes and fluorene-based copolymers using an improved Suzuki coupling reaction. The improved process yields polymers with high molecular weights and low polydispersity (< 2) and requires significantly less time (24 h) than the Suzuki coupling

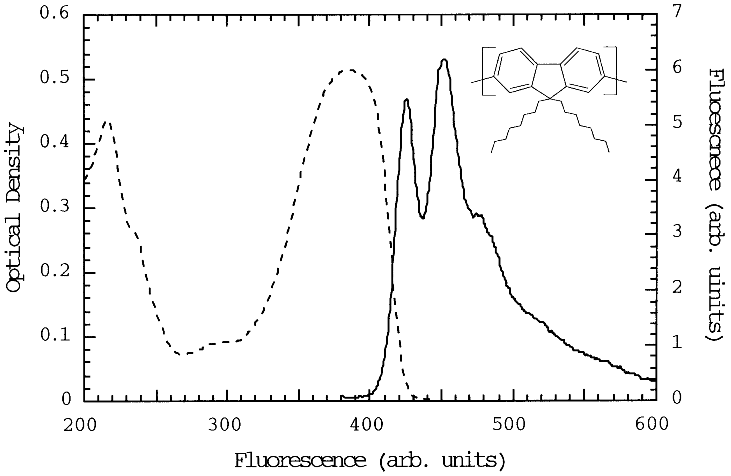

FIGURE 10.3. Absorption (dashed line) and fluorescence (solid line) spectra of a spin-cast PFO film. (From Ref. 10.) Inset: Chemical structure of PFO.

reaction (up to 72 h). For example, poly(9,9-dioctyl-fluroene-2,7-diyl) (PFO)[16] has been synthesized with a molecular weight average of 150,000 g/mol.[1]

10.2.2 Optical and Physical Characterization

This subsection will concentrate on PFO, the most fully characterized polyfluorene. Figure 10.3 shows the absorption and fluorescence spectra of a PFO film prepared by spin-casting from a chloroform solution.[10] The onset of the π–π^* absorption is at 420 nm, rising to a peak at 380 nm, yielding an optical gap of 2.95 eV. The fluorescence spectrum contains vibronic peaks at 426, 452, and 476 nm. The Stokes shift is less than 50 meV, a small value in comparison to most conjugated polymers. This value is similar to that of highly ordered ladder-type poly(*para*-phenylene)[16] and indicative of extended π- conjugation. The fluorescence quantum yield of PFO, measured using a calibrated integrating sphere, has been measured to be $50 \pm 10\%$, depending on the film morphology.[17] The high fluorescence efficiency has led several groups to study laser action in polyfluorenes.[18–20] The photostability and thermal stability of polyfluorene has also been shown to be significantly better than that of poly(*para*-phenylenevinylene) (PPVs).[21,22] Polyfluorenes do not contain the vinylene linkage of PPV, which is especially vulnerable to photo-oxidation, resulting in the formation of fluorescence-quenching carbonyls.

---

[1] The conventional nomenclature for poly(9,9-dioctyl-fluorene-2,7-diyl) would be PDOF. This polymer has also been referred to as PFO by Bradley and co-workers and F8 by Bernius et al. The Bradley naming convention is used here, as this abbreviation has been most commonly used.

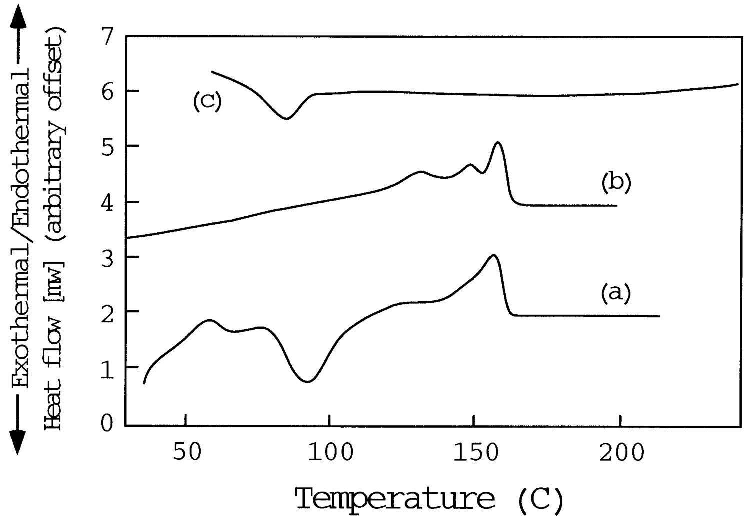

FIGURE 10.4. Differential scanning calorimetric thermograms of PFO for the following thermal cycles: (a) heating at 20°C/min of a quenched film, (b) heating at 20°C/min of a crystallized film, and (c) cooling at 20°C/min after equilibriating at 270°C. (From Ref. 12.)

Grell and co-workers[8,12] have shown that polyfluorenes have liquid-crystalline (LC) phases—a property which can be exploited to produce aligned films with polarized absorption and fluorescence spectra and enhanced charge transport (see below). PFO melts into a birefringent fluid state at 170°C when viewed through a polarization microscope.[12] The fluid becomes isotropic at 270–280°C and shows a reversible transition between LC and isotropic phases. The LC texture is retained if the film is removed from the hot stage and cooled rapidly, indicating that the LC phase can be quenched into a glass without crystallization. Figure 10.4a shows a differential scanning calorimetry (DSC) heating scan for a PFO film that was spin-cast onto a substrate, equilibriated at 220°C, and quenched to room temperature. The quenched sample shows a glass transition, a crystallization exothermal peak at 93°C, and a melting endothermal peak at 156°C. The DSC scan of a film which has been slowly cooled to room temperature at a rate of 0.2°C/min, shown in Fig. 10.4b, has melting peaks but no crystallization peak on heating. The DSC cooling scan, undertaken at a rate of 20°C/min and shown in Fig. 10.4c, shows a exothermal crystallization peak at 81°C. It was found that cooling rates of 50°C/min or more were found to be effective in almost completely suppress crystallization.

To align the LC state of PFO, a film was spin-cast onto a substrate coated with a rubbed polyimide alignment layer. The film was subsequently heated to 200°C and either cooled at 1°C/min to 170°C and then quenched to room temperature (aligned glass) or cooled at 0.2°C/min to room temperature (aligned crystalline film). Figure 10.5 shows the polarized absorption spectra of the resulting films. As-deposited films showed isotropic absorbance, but aligned films showed polarization ratios of 6.6:1 and 6.4:1 and the absorbance maxima (380 nm).

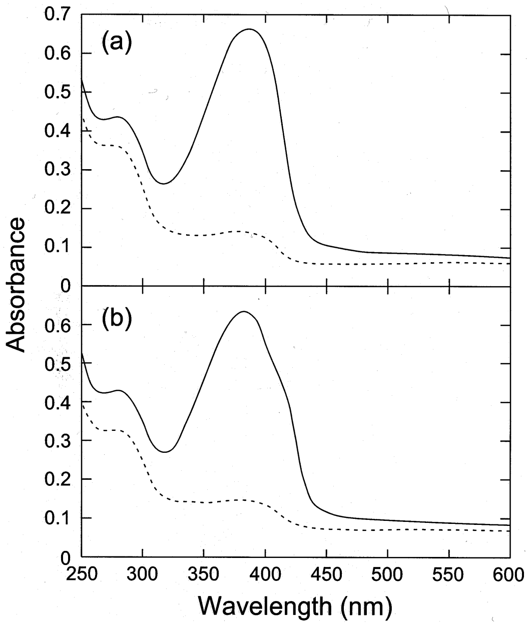

FIGURE 10.5. Polarized absorption spectra of aligned (a) glassy PFO film and (b) crystallized PFO films. The spectra were measured for light polarized parallel (solid line) and perpendicular (dashed line) to the rubbing direction. (From Ref. 12.)

10.2.3 Electronic Characterization

Fukuda et al. noted that polyfluorene was significantly more difficult to dope (by exposure to iodine vapor) than other polymers such as polythiophene. This is a consequence of the large ionization potential. A working knowledge of the ionization potential and electron affinity is necessary for device applications in order to determine appropriate electrodes with low to injection of charge carriers. The oxidation and reduction potentials of PFO were measured by cyclic voltammetry (CV). CV is a method in which the potential applied to an electrochemical cell is scanned and changes in cell current are monitored. Figure 10.6 shows a cyclic voltammogram for a PFO thin film deposited on a glassy carbon working electrode.[23] The reduction and oxidation peaks were measured to be $E_{\text{red}} = -2.54$ V and $E_{\text{ox}} = 1.60$ V. From these measurements, the ionization potential was calculated to be 5.8 eV and the electronic affinity to be 2.12 eV.[23] These values are compared to the workfunctions of possible electrodes in the inset of Fig. 10.6. In a later study, the effect of depositing a metal electrode on the vacuum energy level of PFO was studied.[24]

Although the optical properties of polyfluorenes are attractive, the electrical properties are, if anything, even more so. Charge carrier mobilities are a key factor in determining the performance of polymer LEDs because of the requirement of both balanced injection and transport of electrons and holes. Charge carrier mo-

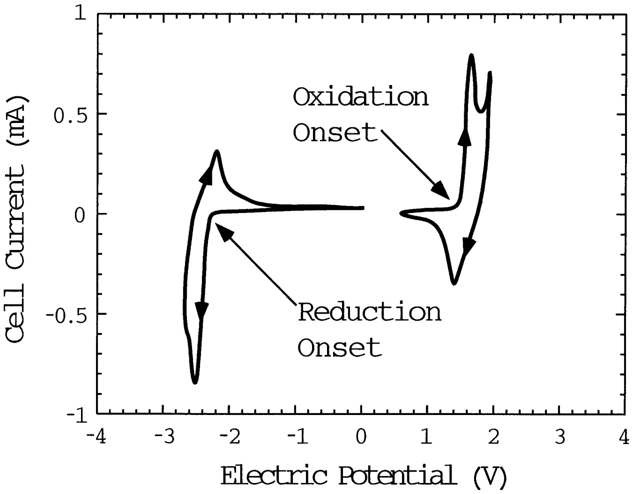

FIGURE 10.6. Cyclic voltammogram. for a PFO thin film deposited on a carbon working electrode, measured relative to a Ag/AgC1 reference electrode. (From Ref. 23.)

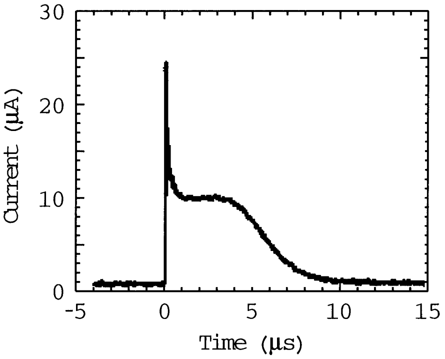

FIGURE 10.7. Time-of-flight current transient for a PFO film. Measurements were performed on a 3-μm-thick film at an electric field of 160 kV/cm. (From Ref. 25.)

bilities in PFO have been studied by the time-of-flight[7,25] (TOF) method and in field-effect transistors (FETs).[26] The TOF experiment involves the photogeneration of a packet of charge carriers by illumination of a sample sandwiched between two electrodes. The drift of carriers under an external bias to the collecting electrode results in a time-dependent current that is monitored across an external load resistor.[27]

Figure 10.7 shows a hole current transient, recorded at an electric field of 160 kV/cm and at room temperature.[27] The initial current spike is followed by a constant current plateau that corresponds to nondispersive hole transport with a time-independent drift velocity. The observed nondispersive hole transport is an indication of excellent purity and chemical regularity. The drop in current at $t > 4$

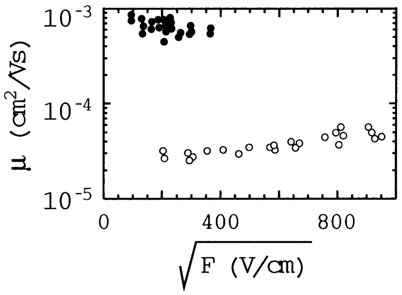

FIGURE 10.8. Calculated hole mobility for PFO as a function of the applied electric field. Open circles are for an isotropic spin-coated film (data from Ref. 25) and filled circles are for an aligned, quenched PFO film. (Data from Ref. 7.)

μs is due to the arrival of holes at the indium–tin-oxide (ITO) electrode where they are discharged. The transit time is determined by plotting the intersection of the plateau and dropoff of the current on a double logarithmic scale. The hole mobility (μ) can then be calculated from the transit time (t) by the relation $\mu = d/tF$, where d is the film thickness and, F is the electric field magnitude. The calculated mobility, measured as a function of electric field, is shown in Fig. 10.8. The hole mobility is found to vary from $\mu = 3 \times 10^{-4}$ cm^2/V s at $F = 40$ kV/cm to $\mu = 4.2 \times 10^{-4}$ cm^2/V s at $F = 800$ kV/cm. PFO has one of the highest recorded mobilities for a conjugated polymer and, unlike polythiophenes, combines this with high fluorescence efficiency, which makes it especially attractive for as an emissive element in light-emitting devices (LEDs). The observation of nondispersive hole transport is also highly unusual.

The hole mobility reported for PFO is promising, but it can be improved. Polymers are highly anisotropic media with significantly different intrachain and interchain properties. Time-resolved microwave conductivity measurements showed that the intrachain mobility of electrons and holes on MEH-PPV in solution is orders of magnitude larger than the mobility observed by TOF measurements of conjugated polymer films.[28] PFO exhibits thermotropic liquid crystallinity[12] and can be homogeneously aligned in the nematic phase on a rubbed alignment layer. These properties raise the possibility that hole mobility in PFO could be enhanced by the preparation of aligned PFO films. TOF measurements were performed on an aligned, 2.25-μm-thick PFO film, which was prepared on a 30-nm-thick polyimide alignment layer on an ITO-coated glass substrate. The alignment procedure for PFO is given elsewhere.[7] Semitransparent gold contacts (70 nm thick) were then deposited onto the polymer film. Charge carriers were generated by an excitation source polarized parallel to the alignment direction of the film, which minimizes the penetration depth of the light. A hole current transient at a field of 44 kV/cm is shown in Fig. 10.9. As for the isotropic film, the arrival of holes at the ITO electrode is clearly observed by a drop in the photocurrent at $t \approx 1$ μs after excitation. The calculated hole mobility ranges from $\mu = 5 \times 10^{-3}$ to 9×10^{-3}cm^2/V s, exceptionally large for a soluble polymer (Fig. 10.8).

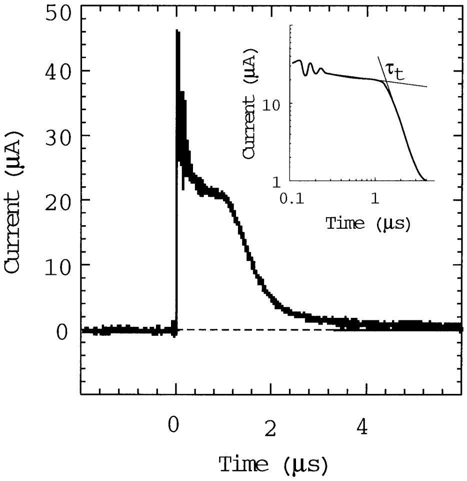

FIGURE 10.9. Time-of-flight current transient for an aligned, 2-μm-thick PFO film at an electric field of 44 kV/cm. (From Ref. 7.)

Field-effect mobilities, measured on an alternating dioctylfluorene–bithiophene copolymer, are equally promising. A mechanically rubbed polyimide alignment layer was deposited onto a glass substrate, followed by the deposition of gold source-drain electrodes by shadow mask evaporation. A 20–30-nm-thick film of poly(9,9′-dioctyl-fluorene-*co*-bithiophene) (F8T2) was spin-cast on top of the alignment layer and annealed at 275–285° C for 3–15 min under nitrogen. Chain alignment is frozen in by quenching the film to room temperature. Finally, a 300–1300-nm gate insulating layer of poly(vinylphenol) is spun from an alcohol solution (in which F8T2 is insoluble) and a gold gate electrode is deposited on top of the structure. The chemical structure of F8T2 and a schematic diagram of the top-gate transistor are shown in Fig. 10.10. Isotropic devices were prepared on areas of the substrate that are not coated by polyimide.

Figure 10.11a shows the transfer characteristics of a top-gate transistor made from an isotropic F8T2 film.[26] The top-gate F8T2 devices exhibit transistor action with on–off current switching ratios exceeding 10^5 and good operating stability. The isotropic devices exhibit mobilities $\mu = (3 - 5) \times 10^{-3}$ cm^2/V s. This mobility is significantly higher than devices in which the F8T2 film underwent no thermal treatment ($\mu < 10^{-3}$ cm^2/V s). Figure 10.11b shows the saturated transfer characteristics of an aligned F8T2 transistor, measured with a source-drain voltage $V_{sd} = -60$ V.[26] High mobilities of 0.009–0.02 cm^2/V s are obtained if the current flow is parallel to the alignment direction. Significantly lower values [$\mu = (1 - 2) \times 10^{-3}$cm^2/V s] were obtained for perpendicular orientation. The mobility anisotropy (5–8) is slightly lower than the dichroic ratio (8–10), measured by polarized absorption. The isotropic device mobility lies between the two aligned values, as might be expected, and is significantly higher than that of an untreated device.

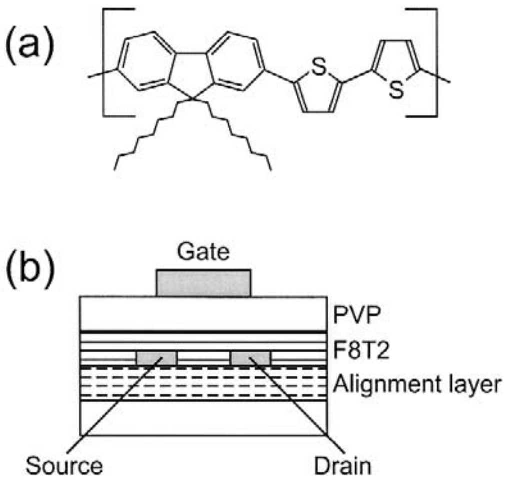

FIGURE 10.10. (a) The chemical structure of F8T2. (b) Schematic diagram of the top-gate polymer FET. (Adapted from Ref. 26.)

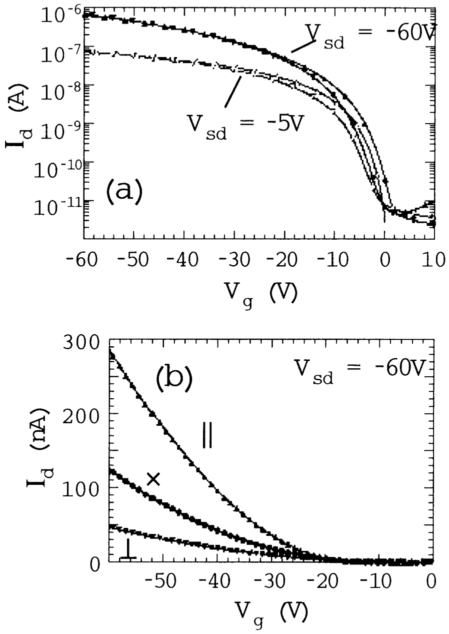

FIGURE 10.11. (a) Transfer characteristics of a glassy, but isotropic top-gate F8T2 transistor with source-drain biases of −5 and −60 V. (b) Saturated transfer characteristics of an aligned F8T2 transistor with channels parallel (upward triangles) and perpendicular (downward triangles). A glassy, but isotropic device without uniaxial alignment is also shown (circles). All characteristics measured with a source-drain bias of −60 V. (From Ref. 26.)

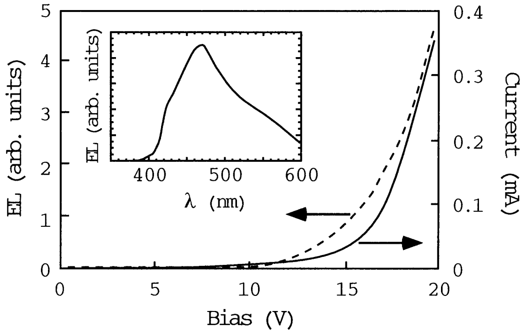

FIGURE 10.12. The current–voltage–luminance characteristics of a PDHF-based LED. The EL spectrum is presented in the inset. (Adapted from Ref. 30.)

10.3 Electroluminescence

10.3.1 Polyfluorene Electroluminescence

10.3.1.1 Polyfluorene LEDs

The report of electroluminescence (EL) from poly(*para*-phenylenevinylene)[3,29] (PPV) spurred fabrication of the first LEDs using polyfluorene as an emissive layer. Ohmori and co-workers prepared an LED by spin-coating a 100–200-nm-thick layer of PDHF onto a glass substrate coated by indium–tin oxide.[30] A magnesium:indium electrode was deposited onto the spin-coated polymer film under vacuum (10^{-7} torr). Figure 10.12 shows the current–voltage–luminance characteristics of the PDHF LED.[11] The turn-on bias of the LED was above 10 V, due to a large injection barrier between the magnesium electrode and the lowest unoccupied molecular orbital (LUMO) of polyfluorene. The EL intensity increased linearly with increasing current density, tending to saturate at higher currents. The electroluminescence spectrum of the LED (inset in Fig. 10.12) follows the fluorescence spectrum of PDHF (Fig. 10.2).

The efficiency of PDHF LEDs was significantly enhanced by adding hole- and electron-transport layers to the device. These devices used *N*,*N*′-diphenyl-*N*,*N*′-(3-methylphenyl)-1,1′-biphenyl-4,4′-diamine (TPD) as a hole-transport layer, 2,(4-biphenylyl)-5-(4-*tert*-butylphenyl)-1,3,4-oxadizole (PBD) as an electron-transport layer, and vapor-deposited PDHF as an emissive layer.[31] The authors note that fluorescence spectrum of vapor-deposited PDHF is modestly blue-shifted from that of a spin-cast film. This indicates that the polymer chain length of the vapor-deposited film is shorter, possibly due to preferential evaporation of shorter-chain macromolecules. Figure 10.13 compares the EL intensity of single-layer PDHF LEDs with vacuum-deposited two-layer (ITO/TPD/PDHF/Ag:Mg) and three-layer (ITO/TPD/PDHF/PBD/Ag:Mg) devices. The turn-on voltages of multiplayer LEDs were still above 10 V, but the relative efficiency of LEDs was enhanced by over an order of magnitude with respect to single-layer LEDs prepared by spin-casting a PDHF film from solution.

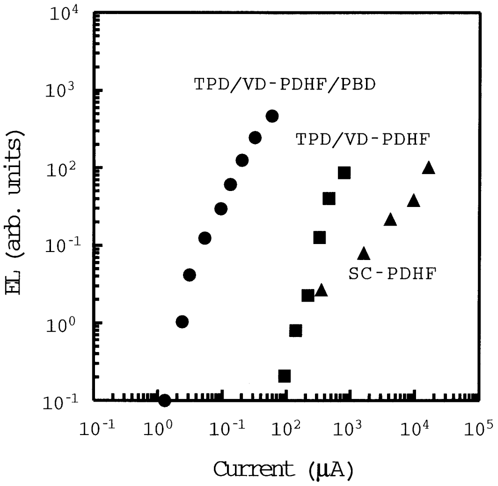

FIGURE 10.13. Dependence of the emission intensity on injection current of one-, two-, and three-layer LEDs. A spin-cast PDHF film was used for the single-layer device and vapor-deposited films were used for the two- and three-layer devices. (From Ref. 31.)

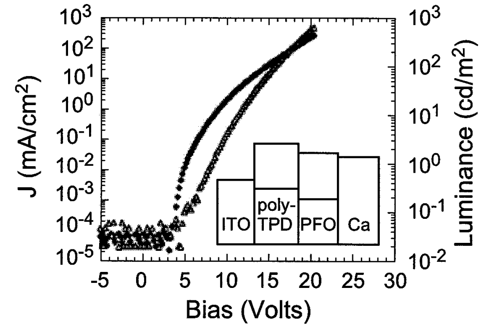

FIGURE 10.14. Current–voltage–luminance characteristics of an ITO/poly-TPD (60 nm)/PFO (200 nm)/Ca LED. The current density (filled diamonds) and luminance (open triangles) are plotted as a function of bias voltage on log-linear axes. The inset shows a schematic energy-level structure for the device. (From Ref. 5.)

10.3.1.2 High-Brightness LEDs

The first quantitative study of the device efficiency of polyfluorene LEDs was reported by Grice and co-workers in 1998.[5] The LED used ITO-coated glass as the anode, a hole-transport layer of a polymeric triphenyldiamene (poly-TPD), an emissive layer of PFO, and a calcium cathode. A schematic energy-level structure for the device is inset in Fig. 10.14. The injection barrier for holes into poly-TPD is approximately 0.3 eV, much less than that for PFO (0.8 eV), and the injection barrier for electrons into PFO is approximately 0.1 eV. Poly-TPD had excellent film-forming properties, was transparent to PFO emission, and was insoluble in

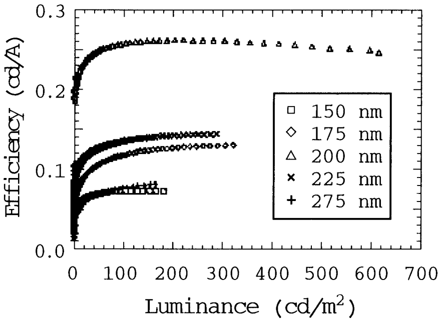

FIGURE 10.15. Efficiency (Cd/A) versus luminance (Cd/m^2) curves for poly-TPD/PFO LEDs with varying thicknesses. The current densities at high bias voltages were limited by the compliance of the power supply. (From Ref. 5.)

xylene, the solvent used to dissolve PFO. The poly-TPD film thickness was 60 nm and varying PFO thicknesses were used to evaluate the effect of film thickness on device efficiency.

Figure 10.14 shows the current–voltage–luminance characteristics of a poly-TPD/PFO device with a 200-nm-thick PFO film. The current turns on at 3.5 V, whereas the EL turn-on bias occurs at 5 V. The luminance reaches 600 Cd/m^2 at drive voltages of 20 V and for a current density of 250 mA/cm^2. The maximum external EL quantum efficiency reaches 0.2% at 150 Cd/m^2 for a 17.5-V bias. The corresponding power efficiency is 0.04 lm/W at 600 Cd/m^2. The EL spectrum closely followed the fluorescence spectrum (Fig. 10.3), although the long-wavelength tail was moderately enhanced. Figure 10.15 shows the luminance dependence of the device efficiency (given in Cd/A) for LEDs with PFO thicknesses between 150 and 275 nm. The best EL performance is achieved for a 200 nm thick PFO layer. A sharp drop in efficiency is seen for devices 25 nm thicker or thinner than this critical thickness.

10.3.1.3 Polyfluorene LECs

Polyfluorene derivatives have also been used in light-emitting electrochemical cells fabricated by Yang and Pei.[32,33] The active material in a light-emitting cell (LEC) is a polymer blend which contains a high concentration of an ionic conductor, usually poly(ethylene oxide) (PEO) complexed with a lithium salt. The PEO–salt complex is very polar and requires the use of a polar solvent. However, most conjugated polymers are not soluble in such solvents and, hence, it is difficult to find a solvent which codissolves both polymers and produces good quality films of such blends without phase segregation. In order to overcome these problems, poly[8,9-bis(3,6-dioxaheptyl)-fluorene-2,7-diyl] (BDOH-PF) was synthesized. The side groups of this polymer are PEO-like units, which allows partial or complete replacement of PEO by the emissive polymer. These side groups also increase the solubility of the polymer in common organic solvents. Figure 10.16 shows the absorption and fluorescence spectra of BDOH-PF in dilute tetrahydrofuran (THF) solution and a

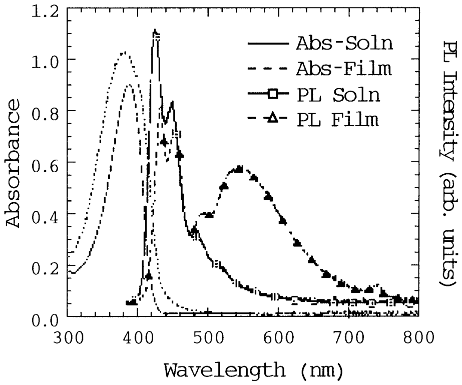

FIGURE 10.16. Optical absorption and fluorescence spectra of BDOH-PF in THF (0.01 mg/ml) and of a thin film spin-cast from THF solution (20 mg/mL). (From Ref. 32.)

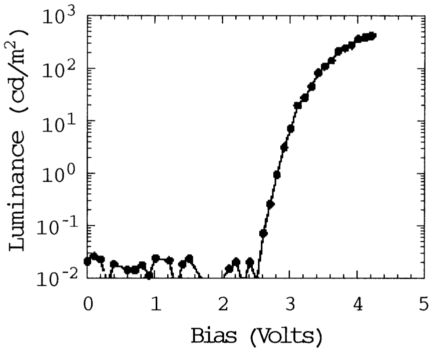

FIGURE 10.17. Luminance–voltage characteristics of an LEC fabricated from BDOH-PF blended with PEO and a Li salt. (From Ref. 33.)

spin-cast film. The chemical structure of BDOH-PF is inset in Figure 10.16. The fluorescence yield of BDOH-PF was measured to be 73% using a calibrated integrating sphere, significantly higher than PFO and other dialkyl-substituted polyfluorenes.

Light-emitting cells were fabricated from a blend of BDOH-PF with PEO lithium triflate, at a weight ratio of ∼ 10:1:2. Figure 10.17 shows the luminance–voltage characteristics of a PDOH-PF LEC. The device turns on at ∼ 2.5 V and reaches 400 Cd/m^2 at 4 V, values considerably lower than the PDHF LEDs reported previously. Figure 10.18 shows the EL spectrum of the LEC. The EL spectrum is dominated by a peak at 560 nm, which has been identified as excimer emission.[34] The EL spectrum is completely dominated by the excimer band if operated at high voltage or after extended operation. One problem with these devices is that the polyfluorene LECs required seconds to start emitting light, far slower than that of LEDs (10^{-9} s) As LED performance has subsequently outperformed that of the LECs, this approach is not being commercially pursued.

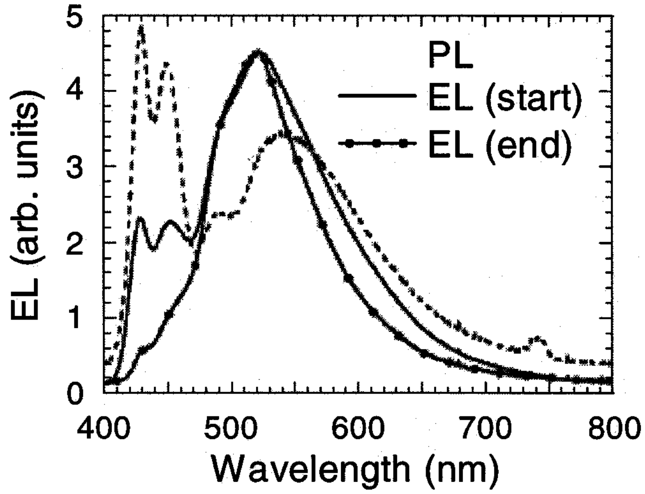

FIGURE 10.18. Electroluminescent spectra of a BDOH-PF LEC: initial EL and the EL after long-term stress. The initial EL is blue and the long-term stress EL changes to bluegreen. The PL spectrum of a thin film of BDOH-PF is also shown for comparison. (From Ref. 33.)

10.3.1.4 Polarized Electroluminescence

The liquid-crystalline properties of polyfluorenes have been exploited in several studies to produce LEDs that emit highly polarized electroluminescence.[4,35] Such devices would be ideal as backlights for liquid-crystal displays. An ideal device would eliminate the need for a polarizer, simplifying construction and effectively doubling the device efficiency. Even if the polarization ratio is insufficient to eliminate the polarizer, there can still be a significant improvement in power efficiency, as the polarizer would absorb much less than 50% of incident light. A polyfluorene with a branched side chain was synthesized in order to achieve a higher polarization than discussed above for PFO. The chemical structure of poly(9,9-di(ethylhexyl)-fluorene-2,7-diyl) (PF2/6) is inset in Fig. 10.19. DSC scans of PF2/6 showed that the polymer is liquid crystalline with a phase transition at 167°C to a birefringent fluid phase. Figure 10.19 shows polarized absorption spectra of PF2/6, aligned into a monodomain on a polyimide layer.[4] The absorption spectra show a very strong dichroism (11:1), well in excess of that reported for PFO (6.5:1, Fig. 10.5).

The conventional method for achieving monodomain alignment in thin films is to deposit onto an alignment layer such as a polyimide which has been rubbed by a cloth. Incorporating an insulating alignment layer can be problematic for producing LEDs. To produce aligned devices, the alignment layer consisted of a rubbed polyimidide (PI) filled with a hole conductor (triphenyldiamine or TPD) which had previously been used in LEDs.[36] The luminance–voltage characteristics for devices fabricated with doped and undoped alignment layers are Inset in Fig. 10.20.

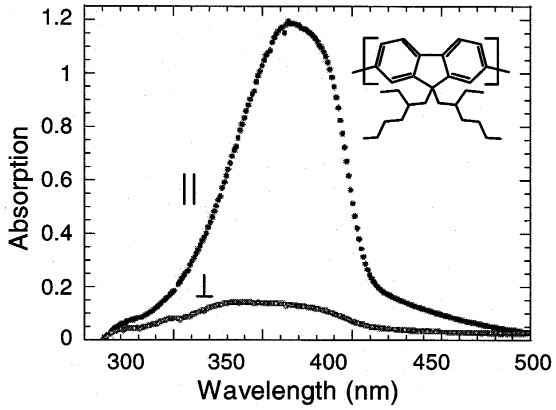

FIGURE 10.19. Polarized absorption spectra for a film of PF2/6 oriented on a rubbed polyimide alignment layer. The spectra were measured for light polarized parallel (filled circles) and perpendicular (open circles) to the rubbing direction. (From Ref. 4.)

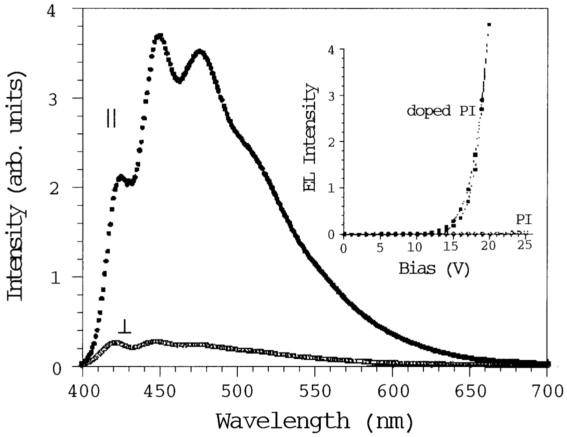

FIGURE 10.20. EL spectra of a thermally aligned ITO:doped-PI:PF2/6:Ca LED with the polarizer aligned parallel (filled circles) or perpendicular (open circles) to the rubbing direction. Inset: Luminance–voltage characteristics for devices with doped (filled squares) and undoped (open circles) PI layers. (From Ref. 4.)

Doping the alignment layer reduces the turn-on voltage and enhances the LED brightness.

Figure 10.20 shows the polarized EL spectra of an aligned PF2/6 LED device measured parallel and orthogonal to the rubbing direction.[4] The parallel EL has peaks at 425, 451, nm 477 nm, with a shoulder at approximately 505 nm. The corresponding spectra for perpendicular detection are blue-shifted by about 5 nm. The most intense peak is at 477 nm and has a polarization ratio of 15, significantly higher than the polarization measured in absorbance. One attractive possibility is that the recombination zone within the LED lies close to the alignment layer, where the polymer will be most highly aligned.

An alternative approach is to use another conjugated polymer as an alignment layers. Jandke et al. mechanically rubbed a partially PPV precursor polymer to prepare aligned PPV film.[37] Devices showed bright EL (200 Cd/m^2 at 20 V) and an EL polarization ratio of 12:1. However, scratches in the film during rubbing caused stability problems. Whitehead et al. prepared a polarized polyfluorene LED by using a PPV alignment layer to prepare highly polarized PFO LEDs.[35] The PPV precursor solution was spin-coated onto a quartz substrate, partially converted for 2 mins in air at 180° C, and then rubbed using a commercial rubbing machine. The PPV was then converted in argon at 165° C to a fully conjugated, insoluble polymer. Finally, a PFO film was spin-coated on top of the PPV alignment layer and converted to a monodomain as discussed above. Figure 10.21 shows the polarized absorption (Fig. 10.21a) and fluorescence (Fig. 10.21b) spectra for a PFO film oriented on a rubbed PPV alignment layer.[35] Polarization ratios of 7:1 in absorbance and 8.5–10:1 in fluorescence were achieved. This dichroism is slightly better than that reported for alignment on a rubbed polyimide layer.[4,9]

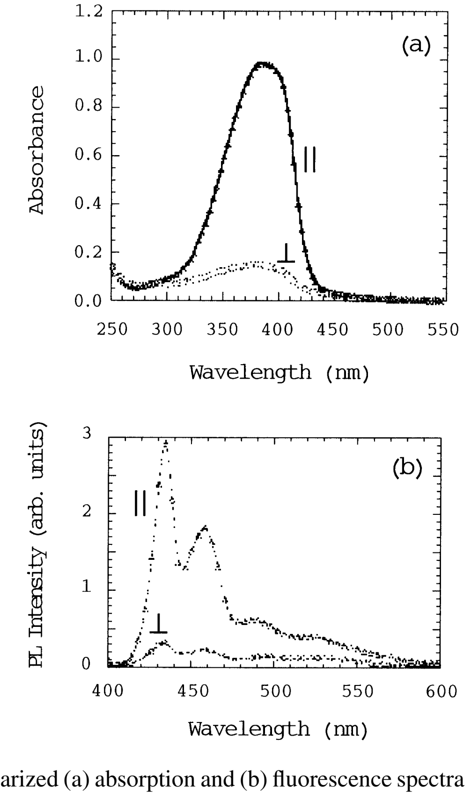

FIGURE 10.21. Polarized (a) absorption and (b) fluorescence spectra for a film of PFO on a rubbed PPV alignment layer. The spectra were measured for light polarized parallel (open triangles) and perpendicular (open circles) to the rubbing direction. (From Ref. 35.)

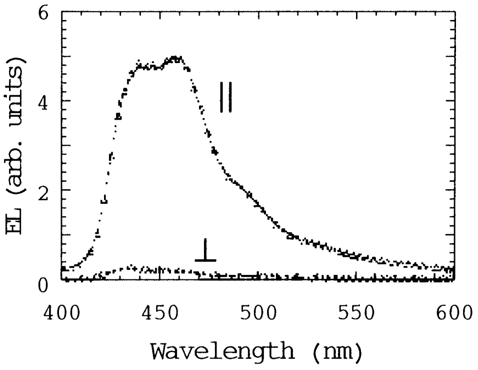

FIGURE 10.22. Polarized electroluminescence spectra from an aligned ITO/PPV/PFO/Ca LED. The spectra were measured for light polarized parallel (open triangles) and perpendicular (open circles) to the rubbing direction. (From Ref. 35.)

A similar protocol was followed for the preparation of LEDs, with the substitution of ITO-coated glass for quartz and evaporation of a calcium cathode on top of the PFO film. Devices were stored and tested in a nitrogen atmosphere. Devices showed a turn-on at 7.5 V and reached a brightness of 350 Cd/m^2 at 19 V. Device efficiencies were found to be somewhat lower than the PFO/poly-TPD devices discussed earlier. Figure 10.22 shows the polarized EL spectra of the PFO/PPV LED.[35] The ratio of the integrated intensities for parallel and perpendicular polarized EL is 19:1, with a peak polarization ratio of 25:1 at the 458-nm peak. These values are double those achieved for fluorescence, which is consistent with the PF6/2-polyimide devices reported earlier. The emission is blue, as expected for PFO, but the spectra shape differs somewhat from the fluorescence spectrum of PFO (Fig. 10.3). The strong peak at 433 nm is significantly weaker. EL must pass through the PPV alignment layer. Given the overlap of the PPV absorption spectrum with PFO fluorescence, this spectral difference is consistent with absorption of EL by the PPV alignment layer. The devices reached a brightness adequate for use as a backlight in a liquid-crystal display.

10.3.2 Fluorene-Based Copolymers

Polyfluorenes show great promise, but the actual devices fall short of performance required for commercial development. There has, however, been great success in producing highly efficient polymer LEDs using alternating copolymers with fluorene moieties. A number of groups have synthesized fluorene-based copolymers and studied their application to LEDs.[38–53] LEDs based on fluorene copolymers produced by Inbasekaran and co-workers will be highlighted here, as these materials were used to produce the polymer displays mentioned at the start of this chapter.[1]

Inbasekaran and co-workers have produced a wide variety of fluorene-based copolymers using the Pd-catalyzed polymerization reaction. Figure 10.23 shows

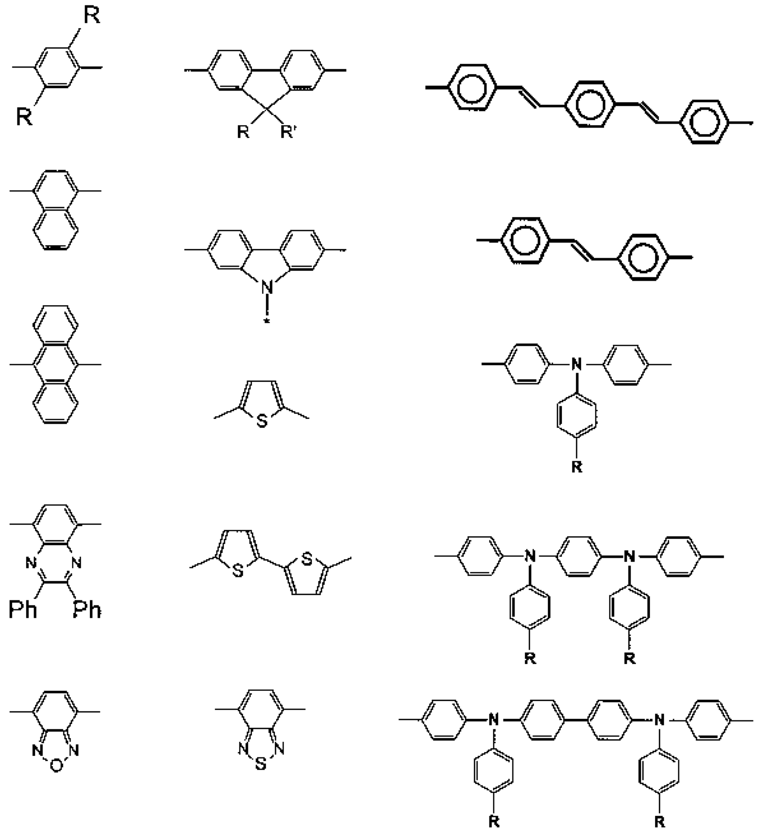

FIGURE 10.23. Molecular subunits used with fluorene in alternating copolymers. (From Ref. 6.)

examples of alternating copolymers produced in this manner. Incorporation of other moieties makes it possible to tune the optical and electronic properties of fluorene polymers. For example, tertiary aromatic amines have excellent hole-transport properties and have been used in photoconductors and LEDs. Amine–fluorene copolymers have hole mobilities up to 10^{-3} cm^2/V s [54–57] suggesting their use as hole-transport materials in LEDs[5] as well as photoconductors.[58] Copolymerization also makes it possible to tune the emission color. A wide range of fluorene copolymers with fluorescence spanning the entire visible spectrum has been synthesized. No other class of fluorescent polymers offers such a wide range of color emission that have been incorporated into LEDs with high efficiency, low operating voltages, and long lifetimes.

Most notable among the Dow copolymers is poly(9,9-dioctylfluorene-*alt*-benzothiadiazole) (F8BT). Figure 10.24 shows the absorption and fluorescence spectra of a blend containing 95% PFO and 5% F8BT; the copolymer repeat unit

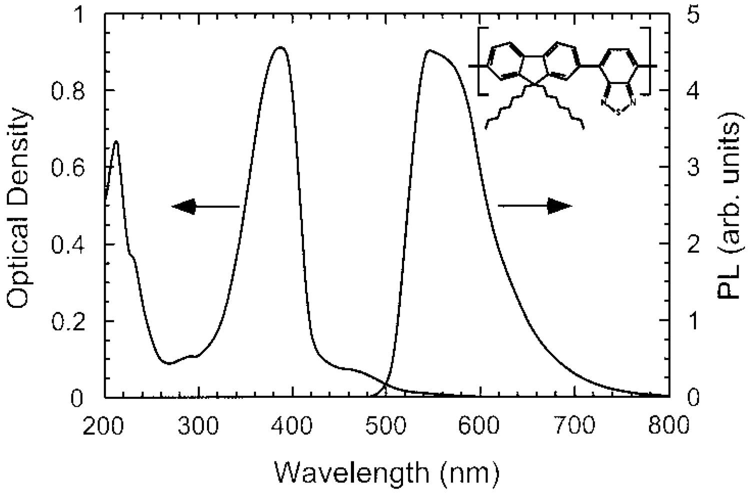

FIGURE 10.24. Absorption and fluorescence spectra of F8BT. The polymer repeat unit is presented in the inset. (From Ref. 59.)

is presented in the inset.[59] The absorption and fluorescence spectra of F8BT are somewhat red-shifted from those of PFO—the absorption peak of F8BT is at 460 nm and the fluorescence peak is at 550 nm. He and co-workers[60,61] have produced high-performance bilayer LEDs using such blends as an emissive layer and poly(9,9-dioctylfluorene-*co*-bis-N,N'-(4-alkoxyphenyl)-N,N'-phenyl-1,4-phenylenediamine), a fluorene–amine copolymer, as a hole-transport layer. Figure 10.25 shows current–voltage characteristics of an F8BT LED.[60] The I–V curve exhibits diodelike behavior, with an on/off current ratio greater than 10^3 at ±25 V. The turn-on voltage for electroluminescence was measured to be $\sim$ 7 V and linearly increased with current density. The EL spectrum of the LED is shown in the inset of Fig. 10.25. The EL spectrum shows a peak at 545 nm with a full-width at half maximum of about 80 nm, in good agreement with the fluorescence spectrum.

Figure 10.26 shows the efficiency of the LED, as a function of the current density. The emission efficiency reaches a peak of 14.5 Cd/A at about 34 mA/cm^2 with 5000 Cd/m^2 luminance. The corresponding external quantum efficiency is 3.86%. The inset of Fig. 10.26 shows the luminous efficiency as a function of the current density. The peak value is 2.26 lm/W at 17 mA/cm^2 with 2400 Cd/m^2 luminance. He and Kanicki later reported higher efficiencies (56.2 Cd/A and 9.0 lm/W) for LEDs using the same emitting and hole-transport layers for an LED fabricated on a flexible, plastic substrate.[61] The turn-on voltage of the LEDs was measured to be $\sim$ 6V.

Color tuning by polymerization is an attractive feature of the Pd-catalyzed polymerization reaction developed by Inbasekaran and co-workers. Fig. 10.27 shows

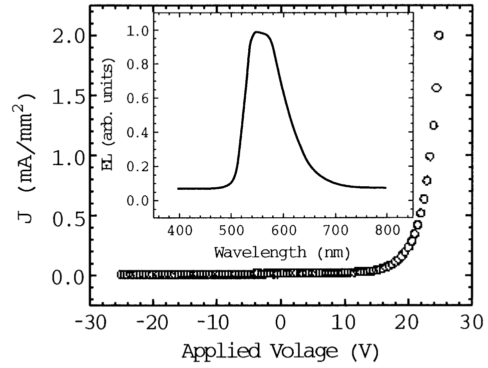

FIGURE 10.25. *I–V* characteristics of bilayer LEDs. The device structure is Al/140 nm F8BT/70 nm PFMO/ITO and the EL spectrum is presented in the inset. (From Ref. 60.)

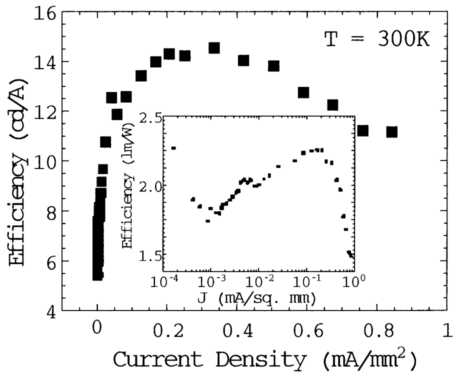

FIGURE 10.26. Emission and luminous efficiency (inset) of the F8BT LEDs as a function of current density. (From Ref. 61.)

the device characteristics and EL spectra of two such devices.[6] The green LED has a maximum EL peak at 534 nm and the red device has its maximum emission at 634 nm. The CIE (Commission Internationale de 1'Eclairage) color coordinates are (0.385, 0.579) for the green LED and (0.683, 0.313) for the red LED. Both devices use 40 nm of poly(ethylenedioxythiophene)/polystyrenesulphonic acid (PEDOT/PSS) as the hole injection/transport layer and 80 nm of the fluorene copolymer as an emissive layer. Both LEDs turn on below 3 V and possess relatively constant efficiency over a wide luminance range.[6] Fig. 10.28 shows a plot of the device efficiency (Cd/A) for the green LED over a luminance range of up to 30,000 Cd/m^2. A similar plot for the red emitter is less favorable owing to the reduced sensitivity of the eye at longer wavelengths.

The stability of LEDs is a critical parameter for commercialization that is not reported in most academic studies of polymer LEDs. In this aspect, polyfluorenes have proven to be exceptional. Fig 10.29 shows the lifetime plot of a red polymer

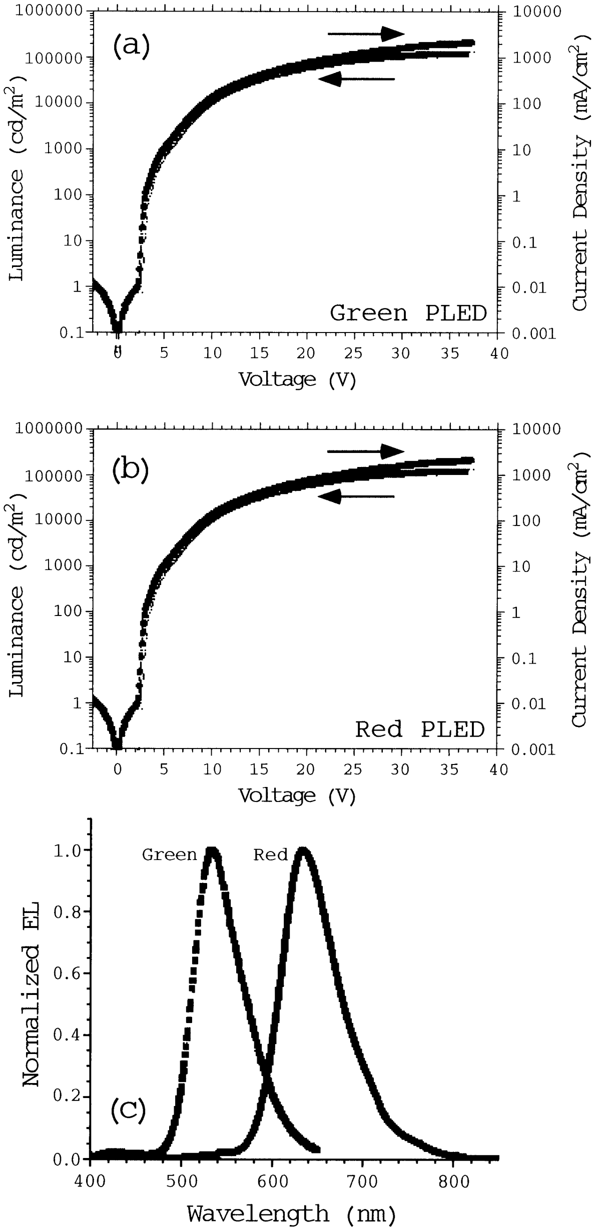

FIGURE 10.27. Current–voltage–luminance characteristics of polyfluorene copolymer LEDs using (a) green and (b) red emitters. (c) EL spectra of the respective LEDs. (From Ref. 6.)

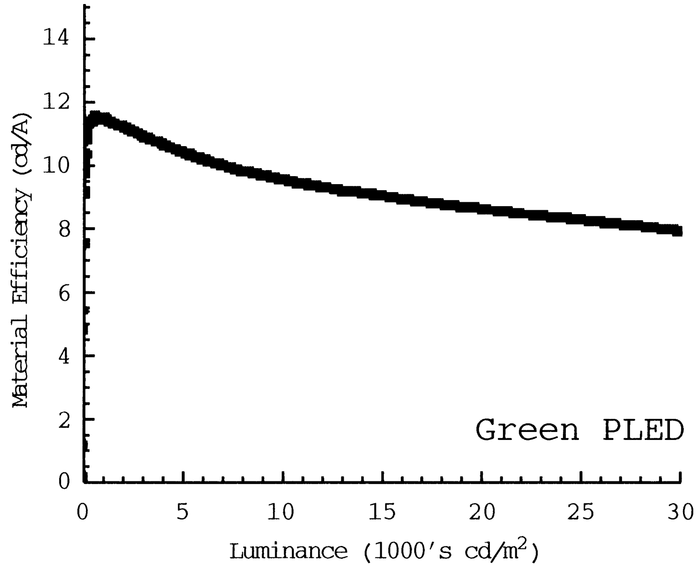

FIGURE 10.28. Plot of the material efficiency (Cd/A) against luminance (Cd/m^2) for the green LED shown in Ref. 27. (From Ref. 6.)

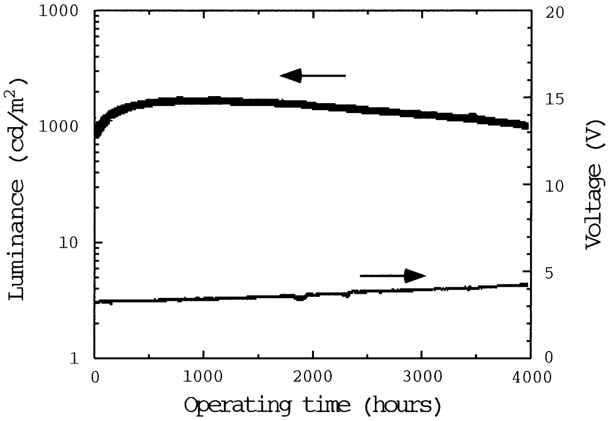

FIGURE 10.29. Stability measurements of a LED based on a red fluorene copolymer, showing the luminance decay and voltage rise with time. All measurements were performed at a luminance of 100 Cd/m^2. (From Ref. 6.)

LED, operated continuously at a brightness of 100 Cd/m^2. When plotted on a double-logarithmic axis, a half-life of 5500 h was obtained for this device. The operating voltage was observed to gradually rise with time, as has been reported elsewhere[62] and attributed to the formation of deep traps in the polymer film as the device ages.[63] The superior photostability of polyfluorenes is likely a contributing factor to device stability. Studies of a series of devices correlated the device half-life with the reciprocal square of the initial luminance.

10.3.3 Doped Polyfluorene Light-Emitting Diodes

10.3.3.1 Fluorescent Dopants

An alternate approach to color tuning by copolymerization is the use of a doped polymer film. Doping is widely used for molecular LEDs and has been assumed to rely on energy transfer from a host to a guest (donor to acceptor). Förster transfer is a resonant dipole coupling process that transfers energy between singlet states and conserves the spin state of the donor and the acceptor chromophores. It is dependent on the energetic overlap between the donor emission spectrum and the acceptor absorption spectrum and has an inverse sixth-power dependence on the donor–acceptor separation.[64] The efficacy of energy transfer between two materials can be characterized by a Förster-transfer radius, R_0. This corresponds to the average separation between donor and acceptor for which the probability of transfer is equal to the probability of recombination on the donor. The Förster radius can be calculated from the fluorescence spectrum of PFO with the absorption spectrum of PtOEP. The expected relation is

$$(R_0)^6 = \frac{cK^2}{N_A n^4} \frac{\int F_m(E)\varepsilon_Q(E)\,dE}{E^4}, \tag{1}$$

where K^2 is an orientation factor (2/3 for random orientation), N_A is Avogadro's number, n is the refractive index of the host, F_m is the normalized fluorescence spectrum of the host, ε_Q is the molar decadic extinction coefficient of the guest, and E is the energy in wave numbers.[65]

Figure 10.30 shows the absorption and fluorescence spectra of 5,10,15,20-tetraphenyl-21H,23H-porphine (TPP).[17] The chemical structure of TPP is inset. The porphyrin Soret band is seen as a strong, narrow absorption peak at 418 nm. The weaker absorption peaks at 512 and 550 nm are the Q bands, also typical of porphyrins. The fluorescence spectrum has peaks at 653 and 714 nm and the fluorescence quantum yield has been measured to be 11% in solution exposed to air.[66] The Soret absorption band has strong overlap with the fluorescence spectrum of PFO, resulting in efficient Förster transfer. The Förster-transfer radius has been calculated from the relative overlap of these spectra to be 4.8 nm.

Only a very low concentration of TPP in PFO is needed to entirely quench PFO fluorescence. Figure 10.31 show the fluorescence quantum yields for TPP and PFO emission components of the spectra as a function of TPP concentration in the blend film. The effective distance between TPP molecules is given on the upper horizontal axis, assuming a uniform dispersion of TPP in the film ($1/n = \frac{4}{3}\pi r^3$). The crossover point from PFO to TPP occurs at 5.4 nm separation, in rough agreement with the calculated Förster-transfer radius.

Light-emitting devices were fabricated by depositing a hole-transport layer of fluorene copolymer:poly(9,9-dioctyl-*co*-bis-N,N'-(3-carboxyphenyl)-bis-N,N'-

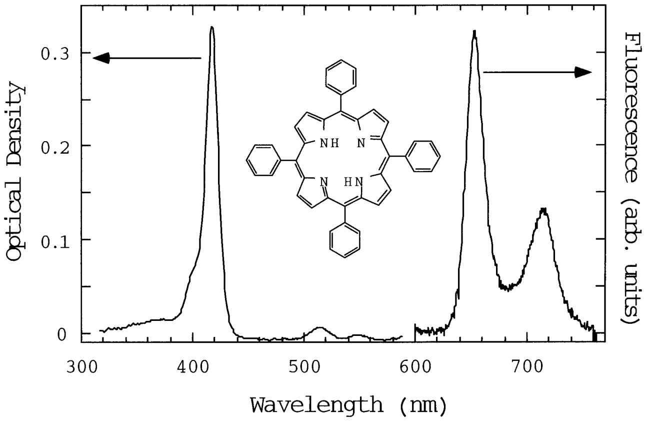

FIGURE 10.30. The absorption (left axis) and fluorescence (right axis) spectra of a film of TPP doped into a PMMA host matrix at 5 wt% concentration. The chemical structure of TPP is presented in the inset. (From Ref. 17.)

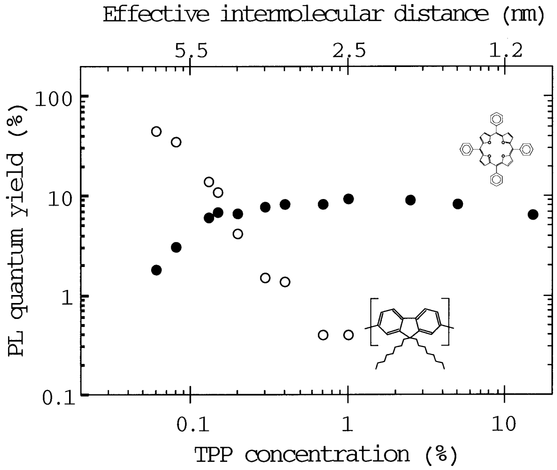

FIGURE 10.31. The fluorescence quantum yields of TPP (filled circles) and PFO (open circles) in a blend film as a function of TPP concentration by weight. The upper *x*-axis shows the TPP intermolecular distance. (From Ref. 17.)

phenylbenzidine) (BFA) onto an ITO-coated glass substrate and then spin-coating a 150-nm-thick PFO:TPP film having a dopant concentration of 2.5% by weight. Figure 10.32 shows a plot of the current density as a function of applied bias for a PFO:TPP LED and a similarly constructed PFO LED. The brightness of the doped LED reaches a luminance of 1 Cd/m^2 at 20 V (0.25 mA/cm^2) and 90 cd/m^2 at 33 V (60 mA/cm^2). The calculated EL quantum efficiency is 0.9%. Although the EL quantum yield of the TPP-doped LED is nearly five times higher than that with PFO alone, the operating bias has increased by approximately 10 V.

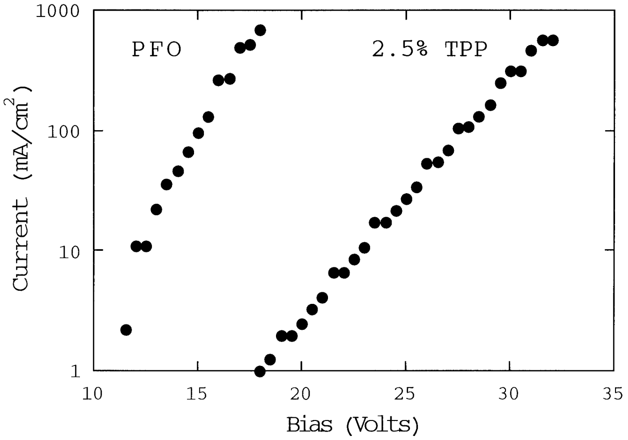

FIGURE 10.32. Current density as a function of applied bias for PFO and PFO:TPP blend LEDs. The TPP concentration was 2.5% by weight and the devices were otherwise identical. (From Ref. 17.)

In order to further investigate this result, time-of-flight studies were conducted on doped PFO:TPP films.[67] The experimental conditions were similar to those discussed earlier for TOF measurements of PFO films.[7] Figure 10.33 compares the TOF transient for an undoped PFO film (Fig. 10.33a) and one doped by 2.5% TPP by weight (Fig. 10.33b). The forward-bias transient of the undoped film shows a current plateau as earlier, indicating nondispersive hole transport. In contrast, the reverse-bias transient of the undoped film shows no such plateau, indicating dispersive transport of electrons at much lower mobilities. Upon doping a PFO film by TPP, both the forward- and reverse-bias transients show highly dispersive transport and reduced mobility. Hole mobility has been dramatically reduced and the current plateau has been lost, indicating that charge transport in the doped film has become highly dispersive. This indicates a large increase in the density of traps upon doping a PFO film. The large increase in the operating voltage of the blend LEDs and the reduced carrier mobility in PFO:TPP blends is strong evidence for charge trapping in such films.

Sainova et al. undertook a complementary study in the effect of blending an emissive layer of PF2/6 (Fig. 10.19) with hole-transporting molecules with different oxidation potentials.[68] LEDs were prepared from PF2/6 and PF2/6 doped at 3% by weight with a triphenylarnine derivative (TPTE), a starburst amine (ST 755), and N,N'-diphenyl-N,N'-bis-α-naphtylbenzidide (ST 16/7). All devices were fabricated at ambient conditions by spin-coating a 25-nm-thick layer of PEDOT/PSS onto an ITO substrate and then spin-coating the polymer (blend) solution and capping with a Ca/Al top electrode. Typical emission-layer thicknesses were 90 nm. Figure 10.34 compares the current–voltage characteristics of the doped LEDs with a PF2/6 LED. The current density significantly decreases upon blending a hole-transport material into PF2/6. The ionization potential (IP) of the hole-transport materials are 4.96 eV for TPTE, 5.3 eV for ST 755, and 5.5 eV for ST 16/7 as

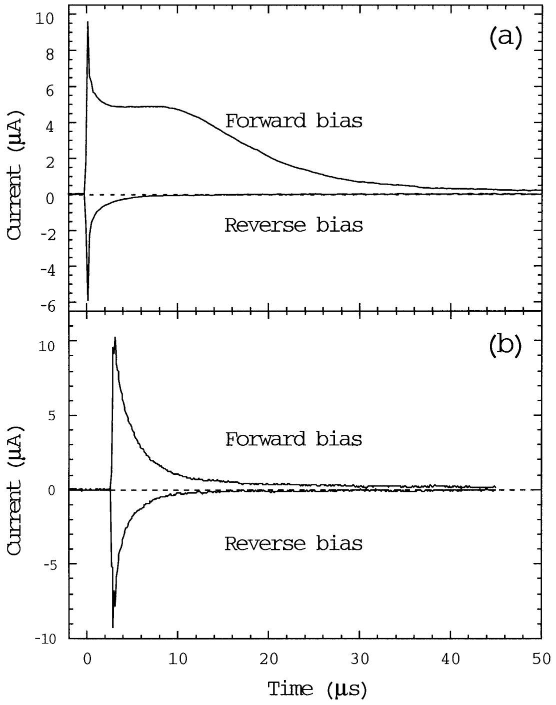

FIGURE 10.33. Time-of-flight transients for (a) a neat PFO film and (b) a PFO film doped with 2.5% TPP by weight. (From Ref. 67.)

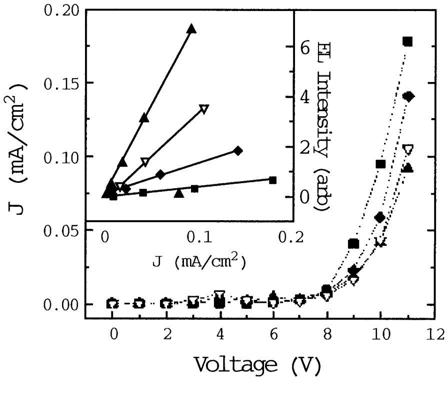

FIGURE 10.34. Current–voltage characteristics of the LEDs based on PF2/6 and blends with different hole-transport materials. Filled squares: PF2/6; filled triangles: PF2/6+TPTE; filled diamonds: PF2/6+ST 755; open triangles: PF2/6+ST 16/7. Inset: The EL intensity versus current characteristics. (From Ref. 68.)

compared to an IP of 5.8 eV for PF2/6. All hole-transport materials will act as hole traps, but only ST 16/7 has a larger electron affinity and thus might act as an electron trap.

Although the current density at a given bias is reduced by blending, the luminous efficiency of the devices sharply increases. The inset to Fig. 10.34 plots the EL intensity versus current density for all four devices. All three doped LEDs show much higher EL output at a given current density. Both of these phenomena can be attributed to better current balance. It has been proposed that trapping of holes will cause a space-charge field to develop under bias, which reduces the total electric field at the anode and increases the field at the cathode.[69] This additional field will block hole injection and facilitate electron injection. As holes are the majority carrier, the overall current density will decrease, but the carrier balance is much improved. The device efficiency (Cd/A) consequently increases from 0.04 for the PF2/6 LED to 0.08 for ST 755, 0.15 for ST 16/7, and 0.87 for TPTE. Thus, a 22-fold improvement of device efficiency was obtained. The color purity of the blend LEDs was also observed to improve with a reduction of the polyfluorene excimer band at 560 nm.

10.3.3.2 Electrophosphorescence

Reports of phosphorescence from doped molecular LEDs[70,71] have spurred much interest owing to the potential for improved efficiency by obtaining emission from otherwise nonemissive triplet excitons. Radiative recombination of both singlet and triplet states substantially increases the theoretical electroluminescence efficiency of organic LEDs. Spin-orbit coupling induced by the heavy atom in such molecules mixes singlet and triplet states, and phosphorescence, the radiative recombination of triplet states, becomes allowed. Dexter transfer of triplet excitons requires quantum mechanical tunneling of electrons between the donor and acceptor. It is therefore a short-range process requiring a separation of less than 1 nm. This can occur when there is spectral overlap between the phosphorescence emission spectrum of the host and the singlet ground state to first triplet excited state absorption spectrum of the guest. This ensures an energetic overlap of the states between which tunneling occurs.

Platinum–porphyrin complexes such as 2,3,7,8,12,13,17,18-octaethyl-21H,23-H-porphine platinum(II) (PtOEP) have been used in such LEDs. The absorption and phosphorescence spectra of PtOEP are shown in Fig. 10.35. The chemical structure of PtOEP is inset. The phosphorescence peak of PtOEP is at 646 nm, requiring a polymer with a triplet-state energy greater than 2 eV. Because the singlet-triplet splitting in conjugated polymers is quite large (> 0.5 eV),[72] a polymer with a fluorescence peak below 480 nm (2.6 eV) is needed. Polyfluorene is an energetically suitable material for such transfer and has been used by several groups to fabricate electrophosphorescent polymer LEDs.[72–75]

Figures 10.36 and 10.37 show the dependence of the current density and luminance, respectively, on the applied bias for an undoped PFO LED[5] and for doped

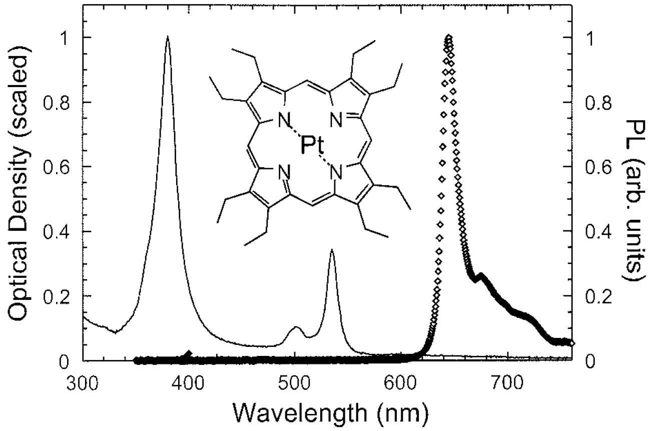

FIGURE 10.35. The absorption (line) and phosphorescence spectra (symbols) of PtOEP. Inset: The chemical structure of PtOEP. (From Ref. 72.)

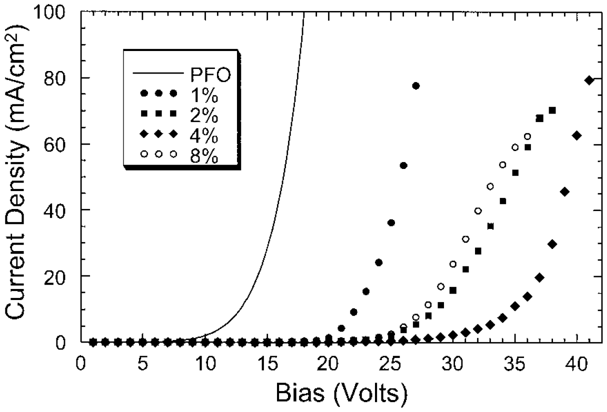

FIGURE 10.36. The current density as a function of applied bias of a PFO LED and PtOEP/PFO LEDs with PtOEP concentrations of 1%, 2%, 4%, and 8% by weight. (From Ref. 72.)

LEDs with PtOEP concentrations of up to 8% by weight. The operating voltage required for charge injection and the onset of electroluminescence increases with doping up to 4 wt% and then decreases for the 8-wt% sample. Tessler et al. have noted that the difference in the ionization potential of PFO and PtOEP is greater than 0.5 V, making PtOEP a recombination center at concentrations as low as 0.01%.[76] The increase of the operating voltage of doped LEDs with PtOEP concentration is clear evidence for charge trapping in the doped system.

It is possible to reduce the operating voltage of the doped LEDs with PtOEP concentrations of 2 wt% and 4 wt% below 8 V by optimizing the thickness of individual layers and incorporating a hole injection layer

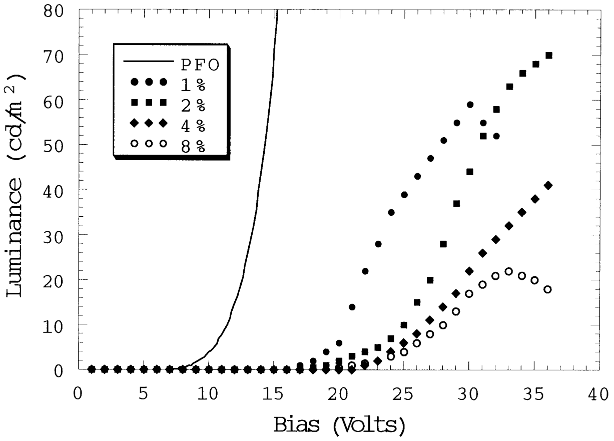

FIGURE 10.37. The luminance as a function of applied bias of a PFO LED and PtOEP/PFO LEDs with PtOEP concentrations of 1%, 2%, 4%, and 8% by weight. (From Ref. 72.)

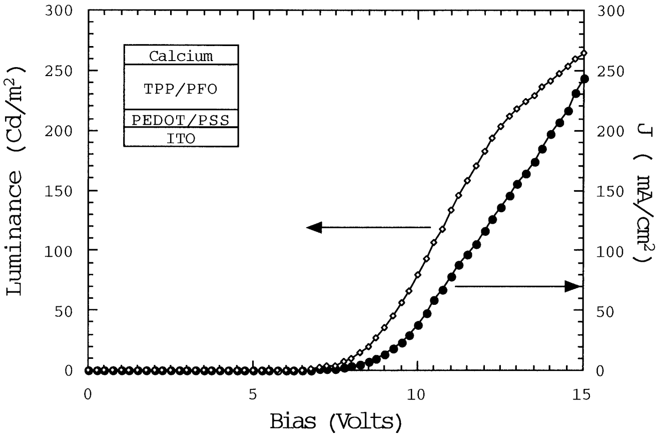

FIGURE 10.38. The current–voltage–luminance characteristics of a ITO/PEDOT:PSS/PFO: PtOEP/Ca LED. (From Ref. 78.)

of poly(3,4-ethylenedioxythiophene)–poly(styrenesulfonate).[77] Fig. 10.38 shows the current–voltage–luminance characteristics of an ITO/PEDT/PFO:PtOEP/Ca LED.[78] The device begins to emit light at 7 V applied bias and reaches a luminance of 100 Cd/m^2 at 10 V. Further improvements in device structure may permit the achievement of commercially competitive operating conditions.

Fig. 10.39 shows the EL spectra of LEDs with concentrations between 0.2% and 8% PtOEP by weight, measured at a current density $J = 22$ mA/cm^2. The spectra are normalized to the EL peak at $\lambda = 646$ nm and offset for ease of comparison. All devices have an EL spectrum characteristic of PtOEP emission, with a peak at 646 nm and vibronic side bands at 685 nm and 718 nm. The 0.2-

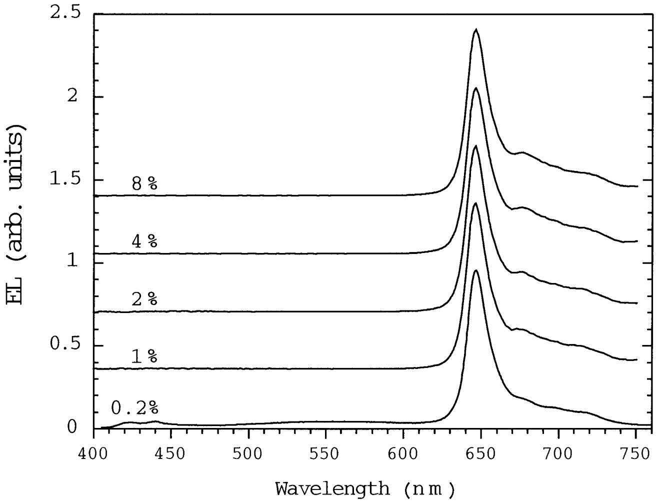

FIGURE 10.39. The electroluminescence spectra of PtOEP/PFO LEDs. The spectra are normalized to the phosphorescence peak at 646 nm and offset for comparison. (From Ref. 72.)

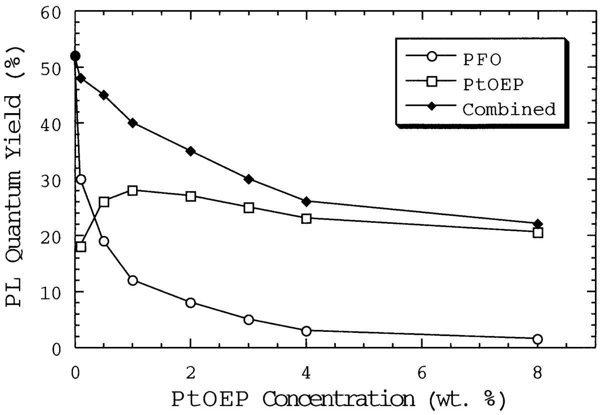

FIGURE 10.40. The PFO fluorescence, PtOEP phosphorescence, and total photoluminescence efficiencies as a function of PtOEP concentration. The excitation source was the 354-nm line of a HeCd laser. (From Ref. 72.)

wt% doped device also shows a weak peak at $\lambda = 430$ nm characteristic of PFO fluorescence and an excimer emission band peaked at 550 nm.[34]

Figure 10.40 shows the fluorescence quantum yield of PFO, the phosphorescence quantum yield of PtOEP, and the total PL yield as a function of PtOEP concentration between 0% and 8% by weight. The samples were excited by a HeCd laser at 354 nm, where PtOEP absorption is quite weak. The PL spectra of the PtOEP/PFO blends are superpositions of the individual spectra of PFO and PtOEP.

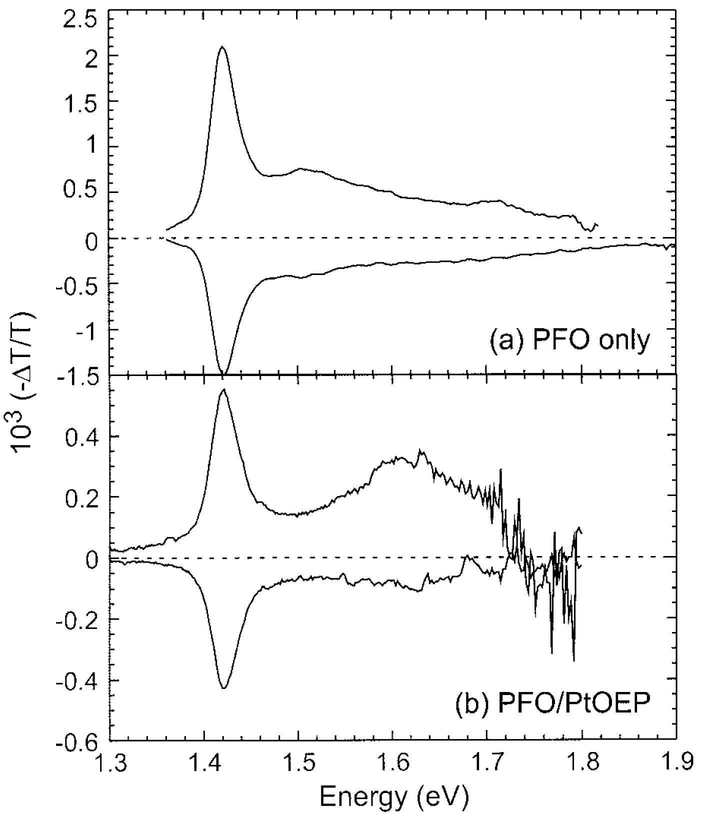

FIGURE 10.41. In-phase (top) and quadrature (bottom) PA spectra of (a) an undoped film of PFO and (b) a blend containing 8wt% PtOEP. (From Ref. 72.)

The contribution of the PFO emission to the PL spectrum decreases significantly as the PtOEP dopant concentration increases. However, even at 8 wt% PtOEP concentration, emission from PFO is not completely quenched. Dominance of the EL spectrum by PtOEP at much lower concentrations than for the PL spectrum indicates that Förster transfer is not an important excitation mechanism for PtOEP molecules in doped LEDs.

The optical properties of polyfluorene make it an ideal system in which to investigate Dexter transfer. Fig. 10.41a shows the PA spectrum of an undoped PFO film, measured at 80 K.[2] The PFO film was excited with a pump beam at

---

[2] In a PA experiment, the excited-state absorption spectrum is measured. The sample was excited by an amplitude- modulated pump beam and changes in the transmission of a probe beam are measured by lockin amplification of a photoreceiver. The 363-nm line of an argon ion laser at a power density of 30 mW/cm^2 was used as the pump beam and a monochromated tungsten white-light source was used as the probe. The pump beam was modulated at 120 Hz by an acousto-optical modulator and the spectra were measured under

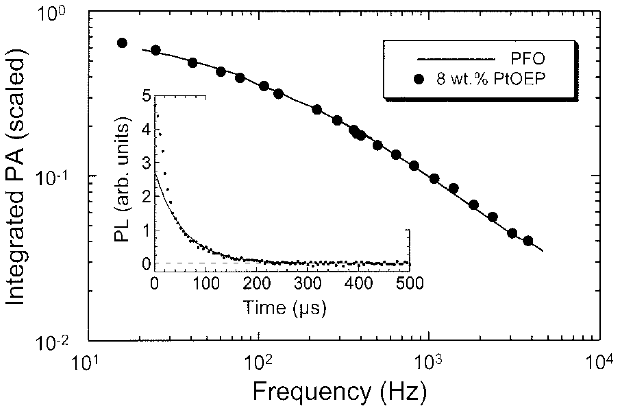

FIGURE 10.42. The dependence of the triplet PA of PFO at 1.43 eV upon the pump modulation frequency for an undoped PFO film (symbols) and one containing 8% PtOEP (solid line). The doped sample is scaled to the undoped sample for comparison. Inset: Phosphorescence decay of a PtOEP/PFO blend following excitation. The symbols show experimental results and the solid line a fit to exponential decay. (From Ref. 72.)

$\lambda = 363$ nm modulated at a frequency of 200 Hz with an optical blade chopper. The PA spectrum is dominated by a sharp transition at 1.43 eV which has been identified as excited-state absorption of triplet excitons.[10] The PA spectrum of a doped PFO film containing 8 wt% PtOEP is shown in Fig. 10.41b. The PFO triplet peak at 1.43 eV is the strongest feature in the PA spectrum of the blend, although there is an additional PA band between 1.5 and 1.7 eV. This additional PA band is correlated with PtOEP, having the same relative weight to the in-phase and quadrature components as the phosphorescence.

The spectrally narrow triplet PA band of PFO makes it possible to compare PFO triplet-state dynamics in the doped and undoped systems in order to look for evidence of Dexter transfer. The PtOEP triplet lifetime in a PFO matrix was determined by measuring the phosphorescence decay following photoexcitation. The phosphorescence decay of a blend containing 1 wt% PtOEP in PFO is inset in Fig. 10.42. The decay could be fit to a lifetime of $55 \pm 2\mu$s, in excellent agreement with pulsed EL measurements.[71]

The lifetime of the excited triplet state of PFO can be determined by measuring the dependence of the triplet PA signal upon the modulation frequency For monomolecular recombination, the excited-state lifetime, τ, can be calculated from the modulation frequency, ω, variation of the PA signal. The ω dependence of the PA amplitude is given by

$$\Delta T \propto \frac{1}{\sqrt{1 + (\omega\tau)^2}} \tag{2}$$

---

vacuum at 80 K. The PA spectrum, defined as the normalized change, ΔT, in transmission of the probe beam, T, is proportional to the photoexcitation density, n.

where τ is the excitation lifetime and ω is the modulation frequency (in rad/s).[79] A series of PA spectra of a PFO film and an 8 wt% PtOEP/PFO blend were measured as a function of the laser modulation frequency between 10 Hz and 4 kHz. The in-phase and quadature PA spectra were integrated over the PFO triplet PA peak between 1.39 and 1.48 eV and the integrated root mean square PA signal was calculated. Figure 10.42 shows the frequency dependence of PFO triplet PA in a neat film of PFO as symbols. The resulting data for PFO could not be fit to a single excitation lifetime, but could be simulated by a bimodal lifetime distribution with lifetimes of 3.2 and 0.3 ms.

The lifetime of PFO triplet excitons is much longer than the phosphorescence lifetime of PtOEP in PFO. Dexter transfer from PFO to PtOEP should reduce the PFO triplet lifetime, because PtOEP molecules decay at a much more rapid rate (56 μs) than PFO triplets (0.3 – 3.2 ms). The solid line in Fig. 10.42 shows the frequency dependence of the PFO triplet PA signal in an 8 wt% doped PFO film, measured under identical conditions as for the undoped film. There is no difference in the frequency dependence of the PA of the two different samples. Thus, if there is any Dexter transfer from PFO to PtOEP, it must be exceedingly weak. This conclusion is supported by the fact that there was no evidence for phosphorescence originating from Dexter transfer of relatively long-lived PFO triplets.

Studies of doped polyfluorene LEDs show that charge trapping is an important, if not dominant, mechanism in doped LEDs. The nondispersive nature of hole-transport in undoped polyfluorene films makes it an ideal system for studying charge trapping in doped LEDs. The sharp triplet PA spectrum of PFO is such that it is an ideal system for studying energy-transfer mechanisms of singlet and triplet excitons.

10.4 Concluding Remarks

Polyfluorene and its copolymers are clearly among the most promising conjugated polymers for device applications. These have a unique combination of high fluorescence efficiency, excellent photostability, and high charge carrier mobility along with attractive physical properties. Given these properties, it is not surprising that such rapid progress has been made with polyfluorene-based LEDs.

Acknowledgments

The author would like to thank Donal Bradley, Mark Bernius, and David Lidzey for many valuable discussions. The author apologizes in advance to any authors whose work has been inadvertently omitted.

References

[1] http://www.dow.com/dow_news/prodbus/200010]2a_pb.html

[2] M Fukuda, K. Sawada, and K. Yoshino, Jpn. J. Appl. Phys. 28, L1433–L1435 (1989).

[3] J. H. Burroughes, D. D. C. Bradley, A. R. Brown, R. N. Marks, K. Mackay, R. H. Friend, P. L. Burns, and A. B. Holmes, Nature 347, 539 (1990).

[4] M. Grell, W. Knoll, D. Lupo, A. Meisel, T. Miteva, D. Neher, H.-G. Nothofer, U. Scherf, and A. Yasuda, Adv. Mater. 11, 671–675 (1999).

[5] A. W. Grice, D. D. C. Bradley, M. Bernius, M. Inbasekaran, W. Wu, and E. P. Woo, Appl. Phys. Lett. 73, 629–631 (1998).

[6] M. T. Bernius, M. Inbasekaran, J. O'Brien, and W. Wu, Adv. Mater. 12, 1737–1750 (2000).

[7] M. Redecker, D. D. C. Bradley, M. Inbasekaran, and E. P. Woo, Appl. Phys. Lett. 74, 1400–1402 (1999).

[8] M. Grell, D. D. C. Bradley, X. Long, T. Chamberlain, M. Inbasekaran, E. P. Woo, and M. Soliman, Acta Polym. 49, 439–444 (1998).

[9] M. Grell, D. D. C. Bradley, G. Ungar, J. Hill, and K. S. Whitehead, Macromolecules 32, 5810–5817 (1999).

[10] A. J. Cadby, P. A. Lane, H. Mellor, S. J. Martin, M. Grell, C. Giebeler, D. D. C. Bradley, M. Wohlgenannt, C. An, and Z. V. Vardeny, Phys. Rev. B 62, 15,604–15,609 (2000).

[11] M Fukuda, K. Sawada, and K. Yoshino, J. Polym. Sci 31, 2465–2471 (1993).

[12] M. Grell, D. D. C. Bradley, M. Inbasekaran, and E. P. Woo, Adv. Mater. 9,798 (1997).

[13] M. Bernius, M. Inbasekaran, E. Woo, W. Wu, and L. Wujkowski, J. Mater. Sci. Mater. Electron. 11, 111 (2000).

[14] M. T. Bernius, M. Inbasekaran, J. O'Brien, and W. Wu, Adv. Mater. 12, 1737 (2000).

[15] N. Miyaura, T. Yanagi, and A. Suzuki, Synth. Commun. 11, 513 (1981).

[16] W. Graupner, M. Mauri, J. Stampfl, O. Unterweger, and G. Leising, Mol. Cryst. Liq. Cryst. Sci. Technol., Sect. A 256, 431 (1994).

[17] T. Virgili, D. G. Lidzey, and D. D. C. Bradley, Adv. Mater. 12, 58 (2000).

[18] X. Long, A. Malinowski, D. D. C. Bradley, M. Inbasekaran, and E. P. Woo, Chem. Phys. Lett. 272, 6 (1997).26

[19] M. N. Shkunov, R. Österbacka, A. Fujii, K. Yoshino, and Z. V. Vardeny, Appl. Phys. Lett. 74, 1648 (1999).

[20] M. Theander, T. Granland, D. M. Johanson, A. Ruseckas, V. Sundsträm, M. R. Anderson, and O. Inganäs, Adv. Mater. 13, 323 (2001).

[21] M. Kreyenschmidt, G. Klaerner, T. Fuhrer, J. Ashenhurst, S. Karg, W. D. Chen, V. Y. Lee, J. C. Scott, and R. D. Miller, Macromolecules 31, 1099–1103 (1998).

[22] V. N. Bliznyuk, S. A. Carter, J. C. Scott, G. Klärner, R. D. Miller, and D. C. Miller, Macromolecules 32, 361–369 (1999).

[23] S. Janietz, D. D. C. Bradley, M. Grell, C. Giebeler, M. Inbasekaran, and E. P. Woo, Appl. Phys. Lett. 73, 2453 (1998).

[24] G. Greczynski, M. Fahlman, and W. R. Salaneck, J. Chem. Phys. 113, 2407 (2000).

[25] M. Redecker, D. D. C. Bradley, M. Inbasekaran, and E. P. Woo, Appl. Phys. Lett. 73, 1565 (1998).

[26] H. Sirringhaus, R. J. Wilson, R. H. Friend, M. Inbasekaran, W. Wu, E. P. Woo, M. Grell, and D. D. C. Bradley, Appl. Phys. Lett. 77, 406 (2000).

[27] P. M. Borsenberger and D. S. Weiss, *Organic Photoreceptors for Imaging Systems*, Marcel Dekker, NY, 1993.

[28] R. J. O. M. Hoofman, M. P. deHaas, L. D. A. Siebbeles, and J. M. Warman, Nature 392, 54 (1998).

[29] D. Braun and A. J. Heeger, Appl. Phys. Lett. 58, 1982 (1991).

[30] Y. Ohmori, M. Uchida, K. Muro, and K. Yoshino, Jpn. J. Appl. Phys. 30, L1941 (1991).

[31] Y. Ohmori, M. Uchida, C. Morishima, A. Fujii, and K. Yoshino, Jpn. J. Appl. Phys. 32, L1663 (1993).

[32] Q. Pei and Y. Yang, J. Am. Chem. Soc. 118, 7416 (1996).

[33] Yang and Q. Pei, J. Appl. Phys. 81, 3294 (1997).

[34] J. Teetsov and M. A. Fox, J. Mater. Chem. 9, 2117 (1999).

[35] K. S. Whitehead, M. Grell, D. D. C. Bradley, M. Jandke, and P. Strohriegl, Appl. Phys. Lett. 76, 2946 (2000).

[36] H. Lim, H. Park, J. G. Lee, Y. Kim, W. J. Cho, and C. S. Ha, Proc. SPIE 345, 3281 (1998).

[37] H. Jandke, P. Strohriegl, J. Gmeiner, W. Brütting, and M. Schwoerer, Adv. Mater. 11, 1518 (1999).

[38] H. N. Cho, D. Y. Kim, Y. C. Kim, J. Y. Lee, and C. Y. Kim, Adv. Mater. 9, 326 (1997).

[39] G. Klaerner, M. H. Davey, W. D. Chen, J. C. Scott, and R. D. Miller, Adv. Mater. 10, 993 (1998).

[40] M. Ranger, D. Rondeau, and M. Leclerc, Macromolecules 30, 7686 (1997).

[41] H. N. Cho, J. K. Kim, D. Y. Kim, C. Y. Kim, N. W. Song, and D. Kim, Macromolecules 32, 1476 (1999).

[42] M. Ranger and M. Leclerc, Macromolecules 32, 3306 (1999).

[43] J. K. Kim, J. W. Yu, J. M. Hong, H. N. Cho, D. Y. Kim, and C. Y. Kim, J. Mater. Chem. 9, 2171 (1999).

[44] A. Donat-Bouillud, I. Lévesque, Y. Tao, M. D'Iorio, S. Beaupré, P. Blondin, M. Ranger, J. Bouchard, and M. Leclere, Chem. Mater. 12, 1931 (2000).

[45] X. Jiang, S. Liu, H. Ma, and A. K.-Y. Jen, Appl. Phys. Lett. 76, 1813 (2000).

[46] G. Klaerner, M. Trollsas, A. Heise, M. Husemann, B. Atthoff, C. J. Hawker, J. Hedrick, and R. D. Miller, Macromolecules 32, 8227 (1999).

[47] N. G. Pschirer and U. H. F. Bunz, Macromolecules 33, 3961 (2000).

[48] P. Blondin, J. Bouchard, S. Beaupré, M. Belletête, G. Durocher, and M. Leclerc, Macromolecules 33, 5874 (2000).

[49] B. Liu, W.-L. Yu, Y.-H. Lai, and W. Huang, Macromolecules 33, 8945 (2000).

[50] R. B. Fletcher, D. G. Lidzey, D. D. C. Bradley, M. Bernius, and S. Walker, Appl. Phys. Lett. 77, 1262 (2000).

[51] J. Birnstock, J. Blässing, A. Hunze, M. Scheffel, M. Stößel, K. Heuser, G. Wittmann, J. Wörle, and A. Winnacker, Appl. Phys. Lett. 78, 3905 (2001).

[52] J. P. Chen, G. Klaerner, J.-I. Lee, D. Markiewicz, V. Y. Lee, R. D. Miller, and J. C. Scott, Synth. Met. 107, 129 (1999).

[53] J. S. Kim, R. H. Friend, and F. Cacialli, Appl. Phys. Lett. 74, 3084 (1999).

[54] M. Redecker, D. D. C. Bradley, M. Inbasekaran, W. Wu, and E. P. Woo, Adv. Mater. 11, 241 (1999).

[55] M. Redecker, D. D. C. Bradley, K. Baldwin, D. Smith, M. Inbasekaran, W. Wu, and E. P. Woo, J. Mater. Chem. 9, 2151 (1999).

[56] A. J. Campbell, D. D. C. Bradley, H. Antoniadis, M. Inbasekaran, W. W. Wu, and E. P. Woo, J. Mater. Chem. 9, 2151 (1999).

[57] A. J. Campbell, D. D. C. Bradley, and H. Antoniadis, J. Appl. Phys. 89, 3343 (2001).

[58] J. J. M. Halls, A. C. Arias, J. D. MacKenzie, W. Wu, M. Inbasekaran, E. P. Woo, and R. H. Friend, Adv. Mater. 12, 498 (2000).

[59] R. B. Fletcher, S. J. Martin, D. G. Lidzey, D. D. C. Bradley, and P. A. Lane, Appl. Phys. Lett. (in press).

[60] Y. He, S. Gong, R. Hattori, and J. Kanicki, Appl. Phys. Lett. 74, 2265 (1999).

[61] Y. He and J. Kanicki, Appl. Phys. Lett. 76, 661 (2000).

[62] A. Berntsen, Y. Croonen, C. Liedenbaum, H. Schoo, R. J. Visser, J. Vleggaar, and P. vandeWeijer, Opt. Mater. 9, 125 (1998).

[63] C. Giebeler, S. A. Whitelegg, D. G. Lidzey, P. A. Lane, and D. D. C. Bradley, Appl. Phys. Lett. 75, 2144 (1999).

[64] D. L. Dexter, J. Chem. Phys. 21, 836 (1953).

[65] A. Shoustikov, Y. You, P. Burrows, M. E. Thompson, and S. R. Forrest, Synth. Met. 217, 1 (1997).

[66] T. L. C. Figueiredo, R. A. W. Johnstone, A. M. P. S. Sorensen, D. Burget, and P. Jacques, Photochem. Photobiol. 69, 517–528 (1999).

[67] A. J. Campbell and D. D. C. Bradley, unpublished results.

[68] D. Sainova, T. Miteva, H. G. Nothofer, U. Scherf, I. Glowacki, J. Ulanski, H. Fujikawa, and D. Neher, Appl. Phys. Lett. 76, 1810 (2000).

[69] S. Berleb, W. Brütting, M. Schwoerer, R. Wehrmann, and A. Elschner, J. Appl. Phys. 83, 4403 (1998).

[70] M. A. Baldo, D. F. O'Brien, Y. You, A. Shoustikov, S. Sibley, M. E. Thompson, and S. R. Forrest, Nature 395, 151 (1998).

[71] D. F. O'Brien, M. A. Baldo, M. E. Thompson, and S. R. Forrest, Appl. Phys. Lett. 74, 442 (1999).

[72] P. A. Lane, L. C. Palilis, D. F. O'Brien, C. Giebeler, A. J. Cadby, D. G. Lidzey, A. J. Campbell, W. Blau, and D. D. C. Bradley, Phys. Rev. B 63, 235206:1–8 (2001).

[73] V. Cleave, G. Yahioglu, P. LeBarny, R. H. Friend, and N. Tessler, Adv. Mater. 11, 285 (1999).

[74] D. F. O'Brien, C. Giebeler, R. B. Fletcher, A. J. Cadby, L. C. Palilis, D. G. Lidzey, P. A. Lane, D. D. C. Bradley, and W. Blau, Proc. 4th Intl. Conf. on Optical Probes of Conjugated Polymers and Photonic Crystals, Synth. Met. 116, 379 (2001).

[75] T.-F. Guo, S.-C. Chang, Y. Yang, R. C. Kwong, and M. E. Thompson, Org; Electron. 1 (2001).

[76] N. Tessler, P. K. H. Ho, V. Cleave, D. J. Pinner, R. H. Friend, G. Yahioglu, P. Le Barny, J. Gray, M. de Souza, and G. Rumbles, Thin Solid Films 363, 64 (2000).

[77] L. Palilis, Ph. D. thesis, University of Sheffield, 2001.

[78] L. C. Palilis, P. A. Lane, D. G. Lidzey, and D. D. C. Bradley, unpublished work.

[79] C. Botta, S. Luzzati, R. Tubino, D. D. C. Bradley, and R. H. Friend, Phys. Rev. B 48, 14,809 (1993).

Index

ACTFEL (ac thin-film EL) device, 195
ac thin-film EL (ACTFEL) device, 195
Aging processes on OLED, effect of, on performance, 95–98
AlMq$_3$, *see* Aluminum (III) 4-methyl hydroxyquinoline
Alternating current light-emitting devices based on pyridine-containing conjugated polymers, 245–262
Aluminum (III) 8-hydroxyquinoline (Alq$_3$), 17, 107
  chemical degradation and physical aging of, 71–98
  crystallization of, 86–89
  crystallization of films of, 88
  electrochemical degradation of, 78–85
  hydrolytic decomposition of, 73
  molecular structure of, 2
  thermal hydrolysis of, 72–78
Aluminum (III) 4-methyl hydroxyquinoline (AlMq$_3$), 91
  crystallization and aging of, 92–95
Amorphous materials selection, guidelines for, 89–92
Amplified spontaneous emission (ASE), 212
Anode, ITO-PEDOT, 171, 172
Aromatic solvents, MEH-PVV processed using, 176–178
ASE (amplified spontaneous emission), 212

Binding energy, exciton, 129–130

Carrier densities, 46
Carrier hopping, polaron versus disorder models for, 24–25
Carrier injection, 26–28
Carrier mobilities, 141
Carrier recombinaiton and emission process, 50
Carrier transport in OLEDs, 23–29
Cathode, 168
Cathode buffer materials, 21–22
Charge-balance factor, 51
Charge carrier injection and transport, 46–49
Charge-injection energy barriers, 167–172
Chemical defects on polymer chain, 219

Chemical stability of materials for OLEDs, 72–85
CN-PPV
  chemical structure of, 131
  synthesis of, 133
Color conversion technique
  external, 227
  internal, 229
Concentration regions, 157–158
Conductivity of polymer film, 166–167
Conjugated polymers, pyridine-containing, *see* Pyridine-containing conjugated polymers
Conjugation lengths, 130
  effective, 211
Copolymers
  fluorene-based, 282–288
  main-chain, 208
  side-chain, 208
Copper phthalocyanine (CuPc), 14
  molecular structure of, 2
Crystallization
  and aging of $AlMq_3$, 92–95
  of Alq_3, 86–89
  of Alq_3 films, 88
CuPc, *see* Copper phthalocyanine
Current-injection voltage, 172–174

Dark spot formation, 31
Decay channels, nonradiative, 144
Degradation mechanisms, 31–33
Degradation processes, molecule-specific, 33
Dexter transfer, 297
DH OLED structure, 53
DHQQ (dihydroquinolinequinone), 84–85
Dihydroquinolinequinone (DHQQ), 84–85
Direct current light-emitting devices based on pyridine-containing conjugated polymers, 245–262
Disorder, 6
Disorder models versus polaron models for carrier hopping, 24–25
Distyrylarylenes, 17
DMs (dopant materials), 60–62
Doctor blade technique, 11
Dopant materials (DMs), 60–62
Dopants, fluorescent, 288–292
Doped polyfluorene light-emitting diodes, 288–298
Double layer, organic, 45
Double light spikes from polymer OLEDS, 187–203
DPVBi, molecular structure of, 2

EB (emeraldine base), 246
  molecular structure of, 3
Effective conjugation length, 211
Effective mobilities, 141
Efficiency
  of OLEDs, 29–31
  quantum, *see* Quantum efficiency
  of singlet-exciton formation, 231
EL, See Electroluminescence
Electrical breakdown, 33
Electrochemical degradation of Alq_3 and Hq, 78–85
Electrodes, transparent, 147
Electroluminescence (EL), v, 1, 220–238
  polarized, 279–282
  polyfluorene, 275–282
  spectra, 4
Electron, 187
  term, 129
Electron mobilities, 15
Electron-transporting and emitting small molecules, 17
Electron transport layer, *see* ETL *entries*
Electron-transport materials (ETMs), 58–60
Electron-withdrawing -CN groups, 139
Electrophosphorescence, 292–298
Electrophosphorescent organic light-emitting devices, 19
Emeraldine base, *see* EB
Emission color, quantum efficiency and, 182
Emission spectrum, 176–180
Emitter materials (EMs), 60
Emitting dipoles, location of, 112
EMs (emitter materials), 60
ETL (electron transport layer), 9, 138–139

ETL-C, molecular structures adequate for, 59
ETL-E, molecular structures adequate for, 59
ETMs (electron-transport materials), 58–60
Evaporation of molecules, 206
Excimers, 223
Exciplex formation, 50
Exciton binding energy, 129–130
Exciton lifetimes, 117–118
Excitons, 128, 187
Ex-I species, 180
External color conversion technique, 227
External quantum efficiency, estimation of, 50–53

Fabry-Perot microcavity, planar, 104–105
Failure modes for OLEDs, 71–72
F8BT, 283
  absorption and fluorescence spectra of, 284
Fermi-Dirac function, 195
Field-effect mobilities, 273
Film thickness, 189
Fluorene-based copolymers, 282–288
Fluorene-based polymers, *see* Polyfluorenes
Fluorescent dopants, 288–292
Fluorescent polymers, 19–21
Förster radius, 288
Förster transfer, 130–131, 288
Fowler-Nordheim theory, 136
Fowler-Nordheim tunneling injection, 47–48
"Frozen junction" LECs, 236–237
F8T2, 273–274
  chemical structure of, 274
Full width at half-maximum (FWHM), 109
FWHM (full width at half-maximum), 109

Gibbs energy, 90
Glass transition temperature, 15

High-brightness LEDs, 276–277
High-performance OLEDs, molecular materials for, 43–65
Hole, 187
  term, 129
Hole mobilities, 15
Hole transport layer, *see* HTL *entries*
Hole-transport materials (HTMs), 55–58
HOMO, 22, 46, 128
HOMO levels, 15
HOMO-LUMO distances, 214
HTL (hole transport layer), 9
HTL/ETL interface, 54
HTM-A, molecular structures adequate for, 57
HTM-E, molecular structures adequate for, 57
HTMs (hole-transport materials), 55–58
Huang Rhys factors, 213
Hydrolytic decomposition of Alq_3, 73
Hydroxyquinoline (Hq)
  aluminum (III), *see* Aluminum (III) 8- hydroxyquinoline (Alq_3)
  electrochemical degradation of, 78–85

‘‘Image force” potential, 26
Indium-tin-oxide (ITO), 12–13
Injection-limited current mechanisms, 28–29
Inkjet printing, 12
Interdiffusion range, 225
Internal color conversion technique, 229
Internal quantum efficiency, estimation of, 50–53
Intrinsic semiconductor, 218
ITO (indium-tin-oxide), 12–13
ITO-PEDOT anode, 171, 172

LC (liquid-crystalline) phases, 269
LEB, molecular structure of, 3
LECs, *see* Polymer light-emitting electrochemical cells
LEDs, *see* Light-emitting diodes
Lifetimes
  exciton, 117–118
  operating, 149
Light-emitting diodes (LEDs)
  doped polyfluorene, 288–298

Light-emitting (*continued*)
  high-brightness, 276–277
  microcavity, *see* Organic microcavity light-emitting diodes
  organic, *see* Organic light-emitting devices
  planar microcavity, *see* Planar microcavity LEDs
  polyfluorene, 275
  polymer organic, *see* Polymer OLEDS
Light-emitting voltage, 174–175
"Line-narrowing," 146
Liquid-crystal displays, v
Liquid-crystalline (LC) phases, 269
Long-range correlations, 25–26
LPPP, 217
LUMO, 22, 46, 128
LUMO levels, 15

Main-chain copolymers, 208
MEH-PPV, 133
  chemical structure of, 159–160
  contact angles and surface tension of films of, 165
  molecular structure of, 3
  processed using aromatic solvents, 176–178
  processed using nonaromatic solvents, 178–180
Metal atom migration, 33
Metal-on-polymer (MOP)-type contact, 168
Metal-polymer interface, 168–170
Microcavities, 103
Microdisk, 105
m-LPPP, 223
  molecular structure of, 3
Mobilities
  carrier, 141
  field-effect, 273
Molecular materials
  for high-performance OLEDs, 43–65
  for OLEDs, 55–64
Molecular tuning
  for high EL durable OLED, 63–64
  for high EL efficiency, 62–63
Molecules, evaporation of, 206
Molecule-specific degradation processes, 33
Monodomain alignment, 279
MOP (metal-on-polymer)-type contact, 168
Multilayer OLEDs, 138–140, 225–229
Multilayer structures, design of, 53–55

NAPOXA, 121–122
Nonaromatic solvents, MEH-PVV processed using, 178–180
Nonradiative decay channels, 144
NPB, molecular structure of, 2
NPD, molecular structure of, 2

OAM (oligoazomethine), 226
ODMR (optically detected magnetic resonance) studies, 8
Ohmic contact, 167
OLEDs, *see* Organic light-emitting devices
Oligoazomethine (OAM), 226
Oligophenylenes, 205
Oligophenyls, physical properties of, 206
Operating lifetimes, 149
Optically detected magnetic resonance (ODMR) studies, 8
Organic double layer, 45
Organic light-emitting devices (OLEDs), v-vi, 1
  basic operation of, 22–23
  basic structure of, 9–10
  carrier transport in, 23–29
  chemical stability of materials for, 72–85
  development from 1960s to 1980s, 43–45
  effect of aging processes on performance of, 95–98
  efficiency of, 29–31
  electrophosphorescent, 19
  fabrication procedures, 10–12
  failure modes for, 71–72
  future possibilities of, 64–65
  high-performance, molecular materials for, 43–65
  introduction to, 1–34
  materials for, 12–22

  microcavity, *see* Organic microcavity light-emitting diodes
  molecular materials for, 55–64
  multilayer, 138–140, 225–229
  novel structures for, 146–148
  optical properties of, 143–146
  outlook for, 33–34
  single-layer, *see* Single-layer OLEDs
  thermal stability of, 85–95
  transport and recombination in, 140–143
  white, 18–19
  working mechanisms of, 45–53
Organic microcavity light-emitting diodes, 103–124
  materials for displays, 121–123
  planar, *see* Planar microcavity LEDs
  types of, 104–106
Oxadiazoles, 17

PANI, *see* Polyaniline
P3AT, 20
  molecular structure of, 3
PBG (photonic bandgap) structures, 105
PDPA, 20–21
  molecular structure of, 3
PEDOT, chemical structure of undoped form of, 137
PEDOT-PSS, 14
  molecular structure of, 3
PEO (poly(ethylene oxide)), 234, 277
PFO, molecular structure of, 3
PFO films, 290
Phosphorescent small molecules, 19
Photoexcitation, processes following, 7
Photoluminescence (PL), spectra, 4
Photoluminescence efficiencies, 134
Photonic bandgap (PBG) structures, 105
Photooxidation, 32
PHP, 225
π-conjugated materials, basic electronic structure and dynamics of, 5–8
Planar Fabry-Perot microcavity, 104–105
Planar microcavity LEDs, 106–110
  intensity and angular dependence in, 114–121
  single mode and multimode, 110–114
Platinum, 13
Platinum-porphyrin complexes, 292–297
PLEDs, *see* Polymer OLEDS
PM (pyrromethene) 580, 107
PMMA, 227–228
  molecular structure of, 3
PNB, molecular structure of, 3
Polarization, 199–200
Polarized electroluminescence, 279–282
Polaronic relaxation, 24
Polarons, 7, 129, 187, 215
Polaron versus disorder models for carrier hopping, 24–25
Polyaniline (PANI), 3, 13
  chemical structure of undoped form of, 137
Poly(ethylene oxide) (PEO), 234, 277
Polyfluorene, 224, 265–298
  electroluminescence, 275–282
  electronic characterization, 270–274
  LEDs, 275 doped, 288–298
  optical and physical characterization, 268–270
  polymer light-emitting electrochemical cells (LECs), 277–279
  synthesis of, 266–268
Polymer aggregation, solvation effect and, 182
Polymer blends, polymer OLEDS based on, 229–233
Polymer chain, chemical defects on, 219
Polymer electronics, polymer morphology in, 155–183
Polymer film, conductivity of, 166–167
Polymer light-emitting electrochemical cells (LECs)
  based on PPP, 233–238
  "frozen junction," 236–237
  polyfluorene, 277–279
Polymer morphology
  control of, 157–167
  control of device performance via, 166–181
  control of thin films via spin-coating process, 161–166
  in polymer electronics, 155–183
Polymer OLEDS (PLEDs), vi, 155

Polymer (*continued*)
  based on polymer blends, 229–233
  double light spikes from, 187–203
  materials for, 12–22
  turn-on voltage of, 183
Polymer-on-metal (POM) contact, 168–169
Polymer-polymer interactions in solutions, 157–161
Polymers
  conjugated, pyridine-containing, *see* Pyridine-containing conjugated polymers
  fluorene-based, *see* Polyfluorenes
  precursor, 207
Poly(*para*-phenylenes) (PPP), 20, 205–238, *see also* PPP *entries*
  absorption properties, 209–214
  charge transport, 217–220
  dielectric function, 209
  emission colors, 224–225
  emission properties, 214
  excited states, 214–217
  geometric arrangement of, 208–209
  ladder, EL devices based on, 222–223
  physical properties of, 206–220
  polymer light-emitting electrochemical cells based on, 233–238
  processing and stability, 206–208
  soluble, EL devices based on, 222
Poly(*p*-phenylenevinylene) (PPW), 127–150
  applications with, 148–149
  electronic structure of, 128–132
  synthesis of, 132–133
Polythiophenes (PTs), 20
POM (polymer-on-metal) contact, 168–169
PPDB films, 229–232
PPP, See Poly(*para*-phenylenes)
PPP-type oligomers, EL devices based on, 223–224
PPP-type polymers, single-layer OLEDS based on, 220–224
PPV, 19
  molecular structure of, 3
PPV-based block copolymers, 19–20
PPW, *see* Poly(*p*-phenylenevinylene)
Precursor polymers, 207
Primary peak, 191
Pt, *see* Platinum *entries*
PTs (polythiophenes), 20
PVK, 250
  molecular structure of, 3
Pyridine-containing conjugated polymers, 245–262
  direct and alternating current light-emitting devices based on, 245–262
  experiments, 247–249
  results and discussion, 249–261
Pyrromethene (PM) 580, 107

QQ (quinolinequinone), 84–85
Quality factor, 104
Quantum efficiency
  device, 180–182
  emission color and, 182
  external and internal, estimation of, 50–53
Quarter-wave stack (QWS), 107
Quinolinequinone (QQ), 84–85
QWS (quarter-wave stack), 107

Radiative rate, 143
Recrystallization, 32
Red-green-blue (RGB) color dots, realization of, 225
Relaxation time, 199
Resonance wavelengths, 110
RGB (red-green-blue) color dots, realization of, 225
Rigid-band theory, 167
Rubrene, molecular structure of, 2

SCALE device configuration, 253–256
SCALE (symmetrically configured ac light- emitting) devices, 246
Schottky thermal emission, 46–47
SCLC, *see* Space-charge-limited current *entries*
Secondary peaks, 191
Semiconductor, intrinsic, 218
SEs (singlet excitons), 5, 8
SE/TE branching ratio, 7
SH-E OLED structure, 53
SH-H OLED structure, 53

Side-chain copolymers, 208
Side groups, solubilizing, 207–208
Single-layer OLEDs, 134–138
  based on PPP-type polymers, 220–224
Singlet-exciton formation, efficiency of, 231
Singlet excitons (SEs), 5, 8
Small molecular guest dye emitters, 18
Solubilizing side groups, 207–208
Solution concentration, effect of, 162
Solvation effect, polymer aggregation and, 182
Solvents
  aromatic, MEH-PVV processed using, 176–178
  effect of, 159–161, 164–166, 170
  nonaromatic, MEH-PVV processed using, 178–180
Space-charge-limited current (SCLC), 44, 136–137
Space-charge-limited current mechanisms, 28–29
SPAN (sulfonated polyaniline), 247
Spike intensity, 192
  turn-off, 197
Spin-coating, 11
Spin-coating process, polymer morphology control of thin films via, 161–166
Spin speed, effect of, 163–164
Spintronic devices, v
“Starburst molecules,” 14
Structural disorder, 6
Sulfonated polyaniline (SPAN), 247
Superoxide, 79–80
Symmetrically configured ac light-emitting (SCALE) devices, *see* SCALE *entries*

TAD (triphenyl diamine), 107
TDATA, molecular structure of, 2
TEs (triplet excitons), 5, 8
Tetrahydrofuran (THF), 160
Thermal emission, Schottky, 46–47
Thermal hydrolysis of Alq$_3$, 72–78
Thermal stability of OLEDs, 85–95
Thermal vacuum evaporation, 10
THF (tetrahydrofuran), 160
Time-of-flight experiments, 141
TPD, molecular structure of, 2
Transparent electrodes, 147
Transport mechanisms, 188
Trapping states, 6
Triphenyl diamine (TAD), 107
Triplet excitons (TEs), 5, 8
Tunneling injection, Fowler-Nordheim, 47–48
Turn-off spike, 192
Turn-off spike intensity, 197
Turn-on voltage, 172–175
  of PLED device, 183

Vacuum deposition techniques, 10

Wet-casting, 12
Wet-coating techniques, 11
“Whispering gallery modes,” 105
White organic light-emitting devices, 18–19

ZnO, 13